APPENDICE : ARTICLES

Contributions à la physique statistique des systèmes à longue portée : relaxation collisionnelle, systèmes analogues

Mémoire présenté par

Bruno Marcos

Laboratoire de Mathématiques J.A. Dieudonné

presentée en vue d'obtenir

l'Habilitation à diriger les recherches de l'Université Côte d'Azur

Discipline : Physique

Soutenue le 19 janvier 2024

devant un jury composé de :

Alberto Bramati	Professeur, Sorbonne Université	Examinateur
Francisco J. Cao-García	Professeur, Universidad Complutense	Examinateur
Didier Clamond	Professeur, Université Côte d'Azur	Examinateur
Yves Elskens	Professeur, Aix-Marseille Université	Rapporteur
Christophe Pichon	Directeur de Recherche, IAP	Rapporteur
Simona Rota Nodari	Professeur, Université Côte d'Azur	Examinatrice
Stefano Ruffo	Professeur, SISSA	Rapporteur

APPENDIX : PAPERS

Contributions to statistical physics of long-range interacting systems : collisional relaxation, analogue systems

Bruno Marcos

Laboratoire de Mathématiques J.A. Dieudonné

Habilitation Thesis

in Physics

defended on 19th January 2024

jury members :

Alberto Bramati	Professor, Sorbonne Université	Examinateur
Francisco J. Cao-García	Professor, Universidad Complutense	Examinateur
Didier Clamond	Professeur, Université Côte d'Azur	Examinateur
Yves Elskens	Professor, Aix-Marseille Université	Rapporteur
Christophe Pichon	Senior Researcher, IAP	Rapporteur
Simona Rota Nodari	Professor, Université Côte d'Azur	Examinatrice
Stefano Ruffo	Professor, SISSA	Rapporteur

Papers treated in the dissertation

Collisional relaxation

I *"Series expansions of the deflection angle in the scattering problem for power-law potentials"*, D. Chiron and B. Marcos, J. Math. Phys. **60**, 052901 (2019).

II *"Quasi-stationary states and the range of pair interactions"*, A. Gabrielli, M. Joyce, B. Marcos, Phys. Rev. Lett, 105, 210602 (2010).

III *"Formation and relaxation of quasi-stationary states in particle systems with power law interactions"*, B. Marcos, A. Gabrielli and M. Joyce, Phys. Rev. E **96**, 032102 (2017).

IV *"A dynamical classification of the range of pair interactions"*, A. Gabrielli, M. Joyce, B. Marcos, F. Sicard, J. Stat. Phys., **141**, 970 (2010).

V *"Collisional relaxation of two-dimensional self-gravitating systems"*, B. Marcos, Physical Review. E, **88**, 032112 (2013).

VI *"Collisional relaxation in the inhomogeneous Hamiltonian-Mean-Field model: diffusion coefficients"*, F. Benetti et B. Marcos, Phys. Rev. E **95**, 022111 (2017).

VII *"Classical Goldstone modes in Long-Range Interacting Systems"*, T. M. Rocha Filho and B. Marcos, Phys. Rev. E **102**, 032122 (2020).

Analogue long-range systems

VIII *"Breathing mode for systems of interacting particles"*, A. Olivetti, J. Barré, B. Marcos, F. Bouchet, R. Kaiser, Phys. Rev. Lett. 103, 224301 (2009) .

IX *"Breathing Dynamics for Systems of Interacting Particles in the Microcanonical and Canonical Descriptions"*, A. Olivetti, J. Barré, B. Marcos, F. Bouchet and R. Kaiser, Transp. Theo. and Stat. Phys. 39, 524 (2010).

X *"Symmetry Breaking in d-Dimensional Self-Gravitating Systems"*, R. Pakter, B. Marcos, Y. Levin, Physical Review Letters **111**, 230603 (2013).

XI *"Nonequilibrium Phase Transition with Gravitational-like Interaction in a Cloud of Cold Atoms"*, J. Barré, B. Marcos D. Wilkowski, Physical Review Letters, **112**, 133001 (2014).

XII *"Long-range one-dimensional gravitational-like interaction in a neutral atomic cold gas"*, M. Chalony, J. Barré, B. Marcos A. Olivetti,D. Wilkowski, **87**, 013401 (2013).

XIII *"Towards a measurement of the Debye length in very large Magneto-Optical traps"*, J. Barré, R. Kaiser, G. Labeyrie, B. Marcos and D. Metivier, Phys. Rev. A **100**, 013624 (2019).

XIV *"Experimental observation of violent relaxation and the formation of out-of-equilibrium quasi-stationary states"*, M. Lovisetto, M.C. Braidotti, R. Prizia, C. Michel, D. Clamond, M. Bellec, E.M. Wright, B. Marcos and D. Faccio, `arXiv:2205.10948`.

XV *"Integrating factor techniques applied to the Schrödinger-like quations. Comparison with Split-Step methods"*, M. Lovisetto, D. Clamond, B. Marcos, `hal-03483942`.

XVI *"Optimized integrating factor technique for Schrödinger-like equations"*, M. Lovisetto, D. Clamond, B. Marcos, Applied Numerical Mathematics, **178**, 329 (2022).

Part I

Collisional relaxation

Journal of Mathematical Physics | ARTICLE | scitation.org/journal/jmp

Series expansions of the deflection angle in the scattering problem for power-law potentials

Cite as: J. Math. Phys. **60**, 052901 (2019); doi: 10.1063/1.5055713
Submitted: 10 September 2018 • Accepted: 17 April 2019 •
Published Online: 9 May 2019

D. Chiron and B. Marcos

AFFILIATIONS

Université Côte d'Azur, CNRS, LJAD, Nice, France

ABSTRACT

We present a rigorous study of the classical scattering for any two-body interparticle potential of the form $v(r) = g/r^\gamma$, with $\gamma > 0$, for repulsive ($g > 0$) and attractive ($g < 0$) interactions. We first derive an explicit series expansion of the deflection angle in the impact factor b. Then, we study carefully the modifications of the results when a regularization (softening) is introduced in the potential at small scales. We check and illustrate all the results with the exact integration of the equations of motion.

I. INTRODUCTION

Scattering of particles is present in many physical processes in a broad area of physics, such as atomic (e.g., Ref. 1), plasma (e.g., Ref. 2), astrophysics (e.g., Ref. 3), and active matter (e.g., Ref. 4). On this subject, a seminal paper was published by Ernest Rutherford in 1911[5] in which he studied the deflection of α and β particles by an atom. He calculated analytically the angle of deflection of the incident particles with the nucleus. His calculations, compared to experimental data (see Ref. 5 for references), permitted to conclude that the atom is basically "empty" with a charge concentrated in the center, surrounded by the electron cloud, which leads to the "planetary" model of the atom.

These two-body collisions play also a central role in collisional processes in Coulomb plasmas (see, e.g., Ref. 2), in self-gravitating systems (as pointed out by Chandrasekhar in a seminal paper[6]), and, in general, in systems of particles with power law interactions.[7,8] In order to write kinetic equations which describe the evolution of such systems, it is necessary to solve the two-body problem, i.e., to compute the final velocities after a scattering event. For example, let us consider for simplicity that the Boltzmann equation which describes the evolution of the one-point distribution function $f(r, v; t)$ of a system of particles interacting with the interparticle potential

$$v(r) = \frac{g}{r^\gamma}. \tag{1}$$

For simplicity, we will write the Boltzmann equation for a spatially homogeneous and isotropic three dimensional system in which collective effects are neglected. In this case, it has the simple form

$$\frac{\partial \varphi}{\partial t}(\mathbf{v}_1; t) = 2\pi \int d\mathbf{v}_2 \int_0^\infty db\, b\, u\, G(\mathbf{v}_2', \mathbf{v}_1', \mathbf{v}_2, \mathbf{v}_1; t), \tag{2}$$

where $\varphi(\mathbf{v}; t)$ is the velocity probability function and

$$G(\mathbf{v}_2', \mathbf{v}_1', \mathbf{v}_2, \mathbf{v}_1; t) = \varphi(\mathbf{v}_2'; t)\varphi(\mathbf{v}_1'; t) - \varphi(\mathbf{v}_2; t)\varphi(\mathbf{v}_1; t), \tag{3}$$

$\mathbf{v}_1$ and $\mathbf{v}_2$ are the velocities of the particles before the collision, $\mathbf{v}_1'$ and $\mathbf{v}_2'$ are the velocities of the particles after the collision, b is the impact factor, and u is the modulus of the relative velocity, i.e.,

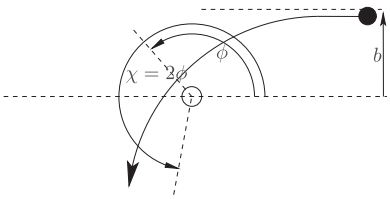

FIG. 1. Collision in the center of mass frame. The black dot represents the fictitious (reduced) particle, and the white dot represents the center of mass of the particles at rest.

$$u = \|\mathbf{v}_2 - \mathbf{v}_1\|. \tag{4}$$

Despite the apparent simplicity of Eq. (2), the main difficulty consists in computing the final velocities $\mathbf{v}_i'$ as a function of the initial ones $\mathbf{v}_i$ ($i = 1, 2$). In the center of mass frame (see Appendix A for details), the angle ϕ (see Fig. 1) can be calculated as a function of the impact factor b using the formula

$$\phi(b) = \int_{r_{min}}^{\infty} \frac{(b/r^2)dr}{\sqrt{1 - (b/r)^2 \mp (b_0/r)^\gamma}}, \tag{5}$$

where r_{min} is the largest root of the denominator. The "minus" sign in the denominator corresponds to a repulsive interaction while the "plus" sign to an attractive one, and b_0 is the characteristic scale

$$b_0 = \left(\frac{2|g|}{mu^2}\right)^{1/\gamma}. \tag{6}$$

In the case of Coulomb and gravitational interaction ($\gamma = 1$), there exists an analytical expression of the deflection angle, the Rutherford formula:[16] for the repulsive case,

$$\phi(b/b_0) = \arctan\left(\frac{2b}{b_0}\right), \tag{7}$$

and for the attractive one,

$$\phi(b/b_0) = \pi - \arctan\left(\frac{2b}{b_0}\right). \tag{8}$$

In the case of different interactions, the process is well known only on the qualitative level or in particular cases (see, e.g., Refs. 1 and 9–14). In the cases in which explicit solutions are not possible to compute, it is natural to perform an asymptotic expansion in the adimensional variable b/b_0. Inspecting, for example, the gravitational case (8), we see that it is possible to write the solution in the form of two asymptotic series: one in powers of b/b_0, valid for $b/b_0 \leq 1/2$, and another one in powers of b_0/b, valid for $b/b_0 \geqslant 1/2$. It is then natural to ask the following questions:

1. Is it possible to write, for $\gamma \neq 1$, an expression in the form of a power series of Eq. (5) for small b/b_0 and for large b/b_0?
2. If the answer of the previous question is positive, what are the exponent(s) of the power series?
3. In the case in which the answer to the previous question is positive, do the coefficients of these power series have simple analytical expressions?
4. If so, do the convergence radii of the two power series for small and large b/b_0 match?

It is not trivial to answer the questions listed above. A naive expansion in power series of b/b_0 of Eq. (5) gives in many cases divergent integrals, which indicates that the series are not in powers of b/b_0. Moreover, special care should be given for attractive interactions and $\gamma > 2$, where the centrifugal barrier could not be sufficient to prevent particles to crash.

In the present paper, we will give the answers to the previous questions. We will derive the full asymptotic power series, one valid for small b/b_0 and another one for large b/b_0, which extend the result[15] valid for $\gamma > 2$, and we will show that their convergence radii match. Moreover, we will study how the trajectories change when introducing a regularization at small scales in the potential.

II. SUMMARY OF THE RESULTS

A. Pure power-law interactions

In this paper, we have derived the full asymptotic series solution of Eq. (5) (in the cases in which it well-defined) for both attractive and repulsive potentials. We first denote

$$\beta = (\gamma/2)^{1/\gamma}|1 - 2/\gamma|^{\frac{2-\gamma}{2\gamma}}. \tag{9}$$

Theorem 1. *We assume repulsive interactions, that is, the minus sign in Eq. (5) with an arbitrary $\gamma > 0$.*

(i) *For $b > \beta b_0$, we have*

$$\phi(b/b_0) = \sqrt{\pi}\sum_{n=0}^{+\infty}\frac{(-1)^n\Gamma((n\gamma+1)/2)}{2n!\Gamma(1+n(\gamma/2-1))}(b_0/b)^{\gamma n}. \tag{10}$$

(ii) *For $b < \beta b_0$, we have*

$$\phi(b/b_0) = \sum_{n=0}^{+\infty}\alpha_n(b/b_0)^{2n+1}, \tag{11}$$

where, for $n \in \mathbb{N}$,

$$\alpha_n = \alpha_n(\gamma) = \frac{(-1)^n\sqrt{\pi}}{(2n+1)n!}\frac{\Gamma(1+(2n+1)/\gamma)}{\Gamma(1/2-n+(2n+1)/\gamma)}.$$

Theorem 2. *We assume attractive interactions, that is, the plus sign in Eq. (5).*

(i) *For $b > \beta b_0$ and $\gamma > 0$ arbitrary, we have*

$$\phi(b/b_0) = \sqrt{\pi}\sum_{n=0}^{+\infty}\frac{\Gamma((n\gamma+1)/2)}{2n!\Gamma(1+n(\gamma/2-1))}(b_0/b)^{\gamma n}. \tag{12}$$

(ii) *For $b < \beta b_0$, $\gamma < 2$, and if*

$$\gamma \notin \left\{2\frac{2k+1}{2\ell+1}, k, \ell \in \mathbb{N}, k < \ell\right\},$$

we have

$$\phi(b/b_0) = \sum_{n=0}^{+\infty}a_n(b/b_0)^{\frac{2\gamma}{2-\gamma}n} + \sum_{q=0}^{+\infty}c_q(b/b_0)^{2q+1}, \tag{13}$$

where, for $q \in \mathbb{N}$,

$$\begin{aligned} c_q &= (-1)^q\binom{-1/2}{q} \times \frac{\Gamma((2q+1)/\gamma+1)\Gamma((q+1/2)(1-2/\gamma))}{(2q+1)\Gamma(q+1/2)} \\ &= \frac{\Gamma((2q+1)/\gamma+1)\Gamma((q+1/2)(1-2/\gamma))}{\sqrt{\pi}(2q+1)q!}, \end{aligned} \tag{14}$$

$$a_0 = \frac{\pi}{2-\gamma}, \tag{15}$$

and, for $n \geqslant 1$,

$$a_n = -\frac{\sqrt{\pi}\Gamma\left(\frac{\gamma n}{\gamma-2}+\frac{1}{2}\right)}{2n\Gamma\left(\frac{2n}{\gamma-2}\right)n!}. \tag{16}$$

(iii) *If $\gamma = \gamma_{k,\ell} = 2\frac{2k+1}{2\ell+1} \in]0, 2[$ for some $k, \ell \in \mathbb{N}$ with $k < \ell$, then*

$$\begin{aligned} \phi(b/b_0) = &\sum_{\substack{n\in\mathbb{N}\text{s.t.}\\ 1+n\frac{2k+1}{k-\ell}\notin -2\mathbb{N}}} a_n(\gamma_{k,\ell})(b/b_0)^{\frac{2\gamma_{k,\ell}}{2-\gamma_{k,\ell}}n} + \sum_{\substack{q\in\mathbb{N}\text{s.t.}\\ (2q+1)\frac{k-\ell}{2k+1}\notin -\mathbb{N}}} c_q(\gamma_{k,\ell})(b/b_0)^{2q+1} \\ &+ \sum_{\substack{n,q\in\mathbb{N}\text{s.t.}\\ (2q+1)(\ell-k)=n(2k+1)}} \frac{\sqrt{\pi}(-1)^q(b/b_0)^{2q+1}}{2n\Gamma(-n-q-1/2)n!q!}\Big(2\ln(b/b_0) \\ &+ \frac{\Gamma'}{\Gamma}(-n-q-1/2)\frac{2}{\gamma_{k,\ell}} + \frac{2}{\gamma_{k,\ell}}\gamma_0 - H_q - \frac{2-\gamma_{k,\ell}}{\gamma_{k,\ell}}(H_n+1/n)\Big). \end{aligned} \tag{17}$$

Here, $H_N = \sum_{p=1}^{N} 1/p$ is the harmonic sum of order N and γ_0 is Euler's constant.

(iv) *For $\gamma \geqslant 2$, particles crash in a finite time if $b \leqslant \beta b_0$. If $b > \beta b_0$, we have*

$$\phi\left(\frac{b}{b_0}\right) = \frac{\pi}{2\sqrt{1-b_0^2/b^2}} \qquad \text{if } \gamma = 2 \text{ and } b > \beta b_0 = b_0, \tag{18a}$$

$$\phi\left(\frac{b}{b_0}\right) \approx -\frac{\ln(1-\beta b_0/b)}{2\sqrt{\gamma-2}} \qquad \text{if } \gamma > 2 \text{ and } b \approx \beta b_0. \tag{18b}$$

Remark 1. Statement (i) *of Theorems 1 and 2 is due to Ref.* 15 *for* $\gamma > 2$. *The formulas extend to arbitrary* γ *positive.*

Remark 2. In Eq. (12) (i), *the coefficient is the same as in Eq.* (10) (i), *up to the* $(-1)^n$ *factor.*

Remark 3. In the statement of Theorem 2 *when* $\gamma < 2$, *we emphasize that in the generic* (ii) *case,* $\gamma \notin \{2\frac{2k+1}{2\ell+1}, k, \ell \in \mathbb{N}, k < \ell\}$, *which we call the unexceptional cases; then,* $\phi(b/b_0)$ *is the sum of two power series with different exponents; one does not depend on* γ, *and the other one does. In particular, for a given* γ, *if we want a first or second order expansion of* ϕ *for* $b/b_0 \ll 1$, *we need to order the exponents in Eqs.* (13) *and* (17). *For instance, noticing that* $2\gamma/(2-\gamma) < 1$ *as soon as* $\gamma < 2/3$, *for hard collisions* ($b/b_0 \ll 1$), *we obtain*

$$\phi = \frac{\pi}{2-\gamma} + \begin{cases} \frac{\Gamma(1+1/\gamma)\Gamma(1/2-1/\gamma)}{\sqrt{\pi}} b/b_0 + o(b/b_0) & \text{if } 2/3 < \gamma < 2, \\ \frac{3}{4}(b/b_0)\ln(b_0/b) + o((b/b_0)\ln(b_0/b)) & \text{if } \gamma = 2/3, \\ -\frac{\sqrt{\pi}\Gamma(1/2-\gamma/(2-\gamma))}{\Gamma(2/(2-\gamma))}(b/b_0)^{2\gamma/(2-\gamma)} + o((b/b_0)^{2\gamma/(2-\gamma)}) & \text{if } 0 < \gamma < 2/3. \end{cases} \tag{19}$$

In the exceptional cases (iii), *then logarithmic corrections appear [see Eq.* (17)*].*

B. Hard collisions with regularized interactions

We have calculated the modification of the above results, at first order and for hard collisions, when a regularization is applied at small scales in the potential (which is a standard procedure, e.g., in molecular dynamics simulations). In this case, the angle ϕ is given by the formula

$$\phi_\epsilon(b, b_0) = \frac{b}{r_{min}} \int_0^1 \frac{dx}{\sqrt{1 - (\frac{bx}{r_{min}})^2 \pm \frac{b_0^\gamma}{\epsilon^\gamma}\mathcal{V}(\frac{r_{min}}{\epsilon x})}}. \tag{20}$$

In the Conclusions, we will give an example of the use of these results. In order to be able to make explicit calculations, we will consider two regularizations commonly used in the astrophysical literature (see, e.g., Refs. 17 and 18), the *Plummer potential*

$$v^{\mathrm{Pl}}(r, \epsilon) = \frac{g}{(r^2 + \epsilon^2)^{\gamma/2}} \tag{21}$$

and the compact softening

$$v^{\mathrm{co}}(r, \epsilon) = \begin{cases} \frac{g}{r^\gamma} & \text{if } r \geqslant \epsilon \\ \frac{g}{\epsilon^\gamma}\mathrm{v}(r/\epsilon) & \text{if } 0 \leqslant r \leqslant \epsilon \end{cases}, \tag{22}$$

where v is a function on [0, 1] such that v(1) = 1. For these regularized potentials, we do not expect series expansions with analytically simple coefficients. We have however been able to compute the following second order expansions (the explicit coefficients are given in Sec. IV):

Theorem 3. *We consider repulsive interactions, that is, the minus sign in Eq.* (20).

(i) *For the Plummer softening, when* $\epsilon < b_0$ *are fixed, we have, for small* b/b_0,

$$\phi_\epsilon(b, b_0) = B^{\mathrm{Pl}}_{\epsilon/b_0}(\gamma)(b/b_0) + \mathcal{O}((b/b_0)^3),$$

where the coefficient $B^{\mathrm{Pl}}_{\epsilon/b_0}(\gamma)$ *is given in Eq.* (45) *in Subsection IV A 1.*

(ii) *For the compact softening, when* $\epsilon < b_0$ *are fixed and for small* b/b_0, *the deflection angle* ϕ_ϵ *is not affected by the softening; hence, we have the same asymptotic behavior as in Eq.* (11), *namely,*

$$\phi_\epsilon(b, b_0) = \alpha_1(\gamma)(b/b_0) + \mathcal{O}((b/b_0)^3).$$

(iii) *For the Plummer (respectively, compact) softening, when* $\epsilon > b_0$ *[respectively,* $\epsilon > b_0(\max \mathrm{v})^{1/\gamma}$*] and* b/ϵ *small, we have*

$$\phi_\epsilon(b, b_0) = \frac{\pi}{2} - \tilde{B}_{\epsilon/b_0}(\gamma) b/\epsilon + o(b/\epsilon),$$

where the coefficient $\tilde{B}_{\epsilon/b_0}(\gamma)$ *is given in Eq.* (48) *in Subsection IV A 2 [respectively, Eq.* (52) *in Subsection IV B 2].*

Theorem 4. *We consider attractive interactions, that is, the plus sign in Eq.* (20) *and either the Plummer or the compact softening. Let us fix* $\epsilon > 0$ *and* $b_0 > 0$ *arbitrary. Then, for* b/ϵ *small, we have*

$$\phi_\epsilon(b, b_0) = \frac{\pi}{2} + C_{\epsilon/b_0}(\gamma) b/\epsilon + o(b/\epsilon),$$

where $C_{\epsilon/b_0}(\gamma)$ is given in Eq. (55) in Subsection IV C.

Remark 4. Let us point out that the statement of Theorem 4 holds true independently whether ϵ/b_0 is small or not.

Proposition 1. We consider the case $\gamma > 2$ with either the Plummer or the compact softening. Then, there exists a threshold $\epsilon_*(b_0, \gamma)$, depending only on b_0 and γ, such that

- *if $\epsilon \leqslant \epsilon_*(b_0, \gamma)$, then the angle ϕ_ϵ diverges to $+\infty$ for some critical impact factor b;*
- *if $\epsilon > \epsilon_*(b_0, \gamma)$, then ϕ_ϵ is a smooth function of b/b_0 for $b/b_0 \geqslant 0$.*

For the Plummer softening, we have

$$\epsilon_*^{\mathrm{Pl}}(b_0, \gamma) = b_0 \left(\frac{\gamma - 2}{\gamma + 2}\right)^{\frac{1}{2} + \frac{1}{\gamma}}, \tag{23}$$

and the expression of $\epsilon_*(b_0, \gamma)$ in the case of compact softening [see Eq. (58)] is slightly more involved but still proportional to b_0.

C. Numerical checking and discussion

First of all, we show in Fig. 2 the truncated series expansions Eqs. (10)–(13) for the pure power-law case for several values of γ: $\gamma = 1/2$ and $\gamma = 7/4$, for repulsive and attractive interactions, and $\gamma = 2/3$ and $\gamma = 6/7$ for attractive interactions, the "exceptional case"; see Eq. (17). We plot the numerical solution ("exact") obtained by numerical integration of Eq. (5) and the truncated series with different number of terms, showing the convergence toward the "exact" solution. In the inset, we show the relative error of the numerical solution and the series with the largest number of terms (nmax) plotted in the main figure. We observe, as expected, that the maximum difference between the two solutions is at the convergence radius of the series, denoted by vertical lines. We observe that the truncation of the respective series to the tenth term provides an excellent approximation for both $b/b_0 \in [0, \beta[$ and $b/b_0 \in]\beta, +\infty[$.

It is interesting to study the different kind of trajectories inspecting the first terms of the asymptotic series. In the case of repulsive potentials, the maximum value that the angle ϕ can take is $\pi/2$, which corresponds to particles coming back in their original direction. In the case of attractive potentials, different cases arise depending on the value of γ:

- For $0 < \gamma < 2$, the leading order value of ϕ for $b/b_0 \ll 1$ is $\pi/(2 - \gamma)$. A number n_{loops} of loops may appear in the trajectory that can be calculated by using the formula

$$n_{loops} = \mathrm{floor}\left(\frac{1}{2 - \gamma}\right). \tag{24}$$

  A typical trajectory for γ close to 2 is illustrated in Fig. 3, with $\gamma = 1.95$ and $b/b_0 = 0.6\beta$, for which $n_{\mathrm{loops}} = 12$.
- For $\gamma > 2$, we have formation of pairs for impact factors smaller than a critical one. For impact factors exactly at the critical one, there is the phenomena of *orbiting* in which the particles are trapped into a circular orbit. For larger impact factors, the collision is well behaved. We illustrate this behavior in Fig. 4.

The numerical checking for regularized potentials can be found in Sec. IV E.

III. SERIES EXPANSIONS FOR PURE POWER-LAW POTENTIALS

For the general case $\gamma \neq 1$, we do not expect to be able to derive an explicit expression through elementary functions for the angle ϕ as a function of b/b_0, as we did for $\gamma = 1$ in Eqs. (7) and (8). However, it is possible to express the integral (5) as a sum of a series. It is important to note that the angle ϕ is a function of the ratio of b and b_0 [see Eq. (A9) in Appendix A]. We will seek therefore for power series of $(b/b_0)^\sigma$ for some suitable σ, not necessarily an integer. As a first step, we perform the substitution $r = r_{min}/x$, $0 < x \leqslant 1$, in Eq. (5), yielding

$$\phi(b/b_0) = \frac{b}{r_{min}} \int_0^1 \frac{dx}{\sqrt{1 - (bx/r_{min})^2 \mp (b_0 x/r_{min})^\gamma}}. \tag{25}$$

We recall that the "minus" sign in the denominator corresponds to a repulsive interaction while the "plus" sign to an attractive one. We will see that it is necessary to use two power series: one valid for the weak scattering regime ($b \gg b_0$) and another one for the strong scattering regime ($b \ll b_0$). We will see that the radii of convergence of both series match and therefore the solution is fully described by the two power series.

The main difficulty in finding the power series is that a naive Taylor expansion in b/b_0 in Eq. (5) does not work. We shall proceed by first identifying an appropriate small parameter, which we call generically δ, and make a first Taylor expansion in δ; then, we expand δ in terms of b/b_0 and substitute in the first expansion. In the following, we detail the procedure for each case.

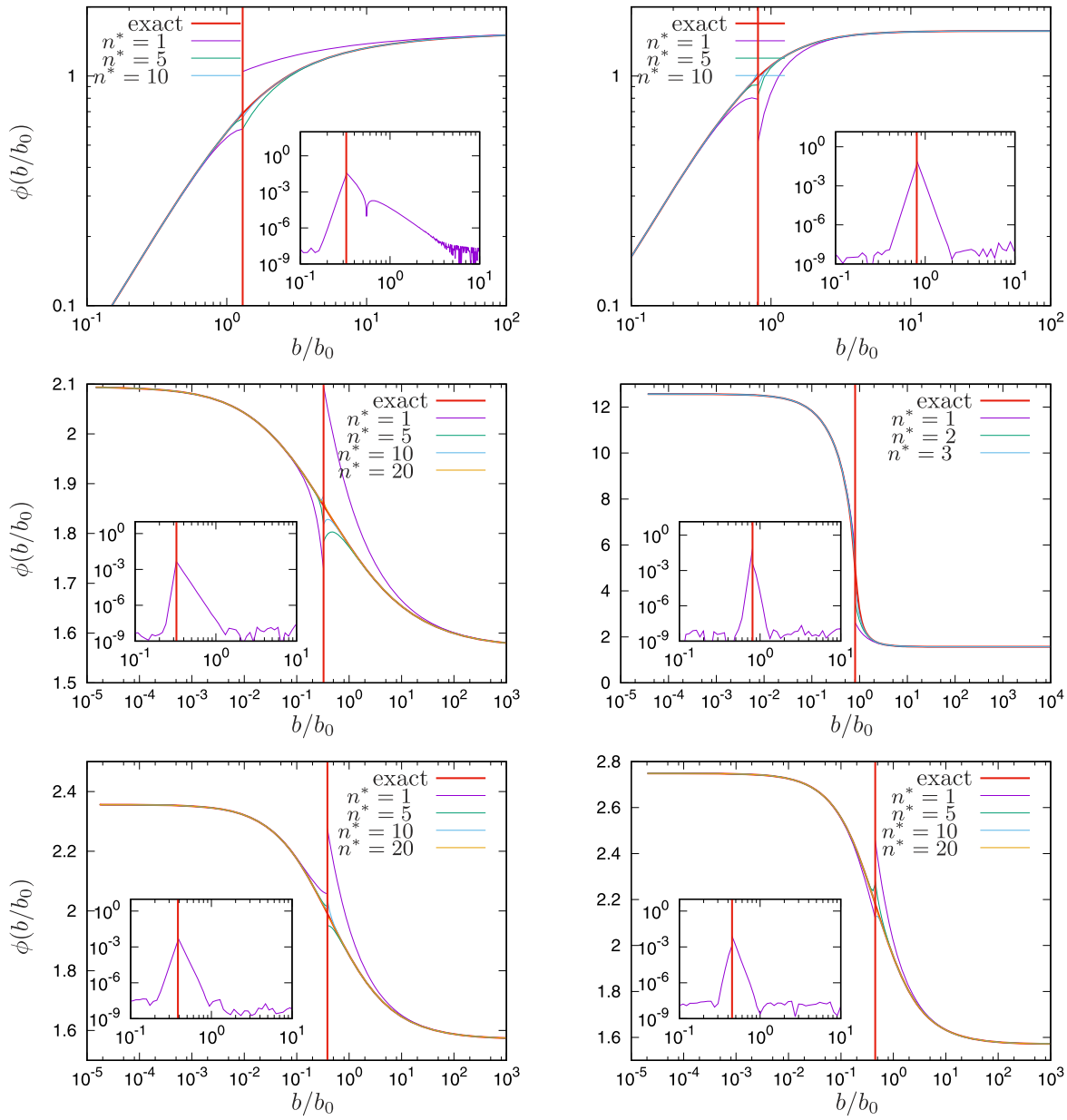

FIG. 2. Top: repulsive interaction, with γ = 1/2 (left) and γ = 7/4 (right). Middle: attractive interaction with the same values of γ. Bottom: two "exceptional" attractive cases [see Eq. (17)], with γ = 2/3 (left) and γ = 6/7 (right). The integer n^* corresponds to the number of terms summed in the first series, and the number of terms summed in the second series is chosen such that the final exponents are as close as possible. Inset: relative error for maximal n^*.

A. The regime of *soft* collisions for attractive and repulsive interactions [Proof of Theorems 1 (i) and 2 (i)]

The regime of *soft* collisions corresponds to the case in which the scale b_0 is small compared to the impact factor b. In this regime, the trajectories of the particles are weakly perturbed. In this subsection, γ is any positive number. In this case, the appropriate small parameter is

$$\delta = (b_0/r_{min})^\gamma = \mp[(b/r_{min})^2 - 1].$$

From Eq. (25), we obtain

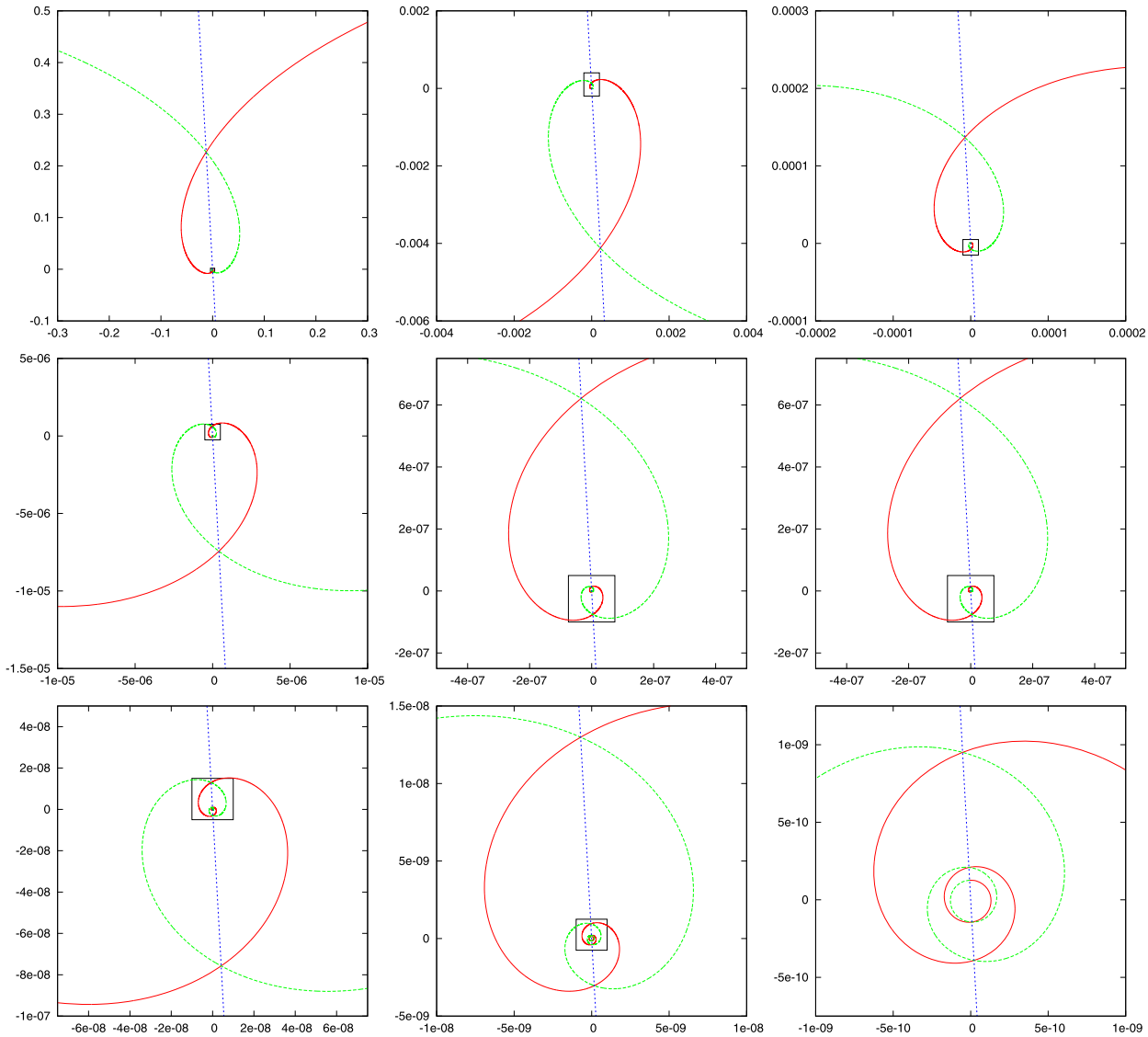

FIG. 3. Near-collision in the center of mass frame for $\gamma = 1.95$ and $b/b_0 = 0.6\beta$. The dotted lines are the axis of symmetry of the trajectory. The squares in each plot represent the frame of the next plot (which has to be read from left to right and top to down). The first half part of the trajectory—from $x = +\infty$ to the axis of symmetry—is plotted in red and the other half of the trajectory in green. The points of intersection of the trajectory lie on the axis of symmetry.

$$\frac{r_{min}}{b}\phi(b/b_0) = \int_0^1 \frac{dx}{\sqrt{1 - x^2 \mp \delta(x^\gamma - x^2)}}.$$

We proceed in two steps: we first prove that ϕ is a power series in $(b_0/b)^\gamma$ for b sufficiently large and then identify the coefficients in the expansion.

We want an expansion of the above integral using that δ is a small parameter. It is then natural to write it under the form

$$\int_0^1 \frac{dx}{\sqrt{1 - x^2}\sqrt{1 \mp \delta \frac{x^\gamma - x^2}{1 - x^2}}}$$

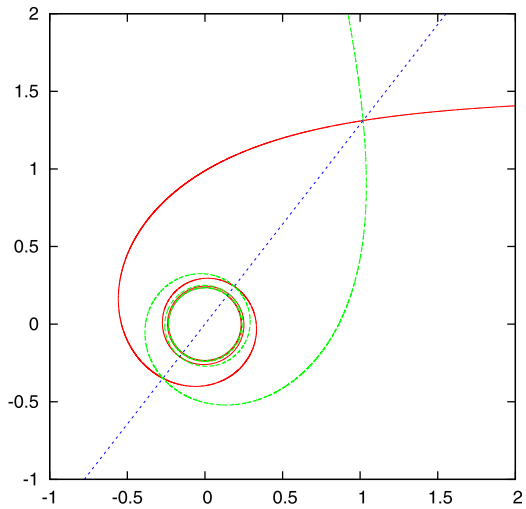

FIG. 4. A trajectory in the center of mass frame for attractive interaction $\gamma = 2.05$ and $b/b_0 = \beta + 1.4 \times 10^{-6}$ (only a portion of the trajectory is plotted). The first half part of the trajectory—from $x = +\infty$ to the axis of symmetry—is plotted in red and the other half of the trajectory in green. The points of intersection of the trajectory lie on the axis of symmetry.

and to expand the second square root in power series. This is possible since the expression $(x^\gamma - x^2)/(1 - x^2)$ is bounded on $[0, 1]$ (for $\gamma > 0$), and this implies that $(r_{min}/b)\phi(b/b_0)$ is actually a power series in δ. Moreover, since

$$\frac{b}{r_{min}} = \sqrt{1 \pm (b_0/r_{min})^\gamma} = \sqrt{1 \pm (b_0/b)^\gamma (b/r_{min})^\gamma},$$

it is easy to show that b/r_{min}, thus also $\delta = \pm((b/r_{min})^2 - 1)$, is itself a power series of the variable $(b_0/b)^\gamma$ (with a positive radius). By substitution and Cauchy product, ϕ is a power series in $(b_0/b)^\gamma$ for b sufficiently large, that is, there exist some coefficients $\kappa_n(\gamma)$, $n \in \mathbb{N}$ such that for b large enough,

$$\phi = \sum_{n=0}^{+\infty} \kappa_n(\gamma)(b_0/b)^{\gamma n}.$$

In addition, from the above computation, we know that each coefficient $\kappa_n(\gamma)$ is a finite sum of the type

$$\sum_{k=0}^{n} C(n,k) \int_0^1 \left(\frac{x^\gamma - x^2}{1 - x^2}\right)^k \frac{dx}{\sqrt{1 - x^2}},$$

the integrals coming from the expansion of the integral $(r_{min}/b)\phi$ in powers of δ and the coefficients $C(n, k)$ of the Cauchy products and the substitution. In particular, each coefficient $\kappa_n(\gamma)$ is an analytic function of γ in $(0, +\infty)$ (and even in the half-space $\{\mathrm{Re} > 0\}$).

We now identify the coefficients $\kappa_n(\gamma)$ by considering the two expansions valid for $\gamma > 2$ and b large

$$\phi = \sqrt{\pi} \sum_{n=0}^{+\infty} \frac{\Gamma((n\gamma + 1)/2)}{2n!\Gamma(1 + n(\gamma/2 - 1))} (\mp (b_0/b)^\gamma)^n = \sum_{n=0}^{+\infty} \kappa_n(\gamma)(b_0/b)^{\gamma n},$$

where the first equality, valid for $\gamma > 2$, comes from Ref. 15. By uniqueness of the power series expansions, we deduce that if $\gamma > 2$, then for all $n \in \mathbb{N}$,

$$\kappa_n(\gamma) = (\mp 1)^n \sqrt{\pi} \frac{\Gamma((n\gamma + 1)/2)}{2n!\Gamma(1 + n(\gamma/2 - 1))}. \tag{26}$$

Since κ_n is an analytic function in $(0, +\infty)$ and both $\gamma \mapsto \Gamma((n\gamma + 1)/2)$ and $\gamma \mapsto 1/\Gamma(1 + n(\gamma/2 - 1))$ are analytic in $(0, +\infty)$, we deduce from the principle of permanence for analytic functions that Eq. (26) holds true for any $\gamma > 0$.

We may now compute the radius of convergence. If $\gamma > 2$, this has been carried out in Ref. 15 using the generalized Stirling formula $\Gamma(s+1) \approx (s/\mathrm{e})^s\sqrt{2\pi s}$ when $s \to +\infty$, showing the convergence of the series for $b_0/b < 1/\beta$. The generalization to $\gamma \leqslant 2$ follows from the same type of computations, combined with Euler's reflection formula $\Gamma(s)\Gamma(1-s) = \pi/\sin(\pi s)$. This proves Eqs. (10) and (12).

B. The regime of *hard* collisions for repulsive interactions [Proof of Theorem 1 (ii)]

This corresponds to the minus sign in Eq. (25). In this subsection again, γ is any positive number. It is then easy to check that $r_{min} \approx b_0$ for small b/b_0. In this case, the appropriate small parameter δ is

$$\delta = (b/r_{min})^2 \sim (b/b_0)^2 \ll 1.$$

Substituting $(b_0/r_{min})^\gamma = 1 - \delta$ in Eq. (25), we obtain the expression

$$\phi(b/b_0) = \sqrt{\delta}\int_0^1 \frac{dx}{\sqrt{1 - x^\gamma + \delta(x^\gamma - x^2)}}.$$

Since the quantity $(x^\gamma - x^2)/(1 - x^\gamma)$ is bounded on $[0, 1]$, the above integral is here again a power series in δ

$$\int_0^1 \frac{dx}{\sqrt{1 - x^\gamma + \delta(x^\gamma - x^2)}} = \sum_{p=0}^{+\infty}\binom{-1/2}{p}\delta^p I_p, \tag{27}$$

where the integrals

$$I_p = \int_0^1 \frac{(x^\gamma - x^2)^p}{(1 - x^\gamma)^{p+1/2}}\,dx,$$

$p \in \mathbb{N}$, may be expressed, after using the substitution $x^\gamma = \cos^2(\vartheta)$, with the help of the Γ function

$$I_0 = \frac{\sqrt{\pi}\Gamma(1+1/\gamma)}{\Gamma(1/2+1/\gamma)}, \qquad I_1 = \frac{2\Gamma(1+3/\gamma)}{3\Gamma(-1/2+3/\gamma)} - \frac{2\Gamma(1+1/\gamma)}{\gamma\Gamma(1/2+1/\gamma)}, \qquad \text{etc.}$$

Furthermore, by the definition of r_{min}, we have

$$\sqrt{\delta} = \frac{b}{b_0}(1-\delta)^{1/\gamma}. \tag{28}$$

This implicit relation provides $\sqrt{\delta}$ as the sum of a power series in b/b_0, i.e.,

$$\sqrt{\delta} = \sum_{n=0}^{\infty}\lambda_n (b/b_0)^{2n+1}. \tag{29}$$

The coefficients λ_n can be calculated inserting Eq. (29) in Eq. (28). We claim therefore that there exist some coefficients α_n ($n \in \mathbb{N}$), depending only on n and γ, such that

$$\phi(b/b_0) = \sum_{n=0}^{+\infty}\alpha_n (b/b_0)^{2n+1}, \tag{30}$$

with

$$\alpha_n = \frac{(-1)^n\sqrt{\pi}}{(2n+1)n!}\frac{\Gamma(1+(2n+1)/\gamma)}{\Gamma(1/2-n+(2n+1)/\gamma)}.$$

The form of α_n can be verified by calculating the coefficients λ_n and inserting Eq. (29) in Eq. (27). The computation of the convergence radius of this series follows from straightforward computations involving, as in Ref. 15, the generalized Stirling formula and (for $\gamma > 2$) Euler's reflection formula. This proves Eq. (11).

C. The regime of *hard* collisions for attractive interactions [Proof of Theorem 2 (ii)–(iv)]

We focus now on the plus sign in Eq. (25) in the regime $b \ll b_0$. As we shall see, the situation is drastically different since the qualitative behavior strongly depends on γ. In this section, we wish to give, for $b \ll b_0$, a series expansion of ϕ analogous to (30). For this regime, we shall consider the small parameter $\delta = (r_{min}/b)^2 \ll 1$ and substitute $(b_0/r_{min})^\gamma = \delta^{-1} - 1$ in Eq. (25) to obtain the expression

$$\phi(b/b_0) = \int_0^1 \frac{dx}{\sqrt{x^\gamma - x^2 + \delta(1 - x^\gamma)}}, \tag{31}$$

which tends, as $\delta \to 0$, to $\int_0^1 (x^\gamma - x^2)^{-1/2} dx$, which is finite only for $0 < \gamma < 2$. This already leads us to study the cases $\gamma < 2$ and $\gamma \geqslant 2$ separately.

1. The case $0 < \gamma < 2, \gamma$ unexceptional (ii)

We use the change of variables $y = x\delta^{-1/\gamma}$ in Eq. (31), which is adapted to our problem, to deduce

$$\phi(b/b_0) = \delta^{\frac{2-\gamma}{2\gamma}} \int_0^{\delta^{-1/\gamma}} \frac{dy}{\sqrt{y^\gamma - \delta^{2/\gamma-1} y^2 + 1 - \delta y^\gamma}}.$$

The idea is now to expand the integrand in power series in $\delta^{2/\gamma-1}$, arguing as in Secs. III A and III B. We obtain

$$\delta^{-\frac{2-\gamma}{2\gamma}} \phi(b/b_0) = \int_0^{\delta^{-1/\gamma}} \frac{dy}{\sqrt{y^\gamma + 1 - \delta y^\gamma}} (1 - \delta^{2/\gamma-1} H_1(y))^{-1/2},$$

with $H_1(y) = y^2/(y^\gamma + 1 - \delta y^\gamma)$. It is elementary to prove that $\delta^{2/\gamma-1} H_1(y)$ is increasing in y from 0 to 1; hence, we may Taylor expand

$$\delta^{-\frac{2-\gamma}{2\gamma}} \phi(b/b_0) = \sum_{n=0}^{+\infty} (-\delta^{2/\gamma-1})^n \binom{-1/2}{n} \int_0^{\delta^{-1/\gamma}} \frac{y^{2n} dy}{(y^\gamma + 1 - \delta y^\gamma)^{n+1/2}},$$

where $\binom{-1/2}{n} = (\prod_{j=0}^{n-1}(-1/2 + j))/n!$. The integral may be expressed through the hypergeometric function (see Ref. 20, Chap. 15) ${}_2F_1 = F$

$$\begin{aligned}
\int_0^{\delta^{-1/\gamma}} \frac{y^{2n} dy}{(y^\gamma + 1 - \delta y^\gamma)^{n+1/2}} &= \frac{\delta^{-\frac{2n+1}{\gamma}}}{2n+1} F\left(n + 1/2, \frac{2n+1}{\gamma}, \frac{2n+1}{\gamma} + 1, 1 - 1/\delta\right) \\
&= \frac{\delta^{-\frac{2n+1}{\gamma}}}{2n+1} \delta^{n+1/2} \frac{2}{2-\gamma} F(n + 1/2, 1, 1 - (n + 1/2)(2-\gamma)/\gamma, \delta) \\
&\quad + \frac{\delta^{-\frac{2n+1}{\gamma}}}{2n+1} \delta^{\frac{2n+1}{\gamma}} \frac{\Gamma((2n+1)/\gamma + 1)\Gamma((n+1/2)(1-2/\gamma))}{\Gamma(n+1/2)} \\
&\quad \times F\left(\frac{2n+1}{\gamma}, 1 + (n+1/2)(2-\gamma)/\gamma, 1 + (n+1/2)(2-\gamma)/\gamma, \delta\right) \\
&= \frac{\delta^{-\frac{2n+1}{\gamma}}}{2n+1} \delta^{n+1/2} \frac{2}{2-\gamma} F(n + 1/2, 1, (n+1/2)(1-2/\gamma) + 1, \delta) \\
&\quad + \frac{\Gamma((2n+1)/\gamma + 1)\Gamma((n+1/2)(1-2/\gamma))}{(2n+1)\Gamma(n+1/2)} (1-\delta)^{-\frac{2n+1}{\gamma}}
\end{aligned}$$

by using the functional relation 15.3.8 in Ref. 20 and the fact that $F(a, b, b, z) = (1 - z)^{-a}$. These formulas hold when $\gamma/2$ is not of the form $(2k + 1)/(2\ell + 1)$ for some $k, \ell \in \mathbb{N}$ with $k < \ell$, since then $1 - (n + 1/2)(2 - \gamma)/\gamma$ is never a nonpositive integer. This is precisely the unexceptional γ's. Reporting these expressions, we infer

$$\phi(b/b_0) = \phi_I(b/b_0) + \phi_{II}(b/b_0),$$

where

$$\phi_I(b/b_0) = \frac{2}{2-\gamma} \sum_{n=0}^{+\infty} \frac{(-1)^n}{2n+1} \binom{-1/2}{n} F(n + 1/2, 1, (n+1/2)(1-2/\gamma) + 1, \delta)$$

and

$$\phi_{II}(b/b_0) = \delta^{\frac{2-\gamma}{2\gamma}} \sum_{n=0}^{+\infty} (-1)^n (\delta^{2/\gamma-1})^n \binom{-1/2}{n} (1-\delta)^{-\frac{2n+1}{\gamma}} \times \frac{\Gamma((2n+1)/\gamma + 1)\Gamma((n+1/2)(1-2/\gamma))}{(2n+1)\Gamma(n+1/2)}.$$

In the series ϕ_{II}, we observe that by the definition of δ, we have $b/b_0 = \delta^{\frac{1}{\gamma} - \frac{1}{2}} (1 - \delta)^{-1/\gamma}$, and thus,

$$\delta^{\frac{2-\gamma}{2\gamma}} (\delta^{2/\gamma-1})^n (1-\delta)^{-\frac{2n+1}{\gamma}} = (b/b_0)^{2n+1}.$$

By using Stirling's formula and the complement formula, we easily obtain

$$(-1)^n \binom{-1/2}{n} \frac{\Gamma((2n+1)/\gamma + 1)\Gamma((n+1/2)(1-2/\gamma))}{(2n+1)\Gamma(n+1/2)} \approx -\frac{\beta^{-2n-1}}{\gamma n \sqrt{2-\gamma} \sin(\pi(n+1/2)(2-\gamma)/\gamma)},$$

where $\beta = (\gamma/2)^{1/\gamma}(2/\gamma - 1)^{\frac{2-\gamma}{2\gamma}}$ [see Eq. (9)]. Therefore,

$$\phi_{II}(b/b_0) = \sum_{n=0}^{+\infty}(-1)^n(b/b_0)^{2n+1}\binom{-1/2}{n} \times \frac{\Gamma((2n+1)/\gamma+1)\Gamma((n+1/2)(1-2/\gamma))}{(2n+1)\Gamma(n+1/2)},$$

which is a power series in b/b_0 of radius β.

Let us now turn to ϕ_I. The series is very slowly converging since $\binom{-1/2}{n} \approx (-1)^{n+1}\sqrt{\pi/n}$. In particular, we know that $\phi(0^+) = a_0(\gamma) = \pi/(2-\gamma)$ and indeed

$$\frac{\pi}{2-\gamma} = \phi_I(0^+) + 0 = \frac{2}{2-\gamma}\sum_{n=0}^{+\infty}\frac{(-1)^n}{2n+1}\binom{-1/2}{n} = \frac{2}{2-\gamma}\arcsin(1),$$

but the remainder $\sum_{n=N+1}^{+\infty}\frac{(-1)^n}{2n+1}\binom{-1/2}{n}$ is of order $1/\sqrt{N}$. If we truncate the series ϕ_I, we then have a quite large error even on the zeroth order term. As a consequence, we shall try to give a power series expansion of ϕ_I in suitable powers of b/b_0. We claim that there exist numbers (depending on γ only) a_n, $n \in \mathbb{N}$, such that

$$\phi_I(b/b_0) = \sum_{n=0}^{+\infty} a_n (b/b_0)^{\frac{2\gamma}{2-\gamma}n}. \tag{32}$$

By expanding the hypergeometric function in power series, it is clear that $\phi_I(b/b_0)$ is a power series in δ with a positive radius, namely,

$$\phi_I(b/b_0) = \frac{2}{2-\gamma}\sum_{p=0}^{+\infty} A_p\delta^p \qquad \text{with} \quad A_p = \sum_{n=0}^{+\infty} d_{n,p},$$

where

$$d_{n,p} = \frac{(-1)^n}{2n+1}\binom{-1/2}{n}\frac{\Gamma(n+1/2+p)\Gamma((n+1/2)(1-2/\gamma)+1)}{\Gamma(n+1/2)\Gamma((n+1/2)(1-2/\gamma)+1+p)}.$$

Moreover, δ is related to b/b_0 through the formula $b/b_0 = \delta^{\frac{1}{\gamma}-\frac{1}{2}}(1-\delta)^{-1/\gamma}$ or

$$(b/b_0)^{\frac{2\gamma}{2-\gamma}} = \delta(1-\delta)^{-\frac{2}{2-\gamma}} = \delta + \frac{2}{2-\gamma}\delta^2 + \ldots = \sum_{k=0}^{+\infty}(-1)^k\binom{-\frac{2}{2-\gamma}}{k}\delta^{k+1};$$

hence, inverting this relation, we see that δ is a power series (with coefficients depending on γ only) of $(b/b_0)^{\frac{2\gamma}{2-\gamma}}$ with a positive radius. The result Eq. (32) then follows by substitution.

We wish now to obtain an explicit expression for the coefficients a_n. The strategy is to equate the coefficients in the expansions in powers of δ in

$$\phi_I(b/b_0) = \sum_{n=0}^{+\infty}\left(\frac{2}{2-\gamma}\sum_{p=0}^{+\infty} d_{n,p}\delta^p\right) \qquad \text{and} \qquad \phi_I(b/b_0) = \sum_{p=0}^{+\infty} a_p\left(\sum_{k=0}^{+\infty}(-1)^k\binom{-\frac{2}{2-\gamma}}{k}\delta^k\right)^p$$

and then solve the linear, upper triangular system relating a_p and A_p (through the coefficients $d_{n,p}$); the sum over n being performed at the end of the calculation. We have then obtained the formulas Eqs. (14), (15), and (16), thus proving Eq. (13).

2. The case $0 < \gamma < 2$, γ exceptional (iii)

It remains to study the case where $\gamma/2$ is of the form $\gamma_{k,\ell}/2 = \frac{2k+1}{2\ell+1}$, which we shall call exceptional. We then fix two integers k, ℓ with $0 \leqslant k < \ell$. The idea will be to pass to the limit in the formula given in Eq. (13) when γ unexceptional tends to $\gamma_{k,\ell}$. Notice that we may write Eq. (13), for γ unexceptional, under the form

$$\phi(b/b_0) = \sum_{\substack{n\in\mathbb{N}\text{s.t.}\\ 1+n\frac{2k+1}{k-\ell}\notin -2\mathbb{N}}} a_n(b/b_0)^{\frac{2\gamma}{2-\gamma}n} + \sum_{\substack{q\in\mathbb{N}\text{s.t.}\\ (2q+1)\frac{k-\ell}{2k+1}\notin -\mathbb{N}}} c_q(b/b_0)^{2q+1}$$
$$+ \sum_{\substack{n,q\in\mathbb{N}\text{s.t.}\\ (2q+1)(\ell-k)=n(2k+1)}}\left(a_n(b/b_0)^{\frac{2\gamma}{2-\gamma}n} + c_q(b/b_0)^{2q+1}\right).$$

Passing to the limit as $\gamma \to \gamma_{k,\ell} = \frac{2(2k+1)}{2\ell+1}$ in the first two sums is immediate, but we have to pay attention to the last sum since Γ is infinite at the nonpositive integers. We fix some $n, q \in \mathbb{N}$ such that $(2q+1)(\ell-k) = n(2k+1)$ (hence $n \geqslant 1$) and denote

$$\sigma = n\frac{\gamma}{2-\gamma} - q - \frac{1}{2} \to 0$$

so that $\gamma - \gamma_{k,\ell} = \sigma(2-\gamma_{k,\ell})^2/(2n) + \mathcal{O}(\sigma^2)$ as $\sigma \to 0$. It follows that

$$\begin{aligned}\frac{2q+1}{\gamma} + 1 &= \frac{2q+1}{\gamma_{k,\ell}} + 1 - \sigma(2q+1)\frac{(2-\gamma_{k,\ell})^2}{2n\gamma_{k,\ell}^2} + \mathcal{O}(\sigma^2)\\ &= q + 1 + n + \frac{1}{2} - \sigma(2q+1)\frac{(2-\gamma_{k,\ell})^2}{2n\gamma_{k,\ell}^2} + \mathcal{O}(\sigma^2)\\ &= q + n + \frac{3}{2} - \sigma\frac{2n}{2q+1} + \mathcal{O}(\sigma^2),\end{aligned}$$

since $2n/(2q+1) = (\ell-k)/(2k+1) = (2-\gamma_{k,\ell})/\gamma_{k,\ell}$, and that

$$(q+1/2)(1-2/\gamma) = -n + \sigma\frac{2-\gamma}{\gamma} = -n + \sigma\frac{2-\gamma_{k,\ell}}{\gamma_{k,\ell}} - \sigma^2\frac{(2-\gamma_{k,\ell})^2}{n\gamma_{k,\ell}^2} + \mathcal{O}(\sigma^3).$$

Then, by using the formula, for $m \in \mathbb{N}$ and $z \to -m$,

$$\Gamma(z) = \frac{(-1)^m}{m!}\left(\frac{1}{z+m} + (H_m - \gamma_0) + \mathcal{O}(z+m)\right),$$

where $H_m = \sum_{j=1}^m 1/j$ and $\gamma_0 = \lim_{m\to+\infty}(H_m - \ln m)$ is Euler's constant; we deduce

$$\begin{aligned}c_q &= \frac{\Gamma((2q+1)/\gamma+1)\Gamma((q+1/2)(1-2/\gamma))}{\sqrt{\pi}(2q+1)q!}\\ &= (-1)^n\frac{\Gamma(q+n+3/2) - \sigma\frac{2n}{2q+1}\Gamma'(q+n+3/2) + \mathcal{O}(\sigma^2)}{\sqrt{\pi}(2q+1)q!n!}\\ &\quad\times\left(\frac{1}{\sigma(2-\gamma_{k,\ell})/\gamma_{k,\ell} - \sigma^2\frac{(2-\gamma_{k,\ell})^2}{n\gamma_{k,\ell}^2}} + (H_n - \gamma_0) + \mathcal{O}(\sigma)\right)\\ &= \frac{(-1)^n\Gamma(q+n+3/2)}{\sqrt{\pi}(2q+1)q!n!\sigma}\frac{\gamma_{k,\ell}}{2-\gamma_{k,\ell}} + \mathcal{O}(1).\end{aligned} \tag{33}$$

Moreover, for $n \neq 0$, we have $2n/(2-\gamma) = n + q + 1/2 + \sigma$; thus,

$$\begin{aligned}a_n &= -\frac{\sqrt{\pi}\Gamma\left(\frac{\gamma n}{\gamma-2} + \frac{1}{2}\right)}{2n\Gamma\left(\frac{2n}{\gamma-2}\right)n!}\\ &= -\frac{\sqrt{\pi}\Gamma(-q-\sigma)}{2n\Gamma(-n-q-1/2-\sigma)n!}\\ &= \frac{\sqrt{\pi}(1+\sigma\Gamma'(-n-q-1/2)/\Gamma(-n-q-1/2) + \mathcal{O}(\sigma^2))}{2n\Gamma(-n-q-1/2)n!}\frac{(-1)^q}{q!\sigma}\left(1 - (H_q - \gamma_0)\sigma + \mathcal{O}(\sigma)\right)\\ &= \frac{\sqrt{\pi}(-1)^q}{2n\Gamma(-n-q-1/2)n!q!\sigma} + \mathcal{O}(1).\end{aligned} \tag{34}$$

We may then check that the two singular terms in a_n and c_q cancel out when $\sigma \to 0$. Indeed, using the reflection formula, we infer

$$\frac{\pi}{\Gamma(-q-n-1/2)} = (-1)^{q+n+1}\Gamma(q+n+3/2),$$

and combining this with the fact that $2n/(2q+1) = (\ell-k)/(2k+1) = (2-\gamma_{k,\ell})/\gamma_{k,\ell}$, we deduce $a_n + c_q = \mathcal{O}(1)$ as $\sigma \to 0$. We shall now inspect the terms of order σ^0. First, we have

$$(b/b_0)^{2n\gamma/(2-\gamma)} = (b/b_0)^{2q+1+2\sigma} = (b/b_0)^{2q+1} + 2\sigma(b/b_0)^{2q+1}\ln(b/b_0) + \mathcal{O}(\sigma^2).$$

Then, going back to Eqs. (33) and (34), we obtain

$$\begin{aligned} c_q &= \frac{(-1)^n\Gamma(q+n+3/2)}{\sqrt{\pi}(2q+1)q!n!\sigma}\frac{\gamma_{k,\ell}}{2-\gamma_{k,\ell}} - \frac{(-1)^n}{\sqrt{\pi}(2q+1)n!q!}\Gamma'(q+n+3/2) \\ &\quad + \frac{(-1)^n}{n!}\frac{\Gamma(q+n+3/2)}{\sqrt{\pi}(2q+1)q!}(H_n-\gamma_0)+\mathcal{O}(\sigma) \\ &= \frac{\sqrt{\pi}(-1)^{q+1}}{2n\Gamma(-n-q-1/2)n!q!\sigma} + \frac{(-1)^q\sqrt{\pi}}{(2q+1)n!q!\Gamma(-n-q-1/2)}\times\frac{\Gamma'(-q-n-1/2)}{\Gamma(-q-n-1/2)} \\ &\quad + \frac{\sqrt{\pi}(-1)^{q+1}}{2n\Gamma(-n-q-1/2)n!q!}\frac{2-\gamma_{k,\ell}}{\gamma_{k,\ell}}(H_n-\gamma_0+1/n)+\mathcal{O}(\sigma), \end{aligned}$$

by using the reflection formula and its logarithmic derivative, and

$$a_n = \frac{\sqrt{\pi}(-1)^q}{2n\Gamma(-n-q-1/2)n!q!\sigma} + \frac{\sqrt{\pi}(-1)^q}{2n\Gamma(-n-q-1/2)n!q!}\left(\frac{\Gamma'(-n-q-1/2)}{\Gamma(-n-q-1/2)} - H_q + \gamma_0\right) + \mathcal{O}(\sigma).$$

Therefore, as $\sigma \to 0$,

$$\begin{aligned} &a_n(b/b_0)^{\frac{2\gamma}{2-\gamma}n} + c_q(b/b_0)^{2q+1} \\ &= (b/b_0)^{2q+1}\left(a_n + c_q + 2\sigma a_n\ln(b/b_0)+\mathcal{O}(\sigma)\right) \\ &\to \frac{\sqrt{\pi}(-1)^q(b/b_0)^{2q+1}}{2n\Gamma(-n-q-1/2)n!q!} \\ &\quad\times\left(\frac{\Gamma'}{\Gamma}(-n-q-1/2)\frac{2}{\gamma_{k,\ell}} + \gamma_0 - H_q + \frac{2-\gamma_{k,\ell}}{\gamma_{k,\ell}}(\gamma_0 - H_n - 1/n) + 2\ln(b/b_0)\right). \end{aligned}$$

This concludes in the exceptional cases.

3. $\gamma = 2$ (iv)

The case $\gamma = 2$ allows explicit computation, and we see that it is a case where the attractive term is strong enough to form pairs when b is small. Of course, this will be also the case when $\gamma > 2$. Actually, when $\gamma = 2$, the behavior of the expression

$$W(r) = 1 - \frac{b^2}{r^2} + \frac{b_0^2}{r^2} = 1 - \frac{b^2 - b_0^2}{r^2}$$

depends on whether $b > b_0$ or $b < b_0$. If $b > b_0$, then W possesses $r_{min} = \sqrt{b^2 - b_0^2}$ as a unique positive zero, and we have the exact value

$$\phi(b/b_0) = \int_{r_{min}}^{+\infty}\frac{(b/r^2)\,dr}{\sqrt{1 - r_{min}^2/r^2}} = \frac{b\pi}{2r_{min}} = \frac{\pi}{2\sqrt{1 - b_0^2/b^2}}. \tag{35}$$

If $b \leqslant b_0$, then $W \geqslant 1$ has no zero. This means that the two particles will crash one onto the other in finite time with a spiraling motion. The integral in the right-hand side of Eq. (5) is then equal to $+\infty$, but the angle ϕ has then no geometrical meaning and the picture given in Fig. 1 is then no longer the good one. The parameter b_0 is then a threshold with the property that particles crash as soon as $b \leqslant b_0$.

4. $\gamma > 2$ (iv)

If $\gamma > 2$, the attractive term is strong enough to form pairs for sufficiently small b, and we shall explicit the threshold. Notice first that when $\gamma > 2$, the function $W(r) = 1 - b^2/r^2 + 2b_0^\gamma/r^\gamma$ decreases on $(0, r_*(b)]$ and increases on $[r_*(b), +\infty)$, with

$$r_*(b) = \left(\frac{\gamma b_0^\gamma}{2b^2}\right)^{\frac{1}{\gamma-2}}.$$

Since $W(r_*(b)) = 1 - b^2/r_*^2(b) + b_0^\gamma/r_*^\gamma(b) = 1 - (b_0/b)^{-\frac{2\gamma}{\gamma-2}}[1 - 2/\gamma](\gamma/2)^{-\frac{2}{\gamma-2}}$, we may then easily check that if

$$b > \beta b_0, \tag{36}$$

where β is defined in (9), then W has a larger positive zero r_{min}, whereas if $b < \beta b_0$, the expression W is positive on $(0, +\infty)$, and if $b = \beta b_0$, the expression W has a double root at $r = r_*(\beta b_0) = b_0(\gamma/2 - 1)^{1/\gamma} > 0$, where $W(r_*(\beta b_0)) = 0$. These three behaviors are illustrated in Fig. 5.

When $\gamma \to 2^+$, we have, as expected, $\beta = (\gamma/2)^{1/\gamma}(1 - 2/\gamma)^{\frac{2-\gamma}{2\gamma}} = (\gamma/2)^{1/\gamma}\exp((1/2)(1 - 2/\gamma)\ln(1 - 2/\gamma)) \to 1$, which is the threshold when $\gamma = 2$. If $b < \beta b_0$, the particles crash in finite time and ϕ has here again no physical or geometrical meaning, despite the fact that the integral

$$\int_0^{+\infty} \frac{(b/r^2)\,dr}{\sqrt{1 - b^2/r^2 + b_0^\gamma/r^\gamma}} = \int_0^{+\infty} \frac{dx}{\sqrt{1 - x^2 + (b_0/b)^\gamma x^\gamma}},$$

where r_{min} has been replaced by 0, converges.

When $b = \beta b_0$, the reduced particle remains asymptotically trapped on a circular orbit of radius $r_*(\beta b_0) > 0$. This phenomenon is called in the atomic physics literature *orbiting* (see, e.g., Ref. 13). The angle ϕ has once again no physical or geometrical meaning, and

$$\int_{r_*(\beta b_0)}^{+\infty} \frac{(b/r^2)\,dr}{\sqrt{1 - b^2/r^2 + b_0^\gamma/r^\gamma}} = +\infty$$

in view of the fact that $1 - b^2/r^2 + b_0^\gamma/r^\gamma \sim (r - r_*(\beta b_0))^2$ for r close to $r_*(\beta b_0)$.

Let us now consider the situation where we take $\gamma > 2$ and b slightly larger than βb_0 so that one expects a divergence in the integral ϕ. We have

$$\phi(b/b_0) = \int_{r_{min}}^{+\infty} \frac{b\,dr}{r^2\sqrt{W_b(r)}},$$

with $W_b(r) = 1 - b^2/r^2 + b_0^\gamma/r^\gamma$ (we have stressed the dependency on b since we are interested in the limit $b \to \beta b_0$). As b approaches βb_0, we have both $r_*(b) \to r_*(\beta b_0) = b_0(\gamma/2 - 1)^{1/\gamma} > 0$ [$r_*(b)$ is the minimum for W_b] and $r_{min} \to r_*(\beta b_0)$ (r_{min} is the largest zero of W_b). In the integral ϕ, the contributions for r close to $r_*(\beta b_0)$ will make the integral diverge since we shall have $W_b(r) \sim (r - r_*(\beta b_0))^2$ (we have a double root when $b = \beta b_0$), whereas the contributions for r much larger than $r_*(\beta b_0)$ will remain of order one. As a consequence, for any small length parameter $\ell > 0$, we have

$$\phi(b/b_0) \approx \int_{r_{min}}^{r_{min}+\ell} \frac{b\,dr}{r^2\sqrt{W_b(r)}},$$

and we may then replace $W_b(r)$ by its second order Taylor expansion near $r_*(b)$

$$W_b(r) = W_b(r_*(b)) + (r - r_*(b))W_b'(r_*(b)) + \frac{1}{2}(r - r_*(b))^2 W_b''(r_*(b)) + \mathcal{O}((r - r_*(b))^3).$$

Since $W_b'(r_*(b)) = 0$ and

$$W_b''(r_*(b)) = \frac{\gamma(\gamma+1)b_0^\gamma}{r_*^{\gamma+2}(b)} - \frac{6b^2}{r_*^4(b)} \approx \frac{2(\gamma-2)b^2}{r_*(\beta b_0)^4} > 0, \tag{37}$$

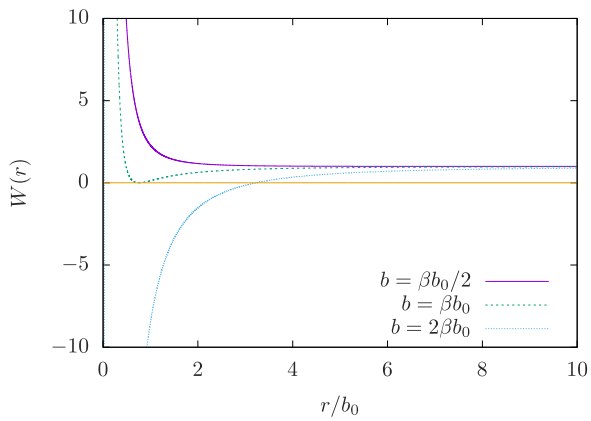

FIG. 5. Graph of W as a function of r/b_0 for different values of b for $\gamma = 5/2$ for the attractive case. Observe that for $b = \beta b_0/2$, there is no root, $b = \beta b_0$ is the limiting case with a double root, and for $b = 2\beta b_0$, there is one root.

this yields

$$\phi(b/b_0) \approx \int_{r_{min}}^{r_{min}+\ell} br^{-2}\, dr/\sqrt{W_b(r_*(b)) + (r - r_*(b))^2 (W_b''(r_*(b))/2 + \mathcal{O}(r - r_*(b)))}.$$

We have $W_b(r_*(b)) < 0 < W_b''(r_*(b))$ with $W_b(r_*(b))$ small but $W_b''(r_*(b))$ of order one. The idea is then to use the substitution

$$z\sqrt{-W_b(r_*(b))} = (r - r_*(b))\sqrt{W_b''(r_*(b))/2 + \mathcal{O}(r - r_*(b))}$$

so that the expression in the square root in the integral becomes simply $-W_b(r_*(b))\,(z^2 - 1)$. This yields

$$\phi(b/b_0) \approx \frac{b}{\sqrt{-W_b(r_*(b))}} \int_1^{z_{max}} \frac{r(z)^{-2}\, dr/dz}{\sqrt{z^2 - 1}}\, dz, \tag{38}$$

where $z_{min} = 1$ and $z_{max} \approx Cte(\ell)/\sqrt{-W_b(r_*(b))} \gg 1$ are the corresponding values to r_{min} and $r_{min} + \ell$ in the z variable. The idea is now that, roughly speaking, $r(z) \approx r_*(b) \approx r_*(\beta b_0)$ and $dr/dz \approx \sqrt{-2W_b(r_*(b))/W_b''(r_*(b))}$, which implies

$$\phi(b/b_0) \approx \frac{b}{r_*(\beta b_0)^2}\sqrt{\frac{2}{W_b''(r_*(b))}} \int_1^{z_{max}} \frac{dz}{\sqrt{z^2 - 1}} \approx \sqrt{\frac{2b^2}{r_*(\beta b_0)^4 W_b''(r_*(\beta b_0))}}\, \ln(z_{max}) \approx -\frac{\ln|W_b(r_*(b))|}{2\sqrt{\gamma - 2}}, \tag{39}$$

in view of Eq. (37) and the fact that $z_{max} \approx Cte(\ell)/\sqrt{-W_b(r_*(b))} \gg 1$. Finally, $W_b(r_*(b)) = 1 - (\beta b_0/b)^{-\frac{2\gamma}{\gamma-2}}$, and we end up with

$$\phi(b/b_0) \approx -\frac{\ln(1 - \beta b_0/b)}{2\sqrt{\gamma - 2}}. \tag{40}$$

For the sake of simplicity, we have included the mathematical details leading to Eq. (39) in Appendix B 1.

IV. LEADING ORDER EXPANSIONS FOR HARD REGULARIZED INTERACTIONS

In this section, we will present the details of the results for regularized hard interactions presented in Sec. II B for the *Plummer potential* Eq. (21) and compact softening Eq. (22). A common feature for both of these potentials is that they fulfill the relation

$$v(r, \epsilon) = \frac{1}{\epsilon^\gamma}\mathcal{V}\left(\frac{r}{\epsilon}\right), \tag{41}$$

with

$$\mathcal{V}^{\mathrm{Pl}}(R) = \frac{1}{(R^2 + 1)^{\gamma/2}}$$

and

$$\mathcal{V}^{\mathrm{co}}(R) = \begin{cases} \dfrac{1}{R^\gamma} & \text{if } R \geqslant 1 \\ \mathrm{v}(R) & \text{if } 0 \leqslant R \leqslant 1. \end{cases}$$

We will show that the results presented below do not depend qualitatively on the explicit form of the regularization used. In what follows, we will study how the angle ϕ is modified by the regularization in the potential, first for repulsive interactions and then for attractive ones.

We recall the angle ϕ_ϵ corresponding to the regularized potential

$$\phi_\epsilon(b, b_0) = \frac{b}{r_{min}} \int_0^1 \frac{dx}{\sqrt{1 - (\frac{bx}{r_{min}})^2 \pm \frac{b_0^\gamma}{\epsilon^\gamma}\mathcal{V}(\frac{r_{min}}{\epsilon x})}}. \tag{42}$$

A. Hard repulsive interactions with the Plummer softening

Here, $\mathcal{V}(R) = \mathcal{V}^{\mathrm{Pl}}(R) = (R^2+1)^{-\gamma/2}$. Then, the function $r \mapsto 1 - b^2/r^2 - b_0^\gamma/\left(r^2 + \epsilon^2\right)^{\gamma/2}$ increases from $-\infty$ to 1 as r increases from 0^+ to $+\infty$ and hence has a single positive zero r_{min}. It is easily checked that r_{min} is an increasing function of b and that the function $r \mapsto 1 - b_0^\gamma/\left(r^2 + \epsilon^2\right)^{\gamma/2}$ possesses a positive zero if and only if $\epsilon < b_0$. Therefore, for small b,

$$r_{min} \approx r_0 = b_0\sqrt{1-(\epsilon/b_0)^2}$$

if $\epsilon/b_0 \leqslant 1$ and

$$r_{min} \approx \frac{b}{\sqrt{1-(\epsilon/b_0)^{-\gamma}}}$$

if $\epsilon/b_0 > 1$. This naturally leads us to distinguish the case $\epsilon < b_0$ and the case $\epsilon > b_0$.

1. The case $\epsilon < b_0$ [Proof of Theorem 3 (i)]

We assume $\epsilon/b_0 < 1$ so that $r_0 > 0$, $r_{min} = r_0(1+\mathcal{O}((b/b_0)^2))$, and consider here again the small parameter $\delta = (b/r_{min})^2 \ll 1$. Substituting

$$\frac{b_0^\gamma}{\epsilon^\gamma} = \frac{1-b^2/r_{min}^2}{\mathcal{V}(r_{min}/\epsilon)} = \frac{1-\delta}{\mathcal{V}(r_{min}/\epsilon)}$$

yields

$$\phi_\epsilon(b,b_0) = \sqrt{\delta}\int_0^1 \frac{dx}{\sqrt{1-\delta x^2-(1-\delta)\frac{\mathcal{V}(r_{min}/(\epsilon x))}{\mathcal{V}(r_{min}/\epsilon)}}} = \sqrt{\delta}\int_0^1 \frac{dx}{\sqrt{F(x,r_{min}/\epsilon)+\delta(1-x^2-F(x,r_{min}/\epsilon))}}, \tag{43}$$

where we have set

$$F(x,r_{min}/\epsilon) = 1-\frac{\mathcal{V}(r_{min}/(\epsilon x))}{\mathcal{V}(r_{min}/\epsilon)}.$$

We prove in Appendix B 2 that the function $x \mapsto \frac{1-x^2}{F(x,r_{min}/\epsilon)}$ is bounded on $[0,1]$ independently of b. This shows that we may apply the Taylor expansion in δ used in Subsection III A and write

$$\phi_\epsilon(b,b_0) = \sqrt{\delta}\int_0^1 \frac{dx}{\sqrt{F(x,r_{min}/\epsilon)}\sqrt{1+\delta(\frac{1-x^2}{F(x,r_{min}/\epsilon)}-1)}} = \sqrt{\delta}\int_0^1 \frac{dx}{\sqrt{F(x,r_{min}/\epsilon)}} + \mathcal{O}(\delta^{3/2}).$$

At this stage, since $r_{min} = r_0(1+\mathcal{O}((b/b_0)^2))$, one could legitimate the expansion

$$\int_0^1 \frac{dx}{\sqrt{F(x,r_{min}/\epsilon)}} = \int_0^1 \frac{dx}{\sqrt{F(x,r_0/\epsilon)}} + \mathcal{O}((b/b_0)^2).$$

Since $r_{min} = r_0(1+\mathcal{O}((b/b_0)^2))$, $\sqrt{\delta} = b/r_{min} = b/r_0(1+\mathcal{O}((b/b_0)^2))$, and thus, when $\epsilon/b_0 < 1$,

$$\phi_\epsilon^{\mathrm{Pl}}(b,b_0) = B_{\epsilon/b_0}^{\mathrm{Pl}}(\gamma)(b/b_0) + \mathcal{O}((b/b_0)^3), \tag{44}$$

where

$$B_{\epsilon/b_0}^{\mathrm{Pl}}(\gamma) = \frac{1}{\sqrt{1-(\epsilon/b_0)^2}}\int_0^1 \frac{dx}{\sqrt{1-\frac{x^\gamma}{(1-(\epsilon/b_0)^2(1-x^2))^{\gamma/2}}}}. \tag{45}$$

Comparing Eq. (44) with the expression in Eq. (11) of the angle of the closest approach without softening, namely, $\phi(b/b_0) = \alpha_1(\gamma)(b/b_0) + \mathcal{O}((b/b_0)^3) = -\frac{\sqrt{\pi}\Gamma(1+3/\gamma)}{3\Gamma(3/\gamma-1/2)}(b/b_0) + \mathcal{O}((b/b_0)^3)$, we observe that the linear dependence (at leading order) of ϕ with respect to b/b_0 is not modified, and only the prefactor changes. It is also easy to check that in the limit $\epsilon \to 0$, we have, as expected, $B_{\epsilon/b_0}^{\mathrm{Pl}}(\gamma) \to \alpha_1(\gamma)$. As expected, the new introduced scale is ϵ.

2. The case $\epsilon > b_0$ [Proof of Theorem 3 (iii)]

In the case $\epsilon > b_0$, we recall that for b small,

$$r_{min} \approx b/\sqrt{1-(\epsilon/b_0)^{-\gamma}} \tag{46}$$

and that

$$\phi_\epsilon(b,b_0) = \frac{b}{r_{min}}\int_0^1 \frac{dx}{\sqrt{1-(bx/r_{min})^2-(b_0^\gamma/\epsilon^\gamma)\mathcal{V}(r_{min}/(\epsilon x))}}.$$

Substituting $1 = b^2/r_{min}^2 + (\epsilon/b_0)^{-\gamma}\mathcal{V}(r_{min}/\epsilon)$ in the integral and considering the small parameter $\delta = r_{min}^2/\epsilon^2 \sim b^2/\epsilon^2$ give

$$\phi_\epsilon(b,b_0) = \int_0^1 \frac{dx}{\sqrt{G_b(x)}},$$

where

$$G_b(x) = 1 - x^2 - \frac{r_{min}^2}{b^2(\epsilon/b_0)^\gamma}\Big(\mathcal{V}(\sqrt{\delta}/x) - \mathcal{V}(\sqrt{\delta})\Big).$$

In view of the fact that $r_{min}^2 \approx b^2/(1-(\epsilon/b_0)^{-\gamma})$ and $b_0 \leqslant \epsilon$, we expect

$$\phi_\epsilon(b,b_0) \approx \int_0^1 \frac{dx}{\sqrt{1-x^2}} = \frac{\pi}{2}.$$

We also see that the situation is similar to the case studied in Subsection III A, but the dependency on the small parameter δ is more intricate. Actually, for the Plummer potential, we have $\mathcal{V}^{\mathrm{Pl}}(R) = (R^2+1)^{-\gamma/2}$; thus, for small R, $\mathcal{V}^{\mathrm{Pl}}(R) = 1 - \gamma R^2/2 + \mathcal{O}(R^4)$. Therefore, for fixed x and small δ, we obtain

$$G_b(x) = 1 - x^2 - \frac{\gamma\delta}{2((\epsilon/b_0)^\gamma - 1)}\left(\frac{1}{x^2} - 1\right) + \mathcal{O}(\delta^2),$$

which is a situation very similar to the case studied in Subsection III A, but unfortunately, the function $x \mapsto (1/x^2 - 1)/(1-x^2) = -1/x^2$ being too singular near the origin, the power series expansion trick used there (see Subsection III A) breaks down.

We divide the correction $\phi\epsilon(b, b_0) - \pi/2$ by δ and write it under the form

$$-\frac{1}{\delta}\left(\phi_\epsilon(b,b_0) - \frac{\pi}{2}\right) = \frac{r_{min}^2 b_0^\gamma \epsilon^2}{b^2}\int_0^1 g_\delta(x)\,dx \approx \frac{1}{(\epsilon/b_0)^\gamma - 1}\int_0^1 g_\delta(x)\,dx$$

by Eq. (46) and with

$$g_\delta(x) = \frac{\mathcal{V}(\sqrt{\delta}) - \mathcal{V}(\sqrt{\delta}/x)}{\delta\sqrt{G_b(x)}\sqrt{1-x^2}\,[\sqrt{G_b(x)} + \sqrt{1-x^2}]} \geqslant 0.$$

Clearly, as b/ϵ goes to 0, $\delta \ll 1$, $G_b(x) \approx 1 - x^2$, and we have

$$\int_0^1 g_\delta(x)\,dx \to \frac{\gamma}{4}\int_0^1 \frac{\frac{1}{x^2} - 1}{(1-x^2)^{3/2}}\,dx = +\infty$$

due to the nonintegrable singularity at the origin. We shall prove that actually $\int_0^1 g_\delta(x)\,dx \sim \delta^{-1/2}$. As a first step, we get rid of the contribution for $1/2 \leqslant x \leqslant 1$. Indeed, $\int_0^1 g_\delta(x)\,dx \to +\infty$, whereas

$$\int_{1/2}^1 g_\delta(x)\,dx \to \frac{\gamma}{4}\int_{1/2}^1 \frac{\frac{1}{x^2} - 1}{(1-x^2)^{3/2}}\,dx < +\infty.$$

As a consequence, using the natural substitution $y = \sqrt{\delta}/x$,

$$\int_0^1 g_\delta(x)\,dx \approx \int_0^{1/2} g(x)\,dx = \frac{1}{\sqrt{\delta}}\int_{2\sqrt{\delta}}^{+\infty} \frac{\mathcal{V}(\sqrt{\delta}) - \mathcal{V}(y)}{D_b(y)}\,dy,$$

where we have denoted

$$D_b(y) = y^2\sqrt{G_b\left(\frac{\sqrt{\delta}}{y}\right)\left(1 - \frac{\delta}{y^2}\right)}\left[\sqrt{G_b\left(\frac{\sqrt{\delta}}{y}\right)} + \sqrt{1 - \frac{\delta}{y^2}}\right].$$

When $\delta \to 0$, we have

$$G_b(\sqrt{\delta}/y) \to G^-_{\epsilon/b_0}(y) = 1 - \frac{1}{(\epsilon/b_0)^\gamma - 1}(\mathcal{V}(y) - \mathcal{V}(0))$$

and one could rigorously justify that

$$\int_0^1 g_\delta(x)\,dx \approx \frac{1}{\sqrt{\delta}}\int_0^{+\infty}\frac{\mathcal{V}(0)-\mathcal{V}(y)}{y^2\sqrt{G^-_{\epsilon/b_0}(y)}\left[\sqrt{G^-_{\epsilon/b_0}(y)}+1\right]}\,dy$$
$$= \frac{(\epsilon/b_0)^\gamma-1}{\sqrt{\delta}}\int_0^{+\infty}\left(1-\frac{1}{\sqrt{1+\frac{1}{(\epsilon/b_0)^\gamma-1}(\mathcal{V}(0)-\mathcal{V}(y))}}\right)\frac{dy}{y^2}.$$

The last integral is indeed convergent since for large y, $\mathcal{V}(y)\to 0$, and thus, the integrand is $\sim 1/y^2$; for small y, $\mathcal{V}^{\mathrm{Pl}}(0)-\mathcal{V}^{\mathrm{Pl}}(y) = 1-(1+y^2)^{-\gamma/2}\approx \gamma/(2y^2)$, and thus, the integrand is continuous at the origin. It then follows that for $b\ll\epsilon$,

$$\phi_\epsilon(b,b_0) = \frac{\pi}{2} - B^{\mathrm{Pl}}_{\epsilon/b_0}(\gamma)b/\epsilon + o(b/\epsilon), \tag{47}$$

with

$$\tilde{B}^{\mathrm{Pl}}_{\epsilon/b_0}(\gamma) = \frac{1}{\sqrt{1-(\epsilon/b_0)^{-\gamma}}}\times\int_0^{+\infty}\left(1-\frac{1}{\sqrt{1+\frac{1}{(\epsilon/b_0)^\gamma-1}(\mathcal{V}^{\mathrm{Pl}}(0)-\mathcal{V}^{\mathrm{Pl}}(y))}}\right)\frac{dy}{y^2} > 0. \tag{48}$$

If $\epsilon\gg b_0$, we justify in Appendix B 3 that

$$\tilde{B}^{\mathrm{Pl}}_{\epsilon/b_0}(\gamma) \approx (\epsilon/b_0)^{-\gamma}\sqrt{\pi}\frac{\Gamma\left(\frac{\gamma+1}{2}\right)}{4\Gamma\left(\frac{\gamma}{2}\right)}. \tag{49}$$

We see here that because $\epsilon\gg b_0$, the value of ϕ is completely different compared to the case $\epsilon\to 0$. As expected, in the limit $b\to 0$, $\phi\to\pi/2$, which means that the particle trajectory is unperturbed compared with the case without softening.

B. Hard repulsive interactions with compact softening

In this subsection, we give the few modifications appearing in the asymptotic expansions when we consider a compact softening Eq. (22). The formulas we shall obtain are qualitatively comparable to those in Subsection IV A for the Plummer softening. The first step is to determine the asymptotic behavior of r_{min}, and here again, we shall distinguish the cases where ϵ/b_0 is small or large.

1. The case $\epsilon < b_0$ [Proof of Theorem 3 (ii)]

Assume that $\epsilon < b_0$. Then, the function $r\mapsto 1-b^2/r^2-b_0^\gamma/r^\gamma$ is increasing on $[\epsilon,+\infty)$ and $1-b^2/\epsilon^2-b_0^\gamma/\epsilon^\gamma<0$ for $b/\epsilon\ll 1$. It follows that this function has a unique zero r_{min} on $[\epsilon,+\infty)$, which satisfies, for $b/b_0\ll 1$,

$$r_{min}\approx b_0>\epsilon.$$

In view of the fact that $r_{min}\approx b_0>\epsilon$, the trajectory never enters into the region $\{r\leqslant\epsilon\}$ where the softening has an effect; hence, we obtain the same asymptotics as in the case without softening [see Eq. (11)]

$$\phi_\epsilon(b,b_0) = \alpha_1(\gamma)(b/b_0)+\mathcal{O}((b/b_0)^3) = -\frac{\sqrt{\pi}\Gamma(1+3/\gamma)}{3\Gamma(3/\gamma-1/2)}(b/b_0)+\mathcal{O}((b/b_0)^3). \tag{50}$$

2. The case $\epsilon > b_0(\max_{\mathbb{R}}\mathcal{V})^{1/\gamma}$ [Proof of Theorem 3 (iii)]

Assume now that $\epsilon > b_0(\max_{\mathbb{R}}\mathcal{V})^{1/\gamma}$, that is, $(\epsilon/b_0)^\gamma > \max_{\mathbb{R}}\mathcal{V} = \max_{[0,1]}\mathcal{V}\geqslant 1$. The function $r\mapsto 1-b^2/r^2-b_0^\gamma/r^\gamma$ is then increasing on $[\epsilon,+\infty)$ from $1-b^2/\epsilon^2-(\epsilon/b_0)^{-\gamma}$ to 1. Since $\epsilon/b_0>1$, we have, for $b\ll\epsilon$, $1-b^2/\epsilon^2-(\epsilon/b_0)^{-\gamma}\approx 1-(\epsilon/b_0)^{-\gamma}>0$; hence, $1-b^2/r^2-b_0^\gamma/r^\gamma$ is positive on $[\epsilon,+\infty)$. On $[0,\epsilon]$, the function $r\mapsto 1-b^2/r^2-(\epsilon/b_0)^{-\gamma}\mathcal{V}(r/\epsilon)$ is >0 for $r=\epsilon$ and tends to $-\infty$ for $r\to 0$, thus has a largest root $r_{min}\leqslant\epsilon$. Moreover, since $b^2/r_{min}^2 = 1-\mathcal{V}(r_{min}/\epsilon)(\epsilon/b_0)^{-\gamma}\geqslant 1-(\epsilon/b_0)^{-\gamma}\max_{\mathbb{R}}\mathcal{V}>0$ by our hypothesis, we have $r_{min}\lesssim b\ll\epsilon$; hence,

$$r_{min} = \frac{b}{\sqrt{1-\mathcal{V}(r_{min}/\epsilon)(\epsilon/b_0)^{-\gamma}}}\approx\frac{b}{\sqrt{1-\mathcal{V}(0)(\epsilon/b_0)^{-\gamma}}}$$

that is close to Eq. (46). We may then carry out computations very similar to those leading to Eq. (47), provided v is $\mathcal{C}^2$ on $[0,1]$, positive on $(0,1]$, and $\mathrm{v}'(0)=0$. This yields

$$\phi_\epsilon(b,b_0) = \frac{\pi}{2} - \tilde{B}^{\mathrm{co}}_{\epsilon/b_0}(\gamma)b/\epsilon + o(b/\epsilon), \tag{51}$$

with

$$\tilde{B}^{\mathrm{co}}_{\epsilon/b_0}(\gamma) = \frac{1}{\sqrt{1-\mathcal{V}^{\mathrm{co}}(0)(\epsilon/b_0)^{-\gamma}}}\int_0^{+\infty}\left(1-\frac{1}{\sqrt{1+\frac{1}{(\epsilon/b_0)^\gamma-\mathcal{V}^{\mathrm{co}}(0)}(\mathcal{V}^{\mathrm{co}}(0)-\mathcal{V}^{\mathrm{co}}(y))}}\right)\frac{dy}{y^2}. \tag{52}$$

Here, we do not claim that $B^{\mathrm{co}}_{\epsilon/b_0}(\gamma)$ is a positive constant. For instance, if $\mathrm{v}(0) = 0$, then $B^{\mathrm{co}}_{\epsilon/b_0}(\gamma) < 0$, whereas if $\mathrm{v}(x) = 1$ on $[0, 1]$, then $B^{\mathrm{co}}_{\epsilon/b_0}(\gamma) > 0$. For a general function v on $[0, 1]$, it may happen exceptionally that $B^{\mathrm{co}}_{\epsilon/b_0}(\gamma)$ vanishes, and in this case, the correction $\phi_\epsilon - \pi/2$ is not of order b/ϵ but smaller. This however does not happen for generic functions v.

C. Hard attractive interactions with a softening (Proof of Theorem 4)

The function $r \mapsto 1 - b^2/r^2 + (\epsilon/b_0)^{-\gamma}\mathcal{V}(r/\epsilon)$ tends to 1 at infinity and to $-\infty$ at 0^+ and hence possesses a largest zero r_{min}, but there may exist several zeros in general. Since $1 \leqslant 1 + (\epsilon/b_0)^{-\gamma}\mathcal{V}(r_{min}/\epsilon) = b^2/r^2_{min}$, we must have $r_{min} \leqslant b \ll \epsilon$, and this in turn implies, independently whether ϵ/b_0 is small or not,

$$r_{min} \approx \frac{b}{\sqrt{1 + \mathcal{V}(0)(\epsilon/b_0)^{-\gamma}}} \tag{53}$$

(whereas, without softening, we had $r_{min} \sim b^{2/(2-\gamma)}$).

Our small parameter here will be $\delta = r^2_{min}/\epsilon^2 \ll 1$ [by Eq. (53)]. Substituting $1 = b^2/r^2_{min} - (\epsilon/b_0)^{-\gamma}\mathcal{V}(r_{min}/\epsilon)$ in the integral gives

$$\phi_\epsilon(b, b_0) = \int_0^1 \frac{dx}{\sqrt{G_b(x)}},$$

where

$$G_b(x) = 1 - x^2 + \frac{r^2_{min}}{b^2(\epsilon/b_0)^\gamma}\Big(\mathcal{V}(\sqrt{\delta}/x) - \mathcal{V}(\sqrt{\delta})\Big).$$

Comparing with Sec. IV A 2, the only difference is a change of sign. Therefore, similar computations to those in that paragraph yield

$$\phi_\epsilon(b, b_0) = \frac{\pi}{2} + C_{\epsilon/b_0}(\gamma)b/\epsilon + o(b/\epsilon), \tag{54}$$

where

$$C_{\epsilon/b_0}(\gamma) = \frac{1}{\sqrt{1 + \mathcal{V}(0)(\epsilon/b_0)^{-\gamma}}} \int_0^{+\infty} \left(\frac{1}{\sqrt{1 - \frac{1}{(\epsilon/b_0)^\gamma + \mathcal{V}(0)}(\mathcal{V}(0) - \mathcal{V}(y))}} - 1 \right) \frac{dy}{y^2}. \tag{55}$$

If $\epsilon \gg b_0$, we can show [as we have done for Eq. (49)] that

$$C_{\epsilon/b_0}(\gamma) \approx (\epsilon/b_0)^{-\gamma}\sqrt{\pi}\frac{\Gamma\left(\frac{\gamma+1}{2}\right)}{4\Gamma\left(\frac{\gamma}{2}\right)}. \tag{56}$$

On the other hand, if $\gamma < 2$ and $\epsilon \ll b_0$, we can show that

$$C_{\epsilon/b_0}(\gamma) \approx \frac{(\epsilon/b_0)^{\gamma/2}}{\sqrt{\mathcal{V}(0)}} \int_0^{+\infty} \left(\sqrt{\frac{\mathcal{V}(0)}{\mathcal{V}(y)}} - 1 \right) \frac{dy}{y^2}.$$

We have then a big difference with the case of repulsive interactions studied in Sec. IV B (and also in Sec. IV A), where $\phi_\epsilon \sim b/\max(\epsilon, b_0)$, displaying the characteristic length ϵ or b_0 depending on which one is the largest one. Here, for attractive interactions, only the softening characteristic length ϵ appears in the first order term $\phi_\epsilon - \pi/2 \sim b/\epsilon$ in Eq. (54).

D. Computation of a threshold in ϵ for attractive potentials with $\gamma > 2$ (Proof of Proposition 1)

When $\gamma > 2$ and without softening in the potential (formally, $\epsilon = 0$), the deflection angle ϕ diverges logarithmically to $+\infty$ when $b > \beta b_0$ approaches βb_0 [Eq. (40)]. This divergence is due to the fact that $r_* \approx R = b_0(2-\gamma)^{1/\gamma}$ becomes a double root of the function W in this limit. The first paragraph of this subsection is devoted to the proof of the existence of some threshold $\epsilon_*(b_0, \gamma) > 0$ for the Plummer softening such that if $\epsilon < \epsilon_*(b_0, \gamma)$, then the angle ϕ_ϵ still diverges for some specific value of b (depending on b_0, γ, and ϵ), whereas for $\epsilon > \epsilon_*(b_0, \gamma)$, the angle ϕ_ϵ no longer diverges and is a smooth function of b/b_0 for all positive values of b/b_0. This means that in order to remove the divergence in ϕ, one has to use a sufficiently large softening ϵ. In the first case, the divergence is here again due to the existence, for some critical value b, of some positive double root in r for the function

$$W_{b,\epsilon}(r) = 1 - \frac{b^2}{r^2} + (\epsilon/b_0)^{-\gamma}\mathcal{V}\left(\frac{r}{\epsilon}\right),$$

which means that we have some jump for r_{min} for this critical value b, whereas for $\epsilon > \epsilon_*(b_0, \gamma)$, the function $W_{b,\epsilon}(r)$ has no double root. In the second paragraph, we will discuss the case of the compact softening.

1. The case of a Plummer softening

We now consider the Plummer softening $\mathcal{V}(R) = \mathcal{V}^{\mathrm{Pl}}(R) = (1+R^2)^{-\gamma/2}$ and are interested in determining under which condition on ϵ the function $W_{b,\epsilon}$ has a unique zero r_{min} for any $b > 0$. We have

$$W'_{b,\epsilon}(r) = \frac{\gamma b_0^\gamma}{r^3}\left(\frac{2b^2}{\gamma b_0^\gamma} - \frac{r^4}{(r^2+\epsilon^2)^{\gamma/2+1}}\right),$$

and denoting $r = \epsilon R$,

$$\frac{r^4}{(r^2+\epsilon^2)^{\gamma/2+1}} = \epsilon^{2-\gamma}\frac{R^4}{(R^2+1)^{\gamma/2+1}}.$$

The function $R \mapsto R^4/(R^2+1)^{\gamma/2+1}$ is increasing on $[0, R_{max}]$ and decreasing on $[R_{max}, +\infty)$ (recall $\gamma > 2$), where $R_{max} = \sqrt{4/(\gamma-2)}$; its maximal value is $M(\gamma) = 16(\gamma-2)^{\frac{\gamma}{2}-1}(\gamma+2)^{-\frac{\gamma}{2}-1}$. Therefore, when $2b^2/(\gamma b_0^\gamma) < \epsilon^{2-\gamma}M(\gamma)$ (case 1), the function $W_{b,\epsilon}$ is increasing on $(0, r_1]$, decreasing on $[r_1, r_2]$, and increasing on $[r_2, +\infty)$; when $2b^2/(\gamma b_0^\gamma) > \epsilon^{2-\gamma}M(\gamma)$ (case 2), the function $W_{b,\epsilon}$ is increasing on $(0, +\infty)$. The two critical points r_1 and r_2 merge for $2b^2/(\gamma b_0^\gamma) = \epsilon^{2-\gamma}M(\gamma)$, and we shall see that the threshold is determined by the sign of $W_{b,\epsilon}$ at this merging point $r_1 = r_2$.

Let us now fix $\epsilon > 0$. For b very small, we are in case 1 and the two positive roots r_1 and r_2 of the equation $2b^2/(\gamma b_0^\gamma) = r^4/(r^2+\epsilon^2)^{\gamma/2+1}$ are r_1 (very small) and r_2 (very large). The function $W_{b,\epsilon}$ has then a local minimum $W_{b,\epsilon}(r_2) \approx 1$. When b increase and $W_{b,\epsilon}$ decrease, the two critical points r_1 and r_2 merge when $2b^2/(\gamma b_0^\gamma) = \epsilon^{2-\gamma}M(\gamma)$, and for larger b, $W_{b,\epsilon}$ is increasing on $(0, +\infty)$.

Let us consider the special value of b_{crit} where $2b_{crit}^2/(\gamma b_0^\gamma) = \epsilon^{2-\gamma}M(\gamma)$ for which the two critical points r_1 and r_2 merge: $r_1 = r_2 = r_{crit} = \epsilon R_{max}$. If $W_{b_{crit},\epsilon}(r_{crit}) > 0$, then by monotonicity in b, for any $b > 0$, the function $W_{b_{crit},\epsilon}$ has a largest positive zero r_{min} which is never a double root. If now $W_{b_{crit},\epsilon}(r_{crit}) < 0$, then, still by monotonicity in b, for b smaller but close to b_{crit}, $W_{b,\epsilon}$ has two critical points $0 < r_1 < r_2$ with $0 > W_{b,\epsilon}(r_1) > W_{b,\epsilon}(r_2)$. As b decreases, the critical value $W_{b,\epsilon}(r_2)$ will be zero for some particular value of $b = b_\sharp$ for which r_2 has become a double root of $W_{b_\sharp,\epsilon}$, yielding a logarithmic divergence in ϕ_ϵ. As a consequence, we simply need to determine the sign of

$$W_{b_{crit},\epsilon}(r_{crit}) = 1 - \frac{b_{crit}^2}{\epsilon^2 R_{max}^2} + \frac{b_0^\gamma}{(\epsilon^2 R_{max}^2+\epsilon^2)^{\gamma/2}} = 1 - \frac{\epsilon^{-\gamma}M(\gamma)\gamma b_0^\gamma}{2R_{max}^2} + \frac{b_0^\gamma \epsilon^{-\gamma}}{(R_{max}^2+1)^{\gamma/2}} = 1 - (\epsilon_*(b_0,\gamma)/\epsilon)^\gamma,$$

where the threshold is given by

$$\epsilon_*(b_0,\gamma) = b_0\left(\frac{\gamma-2}{\gamma+2}\right)^{\frac{1}{2}+\frac{1}{\gamma}}. \tag{57}$$

It follows that if $\epsilon > \epsilon_*(b_0,\gamma)$, then ϕ_ϵ is a smooth function of b (see Fig. 8), whereas if $\epsilon < \epsilon_*(b_0,\gamma)$, then ϕ_ϵ diverges as b approaches some value $b_\sharp = b_\sharp(\epsilon)$ corresponding to the case where $W_{b,\epsilon}$ has zero as a local minimum. By computations very similar to those in Sec. III C, we see that the divergence is indeed logarithmic. One may also check that if $\epsilon = \epsilon_*(b_0,\gamma)$, then ϕ_ϵ is a diverging function of b for some $b_\sharp = b_\sharp(\epsilon)$. In other words, in order to regularize the divergence in the case $\gamma > 2$, we have to use a sufficiently large softening parameter, namely, $\epsilon > \epsilon_*(b_0,\gamma)$.

Let us finally consider the case $\gamma = 2$. Notice that formally, $\epsilon_*(b_0,\gamma) \to 0$ as $\gamma \to 2$; hence, we may think that ϕ_ϵ is a smooth function of b for any $\epsilon > 0$, and this is indeed the case. Actually, in the case $\gamma = 2$, the function $R \mapsto R^4/(R^2+1)^2$ is increasing on $[0, +\infty)$ and tends to 1 at infinity. Therefore, either $b/b_0 < 1$ and then the function $W_{b,\epsilon}$ is increasing on $(0, r_1]$ and decreasing on $[r_1, +\infty)$ or $b/b_0 \geqslant 1$ and then the function $W_{b,\epsilon}$ is increasing on $(0, +\infty)$. In any case, $W_{b,\epsilon}$ has a single zero r_{min} and we never have a double root. It follows that ϕ_ϵ is a smooth function of b.

2. The case of a compact softening

For a general compact softening $\mathcal{V} = \mathcal{V}^{\mathrm{co}}$, computations are much less explicit. We first have

$$W'_{b,\epsilon}(r = \epsilon R) = \frac{b_0^\gamma}{R^3\epsilon^{\gamma+1}}\left(\frac{2b^2\epsilon^{\gamma-2}}{b_0^\gamma} + R^3\mathcal{V}'(R)\right),$$

and we then need to know the behavior of the function $R \mapsto -R^3\mathcal{V}'(R)$, which certainly has a positive maximum $M = M(\mathrm{v})$ attained at some $0 < R_{max} \leqslant 1$ since $\gamma > 2$. If, for instance, the function $R \mapsto -R^3\mathcal{V}'(R)$ is, for some $0 \leqslant R_+ \leqslant R_{max}$, nonpositive on $[0, R_+]$, then increasing on $[R_+, R_{max}]$, and then decreasing on $[R_{max}, +\infty)$; the behavior is the same as the one previously described for the Plummer softening. Since

$$\begin{aligned} W_{b_{crit},\epsilon}(r_{crit}) &= 1 - \frac{b_0^\gamma M(\mathrm{v})}{2\epsilon^\gamma R_{max}^2} + \frac{b_0^\gamma}{\epsilon^\gamma}\mathcal{V}(R_{max}) = 1 - \frac{b_0^\gamma}{2\epsilon^\gamma}\left(\frac{M(\mathrm{v})}{R_{max}^2} - 2\mathcal{V}(R_{max})\right) \\ &= 1 + \frac{b_0^\gamma}{2\epsilon^\gamma}\left(R_{max}\mathcal{V}'(R_{max}) + 2\mathcal{V}(R_{max})\right), \end{aligned}$$

TABLE I. Summary of the expansions of the angle ϕ_ϵ with a Plummer softening in the potential for hard collisions.

Repulsive potential		Attractive potential
$\phi\epsilon \sim b/b_0$ when $b \ll b_0$	if $\epsilon/b_0 < 1$	$\phi_\epsilon - \pi/2 \sim b/\epsilon$ when $b \ll \epsilon$
$\phi\epsilon - \pi/2 \sim -b/\epsilon$ when $b \ll \epsilon$	if $\epsilon/b_0 > 1$	

there exists a threshold if and only if $M(\mathrm{v})/R_{max}^2 = -R_{max}\mathcal{V}'(R_{max}) > 2\mathcal{V}(R_{max})$, in which case the threshold is given by

$$\epsilon_*^{\mathrm{co}}(b_0,\gamma) = b_0\left(\frac{M(\mathrm{v})}{2R_{max}^2} - \mathcal{V}(R_{max})\right)^{1/\gamma}, \tag{58}$$

and otherwise, we never have a double root for $W_{b,\epsilon}$ and hence no divergence in ϕ_ϵ. The example below illustrates the first case.

If $\gamma = 3$ and $\mathrm{v}(R) = 21R^2 - 35R^3 + 15R^4$ for $0 \leqslant R \leqslant 1$, then $R \mapsto -R^3\mathcal{V}'(R)$ is decreasing and negative on $[0, \approx 0.474]$, increasing on $[\approx 0.474, \approx 0.984]$, and decreasing on $[\approx 0.984, +\infty)$ and hence has maximum value $M(\mathrm{v}) \approx 3.023$ attained at $R_{max} \approx 0.984$. Moreover, $M(\mathrm{v})/R_{max}^2 - 2\mathcal{V}(R_{max}) \approx 1.023 > 0$; thus, the variations of $W_{b,\epsilon}$ are the same as for the Plummer softening, with a threshold given by

$$\epsilon_*(b_0,\gamma) = b_0\left(\frac{M(\mathrm{v})}{2R_{max}^2} - \mathcal{V}(R_{max})\right)^{1/3} \approx 0.855 b_0.$$

E. Summary of the results and numerical checking

We summarize in Table I the results obtained in this section for the Plummer softening. We have shown that the effect of the softening does not depend strongly on the form of the softening, obtaining the same qualitative results for the two softening considered—the Plummer one and compact one. There is an exception for repulsive interactions and $\epsilon < b_0$, in which case the compact softening does not modify the trajectory of the particles because they do not reach the region in which the potential is regularized.

In the case of repulsive interactions, we have seen that two different behaviors are shown depending whether ϵ/b_0 is larger than 1 or not. In the case $\epsilon/b_0 < 1$, the softening does not modify strongly the angle ϕ: it behaves linearly for $b \ll b_0$, and only its slope is modified with ϵ. In the case in which $\epsilon/b_0 > 1$, hard collisions are radically modified, obtaining $\lim_{b/b_0\to 0}\phi_\epsilon = \pi/2$. The change of behavior occurs sharply at $\epsilon/b_0 = 1$ as we show in Fig. 6 in which ϕ is plotted as a function of ϵ at fixed b for some values of γ. The range of validity in b of the linear correction is given by the *largest* value of b_0 and ϵ. In Fig. 7 (top), we show the comparison between the numerical integration of ϕ_ϵ in Eq. (20) with the asymptotic predictions Eqs. (44) and (47). We see a very good matching between the curves.

For the case of attractive interactions, the range of validity in b of the linear correction is always given by ϵ. In Fig. 7 (bottom), we show a very good agreement matching between the exact integration Eq. (20) with the asymptotic predictions Eqs. (44) and (54).

We have also studied, for $\gamma > 2$, for which values of the softening there is no formation of pairs for any value of b. We have seen that introducing a softening $\epsilon > 0$ but smaller than some critical one $\epsilon_*(b_0,\gamma)$ automatically regularizes the angle ϕ for any value b, except one for which there is *orbiting*. If $\epsilon > \epsilon_*(b_0,\gamma)$, then the problem is completely regularized. In Fig. 8, we illustrate this behavior. The continuous purple

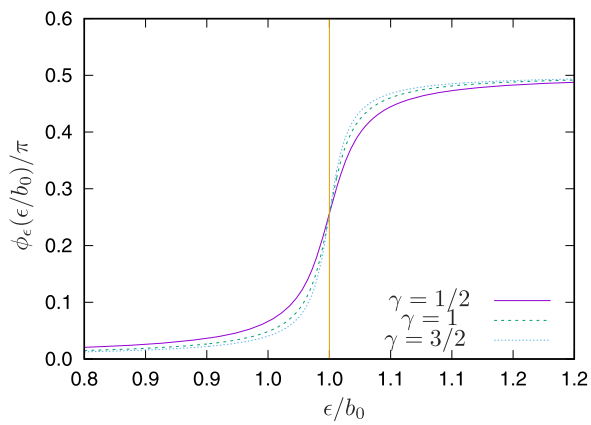

FIG. 6. Value of ϕ for $b/b_0 = 10^{-2}$. The vertical line corresponds to $\epsilon/b_0 = 1$.

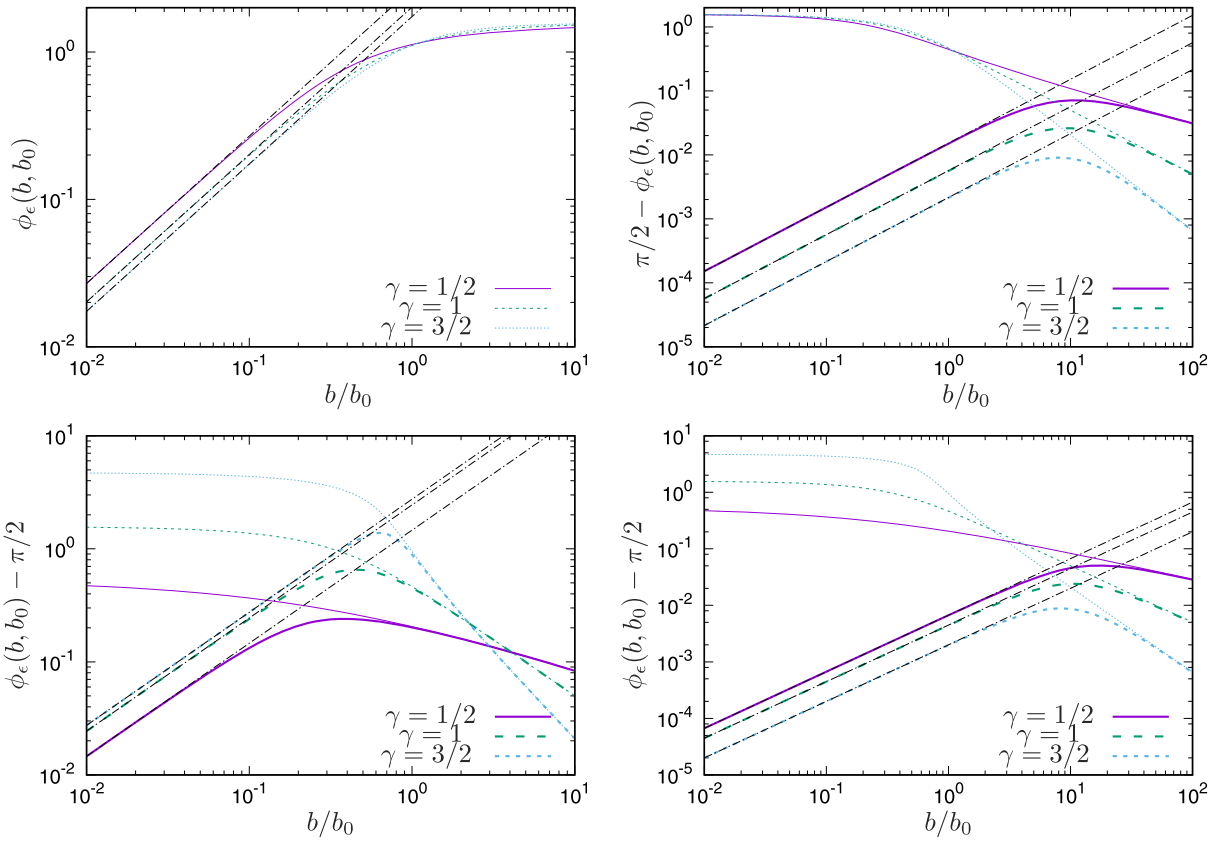

FIG. 7. Top: Numerical computations for repulsive potentials with the Plummer softening. Left: Graph of ϕ_ϵ as a function pf b/b_0 and of the leading order term (dotted-dashed lines) given in Eq. (44) for different values of γ and ϵ/b_0 = 1/10. Right: Graph of ϕ_ϵ for ϵ/b_0 = 10 (thick lines) and the leading order expansion given in Eq. (47) (black dotted-dashed lines). The thin curves correspond to ϕ_0. Bottom: Numerical computations for attractive potentials with the Plummer softening (hard scattering). Left: Graphs of ϕ_ϵ (thick curves) and the theoretical prediction Eq. (44) (black dotted-dashed lines) as a function of b/b_0 for different values of γ and ϵ/b_0 = 1/10. The thin curves correspond to ϕ_0. Right: The same quantity for ϵ/b_0 = 10 and the theoretical prediction Eq. (47) (black dotted-dashed lines). The thin curves correspond to ϕ_0.

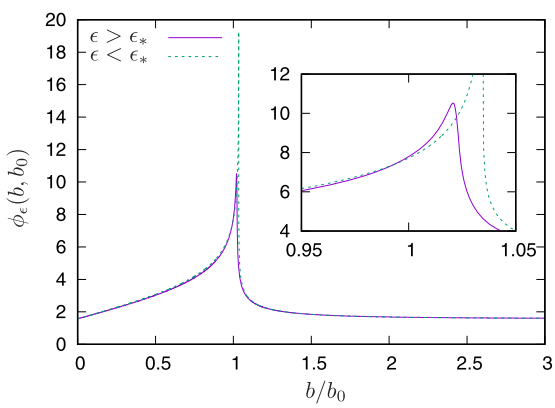

FIG. 8. Plot of ϕ_ϵ as a function of b/b_0 for γ = 5/2 and two different values of the softening. The purple continuous curve corresponds to a value of ϵ slightly larger than $\epsilon_*(b_0, \gamma)$ and the dashed green one to a value of ϵ slightly smaller than $\epsilon_*(b_0, \gamma)$.

curve corresponds to the case in which $\epsilon > \epsilon_*(b_0, \gamma)$. In this case, ϕ_ϵ is a regular function of b, as it can be seen in the inset. The dashed green curve corresponds to the case in which $\epsilon < \epsilon_*(b_0, \gamma)$, for which ϕ_ϵ diverges for $b = b_\sharp(\epsilon)$, which is related to some jump for r_{min} at $b = b_\sharp(\epsilon)$.

V. CONCLUSIONS AND APPLICATIONS

In this paper, we have studied the scattering of two particles interacting with a central potential $v(r) \sim 1/r^\gamma$. This is a generalization of the Rutherford formula of the scattering of two particles interacting via a Coulomb or gravitational force. Unlike the original case, it is not possible to compute in general the deflection angle of the particles explicitly for general $\gamma \neq 1$. We have seen that the problem can be solved in the form of power series, both for the attractive and repulsive case: one for the *weak scattering regime* ($b/b_0 > \beta$) and another one (or two) for the *hard scattering regime* ($b/b_0 < \beta$). We have also studied the case in which the exponent γ of the attractive potential is larger than 2 for which the angular momentum term cannot, in general, prevent the system to collapse and the particles crash. Studying the distance of the closest approach r_{min}, we have found two different behaviors whether γ is smaller or larger than 2:

- If $\gamma < 2$, in the limit $\gamma \to 2^-$ (for any b smaller than some critical value which we have calculated explicitly), the value of r_{min} tends to 0. The trajectories in this limit are a succession of smaller and smaller loops embedded one in the other. An example of such trajectory was given in Fig. 3.
- If $\gamma > 2$, the particles do not crash if the impact factor is larger than some critical value, which we have calculated. For the impact factor slightly larger than this critical value, we have trajectories with $r_{min} \sim b_0$. The particles then *orbit* with distance r_{min} forming a binary, which will be destroyed in a finite time. We gave an example of such trajectories in Fig. 4.

We have also studied the effect of introducing a regularization at small scales in the potential. The conclusions are detailed in Subsection IV E.

One of the motivations of the paper was the computation of the Boltzmann collision operator Eq. (3). With the expressions given in the paper, knowing the velocity distribution function $\varphi(v; t)$, it is straighforward to write a full series expansion of it in the case of pure power-law potentials.

In what follows, we will give an example of application of the results for softened potentials, developed recently in Refs. 7 and 8. In the context of astrophysics or plasma physics, it is natural to be interested in calculating the average change of velocity due to the collisions. It is classical (see, e.g., Ref. 3) to decompose the relative velocity of the particles before the collisions V as the sum of its component along the direction of the initial relative velocity $\mathbf{e}_\parallel$ and the component perpendicular to it $\mathbf{e}_\perp$, i.e.,

$$\mathbf{V} = V_\perp \mathbf{e}_\perp + V_\parallel \mathbf{e}_\parallel. \tag{59}$$

It is possible to compute the average change of velocity $\Delta V_\perp$ and $\Delta V_\parallel$ after a collision has been completed integrating over all the impact factors b

$$\frac{\Delta V_\perp}{V} = \sin(2\phi), \tag{60a}$$

$$\frac{\Delta V_\parallel}{V} = 1 + \cos(2\phi). \tag{60b}$$

One quantity of interest is the average change velocity square, which can be expressed by the integral over all the impact factors, i.e.,

$$\langle \Delta V_\perp^2 \rangle \sim \int_0^R dbb^{d-2} \sin^2\left(2\phi_\epsilon\left(\frac{b}{b_0}\right)\right), \tag{61a}$$

$$\langle \Delta V_\parallel^2 \rangle \sim \int_0^R dbb^{d-2} \left[1 + \cos\left(2\phi_\epsilon\left(\frac{b}{b_0}\right)\right)\right]^2, \tag{61b}$$

where $d > 1$ is the physical dimension and R the size of the system, which is the maximal impact factor available.

In astrophysical or cosmological N-body simulations, the goal is to simulate *collisionless* dynamics sampling a continuous distribution with macroparticles (see, e.g., Ref. 19). The softening used in these simulations is much larger than b_0 (in order to suppress collisional effects), and hence (see Sec. IV), $\phi - \pi/2 \ll 1$. We can therefore write

$$\langle \Delta V_\perp^2 \rangle \sim 4 \int_0^R dbb^{d-2} \left[\phi_\epsilon\left(\frac{b}{b_0}\right) - \frac{\pi}{2}\right]^2 \tag{62}$$

and $\langle \Delta V_\parallel^2 \rangle \ll \langle \Delta V_\perp^2 \rangle$. We can estimate Eq. (62) using the following approximate expression [see Sec. II B and Eq. (12)] for the angle ϕ_ϵ (we will consider explicitly attractive interactions with the Plummer softening to simplify notations, and the compact softening or repulsive case is analogous):

$$\phi_\epsilon - \frac{\pi}{2} \simeq \begin{cases} C_{\epsilon/b_0}(\gamma)\frac{b}{\epsilon} & \text{if } b < \epsilon \\ A(\gamma)\left(\frac{b_0}{b}\right)^\gamma & \text{if } b > \epsilon. \end{cases} \tag{63}$$

Using Eq. (63) to compute integral (62), considering softenings such that $b_0 \ll \epsilon \ll R$, we get the scaling, for $\gamma > (d-1)/2$,

$$\langle \Delta V_\perp^2 \rangle \sim b_0^{2\gamma} \epsilon^{d-1-2\gamma}, \tag{64}$$

where we have used the asymptotic value of $C_\epsilon(\gamma)$ Eq. (56). Notice that impact factors smaller or larger than ϵ contribute to the scaling (64). In the limiting case $\gamma = (d-1)/2$, we get

$$\langle \Delta V_\perp^2 \rangle \sim b_0^2 \ln\left(\frac{R}{\epsilon}\right). \tag{65}$$

In this case, contributions of collisions with $b < \epsilon$ are negligible. For $\gamma < (d-1)/2$, the effect of the softening is negligible because the main contribution to the change of velocity is given by impact factors $b \sim R$.

ACKNOWLEDGMENTS

We thank M. Joyce for many useful discussions and comments.

APPENDIX A: DERIVATION OF THE SCATTERING FORMULA

Let us consider the scattering of two isolated particles. It is convenient to use the center of mass frame to transform the two-particle problem into a one-particle one. Let us consider that particles have masses m_1 and m_2, and their positions are $\mathbf{r}_1$ and $\mathbf{r}_2$, respectively. We define their relative position as

$$\mathbf{r} = \mathbf{r}_1 - \mathbf{r}_2 \tag{A1}$$

and fix the origin of the frame at the center of mass, i.e.,

$$m_1\mathbf{r}_1 + m_2\mathbf{r}_2 = \mathbf{0}. \tag{A2}$$

The relation between the positions of the particles in the center of mass frame r and in the laboratory frame is, using Eqs. (A1) and (A2),

$$\mathbf{r}_1 = \frac{m}{m_1}\mathbf{r}, \tag{A3a}$$

$$\mathbf{r}_2 = -\frac{m}{m_2}\mathbf{r}, \tag{A3b}$$

where we have defined the reduced mass

$$m = \frac{m_1 m_2}{m_1 + m_2}. \tag{A4}$$

In the center of mass frame, the collision occurs as depicted in Fig. 1 in which appears the definition of the impact factor b, the angle of the closest approach ϕ, and the angle of deflection χ, which is $\chi = 2\phi$. In order to define the angles with the usual mathematical signs, the incident particle comes from $+\infty$. This picture assumes that the two particles are far away from each other for $t \to -\infty$ and for $t \to +\infty$. The angle ϕ can be calculated, as a function of the impact factor b, using the classical formula[16]

$$\phi(b) = \int_{r_{min}}^{\infty} \frac{(b/r^2)dr}{\sqrt{1-(b/r)^2 - 2v(r)/(mu^2)}}, \tag{A5}$$

where u is the asymptotic velocity of the incident particle at $+\infty$ ($u = |\dot{\mathbf{r}}|$). The quantity r_{min} is the largest positive root of the denominator, i.e., of

$$W(r) = 1 - (b/r)^2 - 2v(r)/mu^2. \tag{A6}$$

We consider the pure power-law pair potential

$$v(r) = \frac{g}{r^\gamma}, \qquad \gamma > 0, \tag{A7}$$

with $g \neq 0$, where $g > 0$ corresponds to a repulsive interaction and $g < 0$ to an attractive one. We introduce the characteristic scale

$$b_0 = \left(\frac{2|g|}{mu^2}\right)^{1/\gamma}, \tag{A8}$$

which allows us to rewrite Eq. (A5) as

$$\phi(b) = \int_{r_{min}}^{\infty} \frac{(b/r^2)dr}{\sqrt{1-(b/r)^2 \mp (b_0/r)^\gamma}}. \tag{A9}$$

Now, the "minus" sign in the denominator corresponds to a repulsive interaction while the "plus" sign to an attractive one. By using the change of variables $r = b/x$, it is possible to rewrite Eq. (A9) in the following form:

$$\phi(b/b_0) = \int_0^{x_{max}} \frac{dx}{\sqrt{1 - x^2 \mp (b_0/b)^\gamma x^\gamma}}, \tag{A10}$$

where x_{max} is the smallest positive root of the denominator. Since x_{max} is a function of b/b_0 depending only on γ, Eq. (A10) shows explicitly that ϕ is also a function of b/b_0 depending only on γ. Equation (A9) can be solved explicitly only in few cases (e.g., gravity in $d = 3$ which is given by $\gamma = 1$); for the general case, approximations or numerical computation of the integral should be used.

APPENDIX B: SOME TECHNICAL MATHEMATICAL DETAILS

In this appendix, we give mathematical details of some derivations given in the paper.

1. Justification of the leading order expansion Eq. (39)

To completely justify the expansion Eq. (39), we have to pay attention to the z's close to z_{max}. Notice first that

$$dr/dz = \sqrt{-2W_b(r_*)/W_b''(r_*)}(1 + \mathcal{O}(z/z_{max}))$$

and that

$$r(z)^{-2} = (r_* + \mathcal{O}(z/z_{max}))^{-2};$$

hence, the asymptotics $r(z) \approx r_* \approx r_*(\beta b_0)$ and $dr/dz \approx \sqrt{-2W_b(r_*)/W_b''(r_*)}$ are not completely true for $z \sim z_{max}$. We therefore split the right-hand side of Eq. (38) as

$$I_1 + I_2 = \frac{b}{\sqrt{-W_b(r_*)}} \int_1^{z_{max}/\ln(z_{max})} \frac{r(z)^{-2}\, dr/dz}{\sqrt{z^2 - 1}}\, dz + \frac{b}{\sqrt{-W_b(r_*)}} \int_{z_{max}/\ln(z_{max})}^{z_{max}} \frac{r(z)^{-2}\, dr/dz}{\sqrt{z^2 - 1}}\, dz.$$

In I_1, we have $0 \leqslant z/z_{max} \leqslant 1/|\ln z_{max}| = o(1)$; thus,

$$dr/dz = \sqrt{-2W_b(r_*)/W_b''(r_*)}(1 + o(1))$$

and

$$r(z)^{-2} = (r_* + o(1))^{-2} = r_*(\beta b_0)^{-2} + o(1),$$

which yield

$$I_1 \approx b\sqrt{\frac{2}{W_b''(r_*(\beta b_0))}} \int_1^{z_{max}/\ln(z_{max})} \frac{r_*(\beta b_0)^{-2}\, dz}{\sqrt{z^2 - 1}} \approx \sqrt{\frac{2}{r_*(\beta b_0)^4 W_b''(r_*(\beta b_0))}} \ln(z_{max}).$$

Turning back to I_2, where $1 \ll z_{max}/\ln(z_{max}) \leqslant z \leqslant z_{max}$, we simply use that $r(z)^{-2} = \mathcal{O}(1)$ and that $dr/dz = \sqrt{-2W_b(r_*)}\mathcal{O}(1)$; thus,

$$I_2 = \mathcal{O}\left(\int_{z_{max}/\ln(z_{max})}^{z_{max}} \frac{dz}{z}\right) = \mathcal{O}(\ln(\ln z_{max})) \ll \ln(z_{max}).$$

This concludes the justification of Eq. (39).

2. Bounding the function $\frac{1-x^2}{F(x,r_{min}/\epsilon)}$

We prove here that the function $x \mapsto \frac{1-x^2}{F(x,r_{min}/\epsilon)}$ is bounded on $[0, 1]$, independently of $b \ll b_0$ (for the Plummer softening). We recall that for the regime ($\epsilon < b_0$ and $b \ll b_0$), we are studying $r_{min} \approx b_0\sqrt{1 - (\epsilon/b_0)^2}$, thus $r_{min}/\epsilon \approx (\epsilon/b_0)^{-1}\sqrt{1 - (\epsilon/b_0)^2}$.

Let us first work on the interval $[0, 1/2]$. Then, $F(x, r_{min}/\epsilon) = 1 - \mathcal{V}^{\mathrm{Pl}}(r_{min}/(\epsilon x))/\mathcal{V}^{\mathrm{Pl}}(r_{min}/\epsilon)$ is decreasing with respect to x since $\mathcal{V}^{\mathrm{Pl}}(R) = (1 + R^2)^{-\gamma/2}$ is decreasing on $[0, +\infty)$; hence, for $0 \leqslant x \leqslant 1/2$,

$$0 \leqslant \frac{1 - x^2}{F(x, r_{min}/\epsilon)} \leqslant \frac{1}{F(x, r_{min}/\epsilon)} \leqslant \frac{1}{F(1/2, r_{min}/\epsilon)}.$$

The right-hand side does not depend on x and is equal to

$$\left(1-\frac{\mathcal{V}^{\mathrm{Pl}}(2r_{min}/\epsilon)}{\mathcal{V}^{\mathrm{Pl}}(r_{min}/\epsilon)}\right)^{-1}\approx\left(1-\frac{\mathcal{V}^{\mathrm{Pl}}(2(\epsilon/b_0)^{-1}\sqrt{1-(\epsilon/b_0)^2})}{\mathcal{V}^{\mathrm{Pl}}((\epsilon/b_0)^{-1}\sqrt{1-(\epsilon/b_0)^2})}\right)^{-1},$$

which gives the desired upper bound on [0, 1/2].

We now work on [1/2, 1] and use that $\frac{d}{dx}\mathcal{V}^{\mathrm{Pl}}(r_{min}/(\epsilon x)) = -(r_{min}/(\epsilon x^2))(\mathcal{V}^{\mathrm{Pl}})'(r_{min}/(\epsilon x)) \geqslant m$ for some positive constant $m = m(\epsilon/b_0)$ independent of b since $\mathcal{V}^{\mathrm{Pl}}$ is decreasing on $[0, +\infty)$. As a consequence of the mean value theorem, we get

$$0 \leqslant \frac{1-x^2}{F(x, r_{min}/\epsilon)} = \frac{(1+x)(1-x)}{F(x, r_{min}/\epsilon) - F(1, r_{min}/\epsilon)} \leqslant \frac{2}{m}.$$

This concludes the proof of the upper bound on [0, 1/2].

3. Justification of the relation Eq. (49)

If $\epsilon/b_0 \gg 1$, we may use, for instance, the Taylor expansion of the square root to deduce

$$\begin{aligned}\tilde{B}_{\epsilon/b_0}(\gamma) &\approx \int_0^{+\infty}\left(1-\frac{1}{\sqrt{1+\frac{1}{(\epsilon/b_0)^\gamma-1}\left(\mathcal{V}^{\mathrm{Pl}}(0)-\mathcal{V}^{\mathrm{Pl}}(y)\right)}}\right)\frac{dy}{y^2} \approx \frac{1}{(\epsilon/b_0)^\gamma-1}\int_0^{+\infty}\frac{\mathcal{V}^{\mathrm{Pl}}(0)-\mathcal{V}^{\mathrm{Pl}}(y)}{2y^2}\,dy\\ &\approx \frac{1}{(\epsilon/b_0)^\gamma}\int_0^{+\infty}\frac{1-(1+y^2)^{-\gamma/2}}{2y^2}\,dy = \frac{\gamma}{4(\epsilon/b_0)^\gamma}\int_0^{+\infty}(1+y^2)^{-\gamma/2-1}\,dy\\ &= \frac{\gamma}{4(\epsilon/b_0)^\gamma}\int_0^{\pi/2}\cos^\gamma(\vartheta)\,d\vartheta = \frac{\sqrt{\pi}}{4(\epsilon/b_0)^\gamma}\frac{\Gamma\left(\frac{\gamma+1}{2}\right)}{\Gamma\left(\frac{\gamma}{2}\right)}\end{aligned}$$

by first integration by parts and then the use of the substitution $y = \tan\vartheta$.

REFERENCES

[1] R. M. Eisberg and C. E. Porter, "Scattering of alpha particles," Rev. Mod. Phys. **33**, 190–230 (1961).
[2] R. Balescu, *Statistical Mechanics: Matter Out of Equilibrium* (Imperial College Press, 1997).
[3] J. Binney and S. Tremaine, *Galactic Dynamics* (Princeton University Press, 2008).
[4] I. Karamouzas, B. Skinner, and S. J. Guy, "Universal power law governing pedestrian interactions," Phys. Rev. Lett. **113**, 238701 (2014).
[5] E. Rutherford, "The scattering of α and β particles by matter and the structure of the atom," Philos. Mag. **21**(6), 669 (1911).
[6] S. Chandrasekhar, *Principles of Stellar Dynamics* (University of Chicago Press, 1942).
[7] A. Gabrielli, M. Joyce, and B. Marcos, "Quasistationary states and the range of pair interactions," Phys. Rev. Lett. **105**(21), 210602 (2010).
[8] B. Marcos, A. Gabrielli, and M. Joyce, "Formation and relaxation of quasi-stationary states in three dimensional systems with long-range pair interactions," Phys. Rev. E **96**, 032102 (2017).
[9] E. W. McDaniel, *Collision Phenomena in Ionized Gases* (Wiley, 1964).
[10] *Springer Handbook of Atomic, Molecular, and Optical Physics*, edited by W. F. Drake Gordon (Springer-Verlag New York, 2006).
[11] R. G. Newton, *Scattering Theory of Waves and Particles* (Dover Publications, Inc., Mineola, NY, 2002).
[12] J. Kunc, "A general relationship between the scattering angle and the impact parameter in collisions driven by repulsive potentials," J. Phys. D: Appl. Phys. **30**, 1334–1340 (1997).
[13] H. Friedrich, *Scattering Theory* (Springer-Verlag Berlin Heidelberg, 2013), Vol. 872.
[14] E. T. Whittaker, *A Treatise on the Analytical Dynamics of Particles and Rigid Bodies*, Cambridge Mathematical Library, 4th ed. (Cambridge University Press, Cambridge, 1947).
[15] H. M. Mott-Smith, "Collision trajectories for inverse power intermolecular potentials," Phys. Fluids **3**, 721–724 (1960).
[16] L. D. Landau and E. M. Lifshitz, *Mechanics* (Butterworth-Heinemann, 1976).
[17] E. Athanassoula, C. L. Vozikis, and J. C. Lambert, "Relaxation times calculated from angular deflections," Astron. Astrophys. **376**, 1135–1146 (2001).
[18] V. Springel *et al.*, "Simulating the joint evolution of quasars, galaxies and their large-scale distribution," Nature **435**, 629–636 (2005).
[19] E. Athanassoula, E. Fady, J. C. Lambert, and A. Bosma, "Optimal softening for force calculations in collisionless N-body simulations," Mon. Not. R. Astron. Soc. **314**, 475–488 (2000).
[20] M. Abramowitz and I. Stegun, *Handbook of Mathematical Functions with Formulas, Graphs, and Mathematical Tables*, National Bureau of Standards Applied Mathematics Series (U.S. Government Printing Office, Washington, D.C., 1964), Vol. 55.

Quasistationary States and the Range of Pair Interactions

A. Gabrielli,[1,2] M. Joyce,[3,4] and B. Marcos[5]

[1]SMC, CNR-INFM, Physics Department, University "Sapienza" of Rome, Piazzale Aldo Moro 2, 00185-Rome, Italy
[2]Istituto dei Sistemi Complessi—CNR, Via dei Taurini 19, 00185-Rome, Italy
[3]Laboratoire de Physique Nucléaire et Hautes Énergies, Université Pierre et Marie Curie—Paris 6, CNRS IN2P3 UMR 7585, 4 Place Jussieu, 75752 Paris Cedex 05, France
[4]Laboratoire de Physique Théorique de la Matière Condensée, Université Pierre et Marie Curie—Paris 6, CNRS UMR 7600, 4 Place Jussieu, 75752 Paris Cedex 05, France
[5]Laboratoire J.-A. Dieudonné, UMR 6621, Université de Nice—Sophia Antipolis, Parc Valrose 06108 Nice Cedex 02, France

(Received 28 April 2010; revised manuscript received 15 October 2010; published 16 November 2010)

"Quasistationary" states are approximately time independent out of equilibrium states which have been observed in a variety of systems of particles interacting by long-range interactions. We investigate here the conditions of their occurrence for a generic pair interaction $V(r \to \infty) \sim 1/r^\gamma$ with $\gamma > 0$, in $d > 1$ dimensions. We generalize analytic calculations known for gravity in $d = 3$ to determine the scaling parametric dependences of their relaxation rates due to two-body collisions, and report extensive numerical simulations testing their validity. Our results lead to the conclusion that, for $\gamma < d - 1$, the existence of quasistationary states is ensured by the large distance behavior of the interaction alone, while for $\gamma > d - 1$ it is conditioned on the short distance properties of the interaction, requiring the presence of a sufficiently large soft core in the interaction potential.

DOI: 10.1103/PhysRevLett.105.210602 PACS numbers: 05.20.−y, 04.40.−b, 05.45.Pq, 05.90.+m

In recent years there has been renewed interest in the statistical physics of long-range interactions (for a review, see, e.g., [1]), a subject which has been treated otherwise mostly in the astrophysical literature for the specific case of gravity. The defining property of such interactions is the nonadditivity of the potential energy of a uniform system, which corresponds to the nonintegrability at large distances of the associated pair interaction, i.e., a pair interaction $V(r \to \infty) \sim 1/r^\gamma$ with $\gamma < d$ in d space dimensions. The equilibrium thermodynamic analysis of these systems is very different to the canonical one for short-ranged interactions (with $\gamma > d$), leading notably to inhomogeneous equilibria as well as other unusual properties—e.g., nonequivalence of the statistical ensembles, negative specific heat in the microcanonical ensemble. Studies of simple toy models have shown that, like for gravity in $d = 3$, these equilibria (when defined) are reached only on time scales which are extremely long compared to those characteristic of the mean-field dynamics. On the latter time scales one observes typically the formation, through "violent relaxation," of so-called "quasistationary" states (QSS), interpreted theoretically as stable stationary states of the Vlasov equation (which describes the kinetics in the mean-field limit). In this Letter we consider whether the occurrence of such QSS driven by mean-field dynamics can be considered as a behavior arising generically when there are long-range interactions in play. Using both simple analytical results and numerical simulations, we argue for the conclusion that it is only for $\gamma < d - 1$, i.e., when the pair force is absolutely integrable at large separations, that QSS can be expected to occur independently of the short distance properties of the interaction. For $\gamma > d - 1$, on the other hand, their occurrence will be conditioned strongly also on short distance properties, and thus cannot be considered to be a result simply of the long-range nature of the interaction. Our analysis shows the relevance of a classification of the range of interactions according to the convergence properties of forces rather than potential energies which has been formalized in [2].

We proceed by first generalizing a calculation originally given by Chandrasekhar for Newtonian gravity to a system of N particles interacting by a pair potential $V(r) = \frac{g}{r^\gamma}$ (where g is a coupling constant). This calculation, which numerical studies indicate is accurate both parametrically and quantitatively for gravity (see, e.g., [3–7]), will give us an estimate of Γ_2, the relaxation rate due to two-body collisions (i.e., the inverse of the time scale on which a typical particle's velocity is randomized by such interactions). Denoting by $\tau_{\rm mf}$ the characteristic time for the formation of a QSS (i.e., of the mean-field dynamics), the criterion for the existence of QSS we will then study is

$$\Gamma_2 \tau_{\rm mf} \to 0 \quad \text{when } N \to \infty, \tag{1}$$

where the limit $N \to \infty$ corresponds to the mean-field or Vlasov limit [1]. Indeed, if this condition is not satisfied, it implies that there is no mean-field regime in which QSS may form.

Following the treatment for the case of gravity (see, e.g., [3], Sec. 1.2.1) we consider a test particle of velocity v crossing a system in a QSS, assumed spherical and of radius R and approximated as homogeneous. We estimate first the rate of relaxation due to soft two-body collisions by calculating Δv^2, the mean square velocity change of a

particle per crossing (i.e. in a time of order $\tau_{\rm mf}$) due to such collisions. It is straightforward to show that

$$\frac{\Delta v^2}{v^2} \sim N\left(\frac{g}{mv^2R^\gamma}\right)^2 \int_{b_{\rm min}/R}^{b_{\rm max}/R} \frac{dx}{x^{2\gamma-d+2}}, \tag{2}$$

where $b_{\rm min}$ is the minimal impact parameter at which the scattering is soft (i.e., the deflection angle is small), defined by

$$\frac{|g|}{mv^2 b_{\rm min}^\gamma} \sim 1, \tag{3}$$

and $b_{\rm max}$ is the maximal impact parameter for two-body collisions. In these formulas, and in what follows below, we use the symbol $\sim$ to indicate that the numerical factors in all expressions have been dropped, leaving only the parametric dependences which are relevant to our considerations here. In the case of gravity in $d = 3$ the choice of $b_{\rm max}$ has been a source of debate, with numerical simulations indicating that $b_{\rm max} \sim R$ accounts better for results than the more evident choice $b_{\rm max} \sim \ell$, the mean interparticle separation (see, e.g., [4]). We consider in what follows both possibilities, and will see that our central results are not in fact sensitive to which is correct. We have also implicitly assumed $d > 1$ and $\gamma > 0$.

We now write

$$\Gamma_2\tau_{\rm mf} = \Gamma_{\rm soft}\tau_{\rm mf} + \Gamma_{\rm hard}\tau_{\rm mf}, \tag{4}$$

where the first contribution is that considered above, and the second is the remaining one from hard scatterings, i.e., collisions with impact factors $b < b_{\rm min}$. Taking now that $\tau_{\rm mf} \sim \frac{R}{v}$, it is straightforward to deduce from Eq. (2) that, for sufficiently large N,

$$\Gamma_{\rm soft}\tau_{\rm mf} \sim \begin{cases} N^{-1}\left(\frac{b_{\rm max}}{R}\right)^{-2\gamma+d-1} & \text{if } \gamma < (d-1)/2, \\ N^{-1}\left(\frac{R}{b_{\rm min}}\right)^{2\gamma-d+1} & \text{if } \gamma > (d-1)/2, \end{cases} \tag{5}$$

if $b_{\rm min}/b_{\rm max} \ll 1$ for large N. To infer these scalings we need only (as in the corresponding derivation for the case of gravity [3]) use the fact that the QSS is, by definition, a virialized state, i.e., we take

$$\frac{g}{mv^2R^\gamma} \sim \frac{1}{N}\frac{gN^2}{(mNv^2)R^\gamma} \sim \frac{1}{N}\frac{U}{K} \sim \frac{1}{N}, \tag{6}$$

where U, the total potential energy of the QSS, and K, its total kinetic energy, have a fixed ratio because of virialization. This scaling with N corresponds to that in the usual mean-field or Vlasov limit, in which U and K both scale in the same way with N.

Using again the scaling Eq. (6), the definition Eq. (3) gives

$$b_{\rm min} \sim RN^{-(1/\gamma)}. \tag{7}$$

Note first that this implies $b_{\rm min}/b_{\rm max} \to 0$ as $N \to \infty$ for any $\gamma > 0$ if $b_{\rm max} \sim R$, and for any $0 < \gamma < d$ if $b_{\rm max} \sim \ell \sim RN^{-1/d}$, so that Eq. (5) is indeed valid in these cases. Using now again Eq. (7) in Eq. (5) we obtain the scaling

$$\Gamma_{\rm soft}\tau_{\rm mf} \sim \begin{cases} N^{-(1+|\delta|)} & \text{if } \gamma < (d-1)/2, \\ N^{-(d-1-\gamma)/\gamma} & \text{if } \gamma > (d-1)/2, \end{cases} \tag{8}$$

where $\delta = 0$ if $b_{\rm max} \sim R$, and $\delta = (-2\gamma + d - 1)/d$ if $b_{\rm max} \sim RN^{-1/d}$. It follows that, for $\gamma > d - 1$, the contribution of soft two-body scatterings alone diverges at large N, so that the criterion (1) cannot be satisfied in this case for the "candidate" QSS. For any $\gamma < d - 1$, on the other hand, the contribution $\Gamma_{\rm soft}\tau_{\rm mf}$ vanishes as $N \to \infty$. It is simple to show, in this case, that $\Gamma_{\rm hard}\tau_{\rm mf}$ also goes to zero when $N \to \infty$, and thus that the condition (1) for the existence of QSS may be satisfied. To do so it is sufficient to consider that this contribution can be bounded below by that from an "exactly hard" core with radius $\epsilon = b_{\rm min}$, i.e., $V(r) = \infty$ for $r < b_{\rm min}$. Estimating the collision rate on such a core as $\Gamma_{\rm hc} \sim n\sigma v$ where n is the mean density and $\sigma \sim \epsilon^{d-1}$ (the cross section), we obtain

$$\Gamma_{\rm hc}\tau_{\rm mf} \sim N\left(\frac{\epsilon}{R}\right)^{d-1} \sim N^{-(d-1-\gamma)/\gamma} \tag{9}$$

when we take $\epsilon = b_{\rm min}$, with the latter scaling as in Eq. (7). It follows that $\Gamma_{\rm hard}\tau_{\rm mf} \le \Gamma_{\rm hc}\tau_{\rm mf} \to 0$ as $N \to \infty$ for $\gamma < d - 1$. Further it follows from the inferred scaling of $\Gamma_{\rm hc}\tau_{\rm mf}$ that, for $\gamma < d - 1$, the total rate Γ_2 will scale as calculated for $\Gamma_{\rm soft}$ in Eq. (8). In other words, an exact calculation including $\Gamma_{\rm hard}$ should give, at most, a Γ_2 larger than $\Gamma_{\rm soft}$ by a numerical factor.

A corollary of these results, which are summarized in Table I, is that, for a QSS to exist in the case that $\gamma > d - 1$, the pair potential must include a sufficiently large soft core. Indeed to remove the divergence of $\Gamma_{\rm soft}\tau_{\rm mf}$ in this case, we must introduce a smoothing of the potential at a scale ϵ which vanishes more slowly than $b_{\rm min}$ in Eq. (7). In this case $\Gamma_{\rm soft}\tau_{\rm mf}$ is given by the second expression in Eq. (5) but with $b_{\rm min}$ replaced by ϵ. Keeping ϵ/R constant, for example, gives $\Gamma_{\rm soft}\tau_{\rm mf} \sim N^{-1} \to 0$ as $N \to \infty$ for any γ. If the core is "exactly soft," i.e., $V(r) = g/\epsilon^\gamma$ for $r < \epsilon$ we have $\Gamma_{\rm hard} = 0$ and the satisfaction of the condition Eq. (1) follows. If the core is hard, as envisaged above, it is clear that the same is not true. Indeed it is simple to check using Eq. (9) that it is not possible to choose ϵ in order to satisfy both $\Gamma_{\rm hc}\tau_{\rm mf} \to 0$ and $\Gamma_{\rm soft}\tau_{\rm mf} \to 0$ simultaneously as $N \to \infty$ for $\gamma > d - 1$.

TABLE I. Summary of two-body collision rates (without core).

$0 < \gamma < \frac{d-1}{2}$	Soft collisions at $\sim b_{\rm max}$ dominate $\Gamma_{\rm soft}\tau_{\rm mf} \sim N^{-(1+\lvert\delta\rvert)} \gg \Gamma_{\rm hard}\tau_{\rm mf}$
$\frac{d-1}{2} < \gamma < d - 1$	Collisions at $\sim b_{\rm min}$ dominate $\Gamma_{\rm soft}\tau_{\rm mf} \sim N^{-(d-1-\gamma/\gamma)} \ge \Gamma_{\rm hard}\tau_{\rm mf}$
$\gamma > d - 1$	$\Gamma_{\rm soft}\tau_{\rm mf}$ and $\Gamma_{\rm hard}\tau_{\rm mf}$ divergent in N

These results lead then to the primary conjecture of this article: for pair potentials with $V(r \to \infty) \sim 1/r^\gamma$, QSS can always exist if there is a sufficiently large soft core, but only for $\gamma < d - 1$ can they exist when such a core is not present (i.e., when its size $\epsilon \to 0$). The validity of this conclusion rests evidently on the assumption that the dominant correction to the mean-field dynamics is, just as for gravity in $d = 3$, two-body collisionality. More specifically we also require the parametric dependences of the inferred relaxation rates, which have been derived using various simplifying approximations (notably that of homogeneity both in configuration and velocity space). We now present results of numerical simulations (in $d = 3$) which test their validity. We focus here on the crucial result above: the parametric dependence of the two-body scattering rate due to soft scatterings in Eq. (5), for the range $\gamma > (d-1)/2$.

We perform molecular dynamics simulations using a version of the publicly available gravity code GADGET2 [8]. We have modified the force routine in the tree-PM version of the code to treat a generic power-law pair potential with a core. As in the original code we use a soft repulsive core, with compact support: for $r < \epsilon$ $V(r)$ decreases continuously to a minimum at $r \approx \epsilon/2$ and then increases back to a local maximum $V(r = 0) = 0$. In what follows the values of ϵ quoted correspond to the separation at which the force is still attractive but has dropped to approximately 30% of its value in absence of smoothing. We consider here the attractive case (i.e. $g < 0$). The simulations are checked using simple convergence tests on the numerical parameters, and their accuracy is monitored using energy conservation. For the time steps used here it is typically of order 0.1% over the whole run, orders of magnitude smaller than the typical variation of the kinetic or potential energy over the same time. As initial conditions we take the N particles on the sites of a simple cubic lattice of side L_0 and ascribe random velocities uniformly distributed in an interval $[-\Delta, \Delta]$ in each direction (i.e., "waterbag" type initial conditions in phase space). The parameter Δ is chosen so that initial virial ratio is unity, i.e., $2K/|U| = \gamma$. We choose this initial condition because it would be expected to be close to a QSS to which (collisionless) relaxation should occur "gently." The system is enclosed in a cubic box of side $L \approx 2L_0$ (and centered on the same point as the initial cube of particles). Energy conserving "soft" reflecting boundary conditions are used in the dynamics, i.e., at each time step particles which have moved outside the box have the appropriate components of their velocity inverted. The results we report here required runs lasting as long as two weeks on up to 16 processors.

Shown in Fig. 1 is the evolution of the potential energy U as a function of time, for a pair potential with $\gamma = 5/4$ and $\epsilon/L = 0.01$, for the different values of N indicated. We have defined $\tau_{\rm mf} = \sqrt{mL_0^{\gamma+2}/gN}$, which, given that $L_0 \sim R$, is equivalent parametrically to the definition used above, assuming the scaling in Eq. (6). The macroscopic behavior monitored in this plot is clearly very consistent with what has been anticipated, in line with the typical behavior observed in self-gravitating systems and other systems with long-range interactions studied in the literature: there is a first phase of "violent" (collisionless) relaxation towards an approximate equilibrium, the QSS, which then evolves itself in a second phase on a time scale which clearly depends on N. The first phase, on the other hand, should be N independent: as N increases we see that the different curves are increasingly well superimposed at early times.

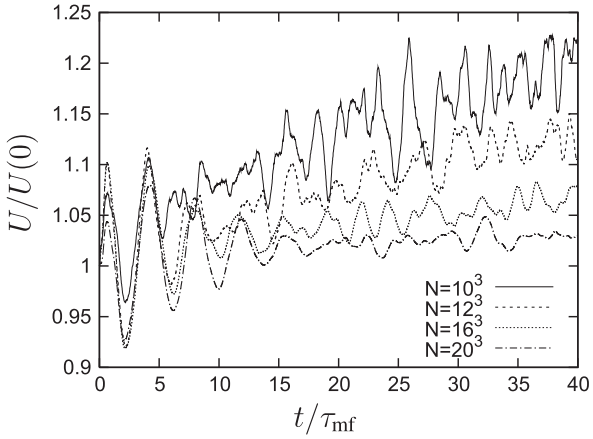

FIG. 1. Temporal evolution of the total potential energy U divided by its initial value $U(0)$, for $\gamma = 1.25$ and a soft core $\epsilon/L = 0.01$, for the different N indicated.

Shown in Fig. 2 are, for the two cases $\gamma = 5/4$ and $\gamma = 3/2$, our measurements of the relaxation rate $\Gamma_{\rm relax}$, as a function of N (upper panel) at a chosen fixed ϵ, and as a function ϵ (lower panel) at fixed chosen N. The estimate of $\Gamma_{\rm relax}$ is obtained simply from the slope of the potential energy plotted as a function of time, in the region in each case where this is well fit by a linear behavior, i.e., we take $\Gamma_{\rm relax} = d(\ln U)/dt$ at $t \to 0$. Each point corresponds to one numerical simulation. Note that for these determinations we consider thus only the evolution away from, but still close to, the QSS. Further results on the longer time evolution of these systems, and, in particular, the compatibility of the fully relaxed states with those predicted analytically for this case in [9] (and related numerical studies in [10]) will be given elsewhere.

The upper panel of Fig. 2 includes a line showing the scaling proportional to $1/N$ predicted by Eq. (5) at fixed $b_{\rm min} = \epsilon$. The agreement is clearly very good. Further it is simple to verify that the results are quantitatively very coherent with the prediction: taking $R \approx L_0/2 \approx L/4$, Eq. (5) fit the normalizations of the plot with a prefactor of order unity in both cases. While the degree of this concordance—despite the many approximations which inevitably limit the accuracy we can expect, and the fact that we have dropped all numerical factors in our derivation—is clearly just fortuitous, this quantitative coherence of the results confirms their solidity.

The lower panel of Fig. 2 shows likewise excellent agreement with the predictions above. On it are shown

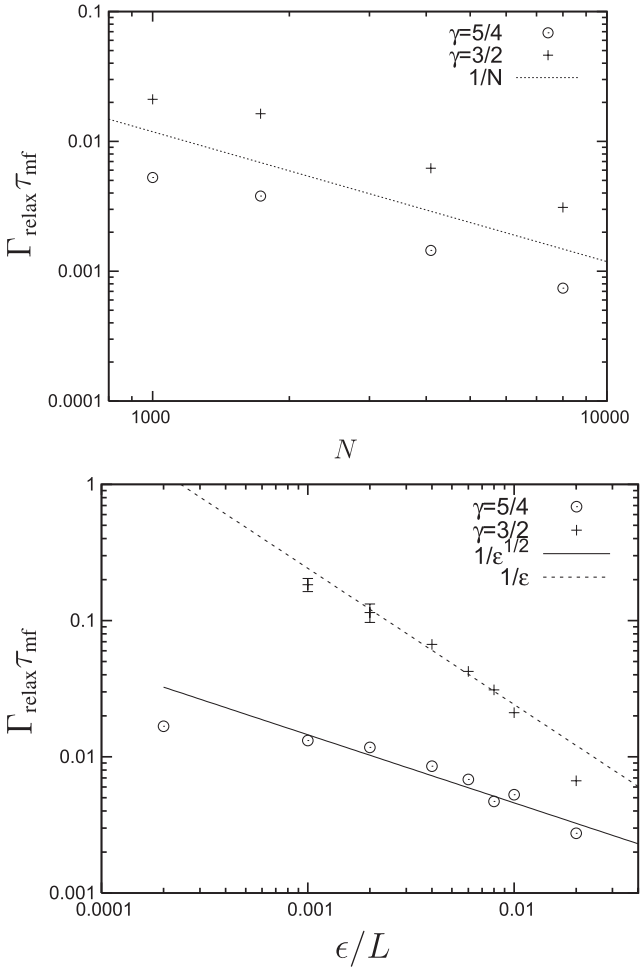

FIG. 2. Estimated relaxation rate $\Gamma_{\rm relax}$ as a function of N at fixed $\epsilon/L = 0.01$ (upper panel), and as a function of ϵ at fixed $N = 10^3$ (lower panel).

lines corresponding to the behavior of Eq. (5) at fixed N, when we replace $b_{\rm min}$ by ϵ. As discussed above, this scaling is predicted to be valid in the regime $b_{\rm min} < \epsilon < b_{\rm max}$. Below $b_{\rm min}$ we expect the rates to reach an asymptotic ϵ-independent value of order those estimated in Eq. (8). The behaviors in the plot are very coherent with these predictions, for values of $b_{\rm min}$ which are in good agreement with Eq. (7), taking again $R \approx L/4$. While we have not predicted the value of $b_{\rm max}$, the downward deviation (corresponding to a reduction in scattering rate) from the fit at larger ϵ occurs at a value very consistent in each case with the measured mean interparticle distance.

We note that this last plot explains why we consider only γ up to $\gamma = 3/2$, and indeed why we have not tried to verify more directly the scalings in Eq. (8) using simulations with $\epsilon \to 0$. The reason is that, in order to measure the relaxation rates, we need to access the regime $\Gamma_{\rm relax}\tau_{\rm mf} \ll 1$, i.e., we need to have a reasonable separation between the times scale of the collisionless dynamics (and formation of QSS) and the relaxation time scale. At $N = 10^3$ we see that $\gamma = 3/2$ is already at this limit for the smallest ϵ, and the error bars on these points reflect the greater difficulty we have in making the measurement in these cases. The only remedy is to increase N, which, however, is prohibitively expensive numerically, in particular, at small ϵ where the proper integration of the (few) hard collisions included requires significant decrease in the time stepping.

Finally, a few remarks on the relation of these results to some of the extensive recent literature on QSS (see [1] for references). The determination of the N dependence of QSS lifetimes has been much emphasized, both as a target for phenomenological studies of toy models, and for theoretical studies of the problem. Our results show that such lifetimes can be expected to depend, in general, not just on N, but also on the parameters characterizing the short distance properties of the potential. While for $\gamma < d - 1$ a limit $\epsilon = 0$ may be defined [and gives the scaling of Eq. (8)], for $\gamma > d - 1$ this is not possible and the scaling of the relaxation rate will depend necessarily on how ϵ scales with N. It would be interesting to extend our numerical simulations to explore the robustness of QSS notably to effects which may come into play in more physically realistic settings: as shown by a recent study [11] of a toy model, the introduction of stochasticity in the dynamics may also destroy QSS. We emphasize that our results here apply only to the particular (albeit broad) class of models considered, and *a priori* not, e.g., to long-range spin models in which there is no equivalent of two-body collisions. It remains an interesting open question to determine in a broader such context the conditions for the existence of QSS on the spatial dependence of the interaction.

We acknowledge many useful discussions with F. Sicard. This work was partly supported by the ANR 09-JCJC-009401 INTERLOP project.

[1] A. Campa, T. Dauxois, and S. Ruffo, Phys. Rep. **480**, 57 (2009).
[2] A. Gabrielli, M. Joyce, B. Marcos, and F. Sicard, J. Stat. Phys. (to be published).
[3] J. Binney and S. Tremaine, *Galactic Dynamics* (Princeton University Press, Princeton, NJ, 1994).
[4] C. Theis, Astron. Astrophys. **330**, 1180 (1998).
[5] C. Theis and R. Spurzem, Astron. Astrophys. **341**, 361 (1999).
[6] J. Diemand, B. Moore, J. Stadel, and S. Kazantzidis, Mon. Not. R. Astron. Soc. **348**, 977 (2004).
[7] Y. Levin, R. Pakter, and F. B. Rizzato, Phys. Rev. E **78**, 021130 (2008).
[8] V. Springel, Mon. Not. R. Astron. Soc. **364**, 1105 (2005).
[9] I. Ispolatov and E. G. D. Cohen, Phys. Rev. E **64**, 056103 (2001).
[10] I. Ispolatov and M. Karttunen, Phys. Rev. E **70**, 026102 (2004).
[11] S. Gupta and D. Mukamel, Phys. Rev. Lett. **105**, 040602 (2010).

Formation and relaxation of quasistationary states in particle systems with power-law interactions

B. Marcos,[1,2,*] A. Gabrielli,[3] and M. Joyce[4]
[1]*Université Côte d'Azur, CNRS UMR 7351, LJAD 06108, France*
[2]*Instituto de Física, Universidade Federal do Rio Grande do Sul, 91501-970, Porto Alegre, Brazil*
[3]*Istituto dei Sistemi Complessi (ISC) - CNR, UoS Sapienza, Dipartimento di Fisica, Università Sapienza; Piazzale Aldo Moro 5, 00185-Rome, Italy*
[4]*Laboratoire de Physique Nucléaire et de Hautes Énergies, UPMC IN2P3 CNRS UMR 7585, Sorbonne Universités, 4, place Jussieu, 75252 Paris Cedex 05, France*
(Received 7 January 2017; published 5 September 2017)

We explore the formation and relaxation of the so-called quasistationary states (QSS) for particle distributions in three dimensions interacting via an attractive radial pair potential $V(r \to \infty) \sim 1/r^\gamma$ with $\gamma > 0$, and either a soft core or hard core regularization at small r. In the first part of the paper, we generalize, for any spatial dimension $d \geqslant 2$, Chandrasekhar's approach for the case of gravity to obtain analytic estimates of the rate of collisional relaxation due to two-body collisions. The resultant relaxation rates indicate an essential qualitative difference depending on the integrability of the pair force at large distances: for $\gamma > d - 1$, the rate diverges in the large particle number N (mean-field) limit, unless a sufficiently large soft core is present; for $\gamma < d - 1$, on the other hand, the rate vanishes in the same limit even in the absence of any regularization. In the second part of the paper we compare our analytical predictions with the results of extensive parallel numerical simulations in $d = 3$ performed with an appropriate modification of the GADGET code, for a range of different exponents γ and soft cores leading to the formation of QSS. We find, just as for the previously well studied case of gravity (which we also revisit), excellent agreement between the parametric dependence of the observed relaxation times and our analytic predictions. Further, as in the case of gravity, we find that the results indicate that, when large impact factors dominate, the appropriate cutoff is the size of the system (rather than, for example, the mean interparticle distance). Our results provide strong evidence that the existence of QSS is robust only for long-range interactions with a large distance behavior $\gamma < d - 1$; for $\gamma \geqslant d - 1$, the existence of such states will be conditioned strongly on the short-range properties of the interaction.

DOI: 10.1103/PhysRevE.96.032102

I. INTRODUCTION

There are many systems of particles interacting with long-range interactions in nature: self-gravitating bodies in astrophysics and cosmology [1], two-dimensional fluid dynamics [2], cold atoms [3], etc. Considering, for simplicity, d-dimensional particle systems, which interact through an isotropic pair potential $v(r)$, long-range systems are usually defined as those for which

$$v(r \to \infty) \sim \frac{g}{r^\gamma}, \tag{1}$$

where $\gamma \leqslant d$, and g is a coupling constant. This characterization of interactions as long-range arises in equilibrium statistical mechanics [4]: in a system of N particles in a volume V, the average energy of a particle is, for $\gamma > d$, independent of the size of the system in the "usual" thermodynamic limit $N \to \infty$, $V \to \infty$ at fixed density N/V. For $\gamma \leqslant d$, a different thermodynamic limit must be taken in order to recover extensivity of the thermodynamic potentials, and N independent intensive properties of the system, as $N \to \infty$. More specifically, the potential energy Φ_i of a particle scales as $\Phi_i \sim gN/V^{\gamma/d}$, and g and V must be scaled appropriately with N so that Φ_i is constant. This is usually called the mean-field thermodynamic limit (or the Vlasov limit when is taken at fixed system size). Using this scaling, the total energy becomes extensive and it is possible to compute thermal equilibrium properties. For the class of systems we consider here, with attractive power-law interactions at large scales in three dimensions, such a treatment has been given in Ref. [5]. For $\gamma < d$, they present unusual features compared to short-range systems: inhomogeneous spatial distributions, inequivalence of the statistical ensembles, negative specific heat in the microcanonical ensemble, etc.[1]

For the case of gravity, it was understood decades ago, however, in the context of astrophysics (through the seminal works of Chandrasekhar, Lynden-Bell, and others), that such considerations based on equilibrium statistical mechanics are only relevant physically on time scales very long compared to those on which such systems evolve dynamically (e.g., the formation and evolution of galaxies) and that the scenario of the dynamics of such systems is completely different to that of short-range systems: on a time scale $\tau_{\rm dyn}$ characteristic of the mean-field dynamics (and independent of N in the mean-field limit described above), one observes the formation, under the effect of a mean-field global interaction through the so-called mean-field relaxation, of very slowly evolving macroscopic states (e.g., galaxies), which are far from thermal equilibrium. For gravity in $d = 3$ dimensions, the time scale for evolution

*Current address: Parc Valrose 06108 Nice Cedex 02, France; Caixa Postal 15051, CEP 91501-970, Porto Alegre, RS, Brazil.

[1]All these considerations are for classical systems. For studies of properties of quantum spin systems with power-law interactions see e.g., Refs. [6,7].

towards equilibrium (or at least increase of the microcanonical entropy for the cases in which thermal equilibrium is not well defined, see Ref. [8]) in which was first estimated by Chandrasekhar [9] to be $\tau_{\rm coll} \sim (N/\ln N)\tau_{\rm dyn}$. Thus, as $N \to \infty$ in the mean-field limit, the system remains trapped in such states and never evolves towards thermodynamic equilibrium. A similar phenomenology has been established in the last years in the study of various other systems with long-range interactions (see, e.g., Refs. [10–13]): relaxation on a mean-field time scale to a "quasistationary state" (QSS) followed by a relaxation towards thermodynamic equilibrium on a time scale which diverges with the particle number N. This scenario has thus been proposed as a kind of paradigm for the dynamics of this class of interactions (e.g., Refs. [4,14,15]).

More formally, the evolution of a system of N particles interacting through the pair potential (1) can be described by the equation

$$\frac{\partial f}{\partial t} + \mathbf{v}(\mathbf{r},t)\cdot\frac{\partial f}{\partial \mathbf{r}} + \mathbf{F}[f]\cdot\frac{\partial f}{\partial \mathbf{v}} = C_N, \tag{2}$$

where $f(\mathbf{r},\mathbf{v},t)$ is the mean phase space density function, i.e., the density of particles at the position $\mathbf{r}$ with velocity $\mathbf{v}$ at time t, and C_N is called the "collision term." In general the latter is a functional of the n-point distribution functions. The term $\mathbf{F}[f]$ is the *mean-field force* which can be written in terms of the pair potential $v(r)$ as

$$\mathbf{F}[f] = -\int f(\mathbf{r}',\mathbf{v},t)\nabla_{\mathbf{r}} v(|\mathbf{r}-\mathbf{r}'|)d\mathbf{r}'d\mathbf{v}. \tag{3}$$

A mean-field dynamical description is valid if, in the mean-field (or Vlasov) limit, we have that

$$\lim_{N\to\infty} C_N = 0 \tag{4}$$

in which case the dynamics is described by the Vlasov equation, known as the "collisionless Boltzmann equation" in the astrophysical literature (e.g., Ref. [1]). QSS are understood as stable stationary solutions of these equations, and mean-field relaxation as the evolution towards such states in the same mean-field framework (on time scales of order $\tau_{\rm dyn}$). Correspondingly, in any finite (but large) N system, the term C_N then describes the "collisional" corrections to the mean-field dynamics.

For long-range interactions, therefore, to show that QSS should exist, one should analyze these collision terms, and determine firstly that they do indeed satisfy the condition (4). Further in order to understand their evolution away from QSS at large but finite N, and (possibly) towards thermal equilibrium, one needs to derive a suitable kinetic theory, which should allow one to infer the scalings of the time scale (or scales) characterizing such evolution as a function of N. Concerning the first step it has been shown rigorously that the Vlasov limit exists for $\gamma < 0$ [16], and for values of γ extending up to $\gamma = 1$ (i.e., the gravitational case in $d = 3$) provided a suitable regularization (i.e., softening) of the potential is imposed at small separations [17–20]. However, these provide only rigorous lower bounds ($\sim \ln N$) to the time scales on which the Vlasov dynamics is valid. They do not allow us to calculate in any practical manner the time scales for collisional relaxation, nor even to determine their parametric scalings. Many attempts have been made in this direction through the construction of explicit kinetic theories [21–29] but, in practice it is difficult to apply these methods to realistic systems to establish the relevant time scales, and in particular their parametric scalings. Moreover, these theories do not take into account strong collisions. Often (e.g., Ref. [15]) it is argued, using such approaches, that the characteristic time scale for collisional relaxation has a generic scaling $\tau_{\rm coll} \sim N\tau_{\rm dyn}$, except for the special case of homogeneous QSS in one dimension.

In this paper, we explore the conditions under which the limit (4) is satisfied for the generic power-law interaction (1). To do so, we use a nonrigorous (but well defined) approach to the problem: we generalize the simple method initiated by Chandrasekhar for the case of gravity [1,9]. This amounts to assuming that the dominant contribution to the collisionality, described by the term C_N, comes from *two-body collisions*. For the gravitational interaction, this simple approach has turned out to account remarkably well for the observed time scales of collisional relaxation (in numerical simulations). We generalize this approach to a generic power-law interaction; and compare the results obtained to the results of numerical simulations of several such systems.

Several important results emerge from this analysis. Firstly, it becomes evident through this approach that, in general, the characteristic time $\tau_{\rm coll}$ for collisional relaxation scales with the particle number N and may depend on the properties of the two-body potential at small distances. Our results for the two-body collisional relaxation lead to the conclusion that, in this respect, an important qualitative distinction can be made between the cases $\gamma < d-1$ and $\gamma > d-1$: in both cases, for unsoftened potentials, $\tau_{\rm coll} \sim N^{\delta}$, where δ is a constant depending on γ and the dimension of space d. However, the sign of δ is positive only if $\gamma < d-1$. This means that when the size of the core is sent to zero, the condition Eq. (4) can be satisfied only for $\gamma < d-1$. The existence of QSS requires the satisfaction of this condition, and therefore such states can exist for $\gamma \geqslant d-1$ only if the rate of collisionality is reduced through the introduction of a sufficiently soft core. In other words, for $\gamma < d-1$ QSS can be considered to occur simply because of the large distance behavior of the potential, while for $\gamma \geqslant d-1$ their existence depends on the details of the short-distance behavior. This leads to what we call a *dynamical* (rather than thermodynamical) classification of the range of interactions, which has been proposed also using different analyses in Refs. [30–33].

The essential result above has already been reported in Ref. [31]. In this paper, we present a more detailed and more extended study of collisional relaxation in these systems, both for the analytical and numerical parts. In the analytical part, we present both a new quantitative treatment of the two-body relaxation including the contribution from hard collisions, and also of the case of different specified soft core regularizations. In the numerical part, we present much more extensive results and detailed analysis, including notably potentials, which decrease more slowly than the gravitational potential, and a full quantitative exploration of the role of softening. The paper is organized as follows: in the next section we give a brief review on the literature of the collisional relaxation in the context of gravitational systems and detail our generalization of Chandrasekhar calculation of the two-body

collisional relaxation rate for the pair potentials (1), with soft or hard regularizations at small distances. This leads us to write parametric scalings which allow us to infer our classification of the range of pair interactions. In the following section, we describe the numerical simulations we use to explore the validity of our analytical results, their initial conditions and the macroscopic quantities we measure to characterize collisional relaxation. In the next section, we present our numerical results, first for the previously studied case of gravity, and then for several cases with $\gamma > 1$ and $\gamma < 1$. We compare then quantitatively the relaxation time obtained theoretically with our simulations and, in the next section, we give numerical evidence indicating that the maximum impact parameter scales with the size of the system. In the final section, we draw our conclusions.

II. RELAXATION RATES DUE TO TWO-BODY COLLISIONS

The parametric dependence of the characteristic time $\tau_{\rm dyn}$ for mean-field evolution is given by that of the typical time a particle needs to cross the system, of size R, under the mean-field force:

$$\tau_{\rm dyn} \simeq \sqrt{\frac{m R^{\gamma+2}}{g N}}, \tag{5}$$

where m is the mass of each particle. The determination of the parametric dependence of the characteristic time of collisionality $\tau_{\rm coll}$—and, as expected, of relaxation towards thermodynamic equilibrium—is much less evident. For the case of gravity ($\gamma = 1$) in three dimensions, Chandrasekhar gave the first estimates in 1943 [34], through a calculation of a diffusion coefficient in velocity space for an infinite homogeneous self-gravitating distribution of particles. The central hypothesis, as for short-ranged systems, was to suppose that the main contribution to the collisional relaxation process arises from *two-body encounters*. He calculated the variation of velocity of a test particle undergoing a "collision" with a particle of the homogeneous distribution, the global relaxation process being the cumulative effect of such "collisions." As we will see in the next subsection the standard notion of *impact parameter* appears in the calculations. Due to the assumption of an infinite homogeneous distribution and to the long-range nature of gravity, Chandrasekhar had to cut off the maximum impact parameter allowed at some scale, which he chose to be given by the typical interparticle separation.

More than twenty years after the paper of Chandrasekhar, Hénon [35] did a new calculation following the hypothesis of Chandrasekhar, but considering that all the impact factors up to the ones of the size of the system would contribute to the relaxation, instead of the ones of the order of the average interparticle distance. There is then no need to introduce artificially an upper cutoff in the impact parameter, as it is naturally fixed by the size of the system. More recent theoretical approaches, like, e.g., Refs. [21,36] (and references therein), have followed a more complete approach, linearizing the Boltzmann equation (2). This approach makes possible to take into account not only local but also collective effects. This approach is, however, very cumbersome analytically and does not lead in practice to definite conclusions about the issues we address here.

On the other hand, N-body computer simulations of the relaxation problem have been performed to test the analytical predictions. In three dimensions, such studies have been developed only for the case of gravitational interaction. We note, amongst others, numerical studies focusing on the cosmological aspect [37], others focusing on the maximum relevant impact parameter in the relaxation process [38–40]. After some controversy, it seems that the appropriate maximal impact parameter is the size of the system (rather than the interparticle distance as postulated initially by Chandrasekhar). The study of the relaxation in softened potentials (see, e.g., Ref. [41]) give more indications in this direction. This is a result we will confirm and provide new evidence for in this paper.

In the rest of this section, we present our generalization of the two body collisional relaxation time for any attractive power-law pair potential of the form (1), with $\gamma > 0$ and a soft or hard core regularization at $r = 0$, and any spatial dimension $d \geqslant 2$. The reasons for these restrictions on γ and d become evident in the calculation below. These calculations give us the parametric dependence for the relaxation rate via two-body collisions, $\Gamma = \tau_{\rm coll}^{-1}$, in a virialized system. As discussed in the introduction, if we assume that these processes are the dominant ones in the collisional dynamics, we can then write the condition for the existence of a regime in which a mean-field (Vlasov) description of the dynamics is valid as [31]

$$\Gamma\, \tau_{\rm dyn} \to 0 \quad \text{when} \quad N \to \infty. \tag{6}$$

Since QSS corresponds to the stationary (and thus virialized) states of the Vlasov equation, condition (6) is also a necessary one for the existence of such states.

A. Generalization of Rutherford scattering for generic power-law interactions

We consider two particles of equal mass m, position vectors $\mathbf{r}_1$ and $\mathbf{r}_2$, and velocity vectors $\mathbf{v}_1 = \dot{\mathbf{r}}_1$ and $\mathbf{v}_2 = \dot{\mathbf{r}}_2$. Their relative position vector is denoted

$$\mathbf{r} = \mathbf{r}_1 - \mathbf{r}_2 \tag{7}$$

and their relative velocity $\mathbf{V} = \dot{\mathbf{r}}$. In their center of mass frame, the velocities of the two particles are given by $\pm(\mathbf{V}/2)$. Thus if $\Delta\mathbf{V}$ is the change in the relative velocity of the particles in the two-body encounter, the changes in velocity of the two particles in the laboratory frame, $\Delta\mathbf{v}_1$ and $\Delta\mathbf{v}_2$, (which are equal to those in the center of mass frame) are

$$\Delta\mathbf{v}_1 = \frac{\Delta\mathbf{V}}{2}, \tag{8a}$$

$$\Delta\mathbf{v}_2 = -\frac{\Delta\mathbf{V}}{2}. \tag{8b}$$

The equations of the relative motion are those of a single particle of mass $m/2$ with position vector $\mathbf{r}(t)$ subject to the central potential.

We decompose $\Delta\mathbf{V}$ as

$$\Delta\mathbf{V} = \Delta V_\perp \mathbf{e}_\perp + \Delta V_\parallel \mathbf{e}_\parallel, \tag{9}$$

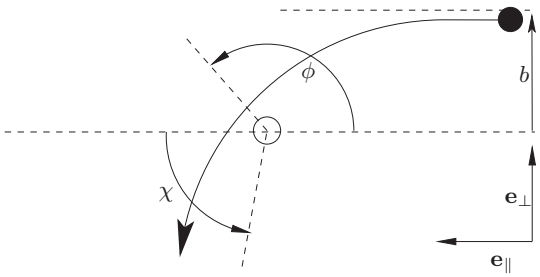

FIG. 1. Trajectory of a particle in a two-body collision in the center of mass frame, with a definition of the relevant quantities for its analysis, notably the deflection angle χ.

where $\mathbf{e}_\parallel$ is a unit vector defined parallel to the initial axis of motion, and $\mathbf{e}_\perp$ a unit vector orthogonal to it, in the plane of the motion (see Fig. 1). In the center of mass frame, the collision occurs as depicted in Fig. 1, which shows the definition of the impact factor b, and the deflection angle $\chi = 2\phi - \pi$. As energy is conserved in the collision, the magnitudes of the initial and final relative velocity, $V = |\mathbf{V}|$, are equal. It follows that

$$\frac{\Delta V_\perp}{V} = -\sin(\chi), \tag{10a}$$

$$\frac{\Delta V_\parallel}{V} = 1 - \cos(\chi). \tag{10b}$$

The angle ϕ can be calculated, as a function of the impact factor b, using the classic formula [42]

$$\phi(b) = \int_{r_{\min}}^{\infty} \frac{(b/r^2)dr}{\sqrt{1-(b/r)^2 - 4v(r)/mV^2}}, \tag{11}$$

where $r_{\min}$ is the positive root of the denominator.

We consider now the case of a pure decaying power-law pair potential,

$$v(r) = -\frac{g}{r^\gamma} \tag{12}$$

and $\gamma > 0$. For $g > 0$, the corresponding force is attractive, while for $g < 0$ it is repulsive. In what follows, we will consider the attractive case, but we will discuss below also the repulsive case. Indeed, it turns out that our essential results hold in both cases.

The integral (11) leads naturally to the definition of the characteristic length scale

$$b_0 = \left(\frac{2|g|}{mV^2}\right)^{1/\gamma}. \tag{13}$$

Considering the attractive case, Eq. (11) may then be rewritten as

$$\phi(b) = \int_{r_{\min}}^{\infty} \frac{(b/r^2)dr}{\sqrt{1-(b/r)^2 + 2(b_0/r)^\gamma}}. \tag{14}$$

Changing to the variable $x = b/r$, we obtain

$$\phi(b/b_0) = \int_0^{x_{\max}} \frac{dx}{\sqrt{1-x^2+2(b_0/b)^\gamma x^\gamma}}, \tag{15}$$

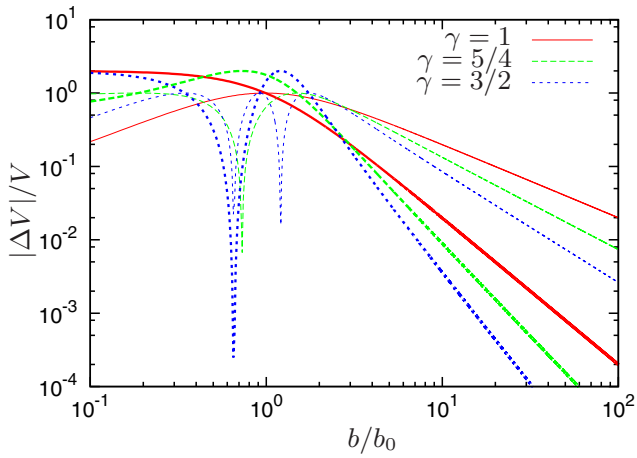

FIG. 2. Absolute value of relative change in the perpendicular (thin lines) and parallel (thick lines) components of the relative velocity in a two-body encounter, for different attractive power-law potentials. The behaviors at small and large values of b/b_0 are well described by the analytical expressions given in the text. Note that for some values of b/b_0 the change of velocity is zero, which corresponds to particles that make one or several loops, with $\chi = 2\pi n$, $n \in \mathbb{N}$.

where now $x_{\max}$ is the positive root of the denominator. Since $x_{\max}$, for given γ, is a function of b/b_0 only, it follows that ϕ is also a function of b/b_0 only.

Equation (14) can be solved analytically only in a few cases, and notably for the case $\gamma = 1$ which corresponds to gravity in $d = 3$. For the general ($\gamma \neq 1$) case, the integral can easily be computed numerically, and $\frac{\Delta V_\perp}{V}$ and $\frac{\Delta V_\parallel}{V}$ can then be calculated. Figure 2 displays the results for a few chosen cases. In order to derive analytically the parametric dependencies of the two-body relaxation rate, it suffices, as we will see, to have analytical approximations in the two asymptotic regimes of soft ($b/b_0 \gg 1$) and hard ($b/b_0 \ll 1$) collisions. The corresponding expressions have been derived in a separate article [43] by one of us (BM) and another collaborator. In what follows, we make use of the relevant results of [43], where the full details of their derivations may be found.

1. Soft collisions ($b \gg b_0$)

When $b \gg b_0$ the particle trajectories are weakly perturbed, and the collision is said to be *soft*. It is shown in Ref. [43] that, in this region, one has

$$\chi(b/b_0) = 2A(\gamma)(b_0/b)^\gamma + \mathcal{O}((b_0/b)^{2\gamma}), \tag{16}$$

where

$$A(\gamma) = \sqrt{\pi}\frac{\Gamma\left(\frac{\gamma+1}{2}\right)}{\Gamma\left(\frac{\gamma}{2}\right)}, \tag{17}$$

with $\Gamma(x)$ being the Euler Gamma function. As the angle of deflection $\chi \ll 1$, it follows that

$$\frac{\Delta V_\perp}{V} = -2A(\gamma)\left(\frac{b_0}{b}\right)^\gamma + \mathcal{O}((b_0/b)^{2\gamma}) \tag{18a}$$

$$\frac{\Delta V_\parallel}{V} = 2A(\gamma)^2\left(\frac{b_0}{b}\right)^{2\gamma} + \mathcal{O}((b_0/b)^{4\gamma}). \tag{18b}$$

In Appendix A, an alternative derivation of Eq. (18a) is presented.

2. *Hard collisions ($b \ll b_0$)*

It is shown in Ref. [43] that, in this asymptotic regime,

$$\chi(b/b_0) = \frac{\gamma\pi}{2-\gamma} + \mathcal{O}((b/b_0)^\alpha), \tag{19}$$

where $\alpha = 2\gamma/(2-\gamma)$ for $\gamma < 2/3$, $\alpha = b/b_0 \ln(b_0/b)$ for $\gamma = 2/3$ and $\alpha = 1$ for $2/3 < \gamma < 2$. If $\gamma \geqslant 2$, collisions are well defined with an asymptotic free state [43] only if

$$b > \beta b_0, \tag{20}$$

where

$$\beta = \gamma^{1/\gamma}\left(1 - \frac{2}{\gamma}\right)^{\frac{2-\gamma}{2\gamma}}. \tag{21}$$

For $b \leqslant \beta b_0$, on the other hand, there is a finite time singularity, i.e., the relative distance of the particles vanishes at a finite time.

The first term in the asymptotic expansion Eq. (19) gives the angle of deflection in the limit of arbitrarily small impact factors, and shows that it depends on γ. While for the case $\gamma = 1$ (i.e., gravity in $d = 3$) each particle velocity is exactly reversed in the center of mass frame ($\chi = \pi$), the general result for the deflection angle is different, and it increases to infinity as $\gamma \to 2$ from below. At $\gamma = 4/3$, each particle performs one full loop around the center of mass and escapes asymptotically in the same direction it arrived in, at $\gamma = 12/7$ each particle performs two full loops etc., and as $\gamma \to 2$ from below the number of such loops diverges.

For $\gamma \geqslant 2$, as noted, there is in fact a singularity, with the particles running into one another at a finite time. To include this case in our treatment we must therefore assume that the pair potential Eq. (12) is regularized at $r = 0$, so that there is a well defined collision for any impact factor. It follows from our analysis that this means that the asymptotic behavior below some arbitrarily small scale must be either repulsive, or, if attractive, diverging more slowly that $1/r^2$. In what follows, this assumption will suffice to extend our results to the range $\gamma \geqslant 2$.

B. Computation of the cumulative effect of many collisions

Following Chandrasekhar, we assume that thermal relaxation is induced by the randomization of particles velocity by two-body collisions. In order to estimate the accumulated effect of two-body collisions on a particle as it crosses the whole system, we estimate first the number of encounters per unit of time with impact parameter b. In doing so, we make the following approximations: (1) the system is treated as a homogeneous random distribution of particles in a d dimensional sphere of radius R and (2) the initial squared relative velocity of colliding particles is given by the variance of the particle velocities in the system.

Each particle is then assumed to perform a simple homogeneous random walk in velocity space, with zero mean change in velocity (because the deflections due to each encounter have no preferred direction), and a positive mean squared velocity which we determine below. In this approximation, we assume that the particles have rectilinear trajectories. This approximation clearly breaks down in the case of hard collisions, in which the trajectory is strongly perturbed. We expect however the estimation of the number of collisions per unit of time to remain correct in this case, because encounters modify only the direction of the velocity, and not its modulus.

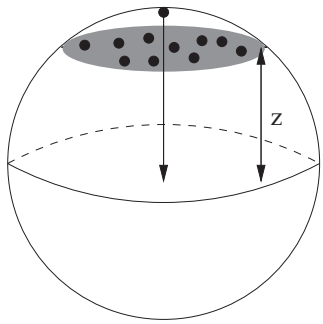

FIG. 3. The system is approximated as a perfectly spherical distribution of particles with radius R.

As illustrated schematically in Fig. 3, we now divide the system in disks of thickness dz, and write the average number of encounters with impact parameter between b and $b + db$ of a particle crossing this disk as

$$\delta n = \frac{B_d N}{R^d} b^{d-2}\, db\, dz, \tag{22}$$

where B_d is a numerical factor which depends on the spatial dimension d (e.g., $B_2 = 2/\pi$, $B_3 = 3/2$).

Multiplying Eq. (22) by the square of Eq. (10) with the condition (15), and integrating from $b = 0$ to $b = \sqrt{R^2 - z^2}$ and then from $z = 0$ to $z = R$, we then estimate the average change in the velocity *during one crossing* of the system, for the perpendicular and parallel components of the velocity, respectively, as

$$\frac{\langle|\Delta V^2_{\perp,\parallel}|\rangle}{|V^2|} = 2B_d N\left(\frac{b_0}{R}\right)^{d-1} \mathcal{I}_{\perp,\parallel}\left(\frac{b_0}{R}\right), \tag{23}$$

where

$$\mathcal{I}_{\perp,\parallel}(x_R) = \int_0^{x_R} dx\, x^{d-2}\, \Theta_{\perp,\parallel}(x)\sqrt{1 - \frac{x^2}{x_R^2}}, \tag{24}$$

where $x = b/b_0$, $x_R = R/b_0$ and

$$\Theta_\perp(x) = \sin^2(\chi(x)), \tag{25a}$$

$$\Theta_\parallel(x) = [1 - \cos(\chi(x))]^2. \tag{25b}$$

Writing the expression for $\frac{\langle|\Delta V^2_{\perp,\parallel}|\rangle}{|V^2|}$ in this way allows a simple and useful comparison with the case of particles interacting by an exact repulsive hard core potential. Indeed, it is straightforward to show (see e.g., Ref. [44]) that for (infinitely) hard particles with a diameter σ, one has

$$\chi(b) = \begin{cases} 2\arccos\left(\frac{b}{\sigma}\right) & \text{if} \quad b \leqslant \sigma \\ 0 & \text{otherwise} \end{cases}. \tag{26}$$

Calculating $\frac{\langle|\Delta V^2_{\perp,\parallel}|\rangle}{|V^2|}$ for this case using exactly the same approach used above, one obtains for the case $\sigma = b_0$, exactly

Eq. (23) with

$$\mathcal{I}_\perp = \frac{8}{(d+3)(d+1)}, \tag{27a}$$

$$\mathcal{I}_\parallel = \frac{4}{d-1}\mathcal{I}_\perp. \tag{27b}$$

Let us return now to the expressions Eq. (24) for the case of (attractive) power-law interactions. Given that $x_R \gg 1$, we can make the approximation

$$\mathcal{I}_{\perp,\parallel}(x_R) \approx \int_0^1 dx\, x^{d-2}\,\Theta_{\perp,\parallel}(x) + \int_1^{x_R} dx\, x^{d-2}\,\Theta_{\perp,\parallel}(x)\sqrt{1-\frac{x^2}{x_R^2}}. \tag{28}$$

The first integral gives the contribution due to hard collisions ($b < b_0$). It is finite provided only that the deflection angle is well defined, i.e., provided only that the two-body collisions is well defined. As we have discussed above this is true for any $\gamma < 2$, and for $\gamma \geqslant 2$ if we assume the singularity at $r = 0$ to be appropriately regularized. Thus this term gives a contribution to $\frac{\langle|\Delta V_{\perp,\parallel}^2|\rangle}{|V^2|}$ which has precisely the parametric dependencies of an exact repulsive hard core, differing only by an overall numerical factor.

Considering now the second term, giving the contribution from soft collisions ($b > b_0$), we see that there are two different cases according to the large x behavior of $\Theta_{\perp,\parallel}$: the integral is convergent as $x_R \to \infty$ if and only if $x^{d-1}\Theta_{\perp,\parallel}(x) \to 0$ as $x \to \infty$. We thus infer from Eq. (18) the following:

(1) For $0 < \gamma < (d-1)/2$,

$$\mathcal{I}_\perp(x_R) \approx 4A^2(\gamma)\int_0^{x_R} dx\, x^{d-2-2\gamma}\sqrt{1-\frac{x^2}{x_R^2}} \tag{29}$$

$$= A^2(\gamma)\sqrt{\pi}\,\frac{\Gamma[d/2-1/2-\gamma]}{\Gamma[d/2+1\gamma]}x_R^{d-1-2\gamma} \tag{30}$$

and $\mathcal{I}_\parallel(x_R) \ll \mathcal{I}_\perp(x_R)$. Thus the integral is dominated by the contribution of soft scatterings, for which the change in the relative velocity is predominantly orthogonal to the initial relative velocity. Replacing Eq. (29) in Eq. (23), we obtain the scaling

$$\frac{\langle|\Delta\mathbf{V}^2|\rangle}{V^2} \approx \frac{\langle|\Delta V_\perp^2|\rangle}{|V^2|} \sim N\left(\frac{b_0}{R}\right)^{2\gamma}, \tag{31}$$

where

$$\frac{\langle|\Delta\mathbf{V}|^2\rangle}{V^2} = \frac{\langle|\Delta\mathbf{V}_\perp|^2\rangle}{V^2} + \frac{\langle|\Delta\mathbf{V}_\parallel|^2\rangle}{V^2}. \tag{32}$$

(2) For $\gamma = (d-1)/2$, which corresponds to gravity in $d = 3$, the contribution from all impact factors from the scale b_0 must be included and

$$\mathcal{I}_\perp(x_R) \approx 4A^2(\gamma)\ln x_R. \tag{33}$$

As in the previous case, $\mathcal{I}_\parallel(x_R) \ll \mathcal{I}_\perp(x_R)$. Note that, given $x_R \gg 1$ this result for $\mathcal{I}_\perp(x_R)$ is very insensitive to precisely where the lower cut-off at $b \sim b_0$ is chosen. We obtain therefore

$$\frac{\langle|\Delta\mathbf{V}^2|\rangle}{|V^2|} \sim N\left(\frac{b_0}{R}\right)^{d-1}\ln\left(\frac{R}{b_0}\right). \tag{34}$$

(3) For $\gamma > (d-1)/2$, we have

$$\mathcal{I}_{\perp,\parallel}(x_R) \approx \mathcal{I}_{\perp,\parallel}(\infty) \approx \int_0^\infty dx\, x^{d-2}\,\Theta_{\perp,\parallel}(x), \tag{35}$$

which is a constant that can be numerically calculated in a straightforward way for any given pair potential in this class. We obtain therefore

$$\frac{\langle|\Delta\mathbf{V}^2|\rangle}{V^2} \sim N\left(\frac{b_0}{R}\right)^{d-1}. \tag{36}$$

In the last case, for sufficiently rapidly decaying potentials, we obtain therefore the same scaling as for the case of hard core particles of diameter b_0.

C. Scalings with N of the relaxation rate in a QSS

Using these results, we now determine how the relaxation rate scales with the parameters of the system. Assuming the system to be in a QSS, we can then obtain its scaling as a function of N alone. For clarity, we drop irrelevant numerical prefactors, but these will be analyzed further in Sec. VI.

We define the relaxation rate Γ as the inverse of the time scale at which the normalized average change in velocity squared due to collisions is equal to one. Given that the estimated $\frac{\langle|\Delta\mathbf{V}|^2\rangle}{V^2}$ is the average change in a crossing time $\tau_{\rm dyn}$, we have therefore

$$\Gamma\tau_{\rm dyn} \simeq \frac{\langle|\Delta\mathbf{V}|^2\rangle}{V^2}. \tag{37}$$

In order to obtain the scaling with N from the above results, we need to determine how the ratio b_0/R scales with N. Using the definition (13) and assuming, as stated above, that the modulus of the relative velocity of colliding particles can be taken to be of the same order as the typical velocity of a single particle v, we have

$$\left(\frac{b_0}{R}\right)^\gamma \sim \frac{g}{mv^2R^\gamma} \sim \frac{1}{N}\frac{gN^2}{(mNv^2)R^\gamma} \sim \frac{1}{N}\frac{U}{K}, \tag{38}$$

where K is the total kinetic energy and U the total potential energy of the system.

If we now assume the system to be in a QSS, i.e., in virial equilibrium, the *virial theorem* gives that

$$2K + \gamma U = 3PV, \tag{39}$$

where P is the pressure of the particles on the boundaries if the system is enclosed, and $P = 0$ if the system is open.

By definition the mean-field scaling with N makes each term in Eq. (39) scale in the same way with N so that the relation remains valid independently of N (up to finite N fluctuations). Thus using this scaling we can infer that

$$b_0 \sim RN^{-1/\gamma}. \tag{40}$$

Using Eqs. (31), (34), and (36), we then infer the following behaviors.

(1) For $0 < \gamma < (d-1)/2$,

$$\Gamma\,\tau_{\rm dyn} \sim N(b_0/R)^{2\gamma} \sim N^{-1}. \tag{41}$$

(2) For $\gamma = (d-1)/2$,

$$\Gamma\,\tau_{\rm dyn} \sim N^{-1}\ln(N). \tag{42}$$

(3) For $\gamma > (d-1)/2$,

$$\Gamma\,\tau_{\rm dyn} \sim N^{-(d-1-\gamma)/\gamma}. \tag{43}$$

It follows that that the condition (6) only holds for potentials with $\gamma < d-1$. Only in this case therefore can the QSS be supposed to exist as we have assumed. For $\gamma \geqslant d-1$, on the other hand, the relaxation induced by two-body collisionality occurs on a time scale which is short compared to a particle crossing time, and a stationary nonthermal state cannot exist on the latter time scale, i.e., a QSS cannot exist.

D. Relaxation rates for softened power-law potentials

We consider now the case in which the power-law potential is "softened" at short distances, i.e., regulated so that the modulus of the force between two particles is bounded above at some finite value. The principle motivation for considering this case here is that, in practice, even for $\gamma < 2$, we are unable numerically to test directly the validity of the scaling predictions Eqs. (36)–(41) for the exact (singular) potentials: the numerical cost of integrating sufficiently accurately hard two-body scatterings over the long time scales required is prohibitive. Instead we will consider power-law potentials softened at a scale ϵ, and study the scaling with both N and ϵ of the relaxation rates in the numerically accessible range for these parameters.

A detailed analysis of the two-body scattering for such softened power-law potentials has been given also in Ref. [43]. We again use the results of this paper to infer, using Eqs. (23)–(25) above, the parametric scalings of the relaxation rate. As in the previous section, we defer until later a discussion of the exact numerical factors, for the specific smoothing functions used in our numerical simulations.

As softening modifies the force below a characteristic scale ϵ, its effect is to modify the deflection angles for impact factor b below a scale of the same order. From the considerations above, it is then evident that, for $\epsilon < b_0$, such a softening does not change the parametric scalings: it can only change the numerical value of the (finite) first integral in Eq. (28). For $\epsilon > b_0$, on the other hand, the second integral in Eq. (28) is modified because the functions $\Theta_{\perp,\parallel}$ are modified up to $x \sim \epsilon/b_0$. Assuming that $\epsilon \ll R$, this will lead to a modification of the parametric scaling of the full expressions for $\frac{\langle|\Delta\mathbf{V}|^2\rangle}{V^2}$ when $\gamma \geqslant (d-1)/2$. In Ref. [43], it is shown that, when $\epsilon \geqslant b_0$, the deflection angle can be approximated as

$$\chi \simeq \begin{cases} 2B(\gamma)\left(\frac{b_0}{\epsilon}\right)^{\gamma}\left(\frac{b}{\epsilon}\right) & \text{if} \quad b < \epsilon^* \\ 2A(\gamma)\left(\frac{b_0}{b}\right)^{\gamma} & \text{if} \quad b > \epsilon^* \end{cases}, \tag{44}$$

where $B(\gamma)$ is a finite constant the exact value of which depends on the functional form of softening used [and $A(\gamma)$ is as defined in Eq. (17)]. The scale ϵ^* is of the same order as ϵ [from continuity of Eq. (44) at $b = \epsilon^*$, their ratio is given by $\epsilon^*/\epsilon \sim (A/B)^{\frac{1}{1+\gamma}}$].

Using Eq. (44), we can now calculate approximately the second integral in Eq. (28) for the cases in which the parametric dependence of their values are modified by the smoothing (with $\epsilon > b_0$).

(1) For $\gamma > (d-1)/2$ (taking $x_R \to \infty$):

$$\mathcal{I}_\perp \simeq \left[\frac{B^2(\gamma)}{d+1} + \frac{A^2(\gamma)}{2\gamma-d+1}\right]\left(\frac{\epsilon}{b_0}\right)^{d-1-2\gamma}, \tag{45a}$$

$$\mathcal{I}_\parallel \simeq \left[\frac{B^4(\gamma)}{4(d+3)} + \frac{A^4(\gamma)}{4\gamma+1-d}\right]\left(\frac{\epsilon}{b_0}\right)^{d-1-4\gamma}, \tag{45b}$$

and therefore $\mathcal{I}_\perp \gg \mathcal{I}_\parallel$ if $\epsilon \gg b_0$.

(2) For $\gamma = (d-1)/2$, assuming $x_R \gg (\epsilon/b_0)$ (i.e., $\epsilon \ll R$), we obtain

$$\mathcal{I}_\perp \simeq A^2(\gamma)\ln\left(\frac{R}{\epsilon}\right), \tag{46}$$

while $\mathcal{I}_\parallel$ is given as Eq. (45b), and $\mathcal{I}_\perp \gg \mathcal{I}_\parallel$ if $\epsilon \gg b_0$.

Using these results we infer finally that the scalings of the relaxation rates of a QSS [with b_0 scaling as in Eq. (40)] in the large N limit are the following.

(1) If $0 < \gamma < (d-1)/2$),

$$\Gamma\,\tau_{\rm dyn} \sim N^{-1}, \tag{47}$$

i.e., the same as in the absence of smoothing.

(2) If $\gamma > (d-1)/2$, then

$$\Gamma\,\tau_{\rm dyn} \sim N^{-1}\left(\frac{\epsilon}{R}\right)^{d-1-2\gamma}. \tag{48}$$

(3) If $\gamma = (d-1)/2$, then

$$\Gamma\,\tau_{\rm dyn} \sim N^{-1}\ln\left(\frac{R}{\epsilon}\right). \tag{49}$$

In summary, the correct parametric scaling for the two-body relaxation rates of a QSS, in the case of a power-law potential softened at a scale $\epsilon > b_0$, are well approximated by simply introducing a cutoff at an impact factor of order ϵ (and therefore considering only the contribution from soft collisions).

For what concerns the existence of QSS, we thus conclude that, with a softened power-law potential, one can satisfy the condition (6) even for any $\gamma \geqslant d-1$. Indeed, taking ϵ/R to be independent of N (i.e., scaling the softening with the system size), we obtain in all cases that $\Gamma_\epsilon\,\tau_{\rm dyn} \sim N^{-1}$. More generally, it is straightforward to deduce what scaling of ϵ with N is required to satisfy the condition (6) in the mean-field limit.

III. NUMERICAL SIMULATIONS

We have performed numerical simulations in $d = 3$ of the evolution of N particle systems, extending to sufficiently long times to observe their collisional evolution.[2] As we have discussed in the previous section, exact power-law interactions with $\gamma \geqslant (d-1)/2$ lead to strong collisions at impact factors $b < b_0$. Indeed, as we have seen, when γ increases much above unity, particles can even make multiple loops around one another during collisions [cf. Eq. (19)]. The smaller

[2]For a recent numerical study of these systems focusing on the shorter time (mean-field) evolution i.e., collisionless relaxation, see Refs. [45,46].

is b, the shorter is the characteristic time for a collision compared to the mean-field time and therefore the greater is the temporal resolution required for an accurate integration (and, in particular, conservation of the energy). This means it is too expensive numerically, even for a few thousand particles, to accurately simulate such a system for times long enough to be comparable to the predicted relaxation times. Indeed, we have seen that the calculation we have done predicts that, even for $(d-1)/2 < \gamma < d-1$ (i.e., $1 < \gamma < 2$ in $d = 3$), relaxation should be dominated by strong collisions with $b \sim b_0$ but nevertheless $\Gamma\,\tau_{\rm dyn}$ diverges in the mean-field limit.

For these reasons, we employ a potential with a softening which is sufficiently large to suppress strong collisions. The predicted scalings we can test are thus those given in Sec. II D, rather than the ones corresponding to pure power-law potentials given in Sec. II C. By studying also the scalings with the softening ϵ at fixed N, however, we can indirectly test in this way the extrapolation to the scalings in Sec. II C.

A. Code

We use a modification of the publicly available gravity code GADGET2 [47]. The force is computed using a modified Barnes and Hut tree algorithm, and we have modified the code in order to treat pair potentials of the form Eq. (1) and softened versions of them (which are those we use in practice). We use an opening angle $\theta = 0.001$, which ensures a very accurate computation of the force. The evolution of the system is computed using a Verlet-type Drift-Kick-Drift symplectic integration scheme. The simulations are checked using simple convergence tests on the numerical parameters, and their accuracy is monitored using energy conservation. For the time steps used here it is typically conserved to within 0.1% over the whole run, orders of magnitude smaller than the typical variation of the kinetic or potential energy over the same time.

B. Initial and boundary conditions

As initial conditions we take the N particles randomly distributed in a sphere of radius $R = 1/2$, and ascribe velocities to particles so that each component is an independent uniformly distributed variable in an interval $[-\xi,\xi]$ (i.e., "water-bag" type initial conditions in phase space). The parameter ξ is chosen so that the initial virial ratio is unity, i.e., $2K/|U| = \gamma$. We make this choice of initial conditions because it is expected to be close to a QSS, to which (collisionless) relaxation should occur "gently," and this is indeed what we observe. We have chosen to enclose the system in a cubic box of size $L = 1$, in order to avoid the complexities associated with particle evaporation. This constraint is imposed in practice using *soft* boundary conditions, which are implemented by changing the sign of the ith component of the velocity when the ith component of the position lies outside the simulation box. We use a time step of the order of $10^{-3}\tau_{\rm dyn}$ (which provides well converged results), where $\tau_{\rm dyn}$ is defined precisely below.

C. Softening

We have performed simulations using two different softening schemes: a "compact" softening and a "Plummer" softening. The former corresponds to a two-body potential

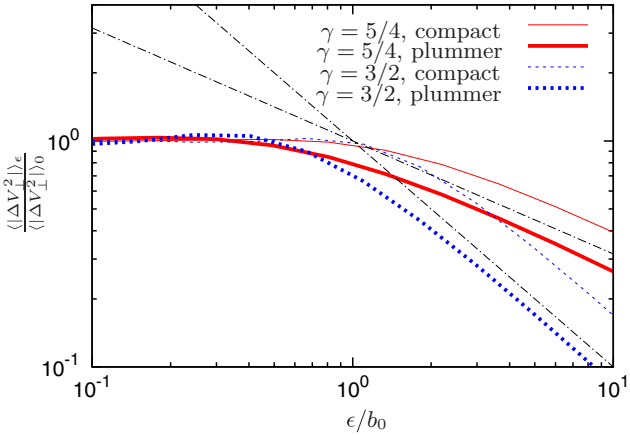

FIG. 4. Numerical evaluation of Eqs. (11) and (23) normalized to the value for $\epsilon/b_0 \to 0$ for $\gamma = 5/4$ and $3/2$. The power-law lines are the theoretical scaling (48).

$$v^{\rm C}(r,\epsilon) = \begin{cases} -\frac{g}{r^\gamma} & \text{if} \quad r \geqslant \epsilon \\ -\frac{g}{\epsilon^\gamma}\mathrm{v}(r/\epsilon) & \text{if} \quad 0 \leqslant r \leqslant \epsilon \end{cases}, \tag{50}$$

where $\mathrm{v}(x)$ is a polynomial, of which the exact expression is given in Appendix B. It is chosen so that the potential and its first two derivatives are continuous at $r = \epsilon$, and it interpolates to a force which vanishes at $r = 0$ via a region in which the force becomes repulsive. The Plummer smoothing corresponds to the simple potential

$$v_\epsilon^P(r) = -\frac{g}{(r^2+\epsilon^2)^{\gamma/2}}, \tag{51}$$

which is everywhere attractive.

As we have noted, it is straightforward to calculate numerically the relaxation rates for these softened potentials, using Eqs. (11) and (23). We show in Fig. 4 the ratio of the resultant $\frac{\langle|\Delta \mathbf{V}_\perp^2|\rangle}{\langle|V^2|\rangle}$ compared to its value for the exact power law, for $\gamma = 5/4$ and $3/2$, as a function of the ratio ϵ/b_0. As described in the previous section, we observe that, for $\epsilon \ll b_0$, the effect of the softening is negligible, while for $\epsilon \gg b_0$, we recover a simple power-law scaling with ϵ, which agrees with that derived above for this regime, cf. Eq. (48). We note that in Fig. 4 the normalization for the asymptotic Plummer curves is greater than for the compact softening.

Performing simulations with these two different softening schemes allows us to test not just the robustness of the agreement with the theoretical scalings derived above, which should not depend on the details of the softening scheme. It also allows us to test more quantitatively for the correctness of the theoretical predictions for the relaxation rates, which predicts also the relative amplitude of the relaxation rate in the regime $\epsilon \gg b_0$. To facilitate this comparison, it is convenient to define an effective softening $\epsilon_{\rm eff}$ obtained by assuming that all the collisions are soft, i.e.,

$$\chi_\epsilon \simeq \begin{cases} 0 & \text{if} \quad b < \epsilon_{\rm eff} \\ 2A(\gamma)\left(\frac{b_0}{b}\right)^\gamma & \text{if} \quad b \geqslant \epsilon_{\rm eff} \end{cases}. \tag{52}$$

Computing the same quantity as in Fig. 4, we can determine, by matching with the result for any other softening scheme,

TABLE I. Factor α [see Eq. (53)] to compute the effective softening $\epsilon_{\rm eff}$ (see text) in units of ϵ, for the two different softening schemes used in this work.

γ	compact core	plummer core
1	0.80	1.69
5/4	0.74	1.55
3/2	0.75	1.50

a value of $\epsilon_{\rm eff}$ in units of ϵ. We can compute therefore an effective softening using

$$\epsilon_{\rm eff} = \alpha\,\epsilon, \tag{53}$$

where the values of α are given in Table I for our two softening schemes, for the values of γ we explore here (in the range $\gamma \geqslant 1$ where the softening plays a role). The result for the case of gravity and the Plummer softening is in agreement with that derived in Ref. [41] (see also Ref. [48]).

Thus our analytical calculations predict that the relaxation rates of QSS measured with the different softening schemes should not only scale in the same way as a function of ϵ (for $\epsilon \gg b_0$) but also they should be equal at values of ϵ corresponding to the same $\epsilon_{\rm eff}$.

D. Sets of simulations

We performed, for each value of γ, and each softening scheme, two different kinds of sets of simulations. One set is at fixed particle number N and a range of different values of the softening ϵ, while in the other set ϵ is kept constant and N is varied. To refer to the simulations, we will use the notation $\mathcal{C}(\gamma; N,\epsilon)$ for a simulation with the compact ("$\mathcal{C}$") softening (1), power-law exponent γ, particle number N, and softening ϵ. Similarly, we denote $\mathcal{P}(\gamma; N,\epsilon)$ a set of simulations with the Plummer ("$\mathcal{P}$") smoothing.

The simulations on which our results below are based are the following.

(1) A set $\mathcal{C}(\gamma; N = 20^3,\epsilon)$ for $\gamma = 1/2$, $\gamma = 1$, $\gamma = 5/4$ and $\gamma = 3/2$ with the values of ϵ listed in the first column of Table II.

(2) A set $\mathcal{C}(\gamma; N,\epsilon/L = 0.005)$ for $\gamma = 1/2$, $\gamma = 1$, $\gamma = 5/4$ and $\gamma = 3/2$ with the values of N listed in the third column of Table II.

(3) A set $\mathcal{P}(\gamma; N = 20^3,\epsilon)$ for $\gamma = 5/4$ and $\gamma = 3/2$ with the values of ϵ listed in the second column of Table II.

(4) A set $\mathcal{P}(\gamma; N,\epsilon/L = 0.005)$ for $\gamma = 5/4$ and $\gamma = 3/2$ with the values of N listed in the third column of table Table II.

E. Numerical estimation of the relaxation rate

To measure numerically the relaxation rate of a QSS, we study the temporal evolution of different appropriate quantities. We consider principally two quite different quantities: on the one hand, the total kinetic (or potential) energy of the system, and on the other hand, the averaged quantity defined as

$$\Delta(t) \equiv \frac{\langle (e(t) - e(t^*))^2 \rangle}{2k^2(t^*)}, \tag{54}$$

TABLE II. List of simulations: the first column gives all the values of the softening parameter ϵ at fixed number of particles $N = 20^3$ for the two sets of simulations $\mathcal{P}$ and $\mathcal{C}$ corresponding to a different kind of softening; the second column gives all the values of the softening parameter ϵ at fixed number of particles $N = 10^3$; and the third gives the values of the number of particles N employed in two sets of simulations $\mathcal{P}$ and $\mathcal{C}$ corresponding to a different kind of softening at fixed $\epsilon/L = 0.014$. The † means that this simulation has been performed only for the case $\gamma = 5/4$, an accurate conservation of energy was not achieved for the other values of γ.

ϵ/L with $N = 20^3$	ϵ/L with $N = 10^3$	N with $\epsilon/L = 0.014$
0.00056†	–	10^3
0.0014	–	12^3
0.0028	–	16^3
0.0056	0.0056	20^3
0.0084	0.0084	26^3
0.0112	0.0112	30^3
0.014	0.014	
0.028	0.028	
0.056	0.056	
0.084	0.084	
0.112	0.112	

where $e(t)$ is the total energy of a single particle (at time t), and $k(t)$ is the kinetic energy per particle. The time t^* is an initial chosen time (and thus $t > t^*$) at which the system has relaxed, starting from the initial condition, to a QSS (typically we have $t^* \sim 10\,\tau_{\rm dyn}$). The brackets $\langle\cdot\rangle$ indicate an average over all the particles in the system.

The variation of the kinetic energy K (or potential energy U) is a simple probe of the macroscopic evolution of the system. For a system evolving through a continuum of virialized QSS, the virial relation (39) holds to an excellent approximation at all times, and thus the variation of K is linked directly to the variation of the pressure on the system wall. Provided this latter term is significant, it will be expected to be a good indicator of the evolution. The second quantity probes more directly the microscopic evolution of the quantities considered in the theoretical calculation. Indeed, the calculation in Sec. II A provides a prediction for the average variation of the velocity of particles due to collisions. The difficulty with measuring this directly is that the velocity of particles also changes continuously because of the mean-field potential. Particle energy, on the other hand, remains exactly constant in a QSS, and its change is in principle due to collisional effects, which we posit here are dominated by the two-body collisions.

F. Other indicators of relaxation

In order to determine whether the system is in a QSS (and hence not in thermal equilibrium), and also to provide further tests of its macroscopic evolution due to collisional effects, we also compute moments of the system's velocity distribution. If the system is at thermal equilibrium, the probability distribution of velocities must be Gaussian for each component with zero mean, and therefore all odd moments of such components must vanish, while even moments of order higher than two are determined as a simple power of

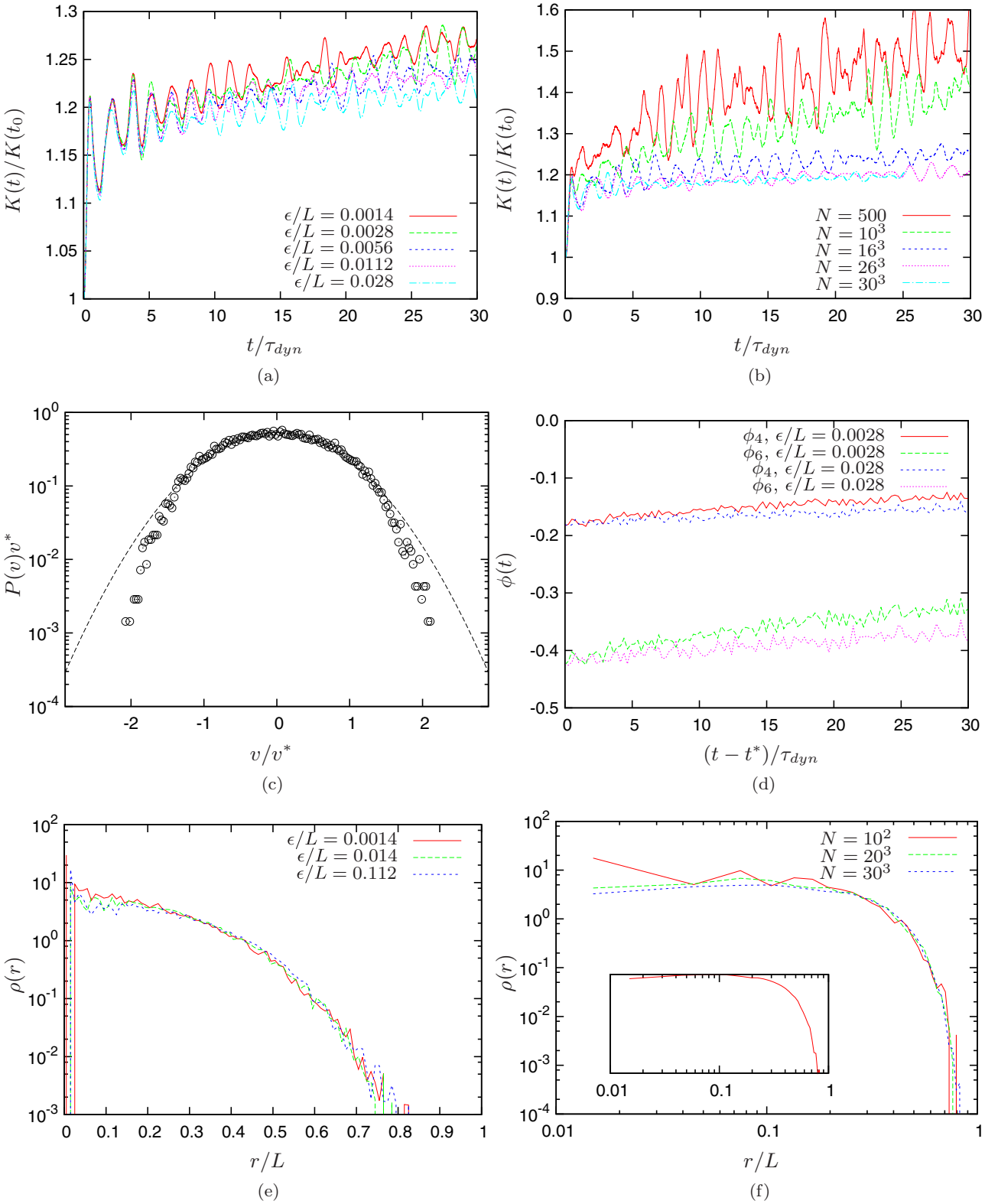

FIG. 5. Results of simulations for the case of gravity ($\gamma = 1$). (a) Evolution of the total kinetic energy normalized to its initial value, for $N = 20^3$ and different values of ϵ, i.e., the set of simulations $\mathcal{C}(1; 20^3, \epsilon/L)$; (b) evolution of the normalized total kinetic energy with $\epsilon = 0.014$ and a range of different values of N, i.e., the set of simulations $\mathcal{C}(1; N, 0.014)$; (c) velocity distribution for the simulation $\mathcal{C}(1; 20^3, 0.0028)$ at $t = 20\tau_{\rm dyn}$; (d) evolution of ϕ_4 and ϕ_6 for the simulations $\mathcal{C}(1; 20^3, 0.0028)$ and $\mathcal{C}(1; 20^3, 0.02)$; (e) density distribution for the simulations $\mathcal{C}(1; 20^3, \epsilon)$ at varying ϵ and $t = 20\tau_{\rm dyn}$; (f) density distribution for the simulations $\mathcal{C}(1; i, 0.01)$ at $t = 20\tau_{\rm dyn}$; and (inset) the same quantity for the simulation $\mathcal{C}(1; 30^3, 0.01)$ in a log-log plot (note the density drops rapidly at $R/L \approx 1/3$).

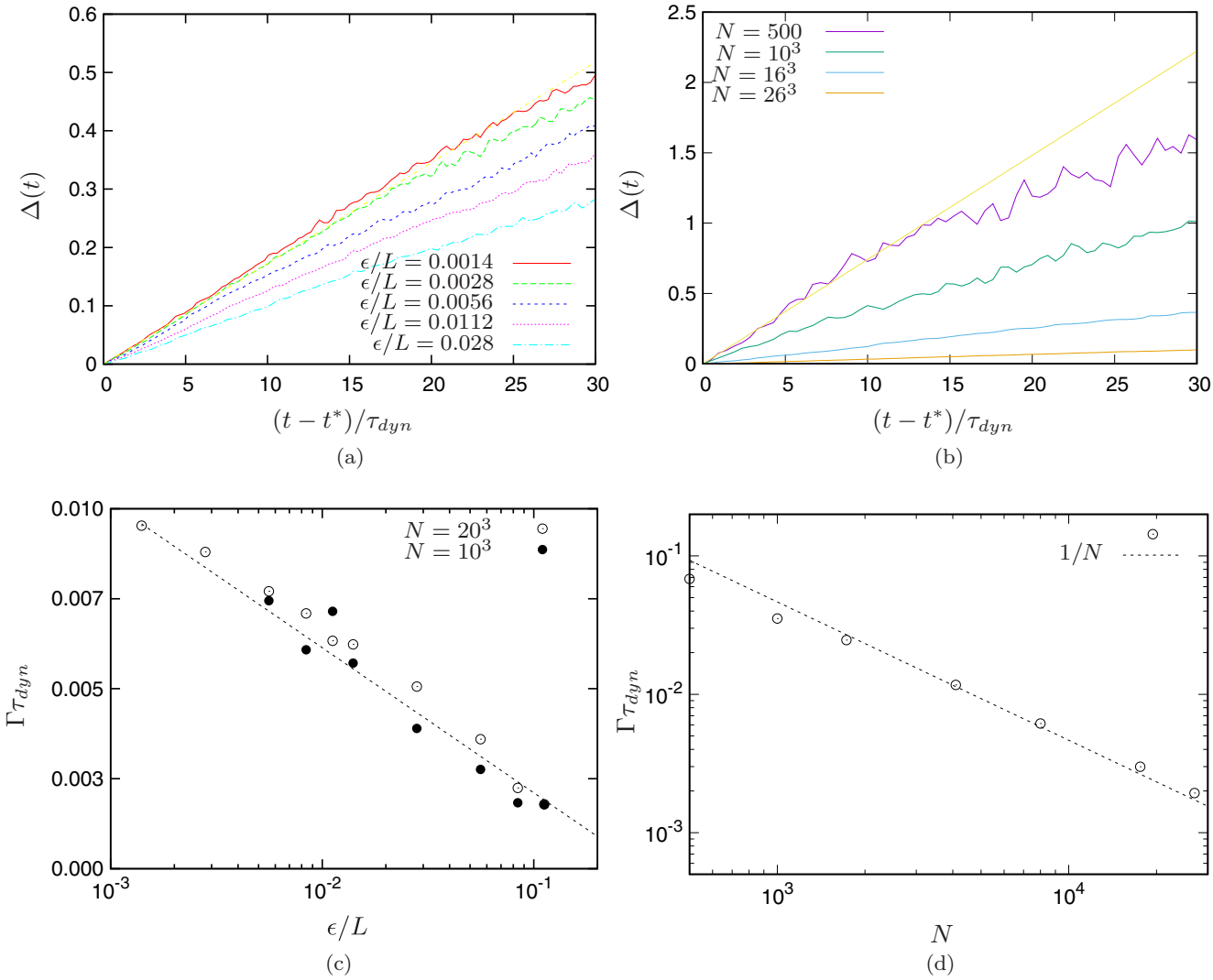

FIG. 6. Measures of relaxation times for the case of gravity ($\gamma = 1$). (a) Evolution of the parameter $\Delta(t)$ for chosen values of ϵ and fixed $N = 20^3$, i.e., in the set of simulations $\mathcal{C}(1;20^3,\epsilon/L)$; (b) evolution of $\Delta(t)$ for the range of N simulated and $\epsilon = 0.014$, i.e., the set of simulations $\mathcal{C}(1;N,0.01)$; and (c) plot of $\Gamma\tau_{\rm dyn}$ as a function of ϵ/L for both $N = 20^3$ and 10^3. In the latter case, following Eq. (49), the amplitude of the relaxation rate has been multiplied by a factor of 8 in order to collapse both the scalings on a single curve; the straight line is the theoretical scaling $\Gamma\tau_{\rm dyn} \sim \epsilon^{-1}$; (d) plot of Γ as a function of N for fixed $\epsilon/L = 0.01$.

the variance:

$$\langle v_i^{2n}\rangle = (2n-1)!!\langle v_i^2\rangle^n.$$

In order to detect the deviation from the Gaussian distribution of the velocity, we use the first two even moments of order larger than two, normalized so that they are zero in the case of a Gaussian distribution:

$$\phi_4 = \frac{\overline{\langle v_i^4\rangle}}{3\overline{\langle v_i^2\rangle}^2} - 1, \tag{55}$$

$$\phi_6 = \frac{\overline{\langle v_i^6\rangle}}{15\overline{\langle v_i^2\rangle}^3} - 1, \tag{56}$$

where $\bar{\cdot}$ denotes average over the coordinates.

G. Units

As noted above, we take the side of the enclosing box $L = 1$. The mean-field characteristic time is defined [following Eq. (5)] as

$$\tau_{\rm dyn} = \sqrt{\frac{mL^{\gamma+2}}{gN}} \tag{57}$$

and we report our results for velocities in units of

$$v^* = \frac{L}{\tau_{\rm dyn}} = \sqrt{\frac{gN}{mL^{\gamma}}}. \tag{58}$$

IV. RESULTS FOR CASE OF GRAVITY ($\gamma = 1$)

In this section, we check our numerical and analytical results using the canonical case of gravity as an established benchmark.

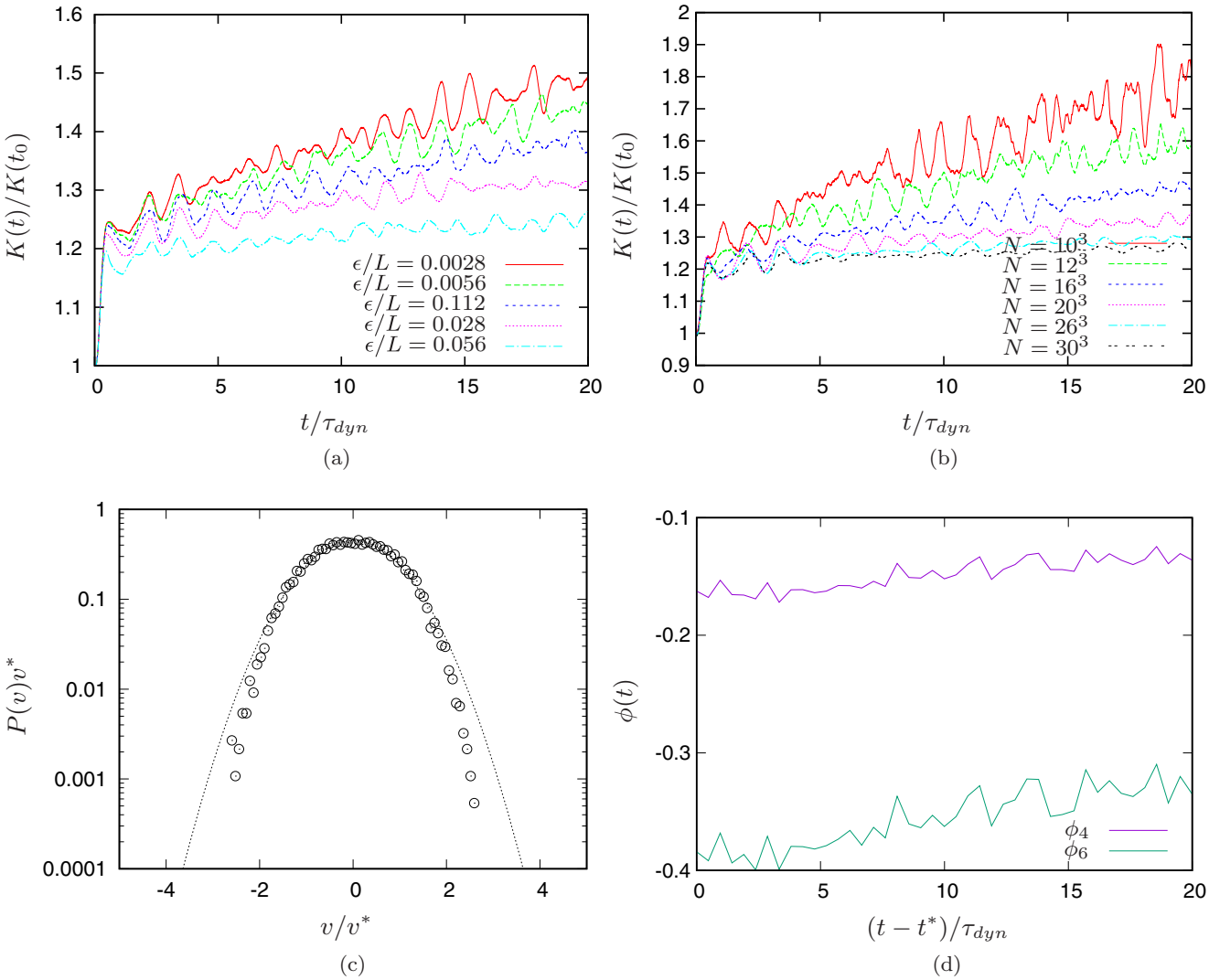

FIG. 7. Results of simulations for the case $\gamma = 5/4$. (a) Evolution of the normalized total kinetic energy for different values of ϵ at fixed $N = 20^3$, i.e., the set of simulations $\mathcal{C}(5/4; 20^3, \epsilon)$; (b) same quantity but for varying N and fixed ϵ/L; (c) velocity distribution for the simulation $\mathcal{C}(5/4; 20^3, 0.0028)$ at $t = 10\tau_{\rm dyn}$; and (d) evolution of ϕ_4 and ϕ_6 for the simulation $\mathcal{C}(5/4; 20^3, 0.0028)$.

A. Qualitative inspection of evolution

Figure 5(a) shows the evolution of the total kinetic energy normalized to its initial value at $t = 0$, for different values of the softening ϵ. We observe that, for sufficiently small softening, and sufficiently short times, the curves match very well. We interpret this to be because they are following the same mean-field evolution. Further, the kinetic energy (and viral ratio) shows a rapid relaxation (by $t \approx \tau_{\rm dyn}$) to relatively small and progressively damped oscillations around an approximately stationary value. This is the familiar mean-field relaxation to a QSS, which in practice we will consider to be established below from $t \approx 10\tau_{\rm dyn}$. For larger times, we observe a slow linear drift in time of the average value of the kinetic energy, which can be interpreted as a signature of the slow collisional relaxation process. In line with the prediction of Eq. (49), this collisional relaxation is suppressed when the softening increases. Figure 5(b) compares the evolution of systems with a fixed (compact) softening but different number of particles. We observe a similar behavior to that in the previous plot, and very consistent with the interpretation given of this evolution as the relaxation to a QSS: we observe a drift away from the almost stationary kinetic energy, which develops more slowly as the number of particles N increases.

Figure 5(c) shows, for the simulation $\mathcal{C}(1; 20^3, 0.0028)$, the velocity distribution at $t = 20\tau_{\rm dyn}$. We observe that the tails of the distribution are clearly non-Gaussian, and thus that the system is not at thermal equilibrium. This is confirmed by the evolution of the functions ϕ_4 and ϕ_6, which are plotted in Fig. 5(d). They are clearly nonzero, indicating a non-Gaussian velocity distribution, and further, show manifestly a slow growth on a longer time scale which is indicative of relaxation towards a Gaussian distribution. Finally, as shown in Figs. 5(e) and 5(f), respectively, the density profile (i.e., mean density in spherical shells centred on the center of mass of the system) at $t = 20\tau_{\rm dyn}$ appear to be independent of the parameters ϵ and

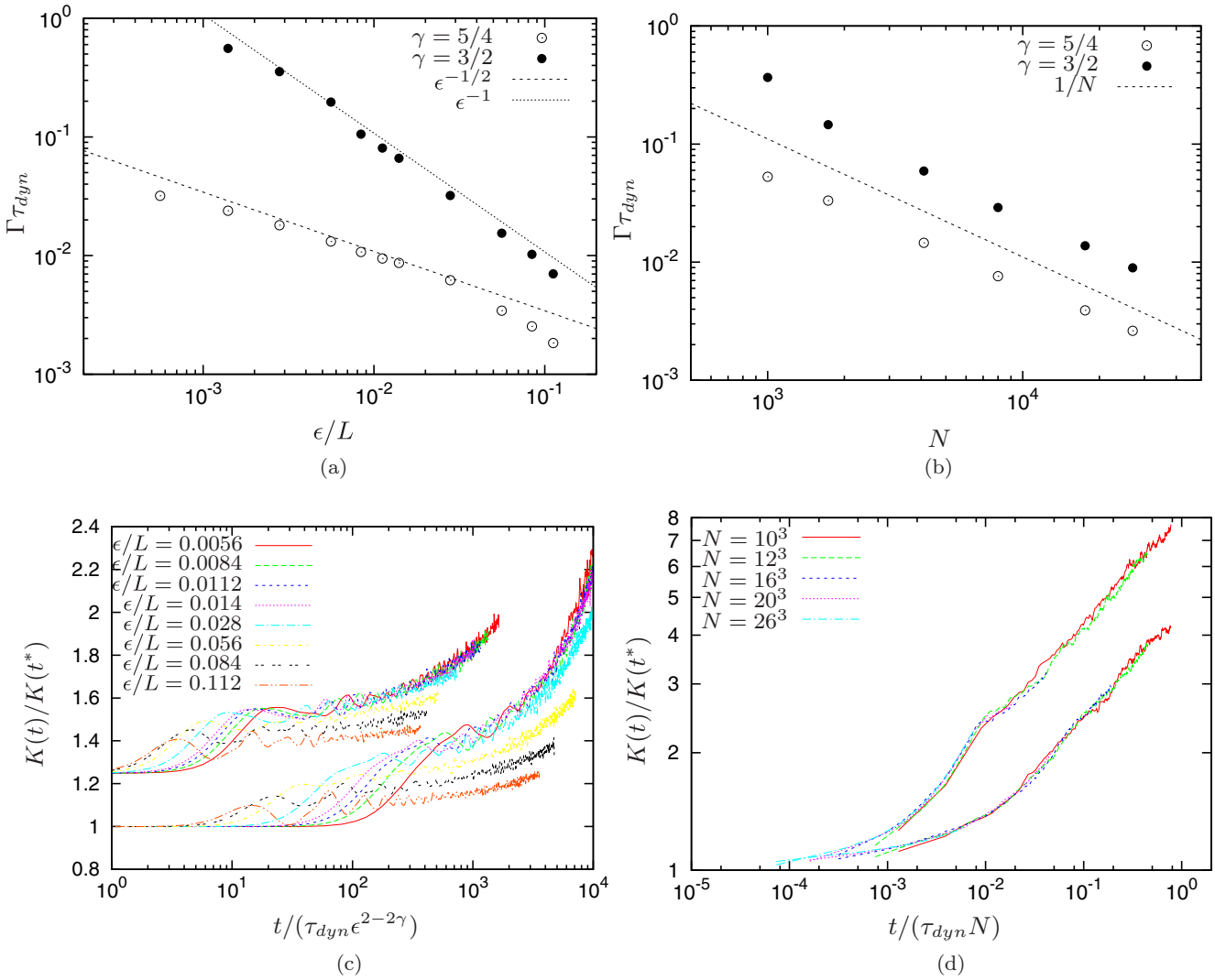

FIG. 8. Tests of scaling of measured relaxation rates: (a) $\Gamma\tau_{\rm dyn}$ as a function of ϵ (compact softening), for the cases $\gamma = 5/4$ and $3/2$ in simulations; and (b) as a function of N for $\gamma = 5/4$ and $3/2$; (c) collapse plot at $N = 20^3$ constant and varying ϵ for $\gamma = 5/4$ (upper curves, all the curves have been multiplied by a factor of 1.25) and $\gamma = 3/2$ (lower curves); and (d) collapse plot at constant $\epsilon/L = 0.1$ and varying N for $\gamma = 5/4$ (lower curve) and $\gamma = 3/2$ (upper curve).

N, as they should be if this profile is indeed characteristic of a QSS.

B. Scaling of the relaxation rate

Figures 6(a) and 6(b) show the evolution of the collisional relaxation parameter $\Delta(t)$, defined in Eq. (54), as a function of time, for different values of ϵ and N. We estimate the relaxation rate as the slope of a linear fit to $\Delta(t)$ at short times. Inspecting Fig. 5(a) or 5(b), we assume that the QSS has been reached at $t = 10\tau_{\rm dyn}$, and we take the reference time t^* to evaluate the slope of $\Delta(t)$ as $t^* = 20\tau_{\rm dyn}$. We can estimate the value of b_0 using Eq. (13) by measuring the relative velocity from the simulation. This gives $b_0/L \approx 8.8 \times 10^{-5}$. As this is considerably smaller even that the smallest softening used, we expect that the relaxation rate will scale as in Eq. (49) rather than Eq. (42). We show in Figs. 6(c) and 6(d) the measured scalings of the relaxation rate with ϵ and N respectively. We observe that there is indeed very good agreement with the theoretical scaling of Eq. (49).

V. RESULTS FOR POTENTIALS WITH $\gamma \neq 1$

We now consider the case of power-law interactions other than gravity. We consider first pair interactions which decrease more rapidly at large separations than the gravitational one, i.e., $\gamma > 1$, and then the case $\gamma < 1$.

A. Interactions decaying faster than gravity ($\gamma > 1$)

We present results for two specific cases: $\gamma = 5/4$ and $3/2$. As discussed above we do not consider larger values because, as predicted by the our analytical calculations, the two-body collision rates increase rapidly as γ does, making it more and more difficult numerically to separate the associated time scale from the mean-field one. Indeed, from Eq. (48), it follows that, at fixed N, the relaxation rate scales as $\epsilon^{-2\gamma}$.

Figures 7(a) and 7(b) display results for the evolution of the total kinetic energy in the case $\gamma = 5/4$. We observe a very similar behavior to that in the gravitational case: the curves are superimposed at the early stage of evolution, and start to separate as time increases. Consistent with the interpretation of this drift as due to two-body relaxation, we observe that it becomes slower for larger N and larger ϵ. Figure 7(c) shows the velocity distribution at $t^* = 10\tau_{\rm dyn}$, and Fig. 7(d) the temporal evolution of the parameters ϕ_4 and ϕ_6 starting from this time. The velocity distribution is clearly initially non-Gaussian but apparently evolves progressively towards a Gaussian. We do not display our results for the case $\gamma = 3/2$, but very similar behaviors are again observed.

We estimate the relaxation rate in the same manner as we did above for the case of gravity, using the evolution of the indicator $\Delta(t)$ (which we do not plot) starting from the reference time t^* (with $t^* = 10\tau_{\rm dyn}$ for $\gamma = 5/4$, and $t^* = 5\tau_{\rm dyn}$ for $\gamma = 3/2$). Estimating again the value of b_0 using Eq. (13), we obtain $b_0/L \approx 3.7 \times 10^{-4}$ for $\gamma = 5/4$, and $b_0/L \approx 8.7 \times 10^{-4}$ for $\gamma = 3/2$. As in the case of gravity, these are therefore smaller than or of the same order as the minimal softening ϵ used, and we thus expect that the scaling of the relaxation rate should be given by Eq. (48).

Figure 8(a) shows the measured relaxation rate for a range of softenings ϵ (for compact softening) at constant particle number $N = 20^3$, for both $\gamma = 5/4$ and $3/2$. Figure 8(b) shows the scaling of the relaxation rate at varying N and constant $\epsilon/L = 0.01$. The error bars have been determined as the statistical error in the fit of Δ, and are smaller than the size of the symbols. We observe that there is very good agreement between the scalings measured and the theoretically predicted one (48). For the largest values of ϵ we observe a departure from the theoretical scaling. This is due to the finite size of the system (when ϵ is around one tenth of the size of the system, where the latter is estimated from the fall-off of the density profile).

We have considered above collisional relaxation over time scales over which the parameters used to monitor evolution change by a small amount. In principle, the predicted scalings should apply also on longer time scales, provided the scale introduced by the softening length is sufficiently small that it does not affect significantly the properties of the QSS. Figure 8(c) shows the temporal evolution of the normalized total kinetic energy for $\gamma = 5/4$ (upper curves) and $\gamma = 3/2$ (lower curves) for a constant particle number N and a range of ϵ. The time axis has been rescaled in line with the theoretically predicted scaling (43). We observe a good superposition of the curves for the smaller values of ϵ, while for softening approaching the size of the system the observed relaxation rate is suppressed compared to the theoretical prediction, just as for the shorter time relaxation [see Fig. 8(a)]. Figure 8(d) shows an analogous collapse plot but for a (small) constant ϵ and varying N, with the time axis now rescaled with N following (43). We observe a very good match between the different curves over the whole duration of the runs.

B. Results: case $\gamma < 1$

In this case, we have seen that the predicted scaling of the relaxation rate is very simple: inversely proportional to N, and independent of the softening [cf. Eq. (47)]. This behavior is a consequence of the fact that the dominant contribution comes from the largest impact factor, which we have assumed to scale with the system size. To test this prediction, we have simulated the case $\gamma = 1/2$. Figure 9(a) shows the evolution of the normalized kinetic energy as a function of time for a range of (compact) softenings ϵ, while Fig. 9(b) shows the same quantity for a range of N at fixed (small) ϵ, as a function of a time variable linearly rescaled with N in accordance with the predicted scaling. We observe that the results are in excellent agreement with the theoretical predictions.

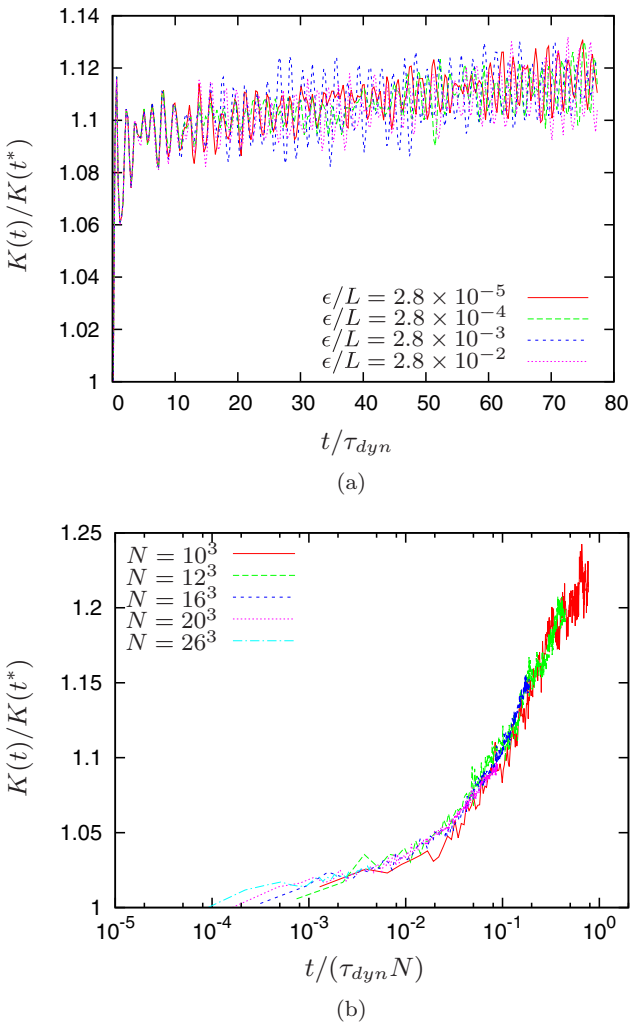

FIG. 9. Evolution of the kinetic energy for systems with $\gamma = 1/2$: (a) for a range of different values of ϵ at fixed $N = 20^3$ and (b) for a range of N different number of particles at fixed $\epsilon = 0.0028$. In the latter plot, the time variable has been rescaled with N in line with the theoretically predicted scaling of Eq. (47).

VI. TESTS OF ANALYTICAL PREDICTIONS: BEYOND SCALING

In the previous sections, we have tested numerically the validity of the theoretical scaling relations derived in the first part of the paper. We now examine further how well

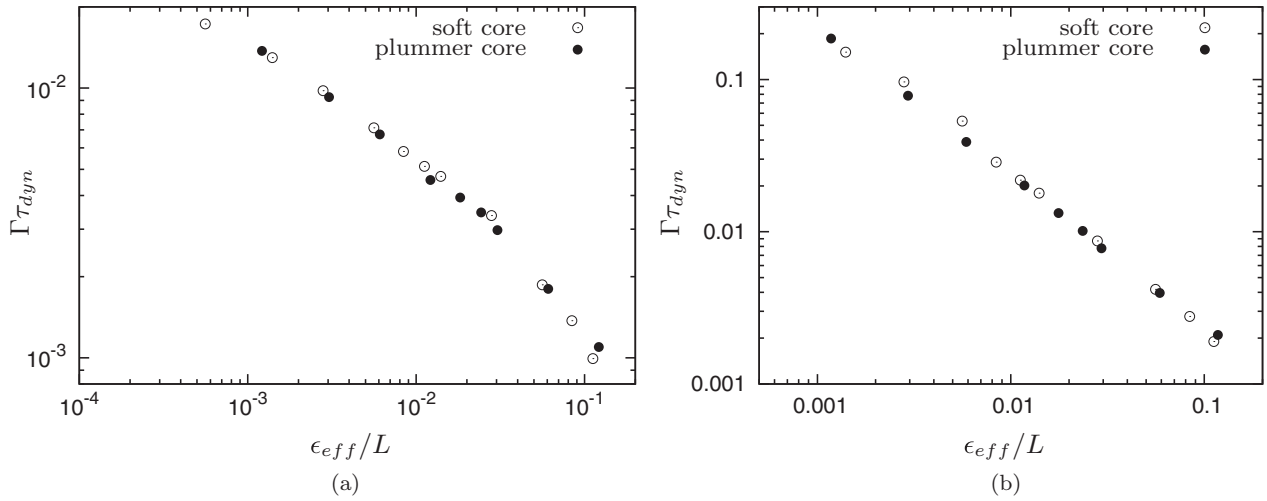

FIG. 10. Measured relaxation rates as a function of $\epsilon_{\rm eff}$ for the two different softening functions, for (a) $\gamma = 5/4$ and (b) 3/2.

the *amplitudes* of the measured relaxation rates match the predictions.

As we have discussed (see also Ref. [13]), the approach we have adopted in deriving two-body collision rates, following that used originally by Chandrasekhar for gravity, makes a number of very strong simplifying assumptions which make the calculation intrinsically inaccurate, notably: spatial homogeneity of the system and the assumption that all collisions take place at a fixed relative velocity given by the velocity dispersion. Further, the "largest impact factor," which we have taken to be given by the system size, is not in fact a precisely defined quantity and indeed it is often treated as a free parameter (see, e.g., Ref. [49] for a discussion in the context of the orbit-averaging technique). Other collisional effects that have been identified through the study of kinetic equations, such as orbit resonances and various collective effects (see e.g., Ref. [23]), are also evidently not taken into account. Thus, even if incoherent two-body scatterings are the dominant collisional process, we cannot expect the calculation method given to provide a very precise prediction for the amplitudes of the relaxation rates. Nevertheless, the fact that the predicted scalings turn out to be in such good agreement with those observed, one would expect the quantitative discrepancies might not to be too large.

A. Effect of softening function

In Secs. II D and III C, we have discussed how the softening of the potential at small scales affects the predicted relaxation rate. The predicted modification depends, in general, not just on the value of the softening scale, but on the detailed form of the softened potential. We have noted, however, that, for $\epsilon \gg b_0$, the effect of any such smoothing is an overall amplitude shift [cf. Fig. (4)]. This allowed us to define, for any softening potential, a constant α giving an effective softening $\epsilon_{\rm eff} = \alpha\epsilon$. The latter is the value of the softening of a reference softened potential which is sharply cutoff at $\epsilon_{\rm eff}$, which gives the same predicted relaxation rate as the actual softened potential. The values of α for the two potentials (compact and Plummer) we have employed are given in Table I.

Thus the theoretical calculations of the two-body relaxation rates make a prediction about the *relative amplitude* of the relaxation rates for our two different smoothings, which we should expect to hold even if the prediction of the absolute amplitude of both may be incorrect. Figures 10(a) and 10(b) shows the relaxation rate measured in simulations with $N = 20^3$, as a function of the calculated $\epsilon_{\rm eff}$ over a wide range. The superposition of the two curves is almost perfect, in line with the theoretical prediction.

B. Detailed comparison of relaxation rates

We now compare directly the amplitudes of the predicted and measured relaxation rates. Table III shows, for the different values of γ we have simulated, the results of this comparison. The second column gives the numerical value of $b_0 \approx (g/(m\langle v^2\rangle))^{1/\gamma}$, where $\langle v^2\rangle$ is the velocity dispersion measured at $t = 20\tau_{\rm dyn}$ in the simulations (we have used that $\langle V^2\rangle \simeq 2\langle v^2\rangle$). Using this value for b_0, and taking $R = 0.3$ for the system size [cf. Figs. 5(e) and 5(f)], we have calculated numerically the predicted $\Gamma\tau_{\rm dyn}$ shown in the third column ("Theory") using Eq. (23). The fourth column ("Numerics") gives the value of $\Gamma\tau_{\rm dyn}$ estimated in our simulations from the short time evolution of the normalized total kinetic energy $K(t)/K(t_0)$ as described in Sec. IV B. Comparing the last columns we find that, despite the many crude approximations

TABLE III. Comparison of the theoretical and measured relaxation rates in the simulations. The second column corresponds to an estimation of b_0, the third one to the estimation of $\langle|\Delta\mathbf{V}^2|\rangle/|V^2|$ using Eq. (23) and the fourth one the relaxation time measured in the simulations (see text).

γ	$b_0 \approx (g/(2m\langle V^2\rangle))^{1/\gamma}$	Theory	Numerics
1/2	9.2×10^{-8}	7.4×10^{-3}	4.6×10^{-4}
3/4	8.4×10^{-6}	1.4×10^{-2}	1.1×10^{-3}
1	8.8×10^{-5}	0.016	4.6×10^{-3}
5/4	3.7×10^{-4}	0.059	0.023
3/2	8.7×10^{-4}	0.017	0.24

performed in the derivation of the relaxation rate we obtain, as we have seen, not only the right scaling with the relevant parameters, but also a relatively good quantitative agreement for the amplitudes for all the cases simulated, with an overall discrepancy in the normalization varying between a factor one and eight.

C. Constraining the maximum impact factor

Going back to the original derivation of the two-body relaxation rate by Chandrasekhar, there has been a debate about the correct choice of the *maximum* impact parameter. In Sec. II A, we have argued that it should be assumed to be of the order of the size of the system, and we have obtained our results making this hypothesis.

For the case $\gamma \leqslant (d-1)/2$, which is dominated by the largest impact factors, we can in principle test this hypothesis. If, instead of Eq. (41), we fix an arbitrary maximum parameter $b_{\max}$, it is straightforward to show that we obtain

$$\Gamma\tau_{\rm dyn} = \tilde{C} N^{-1}\left(\frac{R}{b_{\max}}\right)^{2\gamma-d+1}, \tag{59}$$

where $\tilde{C}$ is a numerical coefficient (depending only on γ and d). If we now assume that $b_{\max} \sim RN^{-\lambda}$, we obtain

$$\Gamma\tau_{\rm dyn} \sim N^{\mu}, \tag{60}$$

where $\mu = \lambda(2\gamma - d + 1) - 1$. The case $\lambda = 0$ corresponds to the assumption we have made up to now, and the result (41). The case $\lambda = 1/d$ corresponds, on the other hand, to the assumption that $b_{\max}$ scales in proportion to the interparticle distance (as originally assumed by Chandrasekhar [9]). Now our numerical results in Sec. V indicate that, for the cases $\gamma = 1/2$ and $\gamma = 3/4$, that $\Gamma\tau_{\rm dyn} \sim N^{-1}$, which corresponds to $\mu = -1$ and therefore $\lambda = 0$.

In the specific case $\gamma = (d-1)/2$, i.e., gravity in $d = 3$, it is in fact possible to *quantify* the maximum impact factor rather than just its scaling. Instead of Eq. (49) (replacing ϵ by $\epsilon_{\rm eff}$ following the discussion in Sec. III C), we have

$$\Gamma\tau_{\rm dyn} = \tilde{D} N^{-1} \ln\left(\frac{b_{\max}}{\epsilon_{\rm eff}}\right), \tag{61}$$

where $\tilde{D}$ is a (calculable) numerical coefficient. Using the simulations presented in Sec. IV, we can fit very well the relaxation rate with

$$\Gamma\tau_{\rm dyn} = \ln\left(\frac{L}{3\epsilon_{\rm eff}}\right)\frac{7.2}{N}. \tag{62}$$

Comparing these last two equations, we have that $\alpha \approx 0$, and, further, that $b_{\max} \approx L/3 \approx R/3$. This size corresponds with the sharp fall-off of the density profile shown in the inset of Fig. 5(f). To check that $b_{\max}$ does not depend on N, we did another set of simulations with the same parameters, but $N = 10^3$ particles. From these we obtained the scaling of the relaxation rate as a function of ϵ plotted in Fig. 6(c), in which, following Eq. (49), the relaxation rate has been multiplied by a factor of eight. We thus obtain very good agreement with the predicted scaling. Our findings confirm therefore the results of Farouki and Salpeter [38,40], who found that the maximum impact parameter should be taken of order of the size of the system.

VII. CONCLUSION

In this paper, we have studied collisional relaxation in systems of particles interacting with a power-law potential $v(r \to \infty) \sim 1/r^{\gamma}$ (1), introducing a regularization of the singularity in the force as $r \to 0$ when necessary. In our analytical calculations, we have generalized the "Chandrasekhar approach" in the case of gravity to such potentials. We have also included the contribution of hard collisions rather than just weak collisions, in which the mean-field trajectories of the particles are weakly perturbed, which is the approximation usually found in the literature, see e.g., Ref. [23]. We have found that the collisional dynamics is dominated by (1) weak collisions, if $\gamma < (d-1)/2$, and (2) hard collisions, if $\gamma > (d-1)/2$, while the case $\gamma = (d-1)/2$, which corresponds to gravity in $d = 3$, is at the threshold. Moreover, we considered the large N, mean-field (or Vlasov) limit scaling of the two-body relaxation rate, assuming the considered particle system to be in viral equilibrium. *In absence of force regularization* (other than an infinitesimal one assumed implicitly to make two-body collisions defined for $\gamma > 2$), we found that this rate, expressed in units of the characteristic time for mean-field dynamics $\tau_{\rm dyn}$, vanishes in the large N for $\gamma < d-1$, and diverges in this limit for $\gamma > d-1$. This means that only in the former case does the mean-field limit of the dynamics exists for a virialized system; in the latter case it does not exist because the collisional relaxation completely dominates the mean-field dynamics. Only in the former case, therefore, can a QSS be expected to exist on a physically relevant time scale. This leads to the following *dynamical* classification of power-law interactions, as (1) *dynamically long-range* for $\gamma < d-1$: in this case $\tau_{\rm dyn} \ll \tau_{\rm coll}$ for sufficiently large N (and $\lim_{N\to\infty}\Gamma\tau_{\rm dyn} = 0$), and (2) *dynamically short-range* for $\gamma \geqslant d-1$: in this case $\tau_{\rm coll} \ll \tau_{\rm dyn}$ for sufficiently large N.

This classification was proposed initially [32] on the basis of a formal analysis of convergence properties of the force on a particle in the thermodynamic limit, and subsequently in Ref. [31] on the basis of the analysis detailed here. It has also been justified using different analytical approaches to the full kinetic theory of such systems [30,33]. As noted in Introduction, this classification differs from the usual one used to distinguish long-range from short-range interactions in the context of a thermodynamic analysis, in which the important feature is the integrability of the *pair potential*. There is therefore a range of γ, $d-1 < \gamma < d$, in which the interaction is *dynamically* short-range, but long-range according to its thermal equilibrium properties. In this case, if the number of particles is sufficiently large, there will be no QSS (as in short-range systems), but the thermal equilibrium state will present the typical features of a long-range system, i.e., spatial inhomogeneity, inequivalence of ensembles, etc.

We note that the more sophisticated approach using the Landau equation (without collective effects) or the Lenard-Balescu one (with collective effects) give rise to the same thresholds at $\gamma = (d-1)/2$ and $\gamma = d-1$, respectively (see, e.g., Ref. [30]). We emphasize, however, that these equations *cannot* make any prediction for the regimes in which strong collisions occur because they assume that collisions are weak, i.e., the orbits of particles are weakly perturbed because of the collisions. Therefore their prediction for the scaling of the collisional relaxation time is always $\tau_{\rm coll} \sim N^{-1}\tau_{\rm dyn}$.

We have also generalized these scalings when the interparticle potential is regularized ("softened") at small scales. With this regularization the case $\gamma \geqslant 2$ (in which the potential barrier cannot prevent the particles to collide for pure power–law potentials) becomes well defined. In this case, the relaxation rate depends on the value of the softening length ϵ for interactions in which small impact factors play a predominant role, i.e., $\gamma \geqslant (d-1)/2$.

We have presented, for $d = 3$, detailed numerical results which support our theoretical findings. We have confirmed previous results in the literature for the gravitational case $\gamma = 1$, notably for the scaling relations satisfied by the relaxation rate as function of the softening ϵ and the number of particles N. Furthermore, using the scaling of the relaxation rate with ϵ, we have found very strong numerical evidence that the maximum impact parameter is related with the size of the system and not microscopic scales such as the interparticle distance. We have simulated also the dynamically long-range cases $\gamma = 5/4$ and $3/2$, in which the collisional relaxation is dominated by collisions around the minimum impact parameter, obtaining again very good agreement with the theoretical scalings. For dynamically long-range systems dominated in our calculations by collisions with the largest impact parameter, we have found, as predicted, that a softening in the potential does not affect the relaxation rate.

The natural extension of this work is the numerical study of collisional relaxation allowing strong collisions, in order to check the scalings of this regime derived in this paper. For such study, it is necessary to develop very refined integration schemes in order to integrate properly such collisions. It would also be interesting in particular to explore the case of gravity with a hard cord regularization, for which the thermodynamic analysis has been considered in the literature (see e.g., Refs. [50,51]). Another interesting perspective is to study the problem with a more rigorous approach using the angle-action variables (with probably also many approximations because it is a very complicated formalism) in order to describe more precisely the relaxation dynamics, and in particular study more precisely the validity of the Chandrasekhar approximation as a function of the range of the interaction γ.

ACKNOWLEDGMENTS

We acknowledge many useful discussions with J. Morand, F. Sicard, and P. Viot. This work was partly supported by the ANR 09-JCJC-009401 INTERLOP project and the CNPq (National Council for Scientific Development, Brazil). Numerical simulations have been performed at the cluster of the SIGAMM hosted at "Observatoire de Côte d'Azur", Université de Nice – Sophia Antipolis and the HPC and visualization resources of the Centre de Calcul Interactif hosted by Université Nice Sophia Antipolis.

APPENDIX A: AN ALTERNATIVE DERIVATION OF THE CHANGE IN PERPENDICULAR VELOCITY DUE TO A COLLISION

It is interesting to derive Eq. (18a) with a simpler method which can give more physical insight. We can compute the change in perpendicular velocity integrating the perpendicular component of the force for all the duration of the collision, assuming that the relative trajectories are unperturbed with constant relative velocity V:

$$F_\perp = \frac{\gamma g}{b^{\gamma+1}}\left[1+\left(\frac{Vt}{b}\right)^2\right]^{-(\frac{\gamma}{2}+1)}. \tag{A1}$$

The change in the perpendicular component of the velocity in a time $2t_c$ is thus

$$|\Delta \mathbf{V}_\perp| = \frac{\gamma g}{m b^{\gamma+1}}\int_{-t_c}^{t_c} dt\left[1+\left(\frac{Vt}{b}\right)^2\right]^{-(\frac{\gamma}{2}+1)} \tag{A2}$$

$$= \frac{\gamma g}{m b^{\gamma} V}\int_{\frac{Vt_c}{b}}^{-\frac{Vt_c}{b}} ds(1+s^2)^{-(\frac{\gamma}{2}+1)} \tag{A3}$$

$$\simeq \gamma\left(\frac{b_0}{b}\right)^{\gamma}\int_{-\infty}^{\infty} ds(1+s^2)^{-(\frac{\gamma}{2}+1)}. \tag{A4}$$

Taking the limit $t_c \to \infty$ and performing the integral we obtain exactly (18a).

APPENDIX B: EXACT FORM OF THE POTENTIAL WITH A SOFT CORE

The potential $v(r,\epsilon)$ is, for $r \geqslant \epsilon$, exactly

$$v(r \geqslant \epsilon,\epsilon) = \frac{g}{r^\gamma}. \tag{B1}$$

We define $u = r/\epsilon$. For $u < 1$, we use the following form of the potential for *soft* core softenings (see Fig. 11):

(1) $\gamma = 1/2$:

$$v(u,1)\epsilon^{1/2} = 15.75u^2 - 22.5u^3 + 8.75u^4; \tag{B2}$$

(2) $\gamma = 3/4$:

$$v(u,1)\epsilon^{3/4} = 11.875u^2 - 17.4167u^3 + 6.875u^4; \tag{B3}$$

(3) $\gamma = 1$:

$$v(u,1)\epsilon = 10u^2 - 15u^3 + 6u^4; \tag{B4}$$

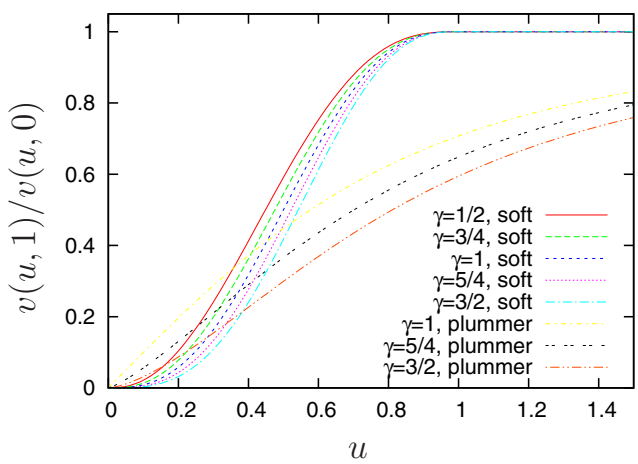

FIG. 11. Softened potentials used in the paper normalized to the unsoftened one.

(4) $\gamma = 5/4$:

$$v(u,1)\epsilon^{5/4} = 8.925u^2 - 13.65u^3 + 5.525u^4; \tag{B5}$$

(5) $\gamma = 3/2$:

$$v(u,1)\epsilon^{3/2} = 8.25u^2 - 12.8333333u^3 + 5.25u^4. \tag{B6}$$

[1] J. Binney and S. Tremaine, *Galactic Dynamics* (Princeton University Press, Princeton, 2008).
[2] P. H. Chavanis, *Dynamics and Thermodynamics of Systems with Long-Range Interactions* (Springer, New York, 2002).
[3] M. Chalony, J. Barré, B. Marcos, A. Olivetti, and D. Wilkowski, Phys. Rev. A **87**, 013401 (2013).
[4] A. Campa, T. Dauxois, and S. Ruffo, Phys. Rep. **480**, 57 (2009).
[5] I. Ispolatov and E. G. D. Cohen, Phys. Rev. E **64**, 056103 (2001).
[6] M. Kastner, Phys. Rev. Lett. **106**, 130601 (2011).
[7] L. Cevolani, G. Carleo, and L. Sanchez-Palencia, New J. Phys. **18**, 093002 (2016).
[8] V. A. Antonov, Vest. Leningr. Gos. Univ. **7**, 135 (1962).
[9] S. Chandrasekhar, *Principles of Stellar Dynamics* (University of Chicago Press, Chicago, 1942).
[10] Y. Y. Yamaguchi, J. Barré, F. Bouchet, T. Dauxois, and S. Ruffo, Physica A **337**, 36 (2004).
[11] M. Joyce and T. Worrakitpoonpon, J. Stat. Mech.: Theory Exp. (2010) P10012.
[12] T. N. Teles, Y. Levin, R. Pakter, and F. B. Rizzato, J. Stat. Mech.: Theory Exp. (2010) P05007.
[13] B. Marcos, Phys. Rev. E **88**, 032112 (2013).
[14] Y. Levin, R. Pakter, F. B. Rizzato, T. N. Teles, and F. P. d. C. Benetti, Phys. Rep. **535**, 1 (2014).
[15] P.-H. Chavanis, Astron. Astrophys. **556**, A93 (2013).
[16] M. Hauray and P. E. Jabin, Arch. Ration. Mech. Anal. **183**, 489 (2007).
[17] W. Braun and K. Hepp, Commun. Math. Phys. **56**, 101 (1977).
[18] H. Spohn, *Large Scale Dynamics of Interacting Particles* (Springer-Verlag, Berlin, 1991).
[19] N. Boers and P. Pickl, J. Stat. Phys. **164**, 1 (2016).
[20] D. Lazarovici and P. Pickl, Arch. Rational Mech. Anal. **225**, 1201 (2017).
[21] M. D. Weinberg, Astrophys. J. **410**, 543 (1993).
[22] J. Heyvaerts, Mon. Not. R. Astron. Soc. **407**, 355 (2010).
[23] P.-H. Chavanis, Physica A **391**, 3680 (2012).
[24] J. B. Fouvry, C. Pichon, J. Magorrian, and P. H. Chavanis, Astron. Astrophys. **584**, A129 (2015).
[25] J. B. Fouvry, C. Pichon, and P. H. Chavanis, Astron. Astrophys. **581**, A139 (2015).
[26] J.-B. Fouvry and C. Pichon, MNRAS **449**, 1982 (2015).
[27] J.-B. Fouvry, C. Pichon, and J. Magorrian, Astron. Astrophys. **598**, A71 (2017).
[28] J.-B. Fouvry, C. Pichon, and P.-H. Chavanis, arXiv:1605.03384.
[29] F. P. C. Benetti and B. Marcos, Phys. Rev. E **95**, 022111 (2017).
[30] P.-H. Chavanis, Eur. Phys. J. Plus **128**, 128 (2013).
[31] A. Gabrielli, M. Joyce, and B. Marcos, Phys. Rev. Lett. **105**, 210602 (2010).
[32] A. Gabrielli, M. Joyce, B. Marcos, and F. Sicard, J. Stat. Phys. **141**, 970 (2010).
[33] A. Gabrielli, M. Joyce, and J. Morand, Phys. Rev. E **90**, 062910 (2014).
[34] S. Chandrasekhar, Astrophys. J. **97**, 255 (1943).
[35] M. Hénon, Ann. Astrophys. **21**, 186 (1958).
[36] P.-H. Chavanis, J. Stat. Mech.: Theory Exp. (2010)5, 19.
[37] J. Diemand, B. Moore, J. Stadel, and S. Kazantzidis, Mon. Not. R. Astron. Soc. **348**, 977 (2004).
[38] R. T. Farouki and E. E. Salpeter, Astrophys. J. **253**, 512 (1982).
[39] H. Smith, Jr., Astrophys. J. **398**, 519 (1992).
[40] R. T. Farouki and E. E. Salpeter, Astrophys. J. **427**, 676 (1994).
[41] C. Theis, Astron. Astrophys. **330**, 1180 (1998).
[42] L. D. Landau and E. M. Lifshitz, *Mechanics* (Butterworth-Heinemann, Oxford, 1976).
[43] D. Chiron and B. Marcos, arXiv:1601.00064.
[44] R. Balescu, *Statistical Mechanics. Matter out of Equilibrium* (Imperial College Press, London, 1997).
[45] P. Di Cintio, L. Ciotti, and C. Nipoti, Mon. Not. R. Astron. Soc. **431**, 3177 (2013).
[46] P. Di Cintio, L. Ciotti, and C. Nipoti, J. Plasma Phys. **81**, 495810504 (2015).
[47] V. Springel, Mon. Not. R. Astron. Soc. **364**, 1105 (2005).
[48] S. D. M. White, MNRAS **184**, 185 (1978).
[49] D. Meritt, *Dynamics and Evolution of Galactic Nuclei* (Princeton University Press, Princeton, 2013).
[50] P.-H. Chavanis, Eur. Phys. J. B **87**, 9 (2014).
[51] M. Champion, A. Alastuey, T. Dauxois, and S. Ruffo, J. Phys. A **47**, 225001 (2014).

J Stat Phys (2010) 141: 970–989
DOI 10.1007/s10955-010-0090-x

A Dynamical Classification of the Range of Pair Interactions

A. Gabrielli · M. Joyce · B. Marcos · F. Sicard

Received: 4 April 2010 / Accepted: 1 November 2010 / Published online: 16 November 2010

Abstract We formalize a classification of pair interactions based on the convergence properties of the *forces* acting on particles as a function of system size. We do so by considering the behavior of the probability distribution function (PDF) $P(\mathbf{F})$ of the force field $\mathbf{F}$ in a particle distribution in the limit that the size of the system is taken to infinity at constant particle density, i.e., in the "usual" thermodynamic limit. For a pair interaction potential $V(r)$ with $V(r \to \infty) \sim 1/r^{\gamma}$ defining a *bounded* pair force, we show that $P(\mathbf{F})$ converges continuously to a well-defined and rapidly decreasing PDF if and only if the *pair force* is absolutely integrable, i.e., for $\gamma > d - 1$, where d is the spatial dimension. We refer to this case as *dynamically short-range*, because the dominant contribution to the force on a typical particle in this limit arises from particles in a finite neighborhood around it. For the *dynamically long-range* case, i.e., $\gamma \leq d - 1$, on the other hand, the dominant contribution to the force comes from the mean field due to the bulk, which becomes undefined in this limit. We discuss also how, for $\gamma \leq d - 1$ (and notably, for the case of gravity, $\gamma = d - 2$) $P(\mathbf{F})$ may, in some cases, be defined in a weaker sense. This involves a regularization of the force summation which is generalization of the procedure employed to define gravitational forces

A. Gabrielli
Istituto dei Sistemi Complessi (ISC)—CNR, Via dei Taurini 19, 00185 Rome, Italy

A. Gabrielli
ISC-CNR, Physics Department, University "Sapienza" of Rome, Piazzale Aldo Moro 2, 00185 Rome, Italy

M. Joyce (✉) · F. Sicard
Laboratoire de Physique Nucléaire et Hautes Énergies, Université Pierre et Marie Curie—Paris 6, CNRS IN2P3 UMR 7585, 4 Place Jussieu, 75752 Paris Cedex 05, France
e-mail: joyce@lpnhep.in2p3.fr

M. Joyce
Laboratoire de Physique Théorique de la Matière Condensée, Université Pierre et Marie Curie—Paris 6, CNRS UMR 7600, 4 Place Jussieu, 75752 Paris Cedex 05, France

B. Marcos
Laboratoire J.-A. Dieudonné, UMR 6621, Université de Nice—Sophia Antipolis, Parc Valrose, 06108 Nice Cedex 02, France

in an infinite static homogeneous universe. We explain that the relevant classification in this context is, however, that which divides pair forces with $\gamma > d - 2$ (or $\gamma < d - 2$), for which the PDF of the *difference in forces* is defined (or not defined) in the infinite system limit, without any regularization. In the former case dynamics can, as for the (marginal) case of gravity, be defined consistently in an infinite uniform system.

Keywords Long range interactions · Clustering dynamics · Thermodynamic limit · Classification

1 Introduction

Interactions are traditionally classified as long-range (or short-range) with respect to the non-additivity (or additivity) of the *potential energy* in the usual thermodynamic limit, i.e., when the number of particles N and volume V are taken to infinity at constant particle density. This is the property which determines the way in which standard instruments of statistical mechanics are applied to determine *equilibrium* properties (see e.g. [1–3]). Indeed in the case of long-range interactions, these instruments are applied using an appropriately generalized thermodynamic limit, in which the coupling or density are also scaled with system size. Such an analysis gives rise generically to features at equilibrium which are qualitatively different from those in short-range systems—inhomogeneous statistical equilibria, non-equivalence of statistical ensembles, negative specific heat in the microcanonical ensemble (see e.g. [2, 3]). Most of these unusual features were first noted and studied in the context of the study of gravitating systems in astrophysics (see e.g. [4, 5] for reviews), and it has been realized in recent years that they are more generic in long-range interacting systems. This thermodynamic analysis extended to long-range systems is believed to determine, however, the behavior of such systems only on time scales which diverge as some power of N (when expressed in terms of the characteristic dynamical time scales). On shorter times scales—usually those of interest in practical applications—study of several such systems (see e.g. [6–10] and references therein) shows that they appear generically, like in the well-documented case of gravity, to relax from almost any initial conditions to (almost) time-independent states—referred to variously as "meta-equilibria", "quasi-equilibria" or "quasi-stationary states" (QSS). The physics of these states, which are generically very different from those at thermal equilibrium, is understood to be the result of evolution in the collisionless regime described by Vlasov equation (usually referred to as the "collisionless Boltzmann equation" in the astrophysical literature [11]). Both the genesis of these states and their long-time relaxation are poorly understood, and are the subject of active study (see e.g. [12–16]).

In this article we consider a simple classification of pair interactions different to this usual thermodynamic one. Instead of considering the convergence properties of *potential energy* in the usual thermodynamic limit, we consider those of the *force*, in the same limit. The resulting classification can, like the usual one, be understood easily from simple considerations. To see this let us consider, as illustrated schematically in Fig. 1, a uniform system of particles interacting by a pair potential $V(r \to \infty) \sim 1/r^{\gamma}$, and divided into two pieces, A and B. For the usual thermodynamic classification one can consider that when the potential $V(r)$ is integrable at large r, i.e., $\gamma > d$ where d is the spatial dimension, the potential energy of a typical particle comes essentially from its interaction with particles in a finite region about it. The energy of a particle (e.g. P or P') in A is thus insensitive to whether B is present or not (and thus the total energy is equal, up to surface effects, to the sum of the

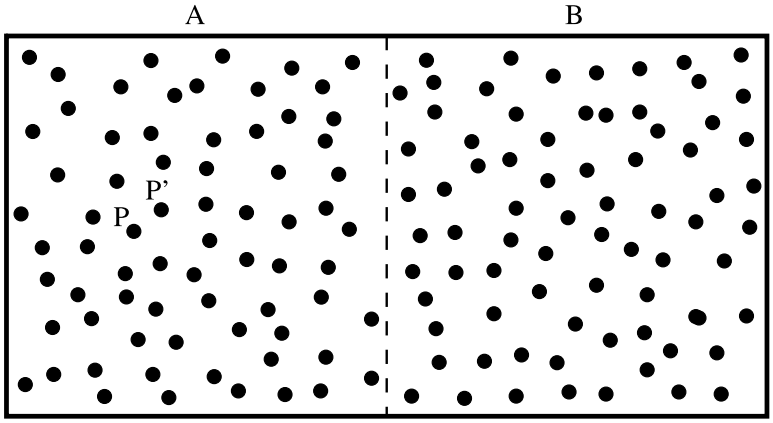

Fig. 1 An (approximately) uniform system consisting of two sub-systems **A** and **B**

energies of the subsystems): from an energetic point of view a particle "does not care" what the size of the system is, and the interaction is in this sense short-range. The distinction we consider is the analogous one deduced when one reasons in terms of *force* (or acceleration) rather than potential energy, and since forces are the primary physical quantities in dynamics, we refer to the corresponding classification as one of *dynamical* range. It is straightforward to see that in such a system, if the pair force is absolutely integrable, i.e., $\gamma > d - 1$, the force acting on a typical particle is due essentially to its interaction with particles in a finite neighborhood around it, while if $\gamma < d - 1$ this is not the case. Thus in the former case a particle in A "does not care" whether the sub-system B is present or not, and in this sense the interaction is "dynamically short-range". The classification differs from the standard one for interactions with $d < \gamma < d - 1$: for such interactions the potential energy "sees the bulk", but the force, which is its derivative, does not.

While the principle motivation for defining such a classification is that it may be relevant to understanding the qualitative behaviors of the out of equilibrium dynamics of such systems, it is *not* the aim of this article to establish that this is the case. We will limit ourselves in this respect to some brief remarks in our conclusions below. Our goal here is to provide a precise formulation of such a classification of the range of interactions based on the convergence properties of forces. While in the usual thermodynamic classification case one considers (see e.g. [1]) the mathematical properties of essential functions describing systems at equilibrium in the limit $N \to \infty$, $V \to \infty$ at fixed particle density $n_0 = N/V$ (i.e. the usual thermodynamic limit), we will consider the behavior of functions characterising the forces in this same limit. More specifically we consider, following an approach introduced by Chandrasekhar for the case of gravity [17, 18], the definedness of the probability distribution function (PDF) of the force field in statistically homogeneous particle distributions as the size of the system becomes arbitrarily large. Such distributions and this limit may be described mathematically using the language of stochastic point processes, considering the class of such processes which have a well defined positive mean density when the infinite size limit is considered. To avoid any confusion we will refer to the usual thermodynamic limit in this context simply as the *infinite system limit*. Indeed the existence or non-existence of the quantities we are studying in this limit has no direct relation here to the determination of properties at thermal equilibrium. Further, in the context of the literature on long-range interactions the term "thermodynamic limit" is now widely associated with the generalized such limit, which involves adopting a different scaling of V (or possibly coupling constants) with N (for a discussion see e.g. [19]).

In this article we also discuss, in Sect. 4, a further (and different) classification which can be given of pair interactions according to their range. This is relevant when one addresses more generally, for any given pair interaction, a question which arises for Newtonian gravity

in a cosmological setting: can a consistent dynamics be defined in an infinite system with non-zero density? A rigorous approach to the same question and the connection with the possibility of defining a *statistical mechanical* state for the system has been developed in [20, 21] in the particular case of a short range non-negative pair potential with finite support. Our conclusion, which generalizes a previous discussion given by two of us in [22], is that the answer to this question is that a necessary and sufficient condition for such a dynamics is not the integrability of the pair force, but instead the integrability of its gradient. This means that one requires $\gamma \geq d-2$, with gravity in any dimension (i.e. $\gamma = d-2$, the interaction potential solving the appropriate d-dimensional Poisson equation) being the marginal case in which such an infinite system limit may be defined. The reason is simply that, in an infinite system without any preferred point (i.e. when this limit is defined respecting statistical translational invariance), the physically meaningful quantity is the relative position of particles (as there is no meaning to absolute position). It is thus the convergence of relative forces on particles with system size which matters. In terms of the schema given above the distinction arises thus when one considers two close-by points (e.g. P and P' in Fig. 1) in sub-system A, say, and asks whether their relative forces—and thus relative motions—depend on the presence of B or not (or, equivalently, on the size of the system). The answer is that this difference of forces does not essentially depend on B if the gradient of the pair force is absolutely integrable, i.e., $\gamma > d-2$, as in this case this difference is dominated by the contribution from particles in a finite neighborhood around them. Thus for the case that $d-2 < \gamma \leq d-1$ the forces acting on two such particles become ill defined as the size of the system is extended to infinity, but their difference remains finite. Indeed, as has been discussed in [22] in the context of gravity in one dimension, the diverging component of the force on a particle represents a force on their centre of mass, which has no physical relevance in an infinite system without a preferred origin.

The paper is organized as follows. In the next section we recall the essential properties of stochastic point processes of relevance to our considerations, and then consider the general analyticity properties of the PDF of the total force at an arbitrary spatial point in such a particle distribution. We show that, for any pair force which is bounded, this PDF in the infinite volume limit is either well defined and rapidly decreasing, or else vanishes pointwise, i.e., the total force is an ill defined stochastic quantity. This means that it suffices, when studying pair potentials with different possible behaviors at large scales, to show that some chosen moment of the PDF converges to a finite value in this limit (or diverges) in order to establish that the whole PDF itself is well-defined (or ill defined). In Sect. 3 we give a general and formal expression for the variance of the total force PDF in a generic infinite uniform stochastic process in terms of the pair force and the two-point correlation properties of the SPP. From this we then deduce our principal result that the force PDF exists strictly in the infinite system limit if and only if the pair force is absolutely integrable at large separations (i.e. $\gamma \leq d-1$) , while it can be defined only in a weaker sense, introducing a regularization, when the pair force is not absolutely integrable. In the following section we discuss the physical relevance of the use of such a regularization, which is the generalization of a simple formulation given by Kiessling [23] of that originally introduced by Jeans for the case of gravity [24], often misleadingly referred to as the "Jeans swindle" [11, 23]. By analyzing the evolution of density perturbations in an infinite system, we show that the physical relevance of such a regularization of the forces requires also a constraint on the behavior of the PDF of total *force differences* as a function of system size. This leads to the conclusion that $\gamma \leq d-2$ is the necessary and sufficient condition in order for it to be possible to have a well defined infinite system limit at constant density for dynamics under a given pair interaction. In the conclusions we review briefly the relation of our results to previous

work in the literature, and comment a little more on the possible relevance of our principle classification of interactions into *dynamically short-range* and *dynamically long-range* to the study of the out of equilibrium dynamics of such systems.

2 The Force PDF in Uniform Stochastic Point Processes: General Results

We first recall the definitions of some basic quantities used in the statistical characterization of a stochastic point process and define the total force PDF (see e.g. [18] for a detailed discussion). We then derive some results on the analyticity properties of the latter quantity which we will exploit in deriving our central results in the next section.

2.1 Stochastic Point Processes

In order to study the properties of the force field in the infinite system limit given by $N \to \infty$, $V \to \infty$ with fixed average density $n_0 > 0$ for a large scale uniform and spatially homogeneous particle system, we generalize the approach introduced by Chandrasekhar in [17] for the total gravitational field in a homogeneous Poisson particle distribution to more general cases and spatial dimensions. To do so we need to characterize statistically point-particle distributions in this limit, and we do this using the language of stochastic point processes (SPP). The microscopic number density of a single realization of the process is

$$n(\mathbf{x}) = \sum_i \delta(\mathbf{x} - \mathbf{x}_i), \tag{1}$$

where δ is the d-dimensional Dirac delta function, $\mathbf{x}_i$ is the position of the ith system particle and the sum runs over all the particles of the system. We will limit our discussion to particle distributions in a Euclidean d-dimensional space which are (i) statistically translationally invariant (i.e. spatially homogeneous or stationary) and (ii) large scale uniform in the infinite volume limit. Property (i) means that the statistical properties around a given spatial point of the particle distribution do not depend on the location of the point. In other words the statistical weights of two realizations of the point process, of which one is the rigidly translated version of the other, are the same and do not depend on the translation vector. In particular this implies that the ensemble average (i.e. average over the realizations of the SPP) $\langle n(\mathbf{x})\rangle$ of the microscopic number density takes a constant value $n_0 > 0$ independent of $\mathbf{x}$. Moreover the two-point correlation function of the microscopic density $\langle n(\mathbf{x})n(\mathbf{x}')\rangle$ depends only on the vector distance $\mathbf{x} - \mathbf{x}'$. Feature (ii) means that the average particle number fluctuation $\delta N(R) = (\langle N^2(R)\rangle - \langle N(R)\rangle^2)^{1/2}$ in a sphere of radius R increases slower with R than the average number $\langle N(R)\rangle_0 \sim V(R)$ with R, where $V(R) \propto R^d$ is the volume of the d-dimensional sphere.

Let us start by considering a generic realization of the particle distribution in a finite volume V and let the total number of particles of the given realization be N. The particle positions $\mathbf{x}_i$ are fully characterized statistically by the joint probability densty function (PDF) $\mathcal{P}_N(\{\mathbf{x}_i\})$ conditional to having N particles in the realization ($\{\mathbf{x}_i\}$ indicates the set of positions of all system particles in the given realization). As a simple, but paradigmatic example we can think of the homogeneous d-dimensional Poisson point process. In this case $\mathcal{P}_N(\{\mathbf{x}_i\}) = V^{-N}$ simply and independently of the value of n_0. Given a function $X(\{\mathbf{x}_i\})$ of the N particle positions in thevolume V its average, conditional to the value of N, can be written as

$$\langle X\rangle_N \equiv \int_V \left[\prod_{i=1}^N d^d x_i\right] \mathcal{P}_N(\{\mathbf{x}_i\}) X(\{\mathbf{x}_i\}),$$

where the position of each particle is integrated in the volume V. In order to evaluate the *unconditional* average of the property X, for which all possible outcomes of the value N are considered, one would need the probability q_N of having N particles in the volume V, which permits to write:

$$\langle X \rangle = \sum_{N=0}^{\infty} q_N \langle X \rangle_N, \tag{2}$$

in a strict analogy with the grand canonical ensemble average in equilibrium statistical mechanics. However, since we are restricting the discussion to large scale uniform particle distributions, for which $\delta N(R)/\langle N(R) \rangle$ vanishes for asymptotically large R, we expect that the larger the volume V the narrower will be the peak around $N = \langle N(V) \rangle = n_0 V$ in which the measure q_N will be concentrated (for simplicity we have indicated with V both the region and its size). Asymptotically we expect that only the term of index $N_0 V$ will contribute to the sum in (2), i.e., for sufficiently large V we can write:

$$\langle X \rangle \simeq \langle X \rangle_{N_0 V}.$$

In other words we can consider that for sufficiently large V the conditional PDF $\mathcal{P}_{n_0 V}(\{\mathbf{x}_i\})$ characterizes completely the statistical properties of the particle distribution in the finite volume V and use this to evaluate in the following subsection the statistical properties of the total force. This is exactly what has been done, for instance, by Chandrasekhar in [17] to calculate the total gravitational force PDF in the Poissonian case.

In Appendix A we recall some of the basic definitions and properties of the statistical characterizations of uniform SPP. We will use below notably two essential properties of $S(\mathbf{k})$, the *structure factor* (SF), which follow from its definition:

- $$\lim_{k \to 0} k^d S(\mathbf{k}) = 0, \tag{3}$$

  i.e., the SF is an integrable function of $\mathbf{k}$ at $k = 0$, and
- $$\lim_{k \to \infty} S(\mathbf{k}) = 1. \tag{4}$$

2.2 General Expression for the Force PDF

Let us consider now that the particles in any realization of the SPP interact through a pair force $\mathbf{f}(\mathbf{x})$, i.e., $\mathbf{f}(\mathbf{x})$ is the force exerted by a particle on another one at vectorial separation $\mathbf{x}$. Further we will assume that the pair force is

- *central*, i.e.,

  $$\mathbf{f}(\mathbf{x}) = \hat{\mathbf{x}} f(x), \tag{5}$$

  where $\hat{\mathbf{x}} = \mathbf{x}/x$, and
- *bounded*, i.e., there exists $f_0 < \infty$ such that $|\mathbf{f}(\mathbf{x})| = f(x) \leq f_0$ for all $\mathbf{x}$.

These assumptions simplify our calculations considerably, but do not limit our aim which is to establish the relation solely between the statistical properties of the force field and *the behavior of the pair interaction at large distances*. Note that the second assumption means that, in cases such as the gravitational or the Coulomb interaction, the divergence at zero

separation is assumed appropriately regularized. We will briefly describe in our conclusions below how our results could be generalized to include such singularities.

Let us assume for the moment that the system volume V is *finite*. As shown above, if V is sufficiently large, one can consider that the number of particles in this volume is deterministically $N_0 V$. We will deal with the important problem of the infinite volume limit defined by $N, V \to \infty$ with $N/V \to n_0 > 0$ in the next subsection, by studying directly the limit $V \to \infty$ with fixed $N_0 V$. The total force field $\mathbf{F}(\mathbf{x})$ at a point $\mathbf{x}$, i.e., the force on a test particle placed at a point $\mathbf{x}$, may thus be written

$$\mathbf{F}(\mathbf{x}) = \sum_{i=1}^{N} \mathbf{f}(\mathbf{x} - \mathbf{x}_i) = \sum_{i=1}^{N} \frac{\mathbf{x} - \mathbf{x}_i}{|\mathbf{x} - \mathbf{x}_i|} f(|\mathbf{x} - \mathbf{x}_i|). \tag{6}$$

The force field $\mathbf{F}(\mathbf{x})$ may be considered as a stochastic variable with respect to the SPP. Choosing arbitrarily the origin as the point where the total force is evaluated, the PDF of this force is formally defined by[1]

$$P_N(\mathbf{F}) = \int_V \left[\prod_{i=1}^{N} d^d x_i \right] \mathcal{P}_N(\{\mathbf{x}_i\}) \delta\left[\mathbf{F} + \sum_i \mathbf{f}(\mathbf{x}_i) \right],$$

where we have used, as assumed, that $\mathbf{f}(-\mathbf{x}_i) = -\mathbf{f}(\mathbf{x}_i)$. Using the identity

$$\delta(\mathbf{y}) = \frac{1}{(2\pi)^d} \int d^d q \, e^{i\mathbf{q}\cdot\mathbf{y}} \tag{7}$$

this can be rewritten as

$$P_N(\mathbf{F}) = \frac{1}{(2\pi)^d} \int d^d q \, e^{i\mathbf{q}\cdot\mathbf{F}} \int_V \left[\prod_{i=1}^{N} d^d x_i \, e^{i\mathbf{q}\cdot\mathbf{f}(\mathbf{x}_i)} \right] \mathcal{P}_N(\{\mathbf{x}_i\}).$$

The integral over the spatial coordinates in the above equation defines the *characteristic function* of the total field $\mathbf{F}$

$$\tilde{P}_N(\mathbf{q}) = \int_V \left[\prod_{i=1}^{N} d^d x_i \, e^{i\mathbf{q}\cdot\mathbf{f}(\mathbf{x}_i)} \right] \mathcal{P}_N(\{\mathbf{x}_i\}), \tag{8}$$

so that

$$P_N(\mathbf{F}) = \frac{1}{(2\pi)^d} \int d^d q \, e^{i\mathbf{q}\cdot\mathbf{F}} \tilde{P}_N(\mathbf{q}).$$

The integral over spatial configurations in (8) can be conveniently rewritten as an integral over the possible values of the pair forces due to each of the $i = 1, \ldots, N$ particles:

$$\tilde{P}_N(\mathbf{q}) \equiv \int \left[\prod_{i=1}^{N} d^d f_i \, e^{i\mathbf{q}\cdot\mathbf{f}_i} \right] \mathcal{Q}_N(\{\mathbf{f}_i\}), \tag{9}$$

[1] We consider here the *unconditional* force PDF, i.e., the force is that at an arbitrary spatial point, rather than that on a point occupied by a particle which belongs to the particle distribution. It is the latter case, of the *conditional* force PDF, which is often considered in calculations of this kind (see e.g. [25–27]). The distinction is not important here as the constraints we derive, which depend on the *large scale* correlation properties of the particle distribution, would be expected to be the same in both cases.

where

$$\mathcal{Q}_N(\{\mathbf{f}_i\}) = \int_V \left[\prod_{i=1}^{N} d^d x_i\right] \mathcal{P}_N(\{\mathbf{x}_i\}) \prod_{i=1}^{N} \delta[\mathbf{f}_i - \mathbf{f}(\mathbf{x}_i)] \tag{10}$$

is the joint PDF for the pair forces $\mathbf{f}_i$. Note that, since $\mathbf{F}$ is the sum of the variables $\{\mathbf{f}_i\}$ its characteristic function $\tilde{P}_N(\mathbf{q})$ can be given as

$$\tilde{P}_N(\mathbf{q}) = \tilde{\mathcal{Q}}_N(\{\mathbf{q}_i = \mathbf{q}\}), \tag{11}$$

where $\tilde{\mathcal{Q}}_N(\{\mathbf{q}_i\})$ is the Nd-dimensional FT of the joint pair forces PDF $\mathcal{Q}_N(\{\mathbf{f}_i\})$, i.e.,

$$\tilde{\mathcal{Q}}_N(\{\mathbf{q}_i\}) = \int \left[\prod_{i=1}^{N} d^d f_i \, e^{i\mathbf{q}_i \cdot \mathbf{f}_i}\right] \mathcal{Q}_N(\{\mathbf{f}_i\}). \tag{12}$$

2.3 Analyticity Properties of the Force PDF

From the fact that the pair force is *bounded* it follows that $\mathcal{Q}_N(\{\mathbf{f}_i\})$ has a compact support, and, since it is absolutely integrable (by definition), FT theory (see e.g. [28]) implies that its characteristic function $\tilde{\mathcal{Q}}_N(\{\mathbf{q}_i\})$ is an analytic function of the variables $\{\mathbf{q}_i\}$. Consequently $\tilde{P}_N(\mathbf{q})$ is an analytic function of $\mathbf{q}$. Again from FT theory one has therefore that $P_N(\mathbf{F})$ is a rapidly decreasing function of $\mathbf{F}$:

$$\lim_{F\to\infty} F^\alpha P_N(\mathbf{F}) = 0, \quad \forall \alpha > 0.$$

Thus $P_N(\mathbf{F})$ is a well-defined function of which all moments finite, i.e., $0 < \langle |\mathbf{F}|^n \rangle < +\infty$ for any $n \geq 0$.

Let us now consider what happens when we take the limit $V \to \infty$ with $N_0 V$. On one hand the joint PDF $\mathcal{Q}_N(\{\mathbf{f}_i\})$ remains non-negative and absolutely integrable at all increasing V. On the other hand the support of this function remains compact with a diameter unaffected by the values of V, but fixed only by f_0. Therefore we expect that the FT theorem keeps its validity also in the infinite system limit resulting in an analytical

$$\tilde{P}(\mathbf{q}) \equiv \lim_{\substack{V\to\infty \\ N/V_0}} \tilde{P}_N(\mathbf{q}).$$

Therefore we will have that

$$P(\mathbf{F}) \equiv \lim_{\substack{V\to\infty \\ N_0 V}} P_N(\mathbf{F})$$

satisfies

$$\lim_{F\to\infty} F^\alpha P(\mathbf{F}) = 0, \quad \forall \alpha > 0.$$

There are then only two possibilities for the behavior of $\tilde{P}_N(\mathbf{q})$ in the infinite system limit:

1. It converges to an absolutely integrable function which is *not identically zero* everywhere, giving a $P(\mathbf{F})$ which is normalizable and non-negative on its support. Further all the integer moments of $|\mathbf{F}|$ are positive and finite.

2. It converges to zero everywhere, giving $P(\mathbf{F}) \equiv 0$. More specifically $P_N(\mathbf{F})$ with $N_0 V$ converges point-wise to the null function: it becomes broader and broader with increasing N (and V), but with an amplitude which decreases correspondingly and eventually goes to zero in the limit.

This latter case is analogous to the case of the sum of identically distributed uncorrelated random variables: if this sum is not normalized with the appropriate power of the number N of such variables, the PDF of the sum vanishes point-wise in a similar way in the limit $N \to \infty$.

In summary it follows from these considerations of the analyticity properties of $\tilde{P}_N(\mathbf{q})$ at increasing V that the case of a well defined, but fat tailed $P(\mathbf{F})$, can be excluded: in the infinite system limit the force PDF, if defined, is expected to be a normalizable and rapidly decreasing function.

3 Large Distance Behavior of Pair Interactions and the Force PDF

In this section we use the result derived in the previous section to infer the main result of this paper: the relation between the large scale behavior of the pair interaction and the force PDF in the infinite system limit.

We thus consider, as above, a central and bounded pair force such that

$$f(x) \simeq \frac{g}{x^{\gamma+1}} \quad \text{for } x \to \infty, \tag{13}$$

or, equivalently, a pair interaction corresponding to a two-body potential $V(x) \simeq g/(\gamma x^{\gamma})$ at large x for $\gamma \neq 0$ (and from $V(x) \simeq -g \ln x$ for $\gamma = 0$). Since the pair force is bounded, we have $\gamma > -1$.

Given the final result derived in the previous section, it follows that, to determine whether the force PDF exists, it is sufficient to analyze a single *even* moment of this PDF: because the PDF, when it exists, is rapidly decreasing, any such moment is necessarily finite and non-zero in this case, and diverges instead when the PDF does not exist. We choose to analyze the behavior of the second moment, $\langle F^2 \rangle$, which is equal to the variance of the PDF since the first moment $\langle \mathbf{F} \rangle$ is zero (see below). We choose this moment because, as we will now see, it can be expressed solely in terms of the FT of $\mathbf{f}(\mathbf{x})$ and of the SF of the microscopic density of the particle distribution. From these expressions we can then infer easily our result.

3.1 Variance of the Force in Infinite System Limit

The formal expression of the total force acting on a test particle (i.e. the force field) at $\mathbf{x}$ in the infinite system limit may be written

$$\mathbf{F}(\mathbf{x}) = \int d^d x' \, \frac{\mathbf{x} - \mathbf{x}'}{|\mathbf{x} - \mathbf{x}'|} f(|\mathbf{x} - \mathbf{x}'|) n(\mathbf{x}'), \tag{14}$$

where the integral is over the infinite space and $n(\mathbf{x})$, given in (1), is the density field in a realization of the general class of *uniform* SPP we have discussed with positive mean density n_0.

It is simple to show, using (14) and the definition of the SF given above in (A.1), that formally

$$\langle \mathbf{F}^2 \rangle = \frac{1}{(2\pi)^d} \int d^d k \, |\tilde{\mathbf{f}}(\mathbf{k})|^2 S(k), \tag{15}$$

where $\tilde{\mathbf{f}}(\mathbf{k})$ is the (d-dimensional) FT of $\hat{\mathbf{x}} f(x)$. It is straightforward to show that $\tilde{\mathbf{f}}(\mathbf{k}) = \hat{\mathbf{k}} \tilde{f}(k)$, where the explicit expression for $\tilde{f}(k)$ is given in the appendix.[2] We can thus write

$$\langle \mathbf{F}^2 \rangle = \frac{1}{(2\pi)^d} \int d^d k \, |\tilde{f}(k)|^2 S(k) = \frac{1}{2^{d-1}\pi^{d/2}\Gamma(d/2)} \int_0^\infty dk \, k^{d-1} |\tilde{f}(k)|^2 S(k), \quad (16)$$

where $\Gamma(x)$ is the usual Euler Gamma function.

3.2 Force PDF for an Integrable Pair Force

Let us now consider the integrability of the integrand in (16). We start with the case in which $f(x)$ is not only bounded but integrable in $\mathbb{R}^d$, i.e., with $\gamma > d - 1$. Given these properties, it is straightforward to verify, using the conditions (3) and (4) on $S(k)$ and standard FT theorems, that the function $|\tilde{f}(k)|^2 S(k))$ is also integrable in $\mathbb{R}^d$. The variance is therefore finite, from which it follows that the PDF exists, and furthermore that all its moments are finite.

3.3 Force PDF for a Non-integrable Pair Forces

For a pair force which is absolutely non-integrable, i.e., $\gamma < d - 1$, the FT $\tilde{\mathbf{f}}(\mathbf{k})$ of $\mathbf{f}(\mathbf{x})$ in (16) is defined only in the sense of distributions, i.e., the integrals over all space of $f(x)$ must be defined by a symmetric limiting procedure. Physically this means that the expression (14) for the force on a particle in infinite space must be calculated as

$$\mathbf{F}(\mathbf{x}) = \lim_{\mu \to 0^+} \lim_{V \to \infty} \int_V \frac{\mathbf{x} - \mathbf{x}'}{|\mathbf{x} - \mathbf{x}'|} f(|\mathbf{x} - \mathbf{x}'|) e^{-\mu|\mathbf{x}-\mathbf{x}'|} n(\mathbf{x}') \, d^d x', \quad (17)$$

where the two limits do not commute. In other words, $\mathbf{F}(\mathbf{x})$ is defined as the zero screening limit of a screened version of the simple power law interaction in an infinite system. The expression (16) is then meaningful when $\tilde{f}(k)$ is taken to be defined in the analogous manner with the two limits $\mu \to 0^+$ of the screening and $V \to \infty$ (i.e. with the minimal non-zero mode $k \sim 1/V \to 0^+$) taken in the same order as indicated in (17).

Let us consider then again, for the case $\gamma < d - 1$, the integrability of the integrand in (16). To do so we need to examine in detail the small k behavior of $\tilde{f}(k)$. It is shown in the appendix that, as one would expect from a simple dimensional analysis, for $f(r \to \infty) \sim 1/r^{\gamma+1}$ we have $f(k \to 0) \sim k^{-d+\gamma+1}$ in any d, for the case of a pair force which is not absolutely integrable, and bounded, i.e., $-1 < \gamma < d - 1$. It follows then from (16) that the variance is finite for a given γ only for a sub-class of uniform point processes, specifically those which satisfy

$$\lim_{k \to 0} k^{-d+2\gamma+2} S(k) = 0, \quad (18)$$

i.e., for $S(k \to 0) \sim k^n$ with

$$n > d - 2\gamma - 2 = -d + 2(d - 1 - \gamma). \quad (19)$$

For uniform point processes violating this condition, i.e., with $S(k \to 0) \sim k^n$ and $-d < n \leq -d + 2(d - \gamma - 1)$, the variance diverges. It follows from the results on the PDF of $\mathbf{F}$

[2] Note that only in $d = 1$ does $\tilde{f}(k)$ coincide with the direct FT of $f(x)$.

presented in the previous section that the total force itself $\mathbf{F}(\mathbf{x})$ is then badly defined in the infinite system limit.

These results of Sects. 3.2 and 3.3 combined are the central ones in this paper, anticipated in the introduction.

Firstly, when pair forces are absolutely integrable at large separations, the total force PDF is well defined in the infinite system limit, while for pair forces which are not absolutely integrable this quantity is ill defined. This has the simple physical meaning anticipated in the introduction: when this PDF is well defined, the force on a typical particle takes its dominant contribution from particles in a finite region around it; when instead the PDF is ill defined far-away contributions to the total force dominate, diverging with the size of the system. Thus absolutely integrable pair forces with $\gamma > d - 1$ are, in this precise sense, "short-range", while they are "long-range" when $\gamma \leq d - 1$. To avoid confusion with the usual classification of the range of interactions based on the integrability properties of the interaction potential, we will adopt the nomenclature that interactions in the case $\gamma > d - 1$ are *dynamically short-range*, while for $\gamma \leq d - 1$ they are *dynamically long-range*. Thus an interaction with $d - 1 < \gamma \leq d$ can be described as *thermodynamically long-range but dynamically short-range*.

Secondly the results in Sect. 3.3 detail how, for $\gamma \leq d - 1$, the force PDF in the infinite system limit may be defined provided an additional prescription is given for the calculation of the force. In the next section we explain the physical meaning and relevance of this result.

4 Definedness of Dynamics in an Infinite Uniform System

The regularization (17) is simply the generalization to a generic pair force with $\gamma \leq d - 1$ of one which is used for the case of Newtonian gravity, often referred to as the "Jeans swindle" (see e.g. [11]). It was indeed originally introduced by Jeans [24] in his treatment of self-gravitating matter in an infinite universe. However, as explained by Kiessling in [23], its denomination as a "swindle" is very misleading, as it can be formulated in a mathematically rigorous and physically meaningful manner, precisely as in (17).

The prescription (17) simply makes the force on a particle defined by setting to zero the ill defined contribution due to the non-zero mean density:

$$\langle \mathbf{F}(\mathbf{x}) \rangle = \lim_{\mu \to 0^+} n_0 \int \frac{\mathbf{x} - \mathbf{x}'}{|\mathbf{x} - \mathbf{x}'|} f(|\mathbf{x} - \mathbf{x}'|) e^{-\mu |\mathbf{x} - \mathbf{x}'|} \, d^d x' = 0. \tag{20}$$

The force on a particle can thus be written as

$$\mathbf{F}(\mathbf{x}) = \lim_{\mu \to 0^+} \int \frac{\mathbf{x} - \mathbf{x}'}{|\mathbf{x} - \mathbf{x}'|} f(|\mathbf{x} - \mathbf{x}'|) e^{-\mu |\mathbf{x} - \mathbf{x}'|} \delta n(\mathbf{x}') \, d^d x', \tag{21}$$

where $\delta n(\mathbf{x}') = n(\mathbf{x}') - n_0$ is the density fluctuation field. It is straightforward to show that the derived constraint (19) corresponds simply to that which can be anticipated by a naive analysis of the convergence of the integral (21): treating $\delta n(\mathbf{x}')$ as a deterministic function (rather than a stochastic field) one can require it to decay at large $|\mathbf{x}'|$ with a sufficiently large exponent in order to give integrability; taking the FT to infer the behavior of $|\tilde{\delta n}(\mathbf{k})|^2$ one obtains the condition (19).

The relevance of the results we have derived for the force PDF in the infinite system limit using this regularization arises thus, as it does in the case of Newtonian gravity, when one addresses the following question: is it possible to define consistently *dynamics* under a given

pair interaction in an infinite system which is uniform at large scales? As we now discuss, generalizing considerations given by two of us in [22] for the specific case of gravity in $d = 1$, the answer to this question is in fact phrased in terms of the definedness of the PDF of *force differences* rather than that of forces. This leads then to our second classification of pair interactions.

4.1 Evolution of Fluctuations and Definedness of PDF

Let us consider first an infinite particle distribution which is such that the total force PDF is defined *at some given time*, i.e., for $\gamma > d - 1$ we may consider any uniform SSP, while for $\gamma < d - 1$ we may consider (employing the regularization discussed) only the class of SSP with fluctuations at large scales obeying the condition (19) *at this time*. The forces on particles at this initial time are then well defined. This will only remain true, however, after a finite time interval, if the evolved distribution continues to obey the same condition (19). Let us determine when this is the case or not.

In order to do so, it suffices to consider the evolution of the density fluctuations, and specifically of the SF at small k, due to the action of this force field. Given that we are interested in the long-wavelength modes of the density field, we can apply the differential form of the continuity equation for the mass (and thus number) density between an initial time $t = 0$ and a time $t = \delta t$:

$$n(\mathbf{x}, \delta t) - n(\mathbf{x}, 0) = \vec{\nabla}[n(\mathbf{x}, 0)\mathbf{u}(\mathbf{x}, 0)], \tag{22}$$

where $\mathbf{u}(\mathbf{x}, 0)$ is the infinitesimal displacement field. Subtracting the mean density n_0 from both sides, and linearizing in $\delta n(\mathbf{x}, \delta t) = [n(\mathbf{x}, \delta t) - n_0]$ and $\mathbf{u}(\mathbf{x}, 0)$, we obtain, on taking the FT,

$$\tilde{\delta} n(\mathbf{k}, \delta t) = \tilde{\delta} n(\mathbf{k}, 0) + i n_0 \mathbf{k} \cdot \tilde{\mathbf{u}}(\mathbf{k}, 0). \tag{23}$$

Taking the square modulus of both sides, in the same approximation we get

$$|\tilde{\delta} n(\mathbf{k}, \delta t)|^2 - |\tilde{\delta} n(\mathbf{k}, 0)|^2 = n_0^2 k^2 |\tilde{\mathbf{u}}(\mathbf{k})|^2 + 2\mathbf{k} n_0 \mathrm{Im}[\tilde{\delta} n(\mathbf{k}, 0)\tilde{\mathbf{u}}^*(\mathbf{k}, 0)]. \tag{24}$$

If the displacements are generated solely by the forces acting (i.e. assuming velocities are initially zero), we have that

$$\mathbf{u}(\mathbf{x}, 0) = \frac{1}{2}\mathbf{F}(\mathbf{x}, 0)\delta t^2 \tag{25}$$

and thus, that $|\tilde{\mathbf{u}}(\mathbf{k})|^2 \propto |\mathbf{F}(\mathbf{k})|^2$. The latter quantity is given, using (15), by

$$|\mathbf{F}(\mathbf{k})|^2 = |\tilde{f}(k)|^2 S(k). \tag{26}$$

In the analysis in the previous section we used the result that at small k, $\tilde{f}(k) \sim k^{-d+\gamma+1}$. Thus $|\tilde{\mathbf{u}}(\mathbf{k})|^2 \sim k^{2m+n}$, where $m = -d + \gamma + 1$, if $S(k) \sim k^n$. It then follows, from (24), that the small k behavior of the time-evolved SF is given by

$$S_{\delta t}(k \to 0) \sim k^n + k^{1+m+n} + k^{2+2m+n}. \tag{27}$$

It can be inferred that the leading small k behavior of the SF is unchanged if and only if $m + 1 \geq 0$, i.e., $\gamma \geq d - 2$. Gravity ($\gamma = d - 2$) is the marginal case is which the long wavelength contribution to the SF generated by the evolution has the same exponent as

the initial SF: this is the well known phenomenon of *linear amplification* of initial density perturbations (see e.g. [11, 29]) which applies[3] in infinite self-gravitating systems (derived originally by Jeans).

If, on the other hand, $\gamma < d - 2$ (i.e. the interaction is "more long-range" than gravity in d dimensions) the exponent of the small k behavior is reduced from n to $n - 2(d - 2 - \gamma)$. Given that our result is for an infinitesimal time δt, this indicates in fact a pathological behavior: in any finite time interval the exponent n should become, apparently, arbitrarily large and negative, while, as shown in Sect. 2, the constraint $n > -d$ is imposed by the assumed large scale uniformity of the SPP. In other words this result means that, in the infinite system limit, when $\gamma < d - 2$, the condition of large scale uniformity is violated immediately by the dynamical evolution. The reason is simply that in this case the *rate of growth of a perturbation at a given scale increases with the scale*. Indeed this is the essential content of the analysis given just above: through the continuity equation, the perturbation to the density field is proportional to the *gradient of the displacement field*, which in turn is simply proportional to the *gradient of the force*. As we now detail more explicitly, when $\gamma < d - 2$, this quantity diverges with the size of the system.

4.2 PDF of Force Differences

Let us consider now the behavior of the PDF of the difference of the forces between two spatial points separated by a fixed vector distance $\mathbf{a}$:

$$\Delta\mathbf{F}(\mathbf{x}; \mathbf{x} + \mathbf{a}) \equiv \mathbf{F}(\mathbf{x}) - \mathbf{F}(\mathbf{x} + \mathbf{a}). \tag{28}$$

If this quantity is well defined in the infinite system limit, its PDF $\mathcal{P}(\Delta\mathbf{F}; a)$ will be independent of $\mathbf{x}$ and will have a parametric dependence only on $a = |\mathbf{a}|$ because of the assumed statistical translational and rotational invariance of the particle distribution.

The analysis of the properties of $\mathcal{P}(\Delta\mathbf{F}; a)$ in the infinite volume limit is formally exactly the same as that given above for the total force $\mathbf{F}$, with the only replacement of the pair force in (13) by the *pair force difference*:

$$\Delta\mathbf{f}(\mathbf{x}, \mathbf{x} + \mathbf{a}) = \mathbf{f}(\mathbf{x}) - \mathbf{f}(\mathbf{x} + \mathbf{a}), \tag{29}$$

i.e., the difference of the pair forces on two points located at $\mathbf{x}$ and $\mathbf{x} + \mathbf{a}$ due to a point at the origin. Assuming again the possible small scale singularities in this pair force difference to be suitably regulated, our previous analysis carries through, the only significant change being that, as $x \to \infty$,

$$\Delta\mathbf{f}(\mathbf{x}, \mathbf{x} + \mathbf{a}) \sim a\hat{\mathbf{x}}/x^{\gamma+2}. \tag{30}$$

Proceeding in exactly the same manner to analyse $\mathcal{P}(\Delta\mathbf{F}; a)$, we find that

- For $\gamma > d - 2$, i.e., if the *gradient of the pair force at fixed a is an absolutely integrable function* of $\mathbf{x}$ at large separations, the PDF $\mathcal{P}(\Delta\mathbf{F}; a)$ is well defined in the infinite system limit, and is a rapidly decreasing function of its argument for any SPP. This is true without any regularization.

[3] The result does not apply, however, when $n > 4$ [29]; the reason is that fluctuations with $S(k \to 0) \sim k^4$ arise generically from any rearrangement of matter due to dynamics which conserves mass and momentum locally. These effects are neglected implicitly above when we use the continuum approximation to the density fluctuation field.

- For $\gamma \leq d-2$, on the other hand, a well defined PDF may be obtained only by using the regularization like that introduced above in (17). Therefore the PDF of the force differences then remains well defined, i.e., the force difference $\Delta\mathbf{F}(\mathbf{x};\mathbf{a})$ remains finite at all $\mathbf{x}$, only in a sub-class of SPP defined by the constraint

$$n > d - 2\gamma - 4 = -d + 2(d-2-\gamma). \tag{31}$$

  For the case of gravity $\gamma = d-2$ this coincides with the full class of uniform SPP, while for any smaller γ, it restricts to a sub-class of the latter.

4.3 Conditions for Definedness of Dynamics in an Infinite System

Our analysis in Sect. 4.1 of the evolution of density perturbations under the effect of the mutual pair forces gave the sufficient condition $\gamma \geq d-2$ for the consistency of the dynamics in the infinite system limit, but with the assumption that the total force PDF was itself defined. This means that, in the range $d-2 \leq \gamma < d-1$, the result derived applies only to the sub-class of infinite uniform particle distributions in which the large scale fluctuations obey the condition (19). It is straightforward to verify, however, that the analysis and conclusions of Sect. 4.1 can be generalized to cover all uniform SPP for $\gamma \geq d-2$. In line with the discussion given above, the analysis requires in fact only assumptions about the behavior of the gradient of the forces, rather the forces themselves. More specifically, the only equation which explicitly contains the force, (25), is a purely formal step which can be modified to include the possibility that the force diverges with system size. Indeed if the force—at a given point—includes such a divergence it is sufficient that this divergence cancels out when we calculate the difference between this force and that at a neighboring point. Physically this means simply that, as discussed above, when we consider the relative motions of particles, it is sufficient to consider relative forces. Further, as we are considering the limit of an infinite system in which there is no preferred point (i.e. statistical homogeneity holds), only relative motions of points has physical significance, and therefore only the spatial variation of the forces can have physical meaning. These latter statements can be viewed as a kind of corollary to Mach's principle: if the mass distribution of the universe is, as it is in the case we consider, such that there is no preferred point in space (and, specifically, no center of mass) inertial frames which give absolute meaning to forces (rather than tidal forces) cannot be defined.

In summary our conclusion is that the necessary and sufficient condition for dynamics to be defined in the infinite system limit—in analogy to how it is defined for Newtonian self-gravitating particles in a infinite universe of constant density—is that the gradient of the pair force be absolutely integrable at large separations. Gravity is the marginal (logarithmically divergent) case in which such a dynamics can be defined, but only by using a prescription such as (17). Further these conditions on the range of pair forces can be expressed simply as one on the existence of the PDF of force differences of points as finite separations in the infinite system limit.

5 Discussion and Conclusions

In conclusion we make some brief remarks on how the results derived here relate to previous work in the literature on force PDFs. In this context we also discuss the important assumption we made throughout the article, that the pair force considered was *bounded*. Finally we

return briefly to the question of the relevance of the classification dividing interactions according to the integrability properties of the pair force, concerning which we have reported initial results elsewhere [30].

The first and most known calculation of the force PDF is that of Chandrasekhar [17], who evaluated it for the gravitational pair interaction in an infinite homogeneous Poisson particle distribution (in $d = 3$). This results in the so-called *Holtzmark distribution*, a probability distribution belonging to the Levy class (i.e. power law tailed with a diverging second moment) with $P(\mathbf{F}) \sim F^{-9/2}$ at large F. According to our results here, a well defined PDF may be obtained for such a force law, which is *not* absolutely integrable at large separations, only by using a prescription for the calculation of the force in the infinite system limit. In his calculation Chandrasekhar indeed obtains the force on a point by summing the contributions from mass in *spheres* of radius R centered on the point considered, and then taking $R \to \infty$ (with n_0 fixed). This prescription is a slight variant of the one we have employed (following Kiessling [23]): instead of the smooth exponential screening of the interaction, it uses a "spherical top-hat" screening so that the force may be written formally as in (17) with the replacement of $e^{-\mu|\mathbf{x}-\mathbf{x}'|}$ by a Heaviside function $\Theta(\mu^{-1} - |\mathbf{x} - \mathbf{x}'|)$. It is straightforward to verify that the result of Chandrasekhar is unchanged if the smooth prescription (17) is used instead. As the Poisson distribution corresponds to an SF $S(k \to 0) \sim k^n$ with $n = 0$, the general condition (19) for the existence of the PDF we have derived, which gives $n > -1$ for gravity in $d = 3$, is indeed satisfied. The fact that the PDF is power-law tailed (and thus *not* rapidly decreasing) arises from the fact that the calculation of Chandrasekhar does not, as done here, assume that the singularity in the gravitational interaction is regularized. Indeed it is simple to show explicitly [18] that this power law tail arises from the divergence in the pair force at zero separation. This can be done by considering the contribution to the total force on a system particle due to its nearest neighbor particle, which turns out to have a power law tail identical, both in exponent and amplitude, to that of the full $P(\mathbf{F})$.

Our analysis shows that it is true in general that well defined, but power-law tailed force PDFs, can arise only when there are singularities in the pair force: for a bounded force we have seen that the PDF is necessarily rapidly decreasing when it exists. More specifically, returning to the analysis of Sect. 2.3, it is straightforward to see that the crucial property we used of $\mathcal{Q}_N(\{\mathbf{f}_i\})$, that it have *compact support*, is no longer valid when the pair force has singularities. The analyticity properties which lead to a rapidly decreasing PDF may then not be inferred. We note that this is true at finite N, and has nothing to do with the infinite volume limit, i.e., the appearance of the associated power-law tail arises from the possibility of having a single particle which give an unbounded contribution rather than from the combination of the contribution of many particles which then diverges in the infinite system limit. The exponent in such a power-law tail will depend on the nature of the divergence at small separation. More specifically, for a central pair force as considered above and now with a singularity $f(x \to 0) \sim 1/x^a$, a simple generalization of the analysis for the case of gravity (see [18]) of the leading contribution to the total force coming from the nearest neighbor particle leads to the conclusion that $P(F \to \infty) \sim F^{-d-\frac{d}{a}}$ (where $F = |\mathbf{F}|$). This implies that the variance diverges (i.e. the PDF becomes fat-tailed) for $a > d/2$.

Force PDFs have been calculated in various other specific cases. Wesenberg and Molmer [25] derived that of forces exerted by randomly distributed dipoles in $d = 3$, corresponding to a pair force with $\gamma = 2$. According to our results this is the marginal case in which a summation prescription is required for the force, and indeed a prescription using spheres, like that used by Chandrasekhar for gravity, is employed. We note that [25] focusses on the power-law tails associated with the singularity at zero separation of the force, which lead in this case (as can be inferred from the result summarized above) to the divergence of the

first moment of the force PDF. One of us (AG) has given results previously [26] for the PDF for a generic power-law interaction in $d = 1$ for $\gamma > -1$ in our notation above. The conditional force PDF is then derived for the case of an infinite "shuffled lattice" of particles, i.e., particles initially on an infinite lattice and then subjected to *uncorrelated* displacements of finite variance, and using again, as Chandrasekhar, a "spherical top-hat" prescription for the force summation (for $\gamma \leq 0$, when the pair force is not absolutely integrable). It is simple to show [18] that such a distribution has an SF with $n = 2$ at small k, and thus the existence of the force PDF in these cases is again in line with the constraint (19) derived. Power-law tails are again observed in these cases, and their exponents related explicitly to the singularity in the assumed power-law force at zero separation.

The calculation of Chandrasekhar has been generalized in [27] to the case of particles on an infinite shuffled lattice. This leads again, in line with condition (19), to a well defined PDF, again with or without power-law tails according to whether the singularities in the pair force are included or not. Chavanis [31] considers, on the other hand, the generalization of Chandrasekhar calculation (for the PDF of gravitational forces in a Poisson distribution) to $d = 2$ and $d = 1$. The condition (19 for gravity ($\gamma = d - 2$) gives $n > -d + 2$, which implies that the force PDF is not defined in the infinite system limit we have considered for $d \leq 2$, and indeed in [31] well defined PDFs are obtained in $d = 2$ and $d = 1$ by using a different limiting procedure involving in each case an appropriate rescaling of the coupling with N. The physical meaning of such a procedure is discussed in [22], which considers in detail the calculation of the force PDF for gravity in $d = 1$ in a Poisson distribution (as in [31]). An exact calculation of the force PDF of the *screened* gravitational force in the infinite system limit is given, which allows one to see in this case exactly how the general result given here is verified in this specific case: all moments of the PDF diverge simultaneously as the screening length is taken to infinity, giving a PDF which converges point-wise to zero. The force PDF for gravity in $d = 1$ for a class of infinite particle distributions generated by perturbing a lattice has been derived recently by three of us in [32]. It is straightforward to show that one of the conditions imposed on the perturbations to obtain the PDF, that the variance of the perturbations be finite, corresponds in fact to the condition $n > 1$ which coincides precisely with the more general condition (19) derived here. Unlike in the other specific cases just discussed, it turns out that in this case (gravity in $d = 1$) it is in fact necessary to use the smooth prescription (17). As explained in detail in [32], the top-hat prescription does not give a well defined result in this case, because surface contributions to the force which do not decay with distance in this case are not regulated by it. We underline that the general result given in the present article are for this specific prescription (17). Further analysis would be required to derive the general conditions in which a top-hat prescription also gives the same (and well-defined) PDF.

Finally let us comment on why we anticipate the classification of pair interactions according to their "dynamical range", formalized here using the force PDF, should be a useful and relevant one physically in the study of systems with long-range interactions. The reason is that this classification reflects, as we have explained, the relative importance of the mean field contribution to the force on a particle, due to the bulk, compared with that due to nearby particles. Now it is precisely the domination by the former which is understood to give the regime of *collisionless* dynamics which is expected to lead to the formation of QSS states, which are usually interpreted to be stationary states of the Vlasov equations describing such a regime of the dynamics (see e.g. [19]). In a recent article [30] by three of us, we have reported a numerical and analytical study which provides strong evidence for the following result, very much in line with this naive expectation: systems of particles interacting by attractive power law pair interactions like those considered here can always give

rise to QSS; however when the pair force is *dynamically short-range* their existence requires the presence of a sufficiently large soft core, while in the *dynamically long-range* case QSS can occur independently of the core, whether hard or soft, provided it is sufficiently small. In other words only in the case of a pair force which is "dynamically long-range" can the occurrence of QSS be considered to be the result only of the long distance behavior of the interaction alone. This finding is very consistent with what could be anticipated from the preceding (naive) argument: the effect of a "soft core" is precisely to reduce the contribution to the force due to nearby particles, which would otherwise dominate over the mean field force in the case of a pair force which is absolutely integrable at large distances. Indeed the meaning of "sufficiently large" specified in [30] is that the size of the soft core must increase in an appropriate manner with the size of the system as the limit $N \to \infty$ is taken, while we have always implicitly assumed it to be fixed in units of the interparticle distance here. Further work on these issues will be reported elsewhere.

Acknowledgements We thank M. Kiessling and T. Worrakitpoonpon for useful conversations, and P. Viot for useful comments on the manuscript.

Appendix A: One and Two Point Properties of Uniform SPP

In this appendix we give the general one and two-point statistical characterization of a SPP which is uniform on large scales.

The description of the correlation properties of a generic uniform SPP is given by the n-point correlation functions of the density field. For our considerations it will turn out to be sufficient to consider only the two-point properties, and more specifically it will be most convenient to characterize them in reciprocal space through the *structure factor* (SF) (or power spectrum). This is defined by

$$S(\mathbf{k}) = \lim_{V\to\infty} \frac{\langle |\tilde{\delta} n(\mathbf{k}; V)|^2 \rangle}{n_0 V}, \tag{A.1}$$

where

$$\tilde{\delta} n(\mathbf{k}; V) = \int_V d^d x\, e^{-i\mathbf{k}\cdot\mathbf{x}} [n(\mathbf{x}) - n_0]. \tag{A.2}$$

With these normalisations the SF of an uncorrelated Poisson process is $S(\mathbf{k}) = 1$. For a statistically isotropic point process $S(\mathbf{k}) \equiv S(k)$, where $k = |\mathbf{k}|$. We recall here that $S(\mathbf{k})$ is the Fourier transform (FT) of the connected two point density correlation function:

$$S(\mathbf{k}) = \int d^d x\, e^{-i\mathbf{k}\cdot\mathbf{x}} C(\mathbf{x}),$$

where

$$C(\mathbf{x}) = \frac{\langle n(\mathbf{x}_0 + \mathbf{x}) n(\mathbf{x}_0) \rangle - n_0^2}{n_0} = \delta(\mathbf{x}) + n_0 h(\mathbf{x}).$$

In the last expression we have explicitly separated in the correlation function $C(\mathbf{x})$ the shot noise term $\delta(\mathbf{x})$, present in all SPP and due to the "granularity" of the particle distribution, from the "off-diagonal" term $n_0 h(\mathbf{x})$ which gives the actual spatial correlations between different particles.

In the paper we study the convergence properties of forces at large distances and are thus mainly interested in the properties of the SF at small k. In this respect we will use the following limit on the SF which follows from the assumed uniformity of the SPP:

$$\lim_{k\to 0} k^d S(\mathbf{k}) = 0,$$

i.e., the SF is an integrable function of $\mathbf{k}$ at $k = 0$. This constraint simply translates in reciprocal space the requirement from uniformity on the decay of relative fluctuations of the number of particles contained in a volume V about the mean at large V:

$$\lim_{V\to\infty} \frac{\langle N(V)^2\rangle - \langle N(V)\rangle^2}{\langle N(V)\rangle^2} = 0.$$

Given that $\langle N(V)\rangle \propto V$, the root mean square fluctuation of particle number N in a volume V must diverge slower than the volume V itself in order that this condition be fulfilled. (This is equivalent to saying that $C(\mathbf{x})$ must vanish at large x.)

We use likewise in the paper only one constraint on the large k behavior of the SF, which is valid for any uniform SPP (see e.g. [18]) and coincides with the shot noise term in the correlation function $C(\mathbf{x})$:

$$\lim_{k\to\infty} S(\mathbf{k}) = 1.$$

Appendix B: Small k Behavior of $\tilde{\mathbf{f}}(\mathbf{k})$

We are interested in the small k behavior of the Fourier transform $\tilde{\mathbf{f}}(\mathbf{k})$ of the pair force in d dimensions in the case where the pair force $\mathbf{f}(\mathbf{x}) = \hat{\mathbf{x}} f(x)$, where $\hat{\mathbf{x}} = \frac{\mathbf{x}}{|\mathbf{x}|}$, is non-integrable but converges to zero at $x \to \infty$, i.e., $f(r) \sim x^{-(\gamma+1)}$ at large x with $-1 < \gamma \le d-1$.

We first show that for a function $\mathbf{f}(\mathbf{x}) = \hat{\mathbf{x}} f(x)$, its Fourier transform, $\tilde{\mathbf{f}}(\mathbf{k}) = \mathrm{FT}[\mathbf{f}(\mathbf{x})](\mathbf{k})$, can be written $\tilde{\mathbf{f}}(\mathbf{k}) = \hat{\mathbf{k}}\ \psi(k)$ where $\psi(k)$ is a function depending only on the modulus of $\mathbf{k}$ and $\hat{\mathbf{k}} = \frac{\mathbf{k}}{|\mathbf{k}|}$. In order to obtain this result, we start by writing

$$\tilde{\mathbf{f}}(\mathbf{k}) = \int d^d x\ \mathbf{f}(\mathbf{x}) e^{-i\mathbf{k}.\mathbf{x}} = \int d^d x\ \hat{\mathbf{x}} f(x) e^{-i\mathbf{k}\mathbf{x}},$$

where this integral is defined in the sense of functions or distributions according to the integrability of $f(x)$.

In the following we denote by $(\hat{\mathbf{e}}_1, \hat{\mathbf{e}}_2, \ldots, \hat{\mathbf{e}}_n)$ the Cartesian vector basis in d-dimension and we define $(r, \theta_1, \theta_2, \ldots, \theta_{d-1})$ the hyper-spherical coordinates of $\mathbf{x}$. Considering $\mathbf{k} = k\hat{\mathbf{e}}_1$ and denoting for simplicity $\theta = \theta_1$, we can write

$$\tilde{\mathbf{f}}(\mathbf{k}) = \int d^d x\, \hat{\mathbf{x}} f(x) e^{-ikx\cos\theta},$$

where

$$d^d x = \left(\prod_{j=0}^{d-1} \sin^j(\theta_{d-j})\, d\theta_{d-j}\right) x^{d-1}\, dx.$$

Projecting $\tilde{\mathbf{f}}(\mathbf{k})$ on the Cartesian basis, it is easy to see that the only non-vanishing term is $\hat{\mathbf{e}}_1.\tilde{\mathbf{f}}(\mathbf{k})$ which gives

$$\hat{e}_1.\tilde{f}(\mathbf{k}) = C_{\theta_{i\neq 1}} \int_0^\infty dx\, x^{d-1} \int_0^\pi d\theta \sin^{n-2}(\theta) \cos\theta f(x) e^{-ikx\cos\theta},$$

where $C_{\theta_{i\neq 1}}$ is a constant term coming from the integration over all the hyper-spherical coordinates θ_i with $i \neq 1$. We thus can write $\tilde{\mathbf{f}}(\mathbf{k}) = \hat{\mathbf{k}}\psi(k)$ where $\psi(k)$ is a function depending only on the modulus of $\mathbf{k}$.

We now focus our attention on the small k behavior of the term

$$\int_0^\infty dx\, x^{d-1} f(r) e^{-ikx\cos\theta}, \tag{B.1}$$

where the function $f(x)$ is non-integrable but converges to zero at $x \to \infty$, i.e., $f(x) \sim x^{-(\gamma+1)}$ at large x with $-1 < \gamma \leq d-1$, and thus can be written $f(x) = x^{-(\gamma+1)} + h(x)$ with $h(x)$ a smooth function, integrable at $x = 0$ and such that $x^{\gamma+1}h(x) \to 0$ for $x \to \infty$. Defining explicitly (B.1) in the sense of distributions, the small k behavior is determined by this leading divergence at $x \to \infty$,

$$\lim_{\mu\to 0} \int_0^\infty dx\, x^{d-1} \frac{e^{-\mu x}}{x^{\gamma+1}} e^{-ikx\cos\theta}, \tag{B.2}$$

where the parameter $\mu > 0$. We define $\alpha = d - \gamma - 2$ which satisfies $-1 \leq \alpha < d-1$ and rewrite (B.2)

$$\lim_{\mu\to 0} \int_0^\infty dx\, x^\alpha e^{-(ik\cos\theta+\mu)x}.$$

This can be easily calculated with Laplace's transform and gives

$$\int_0^\infty dx\, x^\alpha e^{-(ik\cos\theta+\mu)x} = \frac{\Gamma(\alpha+1)}{(\mu + ik\cos\theta)^{\alpha+1}}.$$

We can conclude that

$$\begin{aligned}\lim_{\mu\to 0} &\int_0^\infty dx x^{d-1} \frac{e^{-\mu x}}{x^{\gamma+1}} e^{-ikx\cos\theta} \\ &= i^{-(\alpha+1)} \cos^{-(\alpha+1)}(\theta)\Gamma(\alpha+1)k^{-(\alpha+1)} \sim k^{\gamma-d+1}.\end{aligned}$$

References

1. Ruelle, D.: Statistical Mechanics: Rigorous Results. Benjamin, Elmsford (1983)
2. Dauxois, T., Ruffo, S., Arimondo, E., Wilkens, M.: Dynamics and Thermodynamics of Systems with Long Range Interactions. Springer, Berlin (2002)
3. Campa, A., Giansanti, A., Morigi, G., Sylos Labini, F.: Dynamics and Thermodynamics of Systems with Long Range Interactions: Theory and Experiments. AIP Conference Proceedings. AIP, New York (2008)
4. Thirring, W.: Quantum Mathematical Physics. Springer, Berlin (2002)
5. Chavanis, P.H.: Int. J. Mod. Phys. B **20**, 3113 (2006)
6. Yawn, K.R., Miller, B.N.: Phys. Rev. E **68**, 056120 (2003)
7. Yamaguchi, Y.Y., Barré, J., Bouchet, F., Dauxois, T., Ruffo, S.: Physica A **337**, 36 (2004). cond-mat/0312480
8. Antoniazzi, A., Califano, F., Fanelli, D., Ruffo, S.: Phys. Rev. Lett. **98**, 150602 (2007)

9. Antoniazzi, A., Fanelli, D., Ruffo, S., Yamaguchi, Y.Y.: Phys. Rev. Lett. **99**, 040601 (2007)
10. Yamaguchi, Y.Y.: Phys. Rev. E **78**, 041114 (2008)
11. Binney, J., Tremaine, S.: Galactic Dynamics. Princeton University Press, Princeton (1994)
12. Campa, A., Giansanti, A., Morelli, G.: Phys. Rev. E **76**, 041117 (2007). 0706.3664
13. Baldovin, F., Chavanis, P., Orlandini, E.: Phys. Rev. E **79**, 011102 (2009). cond-mat/0501583
14. Chavanis, P.: J. Stat. Mech. Theory Exp. **5**, 19 (2010). 1002.3268
15. Teles, T.N., Levin, Y., Pakter, R., Rizzato, F.B.: J. Stat. Mech. **5**, 7 (2010). 1004.0247
16. Gupta, S., Mukamel, D.: Phys. Rev. Lett. **105**, 040602 (2010). 1006.0233
17. Chandrasekhar, S.: Rev. Mod. Phys. **15**, 1 (1943)
18. Gabrielli, A., Sylos Labini, F., Joyce, M., Pietronero, L.: Statistical Physics for Cosmic Structures. Springer, Berlin (2004)
19. Balescu, R.: Equilibrium and Nonequilibrium Statistical Mechanics. Wiley, New York (1975)
20. Lanford, O.E. III: Commun. Math. Phys. **9**, 176 (1968)
21. Lanford, O.E. III: Commun. Math. Phys. **11**, 257 (1969)
22. Gabrielli, A., Joyce, M.: Phys. Rev. E **81**, 021102 (2010). 0909.5034
23. Kiessling, M.K.-H.: Adv. Appl. Math. **31**, 132 (2003). astro-ph/9910247
24. Jeans, J.H.: Philos. Trans. R. Soc. **199**, 1 (1902)
25. Wesenberg, J.H., Mølmer, K.: Phys. Rev. Lett. **93**, 143903 (2004). quant-ph/0406178
26. Gabrielli, A.: Phys. Rev. E **72**, 066113 (2005). cond-mat/0506365
27. Gabrielli, A., Baertschiger, T., Joyce, M., Marcos, B., Labini, F.S.: Phys. Rev. E **74**, 021110 (2006). cond-mat/0603124
28. Kolmogorov, A., Fomin, S.: Elements of the Theory of Functions and Functional Analysis. Dover, New York (1999)
29. Peebles, P.J.E.: The Large-Scale Structure of the Universe. Princeton University Press, Princeton (1980)
30. Gabrielli, A., Joyce, M., Marcos, B.: (2010). 1004.5119
31. Chavanis, P.H.: Eur. Phys. J. B **70**, 413 (2009). 0810.1211
32. Gabrielli, A., Joyce, M., Sicard, F.: Phys. Rev. E **80**, 041108 (2009)

Collisional relaxation of two-dimensional self-gravitating systems

Bruno Marcos*

Université de Nice—Sophia Antipolis, Centre National de la Recherche Scientifique, Laboratoire J. A. Dieudonné, UMR 7351, Parc Valrose 06108 Nice Cedex 02, France

(Received 4 December 2012; published 9 September 2013)

Systems with long range interactions present generically the formation of quasistationary long-lived nonequilibrium states. These states relax to Boltzmann equilibrium following a dynamics which is not well understood. In this paper we study this process in two-dimensional inhomogeneous self-gravitating systems. Using the Chandrasekhar—or local—approximation we write a simple approximate kinetic equation for the relaxation process, obtaining a Fokker-Planck equation for the velocity distribution with explicit analytical diffusion coefficients. Performing molecular dynamics simulations and comparing them with the evolution predicted by the Fokker-Planck equation, we observe a good agreement with the model for all the duration of the relaxation, from the formation of the quasistationary state to thermal equilibrium. We observe however an overestimate or underestimate of the relaxation rate of the particles with the slower or larger velocities, respectively. It is due to systematic errors in estimating the velocities of the particles at the moment of the collisions, inherent to the Chandrasekhar approximation when applied to inhomogeneous systems. Theory and simulations give a scaling of the relaxation time proportional to the number of particles in the system.

DOI: 10.1103/PhysRevE.88.032112 PACS number(s): 05.70.Ln, 04.40.−b

I. INTRODUCTION

Systems of particles with long range interactions are those which interparticle potential at large separation decays slower than the dimension d of space, i.e., $v(r \to \infty) \sim 1/r^{\gamma}$ with $\gamma \leqslant d$. There are many examples in nature, such as self-gravitating systems in the cosmological and astrophysical context (the large structure of the universe, galaxies, etc.), interaction between vortices in two-dimensional hydrodynamics, cold classical atoms, and capillary interactions between colloids or granular media (for a review see, e.g., [1]). These kinds of systems present very particular properties in thermal equilibrium, such as negative microcanonical specific heat or inequivalence of statistical ensembles. Their dynamics is also peculiar compared to short range systems: in a first stage there is the generic formation in a few characteristic times $\tau_{\rm dyn}$ of a long-lived nonequilibrium state—during the so-called violent relaxation process. Typical examples of such quasistationary states (QSSs) are galaxies and young globular clusters. Then, a comparatively very slow relaxation to thermodynamical equilibrium occurs—called *collisional relaxation*—in a time scale of order $\tau_{\rm coll} \sim N^{\delta}\tau_{\rm dyn}$, where N is the number of particles and $\delta \geqslant 1$ depends on the system studied.

The mechanism of collisional relaxation is still not well understood. In the context of gravitational systems, Chandrasekhar found theoretically, in a seminal work [2], an estimate of the relaxation time for gravitational systems in three dimensions. He considered a homogeneous system and computed the change in velocity due to successive independent collisions[1] of a test particle in a stationary macroscopic configuration. Because of the hypothesis of homogeneity there is no macroscopic scale in the system, which led to an ongoing controversy about the value of the maximal impact parameter of the collisions and in particular how it should scale with N [3–6]. Following this, several studies considered collective effects (e.g., [7]), but still in homogeneous configurations. An explicit theoretical description of the collisional relaxation in inhomogeneous systems is technically much more difficult to derive, requiring the use of action-angle variables. This description is still lacking, despite recent progress in this direction [8,9] (for a recent review see, e.g., [10]).

The collisional relaxation has also been studied numerically, for a wide variety of systems. For one-dimensional gravity, a scaling of $\tau_{\rm coll} \sim N\tau_{\rm dyn}$ has been measured for the full relaxation process [11], and in the Hamiltonian mean field (HMF) model the scaling has been found to be dependent on the initial condition: $\tau_{\rm coll} \sim N\tau_{\rm dyn}$ [12], $\tau_{\rm coll} \sim N^{1.7}\tau_{\rm dyn}$ [12], or $\tau_{\rm coll} \sim \exp(N)\tau_{\rm dyn}$ [13]. For dimensions larger than $d = 1$, the relaxation has been estimated studying—for numerical reasons—only its early stage, i.e., for times in which the QSS is weakly perturbed (see, e.g., [14,15]), or performing simulations with a simplified dynamics. For gravity in two dimensions, in simulations performed imposing radial symmetry, $\tau_{\rm coll} \sim N^{1.35}\tau_{\rm dyn}$ [16] has been observed. In $d = 3$ dimensions, the Chandrasekhar scaling $\tau_{\rm coll} \sim N/\ln N\tau_{\rm dyn}$ has been verified for gravity (see, e.g., [4,14,17]) and for power-law potential $u(r) = 1/r^{\gamma}$, for which $\tau_{\rm coll} \sim N\tau_{\rm dyn}$ has been found if $\gamma < 2$ (see [15,17]).

In this paper, we study the collisional relaxation of a self-gravitating system in $d = 2$ dimensions. The interacting potential—the solution of the Poisson equation in $d = 2$ dimensions—is $u(r) = g\ln(r)$, where g is the coupling constant. It is an attractive model because it presents the same mechanism of collisions as in $d = 3$ (which is not the case for models in $d = 1$), the system is self-confined (it is not necessary to confine it artificially in a box), thermal equilibrium properties are easily calculated, and numerical simulations are easier to perform than in $d = 3$. Moreover, as mentioned above, it was found in [16], using simulations imposing radial symmetry (particles conserve their initial

*bruno.marcos@unice.fr

[1]We will use here, as in the astrophysical literature, the term "collisions." In the general context of long range systems it would be more appropriate to call them "finite N effects."

angular momentum), that the collisional relaxation scales with the number of particles in the unexpected manner $\tau_{\rm coll} \sim N^{1.35}\tau_{\rm dyn}$. In the way in which these simulations have been performed the actual model is quasi-one-dimensional, and this result may have some connection with the striking relaxation time for the HMF model, which for some initial conditions has been found to scale as $\tau_{\rm coll} \sim N^{1.7}\tau_{\rm dyn}$.

Another question that will be addressed in this paper concerns the fact that it has been observed that the Chandrasekhar approximation—or *local approximation*—gives good estimation of the relaxation time not only in homogeneous systems but also in nonhomogeneous configurations (see [4–6,15]), and in particular how it scales (in a nontrivial way) with the number of particles N and the minimal impact parameter [15]. This suggests the possibility to describe, in a good approximation, the whole collisional relaxation process using this approximation (see, e.g., [10]), in which the system is treated as locally homogeneous.

This paper is organized as follows. In Sec. II, we show that, if the QSS which is collisionally relaxing is approximately homogeneous in its center—as it is for many initial conditions for a gravitational system in $d = 2$ and 3—then treating the system as homogeneous (but finite) is a reasonable approximation. Then, we compute the diffusion coefficients and, neglecting collective effects, we write a Fokker-Planck equation which describes the evolution of the system. In Sec. III, we report simulations using molecular dynamics of the relaxation of the system, for the whole time range between the QSS and the final thermal equilibrium, for two different initial conditions and different numbers of particles. We will see that, despite the many approximations, the evolution of the velocity probability density function (PDF) is reasonably well described by the theory for intermediate values of the velocity. In Sec. IV, we discuss the validity of the Chandrasekhar approximation. In Sec. V, we present the conclusions of this study and further perspectives.

II. THEORETICAL DESCRIPTION

We model the generic evolution of the system using the Boltzmann equation for the one point probability density function $f(\mathbf{r},\mathbf{v},t)$. We can write it formally as

$$\frac{\partial f}{\partial t} + \mathbf{v}\cdot\frac{\partial f}{\partial \mathbf{r}} + \mathbf{F}[f]\cdot\frac{\partial f}{\partial \mathbf{v}} = \Gamma_c[f], \tag{1}$$

where $\Gamma_c[f]$ is the collision operator. During the relaxation process, the system reaches first a QSS and then evolves (comparatively slowly) through an infinity sequence of QSSs, in which

$$\mathbf{v}\cdot\frac{\partial f}{\partial \mathbf{r}} + \mathbf{F}[f]\cdot\frac{\partial f}{\partial \mathbf{v}} = 0. \tag{2}$$

To make Eq. (1) tractable analytically, we will assume that Eq. (2) holds for all times, the force term being implicitly included in the collision term.

We will focus in this paper on the evolution of the velocity PDF:

$$s(\mathbf{v},t) = \int d^2r\, f(\mathbf{r},\mathbf{v},t). \tag{3}$$

We integrate Eq. (1) over the positions, obtaining, in the approximation Eq. (2),

$$\frac{\partial s}{\partial t} = \int d^2r\, \Gamma_c[f]. \tag{4}$$

In the same manner as in the most studied $d = 3$ case, the relaxation is dominated by *weak collisions* (see, e.g., [18]), i.e., the ones for which the trajectories of the particles are weakly perturbed. Moreover, it has been shown that, for times larger than one orbital period, the force correlation function decays rapidly (e.g., as $\sim 1/t^5$ for gravity in $d = 3$ [19]). We may then consider that collisions are independent and the use of a Fokker-Planck approximation of Eq. (4) is therefore justified (see, e.g., [10,20]), which can be written as

$$\frac{\partial s(\mathbf{v},t)}{\partial t} = \frac{\partial}{\partial v_i}[D_{v_i} s(\mathbf{v},t)] + \frac{1}{2}\frac{\partial^2}{\partial v_i \partial v_j}[D_{v_i v_j} s(\mathbf{v},t)], \tag{5}$$

where the diffusion coefficients are defined as the average change of the velocity of the particles per unit of time, i.e.,

$$D_{v_i}(\mathbf{v}) = \frac{\langle \Delta v_i \rangle}{\Delta t}, \tag{6a}$$

$$D_{v_i v_j}(\mathbf{v}) = \frac{\langle \Delta v_i \Delta v_j \rangle}{\Delta t}. \tag{6b}$$

In Eqs. (5) and (6) we have assumed that the diffusion coefficients are a well-defined quantity to describe the relaxation process in an inhomogeneous system. We will see in what follows to what extent it is a good approximation.

The strategy to compute the diffusion coefficients is the following: because collisional relaxation is dominated by weak collisions, i.e., by the ones in which the trajectories of the particles are weakly perturbed (see, e.g., [18]), the diffusion coefficients [Eq. (6)] can be calculated computing changes in velocity of the particles considering that they are evolving on their unperturbed orbits (i.e., the ones which correspond to the mean field $N \to \infty$ limit). In Sec. II A, we first estimate the mean field potential in which the particles are evolving; in Sec. II B, we then compute the change in velocity due to one collision; and finally, in Sec. II C, we compute the diffusion coefficients themselves.

A. Mean field potential

We are going to assume that in the region in which particles are collisionally relaxing the density PDF is homogeneous. This distribution generates a harmonic gravitational field. We will see in our simulations (see Sec. III) that it is a very good approximation. Moreover, this is also true for the thermal equilibrium state, which is the final state the system will reach. At thermal equilibrium the potential generated by the QSS (see, e.g., [16]) is

$$\Psi(r) = \frac{gN}{2}\ln(\lambda^2 + r^2), \tag{7}$$

where λ is a constant which depends on the total energy of the system.[2] For $r \lesssim \lambda$ (which corresponds to a scale which

[2]The $N \to \infty$ limit is taken in such a way that $g \propto N^{-1}$, which is equivalent to keeping the dynamical time of the system invariant

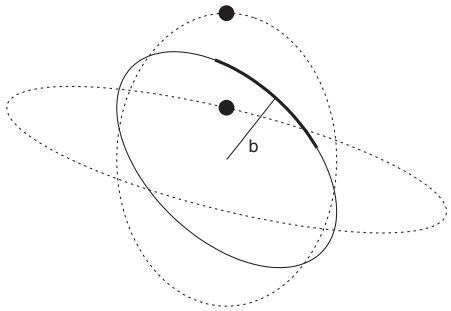

FIG. 1. Sketch of the orbits (dotted curves) of two "colliding" particles (which are plotted at the same arbitrary time). The plain curve represents their relative trajectory, and the thick portion (of length $\sim 2b$) represents the part of the trajectory in which $|\Delta \mathbf{V}_\perp|$ changes significantly (see text).

includes half of the particles), the potential is harmonic, i.e.,

$$\Psi(r) \simeq gN \ln \lambda + \omega^2 r^2, \tag{8}$$

where

$$\omega^2 = \frac{gN}{2\lambda^2}. \tag{9}$$

Under the hypothesis that the potential has the form of Eq. (8), the trajectories of the particles in the central region of the system (where collisional relaxation occurs) can be then well approximated with ellipses. The relative motion of two particles is also therefore an ellipse which can be written as

$$\mathbf{r}(t) = x_0 \sin(\omega t)\hat{x} + y_0 \cos(\omega t)\hat{y}, \tag{10}$$

as shown in Fig. 1. We expect that the hypothesis Eq. (8) is relatively general: it has been shown numerically in $d = 3$ that, for a wide set of initial conditions, the QSS presents also a central homogeneous region which decays rapidly to zero at larger scales [21].

B. Computation of the change of velocity due to one "collision"

In the context of long range systems, we define a "collision" between two particles as the process in which they cross each other in half an orbital period (one crossing of the system). Assuming that the relative orbits have the form of Eq. (10) we can compute the change in relative velocity in the $\hat{y}$ direction of two crossing particles by integrating the gravitational acceleration $\mathbf{F}(t)/m$ projected in the $\hat{y}$ direction over the duration of a collision:

$$\begin{aligned} |\Delta \mathbf{V}_y| &= 2g \int_0^{\frac{\pi}{2\omega}} \frac{\mathbf{F}(t)\cdot\hat{y}}{m} dt \\ &\simeq 2g \int_0^{\frac{\pi}{2\omega}} \frac{y_0 \cos(\omega t)\, dt}{x_0^2 \sin^2(\omega t) + y_0^2 \cos^2(\omega t)} \\ &= 2g \frac{\arctan\left[\sqrt{\frac{x_0^2}{y_0^2} - 1}\right]}{w\sqrt{x_0^2 - y_0^2}}. \end{aligned} \tag{11}$$

changing N [see Eq. (24)]. We keep here the dependence on N to have an explicit dependence on $\tau_{\rm dyn}$ in our equations.

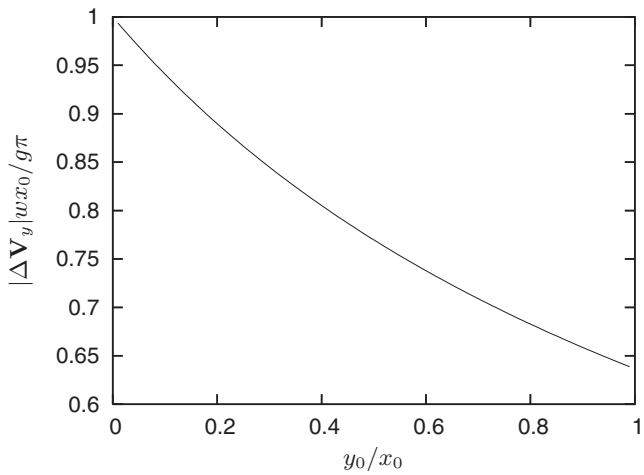

FIG. 2. Change in the relative velocity in the y direction $|\Delta \mathbf{V}_y|$ [Eq. (11)] normalized by its asymptotic value [Eq. (13)] as a function of the ellipticity y_0/x_0.

From geometrical arguments, it is possible to see that most of the orbits will have large ellipticity. For example, in our simulations we find $y_0/x_0 \approx 0.1$ on average (see Sec. IV). If we choose the axis in order $y_0 < x_0$, then, if the condition

$$y_0 \ll x_0 \tag{12}$$

holds, Eq. (11) can be well approximated by

$$|\Delta \mathbf{V}_y| = \frac{g\pi}{\omega x_0}\left[1 + \mathcal{O}\left(\frac{y_0}{x_0}\right)\right]. \tag{13}$$

In Fig. 2 we show how the approximation Eq. (13) becomes better increasing the ellipticity x_0/y_0. For example, a maximal relative error of 35% is made for $x_0/y_0 = 1$, decreasing rapidly to an error of 6% when $x_0/y_0 = 0.1$. From Eq. (11) it is possible to see that the "collision" is localized in space and time: as the integral converges rapidly, an excellent approximation of Eq. (11)—with the condition Eq. (12)—consists in taking as the upper cutoff the integral $\omega t \simeq y_0/x_0$. This means that most of the change of velocity occurs during the interval of time $\Delta t \simeq \omega^{-1} y_0/x_0$ centered around $t = 0$ in our parametrization Eq. (10), in a region of length $\sim 2y_0$.

In order to compute simply averages over the velocity PDF in what follows, it is useful to have an expression of the change of velocity as a function of the velocity of the particle itself. In the same approximation, Eq. (12), we have

$$|\mathbf{V}(t=0)| \equiv V \simeq \omega x_0 \left[1 + \mathcal{O}\left(\frac{y_0}{x_0}\right)\right]. \tag{14}$$

Then

$$|\Delta \mathbf{V}_y| \equiv |\Delta \mathbf{V}_\perp| \simeq \frac{g\pi}{V}, \tag{15}$$

where V is the relative velocity at the distance of closest approach. We use the notation $\mathbf{V}_\perp$ because, in this approximation, $\Delta \mathbf{V}_y$ corresponds to the change of velocity in the perpendicular direction of the velocity of the particle. This result is the one obtained by Chandrasekhar adapted to self-gravitating systems in $d = 2$ dimensions. We will discuss the implications and limitations of this approach in Sec. IV.

It is possible to compute the change in the relative parallel velocity using the fact that, in a weak collision, V does not change during the collision. Then

$$|\Delta \mathbf{V}_\perp| = V \sin\theta, \tag{16a}$$

$$|\Delta \mathbf{V}_\parallel| = V(1-\cos\theta), \tag{16b}$$

where θ is the angle of deflection. In the weak collision approximation $\theta \ll 1$, and thus we have $\sin\theta \simeq \theta$ and $\cos\theta \simeq 1-\theta^2/2$, and then

$$|\Delta \mathbf{V}_\parallel| = \frac{|\Delta \mathbf{V}_\perp|^2}{2V}. \tag{17}$$

Taking into account that particle masses are equal we obtain for the change in velocity of a particle, using Eqs. (15) and (17),

$$|\Delta \mathbf{v}_\perp| \simeq \frac{\pi g}{2V}, \tag{18a}$$

$$|\Delta \mathbf{v}_\parallel| \simeq \frac{\pi^2 g^2}{4V^3}. \tag{18b}$$

C. Computation of the diffusion coefficients

We compute the diffusion coefficients using the standard method used in $d=3$ in the local approximation. As the spatial density PDF is approximately constant up to a scale r^* in radial coordinates (see the discussion and numerical simulations of Sec. III), we can therefore estimate the number η of collisions of a particle in a time interval Δt, on average, as

$$\eta \simeq \frac{2NV\Delta t}{\pi r^*}; \tag{19}$$

the factor $\pi r^*/2$ is the average height of a circle of radius r^*. We are going now to average over the velocity PDF. We will do a somewhat uncontrolled approximation here because Eq. (15) gives the change of relative velocity *at the point of closest approach*. It is not possible to compute exactly this quantity from the velocity PDF because the change in velocity of a particle does not depend on its velocity (as in the homogeneous case) but on the orbit to which it behaves, i.e., on the particular values of x_0 and y_0 corresponding to the particle. To go further, however, we will assume that it is possible to average over the velocity PDF $s(v)$. Introducing, as in the $d=3$ case, the Rosenbluth potential [22]

$$q(v) = \int d^2v' \frac{s(v')}{|\mathbf{v}-\mathbf{v}'|}, \tag{20a}$$

$$p(v) = \int d^2v' s(v')|\mathbf{v}-\mathbf{v}'|, \tag{20b}$$

and assuming that the velocity PDF is isotropic, we obtain, keeping only terms of $\mathcal{O}(g^2)$ (see the Appendix),

$$D_{v_i}(v) = \frac{\langle \Delta v_i\rangle}{\Delta t} = C\frac{\partial q(v)}{\partial v_i}, \tag{21a}$$

$$D_{v_i v_j}(v) = \frac{\langle \Delta v_i \Delta v_j\rangle}{\Delta t} = C\frac{\partial^2 p(v)}{\partial v_i \partial v_j}, \tag{21b}$$

where

$$C = \frac{\pi g^2 N}{2r^*}. \tag{22}$$

As the succession of QSSs has an approximate polar symmetry, it is then useful to write Eq. (5) in polar coordinates. Considering that the Rosenbluth potentials are isotropic, we have, using Eq. (A7),

$$\frac{\partial \tilde{s}}{\partial t} = C\left\{-\frac{\partial}{\partial v}\left[\left(q'(v)+\frac{p'(v)}{2v^2}\right)\tilde{s}\right] + \frac{1}{2}\frac{\partial^2}{\partial v^2}[p''(v)\tilde{s}]\right\}, \tag{23}$$

where $\tilde{s}(v)$ is the velocity PDF in polar coordinates, $v=|\mathbf{v}|$, and the primes denote derivation with respect to v. It is useful to write Eq. (23) in an adimensional form. We define the time unit as the dynamical time of the system:

$$\tau_{\rm dyn} = \frac{1}{\sqrt{gN}}. \tag{24}$$

We define the velocity units v_* using the virial theorem, which states that, for any stationary state (and hence a QSS), the average velocity square of the particles is constant during the evolution (see, e.g., [16,23]):

$$\langle v^2\rangle = \frac{gN}{2}. \tag{25}$$

It is then natural to take as the velocity unit

$$v_* = \sqrt{gN}. \tag{26}$$

Defining the adimensional time and velocities as $\tilde{t} = t/\tau_{\rm dyn}$ and $\tilde{v} = v/v_*$, respectively, we have, from Eq. (23),

$$\frac{\partial \tilde{s}}{\partial \hat{t}} = \hat{C}\left\{-\frac{\partial}{\partial \hat{v}}\left[\left(q'(\hat{v})+\frac{p'(\hat{v})}{2\hat{v}^2}\right)\tilde{s}\right] + \frac{1}{2}\frac{\partial^2}{\partial \hat{v}^2}[p''(\hat{v})\tilde{s}]\right\}, \tag{27}$$

where we have defined

$$\hat{C} = C\frac{\tau_{\rm dyn}}{v_*^3} = \frac{\pi}{2Nr_*}. \tag{28}$$

Equation (27) depends on N through $\hat{C}$, which implies that the relaxation scales as

$$\tau_{\rm coll} \sim N\tau_{\rm dyn}. \tag{29}$$

To compute explicitly the diffusion coefficients we need an explicit form of $\tilde{s}(\hat{v})$. As discussed above, the velocity PDF at the distance of closest approach is unknown. We will use then the standard approximation to take the equilibrium Maxwell-Boltzmann PDF (see, e.g., [10]):

$$\tilde{s}_{\rm MB}(\hat{v}) = 2\hat{v}v_*\beta\exp(-\beta\hat{v}^2), \tag{30}$$

with $\beta = 2$ given by Eq. (25). We obtain in this approximation

$$q(\hat{v}) = e^{-\beta\hat{v}^2/2}\sqrt{\pi\beta}\, I_0\left(\frac{\beta\hat{v}^2}{2}\right), \tag{31a}$$

$$p(\hat{v}) = \frac{1}{2}\sqrt{\frac{\pi}{\beta}}e^{-\beta\hat{v}^2/2}\left[-e^{\beta\hat{v}^2/2} + (1+\beta\hat{v}^2)I_0\left(\frac{\beta\hat{v}^2}{2}\right) + \beta\hat{v}^2 I_1\left(\frac{\beta\hat{v}^2}{2}\right)\right], \tag{31b}$$

where $I_n(x)$ is the modified Bessel function of the first kind. It is possible to verify that the equilibrium PDF Eq. (30) is a stationary solution of Eq. (27) with the diffusion coefficients

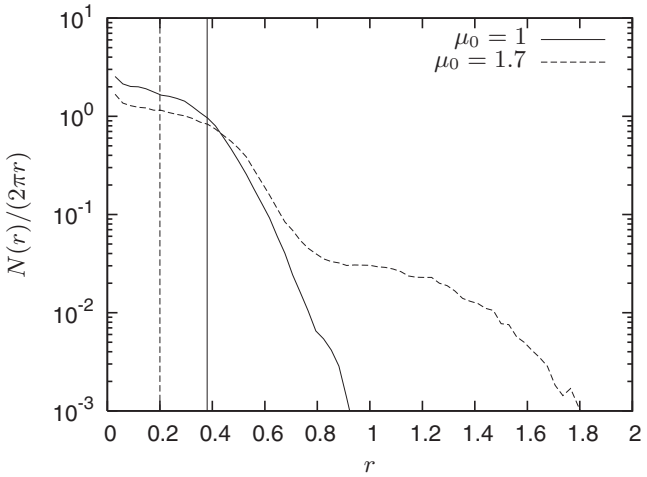

FIG. 3. Density PDF in the QSS at $t = 50\tau_{\rm dyn}$ for both initial conditions. The vertical curves (of the same type as their corresponding density profile) are the values of r^* used in Eq. (19) in order to obtain the measured relaxation rate in the simulations.

given by Eq. (31). Note that we obtain the same result obtained in [24] (see also [25]), in which a different method to compute the diffusion coefficients than Rosenbluth potentials has been used.

III. NUMERICAL SIMULATIONS

We compare the theoretical model with molecular dynamics simulations performed with a modification of the publicly available code GADGET2 [26] to handle the logarithmic interaction. We use a time step of $2.5 \times 10^{-4}\tau_{\rm dyn}$ in order to ensure a very precise energy conservation, which is better than 10^{-5} for the whole duration of the runs. We performed simulations with initial water-bag conditions with different numbers of particles in the interval $N = 100$–8000 and initial virial ratio $\mu_0 = 1$ and 1.7, where

$$\mu_0 = \frac{v_*}{\sqrt{2\langle v_0^2\rangle}}, \tag{32}$$

where $\langle v_0^2\rangle$ is the average of the initial velocity square. The simulations have been performed for times of $5600\tau_{\rm dyn}$ for the systems with the largest N and $7700\tau_{\rm dyn}$ for those with the smallest one. In order to improve statistics, we average the measured velocity PDF over 100 consecutive snapshots in an interval of $2.5\tau_{\rm dyn}$. The system forms a QSS which is approximately homogeneous in its central region, with a rapid decay of the density at larger scale, as shown in Fig. 3 for both initial conditions. We observe that the one with initial virial ratio $\mu_0 = 1$ gives rise to a compact density PDF, whereas the one with initial virial ratio $\mu_0 = 1.7$ gives rise to a core halo distribution. In Fig. 4 we plot the potential energy $\Psi(r)$ generated by the density PDF at time $t = 50\tau_{\rm dyn}$ (the time in which the system has violently relaxed) and $t = 5600\tau_{\rm dyn}$, corresponding to thermal equilibrium for the $\mu_0 = 1.7$ case (an analogous result is obtained for $\mu_0 = 1$). We observe that for the inner part of the system the potential is very well approximated by the potential generated by the system at thermal equilibrium [Eq. (8)]. We monitor how the system

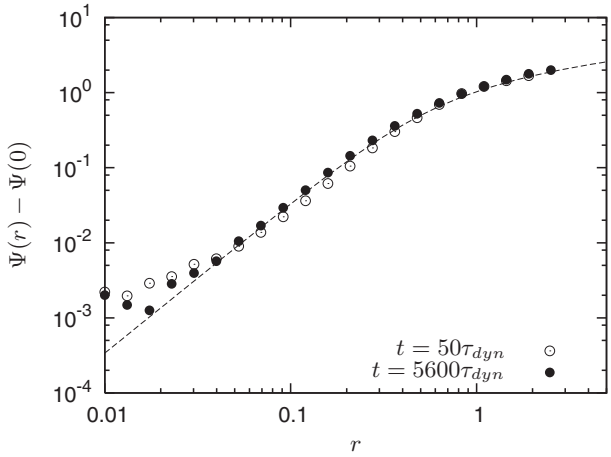

FIG. 4. Potential of the particles as a function of their radial distance for the simulation with $\mu_0 = 1.7$, at $t = 50$ and $5600\tau_{\rm dyn}$. The dashed line is the potential of the distribution at thermal equilibrium [Eq. (7)].

approaches thermal equilibrium using the parameter

$$\xi(t) = \frac{1}{N^2}\int_0^\infty [s(v,t) - s_{\rm MB}(v)]^2 dv. \tag{33}$$

In order to compare simulations with theory we compute the associated Langevin equation of Eq. (27). Therefore, the change in the velocity is given, following the Ito definition, by

$$d\hat{v}(\hat{t}) = \hat{C}\left[\left(q'(\hat{v}) + \frac{p'(\hat{v})}{2\hat{v}^2}\right)d\hat{t} + \sqrt{p''(\hat{v})}dW\right], \tag{34}$$

where dW is a Gaussian stochastic variable delta correlated in time with variance unity. We choose as the initial condition a configuration of the numerical simulation at $t = 50\tau_{\rm dyn}$ (the time in which the system has violently relaxed) and then we compare the evolution predicted by the Langevin equation and the one of the full numerical simulation. We integrate Eq. (34) by a simple Euler procedure. In Fig. 5 we show the evolution of $\xi(t)$, where the time axis has been rescaled by a factor N, which indicates a scaling of the relaxation time as $\tau_{\rm coll} \sim N\tau_{\rm dyn}$. For clarity, of all the simulations with different numbers of particles performed we plot three of them. The part of the curve which flattens corresponds to thermal equilibrium, which is attained first as N decreases. The matching between the curves corresponding to different N is very good in the region out of equilibrium, as has been illustrated for $N = 750$, 12^3, and 16^3, which confirms the prediction of Eq. (27) for the scaling of the relaxation. The plain curves correspond to the theoretical prediction given by Eq. (34) with $r^* = 0.38$ for the simulation with $\mu_0 = 1$ and $r^* = 0.2$ for the simulation with $\mu_0 = 1.7$. These values are, within a factor of 2, close to the scale of the falloff in the density PDF; the density decays to half its center value around $r \approx 0.4$ for both sets of simulations. We emphasize that the difference in the slopes of the curves is essentially due to the different initial conditions considered for each case rather than the value of r^* taken: taking indeed the same intermediate value of $r^* = 0.29$ for both initial conditions the two curves appear to be very different. The full simulation curves decay to a lower value at thermal equilibrium because

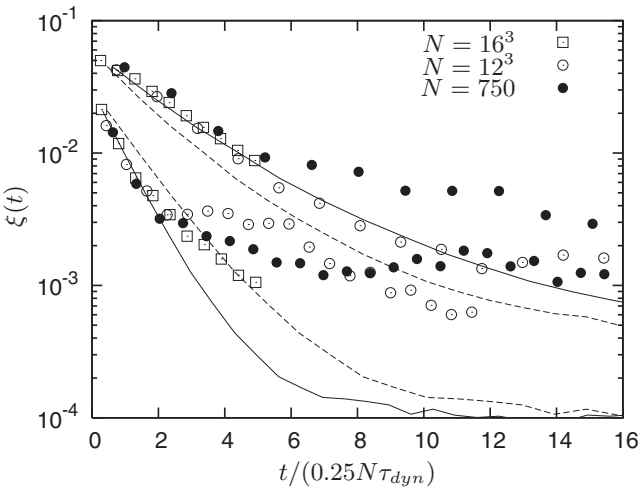

FIG. 5. Upper curves: initial condition with $\mu_0 = 1$. Lower curves: initial conditions with $\mu_0 = 1.7$. Points: evolution of the crossover parameter $\xi(t)$ measured in the molecular dynamics simulations for the two different initial conditions $\mu_0 = 1$ and 1.7. Lines: theoretical prediction calculated using Eq. (34) for each case (see text).

fluctuations appear to be larger in the molecular dynamics simulations than in the Langevin simulation. In Fig. 6 we show the evolution of the full velocity PDF for both the simulation and the theory. The first two rows of the figure correspond to the cases $\mu_0 = 1$ and 1.7, respectively. In the next two rows of the figure we reproduce the same plots but in log-linear scale to appreciate the tails of the distribution. We observe that the model predicts very well the evolution of the velocity PDF for *intermediate* values of the velocities. For low velocities it predicts systematically a relaxation *faster* than that observed in the simulation, whereas for large velocities it predicts systematically a relaxation slower than the one observed in the simulations (in the latter case, especially for the $\mu_0 = 1.7$ system). We discuss this discrepancy in the following section.

IV. THE VALIDITY OF THE CHANDRASEKHAR APPROXIMATION APPLIED TO INHOMOGENEOUS SYSTEMS

It is possible to show that the result Eq. (15) is the same one as the one obtained in the spatial homogeneous case originally treated by Chandrasekhar applied to gravity in $d = 2$. This study considered rectilinear trajectories with constant relative velocity V (see, e.g., [18]), in which the distance of closest approach y_0 is the impact factor b. Then

$$|\Delta \mathbf{V}_\perp| \simeq 2\int_0^\infty \frac{g\,b}{b^2 + (Vt)^2}dt = \frac{g\pi}{V}. \tag{35}$$

The agreement between the results can be understood for two reasons:

(1) Trivially, in the limit $y_0/x_0 \to 0$, the unperturbed trajectories [Eq. (10)] become rectilinear.

(2) An excellent approximation to the integral Eq. (35) is obtained taking $t \simeq b/V$ as the upper cutoff; i.e., the collision is localized in the same sense as the one discussed for the integral Eq. (11).

Therefore we can conclude that, when the relative orbits have large ellipticity, the system can be treated as locally homogeneous and Eq. (35) would be a good approximation. We have checked that this is the case in our system, as shown in Fig. 7. In this figure, we measure from the simulations the value of y_0/x_0 for all the possible relative orbits [i.e., $N(N-1)/2$ in total] at $t = 50\tau_{\rm dyn}$. We stress however that, as discussed above, it is not possible to average properly over velocities: the appropriate velocity PDF which must be used in Eqs. (11) and (35) is not the velocity PDF but the *velocity PDF at the moment of the collision*. Having this idea in mind we obtain a very coherent picture to explain the results obtained in Fig. 6:

(1) Particles with large velocity are very likely to be at the perigee of their orbit, i.e., the portion of the orbit in which the velocity is maximal. Hence, during the successive collisions, it is very probable that they would be in another portion of their orbit, with smaller velocity. Therefore, velocities at the moment of the collisions are systematically overestimated and, using Eq. (13) [or Eq. (31)], the relaxation rate predicted by the Chandrasekhar approximation will be faster than the one which actually happens in the system.

(2) The opposite occurs for low velocities: particles are more likely to be at the apogee of their orbit. Therefore, the velocity in the moment of the collisions is systematically underestimated, and then, for the same reason as above, the Chandrasekhar approximation predicts a relaxation rate slower than the one which actually occurs.

The arguments presented above apply also in $d = 3$, which may explain why the original Chandrasekhar approach gives a good estimate of the relaxation time in inhomogeneous systems, taking as the maximal impact parameter the size of the system (see, e.g., [6,14]). In particular, the following apply:

(1) We expect that, in the same way as in the case studied here, the mean field potential would not change too much during the collisional relaxation process, which essentially makes the dynamical time $\tau_{\rm dyn}$ invariant.

(2) It has been shown numerically in $d = 3$ that, for a wide set of initial conditions, the QSS presents also a central homogeneous region which decays rapidly to zero at larger scales [21]. Our hypothesis in Sec. II A would be therefore fulfilled.

(3) All the arguments in Sec. II B would also be true, and in particular the change of velocity due to one collision would have the same properties as Eq. (11), as we show below.

Because collisions occur also in a plane, we now have

$$|\Delta \mathbf{V}_y| \simeq 2g\int_0^{\frac{\pi}{2\omega}} \frac{y_0\cos(\omega t)\,dt}{\left[x_0^2\sin^2(\omega t) + y_0^2\cos^2(\omega t)\right]^{3/2}} = \frac{2g}{\omega x_0 y_0}. \tag{36}$$

In the limit $y_0/x_0 \to 0$, and using Eq. (14), we get the well-known result of Chandrasekhar [2]:

$$|\Delta V_\perp| \simeq \frac{2g}{Vb}. \tag{37}$$

Collisions are then "local," in the same manner as in the case discussed in the paper; i.e., the change in velocity occurs in

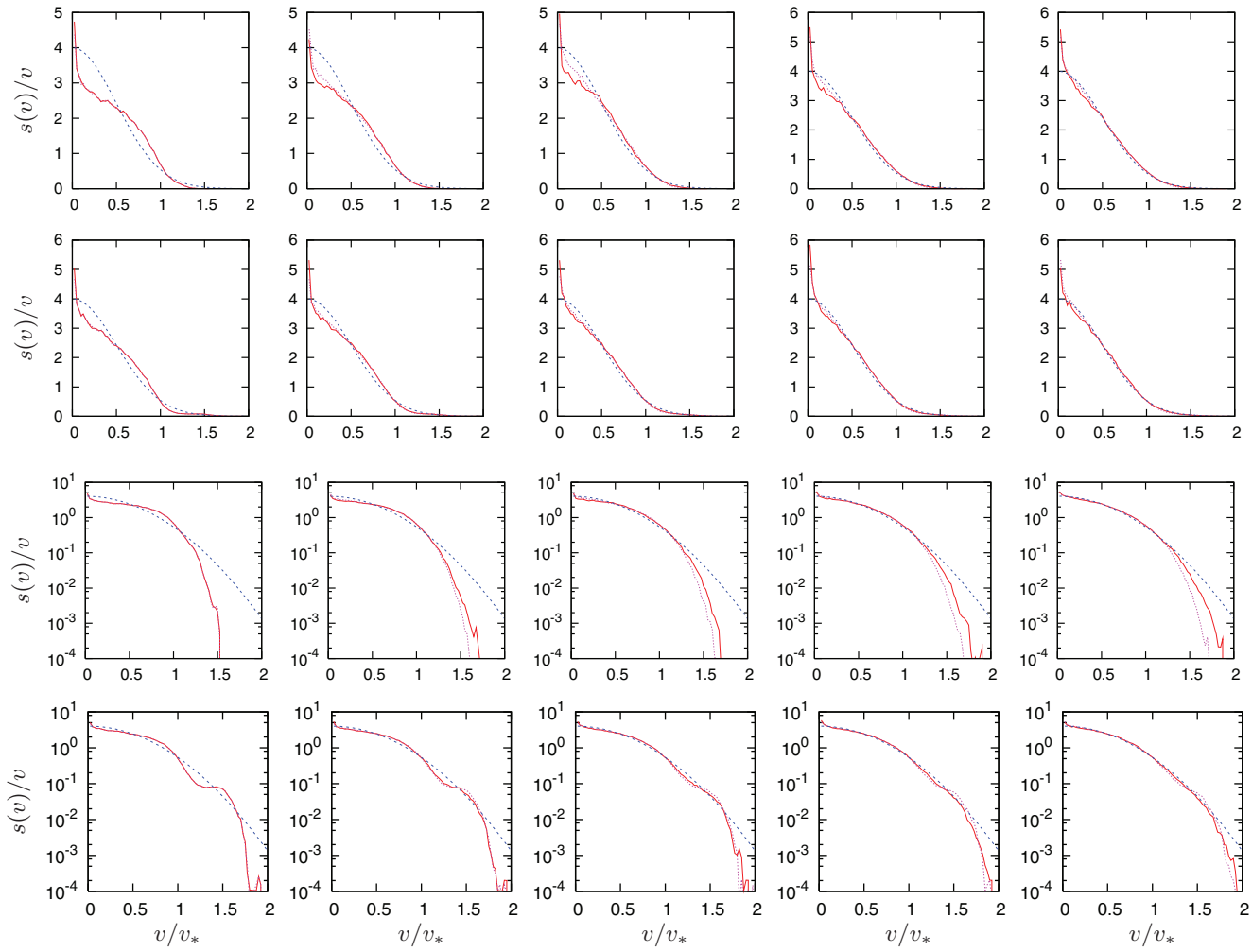

FIG. 6. (Color online) First row of plots: evolution of the velocity PDF for $\mu_0 = 1$ and times $t = 20, 1550, 3100, 4650,$ and $6200\tau_{\rm dyn}$. Second row of plots: evolution of the velocity PDF for $\mu_0 = 1.7$ and times $t = 20, 520, 1030, 1550,$ and $2060\tau_{\rm dyn}$. The second block of plots is exactly the same but in log-linear scale. The plain red curve represents the simulations, the pink dotted one represents the theoretical prediction, and the blue dashed curve represents the thermal equilibrium PDF [Eq. (30)].

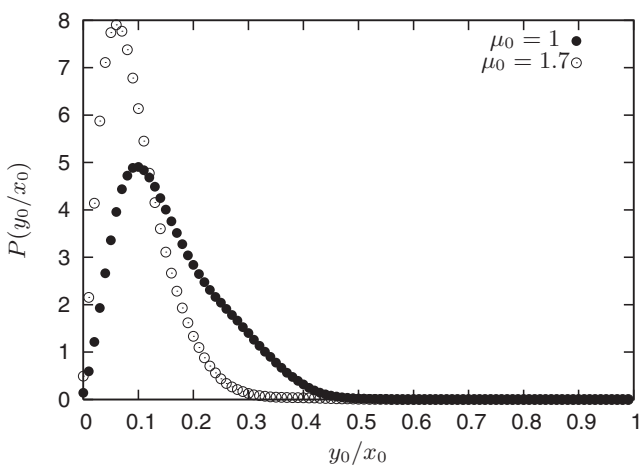

FIG. 7. Distribution of eccentricities $P(y_0/x_0)$ measured at $t = 50\tau_{\rm dyn}$ for both initial conditions.

a region of space of the order of the impact factor. As in the case treated in the paper it is difficult to estimate the statistics of the relative velocities at the distance of closest approach. However, the dependence of the change in velocity with the impact factor is expected to be an excellent approximation. As Eq. (37) factorizes between a part which depends on the velocity and another one on the impact factor b, even if we make an error computing averages over velocities we obtain the Coulomb logarithm $\ln(R/b_{\rm min})$ integrating over the allowed impact factors ($b_{\rm min}$ is the minimal impact factor). This explains why the relaxation rate measured in simulations scales with the Coulomb logarithm, as observed in simulations in gravitational systems in $d = 3$ [4–6,15,17].

V. DISCUSSION

In this paper we have shown that using a "minimal" model—based on the Chandrasekhar approximation—we can

describe well the evolution of the velocity distribution of a gravitational system in $d = 2$, for times from the formation of the QSS to thermal equilibrium. We have derived an explicit kinetic equation neglecting collective effects, in which we slightly adjust a single free parameter r^*. Comparing the evolution of the velocity distribution observed in the simulation and the one calculated with the model, we obtain a good agreement for all times, from the formation of the QSS to thermal equilibrium.

We can conclude, as we anticipated in the Introduction, that the Chandrasekhar (or local) approximation gives a reasonable description of the collisional relaxation in this system. This is due to the fact that many of the relative orbits of the particles can be well approximated by ellipses with large ellipticity, for which the Chandrasekhar approximation is a good one. However, a systematic error is made computing the diffusion coefficients, because the velocity of the particles *during the collisions* does not correspond in general to the velocity of the particle at the moment in which we sample the velocity PDF. Because of that, we have shown that we overestimate systematically the relaxation rate of the particles with small velocity and we underestimate systematically the relaxation rate of particles with large velocities.

We have neglected possible resonances of the particles with the mean field potential. We expect that they are not important, because particles have the same mass, which is a very different situation than the decay of a single much more massive particle inside a QSS formed by much lighter ones, which can excite resonances (see, e.g., [27]). Moreover, the actual potential in which particles are moving is not harmonic but is close to the one of Eq. (7): particles present highly precessing quasiperiodic orbits, which are very unlikely to excite resonances by crossing the system again and again following the same trajectory.

On the other hand, we do not observe numerically the scaling $\tau_{\rm coll} \sim N^{1.35}\tau_{\rm dyn}$ observed in [16]. This is is due to the fact that the authors of that study use a simplified dynamics (polar symmetry is imposed along the entirety of the run and therefore particles conserve their initial angular momentum), appearing not to describe properly the collisional dynamics of the real $d = 2$ system. A possible explanation of this discrepancy is that the model presented in [16] is not truly two dimensional but quasi-one-dimensional. It is known that one-dimensional models like the HMF can present striking scalings of the relaxation time with N, as pointed out in the Introduction. Interestingly, however, the same group gets, using the same simplified dynamics in $d = 3$, the same scaling $\tau_{\rm coll} \sim N\tau_{\rm dyn}$ observed using full numerical simulations [28]. More investigation should be done to understand this discrepancy.

Some conclusions can be made about the maximal impact parameter, which has to be considered in the calculations. In the simulations we do not observe any dependence of r^*—which is directly related with the maximal impact parameters allowed—on the number of particles N. We can conclude then that the maximum impact parameter does not depend on a scale related to the interparticle distance—which scales as $N^{-1/2}$—but on the size of the system. Moreover, we obtain an actual value of r^* which corresponds to the size of the homogeneous part of the system. This result is in agreement with simulations performed in $d = 3$ dimensions [17] with potential interactions $u(r) \sim 1/r^\gamma$ and $\gamma \leqslant 2$, in which the maximal impact parameter to take in the Chandrasekhar approximation was numerically estimated to be one-third the size of the system.

In this paper we have made the assumption that the density distribution is approximately homogeneous in the center of the QSS. We observe this feature in our simulations and, as pointed out above, it is also true for a wide class of initial conditions in $d = 3$. There are however other cases in which the density distribution is more "cuspy," for example when a black hole is located in the center of the system (see, e.g., [29,30]). In this case the problem is more complicated to address than making our hypothesis of homogeneity: the differential equations describing the trajectories of the particles in the mean field are not linear anymore and their relative trajectories [which is the quantity which appears in Eq. (11) and the following ones] cannot be simply obtained subtracting the solution of the individual trajectories. However, in light of our analysis, we expect that the ideas presented in Sec. IV would be valid. As at the distance of closest approach the perpendicular relative velocity $\mathbf{V}_\perp$ is always changing sign by definition, we expect that for a sufficiently small impact factor the relative velocity would also be constant in the region in which integral Eq. (35) [or Eq. (36)] is converging, and then the analysis presented in this paper would hold. It is however difficult to estimate the errors made using the Chandrasekhar approximation in this case. A more detailed numerical analysis should be performed for this kind of QSS.

As a general conclusion of this paper, we can say that in order to obtain a better description of the collisional relaxation the use of action-angle variables is unavoidable. When performing the the calculation of Eq. (11) we are indeed using action-angle variables, the parameters x_0 and y_0 being closely related to the two actions of the system. A complete calculation using canonical perturbation theory is however much more involved.

ACKNOWLEDGMENTS

I am very grateful to M. Joyce and Y. Levin for many discussions which made this work possible. I acknowledge many useful discussions with J. Barré, C. Nardini, R. Pakter, F. Peruani, A. C. Ribeiro Teixeira, T. Teles, and D. Vincenzi. I warmly thank M. Courtney for reading a previous version of the paper. Numerical simulations were performed at the SIGAMM cluster hosted at "Observatoire de Côte d'Azur," Université de Nice—Sophia Antipolis. This work was partly supported by the ANR INTERLOP project (Grant No. 09-JCJC-009401) and the CNPq (National Council for Scientific Development, Brazil).

APPENDIX: COMPUTATION OF THE DIFFUSION COEFFICIENTS

We define a laboratory Cartesian system of coordinates with unit vectors $\hat{e}_i$ $(i = 1,2)$ and another Cartesian system of coordinates $\hat{e}'_i$, in which $\hat{e}'_1$ is in the direction of the initial

relative velocity. We have therefore

$$\Delta \mathbf{v} = -|\Delta \mathbf{v}_{\parallel}|\hat{e}'_1 + |\Delta \mathbf{v}_{\perp}|\hat{e}'_2. \tag{A1}$$

The projection of the velocity in the $\hat{e}_i$ direction is then

$$\Delta v_i = -|\Delta \mathbf{v}_{\parallel}|\hat{e}'_1 \cdot \hat{e}_i + |\Delta \mathbf{v}_{\perp}|\hat{e}'_2 \cdot \hat{e}_i. \tag{A2}$$

Taking into account that, on average, collisions which will give rise to a change of the perpendicular velocity are equally probable in the $\hat{e}'_2$ direction and in the direction opposite to it, we can write

$$\Delta v_i = -|\Delta \mathbf{v}_{\parallel}|\frac{V_i}{V}, \tag{A3a}$$

$$\Delta v_i \Delta v_j = |\Delta \mathbf{v}_{\perp}|^2 \left(\delta_{ij} - \frac{V_i V_j}{V^2}\right), \tag{A3b}$$

where we have kept only the terms of $\mathcal{O}(g^2)$ and used the fact that $\hat{e}'_1 \cdot \hat{e}_i = V_i/V$ and $(\hat{e}'_2 \cdot \hat{e}_i)(\hat{e}'_2 \cdot \hat{e}_j) = \delta_{ij} - V_i V_j/V^2$. The diffusion coefficients are

$$D_{v_i} = \frac{\langle \Delta v_i \rangle}{\Delta t} = -C \int d^2v' s(v') \frac{V_i}{V^3}, \tag{A4a}$$

$$D_{v_i v_j} = \frac{\langle \Delta v_i \Delta v_j \rangle}{\Delta t} = C \int d^2v' \frac{s(v')}{V} \left(\delta_{ij} - \frac{V_i V_j}{V^2}\right). \tag{A4b}$$

Introducing, as in the $d = 3$ case, the Rosenbluth potential, we can write the diffusion coefficient using Eqs. (19) and (22):

$$D_{v_i}(v) = C \frac{\partial q(v)}{\partial v_i}, \tag{A5a}$$

$$D_{v_i v_j}(v) = C \frac{\partial^2 p(v)}{\partial v_i \partial v_j}, \tag{A5b}$$

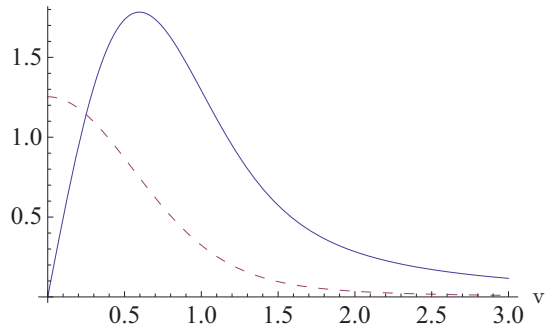

FIG. 8. (Color online) Plot of $q'(v)$ (full line) and $p''(v)$ (dashed line) as a function of v.

where

$$q(v) = \int d^2v' \frac{s(v')}{|\mathbf{v} - \mathbf{v}'|}, \tag{A6a}$$

$$p(v) = \int d^2v' s(v')|\mathbf{v} - \mathbf{v}'|, \tag{A6b}$$

where we have assumed that the velocity PDF is isotropic. Using the fact that the Rosenbluth potentials are isotropic we can simplify Eqs. (A5) using the fact that

$$\frac{\partial q(v)}{\partial v_i} = \frac{v_i}{v} q'(v), \tag{A7a}$$

$$\frac{\partial^2 p(v)}{\partial v_i \partial v_j} = \frac{v_i v_j}{v^2} \left(p''(v) - \frac{p'(v)}{v}\right) + \delta_{ij} \frac{p'(v)}{v}, \tag{A7b}$$

where the prime denotes the derivative with respect to v. In Fig. 8 we plot $q'(v)$ and $p''(v)$, are related to $D_{v_i}(v)$ and $D_{v_i v_j}(v)$, respectively.

[1] A. Campa, T. Dauxois, and S. Ruffo, Phys. Reports **480**, 57 (2009).
[2] S. Chandrasekhar, *Principles of Stellar Dynamics* (University of Chicago Press, Chicago, 1942).
[3] M. Hénon, Annales d'Astrophysique **21**, 186 (1958).
[4] R. T. Farouki and E. E. Salpeter, Astrophys. J. **253**, 512 (1982).
[5] H. Smith, Jr., Astrophys. J. **398**, 519 (1992).
[6] R. T. Farouki and E. E. Salpeter, Astrophys. J. **427**, 676 (1994).
[7] M. D. Weinberg, Astrophys. J. **410**, 543 (1993).
[8] J. Heyvaerts, Mon. Not. R. Astron. Soc. **407**, 355 (2010).
[9] P.-H. Chavanis, Physica A **391**, 3680 (2012).
[10] P.-H. Chavanis, arXiv:1210.5743.
[11] M. Joyce and T. Worrakitpoonpon, J. Stat. Mech. (2010) P10012.
[12] Y. Y. Yamaguchi, J. Barré, F. Bouchet, T. Dauxois, and S. Ruffo, Physica A **337**, 36 (2004).
[13] A. Campa, P.-H. Chavanis, A. Giansanti, and G. Morelli, Phys. Rev. E **78**, 040102 (2008).
[14] J. Diemand, B. Moore, J. Stadel, and S. Kazantzidis, Mon. Not. Roy. Astron. Soc. **348**, 977 (2004).
[15] A. Gabrielli, M. Joyce, and B. Marcos, Phys. Rev. Lett. **105**, 210602 (2010).
[16] T. N. Teles, Y. Levin, R. Pakter, and F. B. Rizzato, J. Stat. Mech. (2010) P05007.
[17] B. Marcos, A. Gabrielli, and M. Joyce (unpublished).
[18] J. Binney and S. Tremaine, *Galactic Dynamics* (Princeton University Press, Princeton, 2008).
[19] L. Cohen and A. Ahmad, Astrophys. J. **197**, 667 (1975).
[20] H. Risken, *The Fokker-Planck Equation. Methods of Solution and Applications*, 2nd ed. (Springer, Berlin, 1989).
[21] F. Roy and J. Perez, Mon. Not. R. Astron. Soc. **348**, 62 (2004).
[22] N. Rostoker and M. N. Rosenbluth, Phys. Fluids **3**, 1 (1960).
[23] P.-H. Chavanis, C. R. Phys. **7**, 331 (2006).
[24] P. H. Chavanis, Eur. Phys. J. B **52**, 61 (2006).
[25] P. H. Chavanis, Eur. Phys. J. Plus **127**, 19 (2012).
[26] V. Springel, Mon. Not. R. Astron. Soc. **364**, 1105 (2005).
[27] J. I. Read, T. Goerdt, B. Moore, A. P. Pontzen, J. Stadel, and G. Lake, Mon. Not. R. Astron. Soc. **373**, 1451 (2006).
[28] Y. Levin, R. Pakter, and F. B. Rizzato, Phys. Rev. E **78**, 021130 (2008).
[29] E. Noyola and K. Gebhardt, Astrophys. J. **132**, 447 (2006).
[30] H. Baumgardt, J. Makino, and T. Ebisuzaki, Astrophys. J. **613**, 1133 (2004).

Collisional relaxation in the inhomogeneous Hamiltonian mean-field model: Diffusion coefficients

F. P. C. Benetti[1,2,*] and B. Marcos[2,†]
[1]*Instituto de Física, Universidade Federal do Rio Grande do Sul, Brazil*
[2]*Université Côte d'Azur, CNRS UMR 7351, LJAD, France*
(Received 12 October 2016; published 8 February 2017)

Systems of particles with long-range interactions present two important processes: first, the formation of out-of-equilibrium quasistationary states (QSS) and, second, the collisional relaxation towards Maxwell-Boltzmann equilibrium in a much longer time scale. In this paper, we study the collisional relaxation in the Hamiltonian mean-field model using the appropriate kinetic equations for a system of N particles at order $1/N$: the Landau equation when collective effects are neglected and the Lenard-Balescu equation when they are taken into account. We derive explicit expressions for the diffusion coefficients using both equations for any magnetization, and we obtain analytic expressions for highly clustered configurations. An important conclusion is that in this system collective effects are crucial in order to describe the relaxation dynamics. We compare the diffusion calculated with the kinetic equations with simulations set up to simulate the system with or without collective effects, obtaining a very good agreement between theory and simulations.

DOI: 10.1103/PhysRevE.95.022111

I. INTRODUCTION

Systems with long-range interactions present the generic evolution in two distinct stages: first, the evolution to a quasistationary state in a process called *collisionless (or violent) relaxation* [1] in a time scale $\tau_{\rm dyn}$, and, second, the evolution towards thermodynamic equilibrium in the so-called *collisional relaxation process*, in a time scale of order $\tau_{\rm coll} \sim N^{\delta}\tau_{\rm dyn}$, where $\delta > 0$ depends on the system considered. The mechanism of collisional relaxation is qualitatively well known since the seminal work of Chandrasekhar [2]: The main elements are *two-body* collisions, which randomizes the velocity of the particles, leading to a Maxwell-Boltzmann velocity distribution. Using simple calculations and approximating the system as spatially homogeneous, Chandrasekhar was able to determine that, for gravitational systems in three dimensions, $\tau_{\rm coll} \sim \tau_{\rm dyn} N/\ln N$. This approach was subsequently used by other authors, notably Hénon in the 1960s (see, e.g., Ref. [3]), and led to the development of Fokker-Planck techniques. All these methods share the same feature of approximating the system as homogeneous. For example, in the *orbit-averaging* approach (see, e.g., Ref. [4]), diffusion coefficients are computed approximating the system as homogeneous, and then they are averaged over the actual orbits of the particles. This method is used because it is technically difficult to compute diffusion coefficients for inhomogeneous configurations, essentially because the trajectories of the unperturbed particles (i.e., in the mean-field limit) would need to be computed, which is generally a very difficult task. Moreover, using this approach, it is not possible to take into account *collective effects*, which can be important for some systems and configurations, which we will see it is the case in the present work.

At the same time, a rigorous kinetic theory for (repulsive, neutral) plasmas was being developed first by Landau (introducing, notably, the concept of *Landau damping*) and subsequently by other authors such as Lenard, Balescu, etc. (see, e.g., Ref. [5]). When the system is neutral, the mean-field configuration is homogeneous, and it is therefore possible to attack the problem in an essentially analytical way, including even collective effects.

Over the past few years a rigorous kinetic theory for inhomogeneous configurations has been developed by different authors [6–10]. In these works, the general procedure in order to compute kinetic equations at order $1/N$ has been described. There are, however, many practical difficulties when trying to compute quantities of interest such as the diffusion coefficients, and this for various reasons. The natural way to write these equations is to use *angle-action* variables (see, e.g., Ref. [11]). To compute them as a function of the natural variables (x,v) is technically equivalent to solving the equations of motion for the unperturbed ($N \to \infty$) potential, which is in general impossible analytically. The subsequent calculation of the diffusion coefficient (which involves, e.g., Fourier transform about the angle variable) becomes (even numerically) very difficult. For this reason, we are only aware of the study of self-gravitating tepid disks [12,13]. In this case, it is possible to make controlled approximations, which makes the semianalytical calculations feasible.

In this paper we have chosen to study *exactly* a sufficiently simple model in order to compute the diffusion coefficients without approximations (up to order $1/N$). To do so, we use the popular *Hamiltonian mean-field model* (HMF) [14], which has widely been used to study long-range systems. Its simplicity permits us to compute some analytical and numerical quantities which would be impossible in more realistic models such as three-dimensional gravity. For this reason, the diffusion coefficients have already been studied in the much simpler spatially homogeneous configuration [15]. Our work has two main objectives: On one side, it will permit us to compare the diffusion coefficients with numerical simulations in order to check the validity of the assumptions made deriving the kinetic equations in the case of spatially inhomogeneous distributions. On the other side, it will set up the method to solve numerically the Lenard-Balescu equation not only for the HMF but also for other more complicated models, as self-gravitating systems.

*Caixa Postal 15051, CEP 91501-970, Porto Alegre, RS, Brazil.
†Parc Valrose, 06108 Nice, Cedex 02, France.

The paper is organized as follows: In the first section we summarize the kinetic theory we will apply in the paper. In the next section, we apply the equations for the HMF to compute the diffusion coefficients, giving also analytical results for some cases. Then we compare the theoretical predictions with molecular dynamics simulations, including or not collective effects, and then we give conclusions and perspectives.

II. KINETIC THEORY

The evolution of an N-body system under Hamiltonian dynamics can be described using kinetic theory. The approach outlined in this section follows that of several previous works (see Introduction) and is summarized in, e.g., Ref. [16].[1] The problem addressed by this kinetic approach is the following: Given a set of N particles of mass m with initial positions $\{\mathbf{r}_i\}$ and velocity $\{\mathbf{v}_i\}$ and their Hamiltonian equations of motion, how and to what steady state will they evolve? We start with the discrete distribution function $f_d(\mathbf{r},\mathbf{v},t)$, which contains all the information of the state of the system at a given time t,

$$f_d(\mathbf{r},\mathbf{v},t) = m\sum_{i=1}^{N}\delta[\mathbf{r}-\mathbf{r}_i(t)]\delta[\mathbf{v}-\mathbf{v}_i(t)]. \tag{1}$$

The evolution of the discrete distribution function is given exactly by the Klimontovich equation [17]

$$\frac{\partial f_d}{\partial t} + \mathbf{v}\cdot\frac{\partial f_d}{\partial \mathbf{r}} - \frac{\partial \phi_d}{\partial \mathbf{r}}\cdot\frac{\partial f_d}{\partial \mathbf{v}} = 0, \tag{2}$$

$$\phi_d(\mathbf{r},t) = \int u(|\mathbf{r}-\mathbf{r}'|)f_d(\mathbf{r}',\mathbf{v}',t)d\mathbf{r}'d\mathbf{v}', \tag{3}$$

where $\phi_d(\mathbf{r},t)$ is the discrete convolution potential, $u(\mathbf{r}-\mathbf{r}')$ is the pair interaction potential between particles at positions $\mathbf{r}$ and $\mathbf{r}'$, and $\frac{\partial f}{\partial \mathbf{u}} = \sum_{i=1}^{d}\frac{\partial f}{\partial u_i}\mathbf{e}_i$ and d is the spatial dimension.

For a given initial distribution $f_0^d(\mathbf{r},\mathbf{v}) = m\sum_{i=1}^{N}\delta[\mathbf{r}-\mathbf{r}_i(t=0)]\delta[\mathbf{v}-\mathbf{v}_i(t=0)]$, the discrete distribution is determined at all future times t. A smooth distribution function can be obtained by averaging over an ensemble of initial conditions,

$$f(\mathbf{r},\mathbf{v},t) = \langle f_d(\mathbf{r},\mathbf{v},t)\rangle \tag{4}$$

and thus $f_d(\mathbf{r},\mathbf{v},t) = f(\mathbf{r},\mathbf{v},t) + \delta f(\mathbf{r},\mathbf{v},t)$.

The same smoothing process can be done for the Klimontovich equation. Since averages over the fluctuations are zero, this leads to

$$\frac{\partial f}{\partial t} + \mathbf{v}\cdot\frac{\partial f}{\partial \mathbf{r}} - \frac{\partial \phi}{\partial \mathbf{r}}\cdot\frac{\partial f}{\partial \mathbf{v}} = \frac{\partial}{\partial \mathbf{v}}\cdot\left\langle \delta f\frac{\partial \delta\phi}{\partial \mathbf{r}}\right\rangle. \tag{5}$$

The above equation gives the evolution of the smooth distribution due to correlation between its own fluctuations and the fluctuation of the smooth potential $\phi(\mathbf{r},t)$, determined by $\phi_d(\mathbf{r},t) = \phi(\mathbf{r},t) + \delta\phi(\mathbf{r},t)$, where

$$\phi(\mathbf{r},t) = \int u(|\mathbf{r}-\mathbf{r}'|)f(\mathbf{r}',\mathbf{v}',t)d\mathbf{r}'d\mathbf{v}', \tag{6}$$

$$\delta\phi(\mathbf{r},t) = \int u(|\mathbf{r}-\mathbf{r}'|)\delta f(\mathbf{r}',\mathbf{v}',t)d\mathbf{r}'d\mathbf{v}'. \tag{7}$$

Subtracting Eq. (5) from the Klimontovich equation and keeping only terms of order lower than $\mathcal{O}(1/N)$ gives the linearized Klimontovich equation,

$$\frac{\partial \delta f}{\partial t} + \mathbf{v}\cdot\frac{\partial \delta f}{\partial \mathbf{r}} - \frac{\partial \delta\phi}{\partial \mathbf{r}}\cdot\frac{\partial f}{\partial \mathbf{v}} - \frac{\partial \phi}{\partial \mathbf{r}}\cdot\frac{\partial \delta f}{\partial \mathbf{v}} = 0. \tag{8}$$

The system of Eqs. (5) and (8) are known as the quasilinear approximation, since in the first equation the correlation term on the right-hand side is of order $1/N$, while in the second equation all terms of order $1/N$ or higher have been neglected.

A. Homogeneous systems

We will first give a brief derivation of the kinetic equations for the spatially homogeneous case. It is technically simpler than the inhomogeneous one while sharing the same ideas. In this case $f = f(\mathbf{v},t)$, so Eqs. (5) and (8) become

$$\frac{\partial f}{\partial t} = \frac{\partial}{\partial \mathbf{v}}\cdot\left\langle \delta f\frac{\partial \delta\phi}{\partial \mathbf{r}}\right\rangle, \tag{9a}$$

$$\frac{\partial \delta f}{\partial t} + \mathbf{v}\cdot\frac{\partial \delta f}{\partial \mathbf{r}} - \frac{\partial \delta\phi}{\partial \mathbf{r}}\cdot\frac{\partial f}{\partial \mathbf{v}} = 0. \tag{9b}$$

The fluctuation terms are more easily dealt with by using the Fourier-Laplace transforms

$$\widetilde{\delta f}(\mathbf{k},\mathbf{v},\omega) = \frac{1}{(2\pi)^d}\int d\mathbf{r}\int_0^\infty dt\, e^{-i(\mathbf{k}\cdot\mathbf{r}-\omega t)}\delta f(\mathbf{r},\mathbf{v},t) \tag{10}$$

and

$$\widetilde{\delta\phi}(\mathbf{k},\omega) = \frac{1}{(2\pi)^d}\int d\mathbf{r}\int_0^\infty dt\, e^{-i(\mathbf{k}\cdot\mathbf{r}-\omega t)}\delta\phi(\mathbf{r},t). \tag{11}$$

Taking the Fourier-Laplace transform of Eq. (9b), we have

$$\widehat{\delta f}(\mathbf{k},\mathbf{v},0) - i(\mathbf{k}\cdot\mathbf{v}-\omega)\,\widetilde{\delta f}(\mathbf{k},\mathbf{v},\omega) + i\mathbf{k}\cdot\frac{\partial f}{\partial \mathbf{v}}\,\widetilde{\delta\phi}(\mathbf{k},\omega) = 0, \tag{12}$$

where

$$\widehat{\delta f}(\mathbf{k},\mathbf{v},0) = \int\frac{d\mathbf{r}}{(2\pi)^d}\,e^{-i\mathbf{k}\cdot\mathbf{r}}\delta f(\mathbf{r},\mathbf{v},0). \tag{13}$$

From the above equation, we can isolate $\widetilde{\delta f}$ and thus find an expression relating the fluctuations of the distribution function and the fluctuations of the potential and the initial condition,

$$\widetilde{\delta f} = \underbrace{\frac{\mathbf{k}\cdot\frac{\partial f}{\partial \mathbf{v}}\widetilde{\delta\phi}(\mathbf{k})}{\mathbf{k}\cdot\mathbf{v}-\omega}}_{\text{collective effects}} + \underbrace{\frac{\widehat{\delta f}(\mathbf{k},\mathbf{v},0)}{i(\mathbf{k}\cdot\mathbf{v}-\omega)}}_{\text{initial conditions}}. \tag{14}$$

Because collective effects are difficult to compute analytically, a common approximation found in the literature consists in neglecting them (see, e.g., Ref. [9]). In this paper we

[1] Here we use the Klimontovich formulism; the same equations may be obtained from the Born-Bogoliubov-Green-Klimontovich-Yvon (BBGKY) hierarchy, see, i.e., Ref. [8].

will consider the complete problem, and we will study their importance in the inhomogeneous HMF.

The next step in the derivation consists in expressing the Fourier transform of the fluctuation of the potential $\widetilde{\delta\phi}(\mathbf{k},\omega)$ as a function of the fluctuation $\widetilde{\delta f}(\mathbf{k},w)$. To do so, we integrate Eq. (14) over $\mathbf{v}$, and, using the Fourier transform of Eq. (7), we get

$$\int_{-\infty}^{\infty} d\mathbf{v}\widetilde{\delta f}(\mathbf{k},\mathbf{v},\omega) = \frac{1}{\epsilon(\mathbf{k},\omega)}\int_{-\infty}^{\infty} d\mathbf{v}\frac{\widehat{\delta f}(\mathbf{k},\mathbf{v},0)}{i(\mathbf{v}\cdot\mathbf{k}-\omega)}, \tag{15}$$

where we have defined the plasma response dielectric function

$$\epsilon(\mathbf{k},\omega) = 1 - \hat{u}(\mathbf{k})\int d\mathbf{v}\frac{\mathbf{k}\cdot\partial f(\mathbf{v})/\partial\mathbf{v}}{\mathbf{v}\cdot\mathbf{k}-\omega}. \tag{16}$$

Using again Eqs. (7) and (15), we get

$$\begin{aligned}\widetilde{\delta\phi}(\mathbf{k},\omega) &= \hat{u}(\mathbf{k})\int_{-\infty}^{\infty} d\mathbf{v}\widetilde{\delta f}(\mathbf{k},\mathbf{v},\omega)\\ &= \frac{\hat{u}(\mathbf{k})}{\epsilon(\mathbf{k},\omega)}\int_{-\infty}^{\infty} d\mathbf{v}\frac{\widehat{\delta f}(\mathbf{k},\mathbf{v},0)}{i(\mathbf{p}\cdot\mathbf{k}-\omega)}.\end{aligned} \tag{17}$$

Inserting Eqs. (14) and (17) into Eq. (9a), after some algebra, we get the Lenard-Balescu equation (using the notation [17]):

$$\begin{aligned}\frac{\partial f}{\partial t} &= \pi(2\pi)^d m\sum_{i,j=1}^{d}\frac{\partial}{\partial v_i}\int d\mathbf{k}d\mathbf{v}' k_i k_j\frac{\hat{u}(\mathbf{k})^2}{|\epsilon(\mathbf{k},\mathbf{k}\cdot\mathbf{v})|^2}\\ &\quad\times\delta[\mathbf{k}\cdot(\mathbf{v}-\mathbf{v}')]\left(\frac{\partial}{\partial v_j}-\frac{\partial}{\partial v'_j}\right)f(\mathbf{v},t)f(\mathbf{v}',t).\end{aligned} \tag{18}$$

When collective effects are neglected, i.e., the first term of Eq. (14) is neglected, it is simple to see from Eq. (16) that $\epsilon(\mathbf{k},\omega) = 1$.

B. Inhomogeneous systems

In inhomogeneous systems, the strategy is to use, instead of the variables $(\mathbf{r},\mathbf{v})$, the angle-action variables $(\mathbf{w},\mathbf{J})$ corresponding to the Hamiltonian $\mathcal{H}$ of smooth dynamics (i.e., the one corresponding to the limit $N\to\infty$) [18]. Using these variables, particles described by the Hamiltonian $\mathcal{H}$ keep their action $\mathbf{J}$ constant during the dynamic and their angle evolves with time as $\mathbf{w} = \Omega(\mathbf{J})t + \mathbf{w}_0$, where $\mathbf{w}_0$ is the angle at $t = 0$ and $\Omega(\mathbf{J}) = \partial\mathcal{H}/\partial\mathbf{J}$ is the angular frequency [19]. The system thus becomes "homogeneous" in the new coordinates [20].

The equations for evolution of smooth distribution function f and its fluctuation δf are [7,10]

$$\frac{\partial f(\mathbf{J})}{\partial t} + [\mathcal{H}(\mathbf{J}),f(\mathbf{J})] = -\langle[\delta\phi,\delta f(\mathbf{J})]\rangle, \tag{19a}$$

$$\frac{\partial\delta f(\mathbf{J})}{\partial t} + [\mathcal{H}(\mathbf{J}),\delta f(\mathbf{J})] + [\delta\phi,f(\mathbf{J})] = 0, \tag{19b}$$

where ϕ is the smooth mean-field potential and $\delta\phi$ is its fluctuation, and $[\mathcal{H},B] = \frac{\partial\mathcal{H}}{\partial\mathbf{J}}\frac{\partial B}{\partial\mathbf{w}} - \frac{\partial\mathcal{H}}{\partial\mathbf{w}}\frac{\partial B}{\partial\mathbf{J}}$ are Poisson brackets with action-angle variables as the canonical coordinates.

Since by construction $\partial\mathcal{H}/\partial\mathbf{w} = 0$ and $\partial f/\partial\mathbf{w} = 0$, the terms in Poisson brackets reduce to

$$[\mathcal{H},\delta f] = \frac{\partial\mathcal{H}}{\partial\mathbf{J}}\frac{\partial\delta f}{\partial\mathbf{w}} = \Omega(\mathbf{J})\cdot\frac{\partial\delta f}{\partial\mathbf{w}}, \tag{20}$$

$$[\delta\phi,f] = -\frac{\partial\delta\phi}{\partial\mathbf{w}}\cdot\frac{\partial f}{\partial\mathbf{J}}. \tag{21}$$

Substituting the above in Eq. (19) and averaging over angles $\mathbf{w}$,

$$\frac{\partial\overline{f}}{\partial t} = \frac{\partial}{\partial\mathbf{J}}\cdot\left\langle\overline{\delta f\frac{\partial\delta\phi}{\partial\mathbf{w}}}\right\rangle, \tag{22a}$$

$$\frac{\partial\overline{\delta f}}{\partial t} + \Omega(\mathbf{J})\cdot\frac{\partial\overline{\delta f}}{\partial\mathbf{w}} - \overline{\frac{\partial\delta\phi}{\partial\mathbf{w}}\cdot\frac{\partial f}{\partial\mathbf{J}}} = 0, \tag{22b}$$

where $\overline{A}$ represents the angle-averaging of A. From now on, we disregard this notation and write $\overline{A} = A$ for simplicity, but we emphasize that the equations from this point further correspond to the angle-averaged quantities.

Observe that Eq. (22) have the same structure as their homogeneous counterpart equation (9) identifying the action $\mathbf{J}$ with the velocity $\mathbf{v}$ and the angle $\mathbf{w}$ with the spatial variable $\mathbf{r}$. The only difference appears in the second term of Eq. (22b) in which the velocity $\mathbf{v}$ is substituted by the frequency of the unperturbed orbit $\Omega(\mathbf{J})$. Following then the same procedure as the one described in the homogeneous case, we get the Lenard-Balescu-type kinetic equation (with collective effects) in action-angle variables [8,10],

$$\begin{aligned}\frac{\partial f}{\partial t} &= \pi(2\pi)^d m\frac{\partial}{\partial\mathbf{J}}\cdot\sum_{\mathbf{k},\mathbf{k}'}\int d\mathbf{J}'\mathbf{k}\frac{\delta[\mathbf{k}\cdot\Omega(\mathbf{J})-\mathbf{k}'\cdot\Omega(\mathbf{J}')]}{|D_{\mathbf{k},\mathbf{k}'}(\mathbf{J},\mathbf{J}',\mathbf{k}\cdot\Omega(\mathbf{J}))|^2}\\ &\quad\times\left(\mathbf{k}\cdot\frac{\partial}{\partial\mathbf{J}}-\mathbf{k}'\cdot\frac{\partial}{\partial\mathbf{J}'}\right)f(\mathbf{J},t)f(\mathbf{J}',t),\end{aligned} \tag{23}$$

where

$$\frac{1}{D_{\mathbf{k},\mathbf{k}'}(\mathbf{J},\mathbf{J}',\omega)} = \sum_{\alpha,\alpha'}\hat{\Phi}_\alpha(\mathbf{k},\mathbf{J})(\epsilon^{-1})_{\alpha,\alpha'}(\omega)\hat{\Phi}^\star_{\alpha'}(\mathbf{k}',\mathbf{J}'), \tag{24}$$

and $\epsilon_{\alpha\alpha'}(\omega)$ is the dielectric tensor

$$\begin{aligned}\epsilon_{\alpha\alpha'}(\omega) &= \delta_{\alpha\alpha'} + (2\pi)^d\sum_{\mathbf{k}}\int d\mathbf{J}\frac{\mathbf{k}\cdot\partial f/\partial\mathbf{J}}{\mathbf{k}\cdot\Omega(\mathbf{J})-\omega}\\ &\quad\times\hat{\Phi}^\star_\alpha(\mathbf{k},\mathbf{J})\hat{\Phi}_{\alpha'}(\mathbf{k},\mathbf{J}).\end{aligned} \tag{25}$$

The indices (α,α') are labels for the biorthogonal basis $\{\rho_\alpha,\Phi_\alpha\}$, where $\rho(\mathbf{r}) = \int f(\mathbf{r},\mathbf{v},t)d\mathbf{v}$, which satisfies [21]

$$\int u(|\mathbf{r}-\mathbf{r}'|)\rho_\alpha(\mathbf{r}')d\mathbf{r}' = \Phi_\alpha, \tag{26}$$

$$\int\rho_\alpha(\mathbf{r})\Phi^\star_{\alpha'}(\mathbf{r})d\mathbf{r} = -\delta_{\alpha,\alpha'}. \tag{27}$$

The terms $\hat{\Phi}_\alpha$ are the Fourier transforms of the potential in the biorthogonal representation with respect to the angles,

$$\hat{\Phi}_\alpha(\mathbf{k},\mathbf{J}) = \frac{1}{(2\pi)^d}\int d\mathbf{w}e^{-i\mathbf{k}\cdot\mathbf{w}}\Phi_\alpha(\mathbf{w},\mathbf{J}). \tag{28}$$

The Lenard-Balescu equation (23) gives the evolution of f due to the inclusion of a finite-N correction to the collisionless

(Vlasov) kinetic equation. From Eq. (23), we see that the evolution, which slowly deforms the orbits of constant $\mathbf{J}$, is driven by resonances between orbital frequencies, $\mathbf{k}\cdot\Omega(\mathbf{J}) = \mathbf{k}'\cdot\Omega(\mathbf{J}')$. This differs from the homogeneous case, Eq. (18), where f evolves due to the resonances $\mathbf{v} = \mathbf{v}'$.

Using the chain rule, the Lenard-Balescu-type equation (23) can be written in the form of a Fokker-Planck equation,

$$\frac{\partial f}{\partial t} = \sum_{i,j=1}^{d} \frac{\partial^2}{\partial J_i \partial J_j} D^{ij}_{\rm dif}(\mathbf{J},t) f(\mathbf{J},t) - \frac{\partial}{\partial \mathbf{J}}\cdot \mathbf{D}_{fr}(\mathbf{J},t) f(\mathbf{J},t), \tag{29}$$

where

$$D^{ij}_{\rm dif}(\mathbf{J},t) = \pi(2\pi)^d m \sum_{\mathbf{k},\mathbf{k}'} \int d\mathbf{J}' k_i k_j \frac{1}{|D_{\mathbf{k},\mathbf{k}'}(\mathbf{J},\mathbf{J}',\mathbf{k}'\cdot\Omega(\mathbf{J}'))|^2} \times \delta[\mathbf{k}\cdot\Omega(\mathbf{J}) - \mathbf{k}'\cdot\Omega(\mathbf{J}')] f(\mathbf{J}',t) \tag{30}$$

is the diffusion coefficient and the friction coefficient is

$$\mathbf{D}_{fr}(\mathbf{J},t) = \pi(2\pi)^d m \sum_{\mathbf{k},\mathbf{k}'} \int d\mathbf{J}' f(\mathbf{J}')\, \mathbf{k}\left(\mathbf{k}\frac{\partial}{\partial \mathbf{J}} - \mathbf{k}'\frac{\partial}{\partial \mathbf{J}'}\right) \times \frac{\delta[\mathbf{k}\cdot\Omega(\mathbf{J}) - \mathbf{k}'\cdot\Omega(\mathbf{J}')]}{|D_{\mathbf{k},\mathbf{k}'}(\mathbf{J},\mathbf{J}',\mathbf{k}'\cdot\Omega(\mathbf{J}'))|^2}. \tag{31}$$

The ith component of the friction coefficient (31) can also be written as the sum of the derivative of the diffusion coefficient, plus a polarization force [10],

$$D^i_{fr}(\mathbf{J},t) = \frac{\partial}{\partial J_i} D^{ij}_{\rm dif}(\mathbf{J},t) + D^i_{\rm pol}(\mathbf{J},t), \tag{32}$$

where the i component of the polarization force is

$$D^i_{\rm pol}(\mathbf{J},t) = \pi(2\pi)^d m \sum_{\mathbf{k},\mathbf{k}'} \int d\mathbf{J}' k_i \mathbf{k}' \frac{1}{|D_{\mathbf{k},\mathbf{k}'}(\mathbf{J},\mathbf{J}',\mathbf{k}'\cdot\Omega(\mathbf{J}'))|^2} \times \delta[\mathbf{k}\cdot\Omega(\mathbf{J}) - \mathbf{k}'\cdot\Omega(\mathbf{J}')] \frac{\partial f(\mathbf{J}',t)}{\partial \mathbf{J}'}. \tag{33}$$

When collective effects are not considered, we have

$$\epsilon_{\alpha\alpha'} = \delta_{\alpha\alpha'}, \tag{34}$$

and therefore the Landau equation is obtained using the *bare*, undressed Fourier transforms of the potential,

$$\frac{1}{\left|D^{\rm bare}_{\mathbf{k},\mathbf{k}'}(\mathbf{J},\mathbf{J}',\mathbf{k}'\cdot\Omega(\mathbf{J}'))\right|^2} = |\hat{\Phi}_\alpha(\mathbf{k},\mathbf{J})\hat{\Phi}^\star_\alpha(\mathbf{k}',\mathbf{J}')|^2. \tag{35}$$

III. KINETIC EQUATIONS FOR THE HAMILTONIAN MEAN-FIELD MODEL

We will compute explicitly the diffusion coefficients for the HMF model. It is given by the Hamiltonian

$$H = \sum_{i=1}^{N} \frac{p^2}{2} - \frac{1}{2N}\sum_{i,j=1}^{N} \cos(\theta_i - \theta_j). \tag{36}$$

The energy of one particle can be written as

$$h(\theta,p) = \frac{p^2}{2} + \phi(\theta) = \frac{p^2}{2} - \frac{1}{N}\sum_{i=1}^{N}\cos(\theta_i - \theta). \tag{37}$$

The potential $\phi(\theta) = -1/N\sum_i \cos(\theta_i - \theta)$ can be rewritten as

$$\phi(\theta) = -\frac{\sum_{i=1}^N \cos\theta_i}{N}\cos\theta - \frac{\sum_{i=1}^N \sin\theta_i}{N}\sin\theta = -M_x\cos\theta - M_y\sin\theta, \tag{38}$$

where $\mathbf{M} = (M_x, M_y)$ is the magnetization vector. Its modulus quantifies how bunched, or clustered, the particles are. Shifting all angles by a phase $\alpha = \arctan(M_y/M_x)$, we can write the potential simply as a function of the modulus of the magnetization M,

$$\phi(\theta^\star) = -M\cos\theta^\star, \tag{39}$$

where $\theta^\star = \theta - \alpha$ and $M = M_x = \sum_{i=1}^N \cos\theta_i^\star$. For simplicity, henceforth we denote $\theta^\star$ as θ.

A. Action-angle variables

Inhomogeneous states of the HMF model have previously been studied using action-angle variables in the case of Vlasov stability [22,23]. We define our action angle variables in the same way as these references. The action J is defined as

$$J = \frac{1}{2\pi}\oint p\,d\theta$$

with $p = \sqrt{2[h - \phi(\theta)]}$, where energy h is the one-particle energy and $\phi(\theta)$ is the mean-field potential, Eq. (39). The potential can be fully specified with a single scalar quantity, the modulus of the magnetization M. It is possible to write simply and in a generic way an expression for the action which depends only on the energy of the particle h and the adiabatic, static magnetization M_0 (see Appendix A),

$$J(\kappa) = \frac{4\sqrt{M_0}}{\pi}\begin{cases} 2[E(\kappa) - (1-\kappa^2)K(\kappa)], & \kappa < 1 \\ \kappa E\left(\frac{1}{\kappa}\right), & \kappa > 1 \end{cases}, \tag{40}$$

where

$$\kappa = \sqrt{\frac{h + M_0}{2M_0}}. \tag{41}$$

The action J is discontinuous at the separatrix $\kappa = 1$, the boundary between rotating and librating orbits (see Fig. 1). Figure 2 shows the action as a function of κ and the discontinuity at the separatrix.

The frequency $\Omega(J)$ is $\Omega(J) = \partial h/\partial J$. Due to the frequency being noninjective in J, and J being a function of elliptical integrals of κ, it is easier to treat all expressions directly as a function of κ. We use the Jacobian $\partial\kappa/\partial J$ to change variables,

$$\left[\frac{\partial J}{\partial \kappa}\right] = \frac{4\sqrt{M_0}}{\pi}\begin{cases} 2\kappa K(\kappa), & \kappa < 1 \\ K\left(\frac{1}{\kappa}\right), & \kappa > 1. \end{cases} \tag{42}$$

Thus the frequency is given by $\Omega(J) = (\partial\kappa/\partial J)(\partial h/\partial\kappa)$,

$$\Omega(\kappa) = \pi\sqrt{M_0}\begin{cases} \frac{1}{2K(\kappa)}, & \kappa < 1 \\ \frac{\kappa}{K\left(\frac{1}{\kappa}\right)}, & \kappa > 1 \end{cases}. \tag{43}$$

The explicit expressions for the action-angle variables is a great advantage of the HMF model for the investigating

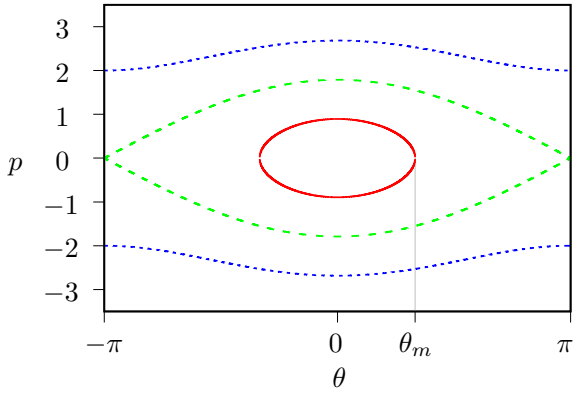

FIG. 1. Examples of a librating orbit (red solid line), for which $\kappa < 1$, a rotating orbit (blue dotted line), for which $\kappa > 1$, and the separatrix orbit (green dashed line), for which $\kappa = 1$. For the librating orbit, $\theta_m = \arccos(1 - 2\kappa^2)$, while for the other orbits $\theta_m = \pi$.

inhomogeneous states. For most systems, this is not possible, a few exceptions in astrophysics being spherical potentials and flat axisymmetric potentials such as razor-thin and tepid disks, as well as some nonaxisymmetric potentials such as Stäckel potentials [18].

B. Kinetic equations

For the HMF model, the pair potential $u(\theta - \theta') = -\cos(\theta - \theta')$ can be written in the two-dimensional biorthogonal representation as $\Phi_c = -\cos[\theta(w,\kappa)]$ and $\Phi_s = -\sin[\theta(w,\kappa)]$, and its Fourier transforms are

$$\begin{aligned}\hat{\Phi}_c(m,\kappa) &= -c_m(\kappa) = \frac{-1}{2\pi}\int_{-\pi}^{\pi}\cos[\theta(w,\kappa)]e^{-imw}dw,\\ \hat{\Phi}_s(m,\kappa) &= -s_m(\kappa) = \frac{-1}{2\pi}\int_{-\pi}^{\pi}\sin[\theta(w,\kappa)]e^{-imw}dw.\end{aligned} \tag{44}$$

These can be written more simply as (see Appendix B)

$$c_n(\kappa) = \begin{cases}\frac{\pi^2}{K(\kappa)^2}\frac{|n|q(\kappa)^{|n|/2}}{1-q(\kappa)^{|n|}} & \kappa < 1,\ n \text{ even},\\ 0 & \kappa < 1,\ n \text{ odd},\\ \frac{2\pi^2\kappa^2}{K(\frac{1}{\kappa})^2}\frac{|n|q(\frac{1}{\kappa})^{|n|}}{1-q(\frac{1}{\kappa})^{2|n|}} & \kappa > 1,\end{cases} \tag{45}$$

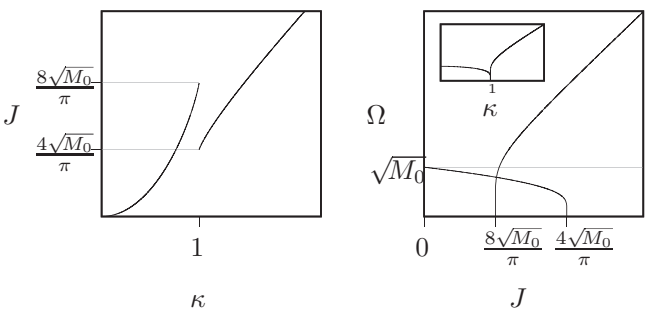

FIG. 2. Action as a function of κ for the HMF model (left), and frequency Ω versus J (inset: Ω vs κ) (right) for the HMF model.

and

$$s_n(\kappa) = \begin{cases}0 & \kappa < 1,\ n \text{ even},\\ -i\frac{\pi^2}{K(\kappa)^2}\frac{nq(\kappa)^{|n|/2}}{1+q(\kappa)^{|n|}} & \kappa < 1,\ n \text{ odd},\\ -i\frac{2\pi^2\kappa^2}{K(\frac{1}{\kappa})^2}\frac{nq(\frac{1}{\kappa})^{|n|}}{1+q(\frac{1}{\kappa})^{2|n|}} & \kappa > 1,\ p > 0,\\ i\frac{2\pi^2\kappa^2}{K(\frac{1}{\kappa})^2}\frac{nq(\frac{1}{\kappa})^{|n|}}{1+q(\frac{1}{\kappa})^{2|n|}} & \kappa > 1,\ p < 0,\end{cases} \tag{46}$$

where $q(k) = \exp[-\pi K(\sqrt{1-k^2})/K(k)]$. To switch variables from J to κ, we use the Dirac δ identity $\delta[f(x)] = \sum_{x^*}\delta(x - x^*)/|\partial f/\partial x|_{x^*}$ [where x^* are the roots of $f(x)$]. Thus, the Lenard-Balescu equation for the HMF model is

$$\begin{aligned}\frac{\partial f}{\partial t} &= \frac{2\pi^2}{N}\left|\frac{\partial J}{\partial \kappa}\right|^{-1}\frac{\partial}{\partial\kappa}\sum_{n,n'=-\infty}^{\infty}\int\frac{d\kappa' n|\partial J'/\partial\kappa'|}{|D_{nn'}(\kappa,\kappa',n\Omega(\kappa))|^2}\\ &\times\sum_{\kappa^\star}\frac{\delta(\kappa'-\kappa^\star)}{\left|n'\frac{\partial\Omega}{\partial\kappa'}\right|_{\kappa^\star}}\left(n\left|\frac{\partial J}{\partial\kappa}\right|^{-1}\frac{\partial}{\partial\kappa} - n'\left|\frac{\partial J'}{\partial\kappa'}\right|^{-1}\frac{\partial}{\partial\kappa'}\right)\\ &\times f(\kappa,t)f(\kappa',t),\end{aligned} \tag{47}$$

where $\kappa^\star$ are the roots of the equation $m\Omega(\kappa) - m'\Omega(\kappa') = 0$, the Jacobian $|\partial J/\partial\kappa|$ is given by Eq. (42), and $\partial\Omega/\partial\kappa$ is

$$\frac{\partial\Omega}{\partial\kappa} = \pi\sqrt{M_0}\begin{cases}\frac{E(\kappa)+(\kappa^2-1)K(\kappa)}{2\kappa(\kappa^2-1)K^2(\kappa)}, & \kappa < 1,\\ \frac{\kappa^2 E(\frac{1}{\kappa})}{(\kappa^2-1)K^2(\frac{1}{\kappa})}, & \kappa > 1.\end{cases} \tag{48}$$

The associated diffusion coefficient is

$$D_{\rm dif}(\kappa) = \frac{2\pi^2}{N}\sum_{n,n'=\infty}^{\infty}\sum_{\kappa^\star}\frac{n^2|\partial J/\partial\kappa|_{\kappa^\star}}{|D_{nn'}(\kappa,\kappa^\star,n\Omega(\kappa))|^2}\frac{f(\kappa^\star,t)}{\left|n'\frac{\partial\Omega}{\partial\kappa'}\right|_{\kappa^\star}} \tag{49}$$

and the polarization coefficient is

$$D_{\rm pol}(\kappa) = \frac{2\pi^2}{N}\sum_{n,n'=-\infty}^{\infty}\sum_{\kappa^\star}\frac{n\,n'}{|D_{nn'}(\kappa,\kappa^\star,n\Omega(\kappa))|^2}\frac{\partial f/\partial\kappa'|_{\kappa^\star}}{\left|n'\frac{\partial\Omega}{\partial\kappa'}\right|_{\kappa^\star}}. \tag{50}$$

Equation (24), which determines $D_{nn'}(\kappa,\kappa',\omega)$, becomes

$$\frac{1}{D_{nn'}(\kappa,\kappa',\omega)} = \frac{c_n(\kappa)c_{n'}(\kappa')}{\epsilon_{cc}(\omega)} - \frac{s_n(\kappa)s_{n'}(\kappa')}{\epsilon_{ss}(\omega)}. \tag{51}$$

If collective effects are neglected, then $\epsilon_{cc} = \epsilon_{ss} = 1$, and we get simply

$$\frac{1}{D^{\rm bare}_{nn'}(\kappa,\kappa')} = c_n(\kappa)c_{n'}(\kappa') - s_n(\kappa)s_{n'}(\kappa'). \tag{52}$$

If collective effects are not neglected, then it is necessary to compute numerically the dielectric tensor, with the procedure we detail below.

C. Numerical computation of the dielectric tensor

The cc and ss components of the dielectric tensor are

$$\epsilon_{cc}(\omega) = 1 + 2\pi\sum_{\ell=-\infty}^{\infty}\int_0^\infty d\kappa\frac{g^{cc}_\ell(\kappa)}{\Omega(\kappa) - \omega/\ell} \tag{53}$$

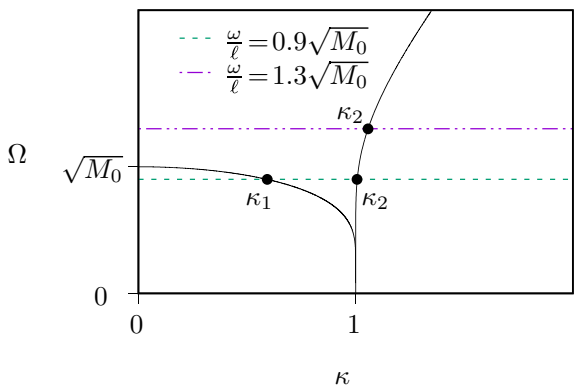

FIG. 3. Poles of integral in the dielectric tensor components (53) and (54). For $\omega/\ell > \Omega_0$ (dash-dotted line), only one pole occurs (κ_2), while for $0 < \omega/\ell < \Omega_0$ (dashed line), there are two (κ_1 and κ_2).

and

$$\epsilon_{ss}(\omega) = 1 + 2\pi \sum_{\ell=-\infty}^{\infty} \int_0^{\infty} d\kappa \frac{g_\ell^{ss}(\kappa)}{\Omega(\kappa) - \omega/\ell}, \tag{54}$$

respectively, where, to simplify the notation, we have defined

$$g_\ell^{cc}(\kappa) = |c_\ell(\kappa)|^2 \partial f/\partial\kappa, \tag{55a}$$

$$g_\ell^{ss}(\kappa) = |s_\ell(\kappa)|^2 \partial f/\partial\kappa. \tag{55b}$$

The off-diagonal terms, involving products of the type $c_n(\kappa)s_{n'}(\kappa')$, are zero after integration.

The integrals in Eqs. (53) and (54) must be performed carefully due to the poles at $\omega = \ell\Omega(\kappa)$. Poles can only occur if ℓ and ω are of the same sign. Moreover, the number of poles depends on the value of ω, since $\Omega(\kappa)$ can have the same value at two different values of κ for $\Omega(\kappa) < \Omega_0$ where $\Omega_0 = \Omega(0) = \sqrt{M_0}$. Therefore, we distinguish among the following cases (see Fig. 3):

(1) $\omega/\ell < 0$: no poles;

(2) $0 < \omega/\ell < \Omega_0$: one pole $\kappa_1 < 1$ and one pole at $\kappa_2 > 1$;

(3) $\omega/\ell > \Omega_0$: one pole at $\kappa_2 > 1$.

For each case, the integrals must be separated into different regions. In all cases we separate between the regions $\kappa \in (0,1)$ and $\kappa \in (1,\infty)$, due to the different expressions of $\Omega(\kappa)$, $c_n(\kappa)$, and $s_n(\kappa)$ in the two domains. Therefore, for case 1, the integrals in Eqs. (53) and (54) are

$$\int d\kappa \frac{g_\ell^{cc/ss}(\kappa)}{\Omega(\kappa) - \omega/\ell} = \int_0^1 d\kappa \frac{g_\ell^{cc/ss}(\kappa)}{\Omega(\kappa) - \omega/\ell} + \int_1^{\infty} d\kappa \frac{g_\ell^{cc/ss}(\kappa)}{\Omega(\kappa) - \omega/\ell}. \tag{56}$$

For case (2), we must use the Landau contour in both regions,

$$\int d\kappa \frac{g_\ell^{cc/ss}(\kappa)}{\Omega(\kappa) - \omega/\ell} = \mathcal{P}\int_0^1 d\kappa \frac{g_\ell^{cc/ss}(\kappa)}{\Omega(\kappa) - \omega/\ell} + i\pi Res\kappa_1 + \mathcal{P}\int_1^{\infty} d\kappa \frac{g_\ell^{cc/ss}(\kappa)}{\Omega(\kappa) - \omega/\ell} + i\pi Res\kappa_2, \tag{57}$$

and, for case (3), only in the second region,

$$\int d\kappa \frac{g_\ell^{cc/ss}(\kappa)}{\Omega(\kappa) - \omega/\ell} = \int_0^1 d\kappa \frac{g_\ell^{cc/ss}(\kappa)}{\Omega(\kappa) - \omega/\ell} + \mathcal{P}\int_1^{\infty} d\kappa \frac{g_\ell^{cc/ss}(\kappa)}{\Omega(\kappa) - \omega/\ell} + i\pi Res\kappa_2, \tag{58}$$

where $\mathcal{P}\int$ denotes the Cauchy principal value and $Resx$ is the residue of the integrand at x.

Equations (49), (51), (53), and (54), with $\Omega(\kappa)$, $s_m(\kappa)$, and $c_m(\kappa)$ determined by equations (43), (45), and (46), respectively, enable us to calculate the diffusion coefficient of the HMF model in action-angle variables, with collective effects. The same can be done neglecting collective effects, using the same equations with $\epsilon_{cc} = \epsilon_{ss} = 1$. The inclusion or exclusion of collective effects greatly affects the resulting diffusion coefficient. This is shown in Fig. 6, where we present diffusion coefficients considering a thermal bath,

$$f(\kappa,t) = C\exp[-\beta M_0(2\kappa^2 - 1)], \tag{59}$$

for two equilibrium configurations (β, M_0), where $C = \sqrt{\beta/(2\pi)^3}/I_0(\beta M_0)$ and $I_n(z)$ is the nth-order modified Bessel function of the first kind. For the numerical results, all sums over n, n', and ℓ are truncated at $n_{\max} = 6$ and $\ell_{\max} = 6$, respectively (although normally $n_{\max} = 4$ and $\ell_{\max} = 2$ suffice).

From the forms of equations of the diffusion coefficients (49), we see that the contributions to the diffusion of a particle with a parameter κ come from its resonances with particles of parameter $\kappa^\star$, where $\kappa^\star$ and κ satisfy $n\Omega(\kappa) = n'\Omega(\kappa^\star)$ and n,n' are integers. In order to see how each resonance contributes to the diffusion coefficient, in Fig. 4 we plot maps showing the normalized contribution of each term in the $\kappa^\star$ sum, for a given κ, for a thermal distribution function corresponding to $M_0 = 0.05$ (top) and $M_0 = 0.9$ (bottom). In other words, if we write the diffusion coefficient as

$$D_{\rm dif}(\kappa) = \sum_{\kappa^\star} \gamma(\kappa,\kappa^\star), \tag{60}$$

then the color map shows $\gamma(\kappa,\kappa^\star)/D_{\rm dif}(\kappa)$.

In the highly inhomogeneous case, $M_0 = 0.9$, almost all the contribution comes from $\kappa^\star < 1$ (inside the separatrix). This is mainly due to the distribution being highly clustered, so most particles are below the separatrix. Consequently, for most particles, the main contribution to their diffusion comes from resonances with particles at their same frequency. This is represented by the strong yellow line at $\kappa^\star < 1$. For the almost-homogeneous case, $M_0 = 0.05$, the particles are not so clustered and so particles with $\kappa^\star \neq \kappa$ also contribute, as demonstrated by the presence of other curves in the top panel.

D. Examples of numerical calculations

In this section we show the predictions for the diffusion coefficients both including or neglecting collective effects. Note that, near the separatrix ($\kappa = 1$), we do not plot the value of the diffusion coefficient. This is because the calculation becomes numerically unstable in this region. Indeed, the

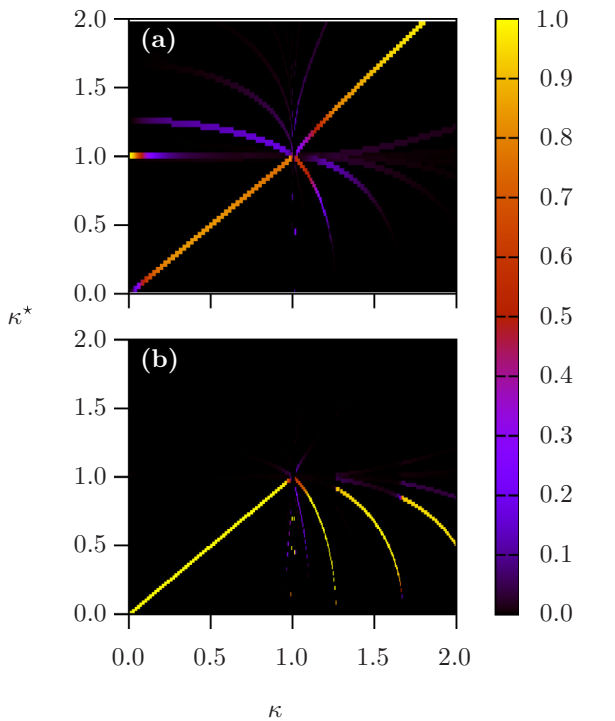

FIG. 4. Normalized contribution to the Lenard-Balescu diffusion coefficient $D_{\rm dif}(\kappa)$, Eq. (49), as a function of $\kappa^\star$. Both panels correspond to thermal equilibrium distributions but with different magnetizations: (a) almost homogeneous, $M_0 = 0.05$, and (b) highly inhomogeneous, $M_0 = 0.9$. In the latter case, most of the contribution comes from resonances at $\kappa^\star < 1.0$ (below the separatrix), while for the nearly homogeneous system this is not the case.

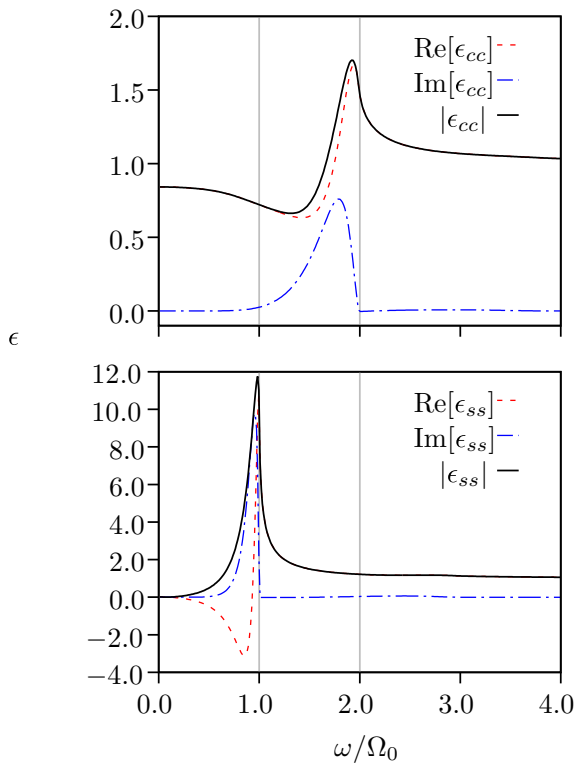

FIG. 5. Cosine (top) and sine (bottom) components of the dielectric tensor $\epsilon(\omega)$, given by Eqs. (53) and (54), respectively. The equilibrium parameters are $(u, M_0) = (-0.1, 0.728)$. The vertical lines show $\omega = \Omega_0$ and $\omega = 2\Omega_0$.

perturbative approach we have used may not be valid [24,25] for particles crossing the separatrix. Since it does not seem to play an important role in the diffusion, we neglect the point $\kappa \approx 1$. First, we notice that, as in the homogeneous case [15], collective effects are very important in this system. To illustrate this behavior, we plot the components of the dielectric tensor in Fig. 5. We observe a characteristic frequency (materialized by a "bump") at a frequency of order $n\Omega_0$, with $n = 1$ for sine perturbations and $n = 2$ for cosine ones. We observe that collective effects are very important for frequencies $\omega \lesssim n\Omega_0$ in this case, i.e., the modulus of the components of the dielectric tensor differs considerably from 1. Inspecting the kinetic equation (47), we see that this implies that for values of κ which correspond to these frequencies (which correspond mainly to librating particles) collective effects are important. However, particles with larger frequencies do not present strong collective effects, because they have frequencies $\omega \gg \Omega_0$ for which the components of the dielectric tensor is close to 1.

This fact is apparent in the computation of the diffusion coefficients for two different magnetizations shown in Fig. 6. For both small magnetization (i.e., system very close to homogeneity) as well as magnetization closer to 1, the diffusion coefficients predicted by the Landau equation (no collective effects) and the Lenard-Balescu equation (collective effects) difrer completely except, as expected, for $\kappa > 1$, which corresponds to particles with frequencies for which the modulus of the components of the dielectric tensor tends to 1.

E. Analytical results for highly magnetized states

It is possible to obtain analytical expressions for the diffusion coefficients for highly magnetized configurations. In this case, all the particles have $\kappa < 1$ and it suffices to perform the sums in the kinetic equations up to $|n| = |n'| = 2$ to obtain a good approximation to the dielectric tensor and the diffusion coefficients. This implies that the position of the resonances are $\kappa^\star = \kappa$, simply.[2] If the system is less magnetized, then there are resonances with particles which are outside the separatrix, and in this case it is necessary to solve numerically the resonance condition $n\Omega(\kappa) = n'\Omega(\kappa^*)$. We will study the case in which collective effects are neglected, and then when collective effects are considered for two paradigmatic cases: a core-halo distribution and a Maxwell-Boltzmann distribution. These two distributions can be considered as prototypes of the two classes of distributions which appears after the violent relaxation process. When initial condition leads to a very "violent" violent relaxation, it results in a core-halo quasiequilibrium, while when the initial condition leads to a "gentle" violent relaxation, a compact distribution similar to a Gaussian one forms [26].

[2]Note that in this approximation the flux associated with Eq. (23) is zero, and hence f does not vary with time.

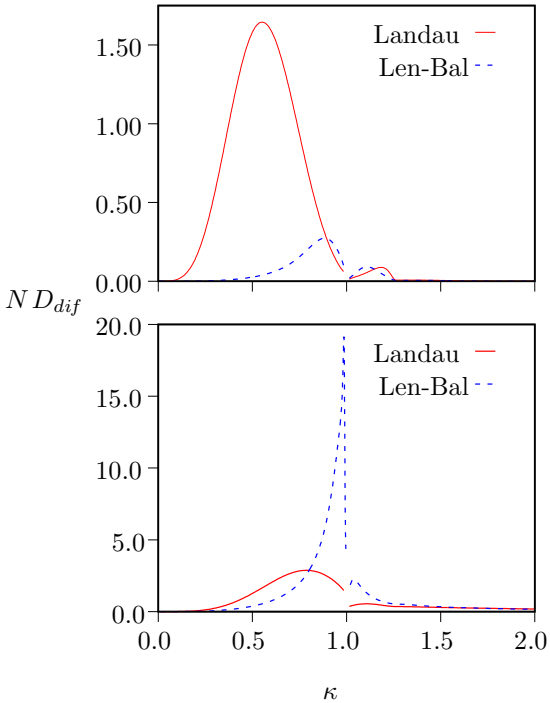

FIG. 6. Diffusion coefficient $D_{\rm dif}(\kappa)$ for two different equilibrium configurations: $(u,M_0) = (-0.1,0.7285)$ (top) and $(u,M_0) = (0.2475,0.0632)$ (bottom). Solid (red) lines show the diffusion coefficient with collective effects, Eqs. (49) and (51), while the dashed (blue) lines show the result without collective effects, Eqs. (49) and (52). Both curves are cut off near $\kappa = 1$ due to numerical instability at the separatrix.

1. Without collective effects

When collective effects are neglected, $\epsilon_{cc} = 1$ and $\epsilon_{ss} = 1$, a very good approximation is given by taking only the first term of Eqs. (49) and (50) (taking higher terms is straightforward). We obtain therefore

$$D_{\rm dif}(\kappa) = \frac{4\pi^8\kappa^2(1-\kappa^2)\mathrm{sech}^4\left[\frac{\pi K(\sqrt{1-\kappa^2})}{2K(\kappa)}\right]}{NK(\kappa)^5[(\kappa^2-1)K(\kappa)+E(\kappa)]}f(\kappa), \tag{61a}$$

$$D_{\rm pol}(\kappa) = \frac{\pi^9\kappa(\kappa^2-1)\mathrm{sech}^4\left[\frac{\pi K(\sqrt{1-\kappa^2})}{2K(\kappa)}\right]}{2N\sqrt{M_0}K(\kappa)^6[(\kappa^2-1)K(\kappa)+E(\kappa)]}\frac{\partial f}{\partial\kappa}(\kappa). \tag{61b}$$

If M_0 is very close to 1, then most of the particles have small κ. It is possible to expand Eq. (61) around $\kappa = 0$, giving the following simple results:

$$D_{\rm dif}(\kappa) = \frac{1}{N}[32\pi^2\kappa^4 + \mathcal{O}(\kappa^6)]f(\kappa), \tag{62a}$$

$$D_{\rm pol}(\kappa) = \frac{1}{N\sqrt{M_0}}[8\pi^2\kappa^3 + \mathcal{O}(\kappa^5)]\frac{\partial f}{\partial\kappa}(\kappa). \tag{62b}$$

2. With collective effects

We will first consider the core-halo distribution. It can be modeled by the sum of two step functions,

$$f_{\rm ch}(\kappa) = \eta_1\Theta[\mu_1 - h] + \eta_2\Theta[\mu_2 - h], \tag{63}$$

where we have assumed that μ_1 and μ_2 corresponds to the energy of particles which are inside the separatrix. Using the definition of $h = M_0(2\kappa^2 - 1)$, we can express Eq. (63) as a function of κ

$$f_{\rm ch}(\kappa) = \eta_1\Theta\big[2M_0\big(\kappa_1^2-\kappa^2\big)\big] + \eta_2\Theta\big[2M_0\big(\kappa_2^2-\kappa^2\big)\big], \tag{64}$$

where $\kappa_i = \sqrt{\mu_i/M_0 + 1}$ and $\kappa_1 < 1$ and $\kappa_2 < 1$.

Computing the dielectric tensor is straightforward because the derivative of $f_{\rm ch}$ about κ involves Dirac δ functions:

$$\frac{\partial f_{\rm ch}}{\partial\kappa} = -2\kappa M_0\big\{\eta_1\delta\big[M_0\big(\kappa_1^2-\kappa^2\big)\big] + \eta_2\delta\big[M_0\big(\kappa_2^2-\kappa^2\big)\big]\big\}. \tag{65}$$

The dielectric tensor is purely real, and it can be calculated inserting Eq. (64) into Eqs. (53) and (54):

$$\epsilon_{cc/ss}(\omega) = 1 + 2\pi\sum_{\ell=-\infty}^{\infty}\left\{\frac{g_\ell^{cc/ss}(\kappa_1)}{\Omega(\kappa_1)-\omega/\ell} + \frac{g_\ell^{cc/ss}(\kappa_2)}{\Omega(\kappa_2)-\omega/\ell}\right\} + (\omega\to-\omega), \tag{66}$$

where $(\omega \to -\omega)$ means to sum the same expression with ω replaced by $-\omega$. Using Eqs. (49) and (50) with Eq. (64) and $\kappa^* = \kappa$, it is straightforward to compute the diffusion coefficients.

It is interesting to compare the diffusion coefficients for an idealized core-halo distribution (64) with a more realistic, smoother version of it, which is the kind of distribution we simulated (see Sec. IV):

$$f_{\mathrm{ch}_i^*}(h) = \frac{\eta_1}{1+\exp[\beta_1(h-\mu_1)]} + \frac{\eta_2}{1+\exp[\beta_2(h-\mu_2)]}. \tag{67}$$

For a given mean energy u and magnetization M_0, plus the normalization constraints, three of the six parameters $\eta_1,\eta_2,\beta_1,\beta_2,\mu_1,\mu_2$ are determined. We have chosen the coefficients $\eta_1 = 0.298$, $\eta_2 = 0.05$, $\mu_1 = -0.517$, and $\mu_2 = 0.19$ for $i = 1,2$; $\beta_1 = 70$ and $\beta_2 = 70$ for $i = 1$; and $\beta_1 = 30$ and $\beta_2 = 10$ for $i = 2$. As the coefficients β_i increase, the step functions become steeper. We observe in the top row of Fig. 7 that for the steeper case ch_1^* the two-step core-halo (64) describes very well both the components of the dielectric tensor and the diffusion coefficient. For the softer case ch_2^*, we observe a correct agreement for the components of the dielectric tensor for most of the frequencies. The disagreement is responsible for the differences observed in the diffusion coefficient for some ranges of κ.

For the case of distributions like the Maxwell-Boltzmann one, the main difficulty consists of computing the dielectric tensor. It is possible to do it analytically for a wide class of functions taking the advantage that if $M_0 \to 1$, most of the particles have small κ. We can thus expand in Taylor series the different quantities which appear in the kinetic equations. We

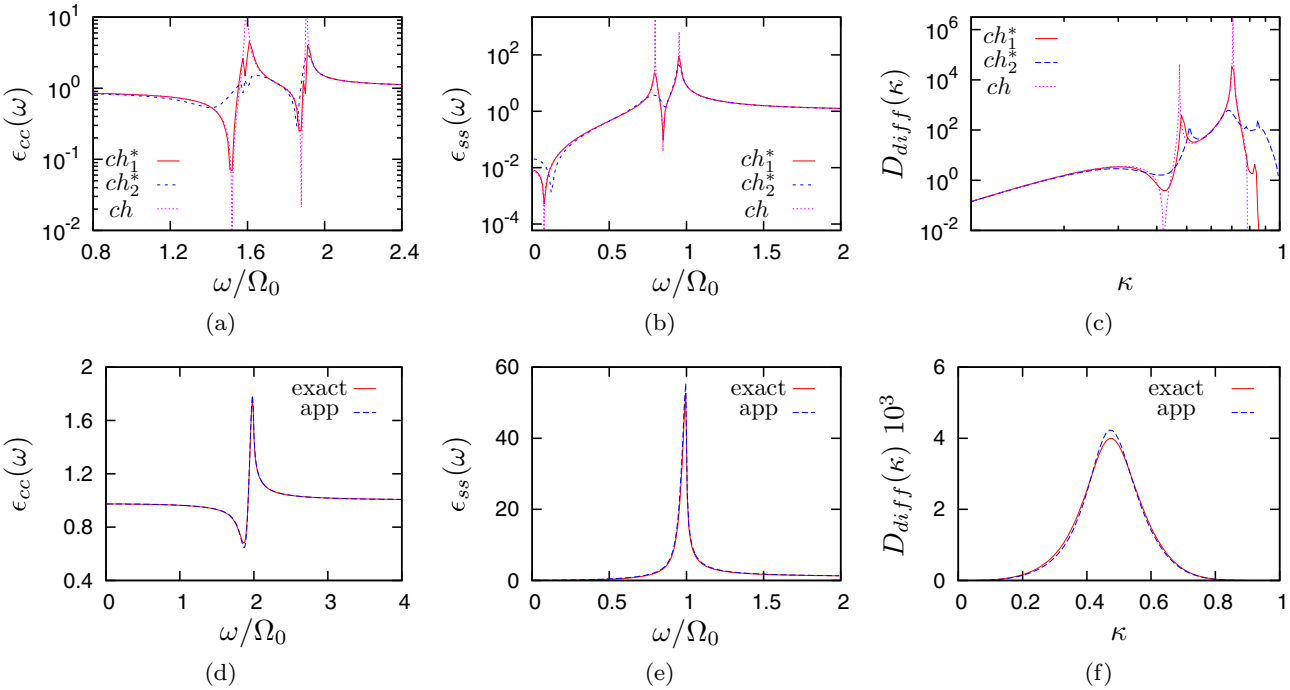

FIG. 7. [(a)–(c)] Comparison of the approximate expressions (C1) and (C2) and the diffusion coefficient for a core-halo system (see text for details), and [(d)–(f)] the same quantities at Maxwell-Boltzmann equilibrium for magnetization $M_0 = 0.95$.

need therefore (valid for $\kappa \leqslant 1$):

$$J(\kappa) = 2\sqrt{M_0}\kappa^2 + \mathcal{O}(\kappa^4), \tag{68a}$$

$$\Omega(\kappa) = \sqrt{M_0}\left[1 - \frac{\kappa^2}{4} + \mathcal{O}(\kappa^4)\right], \tag{68b}$$

$$c_2(\kappa) = \frac{\kappa^2}{2} + \mathcal{O}(\kappa^4), \tag{68c}$$

$$s_1(\kappa) = -i\kappa + \mathcal{O}(\kappa^3). \tag{68d}$$

The components of the dielectric tensor can be approximated as

$$\epsilon_{cc}(\omega) \simeq 1 + \frac{\pi}{2}\int_0^1 d\kappa \frac{\kappa^4 \partial f_{MB}/\partial\kappa}{\sqrt{M_0}\left(1 - \frac{\kappa^2}{4}\right) - \omega/2} + (\omega \to -\omega), \tag{69a}$$

$$\epsilon_{ss}(\omega) \simeq 1 + 2\pi\int_0^1 d\kappa \frac{\kappa^2 \partial f_{MB}/\partial\kappa}{\sqrt{M_0}\left(1 - \frac{\kappa^2}{4}\right) - \omega} + (\omega \to -\omega). \tag{69b}$$

Taking as the distribution function the thermal equilibrium one (59), the integrals can be expressed in terms of trigonometric and exponential integrals (for the explicit expressions, see Appendix C). Using the approximations (C1) and (C2) and the terms of Eqs. (49) and (50) corresponding to n and n' taking the values from -2 to $+2$ we get, for large M_0, a lengthy but analytical approximation (which we do not explicitly write here) of the diffusion coefficients which is very accurate for M_0 close to 1. In the bottom row of Fig. 7 we show the diffusion coefficients for $M_0 = 0.95$.

IV. COMPARISON WITH SIMULATIONS

The previous subsection presents the application of the kinetic equations to the HMF model. In order to compare those analytical results with the Hamiltonian dynamics of the N-body system, we use molecular dynamics, integrating the equations of motion of N particles and tracking their orbits through time.

In order to compare the theoretical results with simulation we adopt the point of view of the Fokker-Planck equation. The idea is to study a test particle evolving in a field composed of the other particles. The effect of the field on the test particle is taken into account by the diffusion and friction coefficients. The mean-field properties of the field evolve adiabatically compared to the time scale of the fluctuations which lead to the test particle's relaxation. In the case of the HMF model, this means that the field's magnetization is $M = M_0 + \delta M$, where M_0 evolves very slowly compared to δM. The test particle's base orbit is thus determined by M_0, whereas the fluctuations δM drive its relaxation. The collective effects represent the reaction of the field to its own perturbations, that is, the field particles are also affected by δM. If we disregard collective effects, the field particles should evolve subject only to the mean magnetization M_0. Therefore, a possible way of testing the importance of collective effects in the HMF model is to simulate two types of N-body dynamics.

The first, which we will refer to as "MD(bath)," is a dynamics *without* collective effects. The system is composed of N_b particles which form a thermal bath and evolve with the adiabatic, static magnetization M_0 (corresponding to the smooth potential),

$$\ddot{\theta}_i^{\,b} = -M_0 \sin\theta_i, \quad i = 1, \ldots, N_b \tag{70}$$

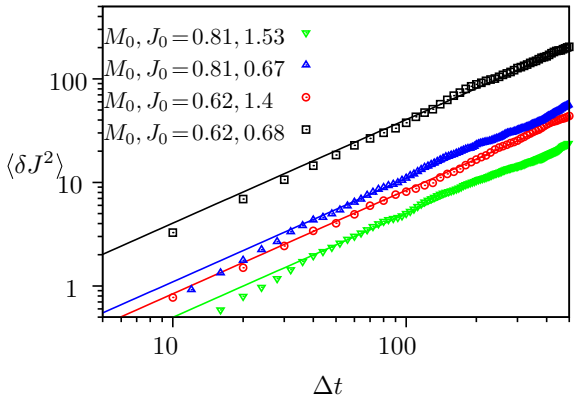

FIG. 8. Variation of J^2, Eq. (75), as a function of time for different values of J_0 and different thermal distributions. Points are molecular dynamics results of the regular HMF model and lines are linear fits. For longer times, the diffusion becomes sublinear.

and N_{tp} independent test particles which evolve under the potential due to the oscillating magnetization of the bath particles,

$$\ddot{\theta}_i^{tp} = -M_x^b \sin\theta_i + M_y^b \cos\theta_i, \quad i = N_b + 1, \ldots, N_b + N_{tp}$$
$$M_x^b = \frac{1}{N_b}\sum_{i=1}^{N_b} \cos\theta_i, \quad M_y^b = \frac{1}{N_b}\sum_{i=1}^{N_b} \sin\theta_i. \tag{71}$$

The bath particles are set up with any initial positions and velocities corresponding to the Vlasov-stable distribution for which we want to measure the diffusion coefficients, e.g., (59) or (67). We detail the procedure for the former case: The initial particle positions and velocities must be distributed according to

$$f_{\rm eq}(\theta, p) = \sqrt{\frac{\beta}{(2\pi)^3}}\, I_0^{-1}(\beta M_0) \exp\left[-\beta\left(\frac{p^2}{2} - M_0 \cos\theta\right)\right]. \tag{72}$$

For each M_0, β must be determined self-consistently by

$$M_0 = \frac{I_1(\beta M_0)}{I_0(\beta M_0)}. \tag{73}$$

Second, we simulate the full N-body simulation of the HMF model—hence *with* collective effects—which we shall refer to as "MD(full)." All N particles in the system evolve according to

$$\ddot{\theta}_i = -M_x \sin\theta_i + M_y \cos\theta_i, \quad i = 1, \ldots, N$$
$$M_x = \frac{1}{N}\sum_{i=1}^{N} \cos\theta_i, \quad M_y = \frac{1}{N}\sum_{i=1}^{N} \sin\theta_i. \tag{74}$$

We have seen from the analytical calculations that collective effects are important in the HMF model. Therefore, these two N-body methods should result in very different diffusion coefficients. We measure the diffusion coefficients of test particles as follows: First, we calculate the initial action $J_i(t_0)$ of each test particle—or simply each particle, in the case of MD(full)—and separate them accordingly into L bins of size ΔJ_0. Then we calculate the mean-square variation of J for each J_0 as a function of Δt,

$$\langle \delta J^2 \rangle_\ell = \frac{1}{N_\ell}\sum_{i=1}^{N_\ell} [J_i(t_0 + \Delta t) - J_0]^2, \quad \ell = 1, \ldots, L \tag{75}$$

where the sum, for each bin ℓ, is over all N_ℓ particles with $J(t_0) \in [(\ell - 1/2)\Delta J_0, (\ell + 1/2)\Delta J_0)$. The diffusion

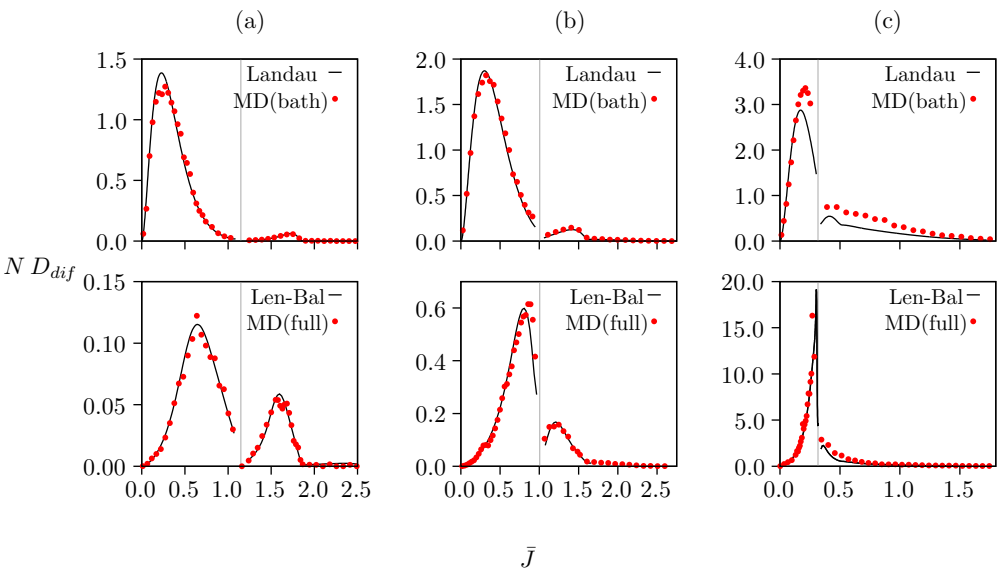

FIG. 9. Diffusion coefficients calculated by molecular dynamics, Eq. (76), compared to the theoretical results, for an equilibrium distribution with parameters (a) $(u, M_0) = (-0.2, 0.816)$, (b) $(u, M_0) = (0.0, 0.622)$, and (c) $(u, M_0) = (0.2475, 0.06)$. On the bottom, MD simulations without collective effects with the prediction of the Landau equation (49). On the top, MD simulations with collective effects with the theoretical curve predicted by the Lenard-Balescu (Len-Bal) equation, using condition (34), and the molecular dynamics given by the regular HMF model, MD(full). The gray vertical line represents the separatrix.

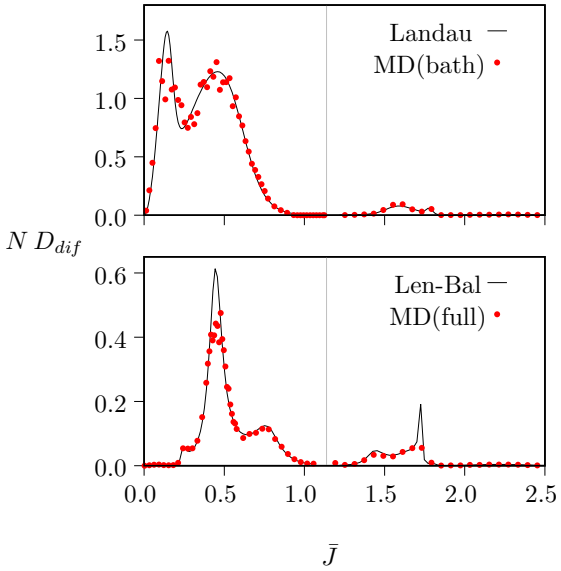

FIG. 10. Diffusion coefficients for a system in a "core-halo" type distribution, given by Eq. (67). On the top, without collective effects: simulation of test particles interacting with the distribution [MD(bath)] and the theoretical curve (Landau). The gray vertical line represents the separatrix. On the bottom, MD simulation results of the regular HMF [MD(full)] with the theoretical curve with collective effects (Len-Bal). The parameters for the distribution are $\beta_1 = 30$, $\beta_2 = 10$, $\eta_1 = 0.298$, $\eta_2 = 0.051$, $\mu_1 = -0.517$, and $\mu_2 = 0.19$, which gives $M_0 = 0.8$.

coefficient for a given J_0 (or, equivalently, for a given bin ℓ), is half of the slope of the linear part of the curve $\langle \delta J^2(\Delta t)\rangle_\ell$,

$$D_{\rm dif}^{\rm MD}(J_0) = \frac{\langle \delta J^2\rangle_\ell}{2\Delta t}. \tag{76}$$

For some values of J_0, care must be taken to calculate the coefficient in the full HMF molecular dynamics: If the magnetization is sufficiently high, then there are little to no particles for higher values of J_0. Therefore, to calculate the coefficient in these regions, we simulate the dynamics of test particles with high J_0 that interact with the full HMF.

Examples of the linear fit are shown in Fig. 8, for two values of J_0. Typically, the fit is done over a time range of $t \in [100,500]$, although this may vary depending on the value of J_0 and M_0. On average, choosing different time ranges does not greatly affect the outcome. For the fits, we took averages of $\langle \delta J^2(\Delta t)\rangle_\ell$ over many time intervals of the dynamics, that is, for many values of t_0. Typically, we used 100 intervals.

In Fig. 9, we compare the molecular dynamics results with the kinetic theory diffusion coefficients for systems in thermal baths.[3]

The top panels show the case without collective effects [MD(bath)] and the Landau diffusion coefficient calculated with (49) and (34), while the bottom panels show the case with collective effects [MD(full)] and the Lenard-Balescu diffusion coefficient (49). Each kind of simulation has been performed with $N = 500\,000$ particles, except for the lowest magnetization case, which was performed with $N = 1\,000\,000$. We see that for magnetizations not close to zero [Figs. 9(a) and 9(b)] the MD fit matches very well the result from the corresponding kinetic equation. In the case of magnetization close to zero [Fig. 9(c)] the match is only reasonably good. This can be explained because in this case the linear diffusion regime is very short and, consequently, the fluctuations larger.

We test also the theoretical results for a core-halo distribution ch_2^* equation (67). For both without collective effects (top) and with collective effects (bottom), the results match very well, see Fig. 10.

V. CONCLUSION

In this paper we have studied the diffusion coefficients corresponding the collisional relaxation in the inhomogeneous HMF model. To perform these calculations we have used the Landau and the Lenard-Balescu equations expressed in action-angle variables. We have described precisely how to perform the calculations and showed that the diffusion coefficients can be easily computed in a very reduced computer time with high precision. Moreover, we have given analytical expressions for the dielectric tensor and the diffusion coefficients for systems with magnetization close to 1, which agree very well with the exact ones.

One of the conclusions of the paper is that, for the cases for which we have calculated the diffusion coefficients, collective effects are very important in the dynamics independently of how much the system is clustered (i.e., magnetized). We note that this is also the case in the homogeneous case [15].

We have also studied which particles "talk to each other" in the collisional relaxation process. For highly clustered systems (i.e., magnetization close to one), the contribution of the relaxation of a given particle comes almost exclusively from particles in the same orbit (i.e., with the same κ). This is a similar behavior than in the homogeneous case, for which it is simple to show that for any long-range one-dimensional system the contribution for the relaxation comes from particles with the same velocity [17]. As the system becomes less clustered, the situation becomes more complicated, and particles in different orbits start to "interact" with one another (see Fig. 4).

In order to test the theoretical predictions, we have computed numerically the diffusion coefficients using molecular dynamics simulations. To check our calculations when the collective effects are neglected, we have set up a simple method to perform simulations in which collective effects are absent. We have found a very good agreement between the theoretical calculations and the simulations both for the dynamics with and without collective effects. We have performed these tests for baths at Maxwell-Boltzmann equilibrium as well as out of equilibrium (core-halo distributions).

The next natural step of this work is to use the diffusion coefficients to compute the whole evolution of the HMF model up to thermalization. With the methods developed in the paper, it is a relatively simple task to compute the evolution with the

[3]For clarity, in the plots of the diffusion coefficients in which the abscissa is the action, we use instead a rescaled action $\bar{J}$,

$$\bar{J} = \begin{cases} J/2 & \kappa < 1 \\ J & \kappa > 1 \end{cases}.$$

Landau or the Lenard-Balescu equation. The magnetization should be computed self-consistently at each time step and then the diffusion coefficient. We stress that the evolution of Eq. (47) could present interesting features because it is nonlinear. This subject will be presented in a forthcoming paper.

We note also that the analytical expressions for the dielectric tensor can be used to study analytically the stability and the mean-field evolution of the HMF model for highly clustered states, computing in an appropriate but straightforward way the pole contributions to the dielectric tensor (see Ref. [22] for a detailed study on the subject).

The extension of our calculations to more complicated interactions, e.g., one-dimensional gravity, is in principle feasible. There are, however, two complications to the calculations compared to the HMF model: first, the biorthogonal basis is not constituted by only two functions but by a infinite number of them. There is, however, the hope that with a suitable choice of family of functions for a given shape of the QSS a reduced number of elements of the basis is sufficient to obtain a good accuracy in the calculations, similarly to the case studied in Refs. [27,28]. Second, we do not expect to have an analytical expression for the Fourier transform of the angle of the element of the basis [Eq. (44)]. These calculations should be performed numerically, which is feasible with a modest computer.

ACKNOWLEDGMENTS

The authors warmly thank J. Barré, D. Chiron, T. M. R. Filho, J. B. Fouvry, A. Galligo, D. Métivier, and T. N. Teles for interesting discussions. This work was partially funded by the Brazilian agencies Conselho Nacional de Desenvolvimento Científico e Tecnológico (CNPq) and Coordenação de Aperfeiçoamento de Pessoa de Nível Superior (CAPES). This work was granted access to the HPC and visualization resources of the Centre de Calcul Interactif hosted by Université Nice Sophia Antipolis, the Mesocentre SIGAMM machine hosted by the Observatoire de la Côte d'Azur, and the Center of Computational Physics CFCIF of the Universidade Federal do Rio Grande do Sul.

APPENDIX A: ACTION-ANGLE VARIABLES OF THE PENDULA

In this Appendix, we present action-angle variables for a pendulum with the Hamiltonian

$$h(\theta,p) = \frac{p^2}{2} - M_0\cos\theta, \tag{A1}$$

using the same conventions as Refs. [22] and [29]. The action J is given by

$$J = \frac{1}{2\pi}\oint p\,d\theta. \tag{A2}$$

If the energy h is greater than the magnetization M_0, then the orbit is rotating: Its momentum will never reach zero. In such cases, the integration over θ will only go from $-\pi$ to π, for positive momentum, or π to $-\pi$, for negative momentum. For librating orbits, which have energy h less than the magnetization M_0, the orbit completes a loop in phase space (see Fig. 1 in the main text), reaching zero momentum at the extreme value of θ, $\pm\theta_m$. The integration starts with positive momentum at $-\theta_m$ and then goes to θ_m and then back to $-\theta_m$ with negative momentum. The action is thus given by

$$J = \frac{1}{2\pi}\begin{cases} 2\int_{-\theta_m}^{\theta_m}\sqrt{2(h+M_0\cos\theta)}d\theta & h < M_0, \\ \int_{-\pi}^{\pi}\sqrt{2(h+M_0\cos\theta)}d\theta & h > M_0. \end{cases} \tag{A3}$$

Using the transformation $x = \theta/2$ and $\cos\theta = 1 - 2\sin^2(\theta/2)$, Eq. (A3) can be written as

$$J = \frac{4\sqrt{M_0}}{\pi}\begin{cases} 2\int_0^{\frac{\theta_m}{2}}\sqrt{\kappa^2-\sin^2 x}dx & \kappa < 1, \\ \kappa\int_0^{\frac{\pi}{2}}\sqrt{1-\frac{1}{\kappa^2}\sin^2 x}dx & \kappa > 1, \end{cases} \tag{A4}$$

where

$$\kappa = \sqrt{\frac{h+M_0}{2M_0}} \tag{A5}$$

and $\theta_m = 2\arcsin(\kappa)$. For $\kappa > 1$, the integral in Eq. (A4) is the complete Legendre elliptic integral of the second kind $E(1/\kappa) = E(\pi/2,1/\kappa)$, where

$$E(\phi,k) = \int_0^{\phi}\sqrt{1-k^2\sin^2\theta}d\theta, \quad k < 1. \tag{A6}$$

For $\kappa < 1$, switching variables with $\sin\theta = \kappa\sin x$, the corresponding integral in Eq. (A4) becomes

$$\int_0^{\theta_m/2}\sqrt{\kappa^2-\sin^2 x}dx = E(\kappa) - (1-\kappa^2)K(\kappa), \tag{A7}$$

where $K(k)$ is the complete elliptic integral of the first kind,

$$K(k) = \int_0^{\pi/2}\frac{d\theta}{\sqrt{1-k^2\sin^2\theta}}. \tag{A8}$$

Therefore, the action is

$$J = \begin{cases} \frac{8\sqrt{M_0}}{\pi}[E(\kappa)-(1-\kappa^2)K(\kappa)], & \kappa < 1, \\ \frac{4\sqrt{M_0}}{\pi}\kappa E\left(\frac{1}{\kappa}\right), & \kappa > 1. \end{cases} \tag{A9}$$

The angle variables, w, satisfy [20]

$$w = \Omega t, \tag{A10}$$

where $\Omega = \partial h/\partial J$ is the angular frequency and t is the time of the pendulum at position θ,

$$t = \int_0^{\theta}\frac{d\theta'}{\sqrt{2(h+M_0\cos\theta')}}. \tag{A11}$$

Integrating $\int dt = \int d\theta/p(\theta,\kappa)$ gives

$$t(\theta,\kappa) = \frac{1}{\sqrt{M_0}}\begin{cases} F(\phi,\kappa) & \kappa < 1,\ p > 0, \\ 2K(\kappa) - F(\phi,\kappa) & \kappa < 1,\ p < 0, \\ \frac{1}{\kappa}F\left(\frac{\theta}{2},\frac{1}{\kappa}\right) & \kappa > 1,\ p > 0, \\ \frac{1}{\kappa}F\left(\frac{\theta}{2},\frac{1}{\kappa}\right) & \kappa > 1,\ p < 0, \end{cases} \tag{A12}$$

where $\phi = \arcsin(\frac{1}{\kappa}\sin\frac{\theta}{2})$. Multiplying by $\Omega(\kappa)$ as given by Eq. (43), we find the angle variables

$$w = \pi \begin{cases} \frac{F(\phi,\kappa)}{2K(\kappa)} & \kappa < 1,\ p > 0, \\ 1 - \frac{F(\phi,\kappa)}{2K(\kappa)} & \kappa < 1,\ p < 0, \\ \frac{F\left(\frac{\theta}{2},\frac{1}{\kappa}\right)}{K\left(\frac{1}{\kappa}\right)} & \kappa > 1,\ p > 0, \\ \frac{-F\left(\frac{\theta}{2},\frac{1}{\kappa}\right)}{K\left(\frac{1}{\kappa}\right)} & \kappa > 1,\ p < 0. \end{cases} \tag{A13}$$

APPENDIX B: ELLIPTIC IDENTITIES FOR FOURIER TRANSFORMS

In this appendix, we show how to obtain the expressions for the Fourier transforms of the orthogonal components of the potential, proportional to $c_n(\kappa)$ and $s_n(\kappa)$ [Eq. (44)], as obtained in Ref. [29]. First, we must find $\cos[\theta(w,\kappa)]$ and $\sin[\theta(w,\kappa)]$ as functions of w and κ directly. These can be obtained from the angle variable (A13), which depends on θ through incomplete elliptic integrals [22]. For the incomplete elliptic integral of the first kind $F(\alpha,k)$, α can be expressed in terms of the Jacobi elliptic functions $sn(u,k)$, $cn(u,k)$, and $dn(u,k)$. In particular, if $F(\alpha,k) = u$, then $\sin\alpha = sn(u,k)$. Applying to Eq. (A13) gives

$$\cos[\theta(w,\kappa)] = \begin{cases} 1 - 2\kappa^2 sn^2\left[\frac{2K(\kappa)w}{\pi},\kappa\right] & \kappa < 1, \\ 1 - 2sn^2\left[\frac{K(1/\kappa)w}{\pi},1/\kappa\right] & \kappa > 1, \end{cases} \tag{B1}$$

and

$$\sin[\theta(w,\kappa)] = \begin{cases} 2\kappa sn\left[\frac{2K(\kappa)w}{\pi},\kappa\right]dn\left[\frac{2K(\kappa)w}{\pi},\kappa\right] & \kappa < 1, \\ 2sn\left[\frac{K(\frac{1}{\kappa})w}{\pi},\frac{1}{\kappa}\right]cn\left[\frac{K(\frac{1}{\kappa})w}{\pi},\frac{1}{\kappa}\right] & \kappa > 1,\ p > 1, \\ -2sn\left[\frac{K(\frac{1}{\kappa})w}{\pi},\frac{1}{\kappa}\right]cn\left[\frac{K(\frac{1}{\kappa})w}{\pi},\frac{1}{\kappa}\right] & \kappa > 1,\ p < 1, \end{cases} \tag{B2}$$

where the properties $sn^2(u,k) + cn^2(u,k) = 1$ and $dn(u,k) = \sqrt{1 - k^2 sn^2(u,k)}$ were used. Finally, (B1) and (B2) can be expressed in terms of the following expansions involving the elliptic functions [30],

$$sn^2(u,k) = \frac{K(k) - E(k)}{k^2K(k)} - \frac{2\pi^2}{k^2K(k)^2}\sum_{n=1}^{\infty}\frac{nq(k)^n}{1 - q(k)^{2n}}\cos\frac{\pi nu}{K(k)}, \tag{B3}$$

$$sn(u,k)dn(u,k) = \frac{2\pi^2}{kK(k)^2}\sum_{n=1}^{\infty}\frac{\left(n - \frac{1}{2}\right)q(k)^{n-\frac{1}{2}}}{1 + q(k)^{2n-1}} \times \sin\frac{\pi\left(n - \frac{1}{2}\right)u}{K(k)}, \tag{B4}$$

$$sn(u,k)cn(u,k) = \frac{2\pi^2}{k^2K(k)^2}\sum_{n=1}^{\infty}\frac{nq(k)^n}{1 + q(k)^{2n}}\sin\frac{\pi nu}{K(k)}, \tag{B5}$$

where $q(k) = \exp[-(\sqrt{1 - k^2})/K(k)]$.

To find $c_n(\kappa)$ and $s_n(\kappa)$, the above expansions should be applied in the equations for $\cos[\theta(w,\kappa)]$ and $\sin[\theta(w,\kappa)]$. This gives the results of Eqs. (45) and (46).

APPENDIX C: DIELECTRIC TENSOR FOR A MAXWELL-BOLTZMANN DISTRIBUTION FOR $M_0 \to 1$

Taking as the distribution function the thermal equilibrium one (59), the components of the dielectric tensor can be approximated as

$$\begin{aligned} \epsilon_{cc}(\omega) &\simeq 1 + \frac{\pi}{2}\int_0^1 d\kappa\,\frac{\kappa^4\partial f_{MB}/\partial\kappa}{\sqrt{M_0}\left(1 - \frac{\kappa^2}{4}\right) - \omega/2} + (\omega \to -\omega) \\ &= 1 + \frac{16\pi\beta C(\omega - 2\sqrt{M_0})^2\alpha_1[Ei(x_1) - Ei(x_2)]}{\sqrt{M_0}} \\ &\quad + \frac{2\pi C[\alpha_2\sinh(\beta M_0) - \beta M_0\cosh(\beta M_0)]}{\beta M_0^{3/2}} \\ &\quad + i\frac{16\pi^2 bC(w - 2\sqrt{M_0})^2\alpha_1\Theta\left(\sqrt{M_0} - \frac{w}{2}\right)\Theta(\omega)}{\sqrt{M_0}} \\ &\quad + (\omega \to -\omega). \end{aligned} \tag{C1}$$

$$\begin{aligned} \epsilon_{ss}(\omega) &\simeq 1 + 2\pi\int_0^1 d\kappa\,\frac{\partial f/\partial\kappa}{\sqrt{M_0}\left(1 - \frac{\kappa^2}{4}\right) - \omega}\kappa^2 + (\omega \to -\omega) \\ &\simeq 1 + 64\pi\frac{\sinh(bM_0)}{\sqrt{M_0}} \\ &\quad - 64\pi b(\sqrt{M_0} - w)\alpha_3[Ei(x_3) - Ei(x_4)] \\ &\quad + i16\pi^3 bC(\sqrt{M_0} - w)\alpha_3\Theta(\sqrt{M_0} - w)\Theta(\omega) \\ &\quad + (\omega \to -\omega), \end{aligned} \tag{C2}$$

where $\alpha_1 = e^{4\beta\sqrt{M_0}\omega - 7\beta M_0}$, $\alpha_2 = -4\beta\sqrt{M_0}\omega + 9\beta M_0 + 1$, $\alpha_3 = e^{8b\sqrt{M_0}w - 7bM_0}$, $x_1 = 6\beta M_0 - 4\beta\sqrt{M_0}\omega$ $x_2 = 8\beta M_0 - 4\beta\sqrt{M_0}\omega$, $x_3 = 8b(M_0 - \sqrt{M_0}w)$, $x_4 = 6bM_0 - 8b\sqrt{M_0}w$, $\Theta(x)$ is the Heaviside step function and $(\omega \to -\omega)$ to sum to the expressions written the same with ω replaced by $-\omega$.

[1] D. Lynden-Bell, Mon. Not. R. Astron. Soc. **136**, 101 (1967).
[2] S. Chandrasekhar, *Principles of Stellar Dynamics* (University of Chicago Press, Chicago, 1942).
[3] M. Henon, in *Saas-Fee Advanced Course 3: Dynamical Structure and Evolution of Stellar Systems*, edited by G. Contopoulos, M. Henon, and D. Lynden-Bell (Observatoire de Genève, Sauverny, Switzerland, 1973), p. 183.
[4] J. Binney and S. Tremaine, *Galactic Dynamics* (Princeton University Press, Princeton, NJ, 2008).
[5] R. Balescu, *Statistical Mechanics: Matter out of Equilibrium* (Imperial College Press, London, 1997).
[6] H. Kandrup, Astrophys. J. **244**, 316 (1981).
[7] J. F. Luciani and R. Pellat, J. Phys. **48**, 591 (1987).
[8] J. Heyvaerts, Mon. Not. R. Astron. Soc. **407**, 355 (2010).

[9] P.-H. Chavanis, Astron. Astrophys. **556**, A93 (2013).
[10] P.-H. Chavanis, Physica A **391**, 3680 (2012).
[11] P. Valageas, Phys. Rev. E **74**, 016606 (2006).
[12] J. B. Fouvry, C. Pichon, and P. H. Chavanis, Astron. Astrophys. **581**, A139 (2015).
[13] J. B. Fouvry, C. Pichon, J. Magorrian, and P. H. Chavanis, Astron. Astrophys. **584**, A129 (2015).
[14] M. Antoni and S. Ruffo, Phys. Rev. E **52**, 2361 (1995).
[15] F. Bouchet and T. Dauxois, Phys. Rev. E **72**, 045103 (2005).
[16] A. Campa, T. Dauxois, and S. Ruffo, Phys. Rep. **480**, 57 (2009).
[17] P. H. Chavanis, Eur. Phys. J. Plus **127**, 19 (2012).
[18] J. Binney and S. Tremaine, *Galactic Dynamics*, 2nd ed. (Princeton University Press, Princenton, NJ, 2008).
[19] H. Goldstein, *Classical Mechanics* (Pearson Education, London, 2002).
[20] A. Lichtenberg and A. Lieberman, *Regular and Chaotic Dynamics*, Applied Mathematical Sciences (Springer, Berlin, 2010).
[21] A. J. Kalnajs, Astrophys. J. **205**, 745 (1976).
[22] J. Barré, A. Olivetti, and Y. Y. Yamaguchi, J. Stat. Mech. (2010) P08002.
[23] S. Ogawa, Phys. Rev. E **87**, 062107 (2013).
[24] J. R. Cary, D. F. Escande, and J. L. Tennyson, Phys. Rev. A **34**, 4256 (1986).
[25] A. I. Neishtadt, Sov. J. Plasma Phys. (Fiz. Plazmy) **12**, 992 (1986).
[26] Y. Levin, R. Pakter, F. B. Rizzato, T. N. Teles, and F. P. C. Benetti, Phys. Rep. **535**, 1 (2014).
[27] J.-B. Fouvry, C. Pichon, and S. Prunet, Mon. Not. R. Astron. Soc. **449**, 1967 (2015).
[28] J.-B. Fouvry and C. Pichon, Mon. Not. R. Astron. Soc. **449**, 1982 (2015).
[29] J. Barré, D. Métivier, and Y. Y. Yamaguchi, Phys. Rev. E **93**, 042207 (2016).
[30] S. C. Milne, Ramanujan J. **6**, 7 (2002).

Classical Goldstone modes in long-range interacting systems

T. M. Rocha Filho *

Instituto de Física and International Center for Condensed Matter Physics, Universidade de Brasília, Campus Universitário Darcy Ribeiro, Asa Norte, 70919-970-Brasília, Brazil

B. Marcos

Université Côte d'Azur, CNRS, Laboratoire J.-A. Dieudonné, 06109-Nice, France

(Received 6 May 2020; accepted 23 July 2020; published 14 September 2020)

For a classical system with long-range interactions, a soft mode exists whenever a stationary state spontaneously breaks a continuous symmetry of the Hamiltonian. Besides that, if the corresponding coordinate associated to the symmetry breaking is periodic, then the same energy of the different stationary states and finite N thermal fluctuations result in a superdiffusive motion of the center of mass for total zero momentum, that tends to a normal diffusion for very long times. As examples of this, we provide a two-dimensional self-gravitating system, a free electron laser, and the Hamiltonian mean-field (HMF) model. For the latter, a detailed theory for the motion of the center of mass is given. We also discuss how the coupling of the soft mode to the mean-field motion of individual particles may lead to strong chaotic behavior for a finite particle number, as illustrated by the HMF model.

DOI: 10.1103/PhysRevE.102.032122

I. INTRODUCTION

Most of the literature on classical statistical mechanics and thermodynamics deals with systems with short-range interparticle interactions, in the sense that the interaction energy at interfaces is negligible with respect to the energy of the bulk of the system. This ensures that energy, as well as entropy, are additive and extensive, two fundamental properties for the theoretical framework of equilibrium statistical mechanics and thermodynamics [1–3]. Yet many real systems fall outside this scope, such as self-gravitating systems, charged plasmas, wave-plasma interaction, dipolar systems, and two-dimensional turbulence [4–9], where the interaction is long-range, i.e., with an interparticle potential $v(r)$ that decays at large distances as $1/r^{\alpha}$, with $\alpha < d$ and d the spatial dimension. As a consequence, the total energy is no longer additive, which can lead to some interesting phenomena as ensemble-inequivalence, negative specific heat, non-Gaussian stationary states (in the limit of an infinite number of particles), and more importantly for the present work, anomalous diffusion.

Let us consider an N-particle systems with Hamiltonian

$$H = \sum_{i=1}^{N} \frac{\mathbf{p}_i^2}{2m} + \frac{1}{N} \sum_{i<j=1}^{N} v(|\mathbf{r}_i - \mathbf{r}_j|), \tag{1}$$

where $\mathbf{r}_i$ and $\mathbf{p}_i$ are the position and conjugate momentum of the ith particle, respectively. The $1/N$ factor in the potential energy term is a Kac factor [10] introduced for the energy to be extensive quantity (on this point see for instance the discussion in chapter 2 of Ref. [9]). Under suitable conditions, in the $N \to \infty$ limit the dynamics described by the Hamiltonian in Eq. (1) is mathematically equivalent to a mean-field description with the one-particle distribution function satisfying the Vlasov equation [11–13], i.e., all particles are uncorrelated.

If the original Hamiltonian is invariant with respect to translation of one coordinate, and the equilibrium (or stationary) state spontaneously breaks this symmetry, then a soft mode, i.e., a Goldstone mode, exists with zero energy cost to go from one equilibrium state to another [14–16]. Besides, if the coordinate associated to the broken symmetry is periodic, then thermal excitations of this soft mode lead to a diffusion of the center of mass of the equilibrium state, as discussed below. Our aim in the present work is then to show how classical Goldstone modes are realized in long-range interacting systems when a symmetry of the Hamiltonian is broken, either for an equilibrium or a nonequilibrium stationary state, and how, in the case of a cyclic coordinate, thermal fluctuations lead to a superdiffusive, ballistic in an initial regime, motion of the center of mass of the system. This behavior is expected to be ubiquitous for all systems with long-range interactions and periodic coordinates, under the stated conditions. We illustrate this phenomenology for three paradigmatic models with long-range interactions: the Hamiltonian mean-field (HMF) model [9,17], two-dimensional self-gravitating particles [18], and the single-pass free-electron laser [9,19–22]. Due to its inherent simplicity, yet retaining the main characteristics of systems with long-range interactions, the HMF model has been extensively studied in the literature. This simplicity will allow us here to present a more detailed theoretical description of this soft mode and of the superdiffusive motion of the center of mass of the system.

The paper is structured as follows: In Sec. II we explain the physical mechanism for the diffusive motion of the center of mass of a statistical stationary state, the thermal excitation

*marciano@fis.unb.br

of the Goldstone mode, and its relation to the diffusion of individual particles. In Sec. III we illustrate this for the HMF model, for both equilibrium and nonequilibrium states, and present a theoretical approach for determining the properties of the diffusive motion of the center of mass. The enhancement of chaos due to the presence of the soft mode is discussed in Sec. IV and illustrated for the HMF model. In Sec. V we show that the same diffusive motion of the center of mass is observed in two other systems with long-range interactions: a two-dimensional self-gravitating system and a free-electron laser, illustrating the generality of this behavior. We close the paper with some concluding remarks and perspectives in Sec. VI.

II. GOLDSTONE MODES IN CLASSICAL STATISTICAL MECHANICS OF SYSTEMS WITH LONG-RANGE INTERACTIONS

Spontaneous symmetry breaking is one of the landmarks of the developments of theoretical physics in the last half-century, occurring from subatomic up to macroscopic systems [14,15], as exemplified by the Brout-Englert-Higgs phenomenon, superconductivity, soft-mode turbulence, phonons in solids, and plasmons, among others [14,15,23,24]. Although usually first introduced for quantum systems, Goldstone modes can also be defined in a classical context [25,26], provided a few conditions are met. The system must have an infinite number of degrees of freedom, with its dynamics having the property that the space of physical states is divided in disconnected islands stable under time evolution. Here disconnected means that a state from one island cannot be reached from a state of a different island by physically realizable process without external intervention. In Statistical Mechanics, each island corresponds to a given state of thermodynamic equilibrium (which is not unique for a given energy if a symmetry is broken), and all those states that evolve into it. For long-range interacting systems one has to also consider islands associated to stationary states other than the Maxwell-Boltzmann (MB) equilibrium distributions. Indeed, in the thermodynamics limit, there are an infinite number of such non-Gaussian states which never evolve to equilibrium, and as a consequence, each such state is part of a disconnected island, again with all states that evolve towards it, in the same sense as for equilibrium states. A symmetry breaking occurs in a given island when it is unstable by the operation of a symmetry subgroup of the whole symmetry group of the system (the symmetries of the Hamiltonian). The Goldstone theorem for classical systems then states (see Ref. [26] for additional mathematical details) that, for each broken symmetry in a given island, there exists a solution of the dynamics satisfying the free wave equation (Goldstone modes).

For a finite but still a large number of particles N, the islands referred above are no longer, strictly speaking, invariant under the system dynamics. A stationary state for finite N acquires a life-time and is now called a quasistationary state (QSS) and can leave an island by evolving in time into the final MB thermodynamic equilibrium [9,27,28]. Although the invariance of the islands is lost, the timescale, i.e., the relaxation time over which the QSS evolves is typically very large, and one can still consider the free wave solution states as long lived Goldstone modes, that slowly relax to the mode corresponding to the final equilibrium state, as discussed below.

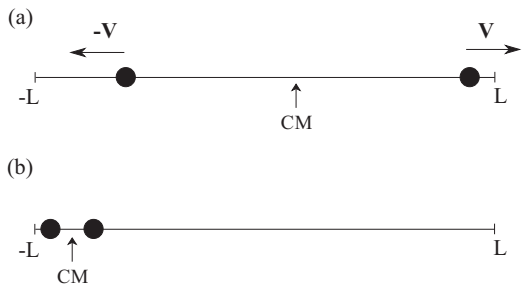

FIG. 1. We consider two particles with a periodic coordinate in the interval $[-L, L)$: (a) In the initial state the total momentum vanishes as both particles have opposite velocities, and the position of the center of mass (CM) is indicated by the vertical arrow. (b) The particles have moved freely, but one of the particles reaches one boundary before the other, and appears at the other side of the periodic one-dimensional space. As a consequence, the center of mass is now at a different position.

Here we are interested in Goldstone modes realized in long-range systems with periodic boundary condition (described using a periodic coordinate). For that purpose, let us suppose that the energy is invariant under translations of a periodic coordinate θ with periodicity 2π, with conjugate momentum p_θ, and that the system is in a (quasi)stationary state or in the true thermodynamic equilibrium. If such a state spontaneously breaks the translation symmetry with respect to θ for a finite number of particles N, then the corresponding Goldstone and thermal fluctuations due to the finite number of particles results in a diffusive motion of the center of mass of the system with vanishing total momentum (see below). This is not a contradictory statement as illustrated by the simple example in Fig. 1. We observe that this is a completely different phenomenon from the nonconservation of angular momentum in simulations with artificial periodic boundary conditions [29]. In the latter case, periodicity is a nonphysical computational artifact to simplify numerical simulations, and has as a side-effect the nonconservation of angular momentum. Here angular momentum is always strictly conserved and the periodic boundary is truly physical.

The equilibrium state (or a quasistationary state) with zero average momentum is represented by the distribution function $f_0(\theta, p)$, considered to be centered initially at $\theta = 0$, with fluctuations described by $\delta f(\theta, p; t)$, that can be considered to be of order $1/\sqrt{N}$ and preserving the total (zero) momentum, i.e.,

$$\int_{-\pi}^{\pi} d\theta \int_{-\infty}^{\infty} dp f_0(\theta, p) = 1, \tag{2}$$

$$\int_{-\pi}^{\pi} d\theta \int_{-\infty}^{\infty} dp\, p\, f_0(\theta, p) = 0, \tag{3}$$

and

$$\int_{-\pi}^{\pi} d\theta \int_{-\infty}^{\infty} dp\, \delta f(\theta, p; t) = \int_{-\pi}^{\pi} d\theta \int_{-\infty}^{\infty} dp\, p\, \delta f(\theta, p; t) = 0, \tag{4}$$

with $f_0 + \delta f \geqslant 0$. As $\theta \in [-\pi, \pi)$ with periodic boundary conditions, we denote the number of particles per unit of time crossing from positive values of θ at the boundary at $\theta = \pi$ as N_+ and the particles crossing by unit of time from negative values of θ at $\theta = -\pi$ as N_-. We then have that

$$N_+ = \int_0^\infty dp[f_0(\pi, p) + \delta f(\pi, p, t)]p, \tag{5}$$

and

$$N_- = -\int_{-\infty}^0 dp[f_0(-\pi, p) + \delta f(-\pi, p, t)]p. \tag{6}$$

The net flux of particles at the boundary $\theta = \pi$ is then given by

$$\Delta N = N_+ - N_- = \int_0^\infty dp[\delta f(\pi, p; t) - \delta f(-\pi, -p; t)]p + \int_{-\infty}^\infty dp f_0(\pi, p)p, \tag{7}$$

where we used explicitly the periodicity in space of $f_0(\theta, p)$. The last term in the right-hand side of Eq. (7) vanishes identically, which is equivalent to say that the net flux of particles at the borders for the unperturbed distribution f_0 is zero. Using the fact that δf must also be periodic in θ, we obtain

$$\Delta N = \int_0^\infty dp[\delta f(\pi, p; t) - \delta f(\pi, -p; t)]p. \tag{8}$$

The important point is that $\delta f(\pi, p; t)$ does not have to be equal to $\delta f(\pi, -p; t)$, but yet complying with a total vanishing momentum. This shows that the periodic boundary conditions together with a nonsymmetric fluctuation with respect to p implies a net movement of the stationary state, which is governed by the nature of finite N fluctuations.

The time derivative of the position of the center of mass $\phi \equiv \langle\theta\rangle$ is then obtained from the considerations in the previous paragraph as

$$\dot{\phi}(t) = -\frac{2\pi}{N}\Delta N = -\frac{2\pi}{N}\int_0^\infty dp[\delta f(\pi, p; t) - \delta f(\pi, -p; t)]p. \tag{9}$$

To show that the motion of the center of mass corresponds to a diffusive process, we write the variance of its position as

$$\sigma_\phi^2(t) = \langle[\phi(t) - \phi(0)]^2\rangle, \tag{10}$$

where

$$\phi(t) = \frac{1}{N}\sum_{i=1}^N \theta_i(t) \tag{11}$$

and $\langle\cdots\rangle$ stands for an average over different realizations for the same (macroscopic) initial state. By choosing the origin such that $\phi(0) = 0$ we have

$$\sigma_\phi^2(t) = \left\langle\left[\frac{1}{N}\sum_{i=1}^N \theta_i(t)\right]^2\right\rangle = \frac{1}{N^2}\left\langle\sum_{i=1}^N \theta_i^2(t)\right\rangle + \frac{1}{N^2}\left\langle\sum_{\substack{i,j=1\\ i\neq j}}^N \theta_i(t)\theta_j(t)\right\rangle. \tag{12}$$

Although the position angles are restricted to the interval $[-\pi, \pi)$, for considering diffusive processes it is useful to consider both the center of mass and particle position to evolve on the whole real axis, and from now, we define ϕ in this way. By folding back to the original interval we recover the motion on the circle. We now note that interparticle correlations for a long-range interacting system with a potential regularized by a Kac factor are of order $1/N$ [12], and therefore $\langle\theta_i\theta_j\rangle = \langle\theta_i\rangle\langle\theta_j\rangle + \mathcal{O}(1/N)$. Since the average of the position of any particle over many realization must vanish by construction, the last term in the right-hand side of Eq. (12) is of order $1/N^3$ and is therefore negligible for large N. From the definition of the variance of the position of the particles in the system,

$$\left\langle\frac{1}{N}\sum_{i=1}^N \theta_i^2\right\rangle = \sigma_\theta^2, \tag{13}$$

we thus have that

$$\sigma_\phi^2(t) = \frac{1}{N}\sigma_\theta^2(t). \tag{14}$$

The particles are initially confined in the interval $-\pi \leqslant \theta < \pi$, and since typically $|\theta|$ gets much greater than π with time, we can write with a minor error that becomes negligible with increasing time that

$$\sigma_\theta^2 \to \frac{1}{N}\sum_{i=1}^N [\theta_i(t) - \theta_i(0)]^2. \tag{15}$$

We conclude that the diffusion of center of mass of the system is due to the diffusion of individual particles viewed as interacting on an infinite space with a periodic interparticle potential. As a consequence, the dynamics of center of mass position can be described by the same type of equations that describe the diffusion in the system. For instance, if a Langevin equation is known for the motion of a single particle, then a corresponding Langevin equation can be written for the center of mass by a simple rescaling by a factor $1/N$. The study of diffusion in position for particles with long-range interactions is not a simple task and was studied in the literature, but a more complete theory is still lacking (see Refs. [30–35] and references therein). However, for the much studied HMF model, a more detailed description of the phenomenon is possible for the initial ballistic diffusion regime, as will be shown in the next section.

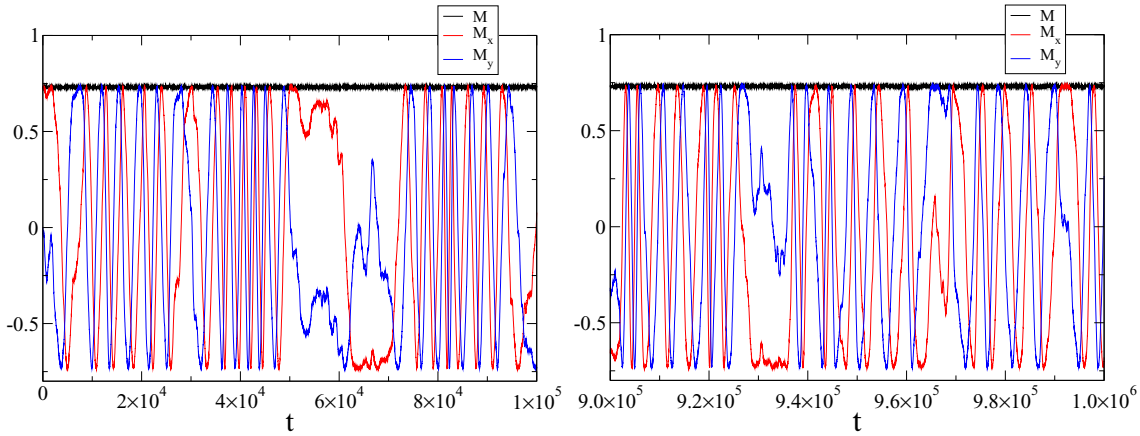

FIG. 2. Total magnetization and component M_x and M_y for the HMF model at thermodynamic equilibrium for two time windows, with energy per particle $e = 0.4$, $N = 10\,000$ particles, time step $\Delta t = 0.5$, and energy relative error of order 10^{-4}.

III. THE HAMILTONIAN MEAN-FIELD MODEL

The HMF model is formed by N particles on a ring globally coupled by a cosine potential and Hamiltonian [9,17]:

$$H = \sum_{i=1}^{N} \frac{p_i^2}{2} + \frac{1}{N} \sum_{i<j=1}^{N} [1 - \cos(\theta_i - \theta_j)]. \tag{16}$$

This model is widely studied in the literature due to its inherent simplicity. Particularly, due to the form of its interparticle potential the numerical effort in molecular dynamics simulations scales linearly with N, instead of N^2, which allows very long simulation times for very large number of particles (see Refs. [4,36] and references therein). The magnetization components for the HMF model are defined by

$$M_x = \frac{1}{N} \sum_{i=1}^{N} \cos(\theta_i), \qquad M_y = \frac{1}{N} \sum_{i=1}^{N} \sin(\theta_i), \tag{17}$$

and the total magnetization by $M = \sqrt{M_x^2 + M_y^2}$. The system is solvable and the one particle equilibrium distribution is given by [17,37]

$$f_{\rm eq}(\theta, p) = \frac{\sqrt{\beta}}{(2\pi)^{3/2} I_0(\beta M)} \times \exp\left\{-\beta\left[\frac{p^2}{2} - M_x \cos(\theta) - M_y \sin(\theta)\right]\right\}, \tag{18}$$

where I_k is the modified Bessel function of the first kind with index k. The magnetization M as a function of the inverse temperature β is obtained from the solution of the equation:

$$M = \frac{I_1(\beta M)}{I_0(\beta M)}. \tag{19}$$

We denote the total energy per particle as $e \equiv H/N$, with H the total Hamiltonian of the system. The system has a second order phase transition from a ferromagnetic phase at lower energies to a homogeneous nonmagnetic phase at higher energies with a critical energy per particle $e = 0.75$. Since only the modulus M is determined for a given temperature, the equilibrium state is infinitely degenerate for $M \neq 0$, and the rotational symmetry of the total Hamiltonian is spontaneously broken.

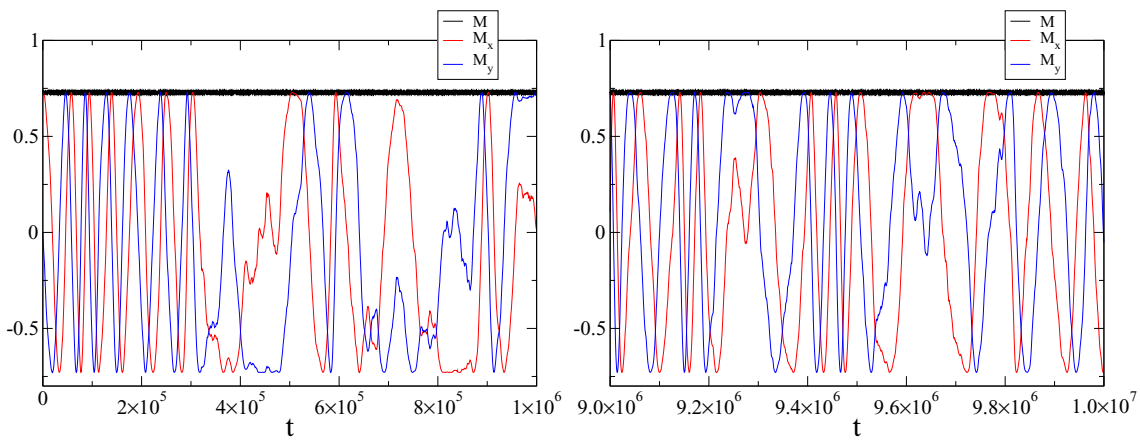

FIG. 3. Same as described in the caption of Fig. 2 but with $N = 1\,000\,000$ particles and energy relative error of order 10^{-5} and final total momentum per particle of order 10^{-7}.

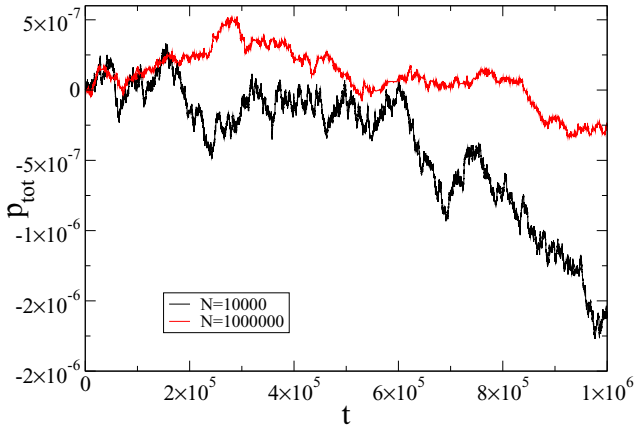

FIG. 4. Total momentum per particle for the simulations described in the captions of Figs. 2 and 3.

As the thermodynamic limit is equivalent to the mean-field description and particles are uncorrelated [11], it is straightforward to show that the time derivatives of M_x and M_y vanish. Nevertheless, for finite N, small correlations are present and result in a slow variation of the magnetization components with time. Figures 2 and 3 show the time evolution of the magnetization components, with a total constant magnetization up to small fluctuations, for an equilibrium magnetized (nonhomogeneous) state for $N = 10\,000$ and $1\,000\,000$, and total energy per particle $e = 0.4$. The total momentum remains zero and constant up to very small numeric errors as shown in Fig. 4. Figure 5 shows the displacement of the angular position of the center of mass, which coincides with the phase of the magnetization given by $M_x + iM_y = M\exp(i\phi)$, for the case in Fig. 2 for $N = 10\,000$, with a typical diffusive random motion behavior. The discrete nature of this motion is evidenced on the right-panel of Fig. 5, as the center of mass jumps by $\pm\pi/N$ for each particle traversing the periodic boundary. Comparing Figs. 4 and 5 it is evident that the motion of the center of mass is orders of magnitude bigger that would be expected from the small errors in the numeric integrator. The oscillations are quasiperiodic with chaotic intermittencies and never damp, as the long time window of the simulation shows clearly. For all times the system is in a degenerate equilibrium state, with a time varying position of its center of mass caused by thermal fluctuations for finite N. This time dependence of the phase of the magnetization was first noted for the HMF model by Ginelli *et al.* in Ref. [38], and also by Manos and Ruffo relating it to the transition from weak to strong chaos for the same model [39]. We will discuss this last point with more details in Sec. IV.

Nonequilibrium states also display the same behavior for finite N as long as the magnetization is not zero. Let us take as initial condition a waterbag state:

$$f(p,\theta) = \begin{cases} 1/(4p_0\theta_0), & \text{if } -p_0 < p < p_0 \\ \quad \text{and} \quad -\theta_0 < \theta < \theta_0, & \\ 0, & \text{otherwise.} \end{cases} \tag{20}$$

Figure 6 shows the dynamical evolution of an initial unstable waterbag state with $M = 0$ ($\theta_0 = \pi$). It goes though an initial violent relaxation and then settles into a magnetized quasistationary state, with a time varying phase of the magnetization similar to the what is observed at thermodynamic equilibrium.

To characterize the diffusive movement of the center of mass of the HMF model we compute the square root displacement $\sigma_\phi(t) = \sqrt{\langle\phi(t)^2\rangle}$, with $\langle\phi(t)\rangle = 0$ [recall that ϕ is defined in the extended space i.e., $\phi \in (-\infty, \infty)$]. Figure 7 shows the results for $e = 0.4$ and $N = 5000$. A power law fit for the initial and final parts of the plot, shows that the motion is initially superdiffusive close to ballistic and tends to normal diffusion asymptotically. The variance of individual particle position $\sigma_\theta^2(t)$ is also shown in the figure rescaled by a factor N, showing a very good agreement with Eq. (14). Figure 8 shows the variance σ_ϕ^2 as a function of time for different values of N and fixed energy (left panel), and different values of the energy per particle e for $N = 5000$. The diffusion is close to ballistic for the time window considered, and tends to disappear for lower energies as the probability of a particle to reach the boundary of the physical space (with respect to the peak of the distribution) goes to zero as $e \to 0$.

The anomalous diffusion of particles in the HMF model and the periodic boundary conditions translate into an anomalous diffusion of the center of mass of the whole system. As commented above, anomalous diffusion in the HMF model

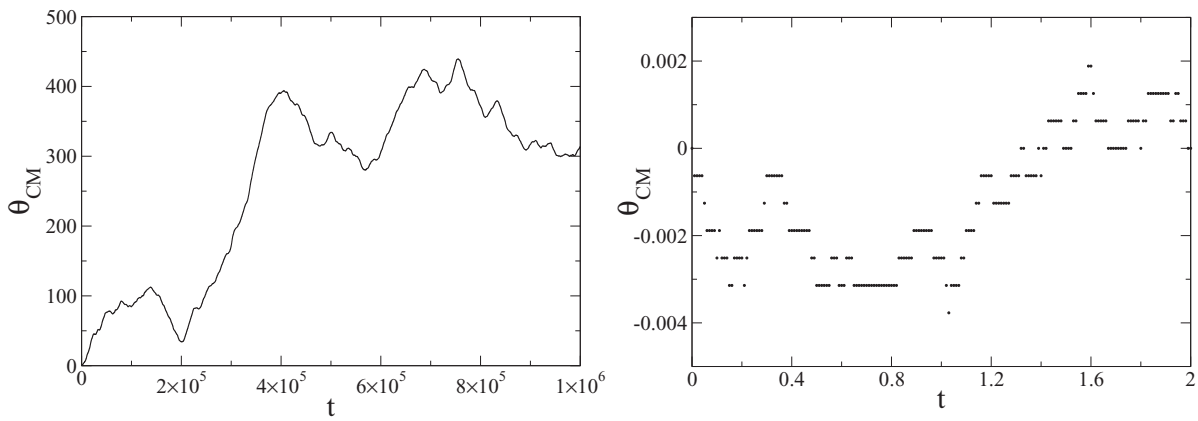

FIG. 5. Left Panel: Center of mass of particles for the same case as in Fig. 2 but with a time step of $\Delta t = 10^{-2}$. Right Panel: Zoom over the initial portion of the graphic in the left panel, showing the discrete nature of the center of mass motion.

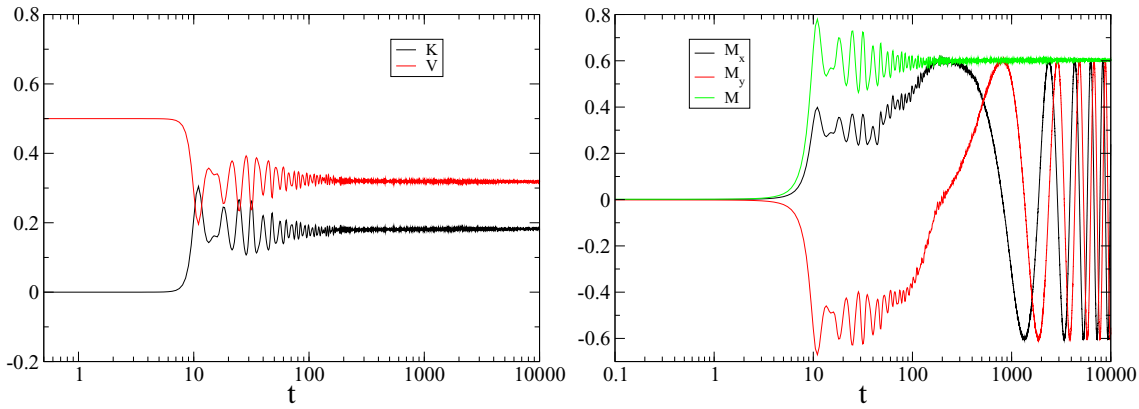

FIG. 6. Left panel: Kinetic (K) and potential (V) energies per particle for an out of equilibrium evolution of waterbag initial state with total energy per particle $e = 0.5$ and initial magnetization $M_0 = 0$ of the HMF model, with $N = 1\,000\,000$. Right panel: total magnetization and its components corresponding to the left panel. The initial violent relaxation is clearly visible, as well as the final oscillatory behavior of the magnetization.

was studied by some authors [30,31,33,40–42], and superdiffusion was shown to be a common feature, even at equilibrium.

A. Dynamics of the center of mass

For the HMF model a complete theoretical characterization of the initial ballistic diffusive motion of the center of mass is possible. We consider here the case of the equilibrium state but the approach can be easily generalized for more general (quasi)stationary states. We first characterize the jumps of the position of the center of mass by showing that is given by the difference of two Poisson processes. Then we discuss how to compute the coefficient of the initial ballistic diffusion and why it tends to normal diffusion due to finite N effects, i.e., collisions or granularity effects.

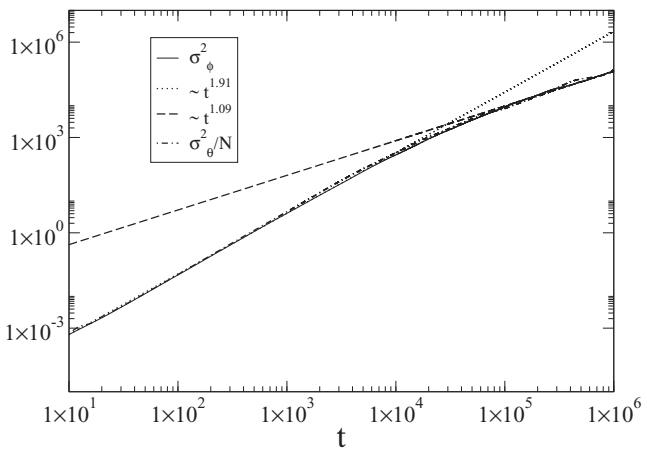

FIG. 7. Variance $\sigma_\phi^2(t)$ for the position of the center of mass at equilibrium for an equilibrium state of the HMF model with $e = 0.4$, $N = 5000$ and 500 realizations. The variance $\sigma_\theta^2(t)$ for the position variables of each individual particle is also shown rescaled by the number of particles N which collapses to the values of $\sigma_\phi^2(t)$, in agreement with Eq. (14).

B. Statistics of the center of mass jumps

Let us consider the equilibrium one-particle distribution function given in Eq. (18), initially centered at $\theta = 0$ ($M_y = 0$ and $M_x = M$). The probability that a given particle crosses at $\theta = \pi$ with $p > 0$ during a small time interval Δt is given by

$$\mathcal{P}_+ = \int_0^\infty dp \int_{\pi - p\Delta t}^{\pi} d\theta\, f_{\rm eq}(\theta, p) = \frac{e^{-\beta M}\Delta t}{(2\pi)^{3/2}\sqrt{\beta} I_0(\beta M)}, \tag{21}$$

and the probability that a given particle traverses at $\theta = -\pi$ with $p < 0$ is

$$\mathcal{P}_- = \int_0^\infty dp \int_{-\pi}^{-\pi + p\Delta t} d\theta\, f_{\rm eq}(\theta, p) = \frac{e^{-\beta M}\Delta t}{(2\pi)^{3/2}\sqrt{\beta} I_0(\beta M)}, \tag{22}$$

which is, obviously, the same as $\mathcal{P}_+$. Thus, the probability that one particle, no matter which, crosses at each one of the boundaries at $\theta = \pm\pi$ is $\mathcal{P} = N\mathcal{P}_+$. Now supposing that for sufficiently small Δt the crossings of particles are independent from each other, the probability that ΔN particles cross at one of the boundaries is given by the Poisson distribution:

$$P(\Delta N) = e^{-\mathcal{P}} \frac{\mathcal{P}^{\Delta N}}{\Delta N!}. \tag{23}$$

The probability for the value of the difference $c = a - b$ of two Poisson distributed random variables a and b, with respective averages $\bar{a}$ and $\bar{b}$, is given by the Skellam distribution [43]:

$$\mathcal{S}(c) = e^{-(\bar{a}+\bar{b})} \left(\frac{\bar{a}}{\bar{b}}\right)^c I_c\left(2\sqrt{\bar{a}\bar{b}}\right), \tag{24}$$

with I_c a modified Bessel function with index c. Now considering that ΔN_+ and ΔN_- particles cross at $\theta = \pi$ and $\theta = -\pi$, respectively, in the time interval Δt, and noting that $\bar{a} = \bar{b} = \mathcal{P}$, the probability that the difference, i.e., the net flux, is $\Delta N = \Delta N_+ - \Delta N_-$ is given by

$$\mathcal{S}(\Delta N) = e^{-2\mathcal{P}} I_{|\Delta N|}(2\mathcal{P}). \tag{25}$$

For a given net flux of particles at the border ΔN, the center of mass moves by $\Delta\phi = -2\pi\,\Delta N/N$. Hence the probability

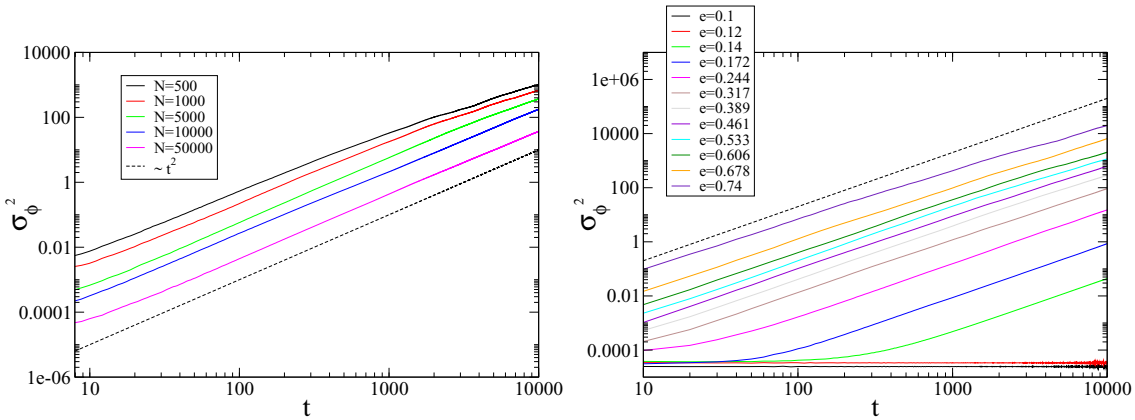

FIG. 8. Left panel: Variance $\sigma_\phi^2(t)$ for the position of the center of mass at equilibrium for an equilibrium state of the HMF model with $e = 0.4$, 100 realizations and a few values of N. The dashed line is proportional to t^2 and is given for comparison purposes. Right panel: Variance $\sigma_\phi^2(t)$ for the equilibrium state for $N = 5000$ and different values of energy per particle. For very low energies there is almost no diffusion, as expected.

that the center of mass moves by $\Delta\phi$ in the same time interval Δt is

$$\mathcal{S}(\Delta\phi) = e^{-2\mathcal{P}} I_{|N\Delta\phi/2\pi|}(2\mathcal{P}). \tag{26}$$

Since the possible values of $\Delta\phi$ are discrete there is no extra multiplication factor resulting from going from Eq. (25) to Eq. (26). Figure 9 shows the frequencies (histograms) of $\Delta\phi$ obtained from a very long run and the theoretical distribution in Eq. (26) with a very good agreement. For ΔN large, the Skellam distribution tends to a Gaussian distribution of the form [43]

$$\mathcal{S}(\Delta\phi) \to \frac{N}{2\pi^{3/2}\sqrt{\mathcal{P}}} \exp\left(-\frac{N^2\Delta\phi^2}{4\pi^2\mathcal{P}}\right). \tag{27}$$

We will see in the next sections that the statistics of the jumps is *not* sufficient to fully characterize the diffusion process. Time-correlation in the jumps are very important, as we will detail below.

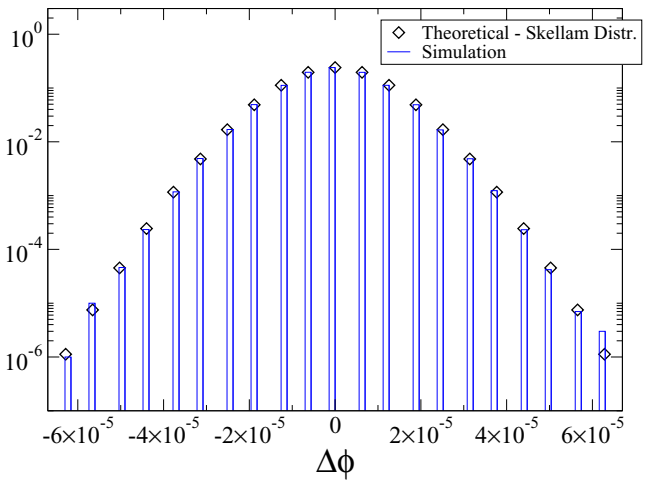

FIG. 9. Normalized histograms (vertical bars) from a numeric simulation for the frequency of increments $\Delta\phi$ of the center of mass position recorded after each time step $\Delta t = 0.01$, total simulation time $t_f = 10^5$, energy $e = 0.4$ and $N = 1000\,000$ compared to the distribution in Eq. (26) (diamonds).

C. The variance of the position of the center of mass ϕ

The variance of the position of the center of mass of the system is written as

$$\begin{aligned}\sigma_\phi^2(t) = \langle[\phi(t)]^2\rangle &= \left\langle \frac{1}{N}\sum_{i=1}^{N}\theta_i(t) \times \frac{1}{N}\sum_{i=j}^{N}\theta_j(t)\right\rangle \\ &= \frac{1}{N^2}\sum_{i,j=1}^{N}\left\langle \int_0^t \mathrm{d}t' p_i(t') \int_0^t \mathrm{d}t'' p_j(t'')\right\rangle \\ &= \frac{t}{N}\int_0^t \mathrm{d}\tau\, \mathcal{C}_p(\tau),\end{aligned} \tag{28}$$

where we used the property $\mathcal{C}_p \equiv \langle p(0)p(\tau)\rangle = \langle p(t)p(t+\tau)\rangle$, valid for a stationary state. In function of the convergence properties of $\mathcal{C}_p$ in Eq. (28), the center of mass ϕ will experiment ballistic or normal diffusion.

D. Ballistic diffusion

Long-term memory of the initial condition is a characteristic property of systems with long-range interactions, and one consequence is anomalous diffusion [44]. The ballistic initial diffusion of the center of mass can be explained by the fact that, for a mean-field system, the momentum autocorrelation function tends to zero after a collisional characteristic time τ_{coll}, which is the time interval collisional effects destroy the memory of the initial state. It is well known that in spatially inhomogeneous configurations of the HMF system, τ_{coll} scales linearly with N [27,28,45]. In particular, in the limit $N \to \infty$, the momentum autocorrelation never vanishes.

In a stationary state in the thermodynamic limit the motion of a particle obeys the equations of a pendulum,

$$\dot{\theta} = p, \quad \dot{p} = -M\sin(\theta), \tag{29}$$

with known closed form solution in terms of an elliptic function for initial conditions $\theta(0) = \theta_0$ and $p(0) = p_0$, and

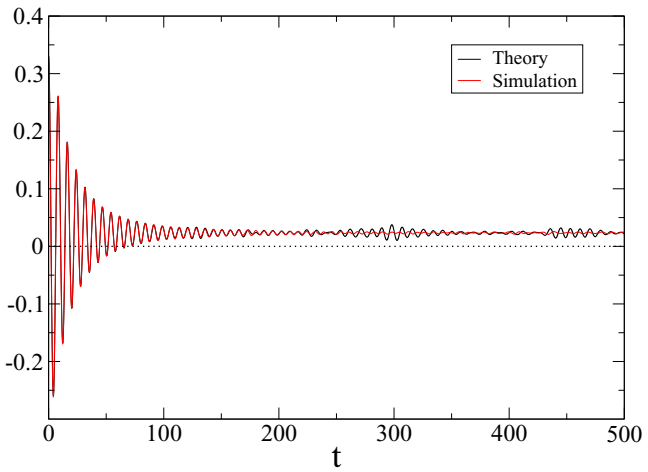

FIG. 10. Momentum autocorrelation function $\mathcal{C}_p(t)$ obtained from Eq. (30) and from a numeric simulation for $e = 0.4$ and $N = 1\,000\,000$. The dotted line was introduced for reference. We see that $\mathcal{C}_p(t)$ tends asymptotically to a nonvanishing value.

therefore the autocorrelation function $\mathcal{C}_p$ for this stationary state can be determined exactly (up to two integrations) as

$$\mathcal{C}_p(\tau) = \int_{-\infty}^{\infty} dp_0 \int_{-\pi}^{\pi} d\theta_0\, f_{\rm st}(\theta_0, p_0)\, p_0\, p(\tau), \tag{30}$$

which is valid for time $t \ll \tau_{\rm coll}$ and where $f_{\rm st}$ denotes the one-particle distribution function for the stationary state. For the equilibrium state $f_{\rm st}$ is given by Eq. (18) and and $p(t)$ is the solution of the equation

$$Q[p(t)] - Q(p_0) = t, \tag{31}$$

with

$$Q(p) \equiv \pm\sqrt{2}\,\frac{\sin(p/2)}{\sqrt{e-M}}\mathcal{F}\left(\cos(p/2), \sqrt{\frac{2M}{M-e}}\right), \tag{32}$$

where $\mathcal{F}$ is the incomplete elliptic integral of the first kind. The plus and minus sign in the right-hand side of Eq. (32) represent the two different branches of the solution. An easy way to overcome the analytical computation of the resulting cumbersome integral in Eq. (30) is to compute it numerically with any desired accuracy and a small numeric effort. Figure 10 shows the autocorrelation function at equilibrium for $e = 0.4$ obtained from Eq. (30), and the same function obtained from a fully numeric molecular dynamics simulation, with a very good agreement. We see that for $t \ll \tau_{\rm coll}$, or equivalently in the limit $N \to \infty$ for any time, the correlation function takes a nonvanishing value $\tilde{\mathcal{C}}_p$. Using Eq. (28) the variance of position of the center of mass is then

$$\sigma_\phi^2(t) = \frac{t}{N}\int_0^t d\tau\, \tilde{\mathcal{C}}_p = \frac{\tilde{\mathcal{C}}_p}{N}\, t^2 \equiv \sigma_N^2\, t^2. \tag{33}$$

This explains why the diffusion is initially ballistic, or close to ballistic for $t \ll \tau_{\rm coll}$. In Fig. 10, we can see that it is indeed the case. After a transient between $t = 0$ and $t \approx 200$, the momentum autocorrelation function takes a constant value. By replacing $f_{\rm eq}$ in the above expression for any stationary state, all results above remain valid.

The value of the constant σ_N^2 can be obtained explicitly using the fact that the one-particle phase space is divided by a separatrix for points corresponding to a libration (outside the separatrix), and bounded motion (inside the separatrix). The separatrix is defined such that the one-particle energy equals the maximum of the mean-field potential. The particles which contribute to the ballistic diffusion are those which are librating, i.e., outside the separatrix. This is because the positions of the particles which are outside the separatrix can increase indefinitely whereas this is not the case for those which lie inside the separatrix. We can therefore write, after a transient time, the position of the center of mass as

$$\phi \simeq \frac{1}{N}\sum_{i=1}^{N^+} \theta_i^+(t), \tag{34}$$

where θ^+ are the N^+ particles which lie outside the separatrix, and thus

$$\langle\phi^2\rangle \simeq \frac{1}{N}\langle(\theta^+)^2\rangle \simeq \frac{1}{N}\langle(v^+)^2\rangle t^2, \tag{35}$$

where $\langle(v^+)^2\rangle$ is the variance of the velocity of the particles outside the separatrix. We have therefore

$$\sigma_N^2 \simeq \langle(v^+)^2\rangle. \tag{36}$$

Note that, as the system is at equilibrium, the quantity $\langle(v^+)^2\rangle$ does not depend on time. We need first to compute the velocity distribution of the particles with an energy larger than the separatrix, which we will call $P^+(v)$. For a system with an average magnetization M, particles are outside the separatrix if their energy e is larger than the average magnetization, i.e.,

$$e = \frac{v^2}{2} - M\cos\theta \geqslant M, \tag{37}$$

where we have used without loss of generality that $M_y = 0$ and then $M = M_x$. The first step in the calculation is to compute the probability density of $\cos\theta$. Using the equilibrium distribution function in Eq. (18) we get

$$\begin{aligned} P(X = \cos\theta) &= \int_0^{2\pi} d\theta \frac{\exp(\beta M\cos\theta)}{2\pi I_0(\beta M)}\delta(X - \cos\theta) \\ &= \frac{1}{\pi I_0(\beta M)}\frac{\exp(\beta M X)}{\sqrt{1-X^2}}. \end{aligned} \tag{38}$$

We are interested in the probability

$$\begin{aligned} P\left(-1 \leqslant \cos\theta \leqslant \frac{v^2}{2M} - 1\right) &\equiv F(v,\beta) \\ &= \frac{1}{\pi I_0(\beta M)}\int_{-1}^{\frac{v^2}{2M}-1} dX \frac{\exp(\beta M X)}{\sqrt{1-X^2}}. \end{aligned} \tag{39}$$

The integral in this equation cannot be performed analytically.

There are two possible cases according to the velocity of the particles:

(1) If $|v| > 2\sqrt{M}$, then the particle automatically lies outside the separatrix.

(2) If $|v| < 2\sqrt{M}$, then the particle is outside the separatrix only if $\cos\theta < v^2/2M - 1$.

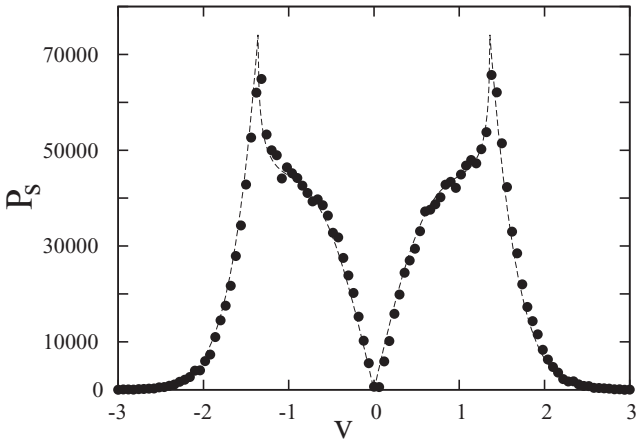

FIG. 11. Comparison of the distribution in Eq. (40) (dashed line) and a numerical realization (circles) with $N = 10^8$ particles and $\beta = 2.26$.

The velocity distribution of the particles outside the separatrix is then

$$P^+(v,\beta)=\begin{cases}\sqrt{\frac{\beta}{2\pi}}\exp(-\beta v^2/2), & \text{if } |v|>2\sqrt{M},\\ \sqrt{\frac{\beta}{2\pi}}\exp(-\beta v^2/2)F(v,\beta), & \text{if } |v|<2\sqrt{M}.\end{cases} \tag{40}$$

The distribution in Eq. (40) is shown in Fig. 11 with a comparison to a numerical realization with $N = 10^6$ particles.

We compute now the variance of the velocity of the particles outside the separatrix:

$$\langle (v^+)^2\rangle = \int_{-\infty}^{\infty} dv\, v^2 P^+(v,\beta). \tag{41}$$

Using Eq. (40), we get to the contribution of the integral for $|v| > 2\sqrt{M}$:

$$2\int_{2\sqrt{M}}^{\infty} dv\, v^2 P^+(v,\beta) = 2\sqrt{\frac{2M}{\pi\beta}} + \mathrm{Erfc}\left(\sqrt{2\beta M}\right). \tag{42}$$

For sufficiently large β (i.e., not too close to the phase transition $\beta = 2$), and using that, for these values of β,

$$M \simeq 1 - \frac{1}{2\beta} + \mathcal{O}(1/\beta^2), \tag{43}$$

this expression can be approximated with

$$2\int_{2\sqrt{M}}^{\infty} dv\, v^2 P^+(v,\beta) = 2\sqrt{\frac{2}{\pi\beta}}e^{1-2\beta+\mathcal{O}(1/\beta)}. \tag{44}$$

To get an analytic approximation of the contribution of integral Eq. (41) for $|v| > 2\sqrt{M}$ it is convenient to invert the order of integration between x and v. We get

$$2\int_0^{2\sqrt{M}} dv\, v^2 P^+(v,\beta) = \frac{1}{\pi I_0(\beta M)}\int_{-1}^{1} dx\, \frac{e^{\beta M x}}{\sqrt{1-x^2}} g(x,\beta), \tag{45}$$

where

$$g(x,\beta) = \frac{\mathrm{Erf}\left(\sqrt{2\beta M}\right) + \mathrm{Erfc}\left(\sqrt{\beta M(x+1)}\right) + \frac{2\left(e^{-\beta M(x+1)}\sqrt{\beta M(x+1)} - \sqrt{2}e^{-2\beta M}\sqrt{\beta M}\right)}{\sqrt{\pi}} - 1}{2\beta}. \tag{46}$$

Since integral Eq. (45) is dominated by the region $x \sim 1$, to get an analytical approximation, it is possible to expand the function $\mathrm{Erfc}[\sqrt{bM(x+1)}]$ in power series around $x = 1$. It is then possible to find an analytical expression for Eq. (45), which is, for sufficiently large β,

$$2\int_0^{2\sqrt{M}} dv\, v^2 P^+(v,\beta) F(v,\beta) = \left[\frac{8}{\pi} - \frac{33}{8\sqrt{2\pi\beta}} + \mathcal{O}\left(\frac{1}{\beta}\right)\right] e^{1-2\beta+\mathcal{O}(1/\beta)}. \tag{47}$$

Combining Eqs. (42) and (47) we obtain that, at leading order,

$$\sigma_N^2 = \frac{\tilde{C}_p}{N} \simeq \frac{8}{\pi}e^{1-2\beta}. \tag{48}$$

A comparison of $\tilde{C}_p$ obtained from Eq. (41) with numeric simulations for different values of β is shown in the left-panel of Fig. 12 with a good very agreement. The spatial distribution function obtained using Eq. (18) is

$$\rho(\theta,t) = \frac{1}{2\pi I_0(\beta M)} e^{\beta M \cos[\theta+\phi(t)]} \tag{49}$$

and is shown on the right-hand panel of the same figure. From Eq. (21) we have that the number of particles that cross at the boundary at $\theta = \pi$ during the time interval Δt is thus given by

$$\mathcal{P}_+ = \frac{\Delta t}{\sqrt{2\pi\beta}}\rho(\pi). \tag{50}$$

We see that σ_N^2 is roughly proportional to $\rho(\pi)$, the value of the spatial density at $\theta = \pi$ for $\phi = 0$. This illustrates the fact that the diffusive ballistic motion is indeed due to an excess of particles crossing at the boundaries into different directions at the boundary of the periodic variable θ.

E. Normal diffusive regime

For finite N, collisional effects destroy the memory of the initial state on a timescale proportional to the order of the strength of the interaction, which for nonhomogeneous states is $1/N$ [27,28,45], causing the autocorrelation function to slowly approach zero, as exemplified in Fig. 13. Consequently the diffusion tends to normal in this same timescale, after which the variance of the center of mass position satisfies $\sigma_\phi(t)^2 = Dt$, with D the (normal) diffusion coefficient. The precise theoretical determination of the crossover time between anomalous and normal diffusion and the value of D is a very difficult task in kinetic theory, and well beyond the scope

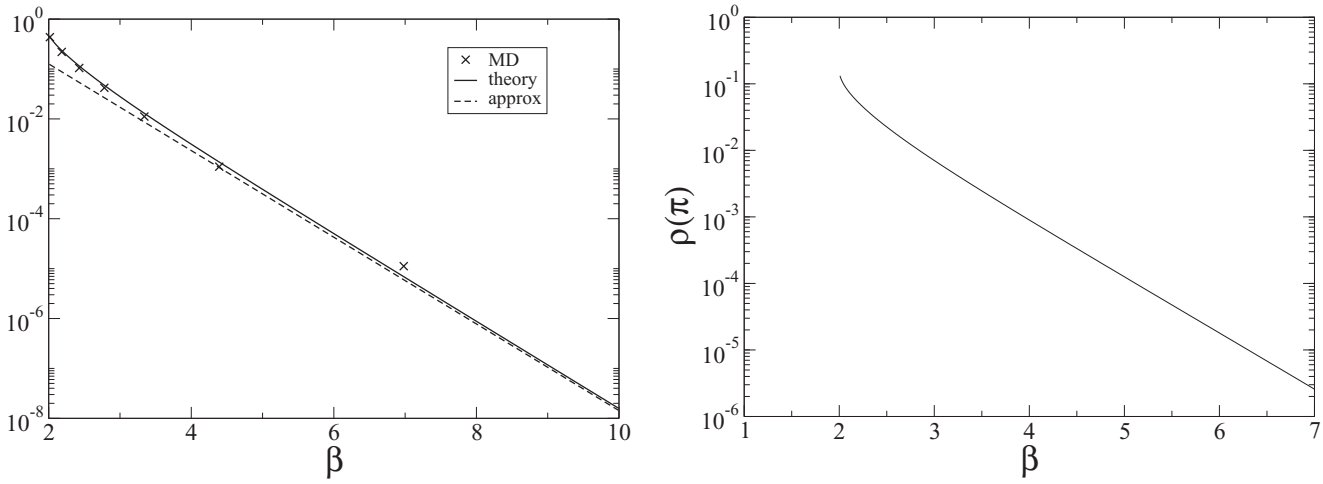

FIG. 12. Left panel: Ballistic diffusion coefficient $\tilde{\mathcal{C}}_p$ from Eq. (30), molecular dynamics (MD) simulations, theoretical prediction Eqs. (36) and (41), and analytical approximation Eq. (48). Right panel: Spatial distribution function at $\theta = \pi$ from Eq. (49). We see that σ_N^2 is roughly proportional to $\rho(\pi)$ when the center of mass is located at the origin, as expected, and the flow of particles is proportional to $\rho(\pi)$.

of the present work. We can, however, determine the diffusion coefficient using an approximation for the exact expression for the variance of position of the center of mass:

$$\sigma_\phi^2(t) = \frac{t}{N}\int_0^\infty d\tau\, \mathcal{C}_p(\tau). \tag{51}$$

We know that the correlation coefficient has the form

$$\mathcal{C}_p(\tau) = \tilde{\mathcal{C}}_p f(\tau, \beta), \tag{52}$$

where $f(\tau, \beta)$ is an unknown function of time and β related to the collisional relaxation process with $f(0, \beta) = 1$, $f(\tau \to \infty, \beta) = 0$ and $\tilde{\mathcal{C}}_p$ defined in Eq. (33). This describes the behavior of the correlation function observed in Fig. 13 for a particular value of β. If we assume that the function f does not depend strongly on β, then we can write

$$\mathcal{C}_p(\tau) \simeq \tilde{\mathcal{C}}_p f(\tau), \tag{53}$$

and then for the variance of position of the center of mass,

$$\sigma_\phi^2(t) \simeq \frac{t}{N}\int_0^\infty d\tau \tilde{\mathcal{C}}_p f(\tau) = \frac{\tilde{\mathcal{C}}_p}{N}\, t \int_0^\infty d\tau f(\tau). \tag{54}$$

We compute numerically the last integral in the right-hand side of Eq. (54) for $e = 0.4$, obtaining

$$\int_0^\infty d\tau f(\tau) \approx 730. \tag{55}$$

Using this result and the analytical expression for $\tilde{\mathcal{C}}_p$ in Eq. (48) we show in Fig. 14 the normal diffusion coefficient D a function of β with a good agreement between theory and simulation. Note that to obtain the numerical estimate requires a considerable numeric effort with very long integration times, and with the caveat that the higher the value of N the higher

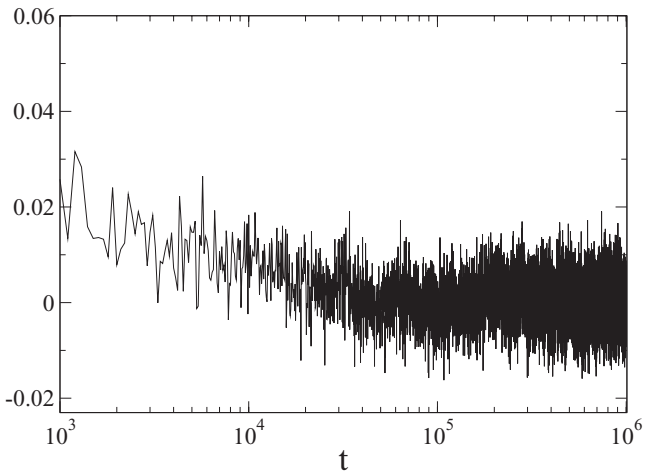

FIG. 13. Momentum autocorrelation function $\mathcal{C}_p(t)$ at equilibrium for very long times, $e = 0.4$, $N = 10\,000$. Note that the time required for $\mathcal{C}_p$ to reach zero corresponds to the crossover time from nonnormal to normal diffusion in Fig. 7

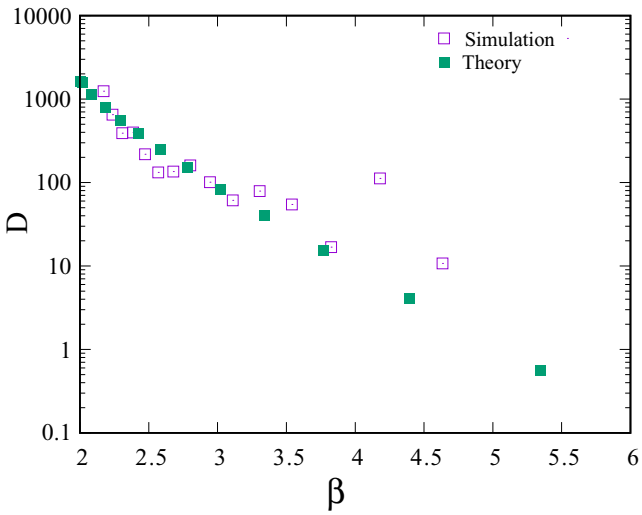

FIG. 14. Normal diffusion coefficient D at equilibrium of the center of mass as a function of β. The simulation has been performed for $N = 1000$, 50 realizations and total simulation time $t_f = 10^6$.

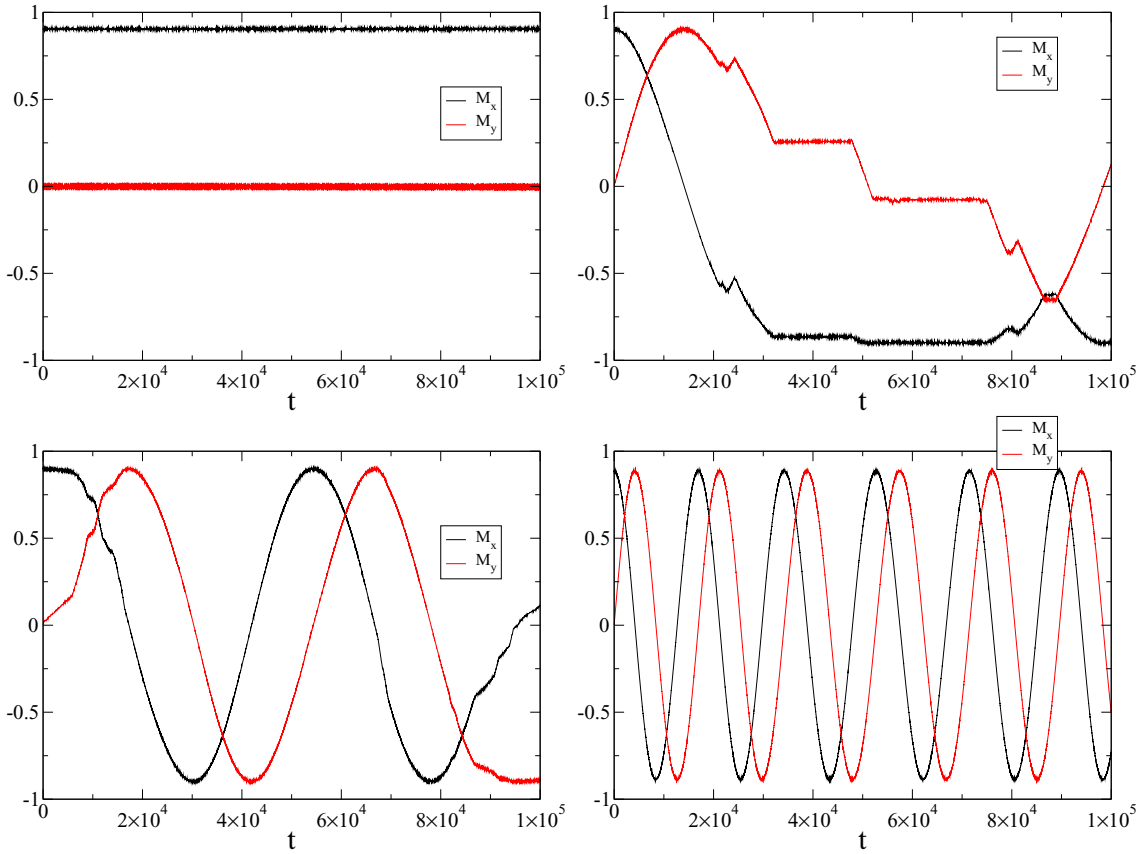

FIG. 15. Magnetization components for the HMF model with $N = 10\,000$ and energies per particle $e = 0.17$ (a), $e = 0.175$ (b), $e = 0.18$ (c), and $e = 0.2$ (d).

the crossover time. As expected, D tends to zero for decreasing energy (increasing β).

IV. CLASSICAL GOLDSTONE MODES AND CHAOS

In nematic liquid crystals the coupling of a roll pattern of electroconvection with a Goldstone mode, due to the symmetry breaking of the alignment of the nematic molecules, results in what is known as soft-mode turbulence [46]. We show now that, similarly, the coupling of the thermal excitations of a Goldstone mode, related to a periodic coordinate in long-range systems, to the mean-field motion of the particles, may lead to what is called strong chaotic behavior.

In the thermodynamic limit $N \to \infty$, the dynamics being exactly described by a mean-field approach, the motion of each particle is statistically uncorrelated from that of all other particles, with the force given by the mean-field force as the statistical average of the forces due to all other particles in the system. Let us consider the case of the HMF model where the equations of motion of particle i are given by

$$\dot{\theta}_i = p_i,$$
$$\dot{p}_i = -M_x \sin\theta_i + M_y \cos\theta_i = -M \sin(\theta_i + \phi). \quad (56)$$

In an equilibrium or stationary state in the thermodynamic limit, the magnetization M and phase ϕ are constant and each particle behaves as a pendulum subject to a constant force M in the direction specified by the phase of the magnetization. As a result, all particles act as uncoupled pendula, and the system is integrable, i.e., nonchaotic. For finite N the system is chaotic as its largest Lyapunov exponent [47] does not vanish [48–50]. Manos and Ruffo [39] showed that a crossover from weak to strong chaos, corresponding to a fraction of chaotic orbits less than 1% (weak chaos) and close to 100% (strong chaos), occurs at an energy value such that the time dependence of the phase, i.e., the excitation of the Goldstone mode, becomes important. This is also reflected by the value of the Lyapunov exponent as a function of energy [39,48,49]. In fact, for energies above the phase transition, where the magnetization vanishes in the thermodynamic limit, the Lyapunov exponent tends to zero very fast with increasing N, according to a power law $N^{-\gamma}$, with $\gamma \approx 1/3$, while for energy values corresponding to strong chaos, the decrease of Lyapunov exponent is at least one order of magnitude slower as given by the exponent γ [49]. Figure 12 at the right shows the value of the equilibrium spatial distribution function in Eq. (49) at $\theta = \pi$ with $\phi = 0$. If $\rho(\pi)$ is not significantly different from zero, then the net flux of particles at the boundary is also very small, and the Goldstone mode is not excited. As a consequence, no net motion of the center of mass of the system is observed for energies below a threshold. Figure 15 shows the behavior of the magnetization components for a few energy values at equilibrium. A significant diffusive motion of the center of mass of the system starts for energies greater than

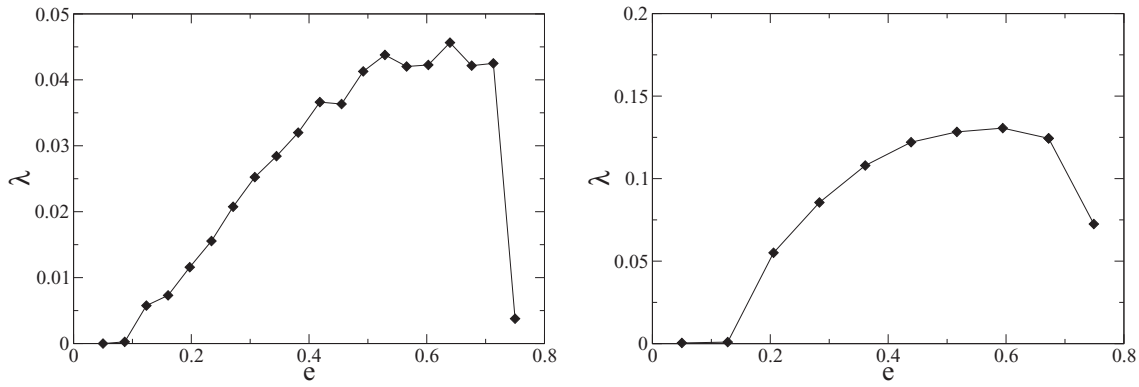

FIG. 16. Left panel: Largest Lyapunov exponent for the pendulum with phase given by a Gaussian colored noise corresponding to the equation of motion in Eq. (56) with $\alpha = 0.01$. Right Panel: Largest Lyapunov exponent for the HMF model in an equilibrium state with $N = 1\,000\,000$.

$e_g \approx 0.17$, the energy value corresponding to the crossover from weak to strong chaos.

To illustrate the relation of the coupling of the diffusive motion of the center of mass and chaos, let us consider a single oscillator with the same equations of motion as in Eq. (56) and phase ϕ given by

$$\phi(K\Delta t) = \sum_{i=1}^{K} \Delta\phi_i, \tag{57}$$

with Δt a small fixed time interval, K an integer, $\Delta\phi_i$ a realization of an exponentially correlated colored noise, i.e., given by a random variable with zero mean, a Gaussian distribution and exponential correlation function

$$\langle \Delta\phi_i \Delta\phi_j \rangle = e^{-K(j-i)\alpha}, \tag{58}$$

with α constant. The variance of the Gaussian distribution of the random variable $\Delta\phi$ is chosen to be the same as the Gaussian distribution for jumps of the center of mass of the HMF model in Eq. (27). The numerical algorithm for generating such a random number is given in Ref. [51]. The largest Lyapunov exponent can be obtained from standard methods [52] and is shown as a function of energy in Fig. 16. The dynamics of the HMF model for finite N is of course much more complex than that of a single pendulum with constant force intensity and random phase, as different particles interact with each other and with fluctuations in the total magnetization, creating feedback effects. The timescales are also different, which are relevant for the magnitude of the Lyapunov exponent. Despite that, a comparison of the graphics in Fig. 16 with Fig. 2 of Ref. [48] shows that the coupling of the Goldstone mode to the motion of a single particle is related to the strong chaotic behavior in the nonhomogeneous phase, with the Lyapunov exponent increasing rapidly for energies above the crossover from weak to strong chaos.

It is an interesting question for further studies to understand in closer details the chaos enhancing mechanism for the HMF model and other long-range interacting systems where the thermal excitation of a similar soft mode also occurs, such as in self-gravitating systems and a free electron laser. This change of regime from weak to strong chaos can also be associated to the flow of particles close to the separatrix, into and outside the region inside it, which are the particles that most contribute to the Lyapunov exponent [50]. This flow of particles determines the diffusive properties of the particles in the system, and therefore also that of the center of mass.

V. GOLDSTONE MODE IN OTHER LONG-RANGE SYSTEMS WITH A PERIODIC COORDINATE

We discussed above that the spontaneous symmetry breaking in a long-range interacting system leads to a Goldstone mode, and if the spatial coordinate associated to the broken symmetry is periodic, then a diffusive motion of the center of mass of the system ensues. To illustrate the generality of this phenomenon we show that it occurs also in two very different systems: a self-gravitating system in two dimensions and a free electron laser.

A. Two-dimensional self-gravitating systems

To show how generic this phenomena is we first turn our attention to two-dimensional self-gravitating systems, with Hamiltonian [18,53,54]

$$H = \sum_{i=1}^{N} \frac{\mathbf{p}_i^2}{2} + \frac{1}{2N} \sum_{i<j=1}^{N} \log(\mathbf{r}_i - \mathbf{r}_j + \epsilon), \tag{59}$$

where $\mathbf{r}_i$ is the vector position of particle i in $\mathbb{R}^2$ and $\mathbf{p}_i$ its conjugate momentum. A small softening parameter ϵ was introduced in the argument of the logarithm function in Eq. (59) to avoid divergences in numerical simulations at zero interparticle distance. Conditions for an instability threshold for spontaneous symmetry breaking after the violent relaxation in self-gravitating systems were discussed in Ref. [55]. We consider an initial state with all particles at rest, and spatially uniform on an annulus with inner and outer radius R_1 and R_2, respectively. After going through a violent relaxation, the system settles on a quasistationary sate with a broken rotational symmetry forming a bar structure, as shown in Fig. 17 for some different time values, where we observe an effective (differential) rotation of the bar, similar to what was discussed above for the HMF model. This is caused by thermal fluctuations of the distribution function and can

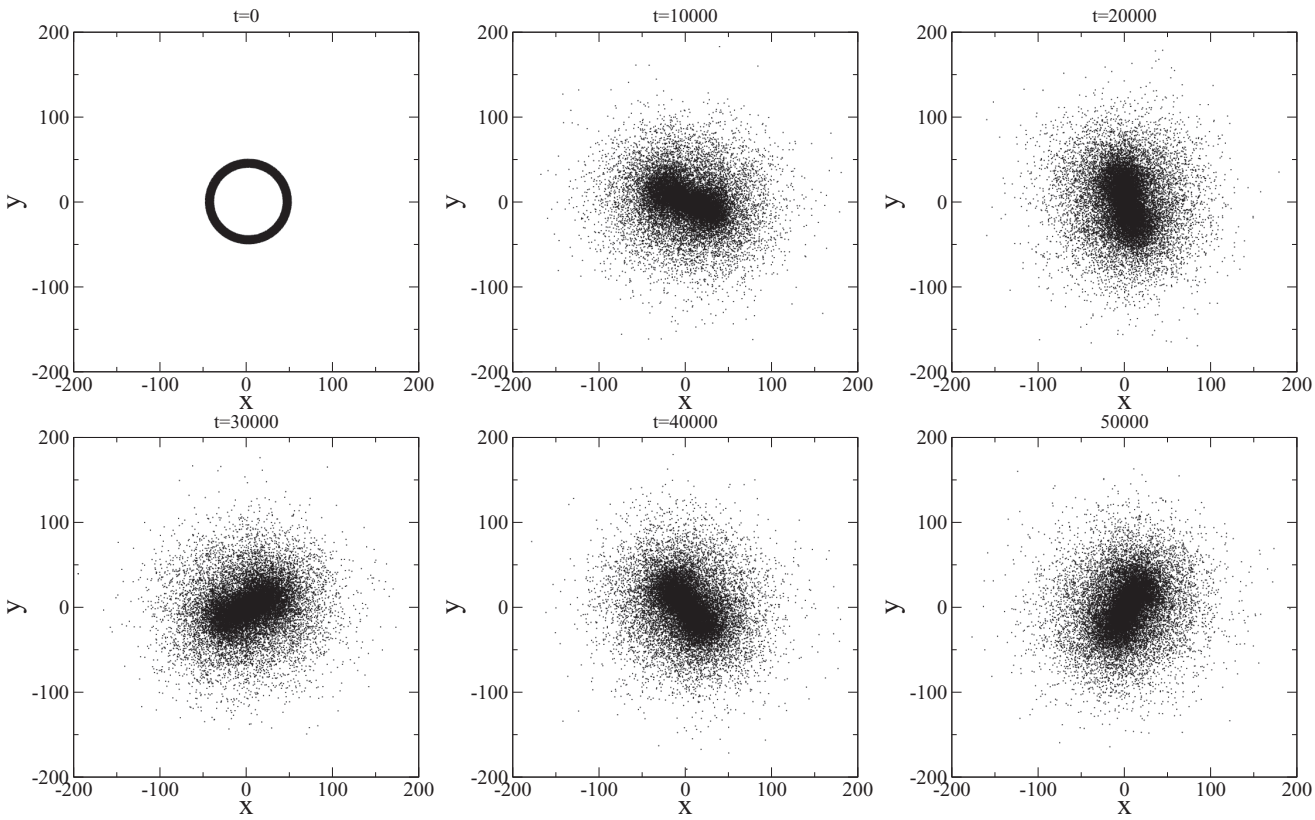

FIG. 17. Positions of particles in the two-dimensional self gravitating system with vanishing total angular momentum for $N = 32\,768$, time step $\Delta t = 0.05$, $\epsilon = 10^{-5}$ and a uniform spatial initial distribution in a circular strip with inner and outer radius $R_1 = 40.0$ and $R_2 = 50.0$ with all particles at rest. The system evolves through the violent relaxation and reaches a quasistationary state displaying a symmetry breaking.

be better understood by using polar coordinates and writing down the one-particle distribution function as $f(p_r, p_\theta, r, \theta)$, where r and θ are the radial and angular coordinates, and p_r and p_θ their canonically conjugate momenta, respectively. The same reasoning as for the HMF model applies here for the angular coordinate. The asymmetry of f with respect to θ induced by momentum preserving fluctuations causes a motion of the preferred direction with zero total angular momentum. This motion can be characterized using the inertia moments with respect to two orthogonal axis, say x and y, divided by the total mass, and given by

$$\sigma_x = \frac{1}{N}\sum_{i=1}^{N} x_i^2,$$
$$\sigma_y = \frac{1}{N}\sum_{i=1}^{N} y_i^2. \tag{60}$$

Figure 18 shows the time evolution of σ_x and σ_y. The rotation of the system is evident albeit the vanishing total angular momentum.

This classical Goldstone mode is the outcome of a symmetry breaking with respect to a periodic coordinate, and its motion is a result of excitations by thermal fluctuations. Since the equilibrium state has no symmetry breaking, the oscillations for the present case are slowly damped with time and vanish once the system reaches thermodynamic equilibrium. Figure 19 shows the standard deviation σ_ϕ for the position angle. The relation in Eq. (14) remains valid here for the angular variable. The position angle of the bar structure in Fig. 18 varies in time with an approximately constant angular velocity, at least for the small time window

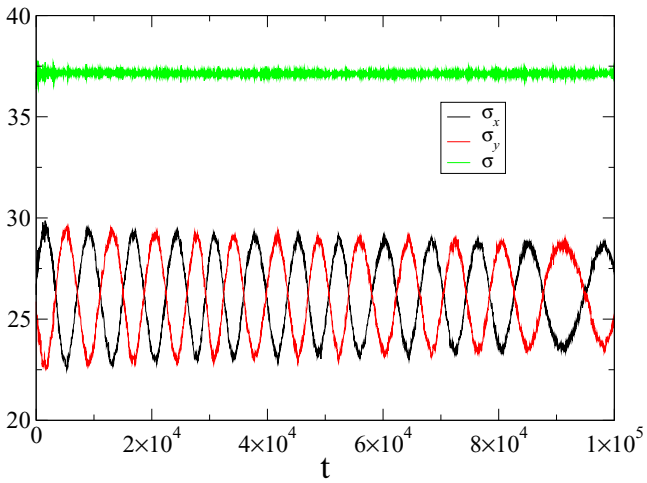

FIG. 18. Position standard deviation $\sigma = \sqrt{\sigma_x^2 + \sigma_y^2}$, and standard deviations for the x and y coordinates for the same simulation as in Fig. 17. The system is initially left to evolve though the initial violent relaxation for a total time of $t = 1000$.

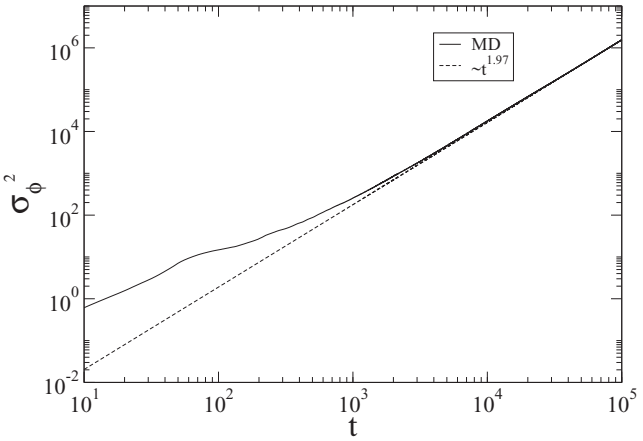

FIG. 19. Variance σ_ϕ^2 of the angular position ϕ of the particles for the same simulation as in Fig. 18. The initial position for computing the displacement $\phi(t) - \phi(0)$ is taken at time $t = 1000$, so that the initial violent relaxation has ended and the system has settled in a quasistationary state. A least squares fit of a power law, shown in the figure as a dashed line, yields $\sigma_\theta^2 \propto t^{1.97}$, i.e., close to the ballistic diffusion.

of the simulation. From the discussion in the previous section, this is a consequence of the ballistic diffusion of the individual particles in the angular direction. Figure 19 shows the variance $\sigma_\phi(t)^2 = (1/N)\sum_{i=1}^N \phi_i(t)$ of the position angular variables $\phi_i(t)$, $i = 1, \ldots, N$ as a function of time, and as expected it scales almost as t^2, i.e., very close to ballistic diffusion. A more detailed study of gravitational systems is beyond the scope of the present work, and will be the subject of a future publication.

B. Free electron laser

A free electron laser is a tunable source of coherent radiation that uses a relativistic electron beam as a lasing medium. This beam propagates in a periodic external magnetostatic field due to an undulator (or wiggler) inducing an oscillatory motion of the electrons, which then emit synchrotron radiation that is amplified as the beam moves along the undulator [19,56]. Assuming a one-dimensional motion along the undulator, the equations governing the motion of the electrons in a single pass FEL for small beam current and emittance are given by [9,19–22]

$$\begin{aligned} \frac{d\theta_j}{dz} &= p_j, \\ \frac{dp_j}{dz} &= -\sum_h F_h\left(A_h e^{ih\theta_j} + A_h^* e^{-ih\theta_j}\right), \\ \frac{dA_h}{dz} &= F_h b_h, \end{aligned} \tag{61}$$

where z is the distance along the undulator, $A_h = A_h^x + iA_h^y$ is the hth harmonic of the field with A_h^x and A_h^y its transverse components, F_h are coupling parameters and b_h the bunching parameters given by

$$b_h = -\frac{1}{N}\sum_{j=1}^N e^{-ih\theta_j}. \tag{62}$$

Equations (61) derive from the Hamiltonian

$$H = \sum_{j=1}^N \frac{p_j^2}{2} - i\sum_h \sum_{j=1}^N \frac{F_h}{h}\left[A_h e^{ih\theta_j} - A_h^* e^{-ih\theta_j}\right], \tag{63}$$

with canonically conjugate variables (θ_j, p_j) and $(\sqrt{N}A_j, \sqrt{N}A_j^*)$. The phase of the jth particle with respect to the hth harmonic is given by $h\theta_j$. Here the spatial coordinate z assumes the role of the time variable. In this sense, besides the Hamiltonian in Eq. (63), the total momentum $P = \sum_j p_j + I$ is also conserved, where the total field intensity is given by $I = \sum_h |A_h|^2$.

A diffusive motion of the center of mass of the electrons in the coordinate θ can be observed along the undulator coordinate z, analogous to what we observed in the HMF model, but with nonvanishing total momentum of the electrons $\sum_j p_j$, and approaching a constant value as the total field intensity I tends to a constant. We again define the average value of the angular coordinate using Eq. (11) with z replacing t. By performing different realizations of simulations with the same macroscopic initial conditions, the diffusion process of the center of mass then shows up as small deviations around $\langle\phi(z)\rangle$ along the coordinate z, and can be quantified by the variance

$$\sigma_\phi^2(z) = \langle(\phi(z) - \langle\phi(z)\rangle)^2\rangle. \tag{64}$$

The left panel of Fig. 20 shows the variance σ_ϕ^2 as a function of z, where a superdiffusive behavior is clearly observed. The evolution value of $\phi(z)$ for one of the realizations is shown on the right panel.

A more thorough study of this system using the methods introduced above will also be the subject of future research, as for other long-range systems.

VI. CONCLUDING REMARKS

We showed that, for a many-particle system with long-range interactions, if the equilibrium or a (quasi)stationary state spontaneously breaks a symmetry of the Hamiltonian, then a soft (Goldstone) mode exists with zero energy cost to go from one equilibrium states to another equivalent one. Besides that, if the coordinate associated to this symmetry breaking is periodic, then this mode can be excited by thermal fluctuations due to finite N effects, resulting in a superdiffusive motion of the center of mass of the system at zero momentum, due to the ambiguity of the position of center of mass. The existence of this soft mode was illustrated for a two-dimensional self-gravitating system, a free electron laser, and, in more details, for the HMF model. For the latter, a theory for the ballistic motion of the center of mass was given, with expressions for relevant quantities. An equivalent theory for more general systems rests on the development of a theory for diffusion of nonhomogeneous states, which has still to be developed. Such finite N effects cannot be described from a purely kinetic equation approach, similarly to the case of a

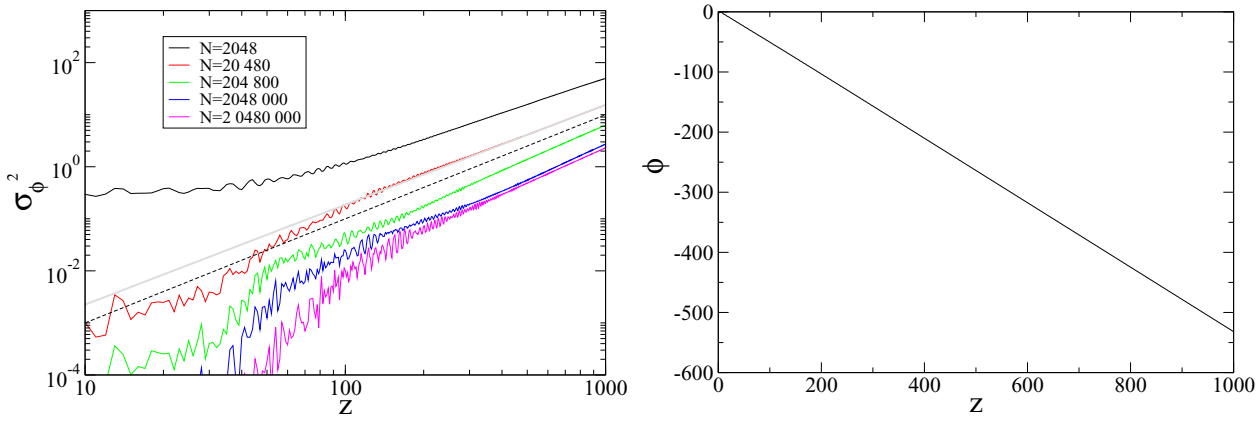

FIG. 20. Left panel: Variance $\sigma_\phi^2(z)$ in Eq. (64) considering a single harmonic and a waterbag initial condition with $p_0 = 0.5$ and $\theta_0 = 0.1$, for a few values of N and 100 realizations, with a time step $\Delta t = 0.05$. The dashed line introduced for reference is proportional to z^2. Right panel: value of $\phi(z)$ for one of the realizations as given by Eq. (11) for $N = 20\,480\,000$ along the undulator.

single wave propagating in a plasma system, where separatrix crossing also plays an important role [57].

We also discussed how the coupling of the Goldstone mode to the mean-field motion of individual particles may enhance the chaotic behavior of the system, and illustrated this possibility again for the HMF model. This seems to be an important mechanism of chaos enhancement in systems with long-range interactions with spontaneous symmetry breaking with respect to a periodic coordinate, and is certainly also a point worth of further research for other similar systems.

ACKNOWLEDGMENTS

The authors are indebted to J. B. Fouvry for many discussions and comments. They thank S. Ruffo for fruitful discussions and also Y. Elskens for the long discussions and for carefully reading our manuscript. T.M.R.F. also acknowledges partial financial support from CNPq (Brazil) Grant No. 305842/2017-0, from Laboratoire J.A. Dieudonné and from the "Fédération Doeblin." B.M. acknowledges support by the Grant Segal ANR-19-CE31-0017 of the Agence Nationale de la Recherche (France).

[1] J. W. Gibbs, *Elementary Principles in Statistical Mechanics* (Charles Scribner's Sons, New York, 1902).
[2] D. Ruelle, *Statistical Mechanics: Rigourous Results* (World Scientific, Singapore, 1999).
[3] H. B. Callen, *Thermodynamics and Introduction to Thermostatistics*, 2nd ed. (John Wiley, New York, 1985).
[4] A. Campa, T. Dauxois, and S. Ruffo, Phys. Rep. **480**, 57 (2009).
[5] Y. Levin, R. Pakter, F. B. Rizzato, T. N. Teles, and F. P. C. Benetti, Phys. Rep. **535**, 1 (2014).
[6] *Dynamics and Thermodynamics of Systems with Long-Range Interactions*, T. Dauxois, S. Ruffo, E. Arimondo, and M. Wilkens Eds. (Springer, Berlin, 2002).
[7] *Dynamics and Thermodynamics of Systems with Long-Range Interactions: Theory and Experiments*, edited by A. Campa, A. Giansanti, G. Morigi, and F. S. Labini, AIP Conference Proceedings, Vol. 970 (2008).
[8] *Long-Range Interacting Systems, Les Houches 2008, Session XC*, edited by T. Dauxois, S. Ruffo, and L. F. Cugliandolo (Oxford University Press, Oxford, 2010).
[9] A. Campa, T. Dauxois, D. Fanelli, and S. Ruffo, *Physics of Long-Range Interacting Systems* (Oxford University Press, Oxford, 2014).
[10] P.C. Hemmer, M. Kac, and G. Uhlenbieck, J. Math. Phys. **5**, 60 (1964).
[11] W. Braun and K. Hepp, Commun. Math. Phys. **56**, 101 (1977).
[12] T. M. Rocha Filho, M. A. Amato, A. E. Santana, A. Figueiredo, and J. R. Steiner, Phys. Rev. E **89**, 032116 (2014).
[13] L. Brenig, Y. Chaffi and T. M. Rocha Filho, Long velocity tails in plasmas and gravitational systems, arXiv:1605.05981.
[14] J. Goldstone, Nuovo Cimento **19**, 154 (1961).
[15] J. Goldstone, A. Salam, and S. Weinberg, Phys. Rev. **127**, 965 (1962).
[16] Ch. Gruber and P. A. Martin, *Goldstone Theorem in Statistical Mechanics, in Mathematical Problems in Theoretical Physics* (Springer, Berlin Conference, 1981).
[17] M. Antoni and S. Ruffo, Phys. Rev. E **52**, 2361 (1995).
[18] B. N. Miller, K. Yawn, and P. Youngkins, Ann. N. Y. Acad. Sci. **867**, 268 (2008).
[19] R. Bonifacio, F. Casagrande, G. Cerchioni, L. De Salvo Souza, P. Pierini and N. Piovella, Riv. Nuovo Cimento **13**, 1 (1990).
[20] M. Antoni, Y. Elskens, and D. F. Escande, Phys. Plasmas **5**, 841 (1998).
[21] M.-C. Firpo and Y. Elskens, J. Stat. Phys. **93**, 193 (1988).
[22] A. Antoniazzi, Y. Elskens, D. Fanelli, and S. Ruffo, Eur. Phys. J. B **50**, 603 (2006).
[23] G. Morchio and F. Strocchi, Ann. Phys. **170**, 310 (1986).
[24] A. G. Rossberg, A. Hertrich, L. Kramer, and W. Pesch, Phys. Rev. Lett. **76**, 4729 (1996).
[25] F. Strocchi, Phys. Lett. A **267**, 40 (2000).
[26] F. Strocchi, *Symmetry Breaking, Lect. Notes Phys.* vol. 643 (Springer, Berlin/Heidelberg, 2005).
[27] T. M. Rocha Filho, A. E. Santana, M. A. Amato, and A. Figueiredo, Phys. Rev. E **90**, 032133 (2014).

[28] A. S. Freitas and D. F. de Albuquerque, Phys. Rev. E **91**, 012117 (2015).
[29] Z. A. Kuzkin, Z. Angew. Math. Mech. **95**, 1290 (2015).
[30] Y. Y. Yamaguchi, F. Bouchet, and T. Dauxois, J. Stat. Mech. (2007) P01020.
[31] Y. Y. Yamaguchi, Phys. Rev. E **68**, 066210 (2003).
[32] F. Bouchet and T. Dauxois, Phys. Rev. E **72**, 045103(R) (2005).
[33] L. G. Moyano and C. Anteneodo, Phys. Rev. E **74**, 021118 (2006).
[34] P.-H. Chavanis, Physica A **377**, 469 (2007).
[35] F. P. C. Benetti and B. Marcos, Phys. Rev. E **95**, 022111 (2017).
[36] T. M. Rocha Filho, Comp. Phys. Comm. **185**, 1364 (2014).
[37] T. M. Rocha Filho, J. Phys. A **42**, 165001 (2009).
[38] F. Ginelli, K. A. Takeuchi, H. Chaté, A. Politi, and A. Torcini, Phys. Rev. E **84**, 066211 (2011).
[39] T. Manos and S. Ruffo, Transp. Theory Stat. Phys. **40**, 360-381 (2011).
[40] V. Latora, A. Rapisarda, and S. Ruffo, Phys. Rev. Lett. **83**, 2104 (1999).
[41] F. Bouchet and T. Dauxois, J. Phys. Conf. Ser. **7**, 34 (2005).
[42] P.-H. Chavanis, Eur. Phys. B **52**, 47 (2006).
[43] J. G. Skellam, J. Royal Stat. Soc. **109**, 296 (1946).
[44] R. Morgado, F. A. Oliveira, G. G. Batrouni, and A. Hansen, Phys. Rev. Lett. **89**, 100601 (2002).
[45] R. Balescu, *Statistical Dynamics—Matter out of Equilibrium* (Imperial College Press, London, 1997).
[46] Y. Hidaka, K. Tamura, and S. Kai, Prog. Theor. Phys. Suppl. **161**, 1 (2006).
[47] E. Ott, *Chaos in Dynamical Systems* (Cambridge University Press, Cambridge, 1993).
[48] M.-C. Firpo, Phys. Rev. E **57**, 6599 (1998).
[49] L. H. Miranda Filho, M. A. Amato, and T. M. Rocha Filho, J. Stat. Mech. (2018) 033204.
[50] L. H. Miranda Filho, M. A. Amato, Y. Elskens and T. M. Rocha Filho, Commun. Nonlin. Sci. Numer. Simulat. **74**, 236 (2019).
[51] R. F. Fox, I. R. Gatland, R. Roy, and G. Vemuri, Phys. Rev. A **38**, 5938 (1988).
[52] T. S. Parker and L. O. Chua, *Practical Numerical Algorithms for Chaotics Systems* (Springer-Verlag, New York, 1989).
[53] T. N. Teles, Y. Levin, R. Pakter, and F. Rizzato, J. Stat. Mech. (2010) P05007.
[54] R. Pakter, B. Marcos, and Y. Levin, Phys. Rev. Lett. **111**, 230603 (2013).
[55] B. Marcos, Phys. Rev. E **88**, 032112 (2013).
[56] W. B. Colson, Phys. Lett. **59**, 187 (1976).
[57] M-C. Firpo, F. Doveil, Y. Elskens, P. Bertrand, M. Poleni, and D. Guyomarc'h, Phys. Rev. E **64**, 026407 (2001).

Part II

Analogue long-range systems

Breathing Mode for Systems of Interacting Particles

Alain Olivetti,[1,*] Julien Barré,[1] Bruno Marcos,[1] Freddy Bouchet,[2] and Robin Kaiser[2]

[1]*Laboratoire J. A. Dieudonné, UMR CNRS 6621, Université de Nice-Sophia Antipolis, Parc Valrose, F-06108 Nice Cedex 02, France*

[2]*Institut Non-Linéaire de Nice, UMR CNRS 6618, Université de Nice-Sophia Antipolis, France*

(Received 25 July 2009; published 24 November 2009)

We study the breathing mode in systems of trapped interacting particles. Our approach, based on a dynamical ansatz in the first equation of the Bogoliubov-Born-Green-Kirkwood-Yvon hierarchy allows us to tackle at once a wide range of power-law interactions and interaction strengths, at linear and nonlinear levels. This both puts in a common framework various results scattered in the literature, and by widely generalizing these, emphasizes universal characters of this breathing mode. Our findings are supported by direct numerical simulations.

DOI: 10.1103/PhysRevLett.103.224301 PACS numbers: 45.50.−j, 05.20.Jj

Systems of trapped interacting particles are studied in many areas of physics: confined plasmas, trapped cold atoms, Bose-Einstein condensates, colloidal particles, trapped ions, astrophysical systems, the latter ones being self-confined by the interactions. The low-lying oscillatory modes of these systems are a natural object of study, as they are an important nondestructive tool to characterize the system and gain insight into the collective effects at work. As a consequence, there is abundant literature on the subject, corresponding to very diverse physical situations: (i) systems with short-range interactions, such as classical gases or shielded Coulomb interaction and (ii) systems with long-range interactions, such as non-neutral plasmas, Coulomb crystals, or astrophysical systems, in which the interactions may be weak (gases) or strong (liquids or crystals).

Diverse approaches and techniques are naturally used to investigate these phenomena. A trapped classical gas of interacting particles is studied using a Boltzmann-Vlasov equation in [1], where the nonlinear dynamics is approximated with a scaling ansatz, which captures the collective effects. Such an ansatz was used earlier for the Gross-Pitaevskii equation in [2,3]. In the confined plasma context, the problem is often studied through hydrodynamical equations, in the so-called "cold fluid approximation" [4], where the dispersion relation for fluid modes in a cold spheroidal plasma is derived. Following an idea of [5], Ref. [6] gives an approximate solution to the breathing mode of a 1D confined plasma beyond the cold fluid approximation, using an *ad hoc* closure of the hydrodynamical equations. Monopole modes of dusty plasmas interacting with a Yukawa potential are investigated in [7,8]. The breathing mode of trapped ions or colloids interacting via Coulomb or Yukawa interactions has been studied in 1D [9,10], 2D [11,12], and 3D [13] for crystallized systems, by a direct diagonalization of the linearized Newtonian equations of motion. Finally, breathing oscillations with attractive interactions have been studied in an astrophysical context using the virial theorem [14].

Each method applies to a specific situation: Newton equations are adapted to a crystallized state with negligible thermal fluctuations, linearization assumes a small amplitude, the Vlasov equation is limited to long-range interactions and weak correlations. Yet in all cases a similar equation for the breathing mode is obtained. In particular, it is intriguing that kinetic descriptions assuming small correlations between particles, fluid descriptions, and perturbative expansions around a crystallized state all yield similar predictions for the breathing mode, at linear and nonlinear levels. This stunning situation calls for a unified theory. In the limit of zero temperature, or equivalently infinitely strong interactions, such an endeavor has recently been undertaken in the linear regime [15]. A more general situation summarizing the different possible regimes for a binary isotropic power-law interparticle force $F(r) \sim 1/r^k$ in d space dimensions is shown in a diagram Fig. 1. We have organized the different cases along two axes. On the

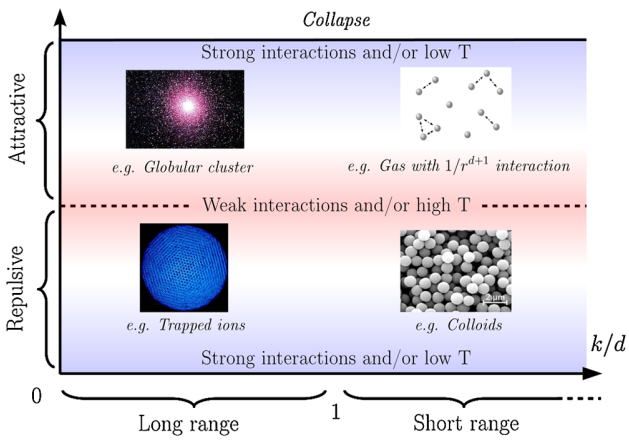

FIG. 1 (color online). Diagram of the different regimes for the breathing mode. On the horizontal axis, the interaction range, measured by k/d. The interaction strength is changing along the vertical axis. Pictures of some physical examples are inserted for illustration.

horizontal axis we represent the interaction range, which we will call long range if $k/d \leq 1$ and short range otherwise. The case $k/d \leq 1$ corresponds to nonintegrable forces at large distances [16]. The vertical axis represents the interaction strength with respect to the thermal energy.

In this Letter, we present a theory of the breathing mode of systems of classical trapped interacting particles which classifies many cases studied in the references cited above in a common framework. The theory is valid both for short-range and long-range interactions, for any dimension, and for various interaction strengths. However, for short-range attractive interactions strong instabilities due to the unregularized short-range singularity are expected, and for strongly attractive long-range interacting systems, a gravitational-like collapse sets in. We did not verify to what extent our model may capture relevant features in these situations. Our theory describes both linear as well as nonlinear oscillations, and isolated systems as well as systems in contact with a thermal bath.

We consider a system of particles confined by a harmonic spherical trapping force $\mathbf{F}_{\text{trap}}(\mathbf{r}) = -\omega_0^2\mathbf{r}$, with binary interaction forces $\mathbf{F}_{\text{int}}$. In the canonical setting, particles are subjected to a positive constant friction k and diffusion D. In the microcanonical setting, $k = 0, D = 0$, and the dynamics is Hamiltonian. To overcome the limitations in the validity of the Vlasov equation, we describe the cloud of particles by its one-particle and two-particles distribution functions $f(\mathbf{r}_1, \mathbf{v}_1, t)$ and $g(\mathbf{r}_1, \mathbf{v}_1, \mathbf{r}_2, \mathbf{v}_2, t)$. We start from the first equation of the Bogolyubov-Born-Green-Kirkwood-Yvon (BBGKY) hierarchy, which we complement by a Fokker-Planck operator [18] to include the temperature in the canonical case:

$$\frac{\partial f}{\partial t} + \nabla_{\mathbf{r}} \cdot (\mathbf{v}f) + \mathbf{F}_{\text{trap}} \cdot \nabla_{\mathbf{v}} f + C[g] = D\Delta_{\mathbf{v}} f + k\nabla_{\mathbf{v}} \cdot (\mathbf{v}f), \tag{1}$$

where $C[g]$ is the interaction term given by

$$C[g](\mathbf{r}_1, \mathbf{v}_1, t) = \int \mathbf{F}_{\text{int}}(\mathbf{r}_1, \mathbf{r}) \cdot \nabla_{\mathbf{v}_1} g(\mathbf{r}_1, \mathbf{v}_1, \mathbf{r}, \mathbf{v}, t) d\mathbf{r} d\mathbf{v}. \tag{2}$$

We stress that Eq. (1), in contrast with the Vlasov equation, can also describe strongly correlated systems. We assume in the following the existence of a stationary state f_0 and g_0, not necessarily the thermodynamic equilibrium [17]. We now drastically simplify the dynamics by using a scaling ansatz [1–3], which we extend here to the two-particles function g:

$$\begin{aligned} f(\mathbf{r}_1, \mathbf{v}_1, t) &= f_0(\varphi(\mathbf{r}_1, \mathbf{v}_1)) \\ g(\mathbf{r}_1, \mathbf{v}_1, \mathbf{r}_2, \mathbf{v}_2, t) &= g_0(\psi(\mathbf{r}_1, \mathbf{v}_1, \mathbf{r}_2, \mathbf{v}_2)), \end{aligned} \tag{3}$$

with $\varphi(\mathbf{r}_1, \mathbf{v}_1) = (\mathbf{R}_1 = \mathbf{r}_1/\lambda, \mathbf{V}_1 = \lambda\mathbf{v}_1 - \dot{\lambda}_{\mathbf{r}_1})$ and $\psi(\mathbf{r}_1, \mathbf{v}_1, \mathbf{r}_2, \mathbf{v}_2) = (\varphi(\mathbf{r}_1, \mathbf{v}_1), \varphi(\mathbf{r}_2, \mathbf{v}_2))$. λ represents the dilatation of the cloud; the choice $\mathbf{R}_1 = \mathbf{r}_1/\lambda$ imposes the ansatz on velocities for consistency. All time dependence in the dynamics is now included in the positive parameter λ. Introducing Eq. (3) into Eq. (1) leads to

$$\sum_{i=1}^{d}\left\{\frac{V_i}{\lambda^2}\frac{\partial f_0}{\partial R_i} - R_i\lambda\frac{\partial f_0}{\partial V_i}(\ddot{\lambda} + \omega_0^2\lambda) - \kappa\frac{\partial(V_i f_0)}{\partial V_i} - \kappa\lambda\dot{\lambda}R_i\frac{\partial f_0}{\partial V_i} - D\lambda^2\frac{\partial^2 f_0}{\partial V_i^2}\right\} + C[g_0 \circ \psi](\mathbf{r}_1, \mathbf{v}_1, t) = 0, \tag{4}$$

where the difficulty is to deal with the interaction term. We now assume that the two-body interaction satisfies

$$\mathbf{F}_{\text{int}}(\lambda\mathbf{r}_1, \lambda\mathbf{r}_2) = \frac{1}{\lambda^k}\mathbf{F}_{\text{int}}(\mathbf{r}_1, \mathbf{r}_2), \tag{5}$$

as, for example, a pure power law. The important step is to replace the interaction term $C[g_0 \circ \psi](\mathbf{r}_1, \mathbf{v}_1, t)$ by a linear combination of f_0 and its derivatives. This is achieved using the condition (5) and the fact that f_0 and g_0 are stationary solutions of Eq. (1). Equation (4) becomes

$$\sum_{i=1}^{d}\left\{V_i\frac{\partial f_0}{\partial R_i}\left(\frac{1}{\lambda^2} - \lambda^{1-k}\right) + D\frac{\partial^2 f_0}{\partial V_i^2}(\lambda^{1-k} - \lambda^2) - R_i\frac{\partial f_0}{\partial V_i}[\lambda(\ddot{\lambda} + \omega_0^2\lambda) - \lambda^{1-k}\omega_0^2 + \kappa\lambda\dot{\lambda}] + \kappa\frac{\partial V_i f_0}{\partial V_i}(\lambda^{1-k} - 1)\right\} = 0. \tag{6}$$

Multiplying the previous equation by $R_j V_j/N$, and integrating over $d\mathbf{R}d\mathbf{V}$, we obtain a constraint on the parameter λ:

$$\ddot{\lambda} + \kappa\dot{\lambda} + \left(\lambda - \frac{1}{\lambda^k}\right)\omega_0^2 - \left(\frac{1}{\lambda^3} - \frac{1}{\lambda^k}\right)\frac{\langle V_j^2\rangle_{f_0}}{\langle R_j^2\rangle_{f_0}} = 0, \tag{7}$$

where j is a coordinate label, and we have set $\langle \mathcal{X}\rangle_f = \frac{1}{N} \times \int \mathcal{X}(\mathbf{r}, \mathbf{v}) f(\mathbf{r}, \mathbf{v}, t) d\mathbf{r} d\mathbf{v}$. In the dynamical equation for λ [Eq. (7)], all parameters are computed as averages over the stationary distribution f_0. For Eq. (7) to be a unique equation, it is necessary that the ratio $\langle V_j^2\rangle_{f_0}/\langle R_j^2\rangle_{f_0}$ does not depend on j, which is true if the trap and interactions are isotropic.

We introduce the dimensionless parameter $p = \langle V_j^2\rangle f_0/(\omega_0^2\langle R_j^2\rangle_{f_0}) \sim k_B T/E_{\text{trap}}$, where $k_B T$ is the thermal energy and E_{trap} the typical potential energy due to the trap. At the canonical equilibrium, $\langle V_j^2\rangle f_0 = \omega_0^2 L^2$, where L is the typical size of the system without interaction. The parameter $p = L^2/\langle R_j^2\rangle_{f_0}$ thus describes change of the square of the size of the trap due to the interactions. The range $p < 1$ ($p > 1$) corresponds to a repulsive (attractive) interaction. A value of the parameter $p \sim 1$ means high temperature or negligible interactions. The limits $p \to 0$ and $p \to +\infty$ correspond to zero temperature or strong repulsive and attractive interaction. We can now rewrite Eq. (7) as $\ddot{\lambda} + \kappa\dot{\lambda} + \phi'(\lambda) = 0$, which corresponds to the

equation of a damped anharmonic oscillator in the potential ϕ:

$$\phi(\lambda) = \begin{cases} \omega_0^2(\frac{1}{2}\lambda^2 + \frac{1}{2}\frac{p}{\lambda^2} + \frac{p-1}{1-k}\lambda^{1-k}) & \text{if } k \neq 1 \\ \omega_0^2(\frac{1}{2}\lambda^2 + \frac{1}{2}\frac{p}{\lambda^2} + (p-1)\log\lambda) & \text{if } k = 1. \end{cases} \quad (8)$$

The first term in Eq. (8) is the quadratic confining potential, the second one corresponds to a pressure term, and the last one is introduced by the two-body interaction. We stress that Eq. (8) does not explicitly depend on d. For repulsive interactions ($p < 1$), ϕ is strictly convex for all $k \geq 0$. It diverges as λ^{-2} when $\lambda \to 0$ and as $\omega_0^2\lambda^2/2$ when $\lambda \to +\infty$. Its unique minimum is $\lambda = 1$. The λ^{-2} divergence at small λ is due to pressure effects for very compressed clouds, and thus does not depend on the interaction. It yields a generic shape for the breathing oscillations in the nonlinear regime. For attractive interactions ($p > 1$), if $0 \leq k \leq 3$, ϕ has exactly the same qualitative properties as in the repulsive case. For $k > 3$, ϕ tends to $-\infty$ when λ goes to zero, indicating a possible collapse of the cloud. However, due to numerical difficulties, we have not tested this prediction.

From Eq. (8), we obtain the general expression of the breathing oscillation frequency in the small friction limit, as a function of the interaction range k and the interaction strength p:

$$\omega(k, p) = \omega_0[(3-k)(p-1)+4]^{1/2}. \quad (9)$$

This expression recovers the well-known limits $\omega = 2\omega_0$ for a noninteracting gas ($p = 1$) and $\omega = \sqrt{3}\omega_0$ for a strongly interacting Coulomb plasma ($p = 0$, $k = 2$) [19]. It provides a generalization to the whole (k, p) plane shown in Fig. 2 and is independent of the dimension. We note that in 3D, the breathing frequency is a decreasing (increasing) function of the interaction strength for repulsive long- (short-)range interactions.

We can now compare the general Eq. (7) to the results found in the literature for various specific situations. Oscillations of crystallized systems [9,10,12,15] correspond to negligible pressure effects; i.e., $p = 0$ and the λ^{-3} term is absent. In [6], the authors consider a 1D plasma ($k = 0$) with p not too small, and introduce a pressure yielding the λ^{-3} term, which leads to the exact equivalent of Eq. (7). Note that Eq. (7) also contains the case of a classical gas with "mean field" interactions [1]. This work considers a Dirac δ potential, which corresponds to an interaction index $k = d + 1$. This result emphasizes that the present theory is not only valid for power-law forces.

In order to test the domain of validity of the ansatz solution, we have performed numerical simulations varying the force index k, parameter p, and amplitude of initial perturbation, in two and three dimensions, with (canonical ensemble) or without (microcanonical ensemble) a thermostat. We simulate the system using a molecular dynamics approach with $N = 4000$ particles. The integrator scheme is a Verlet-leapfrog algorithm [20]. The forces are exactly computed at each time step. As strong short-range singularities for parameters in the upper right corner of Fig. 1 create numerical difficulties, we have not tested the theory in this region. The computer simulations are performed as follows: we first equilibrate the system in a stationary state f_0. Then, at $t = 0$, we introduce a perturbation by rescaling the positions and velocities according to Eq. (3) and we let the system evolve. A similar simulation of a 1D Coulomb system in the microcanonical ensemble has been performed in [6]. The results of our extensive simulations may be summarized as follows. (i) Eq. (7) always picks up quite precisely the oscillation frequency, but not always the amplitude decay. (ii) For strongly repulsive interaction ($p \to 0$), Eq. (7) describes very precisely the whole dynamics. (iii) For a repulsive long-range or short-range interaction and intermediate p (i.e., $p \sim 0.5$) the agreement for the oscillation amplitude is not perfect (see Fig. 3). (iv) For attractive long-range interactions, the accuracy of the ansatz degrades as p increases (Fig. 4).

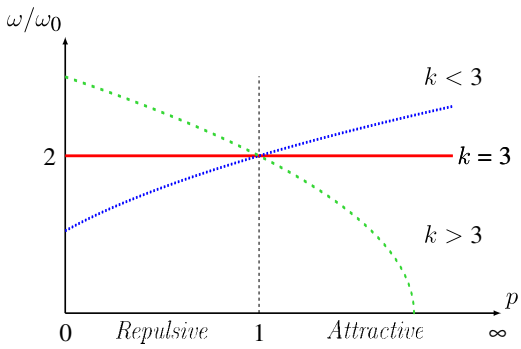

FIG. 2 (color online). Frequency of the linearized breathing mode as a function of the interaction strength p, for different values of interaction range k.

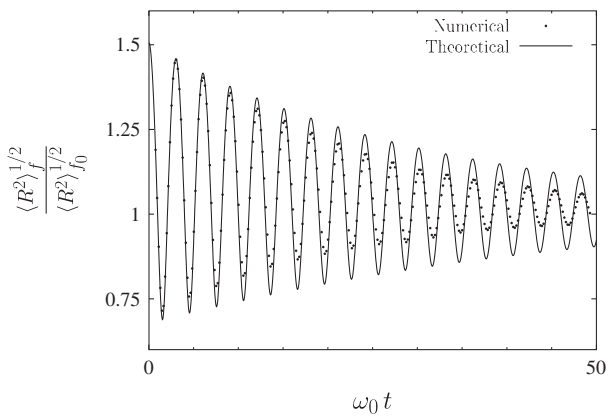

FIG. 3. Evolution of the typical size of the cloud. The space dimension is $d = 2$, and the interactions are repulsive. The parameters are $k = 4$ (short-range interaction), $\omega_0/\kappa = 17.8$ and $p = 0.63$.

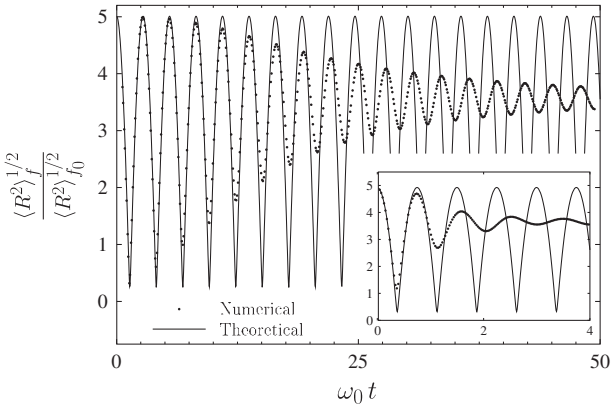

FIG. 4. Evolution of the typical size of the cloud in one of the few negative cases. The space dimension is $d = 3$, and the interactions are attractive. The parameters are $k = 0$ (long-range interaction), $\omega_0 = 17.8$, $\kappa = 0$ (microcanonical ensemble), and $p = 2.2$. Inset: Same parameters, except $p = 70$.

To explain these results, we first stress that in the limit $p \to 0$, Eq. (7) is *exact*. In this case, it may indeed be derived directly from Newton equations, as done in [15] in the linear approximation. The correct generalization for an arbitrary perturbation amplitude is given by Eq. (7). For intermediate p, we attribute the discrepancy between the predicted and simulated oscillation amplitudes to effects that are not taken into account in the simple dynamical ansatz (3), and thus limit the validity of Eq. (7). Indeed, for long-range interactions, one would expect collective effects (Landau damping, phase mixing, etc.) to play a role in the oscillation decay (beyond the friction κ), which are neglected in the ansatz. Similarly, for short-range interactions, two-body collisions should be important. This explanation is supported by the frictionless microcanonical simulations: when there is no amplitude decay in the microcanonical ensemble, which means that phase mixing and two-body collisions are negligible, Eq. (7) correctly predicts the breathing frequency and amplitude, with or without friction. Conversely, amplitude decay or modulation in the microcanonical ensemble is associated with discrepancies between theory and simulations.

In summary, starting from the first equation of the BBGKY hierarchy and a scaling ansatz for the dynamics, we have derived a nonlinear equation describing the breathing oscillations of trapped particles interacting via forces satisfying (5). The derivation and equation are valid independently of the temperature, interaction strength, interaction range, and dimensionality of the physical space, and it is successfully compared to direct numerical simulations. The main limitation is due to phase mixing phenomena for long-range interacting systems and two-body collisions in short-range interacting ones, especially for weak repulsive and attractive interactions, where they introduce damping and loss of coherence, unaccounted for in the scaling ansatz. We have concentrated on power-law interactions, but condition (5) for the force is more general. It includes, for instance, Dirac and dipolar potentials, and some nonpotential forces such as the attenuation force in magneto-optical traps [21]; the ansatz should be useful in such cases. Beyond the breathing mode, a generic study of quadrupolar modes would be very desirable, as harmonic traps are often anisotropic in experimental situations. This is not possible with the scaling ansatz, except in special cases. Even though no real breathing mode [15] exists when interactions are not power law, a generalization of this mode may exist. Following the lines of this Letter, and applying methods used in [8], a more general approach should be possible.

*olivetti@unice.fr

[1] D. Guéry-Odelin, Phys. Rev. A **66**, 033613 (2002).
[2] Y. Castin and R. Dum, Phys. Rev. Lett. **77**, 5315 (1996).
[3] Yu. Kagan, E. L. Surkov, and G. V. Shlyapnikov, Phys. Rev. A **55**, R18 (1997).
[4] D. H. E. Dubin, Phys. Rev. Lett. **66**, 2076 (1991).
[5] D. H. E. Dubin, Phys. Fluids B **5**, 295 (1993).
[6] Sh. Amiranashvili, M. Y. Yu, and L. Stenflo, Phys. Rev. E **67**, 016408 (2003).
[7] T. E. Sheridan, C. R. Buckey, D. J. Cox, R. J. Merrill, and W. L. Theisen, Phys. Lett. A **329**, 88 (2004).
[8] T. E. Sheridan, Phys. Plasmas **11**, 5520 (2004).
[9] D. F. V. James, Appl. Phys. B **66**, 181 (1998).
[10] S. A. Tatarkova, A. E. Carruthers, and K. Dholakia, Phys. Rev. Lett. **89**, 283901 (2002).
[11] V. A. Schweigert and F. M. Peeters, Phys. Rev. B **51**, 7700 (1995).
[12] B. Partoens and F. M. Peeters, Condens. Matter Phys. **9**, 5383 (1997).
[13] S. W. S. Apolinario, B. Partoens, and F. M. Peeters, New J. Phys. **9**, 283 (2007).
[14] S. Chandrasekhar and D. D. Elbert, Mon. Not. R. Astron. Soc. **155**, 435 (1972).
[15] C. Henning, K. Fujioka, P. Ludwig, A. Piel, A. Melzer, and M. Bonitz, Phys. Rev. Lett. **101**, 045002 (2008).
[16] The boundary between long and short range for equilibrium statistical properties is $(k-1)/d = 1$, which corresponds to the integrability limit of the interaction potential [17]. For dynamical properties, it seems preferable to use the present definition.
[17] *Dynamics and Thermodynamics of Systems with Long Range Interactions*, edited by T. Dauxois, S. Ruffo, E. Arimondo, and M. Wilkens, Lecture Notes in Physics Vol. 602 (Springer, Berlin, 2002).
[18] T. D. Frank, *Nonlinear Fokker-Planck Equations: Fundamentals and Applications* (Springer-Verlag, Berlin, 2005).
[19] D. H. E. Dubin and T. M. O'Neil, Rev. Mod. Phys. **71**, 87 (1999).
[20] M. P. Allen and D. J. Tildesley, *Computer Simulation of Liquids* (Clarendon, Oxford, 1987).
[21] T. Walker, D. Sesko, and C. Wieman, Phys. Rev. Lett. **64**, 408 (1990).

Transport Theory and Statistical Physics, 39:524–551, 2010

ISSN: 0041-1450 print / 1532-2424 online
DOI: 10.1080/00411450.2011.567857

BREATHING DYNAMICS FOR SYSTEMS OF INTERACTING PARTICLES IN THE MICROCANONICAL AND CANONICAL DESCRIPTIONS

ALAIN OLIVETTI,[1] JULIEN BARRÉ,[1] BRUNO MARCOS,[1] FREDDY BOUCHET,[2] and ROBIN KAISER[3]

[1]Laboratoire J.A. Dieudonné, UMR CNRS 6621, Université de Nice-Sophia Antipolis, Parc Valrose, F-06108 Nice Cedex 02, France
[2]Laboratoire de Physique, ENS de Lyon, CNRS, Université de Lyon, 46 allée d'Italie, 69364 Lyon cedex 07, France
[3]Institut Non-Linéaire de Nice, UMR CNRS 6618, Université de Nice-Sophia Antipolis, France

By means of a dynamical ansatz, we study the breathing dynamics in systems of trapped interacting particles in a unified context, including a wide range of power law interactions and interaction strengths, at linear and nonlinear levels. We present detailed numerical tests of the general theory, and, motivated by Magneto-Optical Traps modeling, we extend it to the case of space-dependent friction and diffusion.

1. Introduction

Low-lying oscillatory modes are a natural object of study for systems of trapped interacting particles; they are an important tool to understand and characterize the collective effects. As such, they have been studied in many different areas of physics: confined plasmas, trapped cold atoms, Bose-Einstein condensates, colloidal particles, trapped ions, and astrophysical systems—the latter ones being self-confined by the interactions. These systems feature a wide variety of interactions: weak or strong, long or short range.

This work is supported by the ANR-09-JCJC-009401 INTERLOP project.
Address correspondence to Alain Olivetti, Laboratoire J. A. Dieudonné, UMR CNRS 6621, Université de Nice-Sophia Antipolis, Parc Valrose, F-06108 Nice Cedex 02, France. E-mail: alain.olivetti@unice.fr

In this article we will be concerned with the simplest nontrivial oscillatory mode for systems of trapped interacting particles in d dimensions: the breathing mode (Olivetti et al., 2009). It has been tackled in the literature using many different techniques, which we try to partially summarize here:

- A scaling ansatz to approximate the nonlinear dynamics of the Boltzmann-Vlasov equation for a classical gas is used in Guéry-Odelin (2002); this idea was introduced earlier in the context of the Gross-Pitaevskii equation (Castin and Dum, 1996; Kagan et al., 1997).
- In the confined plasma context, the problem is often studied through hydrodynamical equations, in the so-called cold fluid approximation (Dubin, 1991), where the dispersion relation for fluid modes in a cold spheroidal plasma is derived.
- Following an idea of Dubin (1993), Amiranashvili et al. (2003) give an approximate solution to the breathing mode of a $d = 1$ confined plasma beyond the cold fluid approximation, using an *ad hoc* closure of the hydrodynamical equations.
- Linearization of the Newtonian equations of motion around an equilibrium configuration and direct diagonalization have been used to study trapped ions or colloids interacting a Coulomb or Yukawa potential in $d = 1$ (James, 1998; Tatarkova et al., 2002), $d = 2$ (Schweigert and Peeters, 1995; Partoens and Peeters, 1997), and $d = 3$ (Apolinario and Peeters, 2007). It has been generalized recently in (Henning et al., 2008) to a whole class of potentials. However, this technique is a priori restricted to the zero temperature limit and small perturbations.
- Monopole modes of dusty plasmas interacting with a Yukawa potential are investigated in Sheridan and colleagues (Sheridan, 2004; Sheridan et al., 2004), using a kind of mean-field approximation.
- Breathing oscillations with attractive interactions have been studied in an astrophysical context using the Virial theorem (Chandrasekhar and Elbert, 1972).

Each method applies to a specific situation: Newton equations are adapted to a crystallized state with negligible thermal fluctuations, linearization assumes a small amplitude of oscillations, and the Vlasov equation is limited to weak correlations. Yet in all cases a

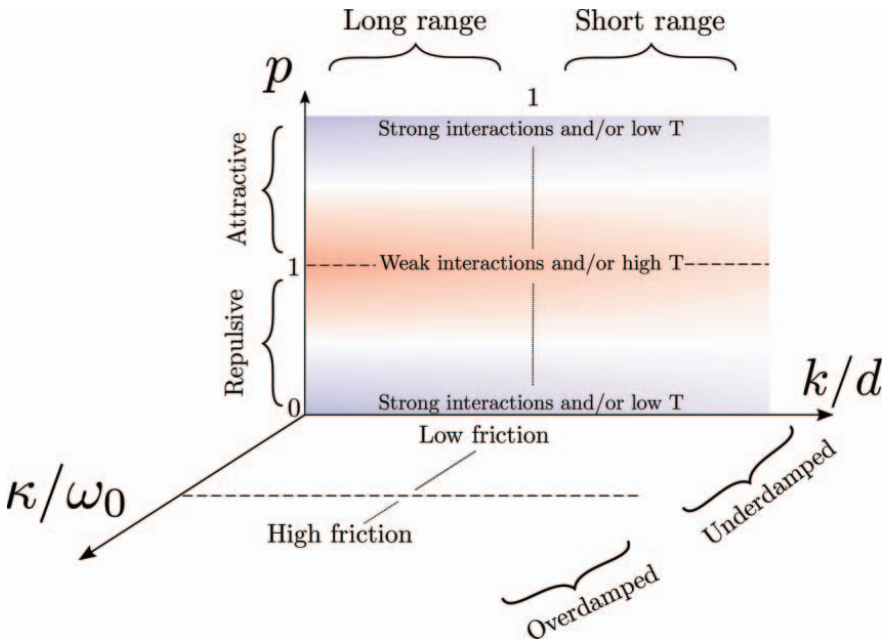

FIGURE 1 (color online). Diagram of the different regimes for the breathing dynamics. On the horizontal axis, the interaction range, measured by k/d. The interaction strength is changing along the vertical axis. The third axis represents the friction normalized by the trap frequency κ/ω_0.

similar equation for the breathing mode is obtained. In Olivetti and colleagues (2009), we introduced a theory based on an extension of the scaling ansatz technique, which classifies many of the previous examples in a common framework. In compensation this theory is mainly (but not entirely) limited to power law interactions and does not give access to more complicated modes beyond the monopole one. Figure 1 summarizes the different regimes we will study in this article, assuming a binary isotropic power-law interparticle force $F(r) \sim 1/r^k$ in d space dimensions. On the horizontal axis is the interaction range, which we will call long-range if $k/d \leq 1$ and short range otherwise. The case $k/d \leq 1$ corresponds to nonintegrable forces at large distances.[1] The vertical axis represents the interaction strength with respect to the thermal energy. The third axis represents the friction, normalized by the trap frequency.

In this article our goals are: *(i)* to present extensive numerical tests of the theory developed in Olivetti and coauthors (2009),

[1]The boundary between long and short range for equilibrium statistical properties is $(k-1)/d = 1$, which corresponds to the integrability limit of the interaction potential (Dauxois et al., 2002). For dynamical properties, it seems preferable to use the present definition.

investigating in particular its limits when the friction is increased; *(ii)* motivated by magneto-optical traps modeling (Labeyrie et al., 2006), to extend it to the case of space-dependent friction and diffusion; and *(iii)* to test this extension of the theory using direct molecular dynamics simulations.

In Section 2, we first review in detail the theory already presented in Olivetti and colleagues (2009), in a frictionless context, and provide comparisons with direct numerical simulations. In Section 3, we introduce some friction and diffusion and show that the equation for the breathing dynamics obtained with the ansatz method is exactly valid in the zero temperature limit, for all friction strength, for repulsive interactions. We then extensively test this equation against direct molecular dynamics simulations, to investigate its domain of validity. In Section 4, we extend the equation for the breathing dynamics to space-dependent friction and diffusion and test our results.

2. Breathing Oscillations Without Friction and Diffusion

2.1. Vlasov Equation

We consider a system of particles confined by an harmonic spherical trapping force $\mathbf{F}_{trap}(\mathbf{r}) = -\omega_0^2\mathbf{r}$, interacting with binary long range interaction forces $\mathbf{F}_{bin}$. Let us first assume that correlations between particles are weak; we can then use the Vlasov equation to model the system in the continuum limit. In this section, we assume that the system is Hamiltonian.

Using the one-particle distribution $f(\mathbf{r}, \mathbf{v}, t)$, the Vlasov equation reads:

$$\frac{\partial f}{\partial t} + \nabla_{\mathbf{r}}.(\mathbf{v} f) + \mathbf{F}_{trap}.\nabla_{\mathbf{v}} f + \mathbf{F}_{int}[f] \cdot \nabla_{\mathbf{v}} f = 0, \tag{1}$$

where $\mathbf{F}_{int}[f]$ is the interaction term given by:

$$\mathbf{F}_{int}[f](\mathbf{r}) = \int \mathbf{F}_{bin}(\mathbf{r}, \tilde{\mathbf{r}})\, f(\tilde{\mathbf{r}}, \mathbf{v}, t)\, d\tilde{\mathbf{r}} d\mathbf{v}. \tag{2}$$

We consider f_0, a stationary state solution of Eq. (1). If $\mathbf{F}_{bin} = -\nabla_{\mathbf{r}} V_{bin}$ is a potential force, then $\mathbf{F}_{int}[f] = -\nabla_{\mathbf{r}} V_{int}[f]$ is also

potential, and a natural choice for f_0 is the statistical equilibrium, parametrized by the inverse temperature β. This statistical equilibrium is implicitly defined by the equation

$$f_0(\mathbf{r}, \mathbf{v}) \propto e^{-\beta \mathbf{v}^2/2} e^{-\beta V_{int}[f_0](\mathbf{r})} e^{-\beta \omega_0^2 \mathbf{r}^2/2}. \tag{3}$$

Such an equilibrium does not always exist when the interaction is attractive. We will consider this statistical equilibrium for f_0 in this subsection, unless explicitly stated. We also assume that f_0 is isotropic in positions.

We now drastically simplify the dynamics by using a scaling ansatz (Guéry-Odelin, 2002; Castin and Dum, 1996; Kagan et al., 1997):

$$f(\mathbf{r}, \mathbf{v}, t) = f_0(\varphi(\mathbf{r}, \mathbf{v})), \tag{4}$$

with

$$\varphi(\mathbf{r}, \mathbf{v}) = (\mathbf{R} = \mathbf{r}/\lambda, \mathbf{V} = \lambda \mathbf{v} - \dot{\lambda} \mathbf{r}). \tag{5}$$

With this hypothesis all the time dependence in the dynamics is now included in the positive parameter λ. This ansatz is tailored to capture the radial dynamics; thus, we will not be able to look at higher order modes of the system, like quadrupole modes.

We justify the ansatz as follows. We assume that the spatial dynamics can be described with the simple scaling ansatz

$$\mathbf{R} = \frac{\mathbf{r}}{\lambda(t)}. \tag{6}$$

In the Hamiltonian description, we require the conservation of the phase space volume, *i.e.*, $d\mathbf{r}d\mathbf{v} = d\mathbf{R}d\mathbf{V}$. This implies that

$$\mathbf{V} = \lambda(t)\mathbf{v} + \mathbf{h}(\mathbf{r}, t), \tag{7}$$

where $\mathbf{h}$ is an arbitrary function of $\mathbf{r}$ and t. Integrating the Vlasov equation over the velocity variable, we obtain the continuity

equation

$$\frac{\partial \rho(\mathbf{r}, t)}{\partial t} + \frac{\partial\,(\mathbf{u}(\mathbf{r}, t)\rho(\mathbf{r}, t))}{\partial \mathbf{r}} = 0, \tag{8}$$

where the space density ρ and the velocity $\mathbf{u}$ are defined by

$$\begin{cases} \rho(\mathbf{r}, t) = \displaystyle\int f(\mathbf{r}, \mathbf{v}, t)\, d\mathbf{v}, \\ \rho(\mathbf{r}, t)\mathbf{u}(\mathbf{r}, t) = \displaystyle\int \mathbf{v} f(\mathbf{r}, \mathbf{v}, t)\, d\mathbf{v}. \end{cases} \tag{9}$$

Calling $\rho_0(\mathbf{r})$ the stationary solution for the density $\rho(\mathbf{r}, t)$, and injecting the scaling ansatz inside Eq. (8), we have:

$$\begin{aligned} &\frac{\partial}{\partial t}\left[\frac{1}{\lambda^d}\rho_0\left(\frac{\mathbf{r}}{\lambda}\right)\right] + \frac{1}{\lambda^{d+1}}\frac{\partial}{\partial \mathbf{r}}\left[\rho_0\left(\frac{\mathbf{r}}{\lambda}\right)\mathbf{u}\left(\frac{\mathbf{r}}{\lambda}, t\right)\right] \\ &\quad - \frac{1}{\lambda^{d+1}}\frac{\partial}{\partial \mathbf{r}}\left[\mathbf{h}(\mathbf{r}, t)\rho_0\left(\frac{\mathbf{r}}{\lambda}\right)\right] = 0. \end{aligned} \tag{10}$$

Assuming that f_0 is even with respect to its velocity variables (which is the case for (3)), the second term of Eq. (10) vanishes. Looking for a condition over $\mathbf{h}$, which separately cancels the terms containing ρ_0 and $\partial_{\mathbf{r}}\rho_0$, we finally obtain

$$\mathbf{h}(\mathbf{r}, t) = -\dot{\lambda}(t)\mathbf{r}. \tag{11}$$

Combining Eq. (6), (7), and (11) leads to the scaling ansatz (4).

After given this justification of the scaling ansatz (4), let us now insert it into Eq. (1). This leads to:

$$\sum_{i=1}^{d}\left\{\frac{V_i}{\lambda^2}\frac{\partial f_0}{\partial R_i} - R_i\lambda\frac{\partial f_0}{\partial V_i}\left(\ddot{\lambda} + \omega_0^2\lambda\right) + \lambda\mathbf{F}_{int}[f_0 \circ \varphi](\mathbf{r}).\nabla_{\mathbf{V}} f_0\right\} = 0. \tag{12}$$

We now assume that the binary interaction is homogeneous with degree $-k$ (we use here and in the following the word

"homogeneous" in its mathematical sense):

$$\mathbf{F}_{bin}(\lambda\mathbf{r}, \lambda\tilde{\mathbf{r}}) = \frac{1}{\lambda^k}\mathbf{F}_{bin}(\mathbf{r}, \tilde{\mathbf{r}}). \tag{13}$$

The previous relation eliminates the function φ in the interaction term:

$$\begin{aligned}\mathbf{F}_{int}[f_0 \circ \varphi](\mathbf{r}) &= \int \mathbf{F}_{bin}(\mathbf{r}, \lambda\tilde{\mathbf{r}})\, f_0(\tilde{\mathbf{r}}, \mathbf{v})\, d\tilde{\mathbf{r}} d\mathbf{v} \\ &= \frac{1}{\lambda^k}\int \mathbf{F}_{bin}(\mathbf{R}, \tilde{\mathbf{r}})\, f_0(\tilde{\mathbf{r}}, \mathbf{v})\, d\tilde{\mathbf{r}} d\mathbf{v} \\ &= \frac{1}{\lambda^k}\mathbf{F}_{int}[f_0](\mathbf{R}).\end{aligned} \tag{14}$$

Finally, using Eq. (14) and the fact that f_0 is a stationary solution of Eq. (1), one can substitute the interaction term by a linear combination of f_0 and its derivatives. Equation (12) becomes

$$\sum_{i=1}^{d} V_i \frac{\partial f_0}{\partial R_i}\left(\frac{1}{\lambda^2} - \lambda^{1-k}\right) - R_i \frac{\partial f_0}{\partial V_i}\left[\lambda\left(\ddot{\lambda} + \omega_0^2\lambda\right) - \lambda^{1-k}\omega_0^2\right] = 0. \tag{15}$$

Multiplying it by $R_j V_j / N$ and integrating over $d\mathbf{R}d\mathbf{V}$ leads to a constraint on the parameter λ:

$$\ddot{\lambda} + \left(\lambda - \frac{1}{\lambda^k}\right)\omega_0^2 - \left(\frac{1}{\lambda^3} - \frac{1}{\lambda^k}\right)\frac{\langle V_j^2\rangle_{f_0}}{\langle R_j^2\rangle_{f_0}} = 0, \tag{16}$$

where j is a coordinate label, and we have set

$$\langle\chi\rangle_f = \frac{1}{N}\int \chi(\mathbf{r}, \mathbf{v})\, f(\mathbf{r}, \mathbf{v}, t)\, d\mathbf{r}d\mathbf{v}. \tag{17}$$

In the dynamical equation for λ (16), all parameters are computed as averages over the stationary distribution f_0. Since f_0 is isotropic in positions and velocities, $\langle V_j^2\rangle_{f_0}$ and $\langle R_j^2\rangle_{f_0}$ do not depend on j: Eq. (16) is the same for the d coordinates.

Taking higher order moments of Eq. (15) would produce different equations for λ, implying that the only solution is the trivial one $\lambda = 1$. This is a consequence of the fact that the ansatz does

not contain any nontrivial exact solution of the Vlasov equation. One may hope however that Eq. (16) satisfactorily describes the breathing dynamics over short times: this will be tested in numerical simulations.

A dimensionless parameter appears naturally in Eq. (16), which we define as

$$p = \frac{\langle V_j^2 \rangle_{f_0}}{\omega_0^2 \langle R_j^2 \rangle_{f_0}}. \tag{18}$$

When f_0 is given by (3), it can be interpreted as the ratio between the thermal energy $k_B T$ and the typical potential energy due to the trap $E_{trap} \sim \omega_0^2 \langle R^2 \rangle_{f_0}$:

$$p \sim \frac{k_B T}{E_{trap}}. \tag{19}$$

Using (3) for a system with and without interactions ($V_{int} = 0$), at the same temperature, we have

$$\langle V_j^2 \rangle_{f_0, V_{int}=0} = \langle V_j^2 \rangle_{f_0} = \omega_0^2 \langle R_j^2 \rangle_{f_0, V_{int}=0},$$

which implies

$$p = \frac{\langle R_j^2 \rangle_{f_0, V_{int}=0}}{\langle R_j^2 \rangle_{f_0}}.$$

We can summarize this:

- $0 < p < 1$ corresponds to repulsive interactions, with $p \ll 1$ the strong interaction regime.
- If $p \sim 1$, the system is weakly interacting.
- For $p > 1$, the interaction is attractive, and $p \gg 1$ corresponds to the strong interaction regime.

We now write (16) as

$$\ddot{\lambda} + \left(\lambda - \frac{p}{\lambda^3} + \frac{p-1}{\lambda^k}\right)\omega_0^2 = 0. \tag{20}$$

2.2. Extension of the Ansatz

In the previous subsection, we started from the Vlasov equation. In order to take into account correlations between particles (and thus describe also short-range interacting systems) we start now from the first equation of the Bogolyubov-Born-Green-Kirkwood-Yvon (BBGKY) hierarchy:

$$\frac{\partial f}{\partial t} + \nabla_{\mathbf{r}}.(\mathbf{v} f) + \mathbf{F}_{trap}.\nabla_{\mathbf{v}} f + C[g] = 0, \tag{21}$$

where $C[g]$ is the interaction term which is given now by:

$$C[g](\mathbf{r}_1, \mathbf{v}_1, t) = \int \mathbf{F}_{bin}(\mathbf{r}_1, \mathbf{r}).\nabla_{\mathbf{v}_1} g(\mathbf{r}_1, \mathbf{v}_1, \mathbf{r}, \mathbf{v}, t)\, d\mathbf{r} d\mathbf{v} \tag{22}$$

and $g(\mathbf{r}_1, \mathbf{v}_1, \mathbf{r}, \mathbf{v}, t)$ the two-particles distribution. We stress that Eq. (21), in contrast with the Vlasov equation, can also describe the dynamics of strongly correlated systems and also short-range interacting systems. Note that Eq. (21) is strictly equivalent to the Hamiltonian equation because we have not yet done any hypothesis on the unknown function g. We assume the existence of a stationary state f_0 and g_0, for instance the statistical equilibrium, and perform the closure using the previous scaling ansatz (4), extended to the two-particles function g, as done in Olivetti and colleagues (2009):

$$\begin{cases} f(\mathbf{r}_1, \mathbf{v}_1, t) = f_0(\varphi(\mathbf{r}_1, \mathbf{v}_1)) \\ g(\mathbf{r}_1, \mathbf{v}_1, \mathbf{r}_2, \mathbf{v}_2, t) = g_0(\psi(\mathbf{r}_1, \mathbf{v}_1, \mathbf{r}_2, \mathbf{v}_2)) \end{cases} \tag{23}$$

with

$$\begin{cases} \varphi(\mathbf{r}_1, \mathbf{v}_1) = (\mathbf{R}_1 = \mathbf{r}_1/\lambda, \mathbf{V}_1 = \lambda \mathbf{v}_1 - \dot{\lambda}\mathbf{r}_1) \\ \psi(\mathbf{r}_1, \mathbf{v}_1, \mathbf{r}_2, \mathbf{v}_2) = (\varphi(\mathbf{r}_1, \mathbf{v}_1), \varphi(\mathbf{r}_2, \mathbf{v}_2)). \end{cases} \tag{24}$$

Once again, the positive parameter λ contains all the time dependence of the dynamics. The computations are similar to those in Subsection 2.1. Introducing the ansatz in Eq. (21) yields:

$$\sum_{i=1}^{d} \left\{ \frac{V_i}{\lambda^2} \frac{\partial f_0}{\partial R_i} - R_i \lambda \frac{\partial f_0}{\partial V_i} \left(\ddot{\lambda} + \omega_0^2 \lambda \right) + C[g_0 \circ \psi](\mathbf{r}_1, \mathbf{v}_1, t) \right\} = 0. \tag{25}$$

The homogeneity of the binary forces (see Eq.(13)) allows us to simplify the interaction term:

$$\begin{aligned} C[g_0 \circ \psi](\mathbf{r}, \mathbf{v}) &= \int \mathbf{F}_{bin}(\lambda \mathbf{R}, \lambda \mathbf{S}).\nabla_{\mathbf{v}} \left[g_0(\mathbf{R}, \mathbf{V}, \mathbf{S}, \mathbf{W}) \right] d\mathbf{S} d\mathbf{W} \\ &= \lambda \int \mathbf{F}_{bin}(\lambda \mathbf{R}, \lambda \mathbf{S}).\nabla_{\mathbf{V}} g_0(\mathbf{R}, \mathbf{V}, \mathbf{S}, \mathbf{W}) d\mathbf{S} d\mathbf{W} \\ &= \lambda^{1-k} C[g_0](\mathbf{R}, \mathbf{V}). \end{aligned} \tag{26}$$

We now multiply by $R_j V_j / N$ and integrate over $d\mathbf{R} d\mathbf{V}$. Introducing, as before, the dimensionless parameter p defined in Eq. (18), we obtain the equation:

$$\ddot{\lambda} + \left(\lambda - \frac{p}{\lambda^3} + \frac{p-1}{\lambda^k} \right) \omega_0^2 = 0, \tag{27}$$

which is exactly the same as Eq. (20).

2.3. Analysis of the Breathing Dynamics

We can rewrite Eq. (20) as an equation of an anharmonic oscillator in the external potential ϕ:

$$\ddot{\lambda} + \phi'(\lambda) = 0 \tag{28}$$

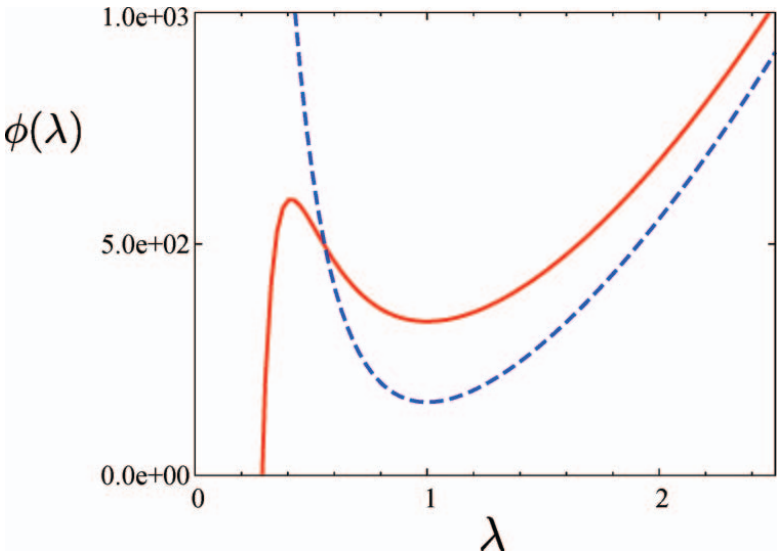

FIGURE 2 (color online). Shape of the potential for two different cases: repulsive (dotted line) and attractive with $k > 3$ (solid line).

with

$$\phi(\lambda) = \begin{cases} \omega_0^2 \left(\frac{1}{2}\lambda^2 + \frac{1}{2}\frac{p}{\lambda^2} + \frac{p-1}{1-k}\lambda^{1-k} \right), & \text{if } k \neq 1, \\ \omega_0^2 \left(\frac{1}{2}\lambda^2 + \frac{1}{2}\frac{p}{\lambda^2} + (p-1)\log\lambda \right), & \text{if } k = 1. \end{cases} \tag{29}$$

The first term in Eq. (29) is the quadratic confining potential, the second one corresponds to a kinetic pressure term (which does no depend on the dimension d considered), and the last one is introduced by the two-body interaction.

The shape of the potential determines the form of the oscillations. For repulsive interactions ($p < 1$), the potential is convex for all k. It diverges as $\phi \sim \lambda^{-2}$ as $\lambda \to 0$ and behaves as $\phi \sim \lambda^2$ as $\lambda \to \infty$, which ensures that the system oscillates around its unique minimum $\lambda = 1$. For attractive ($p > 1$) interactions and $0 \leqslant k \leqslant 3$, the potential presents the same properties. For attractive interactions and $k > 3$, the potential diverges to $-\infty$ as λ^{1-k} for small λ. If $p < 1 - 4/(3-k)$, $\lambda = 1$ is a metastable stationary state, and there exists an unstable stationary state for $\lambda^* < 1$, see Figure 2. For $p > 1 - 4/(3-k)$, $\lambda = 1$ is an unstable stationary state and there is a metastable state for $\lambda > 1$.

From Eq. (16), we obtain the general expression of the linearized breathing oscillation frequency as a function of the

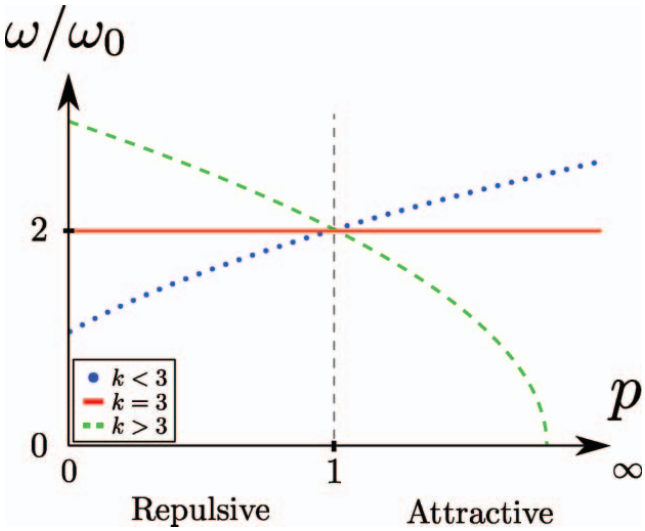

FIGURE 3 (color online). Frequency of the linearized breathing mode as a function of the interaction strength p, for different values of interaction range k.

interaction range k and the interaction strength p:

$$\omega(k, p) = \omega_0 \left[(3 - k)(p - 1) + 4\right]^{1/2}. \tag{30}$$

This expression recovers the well-known limits $\omega = 2\omega_0$ for a non-interacting gas ($p = 1$) and $\omega = \sqrt{3}\omega_0$ for a strongly interacting Coulomb plasma ($p = 0$, $k = 2$) (Dubin and ONeil, 1999). It provides a generalization to the whole (k, p) plane shown in Figure 1 and is independent of the dimension. We note that for $k > 3$ and repulsive interactions ($p < 1$), the breathing frequency is an increasing function of the interaction strength (decreasing function of p); this corresponds in 3 dimensions to short-range interactions ($k > d$). On the other hand, for $k < 3$ it is a decreasing function of the interaction strength (increasing function of p); this corresponds in 3 dimensions to long-range interactions ($k < d$). See Figure 3 for details.

2.4. *Comparison with the Literature*

We can now compare Eqs. (16) and (27) to the results found in the literature for various specific situations. Oscillations of crystallized systems (James, 1998; Tatarkova et al., 2002; Partoens and Peeters, 1997; Henning et al., 2008) correspond to negligible

pressure effects, *i.e.* $p = 0$ and the λ^{-3} term of is absent. In Amiranashvili and colleagues (2003), the authors consider a $d = 1$ plasma ($k = 0$) with p not too small, and introduce a pressure yielding the λ^{-3} term, which leads to the exact equivalent of Eq. (16).

In Guéry-Odelin (2002) considered a classical gas with "mean field" interactions, given by a Dirac δ potential. This corresponds to a homogeneity degree for the force $-k = -d-1$. Equation (16) contains this case, and this emphasizes that the present theory is not only valid for power-law forces.

The Yukawa potential

$$V(\mathbf{r}) \propto \frac{\exp(-|\mathbf{r}|/L_s)}{|\mathbf{r}|}, \tag{31}$$

is not homogeneous, so our method does not work. However, both in the Coulombian limit, where the shielding length L_s is much larger than the system size, and the opposite one, where L_s is much smaller than the system size, the Yukawa potential may be approximated by a homogeneous potential, respectively a Coulomb and a Dirac δ potential. Equation (16) then reproduces the results of Sheridan et al. (2004) and Sheridan (2004), obtained by other means.

2.5. *Comparison with Numerical Simulations*

In order to test the domain of validity of Eq. (27), we have performed several numerical simulations. We have considered different force index k, parameter p, and amplitude of initial perturbation, in one, two, and three dimensions.

We simulate the system using a molecular dynamics approach with $N = 4000$ particles unless otherwise stated. The integrator scheme is a Verlet-leapfrog algorithm (Allen and Tildesley, 1987) in the micro-canonical ensemble. The forces are exactly computed at each time-step.

The computer simulations are performed as follows: we first equilibrate the system in a stationary state using a Langevin thermostat (see Section 3.3). Then, at $t = 0$, we introduce a perturbation by rescaling the positions and velocities according to Eqs. (4) and (5), and we let the system evolve. A similar simulation of

a $d = 1$ Coulomb system has been performed in Amiranashvili and colleagues (2003), corresponding to cases with $k/d = 0$ and $p < 1$. In the following we present the results of the simulations and a comparison with the theory developed here. We have studied most of the possible combinations between *(i)* repulsive or attractive interactions, *(ii)* short or long range interactions, *(iii)* weak or strong interactions, and *(iv)* small or large amplitudes oscillations. Figure 4 shows some of our numerical tests, which we describe in the following:

- We have extensively studied the case in which the interaction is repulsive. The results are the following, classified according to the interaction strength: for *strong interactions* ($p \ll 1$) the ansatz describes very well both the amplitude and frequency of oscillation, for all the cases considered, and that for many oscillations. This is because the ansatz is *exact* in the limit $p \to 0$, as we will show in Subsection 3.1. We include two examples (Figures 4(a) with a very small p and 4(d) for $p = 0.166$), respectively with $d = 3$ and $d = 2$, both of them for small amplitude oscillations and short-range interaction. Long-range and/or large amplitude oscillations lead to the same conclusions.

  When p is of order 1, the ansatz gives a less accurate description of the simulations. It is in general able to predict the frequency of several oscillations, but gives less good results for the amplitudes. The ansatz (4) predicts a self-similar evolution of the density:

$$\rho(\mathbf{r}, t) = \lambda^{-d} \rho_0 \left(\frac{\mathbf{r}}{\lambda} \right). \tag{32}$$

  It is therefore not able to describe, *e.g.*, the evolution of the density if particles that are in a given shell of the initial (spherical) distribution are transported during the evolution to another shell (which is called "shell crossing" in fluid mechanics, see *e.g.*, Buchert, 1992). For long-range interactions, such phenomena occurs during the so-called violent relaxation, which is a well-known process of relaxation to a quasi-stationary state (Lynden-Bell, 1967). Figures 4(c) and 4(d) illustrate this situation for long-range interaction and different initial perturbations. The ansatz predicts no decay of the oscillation amplitude,

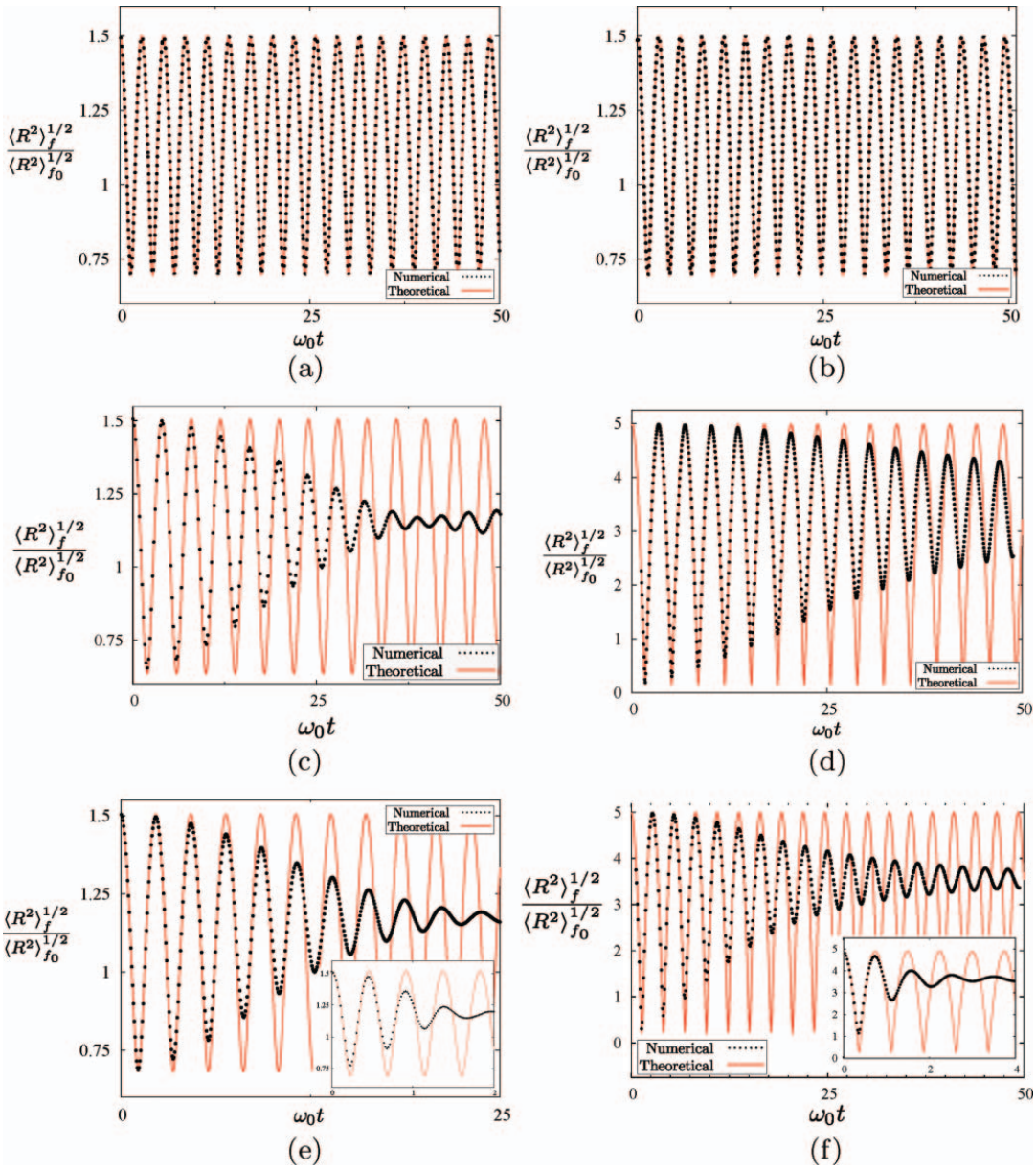

FIGURE 4 (color online). Microcanonical evolution of the typical size of the cloud ($N = 4000$, $\omega_0 = 17.8$). (a) The space dimension is $d = 3$, and the interactions are repulsive. The parameters are $k = 4$ (short range interaction), $p = 1.2 \times 10^{-3}$ and $(\lambda, \dot{\lambda})|_{t=0} = (1.5, 0.0)$. (b) The space dimension is $d = 2$, and the interactions are repulsive. The parameters are $k = 4$ (short range interaction), $p = 1.66 \times 10^{-1}$ and $(\lambda, \dot{\lambda})|_{t=0} = (1.5, 0.0)$. (c) The space dimension is $d = 3$, and the interactions are repulsive. The parameters are $k = 0$ (long range interaction), $p = 4.5 \times 10^{-1}$ and $(\lambda, \dot{\lambda})|_{t=0} = (1.5, 0.0)$. (d) The space dimension is $d = 3$, and the interactions are repulsive. The parameters are $k = 0$ (long range interaction), $p = 4.4 \times 10^{-1}$ and $(\lambda, \dot{\lambda})|_{t=0} = (5.0, 0.0)$. (e) The space dimension is $d = 3$, and the interactions are attractive. The parameters are $k = 0$ (long range interaction), $p = 2.2$ and $(\lambda, \dot{\lambda})|_{t=0} = (1.5, 0.0)$. Same parameters for the inset except $p = 70$. (f) The space dimension is $d = 3$, and the interactions are attractive. The parameters are $k = 0$ (long range interaction), $p = 2.2$ and $(\lambda, \dot{\lambda})|_{t=0} = (5.0, 0.0)$. Same parameters for the inset except $p = 70$.

whereas the simulations show such decay: we may then attribute this to the "violent relaxation" phenomenon. In the case of short-range interactions, a similar approximate description by the ansatz of the simulations is observed. In this case, a mechanism candidate for the loss of coherence in the oscillations (and hence their decay) is two-body collisions, which is an efficient relaxation process in such short-range interacting systems.

- For numerical reasons, we only simulated in the attractive case long-range interacting systems. We show such a numerical experiment in Figure 4(e) and 4(f), for $k = 0$ and $p = 2.2$ ($p = 70$ for inset) in $d = 3$. In these cases the "violent relaxation" is always important, which explains the decay in the oscillation amplitude observed in the simulations and not predicted by the ansatz. Finally remark that a large amplitude oscillation leads to a worse prediction than in the repulsive case.

On Figures 4(c)–4(f), we see that the asymptotic value of $\langle R^2 \rangle_f / \langle R^2 \rangle_{f_0}$ seems to be different from 1, indicating a relaxation to a stationary state different from the initial one. This was to be expected, as the initial perturbation changes the energy of the system with respect to the reference state f_0, and there is no dissipation. Since the ansatz is built on the reference stationary state f_0, one cannot hope that it will be relevant to describe the asymptotic stationary state.

On a 3D system with Coulomb interactions, we have checked that our numerical results do not change significantly performing simulations with $N = 1000$ and $N = 10{,}000$ particles. After 10 oscillations, we observe a difference around 1% in the amplitude and no sizable difference for the frequencies.

3. Breathing Oscillations with Friction and Diffusion

In many cases, it is reasonable to assume that particles, rather than following a Hamiltonian evolution, are subjected to small random uncorrelated forces, and a friction: this situation is conveniently modeled by adding to the Vlasov equation a Fokker-Planck operator with a positive constant friction κ and diffusion D, which amounts to define a temperature.

3.1. Small T Limit for Repulsive Interactions

In this subsection we consider the zero temperature limit of the model for a repulsive interaction, *i.e.*, the limit in which $p \to 0$.[2] This is also the limit where the random force is negligible, so that the dynamics is described by Newton equations.

In this case, the reference stationary state will be a stationary configuration of the particles. Let us consider such a stationary configuration $\{\mathbf{r}_i^0\}_{i=1}^N$ for the N particles. The force $\mathbf{F}_i^0$ on each particle therefore vanishes:

$$\mathbf{F}_i^0 = \mathbf{F}_{trap}\big(\mathbf{r}_i^0\big) + \sum_{j\neq i} \mathbf{F}_{bin}\big(\mathbf{r}_j^0 - \mathbf{r}_i^0\big) = \mathbf{0}. \tag{33}$$

We consider now a breathing dynamics $\mathbf{r}_i(t) = \lambda(t)\mathbf{r}_i^0$. Newton equations read

$$\ddot{\lambda}\mathbf{r}_i^0 = \mathbf{F}_{trap}\big(\lambda(t)\mathbf{r}_i^0\big) - \kappa\dot{\lambda}\mathbf{r}_i^0 + \sum_{j\neq i} \mathbf{F}_{bin}\big(\lambda\mathbf{r}_j^0 - \lambda\mathbf{r}_i^0\big) \tag{34}$$

$$= -\omega_0^2\lambda\mathbf{r}_i^0 - \kappa\dot{\lambda}\mathbf{r}_i^0 + \lambda^{-k}\sum_{j\neq i} \mathbf{F}_{bin}\big(\mathbf{r}_j^0 - \mathbf{r}_i^0\big) \tag{35}$$

$$= -\omega_0^2\lambda\mathbf{r}_i^0 - \kappa\dot{\lambda}\mathbf{r}_i^0 + \omega_0^2\lambda^{-k}\mathbf{r}_i^0. \tag{36}$$

From the first equation to the second one, we have used the homogeneity of the binary force; from the second one to the third, we have used Eq. (33) to express the interaction term as a function of the trap force. This yields an equation for λ

$$\ddot{\lambda} = -\kappa\dot{\lambda} + \omega_0^2(\lambda^{-k} - \lambda), \tag{37}$$

Putting $\kappa = 0$ in Eq. (37) and $p = 0$ in Eq. (20), one finds the same equation. This calculation is very similar to the one done in Henning and colleagues (2008); in this reference, the authors linearize the particles motion, thus limiting themselves to small deviations from the reference state. We have shown here that this restriction is unnecessary.

[2]This limit for an attractive interaction, $p \to \infty$, is trivial: all the particles collapse on a point in the center of the trap.

3.2. Vlasov-Fokker-Planck Equation

When the random force is not negligible, our new starting point is now the Vlasov-Fokker-Planck equation:

$$\frac{\partial f}{\partial t}+\nabla_{\mathbf{r}}.(\mathbf{v}f)+\mathbf{F}_{trap}.\nabla_{\mathbf{v}}f+\mathbf{F}_{int}[f].\nabla_{\mathbf{v}}f = D\Delta_{\mathbf{v}}f+\kappa\nabla_{\mathbf{v}}.(\mathbf{v}f). \quad (38)$$

Once again, we assume the existence of a stationary state f_0 solution of Eq. (38). If the binary interaction is potential and repulsive, there is indeed a unique stationary state of (38), given by the canonical statistical equilibrium (3) (see for instance Bouchet and Corvellec, 2010), appendix E.

As done in Section 2.2, the Vlasov part on the left hand side of Eq. (38) may be replaced by the first equation of the BBGKY hierarchy. We will not repeat these computations here.

Inserting into (38) the same scaling ansatz as in Section 2.1, and performing the same computation, one obtains the following equation:

$$\sum_{i=1}^{d}\Bigg\{ V_i\frac{\partial f_0}{\partial R_i}\left(\frac{1}{\lambda^2}-\lambda^{1-k}\right)+D\frac{\partial^2 f_0}{\partial V_i^2}(\lambda^{1-k}-\lambda^2)-R_i\frac{\partial f_0}{\partial V_i}$$
$$\times\left[\lambda\left(\ddot{\lambda}+\omega_0^2\lambda\right)-\lambda^{1-k}\omega_0^2+\kappa\lambda\dot{\lambda}\right]+\kappa\frac{\partial\,(V_i f_0)}{\partial V_i}(\lambda^{1-k}-1)\Bigg\}=0. \quad (39)$$

Taking the moment R_jV_j of this equation yields the equation for λ:

$$\ddot{\lambda}+\kappa\dot{\lambda}+\left(\lambda-\frac{p}{\lambda^3}+\frac{p-1}{\lambda^k}\right)\omega_0^2=0\,, \quad (40)$$

where we have used for p the same definition as (18). As in the case without friction, taking higher order moments of Eq. (39) yields different equations for λ, implying $\lambda=1$. However, at variance with the case without friction, already the second order moment V_j^2 implies that the only exact solution compatible with the ansatz is $\lambda=1$. We also note that Eq. (40) is compatible with Eqs. (20) and (37) respectively in the limits $\kappa\to 0$ and $p\to 0$.

As a consequence, one may expect Eq. (40) to give useful information on the breathing dynamics at small friction or small p, but its precise domain of validity has to be investigated numerically.

3.3. Comparison with Numerical Simulations

We have performed the numerical simulations in the same setting as in Section 2.5, adding a thermostat. We use a Langevin – Verlet numerical scheme in which the force during each time-step is assumed to vary linearly with time, as the one described in Allen and Tildesley (1987). Our goal is to investigate in which regions of the $(p, k/d, \kappa/\omega_0)$ space the scaling ansatz can be useful, see Figure 1. We have used $N = 1000$ and $N = 5000$ particles considering successively one, two or three space dimension, with $k = 0$. In each case we have performed the simulations varying p and κ following a grid in the plane $(\kappa/\omega_0, p)$, restricting ourselves to repulsive interactions.

In Section 2.5, we have seen that the constant energy simulations showed a very good agreement with the reduced dynamics as far as the oscillation frequency is concerned, and some disagreement concerning the oscillation amplitude. Since we would like to assert here the effect of friction and diffusion, we concentrate on the oscillation frequencies, and use the following criterion to estimate the agreement or disagreement between the simulation and the reduced dynamics Eq. (40):

- In the underdamped regime we consider the relative difference between the theoretical and numerical times for the nth maximum of the oscillation: $|t^n_{theo} - t^n_{num}|/t^n_{theo}$. We choose n to be the last maximum above the noise level.
- In the overdamped regime we consider the half-life time of the initial perturbation: $|t^{1/2}_{theo} - t^{1/2}_{num}|/t^{1/2}_{theo}$.

Figure 5 confirms that for $k = 0$ close to axes $p = 0$ and/or $\kappa/\omega_0 = 0$ the scaling ansatz method leads to reasonable predictions. On the contrary when we approach an overdamped dynamics, the scaling ansatz rapidly fails. We expect a similar picture for different values of k. Figure 6 represents some examples in the underdamped regime for different systems. Frequencies are quite precisely predicted by the ansatz, even if the amplitude's decay is

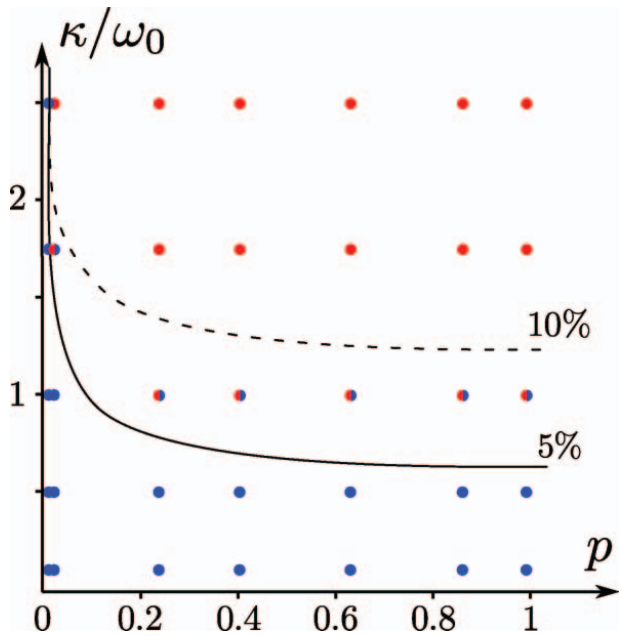

FIGURE 5 (color online). Validity of the scaling ansatz in the plane $(\kappa/\omega_0, p)$ plane. The simulations are done with $N = 5000$ particles and a one-dimensional Coulombian interaction ($k = 0$) with $\omega_0 = 17.8$ and $(\lambda, \dot{\lambda})|_{t=0} = (0.3, 0.0)$. Note that the picture does not appreciably change is we consider instead $N = 1000$ or $d = 2,\ 3$. Blue circle: frequency error $\leq 5\%$; half-blue/red circle: $5\% <$ error $\leq 10\%$; red circle: error $> 10\%$; solid and dashed line represent respectively the qualitative boundaries for 5% and 10% frequency error. For a definition of the frequency error, see text.

not negligible. Note that contrary to simulations done in Section 2.5, the initial state f_0 is also the final one, since the system has a unique stationary state.

4. Space Dependent Friction

We extend in this section the study of the breathing dynamics with the ansatz method to the case where the friction coefficient κ as well as the diffusion constant D are space-dependent. One physical motivation for this extension is the physics of Magneto-Optical Traps (MOTs). In an atomic cloud confined in a MOT, the interaction of atoms with lasers induces a friction and a diffusion; however, it is known that the intensity of these friction and diffusion depends on the atom position and that it may have important dynamical consequences (Labeyrie et al., 2006). Although we will concentrate here on the effect of a space-dependent friction, a precise modeling of a MOT would clearly need to take into account other effects.

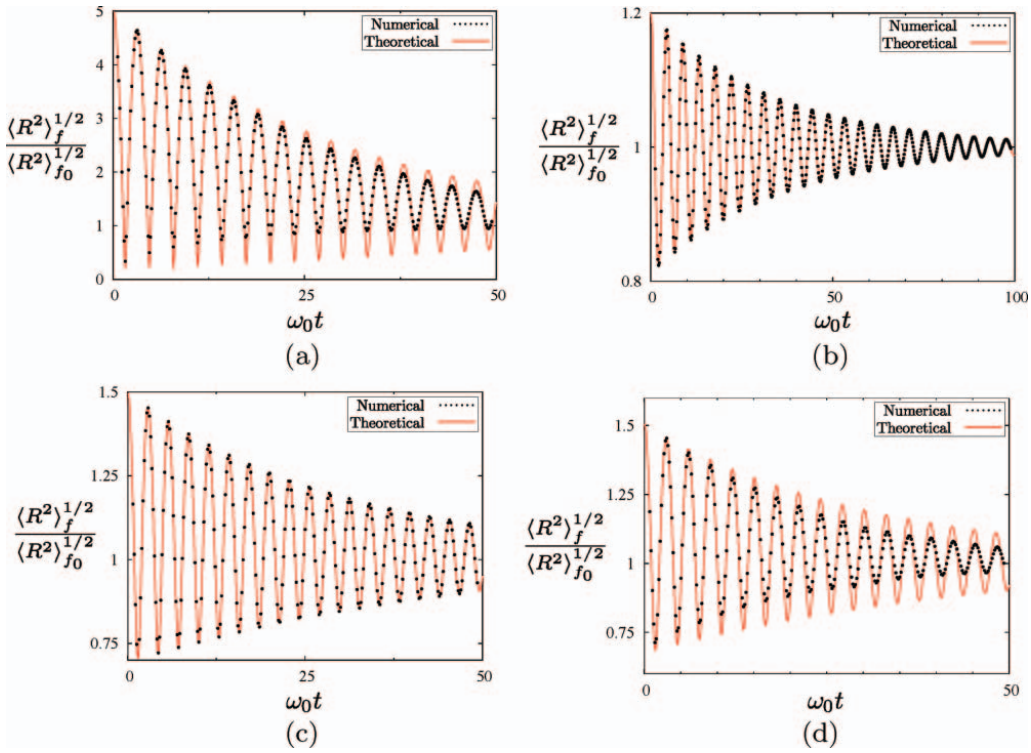

FIGURE 6 (color online). Evolution of the typical size of the cloud in the underdamped case ($N = 4000$, $\kappa/\omega_0 = 5.6 \times 10^{-2}$). (a) The space dimension is $d = 3$, and the interactions are repulsive. The parameters are $k = 1$ (long range interaction), $p = 5.0 \times 10^{-1}$ and $(\lambda, \dot{\lambda})|_{t=0} = (5.0, 0.0)$. (b) The space dimension is $d = 3$, and the interactions are repulsive. The parameters are $k = 1$ (long range interaction), $p = 1.5 \times 10^{-3}$ and $(\lambda, \dot{\lambda})|_{t=0} = (1.2, 0.0)$. (c) The space dimension is $d = 3$, and the interactions are repulsive. The parameters are $k = 4$ (short range interaction), $p = 1.2 \times 10^{-3}$ and $(\lambda, \dot{\lambda})|_{t=0} = (1.5, 0.0)$. (d) The space dimension is $d = 2$, and the interactions are repulsive. The parameters are $k = 4$ (short range interaction), $p = 6.3 \times 10^{-1}$ and $(\lambda, \dot{\lambda})|_{t=0} = (1.5, 0.0)$.

4.1. Dynamical Equation

Our goal is to obtain an effective dynamical equation for the breathing dynamics similar to Eq. (40), which would also be valid in both the small friction and strong repulsive interaction limits.

Eq. (40) was obtained taking the $R_i V_i$ moment of Eq. (39), which in turn came from the use of the dynamical ansatz. When the friction was homogeneous, it was then possible to check that Eq. (40) was compatible with the exact solution at $p = 0$ (or $T = 0$) Eq. (37). When friction and diffusion are not homogeneous, taking the $R_i V_i$ moment after introducing the dynamical ansatz yields an effective equation analogous to Eq. (40) but we do not have an exact solution at $p = 0$ any more to test its consistency.

We will thus rely again on numerical simulations to investigate its domain of validity.

We first introduce the dynamical ansatz into the equation with inhomogeneous friction and diffusion.

We start from the Vlasov Fokker-Planck equation including the space dependence $\kappa(\mathbf{r})$ and $D(\mathbf{r})$ (once again it is straightforward to do the same thing considering the first equation of the BBGKY hierarchy):

$$\frac{\partial f}{\partial t}+\nabla_{\mathbf{r}}.(\mathbf{v}f)+\mathbf{F}_{trap}.\nabla_{\mathbf{v}}f+\mathbf{F}_{int}[f].\nabla_{\mathbf{v}}f=D(\mathbf{r})\Delta_{\mathbf{v}}f+\kappa(\mathbf{r})\nabla_{\mathbf{v}}.(\mathbf{v}f). \tag{41}$$

We assume again the existence of a stationary state f_0. When friction and diffusion are not homogeneous, we have no simple implicit equation for f_0 such as (3).

Using the scaling ansatz method with stationary state f_0 leads to the equivalent equation of Eq. (39):

$$\begin{aligned}\sum_{i=1}^{d}\Bigg\{ & V_i\frac{\partial f_0}{\partial R_i}\left(\frac{1}{\lambda^2}-\lambda^{1-k}\right)+\frac{\partial^2 f_0}{\partial V_i^2}[\lambda^{1-k}D(\mathbf{R})-\lambda^2 D(\lambda\mathbf{R})]\\ & -R_i\frac{\partial f_0}{\partial V_i}\left[\lambda\left(\ddot{\lambda}+\omega_0^2\lambda\right)-\lambda^{1-k}\omega_0^2+\kappa(\lambda\mathbf{R})\lambda\dot{\lambda}\right]\\ & +\frac{\partial\,(V_i f_0)}{\partial V_i}[\lambda^{1-k}\kappa(\mathbf{R})-\kappa(\lambda\mathbf{R})]\Bigg\}=0.\end{aligned} \tag{42}$$

We now multiply Eq. (42) by R_jV_j/N, and integrate over $d\mathbf{R}d\mathbf{V}$. Hence:

$$\begin{aligned}\dot{\lambda}\frac{\left\langle\kappa(\lambda\mathbf{R})R_i^2\right\rangle_{f_0}}{\langle R_i^2\rangle_{f_0}}-\frac{\left\langle\left[\lambda^{1-k}\kappa(\mathbf{R})-\kappa(\lambda\mathbf{R})\right]R_iV_i\right\rangle_{f_0}}{\lambda\left\langle R_i^2\right\rangle_{f_0}}\\ +\ddot{\lambda}+\lambda\omega_0^2-\frac{p}{\lambda^3}\omega_0^2+(p-1)\frac{1}{\lambda^k}\omega_0^2=0,\end{aligned} \tag{43}$$

where we have already introduced the parameter p; thus, we assume here that $\langle V_i^2\rangle_{f_0}/\langle R_i^2\rangle_{f_0}$ does not depend on i. To deal with the new terms we assume that f_0 presents a symmetry of the type $(\mathbb{Z}/2\mathbb{Z})^d$ for velocity variables. In a two-dimensional problem this

corresponds to $f_0(r_x, v_x, r_y, v_y) = f_0(r_x, |v_x|, r_y, |v_y|)$. Under this hypothesis the second term in Eq. (43) vanishes. The same cancellation also happens for instance if f_0 has a spherical symmetry for space variables and the friction $\kappa(\mathbf{r})$ depends only on $|\mathbf{r}|$. These conditions are satisfied for problems with spherical symmetry. The constraint equation then reduces to:

$$\ddot{\lambda} + \lambda\omega_0^2 - \frac{p}{\lambda^3}\omega_0^2 + (p-1)\frac{1}{\lambda^k}\omega_0^2 + \dot{\lambda}\frac{\langle \kappa(\lambda\mathbf{R})R_i^2\rangle_{f_0}}{\langle R_i^2\rangle_{f_0}} = 0. \qquad (44)$$

Note that any explicit dependence on the diffusion disappears, as its effects are averaged out. The diffusion plays a role of course in determining the stationary solution f_0, which in turn appears in the equation. The new qualitative property of Eq. (44) is an effective λ-dependent friction.

A nice feature of Eq. (40) is that the stationary solution f_0 enters in the equation only through the parameter p. The situation is somewhat less favorable for a space-dependent friction, since f_0 also enters into the average $\langle \kappa(\lambda\mathbf{R})R_i^2\rangle_{f_0}$. However a numerical knowledge of f_0 is sufficient to use Eq. (44) in a given problem.

Equation (44) must now be tested against direct numerical simulations.

4.2. Numerical Tests

We now test the validity of Eq. (44) on academic examples of variable frictions.

One problem is the determination of the stationary profile f_0; this is a relatively easy task when friction and diffusion are constant, as f_0 is given by (3). In the present case, we have no analytical expression for f_0, and some numerical help is needed. In the following we will postulate a given density profile and check that it is consistent with the numerics.

We choose to study a one-dimensional plasma with $p \ll 1$, with a constant diffusion and a space-dependent friction. For a constant friction and diffusion, the density profile is then a step function; this is also a one-dimensional analog of an atomic cloud in a Magneto-Optical Trap (Walker et al., 1990). We have checked numerically that a variable friction does not change the

step profile, to our numerical precision. We will then use this step profile, with cut-off length L_i to estimate the averages in Eq. (44).

As a first test let us use the following expression for the friction:

$$\kappa(\mathbf{r}) = \begin{cases} \kappa_0 \left(1 - \dfrac{|\mathbf{r}|}{L_\kappa}\right) & \text{if } |\mathbf{r}| \leq L_\kappa, \\ 0 & \text{if } |\mathbf{r}| > L_\kappa, \end{cases} \tag{45}$$

where L_κ is the cut off for the friction; we do not consider negative friction here. In addition, for $|\mathbf{r}|$ larger than L_κ, the particles feel a diffusion without friction so that the local temperature of the system becomes infinite ($T \sim D/\kappa$). To avoid this nonphysical situation we make sure that particles stay where the friction is nonzero for all time. This condition can be written as $\lambda(t) L_i < L_\kappa$. The constraint equation becomes

$$\ddot{\lambda} + \lambda\omega_0^2 - \frac{p}{\lambda^3}\omega_0^2 + (p-1)\frac{1}{\lambda^k}\omega_0^2 + \dot{\lambda}\kappa_0\left(1 - \frac{3}{4}\frac{\lambda L_i}{L_\kappa}\right) = 0. \tag{46}$$

Let us stress that $p \ll 1$ and we limit the discussion to systems with $\max_{|\mathbf{r}|\in\mathbb{R}}(\kappa(\mathbf{r})) = \kappa_0 \ll \omega_0$. Because satisfying these two conditions with constant friction yields pretty good prediction, it is reasonable to expect that it will be the same in this case.

Figures 7(a) and 7(b) compare numerical simulations with Eq. (46). In these two examples, we are in the *a priori* favorable situation where both $p \ll 1$ and $\max_{|\mathbf{r}|\in\mathbb{R}}(\kappa(\mathbf{r})) = \kappa_0 \ll \omega_0$. We see in Figure 7(a) that the oscillation amplitude and frequency are quite well predicted; for a large amplitude oscillation, the agreement degrades after a few oscillations (see Figure 7(b)). On this figure, the asymptotic value of $\langle R^2\rangle_f/\langle R^2\rangle_{f_0}$ seems to be different from 1, indicating a relaxation to a stationary state different from the initial one. However, after a sufficiently long time, the system actually relaxes to f_0.

We consider now another example of variable friction:

$$\kappa(\mathbf{r}) = \kappa_0\left[1 + \cos\left(\pi\frac{|\mathbf{r}|}{L_\kappa}\right)\right], \tag{47}$$

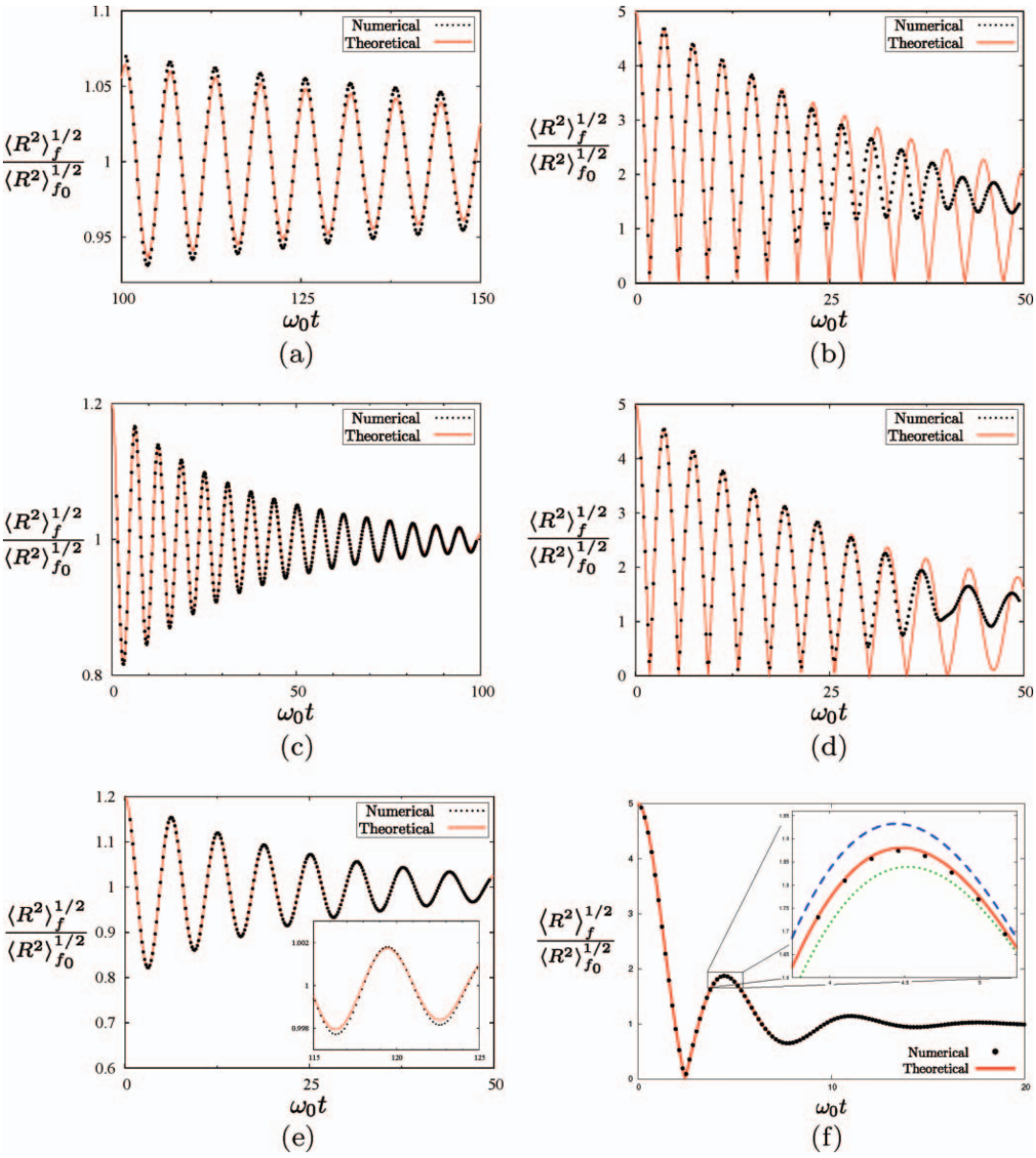

FIGURE 7 (color online). Evolution of the typical size of the cloud with non homogeneous friction in a one dimensional Coulombian system ($N = 4000$, $d = 1$, $k = 0$, $L_i = 12.5$ and $p = 6 \times 10^{-5}$). (a) The friction profile is given by (45). Parameters are $\kappa_0/\omega_0 = 5.6 \times 10^{-2}$, $L_\kappa = 1.25 \times L_i$ and $(\lambda, \dot{\lambda})|_{t=0} = (1.2, 0.0)$. (b) The friction profile is given by (45). Parameters are $\kappa_0/\omega_0 = 5.6 \times 10^{-2}$, $L_\kappa = 5.0 \times L_i$ and $(\lambda, \dot{\lambda})|_{t=0} = (5.0, 0.0)$. (c) The friction profile is given by (47). Parameters are $\kappa_0/\omega_0 = 5.6 \times 10^{-2}$, $L_\kappa = 0.25 \times L_i$ and $(\lambda, \dot{\lambda})|_{t=0} = (1.2, 0.0)$. (d) The friction profile is given by (47). Parameters are $\kappa_0/\omega_0 = 5.6 \times 10^{-2}$, $L_\kappa = 4.0 \times L_i$ and $(\lambda, \dot{\lambda})|_{t=0} = (5.0, 0.0)$. (e) The friction profile is given by (47). Parameters are $\kappa_0/\omega_0 = 5.6 \times 10^{-2}$, $L_\kappa = 0.25 \times L_i$ and $(\lambda, \dot{\lambda})|_{t=0} = (1.2, 0.0)$. (f) The friction profile is given by (47). The dashed blue curve and dotted green curve in the inset are respectively obtained from (44) substituting $\kappa(\lambda\mathbf{R})$ by $\langle\kappa(\mathbf{R})\rangle_{f_0}$ and $\kappa(\mathbf{R})$. Parameters are $\kappa_0/\omega_0 = 5.6 \times 10^{-1}$, $L_\kappa = 0.25 \times L_i$ and $(\lambda, \dot{\lambda})|_{t=0} = (5.0, 0.0)$.

where L_κ represents now the first minimum of $\kappa(\mathbf{r})$. Equation (44) becomes:

$$\ddot{\lambda} + \kappa_0\dot{\lambda} + \lambda\omega_0^2 - \frac{p}{\lambda^3}\omega_0^2 + (p-1)\frac{1}{\lambda^k}\omega_0^2 + \frac{3}{2}\frac{\dot{\lambda}\kappa_0}{L_i^3}\int_0^{L_i}\cos\left(\frac{\pi\lambda R}{L_\kappa}\right)R^2\,dR = 0. \tag{48}$$

The comparison between (48) and simulations yields similar qualitative results: the frequency is always obtained with very good precision (see Figures 7(c), 7(d), and 7(e)) at least for several oscillations. In Figure 7(f), the condition $\kappa_0 \ll \omega_0$ is relaxed, and the agreement remains almost perfect.

The main novelty of Eq. (44) with respect to Eq. (40) is the appearance of an effective nonlinear friction, which depends on λ. We have compared the numerical results (for $d = 1$, $k = 0$) with both Eq. (44) and Eq. (40), using two *ad hoc* effective frictions, independent of λ: $\kappa_{eff}^{(1)} = \langle\kappa(\mathbf{r})\rangle_{f_0}$ and $\kappa_{eff}^{(2)} = \langle\kappa(\mathbf{r})r_1^2\rangle_{f_0}/\langle r_1^2\rangle_{f_0}$. The difference induced by the nonlinear friction is small, but the prediction of Eq. (44) is better (see the inset of Figure 7(f)).

5. Conclusion

Starting from the first equation of the BBGKY hierarchy and a scaling ansatz for the dynamics, a nonlinear equation describing the breathing oscillations of trapped particles interacting *via* homogeneous forces was derived in Olivetti and colleagues (2009). The derivation and equation should be valid independently of the temperature, interaction strength, interaction range and dimensionality of the physical space in the underdamped limit.

In this article, we show that this equation also exactly describes the breathing dynamics of particles interacting through repulsive interactions in the zero temperature limit, for all values of the friction. We then have compared the predictions of this equation with direct numerical simulations, testing a wide range of parameters, to investigate its domain of validity. It appears that in the underdamped regime the main limitation is due to violent relaxation phenomena (sometimes called phase mixing) for long-range interacting systems and two-body collisions in short

interacting ones, especially for weak repulsive and attractive interactions, where they introduce damping and loss of coherence, unaccounted for in the scaling ansatz. In the overdamped regime, the equation is valid only at very small temperature, for repulsive interactions.

Motivated by the physics of Magneto-Optical Traps, we have extended the breathing mode theory to the case of space-dependent friction and diffusion. The predictions are again in good agreement with molecular dynamics simulations in the underdamped and small temperature (in the repulsive case) limits.

References

Allen, M. P., Tildesley, D. J. (1987). *Computer simulation of liquids*, Oxford: Clarendon Press.

Amiranashvili, S., Yu, M. Y., Stenflo, L. (2003). Nonuniform non-neutral plasma in a trap. *Phys. Rev. E* 67:016408.

Apolinario, S. W. S., Partoens, B., Peeters, F. M. (2007). Structural and dynamical aspects of small three-dimensional spherical Coulomb clusters. *New J. Phys.* 9:283.

Buchert, T. (1992). Lagrangian theory of gravitational instability of Friedman–Lemaitre cosmologies and the 'Zel'dovich approximation' *Mon. Not. Roy. Astron. Soc.* 254:729.

Bouchet, F., Corvellec, M. (2010). Invariant measures of the 2D Euler and Vlasov equations. *J. Stat. Mech.* P08021.

Castin, Y., Dum, R. (1996). Bose–Einstein Condensates in Time Dependent Traps. *Phys. Rev. Lett.* 77:5315.

Chandrasekhar, S., Elbert, D. D. (1972). Some elementary applications of the virial theorem to stellar dynamics. *Monthly Notices of the Royal Astronomical Society* 155:435.

Dauxois, T., Ruffo, S., Arimondo, E., Wilkens, M. (Eds). (2002). *Dynamics and Thermodynamics of Systems with Long Range Interactions. Lecture Notes in Physics 602.* Berlin: Springer.

Dubin, D. H. E. (1991). Theory of electrostatic fluid modes in a cold spheroidal non-neutral plasma. *Phys. Rev. Lett.* 66:2076.

Dubin, D. H. E. (1993). Equilibrium and dynamics of uniform density ellipsoidal non-neutral plasmas. *Phys. Fluids B* 5:295.

Dubin, D. H. E., ONeil, T. M. (1999). Trapped non-neutral plasmas, liquids, and crystals (the thermal equilibrium states). *Rev. Mod. Phys.* 71:87.

Guéry-Odelin, D. (2002). Mean-field effects in a trapped gas. *Phys. Rev. A* 66:033613.

Henning, C., Fujioka, K., Ludwig, P., Piel, A. Melzer, A., Bonitz, M. (2008). Existence and vanishing of the breathing mode in strongly correlated finite systems. *Phys. Rev. Lett.* 101:045002.

James, D. F. V. (1998). Quantum dynamics of cold trapped ions with application to quantum computation. *Appl. Phys. B* 66:181.

Kagan, Y., Surkov, E. L., Shlyapnikov, G. V. (1997). Evolution of a Bose gas in anisotropic time-dependent traps. *Phys. Rev. A* 55:R18.

Labeyrie, G., Michaud, F., Kaiser, R. (2006). Self-sustained oscillations in a large magneto-optical trap. *Phys. Rev. Lett.* 96:023003.

Lynden-Bell, D., (1967). Statistical mechanics of violent relaxation in stellar systems. *Mon. Not. Roy. Astron. Soc.* 136:101.

Olivetti, A., Barré, J., Marcos, B., Bouchet, F., Kaiser, R. (2009). Breathing mode for systems of interacting particles. *Phys. Rev. Lett.* 103:224301.

Partoens, B., Peeters, F. M. (1997). Classical artificial two-dimensional atoms: the Thomson model. *Condens. Matter* 9:5383.

Schweigert, V. A., Peeters, F. M. (1995). Spectral properties of classical two-dimensional clusters. *Phys. Rev. B* 51:7700.

Sheridan, T. E. (2004). Theory for the breathing mode of a complex plasma disk. *Phys. Plasmas* 11:5520.

Sheridan, T. E., Buckey, C. R., Cox, D. J., Merrill, R. J., Theisen, W. L. (2004). Breathing-mode resonance of a complex plasma disk. *Phys. Lett. A* 329:88.

Tatarkova, S. A., Carruthers, A. E., Dholakia, K. (2002). One-dimensional optically bound arrays of microscopic particles. *Phys. Rev. Lett.* 89:283901.

Walker, T., Sesko, D., Wieman, C. (1990). Collective behavior of optically trapped neutral atoms. *Phys. Rev. Lett.* 64:408.

Symmetry Breaking in d-Dimensional Self-Gravitating Systems

Renato Pakter,[1] Bruno Marcos,[1,2] and Yan Levin[1]

[1]*Instituto de Física, Universidade Federal do Rio Grande do Sul, Caixa Postal 15051, CEP 91501-970, Porto Alegre, Rio Grande do Sul, Brazil*

[2]*Université de Nice Sophia-Antipolis, CNRS, Laboratoire J.-A. Dieudonné, UMR 7351, Parc Valrose, 06108 Nice Cedex 02, France*

(Received 14 June 2013; revised manuscript received 18 November 2013; published 6 December 2013)

Systems with long-range interactions, such as self-gravitating clusters and magnetically confined plasmas, do not relax to the usual Boltzmann-Gibbs thermodynamic equilibrium, but become trapped in quasistationary states (QSS) the lifetime of which diverges with the number of particles. The QSS are characterized by the lack of ergodicity which can result in a symmetry broken QSS starting from a spherically symmetric particle distribution. We will present a theory which allows us to quantitatively predict the instability threshold for spontaneous symmetry breaking for a class of d-dimensional self-gravitating systems.

DOI: 10.1103/PhysRevLett.111.230603 PACS numbers: 05.20.−y, 05.45.−a, 05.70.Ln

Lord Rayleigh was probably the first to make an observation that long-range forces can lead to symmetry breaking [1]. Rayleigh was studying the stability of conducting spherical fluid droplets carrying charge Q. He discovered that when Q exceeds a certain critical threshold Q_c, droplets become unstable to symmetry breaking perturbations, elongating and eventually breaking up, emitting jets of fluid that carry away a significant fraction of the charge [2]. Rayleigh instability is now the basis for various technological applications, such as electrospraying and electrospinning. It also helps to understand the conformational structure of charged polymers, such as polyampholytes [3]. For self-gravitating systems a similar instability has been observed in gravitational simulations [4]. It has been found that an initially spherically symmetric self-gravitating system can become unstable, leading to formation of structures of reduced symmetry [4]. This radial orbit instability is believed to be important for the formation of elliptical galaxies [5].

There is, however, a fundamental difference between the Rayleigh instability of charged spherical droplets and the instability of spherically symmetric self-gravitating systems. Since the droplets are in (canonical) thermodynamic equilibrium, their shape must correspond to the minimum of the Helmholtz free energy—in fact, even for Q somewhat below Q_c, a spherical shape is already metastable, with the global minimum corresponding to a strongly prolate ellipsoid [6]. The thermal fluctuations, however, are too small to overcome the barrier that separates the metastable minimum from the global one, so that the spherical shape persists up to the Rayleigh threshold. On the other hand, gravitational systems are intrinsically microcanonical—isolated from environment [7–9]. In the thermodynamic limit, such long-range systems do not evolve to thermodynamic equilibrium but become trapped in quasistationary states (QSS), the lifetime of which diverges with the number of particles [10]. The QSS are characterized by the broken ergodicity, making equilibrium statistical mechanics inapplicable [11]. To explore spontaneous symmetry breaking of systems with long-range forces, therefore, requires a completely different approach [12]. In this Letter we will present a theory which allows us to quantitatively predict the thresholds of symmetry breaking instabilities for systems with long-range interactions. The results of the theory will be compared with extensive molecular dynamics simulations.

To present the theory, we will study a class of self-gravitating systems of N particles of mass m in an infinite d-dimensional space. The interaction potential between the particles is $V(\mathbf{r}) = Gm^2/[(2-d)r^{d-2}]$, where G is the gravitational constant. We will work in thermodynamic limit, $N \to \infty$ and $m \to 0$, while the total mass $M \equiv Nm$ remains fixed. The initial particle distribution is assumed to be a uniform spherically symmetric waterbag in both configuration and velocity space,

$$f_0(\mathbf{r}, \mathbf{v}) = \frac{d^2}{C_d^2 r_m^d v_m^d}\Theta(r_m - r)\Theta(v_m - v), \qquad (1)$$

where Θ is the Heaviside step function, $C_d = 2\pi^{d/2}/\Gamma(d/2)$ is the surface area of a d-dimensional unit sphere, and $\Gamma(x)$ is the gamma function. Since the initial waterbag distribution is not a stationary solution of the collisionless Boltzmann (Vlasov) equation, the systems will evolve with time. We are interested in discovering under what conditions Eq. (1) becomes unstable to small nonaxisymmetric perturbations.

It is convenient to define dimensionless variables by scaling the distance, time, velocities, gravitational potential, and energy with respect to $r_0 = r_m$, $t_0 = \sqrt{r_m^d/GM}$, $v_0 = \sqrt{GM/r_m^{d-2}}$, $\psi_0 = GM/r_m^{d-2}$, and $E_0 = GM^2/r_m^{d-2}$, respectively. This is equivalent to setting $r_m = G = M = 1$.

The particle dynamics is governed by Newton's equations of motion

$$\ddot{\mathbf{r}} = -\nabla\psi(\mathbf{r}, t), \tag{2}$$

where the dot stands for the time derivative and $\mathbf{r} = \sum_i x_i \hat{\mathbf{e}}_i$, $i = 1, \ldots, d$, is the particle position. In the thermodynamic limit, the correlations between the particles can be ignored, so that the force acting on a particle located at $\mathbf{r}$ is $\mathbf{F} = -\nabla\psi(\mathbf{r}, t)$, where $\psi(\mathbf{r}, t)$ is the mean gravitational potential which satisfies the Poisson equation

$$\nabla^2\psi = C_d n(\mathbf{r}, t), \tag{3}$$

where $n(\mathbf{r}, t)$ is the particle number density.

We define the "envelope" of the position and velocity particle distributions to be $X_i(t) = \sqrt{(d+2)\langle x_i^2\rangle}$ and $V_i(t) = \sqrt{(d+2)\langle v_i^2\rangle}$, respectively. The $\langle\cdots\rangle$ corresponds to the average over all the particles. Note that in the reduced units, $X_i(0) = 1$ and $V_i(0) = v_m$ for all i, but as the dynamics evolves, it is possible for the symmetry between the different directions to become broken. Our goal is to determine the equations of evolution for $X_i(t)$ [13]. Taking two time derivatives of $X_i^2(t)$ and one of $V_i^2(t)$ and using the equations of motion, Eq. (2), we obtain

$$\dot{X}_i^2 + X_i\ddot{X}_i = V_i^2 - (d+2)\left\langle x_i \frac{\partial\psi}{\partial x_i}\right\rangle \tag{4}$$

and

$$V_i\dot{V}_i = -(d+2)\left\langle \dot{x}_i \frac{\partial\psi}{\partial x_i}\right\rangle. \tag{5}$$

To calculate the averages appearing in Eqs. (4) and (5), we need to know the mean-gravitational potential. We suppose that the originally spherically symmetric homogeneous distribution can become distorted into an ellipsoidal shape with the semiaxis $\{X_i\}$ and uniform density $n(\mathbf{r}, t) = d/C_d\prod_i X_i(t)$. Using the ellipsoidal coordinate system [14], the gravitational field inside a d-dimensional ellipsoid with the semiaxis $\{X_i\}$ can be calculated explicitly to be

$$\frac{\partial\psi}{\partial x_i} = \frac{d}{2}x_i g_i(X_1, \ldots, X_d), \tag{6}$$

where

$$g_i(X_1, \ldots, X_d) = \int_0^\infty \frac{ds}{(X_i^2 + s)\prod_{j=1}^d (X_j^2 + s)^{1/2}}. \tag{7}$$

Furthermore, for a d-dimensional ellipsoid with a uniform mass distribution, it can be shown that $\langle x_i^2\rangle = X_i^2/(d+2)$. Substituting these results in Eqs. (4) and (5), we obtain a closed set of coupled equations:

$$\dot{X}_i^2 + X_i\ddot{X}_i = V_i^2 - \frac{d}{2}X_i^2 g_i(X_1, \ldots, X_d) \tag{8}$$

and

$$V_i\dot{V}_i = \frac{d}{2}X_i\dot{X}_i g_i(X_1, \ldots, X_d). \tag{9}$$

We define the "emittance" [15] in the ith direction as $\epsilon_i^2(t) \equiv (d+2)^2[\langle x_i^2\rangle\langle\dot{x}_i^2\rangle - \langle x_i\dot{x}_i\rangle^2] = X_i^2V_i^2 - \dot{X}_i^2X_i^2$. Taking a time derivative of $\epsilon_i^2(t)$ and using Eqs. (8) and (9), it is possible to show that the $\epsilon_i(t)$ are the constants of motion, $\epsilon_i(t) = \epsilon_i(0) \equiv \epsilon_i$. Using this observation, the set of Eqs. (8) and (9) reduces to

$$\ddot{X}_i = \frac{\epsilon_i^2}{X_i^3} - \frac{d}{2}X_i g_i(X_1, \ldots, X_d). \tag{10}$$

For the initial waterbag distribution, Eq. (1), $\epsilon_i^2(0) = v_m^2$.

The virial theorem requires that a *stationary* gravitational system in d dimensions must have $2K = (2-d)U$, where K and U are the total kinetic and potential energies, respectively. For the initial waterbag distribution, $K = v_m^2 d/[2(d+2)]$ and the potential energy is $U = d/[(2-d)(d+2)]$, so that the virial condition reduces to $v_m = 1$. Although the initial waterbag distribution is not a stationary solution of the collisionless Boltzmann (Vlasov) equation, we expect that if the virial condition is satisfied, the system will not exhibit strong envelope oscillations. This is indeed what has been observed for gravitational systems in $d = 1$, 2, and 3 [16–19]. On the other hand, if the initial distribution does not satisfy the virial condition, the particle distribution will undergo violent oscillations which will lead to QSS with a core-halo structure [16,18]. To measure how strongly the initial distribution deviates from the virial condition, we define a viral number $\mathcal{R}_0 \equiv (2K/((2-d)U)) = v_m^2$. With this definition the emittance becomes $\epsilon_i^2(t) = \mathcal{R}_0$.

Let us first consider a uniform spherically symmetric mass distribution of radius $R(t)$, i.e., $X_i(t) = R(t)$ for $i = 1, \ldots, d$. In this case the integral in Eq. (7) can be evaluated analytically to yield $g_i = 2R^{-d}/d$, and the equation of evolution for the radius of the sphere becomes

$$\ddot{R} = \frac{\mathcal{R}_0}{R^3} - \frac{1}{R^{d-1}}, \tag{11}$$

with $R(0) = 1$ and $\dot{R}(0) = 0$. We see that, in agreement with the earlier discussion, if the initial distribution satisfies the virial condition, $\mathcal{R}_0 = 1$, the sphere's radius remains constant for all time, $R(t) = 1$ for any d. For $d \leq 3$, this equilibrium is stable because a small deviation from $\mathcal{R}_0 = 1$ will result in small periodic oscillations of R. On the other hand, for $d \geq 4$ the equilibrium is unstable, and any $\mathcal{R}_0 \neq 1$ will lead to either collapse or an unbounded expansion of the particle distribution. These conclusions are in agreement with the old observation of Ehrenfest, who first noted that there are no stable orbits for Newtonian gravity in $d \geq 4$ [20].

To investigate the possible symmetry breaking of an initially spherically symmetric mass distribution, we need, therefore, to only consider $d = 2$ and 3. For $d = 2$, the integral in Eq. (7) can be performed analytically

yielding $g_i(X_1, X_2) = 2/X_i(X_1 + X_2)$. Equation (10) then simplifies to

$$\ddot{X}_i = \frac{\epsilon_i}{X_i^3} - \frac{2}{X_1 + X_2}, \qquad i = 1, 2. \tag{12}$$

The symmetry breaking occurs if an initially vanishingly small fluctuation grows as a function of time. To study this instability, it is convenient to introduce new variables,

$$X_i(t) = \bar{X}(t) + \Delta_i(t), \tag{13}$$

where $\bar{X} = (\sum_i X_i)/d$ is the average of X_i's and Δ_i is the asymmetry along the ith direction. Clearly Δ_i's are related by $\sum_i \Delta_i = 0$. Hence, for $d = 2$ there is only one independent asymmetry variable $\Delta = \Delta_1 = -\Delta_2$. To locate the region of instability, we perform a linear stability analysis of Eq. (12). Noting that $(\epsilon_1^2 - \epsilon_2^2) \sim O(\Delta)$, to leading order in Δ, Eq. (12) simplifies to

$$\ddot{\Delta} + \frac{3(\epsilon_1^2 + \epsilon_2^2)}{2\bar{X}^4(t)}\Delta = \frac{(\epsilon_1^2 - \epsilon_2^2)}{2\bar{X}^3(t)}, \tag{14}$$

while the dynamics of $\bar{X}(t)$ to this order is

$$\ddot{\bar{X}} = \frac{\epsilon_1^2 + \epsilon_2^2}{2\bar{X}^3} - \frac{1}{\bar{X}}. \tag{15}$$

The dynamics of Δ is driven by the oscillations of $\bar{X}(t)$. In particular, if the virial condition is satisfied and $\epsilon_1^2 = \epsilon_2^2 = \mathcal{R}_0 = 1$, the $(\Delta = 0, \dot{\Delta} = 0)$ is a stable fixed point of Eq. (14). Therefore, if $\mathcal{R}_0 \approx 1$, for small initial asymmetry, $\Delta(t)$ will not grow in time. However, if the initial distribution does not satisfy the virial condition, $\bar{X}(t)$ will oscillate and may drive a parametric resonance which can make $\Delta(t)$ unstable. This is precisely what is observed in numerical integration of Eqs. (14) and (15). We find that for sufficiently small (or large) $\mathcal{R}_0$, the amplitude of $\Delta(t)$ oscillations grows without a bound. Note that in Eq. (14) the instability occurs as a consequence of a fluctuation either in the velocity [$\Delta(0) = 0$ and $\epsilon_1 \neq \epsilon_2$], the position [$\Delta(0) \neq 0$], or as a combination of both. For sufficiently small (or large) $\mathcal{R}_0$, we find that any small fluctuation in the initial particle distribution is amplified by the dynamics. Of course, in practice the growth of $\Delta(t)$ will be saturated by the Landau damping [16,18] and will result in a QSS with a broken rotational symmetry.

To precisely locate the instability threshold, it is simplest to consider a small fluctuation with $\Delta(0) \neq 0$ and $\epsilon_1 = \epsilon_2$. Since the $\Delta(t)$ is driven by the periodic oscillations of $\bar{X}(t)$, to study this instability we must work in the Poincaré section [21,22].

Consider a displacement vector from the $(\Delta = 0, \dot{\Delta} = 0)$ fixed point, $\mathbf{X}_\Delta(t) = (\delta\Delta, \delta\dot{\Delta})$. From Eq. (14), we see that its dynamics is governed by $\dot{\mathbf{X}}_\Delta = \mathbf{M} \cdot \mathbf{X}_\Delta$, where

$$\mathbf{M} = \begin{pmatrix} 0 & 1 \\ -\frac{3\mathcal{R}_0}{\bar{X}^4} & 0 \end{pmatrix}, \tag{16}$$

and the dynamics of $\bar{X}(t)$ is given by Eq. (15) with $\epsilon_1^2 = \epsilon_2^2 = \mathcal{R}_0$. If we now define a mapping $\mathcal{M}(t)$ that relates $\mathbf{X}_\Delta(t)$ to its initial condition by $\mathbf{X}_\Delta(t) = \mathcal{M}(t) \cdot \mathbf{X}_\Delta(0)$, and substitute this into the evolution equation for $\mathbf{X}_\Delta$, we obtain

$$\dot{\mathcal{M}} = \mathbf{M} \cdot \mathcal{M}, \quad \text{with} \quad \mathcal{M}(0) = I, \tag{17}$$

where I is the identity matrix. In order to determine the stability of $(\Delta = 0, \dot{\Delta} = 0)$ fixed point, we simultaneously integrate Eqs. (15) and (17) over one period τ_R of the oscillation of $\bar{X}(t)$ (i.e., between two consecutive points in the Poincaré map), and determine the eigenvalues of the mapping matrix $\mathcal{M}(\tau_R)$. If the absolute value of any eigenvalue is larger than 1, then $(\Delta = 0, \dot{\Delta} = 0)$ fixed point will be unstable. We find that the asymmetric instability occurs for $\mathcal{R}_0 < 0.255893\ldots$ and for $\mathcal{R}_0 > 2.55819\ldots$. A more detailed analysis shows that it is produced by a pitchfork bifurcation and is of second order. In Fig. 1 we compare the predictions of the theory with the results of extensive molecular dynamics simulations performed using the state-of-the-art gravitational oriented massively parallel GADGET2 code [23], which has been appropriately modified to integrate gravity in two dimensions. At $t = 0$ the particles are distributed in accordance with Eq. (1). To force the symmetry breaking to occur along the x axis, a small perturbation in this direction is introduced. We then monitor the moments $\langle x^2 \rangle$ and $\langle y^2 \rangle$ as the dynamics evolves. Figure 1 shows the evolution of the moments for two different virial numbers. We find that for $\mathcal{R}_0 = 0.16$ the symmetry is broken, while for $\mathcal{R}_0 = 0.36$ the spherical symmetry is unaffected by the initial perturbation. This is in close agreement with the predictions of the present theory. A similar symmetry breaking transition is also found for

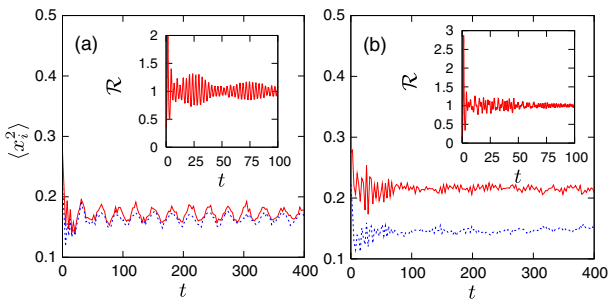

FIG. 1 (color online). The evolution of x and y moments of the mass distribution, $\langle x^2 \rangle$ (red solid curve) and $\langle y^2 \rangle$ (blue dashed curve) obtained using molecular dynamics simulations for a 2D system with $N = 8000$. A small asymmetry in the x direction is introduced in the initial particle distribution. For initial distribution with $\mathcal{R}_0 = 0.36$ (a), the system relaxes to a QSS with a spherical symmetry (see also Fig. 2), while for $\mathcal{R}_0 = 0.16$ (b), spherical symmetry is broken. Similar behavior is found for $\mathcal{R}_0$ above the upper critical threshold; see Fig. 2. The inset shows the evolution of the virial number. Both the symmetric and the asymmetric QSS are fully virialized, $\mathcal{R} = 1$.

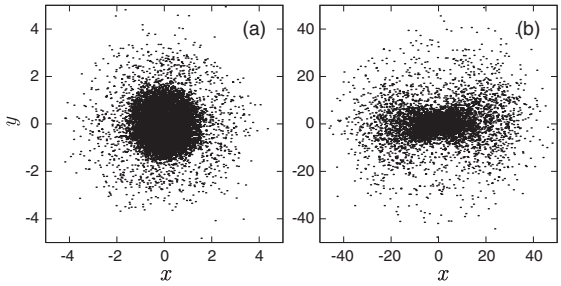

FIG. 2. Snapshots of the x-y particle distribution in a QSS at $t = 200$. In (a) $\mathcal{R}_0 = 2$ and the symmetry remains unbroken, while in (b) $\mathcal{R}_0 = 6.25$ and the QSS has a broken rotational symmetry. Note that the final particle distribution in both cases has a characteristic core-halo structure.

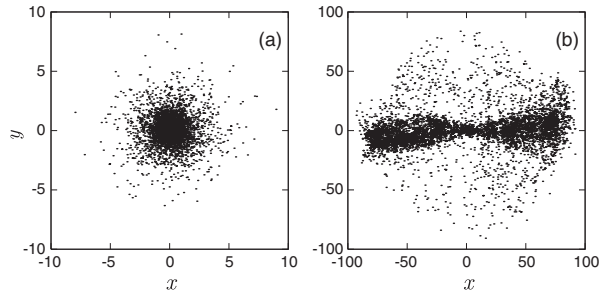

FIG. 3. Snapshots of the x-y projection of the 3D particle distribution ($N = 20000$) at $t = 25$. In (a) $\mathcal{R}_0 = 0.5$, the symmetry remains unbroken, while in (b) $\mathcal{R}_0 = 0.01$ there is a spontaneous symmetry breaking. Note that because of the particle evaporation a 3D system does not relax to a QSS.

large virial numbers; see Fig. 2. Since the transitions are continuous, it is difficult to precisely locate the thresholds of instability using molecular dynamics simulations.

In Fig. 2 we show snapshots of two QSS to which the system relaxes after a few oscillations. In agreement with the theory, depending on the virial number, one of the QSS is spherically symmetric while the other one is not. For $d = 3$ the integral in Eq. (7) cannot be performed in terms of simple analytical functions, and must be evaluated numerically. To locate the instability, we once again make use of the variables defined in Eq. (13) and expand Eq. (10) to linear order in Δ_i. For $d = 3$, there are two independent variables Δ_1 and Δ_2. Numerical integration of these equations shows, once again, the existence of an instability for small and large virial numbers. To precisely locate the instability, we fix $\epsilon_1^2 = \epsilon_2^2 = \epsilon_3^2 = \mathcal{R}_0$. To linear order the dynamics of equations for Δ_1 and Δ_2 then decouples and becomes identical. This means that we can study the stability using a single $\Delta(t)$ variable. The matrix that determines the evolution of the displacement vector from ($\Delta = 0$, $\dot{\Delta} = 0$) fixed point now takes the form

$$\mathbf{M} = \begin{pmatrix} 0 & 1 \\ \frac{R - 15\mathcal{R}_0}{5R^4} & 0 \end{pmatrix}, \tag{18}$$

where $R(t)$ is given by Eq. (11) with $d = 3$. Substituting this matrix in Eq. (17) and adopting the procedure analogous to the one used before, we find that the fixed point ($\Delta = 0$, $\dot{\Delta} = 0$) becomes unstable for $\mathcal{R}_0 < 0.388666\ldots$ and $\mathcal{R}_0 > 1.61133\ldots$. Figure 3 shows two snapshots of the evolution of a 3D gravitational systems. As predicted by the theory, for both small and large virial numbers the spherical symmetry of the initial distribution is broken by the parametric resonances.

For 3D systems finite angular momentum can also lead to breaking of the spherical symmetry. This, however, is not the case in 2D. Furthermore, in our simulations the initial particle distribution has very small angular momentum—in the thermodynamic limit it will be exactly zero. The rotation of the system is, therefore, very slow, while the instability happens very quickly, showing that the residual angular momentum does not play any role for the symmetry breaking studied in this Letter.

It is interesting to compare and contrast the Rayleigh instability of charged conducting droplets and the instability of self-gravitating systems. While the Rayleigh instability is a true thermodynamic transition, the gravitational symmetry breaking is not. When the charge on a droplet exceeds the critical value Q_c, it will undergo a first-order transition to a prolate ellipsoid. On the other hand, the instability of a self-gravitating system is a purely dynamical phenomenon, arising from a parametric resonance that drives an asymmetric mode of oscillation. The magnitude of the instability is saturated by the nonlinear Landau damping [24] which leads to the formation of a nonequilibrium core-halo QSS. If the instability occurs, the broken ergodicity [11] prevents the symmetry from being restored. In $d = 2$, a self-gravitating system with a finite number of particles will eventually relax to thermodynamic equilibrium in which the distribution function will have the usual Boltzmann-Gibbs form [18] and the mean-gravitational potential will once again be spherically symmetric. The relaxation time to equilibrium, however, diverges with N, so that in practice a sufficiently large system (such as an elliptical galaxy) will never evolve to equilibrium, but will stay in a nonequilibrium stationary state forever [25]. For such systems, once the instability occurs, the symmetry will remain irrevocably broken.

This work was partially supported by the CNPq, FAPERGS, INCT-FCx, and by the U.S.-AFOSR under Grant No. FA9550-12-1-0438. Numerical simulations have been performed at the cluster of the SIGAMM hosted at "Observatoire de Côte d'Azur," Université de Nice–Sophia Antipolis.

[1] L. Rayleigh, Philos. Mag. **14**, 184 (1882).
[2] G. I. Taylor, Proc. R. Soc. A **280**, 383 (1964).
[3] Y. Kantor and M. Kardar, Phys. Rev. E **51**, 1299 (1995).
[4] L. Aguilar and D. Merritt, Astrophys. J. **354**, 33 (1990).

[5] E. Athanassoula, R. E. G. Machado, and S. A. Rodionov, Mon. Not. R. Astron. Soc. **429**, 1949 (2013).
[6] G. Ailam and I. Gallily, Phys. Fluids **5**, 575 (1962).
[7] D. H. E. Gross, in *Microcanonical Thermodynamics: Phase Transitions in Small Systems*, Lecture Notes in Phys. Vol. 66 (World Scientific, Singapore, 2001).
[8] I. Ispolatov and E. G. D. Cohen, Phys. Rev. E **64**, 056103 (2001).
[9] P. H. Chavanis and I. Ispolatov, Phys. Rev. E **66**, 036109 (2002).
[10] A. Campa, T. Dauxois, and S. Ruffo, Phys. Rep. **480**, 57 (2009); Y. Levin, R. Pakter, F. B. Rizzato, T. N. Teles, and F. P. da C. Benetti, Phys. Rep., doi:10.1016/j.physrep.2013.10.001 (2013).
[11] F. P. da C. Benetti, T. N. Teles, R. Pakter, and Y. Levin, Phys. Rev. Lett. **108**, 140601 (2012).
[12] T. N. Teles, F. P. da C. Benetti, R. Pakter, and Y. Levin, Phys. Rev. Lett. **109**, 230601 (2012).
[13] F. J. Sacherer, IEEE Trans. Nucl. Sci. **18**, 1105 (1971).
[14] O. D. Kellogg, *Foundations of Potential Theory* (Dover, New York, 1953).
[15] M. Reiser, *Theory and Design of Charged Particle Beams* (Wiley-Inter Science, New York, 1994).
[16] T. N. Teles, Y. Levin, and R. Pakter, Mon. Not. R. Astron. Soc. **417**, L21 (2011).
[17] M. Joyce and T. Worrakitpoonpon, Phys. Rev. E **84**, 011139 (2011).
[18] T. N. Teles, Y. Levin, R. Pakter, and F. B. Rizzato, J. Stat. Mech. (2010) P05007.
[19] Y. Levin, R. Pakter, and F. B. Rizzato, Phys. Rev. E **78**, 021130 (2008).
[20] P. Ehrensfest, Ann. Phys. (Berlin) **366**, 440 (1920).
[21] C. Polymilis and K. Hizanidis, Phys. Rev. E **47**, 4381 (1993).
[22] W. Simeoni, Jr., F. B. Rizzato, and R. Pakter, Phys. Plasmas **13**, 063104 (2006).
[23] V. Springel, Mon. Not. R. Astron. Soc. **364**, 1105 (2005).
[24] Y. Levin, R. Pakter, and T. N. Teles, Phys. Rev. Lett. **100**, 040604 (2008).
[25] B. Marcos, Phys. Rev. E **88**, 032112 (2013).

Nonequilibrium Phase Transition with Gravitational-like Interaction in a Cloud of Cold Atoms

J. Barré,[1] B. Marcos,[1,2] and D. Wilkowski[3]
[1]Laboratoire J.-A. Dieudonné, Université de Nice Sophia-Antipolis, CNRS, 06109 Nice, France
[2]Instituto de Física, Universidade Federal do Rio Grande do Sul, Caixa Postal 15051, CEP 91501-970, Porto Alegre, Rio Grande do Sul, Brazil
[3]Institut Non Linéaire de Nice, Université de Nice Sophia-Antipolis, CNRS, 06560 Valbonne, France; Centre for Quantum Technologies, National University of Singapore, 117543 Singapore, Singapore; PAP, School of Physical and Mathematical Sciences, Nanyang Technological University, 637371 Singapore, Singapore
(Received 10 December 2013; published 31 March 2014)

We propose to use a cloud of laser-cooled atoms in a quasi-two-dimensional trap to investigate a nonequilibrium collapse phase transition in the presence of a gravitational-like interaction. Using theoretical arguments and numerical simulations, we show that, like in two-dimensional gravity, a transition to a collapsed state occurs below a critical temperature. In addition and as a signature of the nonequilibrium nature of the system, persistent particle currents, dramatically increasing close to the phase transition, are observed.

DOI: 10.1103/PhysRevLett.112.133001 PACS numbers: 37.10.De, 04.80.Cc, 05.20.Jj, 37.10.Gh

Nonequilibrium phase transitions have been extensively studied over the years both for their basic understanding and potential applications [1]. Among the numerous examples of nonequilibrium phase transitions, one can quote direct percolation [2], infection spreading [3], geophysical flows [4], complex plasmas [5], surfaces [6] and nanowire growing [7], and traffic jams [8].

For equilibrium phenomena, a systematic approach exists, and powerful tools such as the renormalization group have been developed. In contrast, and despite important progresses in some cases (see Ref. [9] for a textbook account), there is no such general framework so far for nonequilibrium phase transitions [1]. This is an outstanding open problem of statistical physics, since most biological, chemical, and physical systems encountered in nature as well as social phenomena are in nonequilibrium states.

In this Letter, we study a nonequilibrium phase transition driven by an effective gravitational-like interaction, which does not derive from a potential, in a quasi-two-dimensional cloud of laser-cooled atoms. At equilibrium, interparticle long-range interactions are at the origin of dramatic collective effects, such as gravothermal catastrophe or isothermal collapse in self-gravitating systems [10–12] and negative specific heat [11,13]. Systems of Brownian self-gravitating particles in 2D undergo a collapse phase transition, in the sense that the density diverges in finite time below a critical temperature [14,15]. For our nonequilibrium system, we find a similar behavior. In addition, we observe, as a direct signature of the presence of a nonequilibrium state, persistent currents which are rapidly growing close to the transition. Those particularities are explained throughout the Letter.

System.—The starting point of our studies is a simple experimental setup where a cooled atomic gas is located in the x-y plane into one or few two-dimensional traps made of a far off-detuned stationary laser beam (see Fig. 1). The dynamic along the perpendicular axis of the traps is frozen due to a strong confinement. In the x-y plane, the gas is in interaction with two orthogonal contrapropagating pairs of red detuned laser beams providing laser cooling. Hence, the laser beams can be seen as a thermal bath at temperature T. In addition, these cooling beams are absorbed by the gas (shadow effect), leading, in the weak absorption limit, to a gravitational-like interaction in the xy plane, along the axis of the beams [16]. This interaction was experimentally demonstrated in a one-dimensional system [17]. The

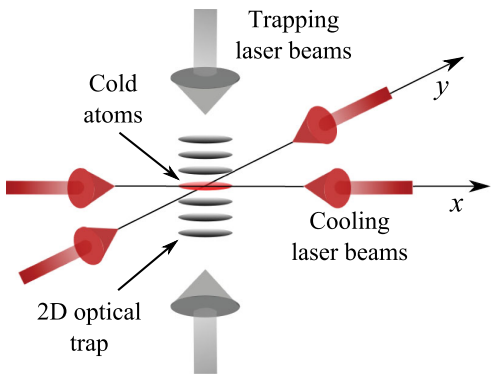

FIG. 1 (color online). Schematic view of the experimental setup. Atoms are confined in strongly anisotropic, quasi-two-dimensional, optical dipole traps: they form one or several pancake-shaped clouds. Two pairs of orthogonal contrapropagating laser beams are in quasiresonance with an atomic transition providing cooling and shadow forces in the x-y plane.

strength of the interaction can be tuned changing the intensity or/and the frequency detuning of the laser beams [see Eq. (2)]. Since the interaction force satisfies the Poisson equation, this system might at first sight be viewed as a tabletop realization of a 2D gravitational-like system in canonical equilibrium. However, the spatial configuration of the laser beams does not preserve the rotational symmetry around the z axis. Hence, the laser-induced long-range force no longer derives from a potential, and the system is fundamentally in a nonequilibrium state.

Modeling.—We describe one cloud of cold atoms by a two-dimensional phase space density $f(\vec{r},\vec{v},t)$, using the notationss $\vec{r}=(x,y)$, $\vec{v}=(v_x,v_y)$. We make the reasonable assumption that cooling can be modeled by a linear friction $-\gamma\vec{v}$, and use a constant velocity diffusion coefficient D to take into account the velocity recoils due to random absorption and fluorescence emission of photons by the atoms. We use the following standard expression for the force $\vec{F}=(F_x,F_y)$ for the shadow effect, which relies on a weak absorption limit [16]:

$$F_x[\rho](x,y) = -C\int \mathrm{sgn}(x-x')\rho(x',y)dx', \tag{1a}$$

$$F_y[\rho](x,y) = -C\int \mathrm{sgn}(y-y')\rho(x,y')dy', \tag{1b}$$

where $\rho(x,y)$ is the surface density of atoms, normalized to 1, and C is a constant characterizing the intensity of the force, which can be computed after integration over the transverse direction [17]:

$$C = \frac{\hbar k\Gamma}{2}\frac{I_0}{I_s}\frac{N}{(1+4\bar{\delta}^2)^2}\frac{\sigma_0}{2\sqrt{\pi}L_\perp}. \tag{2}$$

In this expression, k is the wave number, Γ the width of the atomic transition, $\bar{\delta}$ the normalized frequency detuning, N the number of trapped atoms, $\sigma_0=6\pi/k^2$ the resonant photon absorption cross section, $L_\perp$ the transverse size of the cloud, I_0 the incident laser intensity, and I_s the saturation intensity. Note that the shadow force (1) verifies the same Poisson equation as gravity $\vec{\nabla}\cdot\vec{F}\propto-\rho$, but, contrary to gravity, does not derive from a potential, i.e., $\vec{\nabla}\times\vec{F}\neq\vec{0}$.

The optical dipole traps in the x-y plane are well approximated by harmonic traps at frequency ω_0 and will be modeled accordingly. Moreover, usual experimental configurations correspond to the overdamped regime, i.e., $\omega_0\ll\gamma$. So the velocity distribution quickly relaxes to a Gaussian, and the surface density $\rho(x,y,t)$ evolves according to a nonlinear Smoluchowski equation,

$$\frac{\partial\rho}{\partial t} = \vec{\nabla}\cdot\left[\frac{\omega_0^2}{\gamma}\vec{r}\rho + \frac{1}{m\gamma}\vec{F}[\rho]\rho + \frac{k_BT}{m\gamma}\vec{\nabla}\rho\right], \tag{3}$$

where m is the atomic mass, and the temperature is determined by the relation $k_BT/m=D/\gamma$.

Rescaling time and space as $\tilde{t}=(\omega_0^2/\gamma)t$, $(x,y)=(L\tilde{x},L\tilde{y})$, with $L=\sqrt{C/(m\omega_0^2)}$, Eq. (3) becomes (dropping the tilde for convenience)

$$\frac{\partial\rho}{\partial t} = \vec{\nabla}\cdot[\vec{r}\rho + \vec{F}[\rho]\rho + \Theta\vec{\nabla}\rho]. \tag{4}$$

This equation is the starting point of our theoretical analysis.

Model analysis.—The physics is governed by a single dimensionless parameter

$$\Theta = \frac{k_BT}{C}.$$

The above Eq. (4) is similar to the Smoluchowski-Poisson system describing self-gravitating Brownian particles, or the parabolic-elliptic Keller-Segel model used in chemotaxy theory [18,19]. However, the force does not derive from a potential. It is well known that if the temperature is small enough, a solution to the Smoluchowski-Poisson equation blows up in finite time and forms a Dirac peak. This behavior can also be seen as a phase transition in the canonical ensemble. It is natural to ask if the same phenomenology holds for Eq. (4), the nonpotential generalization of the Smoluchowski-Poisson equation.

To get insight in the behavior of Eq. (4), we compute the time evolution of $S(t)=-\int\rho\ln\rho$. Note that the formation of a Dirac peak corresponds to $S(t)\to-\infty$. Using Eq. (4), $\vec{\nabla}\cdot\vec{F}=-4\rho$, and after integrating by parts, we get

$$\dot{S}(t) = -2 - 4\int\rho^2 d^2\vec{r} + \Theta\int\frac{|\nabla\rho|^2}{\rho}d^2\vec{r}. \tag{5}$$

Writing now $\rho=\sqrt{u}$ and using the functional inequality, valid in 2D [20], $\int u^4\le a\int|\nabla u|^2\times\int u^2$, we have

$$\dot{S}(t) \ge -2 + (\Theta - a)\int\frac{|\nabla\rho|^2}{\rho}d^2\vec{r}, \tag{6}$$

where a is a constant, known numerically, $a\simeq0.171$. If $\Theta>a$, the second term in the right-hand side of the inequality is positive and dominates over the first term above a certain spatial density of the cloud. It ensures that $S(t)$ cannot decrease without bound: collapse is excluded. On the other hand, for $\Theta<a$, collapse becomes possible, even though of course this argument cannot prove that it happens. If it happens, we should not expect 0.171 to be an accurate estimate of the critical parameter Θ_c, but an indication for the behavior of Eq. (4). Indeed, as we describe below, we numerically find indications of a collapse transition at a lower Θ, namely, $\Theta\approx0.12$–0.15.

Numerical simulations.—To simulate Eq. (4), we introduce the following stochastic particles approximation: The position of particle i is denoted by $\vec{r}_i=(x_i,y_i)$, and the dynamical equations are

$$\dot{x}_i = -x_i + F_{i,x} + \sqrt{2\Theta}\eta_{i,x}(t), \tag{7a}$$

$$\dot{y}_i = -y_i + F_{i,y} + \sqrt{2\Theta}\eta_{i,y}(t), \tag{7b}$$

where the $\eta_{i,\cdot}$ are independent Gaussian white noises. To define $F_{i,x}$ and $F_{i,y}$ numerically, we introduce the spatial scale σ. The force is then written as

$$F_{i,x} = -C\sum_{j\neq i}\mathrm{sgn}(x_i - x_j)\delta_\sigma(y_i - y_j), \tag{8a}$$

$$F_{i,y} = -C\sum_{j\neq i}\mathrm{sgn}(y_i - y_j)\delta_\sigma(x_i - x_j), \tag{8b}$$

where $\delta_\sigma(z) = 1$ if $|z| < \sigma$ and zero otherwise. In the limit $\sigma \to 0$, Eq. (8) reduce to the original definition of the force (1). We expect to correctly approximate Eq. (4) when $n\sigma \gg 1$, where n is the number of particles. We integrate the equation of motion using a Euler scheme. The force calculation is sped up using the following procedure: space is discretized with cells of size σ and particles are assigned to cells using the linked-list technique (see, e.g., Ref. [21]); this is a $\mathcal{O}(n)$ operation which does not involve any approximation. Note that the numerical particles should not be seen as direct representations of the atoms in the trap; however, the spatial distribution of the numerical particles should approximate the 2D spatial distribution of atoms described by Eq. (4).

We performed a series of simulations varying initial conditions σ and number of particles n with Θ in the range [0.08,0.3]. In order to keep the strength of the gravitation-like interaction constant when changing the parameters, we keep the quantity $Cn\sigma$ constant. After a time $t \sim 1$, all the simulations reach a stationary state, which we find to be essentially independent of σ, n (for sufficiently large n and small σ) and of the initial conditions. In Fig. 2 are shown snapshots of the particle distributions in the stationary state at $\Theta = 0.14$ and $\Theta = 0.2$. They show a crosslike structure along the diagonals, which is related to the presence of currents, as we will discuss later. To look for a phase transition toward a collapse phase, we plot the central spatial density as a function of Θ, as shown in Fig. 3. We observe an abrupt increase in the density when Θ is decreased, for $\Theta_c \approx 0.12$–0.15.

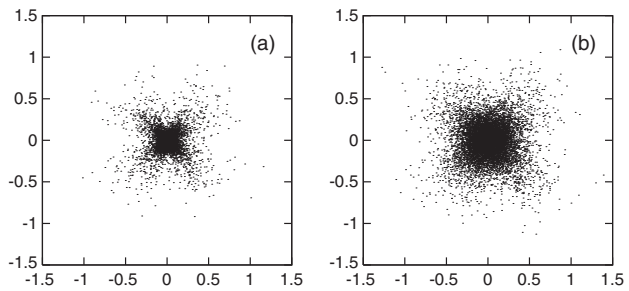

FIG. 2. Snapshot of the particle distribution in the stationary state of a system with $\sigma = 10^{-2}$, $n = 10^4$, a time step $\Delta t = 10^{-5}$, and (a) $\Theta = 0.14$ and (b) $\Theta = 0.2$. The laser beams are along the axes of the figure.

Furthermore, we note that for all simulations with $\Theta > \Theta_c$, the asymptotic state is independent of the time step, suggesting a convergence to a regular stationary state of Eq. (4). In contrast, for $\Theta < \Theta_c$, we have been unable to reach a stationary state independent of the time step. Hence, the numerical results for $\Theta < \Theta_c$ should be taken with caution, since no convergence to a regular solution is achieved. Importantly, this lack of convergence suggests as well that the limit system develops a singularity, indicating the presence of the collapsed phase.

A phase transition toward a collapsed phase at a finite temperature parameter Θ makes our system similar to a 2D self-gravitating gas of Brownian particles, for which the phase transition is predicted at $\Theta_c = 1/(2\pi)$ (see, for example, Ref. [15]), i.e., at a value slightly larger than the one numerically found here. However, in contrast with a 2D self-gravitating gas, the system is truly out of equilibrium; this can be illustrated by computing the current $\vec{J}$ in the stationary state. Using Eq. (4), we have $\vec{J} = \vec{r}\rho + \vec{F}[\rho]\rho + \Theta\vec{\nabla}\rho$, with $\vec{\nabla}\vec{J} = 0$. For interactions deriving from a potential, it is simple to show that, in thermal equilibrium, $\vec{J} = \vec{0}$. In the present case $\vec{J} \neq \vec{0}$, and the inset of Fig. 4 shows their spatial structure. As expected, ingoing currents are along the laser beams where the long-range interaction is maximal. Escaping channels from the trap center are along the diagonals. This current structure explains the crosslike shape found in the particle distribution (see Fig. 2). In the main part of the figure, we see that

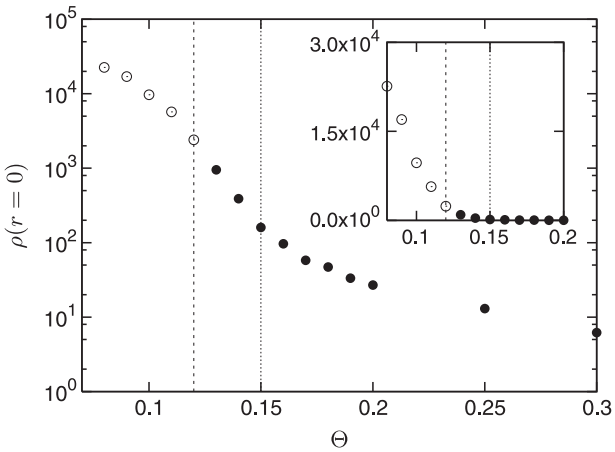

FIG. 3. Density $\rho(r = 0)$ in the center of the trap, as a function of the reduced temperature Θ for $\sigma = 10^{-2}$, $n = 10^4$, and a time step $\Delta t = 10^{-5}$. Filled (empty) points correspond to simulations which have (have not) numerically converged with respect to the time step (see text). Inset: Same quantity plotted in linear-linear scale. The two vertical dashed lines indicate the numerically estimated location of the transition $\Theta_c \approx 0.12$–0.15.

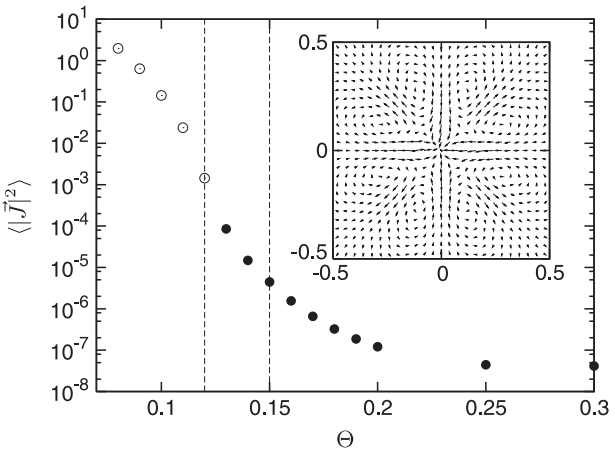

FIG. 4. Spatially averaged square intensity of the currents as a function of Θ for $\sigma = 10^{-2}$, $n = 10^4$, and a time step $\Delta t = 10^{-5}$. Filled (empty) points correspond to simulations which have (have not) numerically converged with respect to the time step (see text). The vertical dashed lines indicate the numerically estimated location of the transition region: $\Theta_c \approx 0.12$–0.15. Inset: Spatial distribution of current $\vec{J}$ in the stationary state, $\Theta = 0.2$. The laser beams are along the axes of the figure.

the current intensity strongly increases as the transition region is approached from above. Like for the central density discussed above, the computed current intensity in the $\Theta < \Theta_c$ region should be taken with caution, since the simulation results still depend on the time step.

Possible experimental realization.—The experiment could be performed following the scheme depicted in Ref. [17]. The starting point would be a ^{88}Sr gas, laser cooled in a magneto-optical trap operating on the narrow $^1S_0 \to {}^3P_1$ intercombination line at 689 nm [22]. The bare linewidth of the transition is $\Gamma/2\pi = 7.5$ kHz. Ultimately, the gas is transferred into one or several 2D dipole traps made with a far off-detuned high power standing optical wave located along the vertical axis. We expect that the interactions between two parallel 2D traps will be weak. In the horizontal plane, two pairs of orthogonal contrapropagating laser beams red detuned with respect to the $^1S_0 \to {}^3P_1$ narrow transition are turned on (see Fig. 1). This setup realizes the proposed 2D gravitational-like interaction. In order to avoid any spatial dependency of the quasiresonant laser beams detuning, the dipole trap wavelength is tuned on the so-called "magic" wavelength, which is $\lambda \sim 900$ nm for our particular case [23]. Importantly, the cold cloud has a horizontal pancake shape. This strong shape asymmetry is necessary to reduce the repulsive interaction mediated by the multiple scattering [24]. In this geometry scattered photons are likely to escape the cloud through the transverse direction. Similar requirements were successfully implemented in the one-dimensional case [17]. They also prevent the generalization of this method to three-dimensional gravitational systems.

We have to check that the regime where the collapse should take place is within reach of current experimental techniques. For this order of magnitude computation, we use a cold cloud with $N = 2 \times 10^6$ atoms at a temperature of $T = 2$ μK. The power of the dipole trap laser beams is 3 W and its waist 300 μm. The trap depth is $k_b/2 \times 10$ μK. The transverse cloud size, frozen by the standing wave trapping, is set to $L_\perp = 5$ μm, whereas the equilibrium longitudinal thermal distribution in the dipole trap and without the quasiresonant laser beams is $L = 100$ μm. Modeling the shadow effect by a long-range gravitationlike force requires a weak absorption of the laser beams, i.e., a low optical depth $b < 1$; it corresponds here to a frequency detuning of $|\delta| > 5.7\Gamma$. In this range, the minimal dimensionless temperature that should be reachable is around $\Theta \sim 0.07$. This is below the theoretical threshold for collapse; thus, the expected phase transition should be observable. One has to make sure, however, that the weak absorption limit is fulfilled, and thus the model is valid, for a large range of spatial density. Indeed, we do not expect, strictly speaking, a collapse of the atomic cloud since above a certain density necessarily $b > 1$. In this latter case, the shadow force becomes short-range and the size of the cloud should remain finite. The modeling we have used also requires a low saturation. For this computation, we have assumed a quasiresonant laser intensity $I = 14I_s$ (where $I_s = 3$ $\mu W/\mathrm{cm}^2$ is the saturation intensity). It corresponds to a saturation parameter $s = (I/I_s)/(4(\delta/\Gamma)^2 + 1) < 0.1$. Thus, the low saturation approximation is fulfilled.

Finally, one notices that the experiment can be, in principle, performed using more standard alkali setup with broad transitions rather than the narrow intercombination line of strontium. However, it is expected to be technically more challenging with the former because "magic" wavelengths are usually more difficult to access [25] and the dipole trap laser should have a much larger power to maintain the higher temperature gas. Moreover, temperatures close to the Fermi temperature have been reported for laser cooling of the ^{87}Sr isotope in a 3D trap [26]. It seems reasonable to believe that the action of laser cooling in combination with the long-range attractive force in the 2D trap might bring the gas closer or even below the degeneracy temperature. If such a condition is fulfilled, like for a white dwarf, the Pauli pressure should play a role in the short-range stabilization of the gas in the collapse phase. The interplay between the nonequilibrium collapse phase and the Pauli pressure remains an open question that should be addressed in a forthcoming publication.

Conclusion.—This work paves the way for experimental observation of a nonequilibrium collapse phase transition, driven by a long-range interaction force. All the characteristic features of the density and the current, should be observable using the current *in situ* or time-of-flight imaging technics. This work also opens the door to outstanding theoretical questions. How could one prove the conjectured collapse? Beyond the entropic computation done here, what could be the tools for such a task? How

could one develop a better numerical scheme when the transition is approached?

We thank Y. Brenier, M. Chalony, D. Chiron, T. Goudon, M. Hauray, P. E. Jabin, and A. Olivetti for useful discussions. This work was partially supported by the ANR 09-JCJC-009401 INTERLOP project and the CNPq (National Council for Scientific Development, Brazil).

[1] G. Ódor, Rev. Mod. Phys. **76**, 663 (2004).
[2] A. Coniglio, Phys. Rev. Lett. **46**, 250 (1981).
[3] H. Hinrichsen, Adv. Phys. **49**, 815 (2000).
[4] M. Berhanu *et al.*, Europhys. Lett. **77**, 59001 (2007).
[5] K. R. Sütterlin *et al.*, Plasma Phys. Controlled Fusion **52**, 124042 (2010).
[6] A. L. Barabási and H. Stanley, *Fractal Concepts in Surface Growth* (Cambridge University Press, Cambridge, England, 1995).
[7] P. Krogstrup, H. I. Jørgensen, E. Johnson, M. H. Madsen, C. B. Sørensen, A. Fontcuberta i Morral, M. Aagesen, J. Nygård, and F. Glas, J. Phys. D **46**, 313001 (2013).
[8] D. E. Wolf, M. Schreckenberg, and A. Bachem, *Traffic and Granular Flow* (World Scientific, Singapore, 1996).
[9] M. Henkel, H. Hinrichsen, and S. Lübeck, *Non-Equilibrium Phase Transitions* (Springer, New York, 2009).
[10] V. Antonov, Vestn. Leningr. Univ., Ser. 1: Mat., Mekh., Astron. **7**, 135 (1962).
[11] D. Lynden-Bell and R. Wood, Mon. Not. R. Astron. Soc. **138**, 495 (1968).
[12] M. Kiessling, J. Stat. Phys. **55**, 203 (1989).
[13] W. Thirring, Z. Phys. A **235**, 339 (1970).
[14] P. H. Chavanis, C. Rosier, and C. Sire, Phys. Rev. E **66**, 036105 (2002).
[15] C. Sire and P. H. Chavanis, Phys. Rev. E **66**, 046133 (2002).
[16] J. Dalibard, Opt. Commun. **68**, 203 (1988).
[17] M. Chalony, J. Barré, B. Marcos, A. Olivetti, and D. Wilkowski, Phys. Rev. A **87**, 013401 (2013).
[18] P. H. Chavanis, Astron. Astrophys. **381**, 340 (2002).
[19] E. F. Keller and L. A. Segel, J. Theor. Biol. **26**, 399 (1970).
[20] M. I. Weinstein, Commun. Math. Phys. **87**, 567 (1983).
[21] D. E. Knuth, *The Art of Computer Programming* (Addison-Wesley, Reading, MA, 1968).
[22] T. Chanelière, L. He, R. Kaiser, and D. Wilkowski, Eur. Phys. J. D **46**, 507 (2008).
[23] H. Katori, T. Ido, and M. Kuwata-Gonokami, J. Phys. Soc. Jpn. **68**, 2479 (1999).
[24] T. Walker, D. Sesko, and C. Wieman, Phys. Rev. Lett. **64**, 408 (1990).
[25] B. Arora, M. S. Safronova, and C. W. Clark, Phys. Rev. A **76**, 052509 (2007).
[26] T. Mukaiyama, H. Katori, T. Ido, Y. Li, and M. Kuwata-Gonokami, Phys. Rev. Lett. **90**, 113002 (2003).

Long-range one-dimensional gravitational-like interaction in a neutral atomic cold gas

M. Chalony,[1] J. Barré,[2,*] B. Marcos,[2,†] A. Olivetti,[2] and D. Wilkowski[1,3,4,‡]

[1]*Institut Non Linéaire de Nice-UMR7335, Université de Nice Sophia-Antipolis, CNRS, 06560 Valbonne, France*

[2]*Laboratoire J.-A. Dieudonné-UMR7351, Université de Nice Sophia-Antipolis, CNRS, 06109 Nice, France*

[3]*Centre for Quantum Technologies, National University of Singapore, 117543 Singapore, Singapore*

[4]*PAP, School of Physical and Mathematical Sciences, Nanyang Technological University, 637371 Singapore, Singapore*

(Received 5 February 2012; published 2 January 2013)

A quasiresonant laser induces a long-range attractive force within a cloud of cold atoms. We take advantage of this force to build in the laboratory a system of particles with a one-dimensional gravitational-like interaction, at a fluid level of modeling. We give experimental evidences of such an interaction in a cold Strontium gas, studying the density profile of the cloud, its size as a function of the number of atoms, and its breathing oscillations.

DOI: 10.1103/PhysRevA.87.013401 PACS number(s): 37.10.De, 04.80.Cc, 05.20.Jj, 37.10.Gh

I. INTRODUCTION

When interactions between the microscopic components of a system act on a length scale comparable to the size of the system, one may call them "long range": for instance, the inverse-square law of the gravitational force between two point masses which is one of the most celebrated and oldest laws in physics. In the many particles world, it is responsible for dramatic collective effects such as the gravothermal catastrophe [1] or the gravitational clustering which is the main mechanism leading to the formation of the structure of galaxies in the present universe. Beyond gravitation, such long-range interactions are present in various physical fields, either as fundamental or as effective interactions: in plasma physics [2], two-dimensional (2D) fluid dynamics [3], degenerated quantum gases [4], ion trapping [5], to cite only these works. Long-range interactions deeply influence the dynamical and thermodynamical properties of such systems. At the thermodynamic equilibrium, long-range interactions are at the origin of very peculiar properties, especially for attractive systems: The specific heat may be negative; canonical (fixed temperature) and microcanonical (fixed energy) ensembles are not equivalent. These special features have been known for a long time in the astrophysics community, in the context of self-gravitating systems.

After the seminal works of Lynden-Bell and Wood [6] and Thirring [7], many contributions followed on this subject (see, for instance, [8] for a recent review), so that the equilibrium characteristics of attractive long-range interacting systems are theoretically well established. This situation is in striking contrast with the experimental side of the problem: There is currently no controllable experimental system exhibiting the predicted peculiarities. There have been some proposals to remedy this situation: O'Dell *et al.* [4] have suggested creating an effective $1/r$ potential between atoms in a Bose-Einstein condensate using off-resonant laser beams; more recently, Dominguez *et al.* [9] have proposed taking advantage of the capillary interactions between colloids to mimic two-dimensional gravity, and Golestanian [10] has suggested experiments using thermally driven colloids. However, these proposals have not been implemented yet, and so far the dream of a tabletop galaxy remains elusive.

The key results of this paper are to show some experimental evidences of a gravitational-like interaction in a quasi-one-dimensional (hereafter 1D) test systems consisting in a cold gas of Strontium atoms in interaction with two contra-propagating quasiresonant lasers. To our knowledge, it is the first experimental realization of the 1D gravitational toy model, which can be compared with the theoretical predictions developed for more than 50 years by the astrophysical and statistical physics community. In the stationary regime, the cloud spatial distribution is in agreement with the well-known sech^2 law for the 1D self-gravitating gas at thermal equilibrium [11]. Moreover, the long-range attractive nature of the force is confirmed studying the cloud's size dependency as a function of the number of atoms. Out of equilibrium, the breathing oscillation frequency increases with the strength of the interaction as it should be for attractive interactions. Quantitatively our experimental results are in agreement with the expected $1/r^\alpha$ force with $\alpha = 0$.

The paper is organized as follows. In Sec. II, we start from the radiation pressure exerted by the lasers and explain under which circumstances this force becomes analog to a 1D gravitational force. We then make some definite theoretical predictions on the size, density profile, and oscillation frequency of the interacting atomic cloud. The experimental setup is described in Sec. III. In the same section, the experimental results are compared with the theory.

II. MODEL AND THEORETICAL PREDICTIONS

The gravitational potential $U(r)$ between two particles can be expressed through the Poisson equation $\nabla^2 U(\mathbf{r}) = A_D G m \delta(\mathbf{r})$, where G is the coupling constant, m the mass of the particle, and A_D a numerical constant which depends on the dimension. The solution of the Poisson equation for the interpaticle potential $U(r)$ in three dimensions is the well-known

$$U(r) = \frac{Gm}{r}, \tag{1}$$

and in 1D,

$$U(r) = Gm|r| \tag{2}$$

*julien.barre@unice.fr
†bruno.marcos@unice.fr
‡david.wilkowski@ntu.edu.sg

(for a review on 1D gravitational systems see, e.g., [12]). After using a mean-field approach (see below), we will show that such a potential should be at play in our experiment, under precise circumstances (see Sec. II B).

We start considering a quasi-1D {cold atomic gas + 1D quasiresonant laser beams} system; an atomic gas, with a linear density $n(z)$, is in interaction with two contra-propagating laser beams. The two beam intensities $I_+(z)$ and $I_-(z)$, where $I_+(-\infty) = I_-(+\infty) \equiv I_0$, respectively, propagating in the positive and negative direction, are much smaller than the atomic line saturation intensity I_s. Thus the atomic dipolar response is linear. The radiation pressure force of the lasers on an atom, having a longitudinal velocity v_z, is given by [13]

$$F_\pm(z,v_z) = \pm\hbar k \frac{\Gamma}{2}\frac{\Gamma^2}{4(\delta \mp k v_z)^2 + \Gamma^2}\frac{I_\pm(z)}{I_s}, \tag{3}$$

where $\hbar$ is the reduced Planck constant, Γ the bare linewidth of the atomic transition, k the wave number, and δ the frequency detuning between an atom at rest and the lasers. For a cloud of N atoms, the attenuation of the laser intensity is given by

$$dI_\pm = \mp\frac{\sigma_\pm}{2\pi L_\perp^2} N I_\pm n(z) dz, \tag{4}$$

where $n(z)$ is the normalized linear density profile and

$$\sigma_\pm = \frac{6\pi}{k^2}\Gamma^2 \int \frac{g(v_z)}{4(\delta \mp k v_z)^2 + \Gamma^2} dv_z \tag{5}$$

is the average absorption cross section for a single atom. $g(v_z)$ is the normalized longitudinal velocity distribution and $2\pi L_\perp^2$ is the transverse section of the cloud. At equilibrium $g(v_z)$ is an even function so $\sigma_- = \sigma_+ \equiv \sigma$. The optical depth is defined as

$$b = \frac{\sigma}{2\pi L_\perp^2} N \int_{-\infty}^{+\infty} n(z) dz = \frac{\sigma N}{2\pi L_\perp^2}. \tag{6}$$

Atoms also experience a velocity diffusion due to the random photon absorptions and spontaneous emissions: This is modeled by a velocity diffusion coefficient D introduced in Eq. (7). In experiments, $\delta < 0$ such that the force, given in Eq. (3), is a cooling force counteracting the velocity diffusion. We now describe the N atoms by their phase space density in 1D, $f(z,v_z,t)$. As in [14], we write a Vlasov Fokker-Planck equation,

$$\frac{\partial f}{\partial t} + v_z \frac{\partial f}{\partial z} - \omega_z^2 z \frac{\partial f}{\partial v_z} + \frac{1}{m}\frac{\partial}{\partial v_z}\{[F_+(z,v_z) + F_-(z,v_z)]f\} = D\frac{\partial^2 f}{\partial v_z^2}, \tag{7}$$

which is, for most of the cases, a reasonable modeling of long-range force systems in the mean-field approximation (see, e.g., [15]). The second term in Eq. (7) is an inertial one, whereas the third one describes a harmonic trapping force being a good approximation of the dipolar trap used in the experiment [16]. Indeed the dipolar potential, in the longitudinal axe of interest, can be written as

$$U_{\rm dip}(z) = \frac{-U_0}{1 + \left(\frac{z}{z_R}\right)^2}, \tag{8}$$

with $z_R = 1.2$ mm, $U_0 = \frac{1}{2}k_B T_{\rm trap}$, and $T_{\rm trap} = 20\,\mu$K. The observed rms longitudinal size being $L_z \lesssim 400\,\mu$m, it is reasonable to perform a Taylor expansion around $z = 0$ to get the harmonic approximation:

$$U_{\rm dip}(z) \approx -U_0\left[1 - \left(\frac{z}{z_R}\right)^2\right], \tag{9}$$

having a characteristic frequency,

$$\omega_z = \left(\frac{k_B T_{\rm trap}}{m z_R^2}\right)^{1/2}. \tag{10}$$

The fourth term of Eq. (7) contains the mean-field force $F_\pm$ divided by the atomic mass m. The right-hand side describes a velocity diffusion. The use of a one-dimensional model is justified by the fact that the ratio between the rms transverse $L_\perp$ and longitudinal L_z size of the cloud measured in the experiment is $L_\perp/L_z \approx 2\times 10^{-2}$. Equation (7) neglects atomic losses and dependencies in position and velocity of the velocity diffusion coefficient.

One notes that the attractive force coming from the beams absorption [Eqs. (3) and (4)] is known since the early days of laser cooling and trapping [17]. However, in an usual three-dimensional (3D) setting this attractive force is dominated by the repulsive force due to photons reabsorption [18], which, in the small optical depth limit, may be seen as an effective repulsive Coulomb force. By contrast, in a 1D configuration with an elongated cloud along the cooling laser beams, the probability of photon reabsorption is reduced by a factor of the order of $L_\perp/L_z$, in comparison with the isotropic cloud having the same longitudinal optical depth. In our experiment, the reduction factor is about 2×10^{-2}, so that the repulsive force can be safely ignored. Similar but weaker reduction of the probability of photons reabsorption is also expected for the 2D geometry, which opens the possibility of experimental systems analogous to 2D self-gravitating systems.

A. Fluid approximation

In order to solve Eq. (7) we assume that the system can be described using a fluid approach: The velocity distribution at time t does not depend on the position, except for a macroscopic velocity $u(z,t)$. We write then the one point distribution function f as

$$f(z,v_z,t) = mNn(z,t)\frac{1}{\Delta(t)} g\left(\frac{v_z - u(z,t)}{\Delta(t)}\right). \tag{11}$$

The velocity distribution $g(v_z)$ is even, centered around u; the velocity dispersion is characterized by a time modulation $\Delta(t)$. Integrating Eq. (7) over dv_z and over $v_z dv_z$, we obtain the fluid equations:

$$\frac{\partial n}{\partial t} + \frac{\partial}{\partial z}(nu) = 0 \tag{12}$$

$$\frac{\partial (nu)}{\partial t} + \frac{\partial}{\partial z}\left[\left(u^2 + \Delta(t)^2 \int v_z^2 g(v_z) dv_z\right) n\right] + \omega_z^2 z n - \frac{1}{m} n \int (F_+ + F_-) g\left(\frac{v_z - u(z,t)}{\Delta(t)}\right)\Delta(t) dv_z = 0. \tag{13}$$

B. Stationary solution

We first look for a stationary solution; this imposes $u = 0$ and $\Delta = 1$. Equation (12) is then automatically satisfied; Eq. (13) for the stationary density $n(z)$ reads

$$\bar{v}_z^2 \frac{\partial n}{\partial z} + \omega_z^2 z n - \frac{1}{m} n \int [F_+ + F_-] g(v_z) dv_z = 0, \quad (14)$$

where we have used the notation $\int v_z^2 g(v_z) dv_z = \bar{v}_z^2$.

Equation (4) is easily integrated, yielding

$$I_+(z) = I_0 e^{-b \int_{-\infty}^{z} n(s) ds}, \quad (15)$$

$$I_-(z) = I_0 e^{-b \int_{z}^{+\infty} n(s) ds}. \quad (16)$$

The exponentials are expanded up to first order, according to the small optical depth hypothesis $b \ll 1$:

$$I_+(z) \simeq I_0 \left(1 - b \int_{-\infty}^{z} n(s) ds\right) \quad (17)$$

$$I_-(z) \simeq I_0 \left(1 - b \int_{z}^{+\infty} n(s) ds\right). \quad (18)$$

Introducing these expressions for $I_\pm$ into Eq. (14), we obtain finally

$$\bar{v}_z^2 \frac{\partial n}{\partial z} + \omega_z^2 z n - N C n \int_{-\infty}^{+\infty} \mathrm{sgn}(s - z) n(s) ds = 0, \quad (19)$$

where

$$C = \frac{3\hbar\Gamma}{2mkL_\perp^2} \frac{I_0}{I_s} \left(\sigma \frac{k^2}{6\pi}\right)^2. \quad (20)$$

Equation (19) is equivalent to an equation describing the stationary density of an assembly of N trapped particles of mass m, with gravitational coupling constant G, in an external harmonic trap of frequency ω_z, in a heat bath at temperature T, with the correspondence:

$$\bar{v}_z^2 \leftrightarrow \frac{k_B T}{m}, \quad (21a)$$

$$C \leftrightarrow Gm, \quad (21b)$$

where k_B is the Boltzmann constant. Two characteristic lengths are identified,

$$L_{ni} = \sqrt{\frac{k_B T}{m \omega_z^2}} \quad (22)$$

is the characteristic size of the noninteracting gas in its external harmonic holding potential. Using Eq. (10) we get

$$L_{ni} = \sqrt{\frac{T}{T_{\mathrm{trap}}}} z_R. \quad (23)$$

The other characteristic length L_i is associated with the interaction strength:

$$L_i = \frac{k_B T}{NCm}. \quad (24)$$

Using these notations we write Eq. (19) as

$$\frac{\partial n}{\partial z} + \frac{z n}{L_{ni}^2} - \frac{n}{L_i} \int_{-\infty}^{+\infty} \mathrm{sgn}(s - z) n(s) ds = 0. \quad (25)$$

The first term of (25) favors the density spreading. In contrast with the 2D and 3D cases, it always prevents the collapse of the cloud [19]. The second term describes an external harmonic confinement coming from the dipole trap in the experiment. The third term is the attractive interaction due to laser beam absorption. It corresponds to a 1D gravitational potential expression in Eq. (2). If the inequality $L_i \ll L_{ni}$ is fulfilled, Eq. (25) is the one expected for a 1D self-gravitating gas at thermal equilibrium [11]. It yields the profile:

$$n(z) = \frac{1}{4L_i} \mathrm{sech}^2 \left(\frac{z}{2L_i}\right). \quad (26)$$

A generalization of Eq. (25) is written as

$$\frac{\partial n}{\partial z} + \frac{1}{k_B T} \frac{\partial U_{\mathrm{dip}}}{\partial z} n - A n \int_{-\infty}^{+\infty} |s - z|^{-\alpha} \mathrm{sgn}(s - z) n(s) ds = 0, \quad (27)$$

including the exact form of the dipole trap (8), and the variation of the interaction exponent α of a $1/r^\alpha$ attractive force. This expression is used to compare theory with experiments in Sec. III. A is a free parameter controlling the interaction strength, and thus the width of the equilibrium profile.

C. Breathing oscillations

To probe the dynamics of the system, we now go back to Eqs. (12) and (13), linearizing these equations with respect to u and $\Delta - 1$, for small amplitude oscillations. One notes that this approximation is much less restrictive than linearizing with respect to the velocity v_z. We then compute $\int [F_+ + F_-] f dv_z$:

$$\int [F_+ + F_-] f dv_z \simeq c_1 (I_+ - I_-) n + c_2 (I_+ + I_-) n u + c_3 (\Delta - 1)(I_+ - I_-) n, \quad (28)$$

where the constants c_i involve integrations with respect to v_z. The first term is the gravitational-like force, as in (19) with $n(z)$ replaced by the time-dependent density $n(z,t)$. The second one is a friction, which *a priori* depends weakly on z through $I_+ + I_-$. Since $I_+ - I_-$ is of order $b \ll 1$, the third term, of order $b(\Delta - 1)$, is neglected. We assume that the dynamics is captured by a single parameter $\lambda(t)$, using the ansatz [20]:

$$f(z, v_z, t) = mNn(z/\lambda) g(\lambda v_z - \dot{\lambda} z). \quad (29)$$

When compared with (11), this amounts to assuming the following: $u = \frac{\dot{\lambda}}{\lambda} z, \Delta = 1/\lambda$. We introduce the notations $\langle \cdot \rangle$ and $\langle \cdot \rangle_0$ for the spatial average of a quantity over the density at time t and the stationary density, respectively. Then

$$\langle z^2 \rangle = \lambda^2 \langle z^2 \rangle_0, \quad \langle zu \rangle = \lambda \dot{\lambda} \langle z^2 \rangle_0, \quad \langle u^2 \rangle = \dot{\lambda}^2 \langle z^2 \rangle_0. \quad (30)$$

We note that Eq. (12) is automatically satisfied by the ansatz (29). To obtain an equation for λ, we integrate Eq. (13) over $z dz$. We obtain, for λ close to 1 (small amplitude oscillations):

$$\ddot{\lambda} + \kappa \dot{\lambda} + \omega^2 (\lambda - 1) = 0, \quad (31)$$

with κ an effective friction and a breathing oscillation frequency:

$$\omega_{\mathrm{br}} = \omega_z (3(p - 1) + 4)^{\frac{1}{2}}. \quad (32)$$

p measures the compression of the cloud:

$$p = \frac{L_{ni}^2}{L_z^2}. \tag{33}$$

In experiments where the effective friction is rather small, Eq. (32) is expected to be a fair approximation for the breathing oscillation frequency. More generally, assuming a power law two-body interaction force in the gas $1/r^\alpha$, the simple relation for $\omega_{\rm br}$ in the weak damping limit becomes [20]

$$\omega_{\rm br} = \omega_z \left[(3-\alpha)(p-1)+4\right]^{\frac{1}{2}}. \tag{34}$$

This formula relates $\omega_{\rm br}$ to α and p, and will be used in Sec. III D. Equation (34) was derived in [20] assuming a velocity independent interaction term, which would be obtained by linearizing the radiation pressure force (3) in velocity. This is not a reasonable approximation in our experiments [21], but we have shown here that (34) is still expected to provide a reasonable approximation for the breathing frequency in the limit of small optical depth.

III. EXPERIMENTS

A. Experimental setup

The sample preparation is done in the same way as depicted in [22]. More details about laser cooling of Strontium in a magneto-optical trap (MOT) can be found in [23]. After laser cooling, around 10^5 atoms at $T \simeq 3\,\mu$K are loaded into a far detuned dipole trap made of a 120-mW single focused laser beam at 780 nm. Analyses are performed using *in situ* images taken with a CCD at different instances of the experimental sequence. The longitudinal profile is obtained averaging over the irrelevant remaining transverse dimension. We directly measure the longitudinal trap frequency $\omega_z = 6.7(0.5)$ Hz from relaxation oscillations of the cold cloud (see example of temporal evolutions in Fig. 1). The radial trap frequency $\omega_\perp = 470(80)$ Hz is deduced from cloud size measurements. The beam waist is estimated at 23(2) μm leading to a potential depth of $T_{\rm trap} \simeq 20\,\mu$K.

Fifty milliseconds after loading the dipole trap (corresponding to $t = 0$ in Fig. 1), a contra-propagating pair of laser beams, red-detuned with respect to the $^1S_0 \to {}^3P_1$ intercombination line at 689 nm (radiative lifetime: 21 μs), is turned on for 400 ms. These beams, aligned with respect to the longitudinal axis of the cloud, generate the effective 1D attractive interaction. When the 1D lasers are on, we apply a $B = 0.3$ G magnetic bias field, for two important reasons: First, the Zeeman degeneracy of the excited state is lifted such that the lasers interact only with a two-level system made out of the $m = 0 \to m = 0$ transition which is insensitive to the residual magnetic field fluctuation. Second, the orientation of magnetic field bias, with respect to the linear polarization of the dipole trap beam, is tuned to cancel the clock (or transition) shift induced by the dipole trap on the transition of interest [22].

The temperature along the 1D laser beams, in our experimental runs, is found to be in the range of 1–3 μK. Even at such low temperatures, and in sharp contrast with standard broad transitions, the frequency Doppler broadening $k\bar{v}_z$ remains larger than Γ. As a direct consequence, the optical depth b depends on the exact longitudinal velocity distribution $g(v_z)$

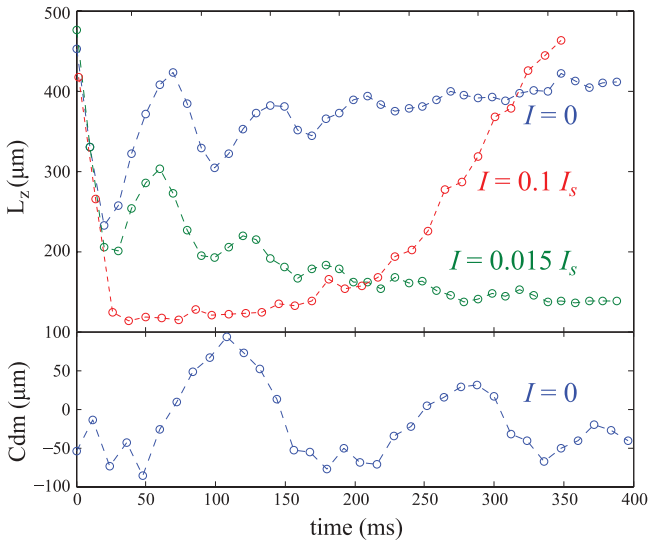

FIG. 1. (Color online) (Top) Typical temporal evolutions of L_z the rms longitudinal size of the atomic cloud for three different 1D beam intensities. The laser detuning is $\delta = -5\Gamma$ for all curves. (Bottom) The center-of-mass (Cdm) position of the atomic gas without the 1D lasers ($I = 0$). The y-axis origin is arbitrary.

[see Eqs. (5) and (6)] which are not necessarily Gaussian [22]. Since we measure only the second moment of the distribution $g(v_z)$, namely, $\bar{v}_z$ or T, one has enough control to assert the $b \ll 1$ limit, thus the occurrence of the self-gravity regime. However, we can perform only qualitative tests of our theory described in Sec. II B.

At $t = -50$ ms, the MOT cooling laser beams are turned off, leaving the trapped atomic cloud in an out-of-equilibrium macroscopic state. Without the 1D lasers, we observed a weakly damped oscillation of the breathing mode and of the center-of-mass position (blue circles in Fig. 1). One notes that damping is caused by anharmonicity of the dipole trap and not by thermalization of the gas which is negligible on the experimental timescale. In the presence of the 1D laser beams, overdamped or underdamped oscillations of the cloud are observed.

B. Stationary state's density profile

Let us first consider the stationary state in the overdamped situation (red circles in Fig. 1). After the transient phase ($t <$ 30 ms), the rms longitudinal size of the atomic gas reaches a plateau at a minimal value of $L_z \simeq 120\,\mu$m with $T \simeq 2\,\mu$K. The slow increase of the cloud's size after the plateau ($t >$ 150 ms) goes with an increase of the temperature up to 4 μK at the end of the time sequence. The origins of the long time scale evolution are not clearly identified, but it is most likely due to coupling of the longitudinal axis with the uncooled transverse dimensions because of imperfect alignment of the 1D laser beams with the longitudinal axis of the trap and nonlinearities of the trapping forces. At the plateau where temperature is around 2 μK the noninteracting gas is expected to have an rms longitudinal size of $L_z = L_{ni} \simeq 370\,\mu$m. Hence, a clear compression of the gas by a factor of three is observed. It is due to the attractive interaction induced by the absorption of the 1D

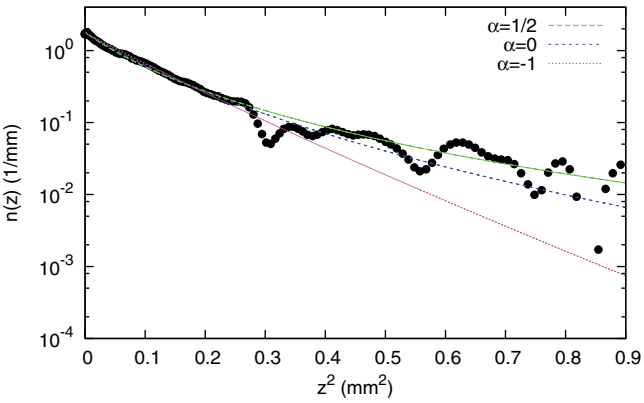

FIG. 2. (Color online) Density linear distribution for $N = 10^5$. The black circles are the experimental data with $I = 0.02I_s$, $\delta = -6\Gamma$, and $b \simeq 0.4$. The profiles were symmetrized to improve the signal-to-noise ratio. The curves are least-square fits of the data using Eq. (27) containing the exact form of the dipole trap and a two-body interaction force $1/r^\alpha$. The fits are performed for each α by fixing the normalization and varying the interaction strength.

laser beams. Moreover, the estimated optical depth is $b < 0.6$. We then approach the two previously mentioned conditions—$b \ll 1$ and $L_z \ll L_{ni}$—for being in the 1D self-gravitating regime as discussed in Sec. II B. In Fig. 2, where $b \simeq 0.4$, we test the effective interaction in the gas by assuming a power law two-body interaction force in the gas $1/r^\alpha$ and fitting the experimental linear density distribution for different values of α in the presence of a dipolar trap; $\alpha = 0$ corresponds to 1D gravity. We see that the best fit seems to be for $\alpha \in [0,1/2]$.

In the absence of the 1D laser beams, we have checked that the experimental linear density distribution has the expected profile of a noninteracting gas in our dipole trap having a $z_R = 1.2(1)$ mm Rayleigh length.

C. Cloud's longitudinal size

In the self-gravitating regime a $1/N$ dependency of L_z is expected at fixed temperature [see Eq. (26) and the definition of L_i]. Figure 3 shows that the cloud's size L_z is in agreement with this prediction for two temperature ranges: 1.5(2) μK (blue circle) and 2.1(2) μK (red star). Fits correspond to the blue dashed line for 1.5(2) μK and the red dashed line for 2.1(2) μK. The fitting expression is

$$N = a\left(1/L_z - L_z/L_{ni}^2\right), \tag{35}$$

where a and L_{ni} are free parameters depending on the temperature of the gas. If $L_{ni} \gg L_z$, the self-gravitating regime is recovered in the fitting expression. However Eq. (35) takes into account the presence of a harmonic trap. Equation (35) can be simply derived using the generalized virial theorem [see Eq. (11) in Ref. [24]] and it is in perfect agreement with numerical integrations of Eq. (25). The fits give $L_{ni} \simeq 0.5$ mm, slightly larger than the expected value of L_{ni} at these temperatures. The $1/N$ dependency of L_z in the self-gravitational regime is consistent with a long-range interaction with $\alpha = 0$. Unfortunately as discussed above, the residual Doppler effect prevents a quantitative comparison with the prediction of our model.

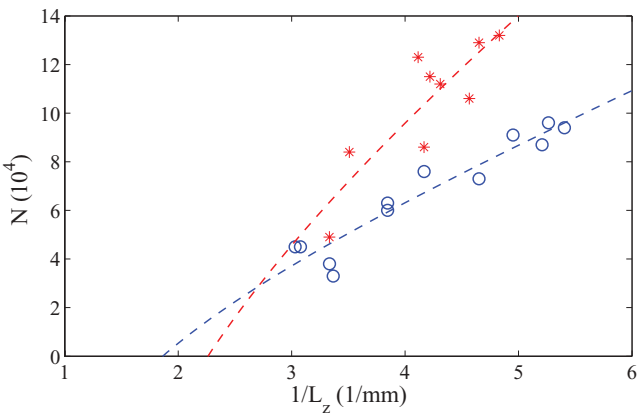

FIG. 3. (Color online) Dependency of the longitudinal size of the cloud with the number of atoms for $\delta = 5.7(5)\Gamma$ and $I = 0.3I_s$. The blue circle (red star) data points correspond to temperature 1.5(2) μK [2.1(2) μK]. The optical depth is in the range of 0.6–0.2 according to atom number variations. The blue and the red dashed lines are fits using Eq. (35).

D. Breathing oscillations

Let us now consider the evolution of the trapped cold cloud in the underdamped situation (as an example, see green circles in Fig. 1). Without the 1D lasers, the ratio of the eigenfrequencies of the breathing mode $\omega_{\rm br}$ and the center of mass ω_z is found to be close to two, as expected for a noninteracting gas in a harmonic trap. As an example the blue curve, shown in Fig. 1, gives $\omega_{\rm br}/\omega_z = 1.9(1)$. If now the attractive long-range interaction is turned on, $\omega_{\rm br}$ is expected to follow Eq. (34) whereas ω_z should remain unchanged.

Figure 4 summarizes the comparisons between the measured ratio $(\omega_{\rm br}/\omega_z)^2$ and the predictions deduced from the relation (34). p is computed from the experimental data in the stationary state. We expect $\alpha = 0$, however, to judge the nature of the long-range attractive interaction; three plots, respectively, for $\alpha = 0,1$, and 2 are shown. If the $\alpha = 2$ case can be excluded, the experimental uncertainty does not allow one to clearly discriminate between $\alpha = 0$ and $\alpha = 1$. In conjunction with Fig. 2, we conclude that the system is

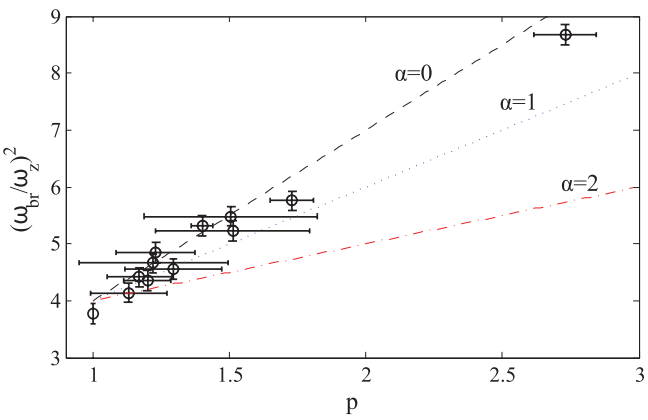

FIG. 4. (Color online) Comparison for $\alpha = 0$, 1, and 2 of the experimental ratio $(\omega_{\rm br}/\omega_z)^2$ and the predictions deduced from the relation (34). The values of p are measured on the experiment.

reasonably well described by a gravitational-like interaction, $\alpha = 0$.

IV. CONCLUSION AND PERSPECTIVES

In this paper, we give strong indications of an 1D gravitational-like interaction in a Strontium cold gas induced by quasiresonant contra-propagating laser beams. First, we show that in the self-gravitating limit, the density distribution follows the theoretically expected profile. Moreover, the scaling of the cloud size with the number of atoms follows the predicted $1/N$ law. Finally, the modification of breathing frequency of the cloud, due to the long-range interaction, is correctly described by a self-gravitating model.

Other phenomena can also be investigated, for example, in relation with plasma physic; Landau damping should be observed studying the return to equilibrium of the system after various perturbations. Moreover, the actual experimental system could be easily extended to 2D geometry suggesting interesting consequences: By contrast with the 1D case, a 2D self-gravitating fluid undergoes a collapse at low enough temperature, or strong enough interaction. Hence, it is conceivable that an experiment similar to the one presented in this paper, in a pancake geometry, would show such a collapse [25].

ACKNOWLEDGMENTS

This work is partially supported by the ANR-09-JCJC-009401 INTERLOP project. D.W. wishes to thank Frédéric Chevy for fruitful discussions.

[1] V. Antonov, Soviet Astr.-AJ **4**, 859 (1961).
[2] Y. Elskens and D. Escande, *Microscopic Dynamics of Plasmas and Chaos* (IOP Publishing, Bristol, 2002).
[3] P. H. Chavanis, in *Dynamics and Thermodynamics of Systems with Long-Range Interactions*, edited by T. Dauxois, S. Ruffo, E. Arimondo, and M. Wilkens (Springer, New York, 2002).
[4] D. O'Dell, S. Giovanazzi, G. Kurizki, and V. M. Akulin, Phys. Rev. Lett. **84**, 5687 (2000).
[5] D. Porras and J. I. Cirac, Phys. Rev. Lett. **92**, 207901 (2004).
[6] D. Lynden-Bell and R. Wood, Mon. Not. R. Astron. Soc. **138**, 495 (1968).
[7] W. Thirring, Z. Phys. A **235**, 339 (1970).
[8] A. Campa, T. Dauxois, and S. Ruffo, Phys. Rep. **480**, 57 (2009).
[9] A. Dominguez, M. Oettel, and S. Dietrich, Phys. Rev. E **82**, 011402 (2010).
[10] R. Golestanian, Phys. Rev. Lett. **108**, 038303 (2012).
[11] G. Camm, Mon. Not. R. Astron. Soc. **110**, 305 (1950).
[12] K. R. Yawn and B. N. Miller, Phys. Rev. E **68**, 056120 (2003).
[13] H. Metcalf and P. van der Straten, Phys. Rep. **244**, 203 (1994).
[14] R. Romain, D. Hennequin, and P. Verkerk, Eur. Phys. J. D. **61**, 171 (2011).
[15] J. Binney and S. Tremaine, *Galactic Dynamics* (Princeton University Press, Princeton, 2008).
[16] S. Chu, J. E. Bjorkholm, A. Ashkin, and A. Cable, Phys. Rev. Lett. **57**, 314 (1986).
[17] J. Dalibard, Opt. Commun. **68**, 203 (1988).
[18] T. Walker, D. Sesko, and C. Wieman, Phys. Rev. Lett. **64**, 408 (1990).
[19] T. Padmanabhan, Phys. Rep. **188**, 285 (1990).
[20] A. Olivetti, J. Barré, B. Marcos, F. Bouchet, and R. Kaiser, Phys. Rev. Lett. **103**, 224301 (2009).
[21] For our experimental data points shown in Fig. 4, $0.3 < k\bar{v}_z/\delta < 1.2$.
[22] M. Chalony, A. Kastberg, B. Klappauf, and D. Wilkowski, Phys. Rev. Lett. **107**, 243002 (2011).
[23] T. Chaneliere, L. He, R. Kaiser, and D. Wilkowski, Eur. Phys. J. D **46**, 507 (2008).
[24] F. Werner, Phys. Rev. A **78**, 025601 (2008).
[25] J. Barré, D. Wilkowski, and B. Marcos (unpublished).

Towards a measurement of the Debye length in very large magneto-optical traps

J. Barré,[1] R. Kaiser,[2] G. Labeyrie,[2] B. Marcos,[3] and D. Métivier[3,*]
[1]*Institut Denis Poisson, Université d'Orléans, Université de Tours, CNRS, France and Institut Universitaire de France*
[2]*Université Côte d'Azur, CNRS, Institut de Physique de Nice, 06560 Valbonne, France*
[3]*Université Côte d'Azur, CNRS, Laboratoire J.-A. Dieudonné, 06109 Nice, France*

(Received 6 August 2018; revised manuscript received 14 May 2019; published 19 July 2019)

We propose different experimental methods to measure the analog of the Debye length in a very large magneto-optical trap, which should characterize the spatial correlations in the atomic cloud. An analytical, numerical, and experimental study of the response of the atomic cloud to an external modulation potential suggests that this Debye length, if it exists, is significantly larger than what was expected.

DOI: 10.1103/PhysRevA.100.013624

I. INTRODUCTION

Magneto optical traps (MOTs), as first realized in 1987 [1], are still a ubiquitous device to manipulate cold atoms. Early studies [2] have shown that when the number of trapped atoms is increased beyond a certain level, the peak density tends to saturate. This unwanted limitation to obtain high spatial densities of laser-cooled atomic samples has been attributed to an effective repulsion between atoms due to multiple scattering of photons. A basic model to describe atoms in a large MOT has then emerged, where atoms, beyond the friction and external trapping force, are subjected to two kinds of effective interaction forces: an effective Coulomb repulsion of [2], which is dominant, and an effective attraction, sometimes called shadow effect, as first described in [3]. Even though the shortcomings of this model are well known (such as a too large optical depth, space dependent trapping parameters [4], subdoppler mechanisms [5,6], light assisted collisions [7], and radiative escape [8,9] or hyperfine changing collisions [10,11]), its predictions on the size and the shape of the atomic clouds are in reasonable agreement with experiments on very large MOTs [12].

It is striking that the above "standard model" describes MOTs as a kind of analog of a non-neutral plasma, as well as an instance of an experimentally controllable system with long-range interactions. This has prompted several studies [13–19], aimed at better probing this analogy and its consequences. We note that these long-range forces stem from the resonant dipole-dipole coupling between atoms [20–26], which if interference can be neglected lead to radiation trapping of light in cold atoms [27–29]. This dipole-dipole coupling is also at the origin of modified radiation pressure on the center of mass [30,31] and of optical binding with cold atoms [32] as well as of supersubradiance [33–35].

Current technologies now allow for larger and larger MOTs, for which long-range interactions become even more important. Hence it becomes feasible to test more quantitatively this plasma analogy. In particular, spatial correlations in plasmas are controlled by a characteristic length, called the Debye length, which depends on charge, density, and temperature. A natural question thus arises: is an experimental observation of a Debye length possible in a large MOT?

In this paper, we propose and analyze three types of experiments to probe spatial correlations in a MOT. We first explain how an analysis of the density profile in the MOT provides an indirect measurement of the Debye length. Then we present a direct measurement by diffraction, and highlight its inherent difficulties: we have not been able to measure spatial correlations this way. Finally, we demonstrate that the cloud's response to an external modulation should also provide an indirect measurement of the Debye length. Our experimental results then show that if the interactions are indeed adequately described by a Coulomb-like interaction, the corresponding Debye length is much larger than what could be expected based on the observed size of the cloud without interaction.

We attempt to characterize density-density correlations in MOTs. This problem has been tackled in various circumstances for quantum gases (see for instance [36,37]); however, in most cases, the density variations of interest were much stronger than those we would like to see in a MOT: a direct imaging of the gas was then often enough to extract the correlations.

In Sec. II, we recall the basic features of the "standard model," based on [2], explain the analogy with non-neutral plasmas, introduce some concepts which will be needed later, and discuss the relevant orders of magnitudes. In Sec. III, we first present our general experimental setup (Sec. III A), then explain the different options to probe the interactions and correlations inside the cloud: (i) analysis of the density profile (Sec. III B), (ii) direct diffraction experiments (Sec. III C), (iii) response to an external modulation (Sec. III D). While method (ii) proves to be not viable with current techniques, comparison of analytical results, simulations, and experiments for methods (i) and (iii) suggest that the Debye length in the cloud may be much larger than expected. The last section, Sec. IV, is devoted to a discussion

*Present address: Center for Nonlinear Studies and Theoretical Division T-4 of Los Alamos National Laboratory, New Mexico 87544, USA.

of these results. Some technical parts are detailed in two Appendices.

II. STANDARD THEORETICAL MODEL AND PLASMA ANALOGY

A. Density-density correlations

Theoretical descriptions and experimental measurements of density-density correlations are present in all fields of condensed matter. We first give below a short introduction to linear response theory and static structure factors, which will play an important role later on (more details can be found for instance in [38]). We define the *one-point probability* distribution function $\rho(\vec{r},t)$, usually called *density*, as the probability to find a particle at the position $\vec{r}$ at time t. If the system is statistically homogeneous the density does not depend on the position and time and $\rho(\vec{r},t)=\rho_c$. We define the *two-point probability* distribution function $\rho^{(2)}(\vec{r},\vec{r}',t)$ as the probability to find one particle at the position $\vec{r}$ and another one at the position $\vec{r}'$ at time t. ρ and $\rho^{(2)}$ can be expressed as statistical averages of the microscopic one-point and two-point distribution functions:

$$\rho(\vec{r},t)=\left\langle\sum_{j=1}^{N}\delta(\vec{r}-\vec{r}_j(t))\right\rangle,$$

$$\rho^{(2)}(\vec{r},\vec{r}',t)=\left\langle\sum_{j,l=1}^{N}\delta(\vec{r}-\vec{r}_j(t))\delta(\vec{r}'-\vec{r}_l(t))\right\rangle.$$

It is customary to introduce the function g defined as

$$g(\vec{r},\vec{r}',t)=\frac{\rho^{(2)}(\vec{r},\vec{r}',t)}{\rho(\vec{r},t)\rho(\vec{r}',t)}. \tag{1}$$

Of central interest in the following will be the structure factor

$$S(\vec{k})=\left\langle\frac{1}{N}\left|\sum_i e^{-i\vec{k}\cdot\vec{r}_i}\right|^2\right\rangle, \tag{2}$$

because it is directly related to the observed diffracted intensity in a diffraction experiment. Both g and S contain information on the density correlations.

If the system is statistically homogeneous, $g(\vec{r},\vec{r}',t)$ depends only on $\vec{r}-\vec{r}'$; if in addition it is statistically isotropic, g depends only on $|\vec{r}-\vec{r}'|$, and will be written $g(r,t)$. In this case, calling ρ_c the constant density, we have

$$\begin{aligned}S(\vec{k})&=1+\rho_c\int g(r)e^{-i\vec{k}\cdot\vec{r}}d\vec{r}\\&=1+N\delta(\vec{k})+\rho_c\int[g(r)-1]e^{-i\vec{k}\cdot\vec{r}}d\vec{r}.\end{aligned} \tag{3}$$

We now introduce the linear-response theory, which describes the response of the system to a small external perturbation. Consider a uniform system of density ρ_c exposed to a weak external potential $\delta\phi(\vec{r})$. Linear-response theory asserts that the density perturbation $\delta\rho$ created by $\delta\phi$ is [38]

$$\delta\hat{\rho}(\vec{k})=-\beta\rho_c[S(\vec{k})-N\delta(\vec{k})]\delta\hat{\phi}(\vec{k}). \tag{4}$$

We will give an approximate theoretical expression for $S(\vec{k})$ in a MOT in Sec. II C, and use these results in Sec. III D.

B. "Coulomb model" for MOTs

In the standard Doppler model, all forces on atoms inside a MOT stem from the radiation pressure exerted by the almost resonant photons. Over long enough time scales, the scattering of many photons produces an average force on the atomic cloud, which may be decomposed as velocity trapping (i.e., friction), spatial trapping, attractive shadow effect, and repulsion due to multiple scattering. The first two are single atom effects, the last two are effective interactions between atoms. The friction force $F_{\rm dop}$ is due to Doppler cooling. Linearizing for small velocities, it reads

$$\vec{F}_{\rm dop}\simeq-m\gamma\vec{v}, \tag{5}$$

with

$$\gamma=\frac{I_0}{I_s}\frac{8\hbar k_{\rm Las}^2}{m}\frac{-\bar{\delta}}{(1+4\bar{\delta}^2)^2},$$

where $I_0, k_{\rm Las}, \bar{\delta}=\delta/\Gamma$ are respectively the laser intensity, wave number, and scaled detuning, I_s is the saturation intensity, and m the atomic mass. This expression assumes a small saturation parameter. γ is positive (actual friction) when the lasers are red detuned ($\delta<0$).

The trapping force $F_{\rm trap}$ is created by the magnetic-field gradient. We will consider a linear approximation to this force:

$$\vec{F}_{\rm trap}\simeq-m\omega_x^2x\vec{e}_x-m\omega_y^2y\vec{e}_y-m\omega_z^2z\vec{e}_z. \tag{6}$$

The anti-Helmholtz configuration of the coils induces a non-isotropic trap, with $\omega_y^2=\omega_z^2=\frac{1}{2}\omega_x^2$. Nevertheless via laser intensity compensations it is possible to obtain a spherical cloud, hence we will use in our modeling $\omega_y=\omega_z=\omega_x=\omega_0$.

The shadow effect, as first studied in [3], results from the absorptions of lasers by atoms with cross section σ_L in the cloud. This force is attractive, and in the small optical depth regime, its divergence is proportional to the density ρ:

$$\vec{\nabla}\cdot\vec{\rm F}_{\rm s}=-6I_0\frac{\sigma_L^2}{c}\rho(x,y,z), \tag{7}$$

where c is the speed of light. Note however that $\vec{\rm F}_{\rm s}$ does not derive from a potential.

The repulsive force [2] is due to multiple scattering of photons. If the optical depth is small, very few photons are scattered more than twice, and the effect of multiple scattering can be approximated as an effective Coulomb repulsion

$$\vec{\rm F}_{\rm c}(\vec{r})=3I_0\frac{\sigma_L\sigma_R}{2\pi c}\frac{\vec{r}}{r^3}, \tag{8}$$

where σ_R is the atomic cross section for scattered photons. The divergence of the force is

$$\vec{\nabla}\cdot\vec{\rm F}_{\rm c}=6I_0\frac{\sigma_L\sigma_R}{c}\rho(x,y,z).$$

The scattered photons actually have complex spectral and polarization properties, and σ_R should rather be understood as an averaged quantity. In all experiments, $\sigma_R>\sigma_L$, with the consequence that the repulsion dominates over the attractive shadow effect. Since repulsion and attraction both have a divergence proportional to the local density, the shadow effect is often considered as a mere renormalization of the repulsive force; note that this involves a further approximation, because

the forces are not proportional, even though their divergences are.

Finally, the spontaneous emission of photons acts as a random noise on the atoms, which induces at the macroscopic level a velocity diffusion. In our experiments, the atomic dynamics is typically overdamped: the velocity damping time is much shorter than the position damping time. The velocity distribution then quickly relaxes to an approximate Gaussian, with temperature T, and the density $\rho(\vec{r},t)$ is described by the Smoluchowsky equation (which is a simplified version of the Fokker-Planck equation in [39]):

$$\partial_t \rho(\vec{r},t) = \vec{\nabla}\cdot\left(\frac{\omega_0^2}{\gamma}\vec{r}\rho - \frac{1}{m\gamma}(\vec{\mathrm{F}}_\mathrm{c}+\vec{\mathrm{F}}_\mathrm{s})[\rho]\rho + \frac{k_\mathrm{B}T}{m\gamma}\vec{\nabla}\rho\right), \tag{9}$$

with a Poisson equation for the force

$$\vec{\nabla}\cdot(\vec{\mathrm{F}}_\mathrm{c}+\vec{\mathrm{F}}_\mathrm{s}) = C\rho \text{ with } C = 6I_0\frac{\sigma_L(\sigma_R-\sigma_L)}{c}. \tag{10}$$

Note finally that in this simplified framework the total force $\vec{\mathrm{F}}_\mathrm{c}+\vec{\mathrm{F}}_\mathrm{s}$ has the same divergence as an effective Coulomb force

$$\tilde{\vec{F}}_c(\vec{r}) = \frac{C}{4\pi}\frac{\vec{r}}{r^3}. \tag{11}$$

One may also represent this situation by attributing an effective charge $q^{\mathrm{eff}} = \sqrt{C\epsilon_0}$ to each atom.

C. Plasma analogy: Temperature and repulsion dominated regimes

The above model describes a large MOT as a collection of particles in a harmonic trap, and the dominant interacting force is a Coulomb-like repulsion. This clearly suggests an analogy with non-neutral plasmas, where trapped electrons interact through real Coulomb forces; for a detailed review, see [40]. The analogy is not perfect: for instance the nonpotential part of the shadow effect is neglected, the friction and diffusion in a MOT are much stronger than in a non-neutral plasma, and the typical optical depth in an experiment is not very small. Nevertheless, it is a basic model to analyze MOT physics, and has been used recently to predict plasma related phenomena in MOTs (see for instance [16,41]).

When the repulsion force is negligible, the trapping force is balanced by the temperature. The cloud has then a Gaussian shape, with atomic density

$$\rho(\vec{r}) = \frac{N}{(2\pi l_g^2)^{3/2}}e^{-\vec{r}^2/2l_g^2}, \text{ with } l_g = \left(\frac{k_\mathrm{B}T}{m\omega_0^2}\right)^{1/2}, \tag{12}$$

where N is the total number of trapped atoms. In the following, l_g will be called the "Gaussian length." For typical MOT parameters, one has as an order of magnitude $l_g \sim 200\ \mu$m. Increasing N, the repulsion increases, and the system enters the repulsion dominated regime, where the trapping force is balanced by the repulsion. Theory then predicts a spherical cloud with constant density ρ_c, and steplike boundaries smoothed over the same length scale l_g defined in Eq. (12) [40]; the radius of the cloud at zero temperature is denoted by L, and we have the expressions

$$\rho_c = \frac{3m\omega_0^2}{C} = \frac{3m\omega_0^2 c}{6I_0\sigma_L(\sigma_R-\sigma_L)},\ L = \left(\frac{3N}{4\pi\rho_c}\right)^{1/3}. \tag{13}$$

The crossover between temperature and repulsion dominated regimes is for $l_g \sim L$. Experimentally, sizes of order $L \sim 1$ cm can be reached (see Sec. III A), which should be well into the repulsion dominated regime. Note that the repulsion dominated regime is not as straightforward to analyze when the trap anisotropy and shadow effect are taken into account; see [42].

D. Plasma analogy: Correlations

To quantify the relative effect of kinetic energy and Coulomb repulsion, it is customary for plasmas to define the "plasma coupling parameter" Γ_p, which is the ratio of the typical potential energy created by a neighboring charge by the typical kinetic energy. For a MOT in the repulsion dominated regime, denoting $a = (4\pi\rho_c/3)^{-1/3}$ a measure of the typical interparticle distance, we have the expression

$$\Gamma_p = \frac{C/(4\pi a)}{k_\mathrm{B}T} = \frac{a^2}{l_g^2}, \tag{14}$$

where we have used Eq. (13), and we recall that $l_g = (k_\mathrm{B}T/m\omega_0^2)^{1/2}$ is the Gaussian length. Using typical experimental values $l_g = 200\ \mu$m, and an atomic density $\rho = 10^{11}$ cm^{-3}, this yields $\Gamma_p \sim 10^{-4}$. A plasma experiences a phase transition from liquid phase to solid phase at $\Gamma_p \simeq 175$, and is considered in a gaslike phase as soon as $\Gamma_p < 1$. The typical value for a MOT experiment is hence very small, well into the gas phase, and the expected correlations are weak. In this regime, and assuming the MOT shape is dominated by repulsion, so that the density in the central region is approximately constant, Debye-Hückel theory can be applied. We give now a short account of this theory. Choosing the origin of coordinates as the position of an atom, the density distribution is given by the Boltzmann factor

$$\rho(\vec{r}) = \rho_c e^{-\psi(\vec{r})/k_\mathrm{B}T}, \tag{15}$$

where $\psi(\vec{r})$ is the *average* potential around $\vec{r}=0$. Using the Poisson equation it is possible to find—self-consistently—the average potential:

$$\nabla^2\psi(\vec{r}) = -C\left[\delta(\vec{r}) - \rho_c + \rho_c e^{-\psi(\vec{r})/k_\mathrm{B}T}\right], \tag{16}$$

where the first term on the right-hand side represents the contribution of the effective point charge of the atom. Using the hypothesis that $\Gamma_p \ll 1$, the Poisson equation can be simplified:

$$\left[\nabla^2 - \kappa_D^2\right]\psi(r) = -C\delta(r), \tag{17}$$

where $\kappa_D = \lambda_D^{-1}$ and

$$\lambda_D = \left(\frac{k_\mathrm{B}T}{\rho_c C}\right)^{1/2}. \tag{18}$$

It is simple to show that the solution of Eq. (17) is

$$\psi(r) = \frac{e^{-r/\lambda_D}}{r}, \tag{19}$$

which yields for the pair-correlation function [38]

$$g(r) = \exp\left(-a\frac{\Gamma_p}{r}e^{-r/\lambda_D}\right). \tag{20}$$

This expression assumes isotropy: this is why the correlation depends only on one distance r. Note that isotropy is certainly not exactly true for a MOT. g vanishes for small r, which is a manifestation of the strong repulsion, and tends to 1 for $r \gg \lambda_D$: correlations disappear in this limit. The excluded volume effect kicks in at very small scales, of order $a\Gamma_p$; at larger scales, the above expression can be replaced by

$$g(r) \simeq 1 - \frac{a\Gamma_p}{r}e^{-r/\lambda_D}. \tag{21}$$

From this expression we can compute the structure factor Eq. (3):

$$S(k) = N\delta(\vec{k}) + \frac{k^2}{k^2 + \kappa_D^2}. \tag{22}$$

For weak plasma parameter $\Gamma_p \to 0$, particles are uncorrelated and Poisson distributed; there is no characteristic correlation length, $\lambda_D \to \infty$ and the structure factor is $S(k) = N\delta(k) + 1$.

Inserting in Eq. (18) the expression for ρ_c Eq. (13), one obtains the expression $\lambda_D = l_g/\sqrt{3}$, and the rough order of magnitude $\lambda_D \sim 100\ \mu$m. Using this and the estimated Γ_p in Eq. (21), we see that the correlations are indeed very small over length scales of order λ_D.

E. Simulations of the "Coulomb model"

We will use in Sec. III numerical simulations to compare the theory with the experiments. We describe here these simulations.

We use Coulomb molecular dynamics (MD), with particles in a harmonic trap interacting through Coulombian interactions (without shadow effect), with friction and velocity diffusion. We use a second-order leapfrog scheme (see, e.g., [43]); the interaction force is implemented in parallel on a GPU. We are not interested in dynamical effects, hence in all cases the simulation is run until the stationary state is reached. To run a simulation, we need to choose the parameters $N^{(\mathrm{sim})}$, $\omega_0^{(\mathrm{sim})}$, $\gamma^{(\mathrm{sim})}$, $m^{(\mathrm{sim})}$, $C^{(\mathrm{sim})}$, $T^{(\mathrm{sim})}$. Ideally, we would choose for these simulation parameters values as close as possible to the experimental ones, which is of course impossible. In particular, the number of simulated particles is imposed by our numerical limitations and is typically $N^{(\mathrm{sim})} = 16\,384$. In order to compare the density profiles in simulations and experiments, we impose $L^{(\mathrm{sim})} = L$ and $\lambda_D^{(\mathrm{sim})} = \lambda_D$. Using Eqs. (13) and (18), this imposes

$$\left(\frac{NC}{m\omega_0^2}\right)^{(\mathrm{sim})} = \frac{NC}{m\omega_0^2}, \quad \left(\frac{k_\mathrm{B}T}{m\omega_0^2}\right)^{(\mathrm{sim})} = \frac{k_\mathrm{B}T}{m\omega_0^2}. \tag{23}$$

In practice, we take for simplicity $m^{(\mathrm{sim})} = 1$, hence $C^{(\mathrm{sim})} = (C/m) \times (N/N^{(\mathrm{sim})})$ and $(k_\mathrm{B}T/\omega_0^2)^{(\mathrm{sim})} = k_\mathrm{B}T/(m\omega_0^2)$. Once the above relations are satisfied, the exact values of $\omega_0^{(\mathrm{sim})}$ and $\gamma^{(\mathrm{sim})}$ are not important since they have no influence on the stationary state we are interested in. We also would like to have the plasma parameter in simulations $\Gamma_p^{(\mathrm{sim})}$ as close as possible to Γ_p. However, from Eqs. (14), (18), and (23), we have

$$\Gamma_p^{(\mathrm{sim})} = \left(\frac{L}{\lambda_D}\right)^2 \frac{(N^{(\mathrm{sim})})^{-2/3}}{3} \simeq 5 \times 10^{-4}\left(\frac{L}{\lambda_D}\right)^2.$$

Hence the plasma parameter in the simulations is imposed by the experimental values of L and λ_D and our choice of $N^{(\mathrm{sim})}$; in particular, it is thus much larger than in the experiments. Nevertheless, all simulations remain safely in the gaslike phase $\Gamma_p \ll 1$.

F. Experimental probes of the "Coulomb" model

Following [2], describing the optical forces induced by multiple scattering as an effective Coulomb repulsion is a standard procedure since the early 1990s. In particular, it satisfactorily explains the important observation that the atomic density in a MOT has an upper limit (preventing for instance the initially sought Bose-Einstein condensation). It also predicts a size scaling $L \sim N^{\sim 1/3}$, which is observed with reasonable precision in the experiments [12,44–46]. However other mechanisms can lead to an upper bound on the density, such as light assisted collisions or other short-range interactions [7,9,47]. Besides the bounded density and size scaling, there are experiments that are consistent with a Coulomb-type repulsion:

(i) A Coulomb explosion in a viscous medium has been observed by measuring the expansion speed of a cold atomic cloud in optical molasses [13,48]. The result shows a good agreement with what is predicted for a similar Coulomb gas.

(ii) Self-sustained oscillations of a MOT have been reported in [14]. The model used to explain the experimental observations assume a cloud with a size increasing with the atom number. This is again consistent with a Coulomb-type repulsion but remains an indirect test of these forces.

All these experiments rely on identifying macroscopic effects of the repulsive force, and microscopic effects such as the building of correlations in the cloud have not been directly observed. This is our goal in the following.

III. LOOKING FOR CORRELATIONS IN EXPERIMENTS

In order to measure directly or indirectly the interaction induced correlations in the atomic cloud, we have performed three types of experiments, which rely on (i) an analysis of the density profile, (ii) a direct measurement of correlations by diffraction, (iii) an analysis of the cloud's response to an externally modulated perturbation. This section gathers our results. Section III A first presents the general experimental setup, which is common to all experiments detailed in Secs. III B, III C, and III D.

A. General experimental setup

The experimental apparatus used in this work as been described in detail elsewhere [12]. ^{87}Rb atoms are loaded in a magneto-optical trap from a dilute room-temperature vapor. The trapping force is obtained by crossing six large laser beams (waist 2.4 cm) at the center of the vacuum chamber, arranged in a two-by-two counterpropagating configuration. These lasers are detuned from the $F = 2 \to F' = 3$ atomic

transition of the $D2$ line by a variable δ, whose value is used to vary the atom number and size of the cloud. Typically, δ is varied from -3Γ to -8Γ, where Γ is the atomic linewidth. The peak intensity in each beam is 5 mW/cm^2. The trapping beams also contain a small proportion (a few %) of "repumping" light, tuned close to the $F = 1 \rightarrow F' = 2$ transition. A pair of coils with opposite currents generate the quadrupole magnetic field necessary for trapping. The magnetic-field gradient along the axis of the coils is 7.2 G/cm. Due to the large diameter of the trapping beams, the maximal number of trapped atoms is large, up to 10^{11}. This results in a large effective repulsive interaction between atoms mediated by scattered photons, making this MOT a good candidate to observe density correlations. Also, the cold atomic cloud is large with a full width at half maximum (FWHM) diameter typically between 10 and 15 mm, depending on the value of δ. The temperature of the cloud is of the order 100–200 μK.

B. Analysis of the density profile

From the theoretical analysis presented in the previous section, we know that our basic model Eq. (9) relates the Debye length λ_D, which controls the correlations, to the Gaussian length l_g, which controls the tails of the density profile: $\lambda_D = l_g/\sqrt{3}$. Fitting the experimental density profile may then provide information on the Debye length. We recall that this is an indirect method and only serves as a guide for a more reliable estimation of the Debye length.

Experimental measurement of the density profile is achieved by imaging the trapping light scattered by the atoms, known as "fluorescence" light, with a charge-coupled device (CCD) camera. However, the spatial distribution of fluorescence light usually does not reflect that of the atomic density, because of multiple scattering [12]. To minimize this effect, we acquire the fluorescence image at a large detuning of -8Γ. The time sequence is as follows: the MOT is operating at a given detuning δ (variable), then the detuning is jumped to -8Γ for a duration of 10 μs, during which the image is recorded. During this short time, the atoms move only by a few 10 μm, which is much smaller than all spatial scales we look for. Furthermore, the experimental data obtained by fluorescence [12] is two dimensional, since the density is integrated over one direction (called z below) hence, we cannot see directly $\rho(r)$ but an integrated quantity; selecting the central part $y \in [-\epsilon, \epsilon]$, where ϵ is about 10% of cloud's width, we obtain the observed density along the x direction:

$$\rho_x(x) = \int_{-\infty}^{\infty} dz \int_{-\epsilon}^{\epsilon} dy \rho(x, y, z).$$

Figure 1 shows, for two values of the detuning δ, this partially integrated experimental density profile ρ_x.

We now compare these profiles with numerical simulations; see Sec. II E. As explained in Sec. II E, in the simulations, L and λ_D can be adjusted independently using the temperature $T^{(\mathrm{sim})}$ and the strength of the repulsive force $C^{(\mathrm{sim})}$. L, the cloud's radius at zero temperature, controls the size of the cloud in the strong interaction regime relevant here; this size can be quantified by the FWHM reported in Fig. 1. λ_D determines the shape of the wings of the density profile. The simulation parameters are adjusted to match

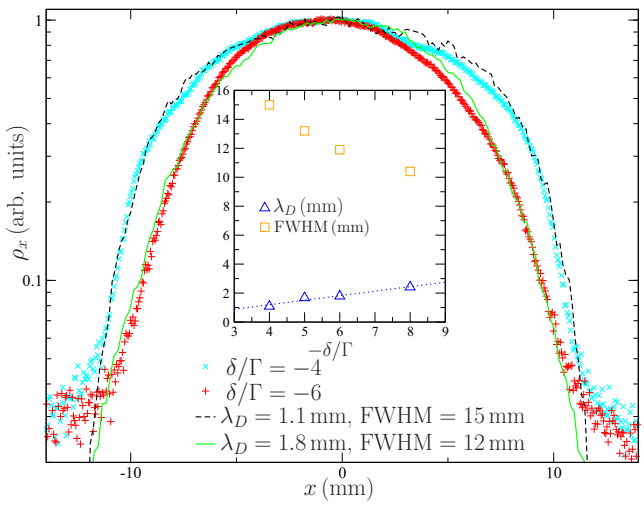

FIG. 1. Density $\rho_x(x)$ obtained by fluorescence for $-\delta/\Gamma = 4, 6$ compared with MD simulation of a trapped Coulomb gas, using $N^{(\mathrm{sim})} = 16\,384$ particles. The inset shows the Debye length λ_D and the cloud FWHM diameter extracted from simulations. (The density plots for $-\delta/\Gamma = 5, 8$ are not shown here.) The simulated plasma parameter ranges from $\Gamma_p \simeq 4 \times 10^{-2}$ for $\delta/\Gamma = -4$ to $\Gamma_p \simeq 5 \times 10^{-5}$ for $\delta/\Gamma = -8$. For all experiments, the number of trapped atoms is of the order of 10^{11}.

simulated and experimental profiles, allowing us to extract the corresponding FWHM and λ_D. Figure 1 shows that the fits are reasonably good, and allow us to extract values for λ_D and L, or, equivalently, for λ_D and the FWHM.

These results suggest a value for the Debye length in the 1–2-mm range—much larger than what was expected on the basis of the experiments in the temperature dominated regime; see Sec. II. However, this method is very model dependent: one could imagine other physical mechanisms or interaction forces producing similar density profiles. To overcome this difficulty, we need methods able to probe more directly the interactions and correlations inside the cloud. This is the goal of Secs. III C and III D.

C. Direct probing of correlations by diffraction

An alternative method to probe spatial correlations of particles and thus access the Debye length is by directly probing two-body correlations via a diffraction experiment: an additional detuned laser beam is sent through the cloud, and the diffracted intensity is recorded. In our experiments, a weak beam of waist $w_{\mathrm{probe}} = 2.2$ mm (much smaller than the cloud's diameter), detuned by several Γ, is sent through the center of the cloud immediately after the trapping beams are shut down. The transmitted far-field intensity distribution is recorded using a CCD camera placed in the focal plane of a lens.

For an incident plane wave, the diffracted intensity I is proportional to the structure factor $S(\vec{k})$ given by Eq. (2), where $\vec{k} = \vec{k}_{\mathrm{inc}} - \vec{k}_{\mathrm{end}}$ is the difference between the incident wave vector $\vec{k}_{\mathrm{inc}} = k_i \vec{e}_z$ and the diffracted one $\vec{k}_{\mathrm{end}} = k_i(\cos\phi_k \sin\theta_k, \sin\phi_k \sin\theta_k, \cos\theta_k)$; this assumes elastic scattering; see Fig. 2 (see [38] for a reference).

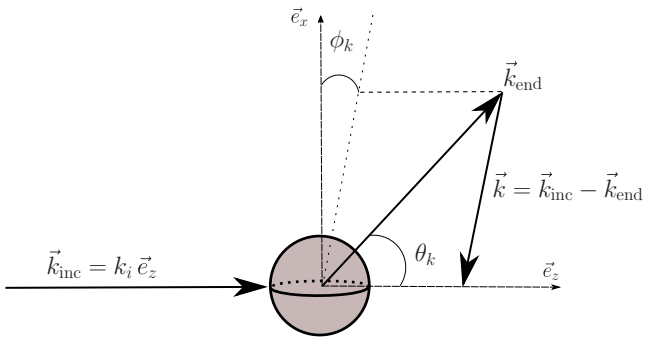

FIG. 2. Sketch of an incident beam $\vec{k}_{\rm inc}$ diffracted on an atom in direction $\vec{k}_{\rm end}$ corresponding to angles θ_k and ϕ_k. We define and show the vector $\vec{k} = \vec{k}_{\rm inc} - \vec{k}_{\rm end}$.

We then have

$$k = |\vec{k}| = 2k_i \sin(\theta_k/2). \tag{24}$$

In an isotropic homogeneous infinite medium the theoretical structure factor would be given by Eq. (22). In the actual experiment, the structure factor Eq. (22) is modified at small k either by the finite size of the cloud, or by the finite waist of the probe beam $w_{\rm probe}$, whichever is smaller (in our case $w_{\rm probe}$ is smaller): the δ function is replaced by a central peak which simply reflects the Fourier transform of the density profile or of the beam profile. Figure 3 shows an example of $S(k)$ for an MD simulation of a trapped Coulomb cloud, with a Gaussian probe beam smaller than the cloud:

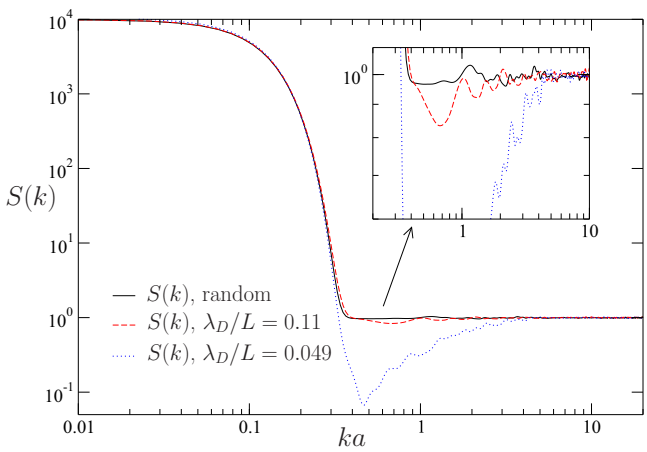

FIG. 3. MD simulations with $N^{(\rm sim)} = 16\,384$ particles of the structure factor $S(k)$, averaged over all $\vec{k}$ such that $|\vec{k}| = k$. The horizontal axis is adimensionalized by the mean interparticle distance a, which is in the simulation $a/L = 0.039$. For the dashed red curve $\Gamma_p \simeq 0.043$ with the same ratio λ_D/L as the black dashed fit in Fig. 1, for the dotted blue curve $\Gamma_p \simeq 0.215$ (these values for the plasma parameter are much higher than expected in the atomic cloud; smaller, more realistic, values are difficult to reach numerically while keeping a small λ_D/L). The waist of the Gaussian probe beam is $w \simeq 0.76L$. The black curve corresponds to randomly distributed particles with the same average density: the two-body correlation obviously vanishes in this case, and accordingly, the characteristic dip is absent.

(i) For small $k \sim 1/w_{\rm probe}$, there is a large smooth peak, corresponding to the Fourier transform of the probe beam's profile.

(ii) For large k, the structure factor tends to 1 [this is clear from Eq. (3)].

(iii) For intermediate $k \sim 1/\lambda_D$, there is a small dip which is the manifestation of the Debye length. It is deeper when the temperature is smaller, since correlations are stronger; see Eqs. (18), (19), and (21). It disappears for large temperature (the black curve in Fig. 3 formally corresponds to an infinite temperature). For values of λ_D/L compatible with Fig. 1 (red dashed curve), the dip is barely visible in the simulations.

This simulation shows that two conditions are necessary for the experimental observation of the signature of the Debye length using this direct diffraction technique. First, the ratio λ_D/L should be small enough to yield a significant dip and also to allow for a reasonable separation in k space between the dip and the central peak. Second, the ratio between the dip depth and the central peak height should not be unreasonably large. Indeed, we observe in the experiment a straight light due to scattering on the optical surfaces (speckle) that cannot be filtered out and that scales like the height of the central peak (probe beam intensity). The typical value of this "noise" is around 10^{-5} relative to the central peak. In Fig. 3, the dip-to-central peak ratio scales as $1/N_{\rm diff}$, where $N_{\rm diff}$ is the number of diffracting atoms. In the experiment, this ratio is of the order of 10^{-9}. The observation of the dip in these conditions thus seems extremely difficult.

D. Response to an external modulation

1. Principle of the experiment

Since a direct measure of correlations inside the cloud is currently not accessible, we have studied indirectly the effect of these correlations, by analyzing the response to an external force. As we will see below, this response is related to the interactions inside the cloud.

The principle of the measurement is illustrated in Fig. 4. A sinusoidal potential is generated by crossing two identical laser beams of waist 2.2 mm and detuning $+20\Gamma$ in the center of the cloud, with an adjustable small angle θ between them [Fig. 4(a)]. The resulting modulation period is $\lambda_e = \lambda_i/\theta$ where $\lambda_i = 780$ nm is the laser wavelength. The intensity of these beams is chosen low enough such that the associated radiation pressure force doesn't affect the functioning of the MOT (no difference in atom number with and without the modulation beams; the induced density modulation is small, at most a few percent). To measure the response of the cloud (in the form of a density grating), we switch off the MOT laser beams and send the probe beam described before through the modulated part of the cloud. The short delay (10 μs) between probing and MOT switching off ensures that the initial density modulation is not blurred by the residual atomic motion. The modulated atomic density acts for the probe as a transmission diffraction grating [Fig. 4(b)]. The zeroth and first diffracted orders are recorded by a CCD camera placed in the focal plane of a lens. Figure 4(c) shows a series of images of the detected diffracted peaks, corresponding to different values of the modulation wavelength λ_e. The zeroth order is blocked to avoid saturation of the CCD. As the diffracted light power

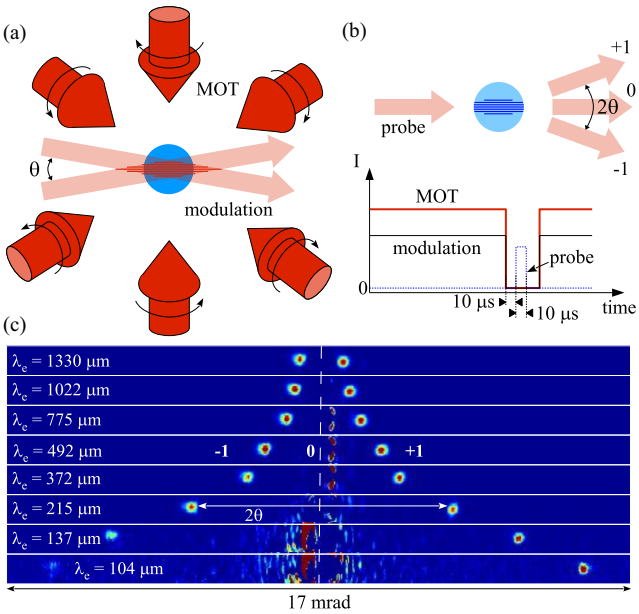

FIG. 4. Principle of modulation experiment. (a) A sinusoidal modulation is applied by crossing two laser beams on the cloud. (b) The atoms are released from the MOT and the diffraction grating due to the atomic density modulation being probed. (c) Images of the ± 1 diffracted orders vs modulation wavelength λ_e. The zeroth order is blocked to avoid saturation of the CCD, and the display is adjusted for each image of the figure to improve readability (see text).

decreases with λ_e, the display is adjusted for each image of the figure to improve readability. The important experimental information is precisely contained in the diffracted power, and will be shown below; see Fig. 5.

2. *Theoretical analysis: Bragg and Raman-Nath regimes*

We now present a theoretical analysis of this modulation experiment, based on the plasma analogy. The static modulation potential in the direction $\vec{e}_x$, with amplitude A, reads

$$\phi_{\text{ext}}(x) = A\sin(k_e x). \tag{25}$$

Experimentally, the depth of the modulation potential was chosen so that the density modulation never exceeded 10%; hence we limit ourselves to a linear-response computation. We are interested in the diffraction profile, which is proportional to the structure factor $S(\vec{k})$. The location of the diffracted peak is given by the modulation wave vector k_e, and the experimentally measured quantity is the integrated diffracted power around k_e, denoted $R(k_e)$. The detailed computations are in Appendix A; we report here the results. The main features are as follows:

(i) There is a crossover between the Bragg regime at small modulation wavelength $\lambda_e < \lambda_e^{(c)}$, or $k_e > k_e^{(c)}$, and the Raman-Nath regime at large modulation wavelength $\lambda_e > \lambda_e^{(c)}$, or $k_e < k_e^{(c)}$. We have

$$\lambda_e^{(c)} = 2\pi\sqrt{\frac{L}{2k_i}} = \sqrt{\pi L \lambda_i} \quad \text{or} \quad k_e^{(c)} = \sqrt{\frac{2k_i}{L}}. \tag{26}$$

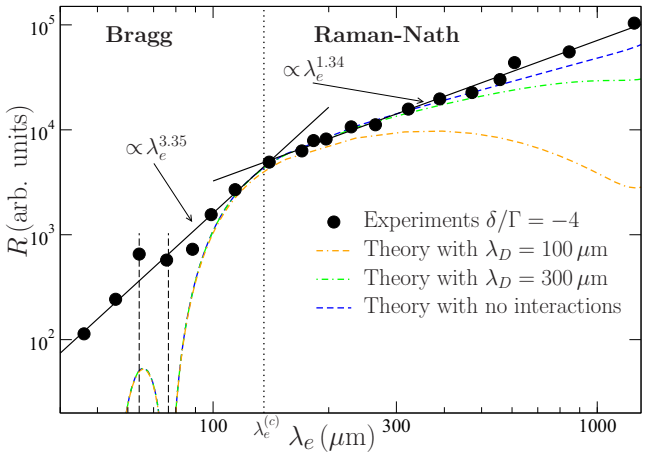

FIG. 5. Comparison of the total diffracted power $R(\lambda_e)$ in the experiment (black dots) and theory (lines). The detuning is $\delta/\Gamma = -4$, $N \sim 10^{11}$, $w = 2.2$ mm. The theoretical curves use $w = 2.2$ mm, and $L = 7.41$ mm, which is the value extracted from Fig. 1 for $\delta/\Gamma = -4$; they are computed with Debye length $\lambda_D = 100$, $300\ \mu$m. The steepness l of the step function in Eq. (A8) is chosen to be $l = 1$ mm (the theoretical curve only weakly depends on l). We also show the theoretical limit case with no interactions $B(\lambda_e) = 1$. The vertical dotted line indicates the theoretical position of the Bragg/Raman-Nath crossover $\lambda_e^{(c)} = 136\ \mu$m. The corresponding experimental value $\lambda_e^{(c),\text{exp}} = 142\ \mu$m is obtained at the intersection of the fitted experimental data (for $\delta/\Gamma = -4$) in the Bragg $\propto \lambda_e^{3.35}$ and Raman-Nath region $\propto \lambda_e^{1.34}$. This latter exponent is not far ($1.34 \simeq 1$) from the prediction of Eq. (27) in the sub-Debye Raman-Nath regime *without interactions*. The exponent in the Bragg regime depends on the specific details of the real experimental profile. The vertical dashed lines indicate a local maximum and a local minimum of the response in the Bragg regime; see Appendix B.

In the Bragg regime, the response is dominated by the longitudinal density profile, whereas in the Raman-Nath regime, the response is dominated by the effect of the interactions inside the cloud: the latter is then of most interest to us. For our experimental conditions, the crossover is around $\lambda_e^{(c)} = 120\ \mu$m.

(ii) We obtain (see Appendix A) the approximate expression for the integrated diffracted power:

$$R(\lambda_e) \propto B(\lambda_e)^2 \times \begin{cases} \lambda_e(\hat{\rho}^0(\lambda_i\pi/\lambda_e^2))^2, & \lambda_e \ll \lambda_e^{(c)} \\ \lambda_e, & \lambda_e^{(c)} \ll \lambda_e \ll L, \end{cases} \tag{27}$$

where

$$B(\lambda_e) = \frac{1}{1 + \lambda_e^2/(2\pi\lambda_D)^2}$$

is the response function containing the effect of the interactions, and $\hat{\rho}^0$ is the Fourier transform of the density profile of the cloud. In the experiments, we use a Gaussian probe beam smaller than the cloud, in order to control the boundary effects in the transverse direction: hence the cloud's density profile is effectively limited in the transverse direction by w, the waist of the probe beam; w is chosen significantly smaller

than the cloud's size, and much larger than the modulation wavelength. In the longitudinal direction, we cannot avoid boundary effects, and accordingly, the diffracted intensity in the Bragg regime explicitly depends on the density profile of the cloud. In practice and to compare with the experiments, we have used expression Eq. (A8) for ρ^0.

(iii) Most importantly, the Raman-Nath regime contains information on the correlations inside the cloud, and this is what we want to exploit. In the sub-Debye Raman-Nath regime $\lambda_e^c < \lambda_e < \lambda_D$, we then expect to see a response $R(\lambda_e) \propto \lambda_e$, whereas in the Raman-Nath regime for $\lambda_e > \lambda_D$, we expect to see $R(\lambda_e)$ *decreasing* with λ_e, ultimately as λ_e^{-3}: this is an effect of the interparticle repulsion. Our strategy is to look for this decreasing region in the experiment, in order to estimate λ_D.

3. Comparison between experiment and theory

We now analyze the experimental results using the above theory. In Fig. 5 we plot the result of an experiment for a detuning $\delta = -3\Gamma$. We compare these results with the theoretical diffraction response of the profile (A8). The parameters L, w, N are chosen to be the same as in the experiment. Indeed, the waist w and atom number N are well controlled and the size of the cloud L can be extracted from a density profile. The smoothing length l appearing in Eq. (A8) is chosen in the range suggested by the density profiles, see Fig. 1, and does not have much influence on the results. The only adjusted parameter here is the vertical amplitude of the theoretical response (in arbitrary units), that we set so it coincides with the experimental curves. The three theoretical curves correspond to three values for the Debye length λ_D: this modifies the response Eq. (27).

The conclusions of this comparison are as follows:

(i) No decrease in the response is observed as the modulation wavelength λ_e is increased: this indicates, if the model used for the analysis is correct, that the Debye length λ_D is larger than the experimentally probed range for λ_e.

(ii) The Bragg/Raman-Nath crossover predicted in (26) is observed in the experiment, at the predicted location.

(iii) In the Raman-Nath regime close to the crossover, the slopes of experiment and theory are both about 1. For larger modulation wavelength, we expect the long-range effects to take place. We indeed see clearly on the theoretical curve with $\lambda_D = 100\ \mu$m a decreasing response. For $\lambda_D = 300\ \mu$m this decrease occurs for larger λ_e and is thus barely visible. For comparison, we plot (blue dashed line) the limit $\lambda_D \to \infty$, corresponding to a noninteracting case. The experimental data show no decrease for large wavelength: hence they are close to the "no interaction" case. More precisely, these data match the Coulomb predictions only if the Debye length is larger than $\sim$400 μm. Unfortunately, probing larger λ_e is difficult and would be hampered by strong finite-size effects.

(iv) In principle, from the analysis of the variations of R with λ_e in the Raman-Nath regime and for $\lambda_e \gg \lambda_D$, we could hope to test the validity of the $1/r^2$ force: this Coulomb model predicts a -3 exponent. However, this $\lambda_e \gg \lambda_D$ regime is not seen in the experiments, and unfortunately the regime which is seen, $\lambda_e < \lambda_D$, is precisely the one where R contains no signature of the interactions.

(v) In the Bragg regime the theoretical response is smaller than what is observed. In this region, the response is sensitive to the details of the density profile, and our simple assumption Eq. (A8) may not be good enough.

(vi) The theoretical analysis predict oscillations in the Bragg regime. While these oscillations are not clearly resolved in the experiments, some hints are visible in Fig. 5 (vertical dashed lines around $\lambda_e = 70\ \mu$m). In Appendix B, we analyze in more detail the theoretical and experimental diffraction profiles, to confirm that the experimental observations are indeed a remnant of the theoretically predicted oscillations.

IV. CONCLUSION

We have proposed in this paper to use the response to an external modulation as an indirect way to measure the correlations inside the atomic cloud, and more generally to probe the effective interactions induced by the multiple photon scattering in large MOTs.

The modulation experiments and comparison with simulations did not show any evidence for a Debye length within the explored range, which could indicate a larger than expected value for λ_D of at least 400 μm for a detuning $\bar{\delta} = -4$. This seems consistent with direct numerical fits of the cloud's density profile, which suggest a Debye length as large as 1 mm. Accordingly, an extension of the modulation experiment to larger wavelengths could be envisioned. These values should be compared to the rough *a priori* estimate $\lambda_D \sim 100\ \mu$m, based on the Coulomb model for the interaction between atoms and the observed size of the cloud. A clear theoretical explanation for the discrepancy between the *a priori* estimate for λ_D and the bounds provided by the experiments is lacking. It is possible that the Coulomb model for the effective interactions between atoms reaches its limits in such large MOTs: the Coulomb approximation relies on a small optical depth, whereas it is around 1 in experiments, or the spatial dependencies of the scattering sections may have to be considered. In either case, a refined model taking these effects into account would be considerably more complicated. It might also be that another mechanism controlling the maximum density, and hence the size of the cloud, is at play beyond multiple diffusion.

ACKNOWLEDGMENTS

D.M. carried out the work at LANL under the auspices of the National Nuclear Security Administration of the U.S. Department of Energy under Contract No. DE-AC52-06NA25396 and was partially supported by DOE/OE/GMLC and LANL/LDRD/CNLS projects.

APPENDIX A: LINEAR RESPONSE COMPUTATIONS FOR THE MODULATION EXPERIMENT

Writing the new density profile as a perturbation around the constant density ρ_c, $\rho(\vec{r}) = \rho_c + \delta\rho(\vec{r})$, we can compute $\delta\rho$ at linear order using Eqs. (3), (4), (22), and (25) (this neglects the

effect of the cloud's boundary):

$$\delta\rho(x,y,z) = \frac{A}{k_{\mathrm{B}}T}\rho_c B(\lambda_e)\sin(k_e x), \tag{A1}$$

where

$$B(\lambda_e) = \frac{1}{1+\lambda_e^2/(4\pi^2\lambda_D^2)}, \lambda_e = \frac{2\pi}{k_e},$$

and A is the small amplitude of the modulating potential. Hence the modulated profile has a clear amplitude dependence on the modulation wavelength λ_e and it is characteristic of Coulomb interactions (another force would have given a different result). When the modulation wavelength is increased beyond the Debye length ($L > \lambda_e > \lambda_D$), the response decreases, which means that large scale inhomogeneities are more difficult to create: this is an effect of repulsive long-range interactions. Therefore, measuring this response function should provide information on the interactions inside the cloud.

The density modulation of the cloud is measured by diffraction: the diffracted amplitude at wavelength λ_e is related to the response function $B(k_e)$. However, this relationship is not straightforward. In particular, we shall see now that there are two distinct diffraction regimes, Bragg at small wavelength, and Raman-Nath at large wavelength.

The diffraction profile is proportional to the structure factor, which is for the modulated cloud, using the definition (2):

$$S(\vec{k}) = S^0(\vec{k}) + \frac{2}{N}\delta\hat{\rho}(\vec{k})\hat{\rho}^0(\vec{k}) + \delta\hat{\rho}(\vec{k})^2 + \mathrm{O(correlation)}, \tag{A2}$$

where S^0, $\hat{\rho}^0$ are respectively the structure factor and the Fourier transform of the effective cloud's profile without external modulation; note that it actually corresponds to the cloud's profile truncated in the x and y direction by the Gaussian probe beam. Hence here N corresponds to the number of diffracted atoms, i.e., within the Gaussian probe beam. We will neglect the correlations because they are very small as we have seen in Sec. III C. The Fourier transform of the modulated cloud $\delta\hat{\rho}(\vec{k})$ can be related to the Fourier transform of the unperturbed cloud $\hat{\rho}^0(\vec{k})$, taking into account the shift in $\vec{k}$ induced by the $\sin(k_e x)$ function $k_x \to k_x \pm k_e$. The diffracted peaks correspond to maxima of the structure factor and are situated around the wave number $|\vec{k}| \simeq |\vec{k}_e|$. To compute their amplitude and shape one can expand in Eq. (A2) around $k = k_e$, and $\phi_k = 0$ or π (these two angles correspond experimentally to the two diffraction peaks observed; see Fig. 2 for definition of k and ϕ_k).

We probe a wave-number region $k_e \in [\sim 10^3, \sim 10^5]\ \mathrm{m}^{-1}$, with $k_i = 2\pi\frac{10^6}{0.78}\ \mathrm{m}^{-1}$, so that $k_e/k_i \ll 1$. This justifies the following expansion:

$$|k_e\,\vec{e}_k - k_e\,\vec{e}_x| = \frac{k_e^2}{2k_i} + k_e \times \mathrm{O}\left(\left(\frac{k_e}{2k_i}\right)^2\right) \simeq k_z \neq 0. \tag{A3}$$

In the perturbed density profile, it yields at the diffracted peak $k \simeq k_e$

$$\hat{\rho}(k_e) \simeq \hat{\rho}^0(k_e) - \frac{A}{2k_{\mathrm{B}}T}B(k_e)\left[\hat{\rho}^0(2k_e) - \hat{\rho}^0\left(\frac{k_e^2}{2k_i}\right)\right]. \tag{A4}$$

Since $\hat{\rho}(k=0) = N$ and the Fourier transform of the profile decreases very quickly to 0 with increasing k [the more regular $\rho(r)$ is, the faster its Fourier transform goes to 0] the dominant term in Eq. (A4) is the last one, provided $NA/(k_{\mathrm{B}}T) \gg 1$ (this is typically the case in experiments) and $k_e \gtrsim 1/L$. Hence the diffracted peak maximum intensity is given by

$$S(k_e) \simeq 1 + \frac{1}{N}\left(\frac{A}{2k_{\mathrm{B}}T}\right)^2 B^2(k_e)\left[\hat{\rho}^0(k_z)\right]^2. \tag{A5}$$

Thus the diffraction response depends on the longitudinal density profile and not only on the response function $B(k_e)$. The density dependence crosses over at $k_z L \sim 1$, which defines a critical modulation wavelength $\lambda_e^{(c)}$ (or wave number $k_e^{(c)}$),

$$\lambda_e^{(c)} = 2\pi\sqrt{\frac{L}{2k_i}} = \sqrt{\pi L \lambda_i} \quad \text{or} \quad k_e^{(c)} = \sqrt{\frac{2k_i}{L}}. \tag{A6}$$

It separates on one side the Raman-Nath regime $k_z L \ll 1$, where the diffracted peak intensity depends only on the response function, and on the other side the Bragg regime $k_z L \gtrsim 1$, where $\hat{\rho}^0(k_z)$ is not constant and decreases quickly to zero. Thus in this latter regime there is an additional dependence related to the Fourier transform of the density profile, that we call the "density effect." Note that in the context of ultrasonic light diffraction this criterion (26) separating Bragg and Raman-Nath regimes is also known [49]. For a cloud of radius $L \approx 6$ mm and a laser $\lambda_i \simeq \lambda_L = 780$ nm, the crossover is expected around $\lambda_e^{(c)} \approx 120\ \mu$m.

It must also be noted that the experimentally measured quantity is not the peak amplitude $S(k_e)$, but rather the diffracted power $R(k_e)$: this brings an extra dependence on k_e. To simply show this, one can expand the structure factor around the peak and, assuming for instance a Gaussian shape around the maximum, deduce a linear dependence on the modulation wavelength $\lambda_e = 2\pi/k_e$ (the precise form of the shape around the maximum does not modify this linear dependence). To summarize, we expect to measure

$$R(k_e) \propto B^2(k_e) \times \begin{cases} \lambda_e[\hat{\rho}^0(\lambda_i\pi/\lambda_e^2)]^2, & \lambda_e \ll \lambda_e^{(c)} \\ \lambda_e, & \lambda_e^{(c)} \ll \lambda_e \ll L. \end{cases} \tag{A7}$$

In this expression, both the density dependence and response function $B(k_e)$ are *a priori* unknown. In order to obtain a well defined theoretical prediction, we assume for the cloud's profile a symmetrized Fermi function [50], i.e., a step smoothed over a length scale l. In the direction perpendicular to the probing beam, the cloud is effectively limited by the waist of the probing laser w; we assume a Gaussian laser profile. This yields a simplified effective density profile

$$\rho^0(r_\perp, z) \propto \frac{l}{L}\frac{\sinh\left(\frac{L}{l}\right)}{\cosh\left(\frac{L}{l}\right) + \cosh\left(\frac{z}{l}\right)}\exp\left(-\frac{2r_\perp^2}{w^2}\right). \tag{A8}$$

Its associated structure factor can be evaluated analytically thanks to [50]. Putting together all the results of this section, we obtain the theoretical predictions shown on Fig. 5.

APPENDIX B: OSCILLATIONS IN THE BRAGG REGIME

In the Bragg regime, the shape of the diffracted beams observed in the experiment shows some variations, as seen in Fig. 6(b): for $\lambda_e = 75.7\ \mu$m, the diffracted beam is split in two; this corresponds to the right dashed vertical line in Fig. 5. Can we explain this observation? One has to remember that the response depends on the longitudinal profile (A4); thus around a peak $k = k_e + \delta k$, the response is

$$S(k) \propto S^0\left(\frac{k_e^2 + 2k_e\delta k}{2k_i}\right).$$

$S^0(k)$ is the Fourier transform of the effective density profile Eq. (A8). In the z direction, this profile is a smoothed step, and this induces oscillations in its Fourier transform and in S^0; the locations of the local minima and maxima of these oscillations mainly depend on the cloud's size L, and only very weakly on the details of Eq. (A8), such as the smoothing length scale l. If $k_e^2/(2k_i)$ happens to correspond to a local minimum of S^0, the diffracted beam can be split in two.

We illustrate this with our theoretical model Eq. (A8), with parameters L and w provided by the experiments, and l chosen to be 1 mm (the results depend very weakly on l). Figure 6(d) shows the theoretical diffracted beam for $\lambda_e = 76.5\ \mu$m, where splitting occurs: this value of λ_e is very close to the one for which splitting is indeed experimentally observed. In Fig. 6(a) we show an experimental image for $\lambda_e = 64.2\ \mu$m (this corresponds to the left vertical dashed line of Fig. 5) where no splitting occurs. The theoretical prediction Fig. 6(c) indeed does not show any splitting.

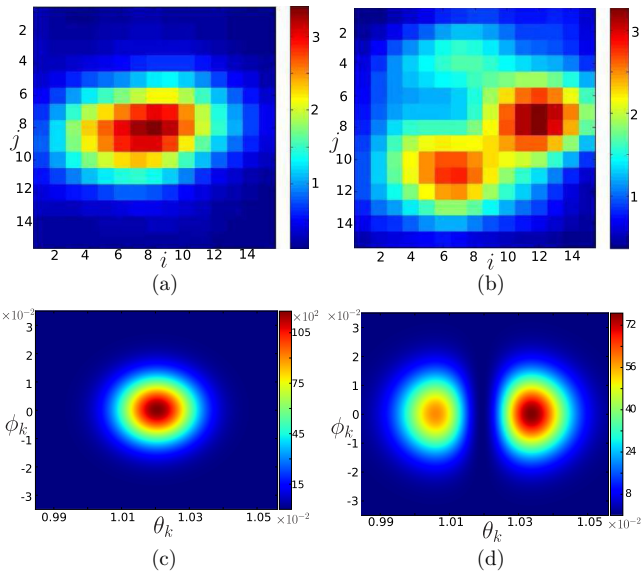

FIG. 6. Experimental (top) and theoretical (bottom) diffracted beams for $\lambda_e = 64.2$ and $75.68\ \mu$m. The color scale is adjusted to improve readability, and i, j are the pixel indexes.

This analysis provides a satisfactory explanation of the experimental observation, and suggests that the Bragg regime is well understood. These features have unfortunately nothing to do with the Debye length we are looking for: they are related to the global cloud's shape.

[1] E. L. Raab, M. Prentiss, A. Cable, S. Chu, and D. E. Pritchard, Phys. Rev. Lett. **59**, 2631 (1987).
[2] T. Walker, D. Sesko, and C. Wieman, Phys. Rev. Lett. **64**, 408 (1990).
[3] J. Dalibard, Opt. Commun. **68**, 203 (1988).
[4] C. G. Townsend, N. H. Edwards, C. J. Cooper, K. P. Zetie, C. J. Foot, A. M. Steane, P. Szriftgiser, H. Perrin, and J. Dalibard, Phys. Rev. A **52**, 1423 (1995).
[5] J. Dalibard and C. Cohen-Tannoudji, J. Opt. Soc. Am. B **6**, 2023 (1989).
[6] K. Kim, H.-R. Noh, H.-J. Ha, and W. Jhe, Phys. Rev. A **69**, 033406 (2004).
[7] J. Weiner, V. S. Bagnato, S. Zilio, and P. S. Julienne, Rev. Mod. Phys. **71**, 1 (1999).
[8] C. C. Bradley, J. J. McClelland, W. R. Anderson, and R. J. Celotta, Phys. Rev. A **61**, 053407 (2000).
[9] A. R. L. Caires, G. D. Telles, M. W. Mancini, L. G. Marcassa, V. S. Bagnato, D. Wilkowski, and R. Kaiser, Braz. J. Phys. **34**, 1504 (2004).
[10] D. Sesko, T. Walker, C. Monroe, A. Gallagher, and C. Wieman, Phys. Rev. Lett. **63**, 961 (1989).
[11] H. J. Lee, C. S. Adams, M. Kasevich, and S. Chu, Phys. Rev. Lett. **76**, 2658 (1996).
[12] A. Camara, R. Kaiser, and G. Labeyrie, Phys. Rev. A **90**, 063404 (2014).
[13] L. Pruvost, I. Serre, H. T. Duong, and J. Jortner, Phys. Rev. A **61**, 053408 (2000).
[14] G. Labeyrie, F. Michaud, and R. Kaiser, Phys. Rev. Lett. **96**, 023003 (2006).
[15] T. Pohl, G. Labeyrie, and R. Kaiser, Phys. Rev. A **74**, 023409 (2006).
[16] J. T. Mendonça, R. Kaiser, H. Terças, and J. Loureiro, Phys. Rev. A **78**, 013408 (2008).
[17] J. T. Mendonça and H. Terças, J. Phys. B: At., Mol. Opt. Phys. **44**, 095301 (2011).
[18] H. Terças, J. T. Mendonça, and R. Kaiser, Europhys. Lett. **89**, 53001 (2010).
[19] J. T. Mendonça and R. Kaiser, Phys. Rev. Lett. **108**, 033001 (2012).
[20] Ph. W. Courteille, S. Bux, E. Lucioni, K. Lauber, T. Bienaimé, R. Kaiser, and N. Piovella, Eur. Phys. J. D **58**, 69 (2010).
[21] T. Bienaimé, M. Petruzzo, D. Bigerni, N. Piovella, and R. Kaiser, J. Mod. Opt. **58**, 1942 (2011).
[22] L. Chomaz, L. Corman, T. Yefsah, R. Desbuquois, and J. Dalibard, New J. Phys. **14**, 055001 (2012).

[23] T. Bienaimé, R. Bachelard, N. Piovella, and R. Kaiser, Fortschr. Phys. **61**, 377 (2013).
[24] B. Zhu, J. Cooper, J. Ye, and A. M. Rey, Phys. Rev. A **94**, 023612 (2016).
[25] S. D. Jenkins, J. Ruostekoski, J. Javanainen, R. Bourgain, S. Jennewein, Y. R. P. Sortais, and A. Browaeys, Phys. Rev. Lett. **116**, 183601 (2016).
[26] L. Corman, J. L. Ville, R. Saint-Jalm, M. Aidelsburger, T. Bienaimé, S. Nascimbène, J. Dalibard, and J. Beugnon, Phys. Rev. A **96**, 053629 (2017).
[27] A. Fioretti, A. Molisch, J. Müller, P. Verkerk, and M. Allegrini, Opt. Commun. **149**, 415 (1998).
[28] G. Labeyrie, D. Delande, C. Müller, C. Miniatura, and R. Kaiser, Opt. Commun. **243**, 157 (2004).
[29] G. Labeyrie, R. Kaiser, and D. Delande, Appl. Phys. B **81**, 1001 (2005).
[30] T. Bienaimé, S. Bux, E. Lucioni, P. W. Courteille, N. Piovella, and R. Kaiser, Phys. Rev. Lett. **104**, 183602 (2010).
[31] J. Chabé, M.-T. Rouabah, L. Bellando, T. Bienaimé, N. Piovella, R. Bachelard, and R. Kaiser, Phys. Rev. A **89**, 043833 (2014).
[32] C. E. Máximo, R. Bachelard, and R. Kaiser, Phys. Rev. A **97**, 043845 (2018).
[33] W. Guerin, M. O. Araújo, and R. Kaiser, Phys. Rev. Lett. **116**, 083601 (2016).
[34] M. O. Araújo, I. Kresic, R. Kaiser, and W. Guerin, Phys. Rev. Lett. **117**, 073002 (2016).
[35] S. J. Roof, K. J. Kemp, M. D. Havey, and I. M. Sokolov, Phys. Rev. Lett. **117**, 073003 (2016).
[36] S. Manz, R. Bücker, T. Betz, Ch. Koller, S. Hofferberth, I. E. Mazets, A. Imambekov, E. Demler, A. Perrin, J. Schmiedmayer, and T. Schumm, Phys. Rev. A **81**, 031610(R) (2010).
[37] C.-L. Hung, X. Zhang, L.-C. Ha, N. Gemelke, and C. Chin, New J. Phys. **13**, 075019 (2011).
[38] J.-P. Hansen and I. R. McDonald, *Theory of Simple Liquids*, 3rd ed. (Elsevier, 2006).
[39] R. Romain, D. Hennequin, and P. Verkerk, Eur. Phys. J. D **61**, 171 (2011).
[40] D. H. E. Dubin and T. M. O'Neil, Rev. Mod. Phys. **71**, 87 (1999).
[41] H. Terças and J. T. Mendonça, Phys. Rev. A **88**, 023412 (2013).
[42] R. Romain, H. Louis, P. Verkerk, and D. Hennequin, Phys. Rev. A **89**, 053425 (2014).
[43] H. Yoshida, Phys. Lett. A **150**, 262 (1990).
[44] D. W. Sesko, T. G. Walker, and C. E. Wieman, J. Opt. Soc. Am. B **8**, 946 (1991).
[45] G. L. Gattobigio, T. Pohl, G. Labeyrie, and R. Kaiser, Phys. Scr. **81**, 025301 (2010).
[46] G. L. Gattobigio, Ph.D. thesis, Università degli studi di Ferrara, Université Nice Sophia Antipolis, 2008.
[47] M. H. Anderson, W. Petrich, J. R. Ensher, and E. A. Cornell, Phys. Rev. A **50**, R3597 (1994).
[48] L. Pruvost, in *International Topical Conference on Plasma Science: Strongly Coupled Ultra-Cold and Quantum Plasmas*, edited by P. K. Shukla, J. T. Mendonça, B. Eliasson, and D. Resedes, AIP Conf. Proc. No. 1421 (AIP, Melville, NY, 2012), pp. 80–92.
[49] W. R. Klein and B. D. Cook, IEEE Trans. Sonics Ultrason. **14**, 123 (1967).
[50] D. W. L. Sprung and J. Martorell, J. Phys. A **30**, 6525 (1997).

Observation of violent relaxation and the formation of an analogue galaxy

M. Lovisetto[1], M.C. Braidotti[2], R. Prizia[2,3], C. Michel[4],
D. Clamond[1], M. Bellec[4], E.M. Wright[5], B. Marcos[1], D. Faccio[2,3]
[1] *Université Côte d'Azur, CNRS, Laboratoire J.-A. Dieudonné, 06109 - Nice, France*
[2] *School of Physics & Astronomy, University of Glasgow, G12 8QQ Glasgow, UK*
[3] *Institute of Photonics and Quantum Sciences, Heriot-Watt University, EH14 4AS Edinburgh, United Kingdom*
[4] *Université Côte d'Azur, CNRS, INPHYNI, France and*
[5] *Wyant College of Optical Sciences, University of Arizona, Tucson, Arizona 85721, USA*

Structures in the Universe, ranging from globular clusters to entire galaxies, are not described by standard statistical mechanics at equilibrium. Instead, they are formed through a process of a very different nature, called *violent relaxation*. This mechanism was proposed theoretically and modelled numerically, but never directly observed in any physical system. We developed a table-top nonlinear optics experiment allowing us to directly observe violent relaxation, leading to the formation of an analogue 2D-galaxy. The experiment allows us to control a range of parameters, including the nonlocal interacting potential, allowing us to emulate the physics of gravitational quantum and classical dark matter models.

Introduction — Structures of the observable Universe, such as galaxies and globular clusters, appear to be macroscopically stationary and, for a long time, were thought to be at thermodynamic equilibrium [1]. However, Chandrasekhar pointed out in 1941 that the time necessary for these objects to reach thermal equilibrium is actually much larger than their age [2]. This has been confirmed by observations determining that these astrophysical structures are indeed far from thermal equilibrium (see, e.g., [3]). In 1967 Lynden-Bell proposed a mechanism, *violent relaxation* that leads to the formation of these out-of-equilibrium structures, called *quasi-stationary states*. These structures evolve towards the quasi-stationary state on a time much faster than that required for full thermodynamic equilibrium [4]. It has been subsequently understood that this mechanism is generic in Hamiltonian systems with a long range interacting potential, i.e., a potential that is not integrable as a result of its extension over large scales [5]. This phenomenon is similar to what arises in plasmas subject to Landau damping, in which there is an exchange of energy between the electromagnetic wave generated by the particles of the plasma and the particles themselves [6]. Landau damping has been observed in plasma experiments [7–13] and in space plasma turbulence [14]. Contrary to Landau damping, violent relaxation is more elusive and has not been observed to date, neither in a repeatable or controllable experiment, nor in situ. Indeed, experimental observation of the dynamics of the formation of quasi-stationary states via violent relaxation is hindered mostly for two reasons. First, there are systems in which it is potentially present, but it is destroyed by the stochastic noise generally present in these systems [16]. Second, there are systems in which violent relaxation is actually present, but the associated timescales are too large to observe it. This is the case of astrophysical systems such as galaxies, independently if it is constituted by classical (non-quantum) dark matter particles (see e.g. [17–20]), or composed by quantum matter (see e.g. [21–25]). In these systems violent relaxation occurs on time scales of the order of millions of years [1].

Violent relaxation has however, been studied numerically for example, by simulating classical N-body systems with nonlocal (e.g. gravitational) interactions that are governed by Vlasov-Poisson equations [26–29]. Whilst these simulations provide confirmation of the process proposed by Lynden-Bell, they provide no guidance of how to observe violent relaxation experimentally.

Here we report the experimental observation of violent relaxation and the subsequent formation of an analogue galaxy. This work is founded on the fact that galaxies are dominated by dark matter, so the underlying classical dynamics are those of an N-body system of self-gravitating particles of dark matter and are described by the Vlasov-Poisson equation [30, 31]. In the corresponding quantum description, the dark matter wavefunction is governed by the Newton-Schrödinger Equation (NSE) that notably has a semi-classical limit that reduces to the Vlasov-Poisson equation and therefore also describes the evolution of classical dark matter [32]. It is this link between the semi-classical limit of the NSE and classical dark matter evolution that allows us to build an experiment to observe violent relaxation. Indeed, the NSE can be experimentally realised in nonlinear optical experiments that have been used to probe gravitational lensing, tidal forces and analogue quantum processes such as Boson star evolution [33, 34]. By choosing the appropriate system parameters, we show that it is possible to experimentally access dominantly the semi-classical limit of the NSE, allowing us to experimentally observe violent relaxation and the formation of a quasi-stationary state in the form of a "table-top galaxy" that bears a close resemblance to the result of an N-body numerical simulation.

Self-gravitating systems. The temporal evolution of self-gravitating particles of dark matter, of mass m, defined

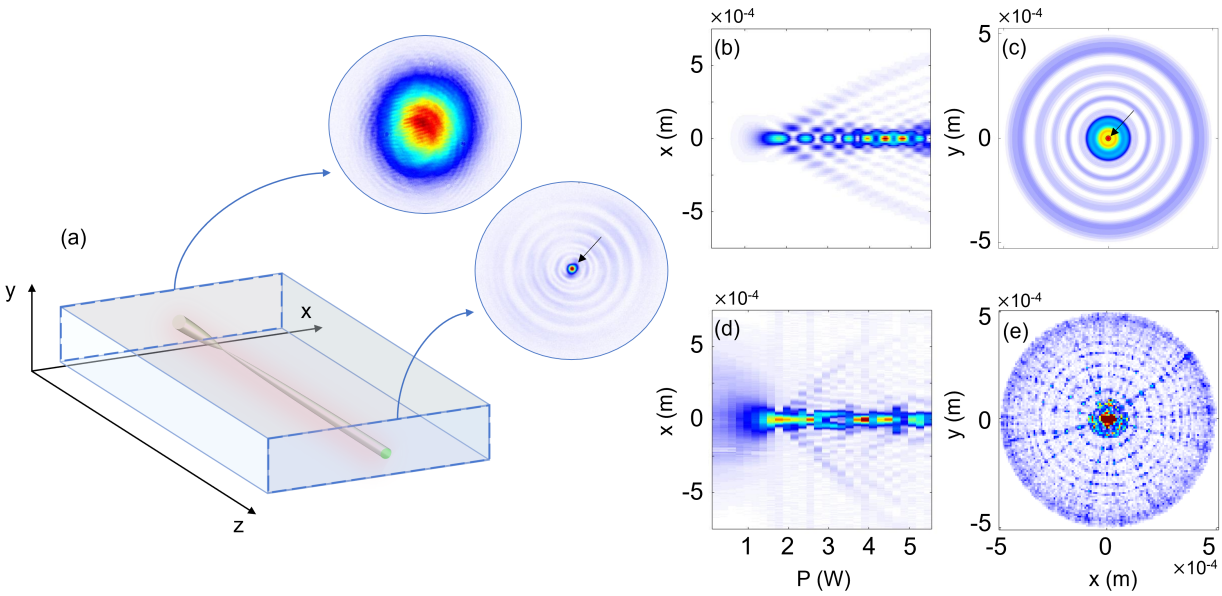

FIG. 1. (a) Sketch of the experiment. A Gaussian laser beam propagates in a lead-doped glass slab. Fully detailed experimental layout is shown in [15]. The diffusion of heat inside the nonlinear medium is represented by the glowing red profile. Insets show measured input and output experimental profiles at $P = 5$ W. (b),(d) $y = 0$ slice of the beam intensity profile as a function of one transverse coordinate x and power, obtained from the numerical simulation (b) and experimental data (d). (c) Simulation of the full transverse plane distribution, $P(x, y)$ at $z = L$ for input power $P = 5$ W. We observe the soliton (red dot indicated by the black arrow) surrounded by the classical part corresponding to $\chi \to 0$. (e) N-body simulation result of under the same conditions performed evolving self-gravitating particles of dark matter. We have used 2^{17} N-body particles and the parameters map directly on to those used in the experiments (see [15] for details), i.e. this galaxy is the particle version of the optical galaxies shown in panel (a) inset (experiment) and (c) (numerical simulation).

by a wavefunction $\psi(\mathbf{r}, t)$, is described in 3D by the Newton–Schrödinger equations (NSE):

$$\mathrm{i}\hbar\partial_t\psi + \frac{\hbar^2}{2m}\nabla^2\psi + m\phi\psi = 0 \tag{1a}$$

$$\nabla^2\phi = -4\pi G|\psi|^2, \tag{1b}$$

where $|\psi|^2$ is the mass density, G the gravitational constant and ∇^2 the three-dimensional (3D) Laplacian. The gravitational potential, ϕ, generated by the mass distribution itself, depends on the constant G and the mass density. When the system is in the semi-classical regime, which corresponds to $\hbar/m \ll 1$, the process of violent relaxation can be observed. This process leads the system towards its quasi-stationary state [1]. Violent relaxation consists in the evolution of the energy distribution due to the variation in time of the potential $\phi(\mathbf{r}, t)$ (being it self-consistently generated by the wavefunction itself, see Eq. (1b)). Observed as part of the evolution towards the quasi-stationary state is phase mixing due to the evolution of the wavefunction in the non-harmonic potential $\phi(\mathbf{r}, t)$. Mixing alone is a relaxation process by itself, despite violent relaxation is much more efficient than mixing alone. When violent relaxation is present, mixing is also generically present, the opposite being not true. Therefore, any demonstration of violent relaxation requires as a minimum, the presence of both of these ingredients: a time varying potential causing the variation of the energy distribution.

In the semi-classical regime, the quasi-stationary solution for violent relaxation process corresponds to the formation of an oscillating solitonic core in the center of the system (defined as the ground state of Eq. (1) of the form $\psi(\mathbf{r}, t) = \hat{\psi}(\mathbf{r})e^{-iE/\hbar t}$, where E is the total energy of the system, see e.g. [35–37]) surrounded by the stationary solution of the classical Vlasov-Poisson equation, which is also the semi-classical limit of the NSE (i.e. the limit $\hbar/m \to 0$ of Eq. (1)) [22, 32]. In order to be sure to be in the proper regime, the soliton has to be small compared to the size of the whole system. When this happens, the system can be considered to be sufficiently semi-classical ($\hbar/m \to 0$) to observe violent relaxation. Therefore, we monitor the degree of classicality with the parameter $\chi = \xi/s$, where ξ is the characteristic size of the soliton [38] and s the size of the whole system. The goal then is (differently from previous studies looking at soliton evolution) to study the behaviour of the broad semi-classical background solution, corresponding to the galaxy, in the potential generated by the total field. In order to do this, we take advantage of the formal identity of Eq. (1) to that describing our optical system.

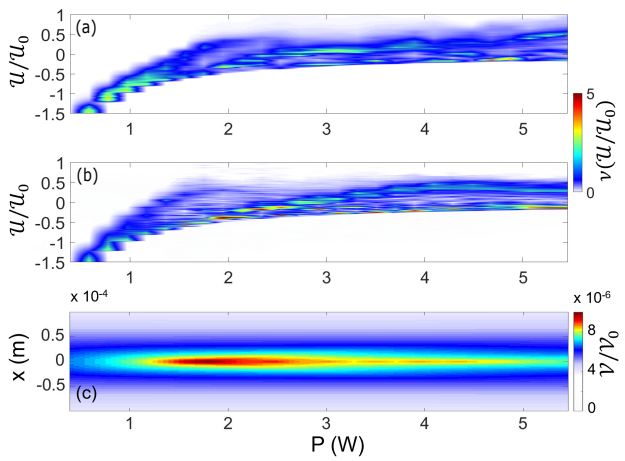

FIG. 2. Distribution of energy density map $\nu(\mathcal{U}/\mathcal{U}_0)$ for the experiment (a) and simulation (b). The energy density units are $\mathcal{U}_0 = (\alpha\beta k_0 P)\,/\,(2\pi\kappa)$. (c) Numerical $y = 0$ slice of the normalized potential $\mathcal{V}/\mathcal{V}_0$, computed at $z = L$, as a function of transverse coordinate x and power P, ($\mathcal{V}_0 = k_0 P$).

Optical system. In the paraxial approximation the propagation of a monochromatic laser beam with amplitude, $\mathcal{E}(\mathbf{r}_\perp, z)$, in a thermally focusing nonlinear medium is described by [33, 34, 39, 40]:

$$\begin{aligned} &\mathrm{i}\partial_z\mathcal{E} + \frac{1}{2k_0 n_b}\nabla_\perp^2\mathcal{E} + k_0\Delta n\mathcal{E} + \mathrm{i}\,\frac{\alpha}{2}\,\mathcal{E} = 0, \\ &\nabla_\perp^2\Delta n = -\frac{\alpha\beta}{\kappa}|\mathcal{E}(\mathbf{r}_\perp, z)|^2, \end{aligned} \tag{2}$$

where $\mathbf{r}_\perp = (x, y)$ is the two-dimensional (2D) position in the plane transverse to the propagation direction z. The operator $\nabla_\perp^2$ is the transverse 2D Laplacian, $k_0 = \frac{2\pi}{\lambda}$ the wave-number of the incident laser with n_b the background refractive index of the medium. The non-local nonlinear refractive index change, Δn, is induced by the beam itself heating the medium. β is the medium thermo-optic coefficient, κ its thermal conductivity and α its absorption coefficient. The last term of Eq. (2) accounts for the absorption in the crystal and in our parameter space, has little effect on the violent relaxation dynamics (see discussion in [15, 41]). We hence neglect it in the following discussion.

Provided that z plays the role of time t, the similarity between Eqs. (1) and (2) underpins the opportunity to directly observe 2D violent relaxation in a laboratory experiment. Notably, the presence of violent relaxation is independent of the dimension of space, and occurs also in 1D [42] and, as is our case, in 2D [43]. Hence, the 2D optical system lends itself to the observation of violent relaxation. The main difference between the 2D optical and 3D gravitational systems is the shape of the potential being logarithmic in the 2D system. However, the mechanism that governs the physics in both systems is the same, i.e. modes or particles that live in a confining potential that is evolving in time can undergo the mode mixing and violent relaxation, leading to the formation of a quasi-stationary state. The optical equivalent of the above-mentioned semi-classical regime is obtained when $\chi = \xi/s \ll 1$. In the optical case, $\xi = \sqrt{z_{\rm nl}/(2k_0 n_b)}$ is the soliton size, defined as the transverse length scale for which both the linear and nonlinear effects are of the same order. $z_{\rm nl} = \kappa/(\alpha\beta k_0 P)$ is the longitudinal length over which the effect of the nonlinear term becomes substantial and $P = \int d\mathbf{r}_\perp\,|\mathcal{E}(\mathbf{r}_\perp, z)|^2$ is the power of the laser beam. Preparing the initial beam with transverse width s dictates the propagation regime of the system (and hence the difference between the soliton-dominated regimes studied in the past where the aim was to generate the soliton solution and hence the waist s was chosen to be close to the soliton waist ξ and generate as less background as possible[39, 44] and the present work that refers to the formation of a significant, surrounding 'background', i.e. the galaxy, hence having $s \ll \xi$).

Moreover, one can define a local energy density of the optical system as

$$\mathcal{U}(\mathbf{r}_\perp, z) = \frac{|\nabla_\perp\mathcal{E}(\mathbf{r}_\perp, z)|^2}{2k\,|\mathcal{E}(\mathbf{r}_\perp, z)|^2} - k_0\Delta n(\mathbf{r}_\perp, z). \tag{3}$$

The first contribution corresponds to the kinetic (linear) energy density $\mathcal{K}(\mathbf{r}_\perp, z)$, the second one to the potential (nonlinear) energy density $\mathcal{V}(\mathbf{r}_\perp, z)$. The total energy $E = \int d\mathbf{r}_\perp\mathcal{E}^*(\mathbf{r}_\perp, z)\left[-\frac{\nabla_\perp^2}{2k} - \frac{k_0}{2}\Delta n(\mathbf{r}_\perp, z)\right]\mathcal{E}(\mathbf{r}_\perp, z)$ is a conserved quantity (if losses are neglected).

In order to characterise and quantify violent relaxation in optical experiments, we define two quantities: firstly, the Wigner transform [45] $F(\boldsymbol{r}_\perp, \boldsymbol{k}_\perp, z)$ of the optical field $\mathcal{E}$, i.e. the density of probability to find a portion of the optical beam at the position $\boldsymbol{r}_\perp$ with wavevector $\boldsymbol{k}_\perp$. We use the evolution of F with respect of z to study the mixing of the phase-space. Secondly, we define the evolution of the distribution of energy density $\nu(\mathcal{U})$ of the optical field $\mathcal{E}$ (see [15] for the mathematical definition), that captures the main signature of the violent relaxation process, i.e. the change in the distribution of the energy due to the variation in the potential $\mathcal{V}(\mathbf{r}_\perp, z) = -k_0\Delta n(\mathbf{r}_\perp, z)$ along z.

Experimental setup. Figure 1(a) shows a schematic representation of the experiment. A continuous-wave laser beam with a Gaussian profile and wavelength $\lambda = 532$ nm propagates in a thermo-optical nonlinear medium made of three aligned identical slabs of lead-doped glass for a total length $L = 30$ cm, represented here as a single slab. The beam width $s = 350$ μm at the sample input facet is chosen experimentally by a system of lenses such that $\chi = 2.3 \times 10^{-2}/\sqrt{P}$, with P measured in Watts and is therefore of order $10^{-2} \ll 1$ over the full evolution (see [15]). This therefore ensures that we satisfy the semi-classical regime requirement.

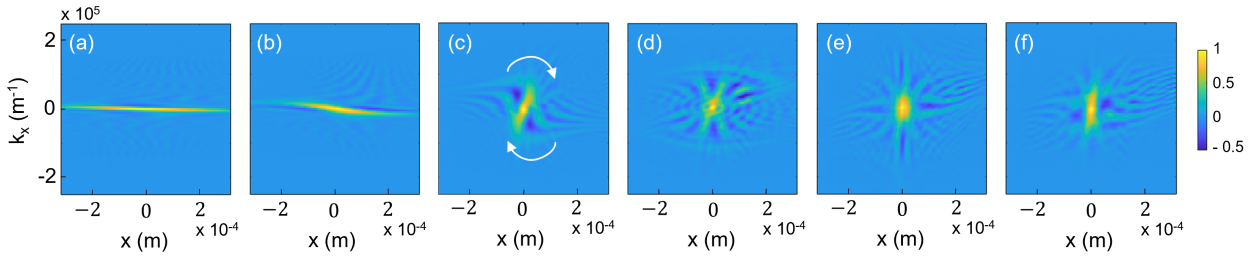

FIG. 3. Results of experiment for the $y = 0, k_y = 0$ profiles of the Wigner distribution at different input powers: (a) $P = 0.2$W, (b) $P = 1$W, (c) $P = 2$W, (d) $P = 3$W, (e) $P = 4$W, (f) $P = 5$W.

When the intense laser beam propagates inside the crystal, it induces a nonlocal interaction (heating) of the medium. The beam at the output facet of the medium is imaged onto a camera, where we collect its interference with a reference beam. By using the Off-Axis Digital Holography technique [46], we measure the spatial distribution of both the intensity and the phase of output field. To explore the full dynamics of the laser beam, we tune the initial power from 0.2 W to 5.5 W. The insets in Fig. 1(a) show the experimental beam intensity profile at the input and output crystal facets for an input power $P = 5$ W.

Experimentally, it is only possible to access the field at the output facet of the sample and not the full nonlinear propagation inside the material. However, there is a direct mapping between power P and propagation length z, when $\chi \ll 1$ and the beam initial phase is negligible (see [15]). This mapping allows us to follow the z-evolution of the amplitude $\mathcal{E}$ by varying the input power of the beam and measuring the intensity at fixed $z = L$ (L is the sample length). We then re-scale the propagation coordinate z in terms of a relevant dynamical characteristic scale $z_{\rm dyn} = s\sqrt{n_b\kappa/\alpha\beta P}$ [15]. Therefore, varying the initial power P and measuring the intensity at fixed $z = L$ is equivalent to measuring the intensity at different steps $z/z_{\rm dyn}$ inside the material at fixed P. Hereafter, we will use P to parameterize the system evolution along z.

Observation of violent relaxation and formation of the quasi-stationary state. Figures 1(b) and (d) depict the numerical and experimental intensity profiles (along $y = 0$) measured at the output of the glass sample as a function of power P, respectively. We observe good qualitative agreement: the initial beam collapse is then followed by a stabilization. In nonlinear optics terms, the optical beam is undergoing self-focusing. The system is trying to stabilize on the solitonic state, by expelling energy in the form of a broad background field composed by the central part plus the outgoing rings. The presence of nonlocality prevents the light from undergoing a catastrophic collapse in this system [47–49]. The semi-classical regime chosen is not ideal for the formation of a soliton, but instead maximizes the generation of the surrounding background that indeed is the result of phase-mixing and violent relaxation (in a gravitational context, this corresponds to the galaxy). A plot of the simulated intensity distribution for an incident power $P = 5$ W is shown in Fig. 1(c), and is in good agreement with the experimental inset in Fig. 1(a)).

Violent relaxation can be identified by looking at the distribution of the energy density $\nu(\mathcal{U}/\mathcal{U}_0)$ and at the phase-space behaviour along the evolution. We expect a variation in the energy density due to a variation in the overall potential $\mathcal{V}(\mathbf{r}_\perp, z)$ [1]. Figure 2 shows the experimental (a) and numerical (b) distribution of the normalized energy density, $\mathcal{U}(\mathcal{E})/\mathcal{U}_0$, obtained for various input powers, P, as well as the potential $\mathcal{V}/\mathcal{V}_0$ evolution (c), computed at $z = L$. Before the collapse (around $P \approx 1.8$ W), we observe a significant variation of the potential $\mathcal{V}$ that then affects the distribution of energy density and is seen to decrease to negative values as it is dominated by the potential and reveals that the system is undergoing violent relaxation. In contrast, after the collapse (after P=3 W), the distribution of energy density exhibits two characteristic 'structures', which persist for the whole subsequent evolution: one at smaller energies, which corresponds to the centre of the beam near the solitonic core; a second 'structure' at higher energies related to the most external rings. It is worth noticing that, after the collapse, the distribution of energy density does not vary significantly, tending asymptotically to a constant profile associated to the quasi-stationary state, formed by the narrow solitonic core plus the broad background analogue galaxy. Therefore, the region in which violent relaxation is most efficient can identified between $P \sim 0.5$ W and P$\sim$ 3 W. Reaching the quasi-stationary state means that the energy density distribution of the system is constant (the system has relaxed), despite the intensity profile keeps evolving (see Fig. 1a). The same happens in the astrophysical context: galaxies can present a slowly evolving energy density, despite showing still a continuing evolution in time of the overall shape.

We study the existence of mixing in the system by analysing the evolution of the phase-space. Figure 3 shows the experimental Wigner distribution $F(\boldsymbol{r}_\perp, \boldsymbol{k}_\perp, z)$ of the full complex-valued optical field [45]. At the input, the system has a Gaussian spatial distribution with a very narrow dispersion along the k_x-axis. As P increases, the phase mixing starts by first twisting the phase-space (indicated by the white arrows) and then forming filaments characteristic of violent relaxation [1]. We have also verified that in a system where only mixing is present (without violent relaxation), such as in the Snyder-Mitchell model [50], the evolution of the system is significantly different [15].

Furthermore, numerical simulations [15] show that the presence of losses, unavoidable in the experiment, do not have a relevant impact on the distribution of energy density.

Conclusions. We have provided experimental evidence of violent relaxation in a long interaction-range system that gives a direct confirmation of the formation of an out-of-equilibrium stationary state that follows the scenario advanced by Lynden-Bell in 1967 [4]. With our table-top experiments, we can directly connect our parameters to those of a particle-based dark matter galaxy, as shown in Fig. 1(e), where we plot the galaxy distribution for a particle system with parameters equivalent to those of the experiment, to be compared with Fig. 1(c).

The next steps may cover further aspects of long range systems such as investigating the effect of angular momentum, studying mergers of structures (which are known as the main mechanism of the formation of spiral galaxies), and simulating systems corresponding to various Dark Matter models.

Methods. Experimental setup. A CW laser with wavelength $\lambda = 532$ nm is split into 2 beams: a reference and a target beam. The reference beam is expanded by a system of lenses and collected by a CMOS camera. Figure 1 in the SM file shows an image of the setup [15]. The target beam is shaped to have waist $s = 350$ μm (waist calculated where the intensity falls of $1/e^2$ - the value has been obtained by a Gaussian fit of the beam intensity at the sample input face - see inset in Fig. 1 in the SM file [15]) and shines onto three aligned identical slabs of lead-doped glass (height $D = 5$ mm, width $W = 40$ mm and length $L_0 = 100$ mm each, hence a total length $L = 300$ mm).

The glass is a self-focusing nonlinear optical medium with background refractive index $n_b = 1.8$, thermal conductivity $\kappa = 0.7$ Wm^{-1}K^{-1}, absorption coefficient $\alpha = 1m^{-1}$, thermo-optic coefficient $\beta = \frac{\partial n}{\partial T} = 2.2 \cdot 10^{-5}$ K^{-1} and transmission coefficient at the sample interface $T = 0.92$. The value of the coefficient β is found by a fit of the experimental beam evolution and results to be 1.6 times larger than the value provided by the manufacturer. The target beam input powers range from $0.2\,W$ to $5.5\,W$, with a $0.25\,W$ step. By means of the off-axis digital holography technique [46], we reconstruct the amplitudes and phases of the target beam.

Acknowledgements. The authors acknowledge financial support from EPSRC (UK Grant No. EP/P006078/2) and the European Union's Horizon 2020 research and innovation program, Grant Agreement No. 820392. D.F. acknowledges financial support from the Royal Academy of Engineering Chair in Emerging Technology programme. M.L. and B.M. acknowledges support by the grant Segal ANR-19-CE31-0017 of the French Agence Nationale de la Recherche. Data is available at DOI:10.5525/gla.researchdata.1320.

Author contributions. B.M. and D.F. conceived the project and ideas. M.L., M.C.B. and R.P. performed the experiments, data analysis and numerical simulations. B.M., M.C.B and E.M.W. performed theoretical analysis. All authors contributed to the manuscript.

[1] J. Binney and S. Tremaine, Galactic Dynamics: Second Edition (Princeton University Press, 2008).
[2] I. S. Chandrasekhar, Astr. J. **93**, 285 (1941).
[3] B. Anguiano, S. R. Majewski, C. R. Hayes, C. A. Prieto, X. Cheng, C. M. Bidin, R. L. Beaton, T. C. Beers, and D. Minniti, The Astronomical Journal **160**, 43 (2020).
[4] D. Lynden-Bell, Monthly Notices of the Royal Astronomical Society **136**, 101 (1967).
[5] A. Campa, T. Dauxois, and S. Ruffo, Physics Reports **480**, 57 (2009).
[6] L. D. Landau, J. Phys. (USSR) **10**, 25 (1946).
[7] J. Malmberg and C. Wharton, Physical Review Letters **13**, 184 (1964).
[8] V. K. Neil and A. M. Sessler, Review of Scientific Instruments **36**, 429 (1965).
[9] L. J. Laslett, V. K. Neil, and A. M. Sessler, Review of Scientific Instruments **36**, 436 (1965).
[10] C. Damm, J. Foote, A. Futch Jr, A. Hunt, K. Moses, R. Post, and J. Taylor, Physical Review Letters **24**, 495 (1970).
[11] K. Gentle and A. Malein, Physical Review Letters **26**, 625 (1971).
[12] M. Sugawa, Physical review letters **61**, 543 (1988).
[13] J. Danielson, F. Anderegg, and C. Driscoll, Physical review letters **92**, 245003 (2004).
[14] C. Chen, K. Klein, and G. G. Howes, Nature communications **10**, 1 (2019).
[15] "The supplementary material provides details of the experimental setup, data analysis and numerical methods.".
[16] M. Chalony, J. Barré, B. Marcos, A. Olivetti, and D. Wilkowski, Phys. Rev. A **87**, 013401 (2013), arXiv:1202.1258 [physics.atom-ph].
[17] F. Zwicky, Helvetica Physica Acta **6**, 110 (1933).
[18] A. Boyarsky, O. Ruchayskiy, D. Iakubovskyi, A. V. Maccio', and D. Malyshev, arXiv e-prints , arXiv:0911.1774

(2009), arXiv:0911.1774 [astro-ph.CO].
[19] Y. Sofue, M. Honma, and T. Omodaka, Publ. Astron. Soc. Jpn. **61**, 227 (2009), arXiv:0811.0859 [astro-ph].
[20] G. Cupani, M. Mezzetti, and F. Mardirossian, Mon. Not. R. Astron. Soc. **403**, 838 (2010), arXiv:0910.2882 [astro-ph.CO].
[21] W. Hu, R. Barkana, and A. Gruzinov, Physical Review Letters **85**, 1158 (2000).
[22] H.-Y. Schive, T. Chiueh, and T. Broadhurst, Nature Physics **10**, 496 (2014).
[23] L. Hui, J. P. Ostriker, S. Tremaine, and E. Witten, Physical Review D **95**, 043541 (2017).
[24] D. J. Marsh and J. C. Niemeyer, Physical review letters **123**, 051103 (2019).
[25] S. Alexander, J. J. Bramburger, and E. McDonough, Physics Letters B **797**, 134871 (2019).
[26] M. Hénon, Annales d'Astrophysique **27**, 83 (1964).
[27] P. J. E. Peebles, Astroph. J. **75**, 13 (1970).
[28] S. J. Aarseth, D. N. C. Lin, and J. C. B. Papaloizou, Astrophys. J. **324**, 288 (1988).
[29] M. Joyce, B. Marcos, and F. Sylos Labini, Mon. Not. R. Astron. Soc. **397**, 775 (2009), arXiv:0811.2752 [astro-ph].
[30] V. C. Rubin, J. Ford, W. K., and N. Thonnard, Astrophys. J. **238**, 471 (1980).
[31] M. Persic, P. Salucci, and F. Stel, Mon. Not. R. Astron. Soc. **281**, 27 (1996), arXiv:astro-ph/9506004 [astro-ph].
[32] P. Mocz, L. Lancaster, A. Fialkov, F. Becerra, and P.-H. Chavanis, Physical Review D **97**, 083519 (2018).
[33] R. Bekenstein, R. Schley, M. Mutzafi, C. Rotschild, and M. Segev, Nature Physics **11**, 872 (2015).
[34] T. Roger, C. Maitland, K. Wilson, N. Westerberg, D. Vocke, E. M. Wright, and D. Faccio, Nature communications **7**, 1 (2016).
[35] I. M. Moroz, R. Penrose, and P. Tod, Classical and Quantum Gravity **15**, 2733 (1998).
[36] C. Rotschild, O. Cohen, O. Manela, M. Segev, and T. Carmon, Phys. Rev. Lett. **95**, 213904 (2005).
[37] C. Rotschild, B. Alfassi, O. Cohen, and M. Segev, Nature Physics **2**, 769 (2006).
[38] "ξ can be estimated by calculating the scale for which the kinetic and potential energies are of the same order of magnitude, giving $\xi = \hbar/m\sqrt{s/8\pi GM}$, where m is the total mass of the system and s the characteristic size of the whole system.".
[39] Y. S. Kivshar and G. P. Agrawa, Optical solitons: from fibers to photonic crystals (Academic press, 2003).
[40] A. Navarrete, A. Paredes, J. R. Salgueiro, and H. Michinel, Physical Review A **95**, 013844 (2017).
[41] M. C. Braidotti, R. Prizia, C. Maitland, F. Marino, A. Prain, I. Starshynov, N. Westerberg, E. M. Wright, and D. Faccio, Phys. Rev. Lett. **128**, 013901 (2022).
[42] M. Joyce and T. Worrakitpoonpon, Phys. Rev. E **84**, 011139 (2011).
[43] T. N. Teles, Y. Levin, R. Pakter, and F. B. Rizzato, Journal of Statistical Mechanics: Theory and Experiment **2010**, P05007 (2010).
[44] S. Trillo, Spatial solitons, Vol. 82 (Springer Science & Business Media, 2001).
[45] E. P. Wigner, in Physical Chemistry, Solid State Physics (Springer, 1997) pp. 110–120.
[46] J. Bertolotti, "Off-Axis Digital Holography Tutorial," `https://jacopobertolotti.com/tutorials.html`.
[47] W. Krolikowski, J. Wyller, and J. Rasmussen, Phys. Rev. E **66**, 046619 (2002).
[48] S. K. Turitsyn, Theor. Math. Phys. (Engl. Transl.) **64**, 797 (1985).
[49] D. Suter and T. Blasberg, Phys. Rev. A **48**, 4583 (1993).
[50] A. W. Snyder and D. J. Mitchell, Science **276**, 1538 (1997).

Observation of violent relaxation and the formation of an analogue galaxy: Supplementary Information

M. Lovisetto[1], M.C. Braidotti[2], R. Prizia[2,3], C. Michel[4],
D. Clamond[1], M. Bellec[4], E.M. Wright[5], B. Marcos[1], D. Faccio[2,3]
[1] *Université Côte d'Azur, CNRS, Laboratoire J.-A. Dieudonné, 06109 - Nice, France*
[2] *School of Physics & Astronomy, University of Glasgow, G12 8QQ Glasgow, UK*
[3] *Institute of Photonics and Quantum Sciences, Heriot-Watt University, EH14 4AS Edinburgh, United Kingdom*
[4] *Université Côte d'Azur, CNRS, INPHYNI, France and*
[5] *Wyant College of Optical Sciences, University of Arizona, Tucson, Arizona 85721, USA*

Supplementary information containing details on both experimental and numerical methods used for this work.

EXPERIMENTAL METHODS

Experiment — The experimental setup is shown in Fig.1. A continuous-wave laser with a Gaussian profile with wavelength $\lambda = 532$ nm is split into 2 components: a reference beam and a target beam. The reference beam is expanded using a 4f-imaging system of lenses and is incident onto a CMOS camera. The target beam is shaped such that its waist is $s = 350$ μm. The waist is calculated by a Gaussian fit of the beam intensity at the sample input plane as the value where the intensity falls of $1/e^2$ - see inset in Fig. 1. The target beam then shines onto three aligned identical slabs of glass (height $D = 5$ mm, width $W = 40$ mm and length $L_0 = 100$ mm each, hence a total length $L = 300$ mm), represented as a single crystal.
The sample is lead-doped glass, having a self-focusing nonlinearity. We report again the material parameters: thermal conductivity $\kappa = 0.7$ Wm^{-1}K^{-1}, background refractive index $n_b = 1.8$, absorption coefficient $\alpha = 1m^{-1}$, thermo-optic coefficient $\beta = \frac{\partial n}{\partial T} = 2.2 \cdot 10^{-5}$ K^{-1} and transmission coefficient at the sample interface $T = 0.92$. We find the value of β by a fit of the experimental beam evolution. With these experimental parameters, we have $z_{\rm nl} \approx 2.7/P$ mm and $\chi = 2.3 \times 10^{-2}/\sqrt{P}$.
As explained in the main text, since it is only possible to measure $\mathcal{E}$ at the end of the sample, in order to explore its value inside the sample we make use of mapping between propagation distance z and power. This mapping holds if the parameter χ is kept constant and therefore it is necessary to vary the width s of the initial condition (see the definition of z_{dyn} and χ in the main paper). However, as shown in the Supplementary Discussion, for sufficiently small values of χ, which is the case in our setup, the experiment is weakly sensitive to a variation of χ. Therefore, we keep s constant when varying P to simplify the experimental procedure.
Data analysis — The experimental intensity profiles are characterized by a background noise - this is removed by

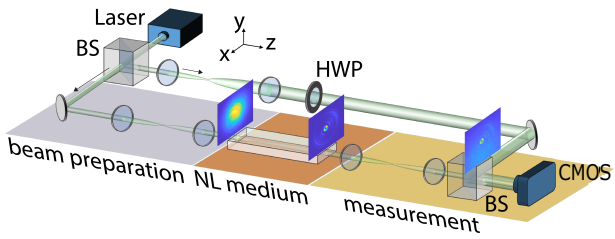

FIG. 1. Experimental setup: a monochromatic laser beam is split into 2 components: a target and a reference beam. The reference beam is expanded using a system of lenses and incident onto a CMOS camera. The target beam is imaged onto the front face of the nonlinear sample through a 4f-imaging system that also allow to choose the input beam waist size. After the nonlinear propagation, the target beam at the output sample face is imaged onto a CMOS camera, where we collect its interference with the reference beam (all beams have the same optical frequency $\lambda = 532$ nm). Half-wave plates ($HWP\lambda/2$) are placed along the beams paths in order to finely tune the beam polarizations in order to have the maximum visibility of the interference fringes. We collect with the CMOS camera the interferograms of the mixed field and the reference. By means of the off-axis digital holography technique [1], we are able to reconstruct the amplitudes and phases of the target beam. Target beam input powers range from $0.2\,W$ to $5.5\,W$, with a $0.25\,W$ step. Top images in the set-up sketch show the experimental intensity profile of the beam at that point in propagation distance: first image from the left is the input beam intensity, then there is the output facet beam profile ($P = 5$ W); last image is the interference of the output target with the reference beam.

averaging out the intensity at pixels that are at the edge of the (x, y) beam profiles; this average is used as an estimate for the background noise and then subtracted from the whole experimental data. We then apply a noise mask, i.e. the intensity points far from the main body of the beam profile are set to zero. On the other hand, the interferograms do not need the noise removal, since the off axis digital holography technique requires a Fourier-transform of the beam which automatically filters all high-frequency contributions from the signal.
z to P mapping — A natural dynamical characteristic length scale $z_{\rm dyn}$ appears in the regime $\chi \ll 1$. This can be calculated writing the corresponding Newton equation of Eq. (2): $n_b k_0 d^2\vec{r}_\perp/dz^2 = k_0 \nabla_\perp \Delta n$, where $\vec{r}_\perp$ is the position in the transverse plane. Using that the typical size $r_\perp \propto s$ and hence $\nabla_\perp \Delta n \propto \Delta n/s$ and the initial velocities $d\vec{r}_\perp/dz \simeq 0$, we get $z_{\rm dyn} = s\sqrt{n_b \kappa/\alpha\beta P}$. This expression allows to map P with z.
Observables — The size of the system is measured using the quantity $R(z) = (P_{y_0})^{-1} \int I(x, y = 0, z)\, |x|\, dx$ with $P_{y_0} = \int I(x, y = 0, z) dx$.

Using the polar symmetry of the beam amplitude, we compute the Wigner transform [6] on the (x, k_x) plane as

$$F(x, k_x, z) = \int dx'\, \mathcal{E}\,(x + x'/2, 0, z)\, \mathcal{E}^*\,(x - x'/2, 0, z)\, e^{ik_x x'}, \tag{1}$$

. where $F(x, k_x, z)$ is a representation of the classical density of probability to find a piece of beam at the position $(x, 0)$ with wavevector $(k_x, 0)$. The distribution of energy density is defined as

$$\nu(\mathcal{U}) = \frac{1}{P} \int d^2 r\, \delta\,[\mathcal{U} - \mathcal{U}(\mathbf{r}, z)]\, I(\mathbf{r}, z), \tag{2}$$

where δ is the Dirac delta function.

NUMERICAL METHODS

Newton–Schrödinger equation

The numerical scheme employed to solve the Newton–Schrödinger equation is a Split-Step algorithm for the propagation along z, combined with a pseudo-spectral method for the integration over the transverse (x, y)-plane. Since in our configuration the boundaries are sufficiently far from the laser beam, we observe a very weak dependence of the simulation results with respect to the boundary conditions used (Fig. 1). Therefore, for simplicity in numerical and analytical calculations, boundary conditions are taken into account by means of the so-called Distribution Loss Model [4], where a degree of non-locality $\sigma = D/2$ is introduced to describe the diffusion of heat in the system. As initial condition for the numerical simulations, we use a fit of the input beam injected into the sample, i.e., the Gaussian field

$$\mathcal{E}_{\rm fit}(x, y, z = 0) \;=\; A\, {\rm e}^{-\frac{(x-x_0)^2+(y-y_0)^2}{2s^2}}\, {\rm e}^{-{\rm i}k_0 \frac{(x-x_0)^2+(y-y_0)^2}{2f}}, \tag{3}$$

where the parameters resulted to be $s = 350\,\mu\mathsf{m}$ and an initial phase $f = -1\,\mathsf{m}$.

Absorption in the material is taken into account introducing an extra term in Eq. (2a) of the main paper:

$${\rm i}\,\frac{\partial \mathcal{E}}{\partial z} \;+\; \frac{1}{2\,k}\,\nabla_\perp{}^2\,\mathcal{E} \;+\; k_0\,\Delta n\,\mathcal{E} \;+\; {\rm i}\,\frac{\alpha}{2}\,\mathcal{E} \;=\; 0, \tag{4}$$

where $\alpha = 1\,\mathsf{m}^{-1}$ for the material used in the experiment. In addition, reflections at the interfaces of the three aligned samples are taken into account introducing a drop in the total intensity by a factor $1 - T$, where $T = 0.92$ is the transmittance at each interface.

N-body method

As explained in the main paper, in the $\hbar/m \to 0$ limit the Newton–Schrödinger equation is equivalent to the classical evolution, given by the Vlasov-Poisson equation. However, the computational cost needed to numerically solve the latter equation is extremely large; for this reason N-Body methods are usually employed [3]. In this case

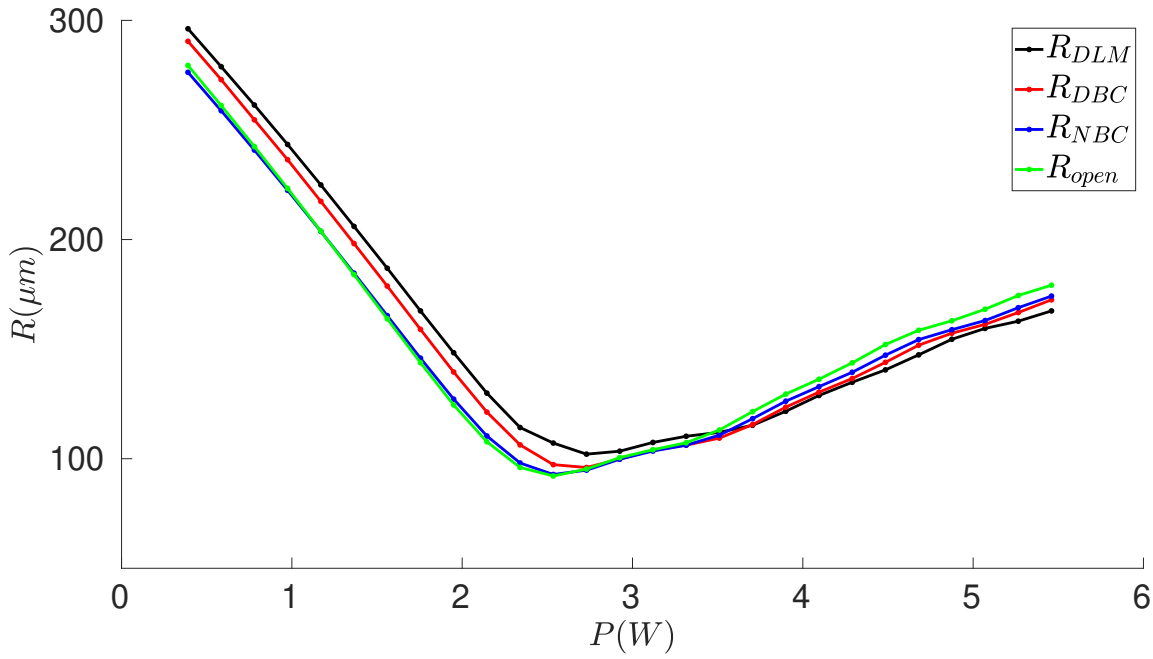

FIG. 2. Comparison between the outputs of the Newton–Schrödinger equation simulation with the Distribution Loss Model (DLM), Dirichlet (DBC), Neumann (NBC) and open boundary conditions (open) for the average size of the beam profile as a function of power at the end of the sample.

the mass distribution function, $f(\boldsymbol{r}, \boldsymbol{v}, t)$ is sampled with a set of N bodies. The sampling procedure is analogue to a Monte-Carlo method. The resulting equations are

$$k \, \frac{d^2 \, \boldsymbol{r}_i}{dz^2} = \frac{\alpha \, \beta \, P}{2 \, \pi \, \kappa \, n_b} \sum_{j=1}^{N} \frac{(\boldsymbol{r}_i - \boldsymbol{r}_j)}{(|\boldsymbol{r}_i - \boldsymbol{r}_j|^2 + \epsilon^2)^{3/2}}, \tag{5}$$

where $\boldsymbol{r}_i = (x_i, y_i)$, P is the power and ϵ is a smoothing parameter. The latter removes the singularities in the potential and suppresses small-scale fluctuations, which are due to the discrete nature of the N-body approach [3]. Notice that, applying the mapping $z \mapsto t$, $k \mapsto m$ and $(\alpha \, \beta \, P)/(2 \, \pi \, \kappa \, n_b) \mapsto G \, m$, (5) corresponds to the classical equation of motion for a system of N self-gravitating particles, all with the same mass $m_i = m$. However, the N bodies must be interpreted as tracers of the phase-space distribution rather than actual particles.

The initial condition is generated performing a Poisson sampling process of the Gaussian appearing (3), while velocities are initialized with the gradient of the initial phase of the complex exponential in (3).

Concerning losses, reflections are taken into account in the same way as in the NSE case, while absorption in the material is introduced multiplying the right hand side of (5) by $\mathrm{e}^{-\alpha \, z}$. The smoothing parameter is set to $\epsilon = 10^{-3} \, s$.

DISCRIMINATION OF THE EVOLUTION OF PHASE SPACE AND DENSITY WITH OR WITHOUT VIOLENT RELAXATION

The mechanism of the mixing process is driven by the existence of a (static) an-harmonic potential. The violent relaxation mechanism, on the other hand, requires the presence of a z-dependence on the potential. In this section, we show that looking at the evolution of the NSE model (which presents phase-space mixing and violent relaxation) and the Snyder–Mitchell model [5] (which presents only phase mixing) leads to different evolutions which gives a strong indication of the existence of violent relaxation in the system. The SM model consists in a Schrödinger equation

coupled with a nonlinear refractive-index profile calculated using the *input* beam profile $\mathcal{E}_0 = \mathcal{E}(\vec{r}_\perp, z = 0)$, namely:

$$\begin{aligned} \mathrm{i}\,\partial_z\,\mathcal{E} \,+\, \frac{1}{2k}\,{\nabla_\perp}^2\,\mathcal{E} \,+\, k_0\,\Delta n\,\mathcal{E} \,=\, 0, \\ {\nabla_\perp}^2\,\Delta n \,=\, -\frac{\alpha\beta}{\kappa}\,I_0, \end{aligned} \tag{6}$$

where $I_0 = |\mathcal{E}_0|^2$.

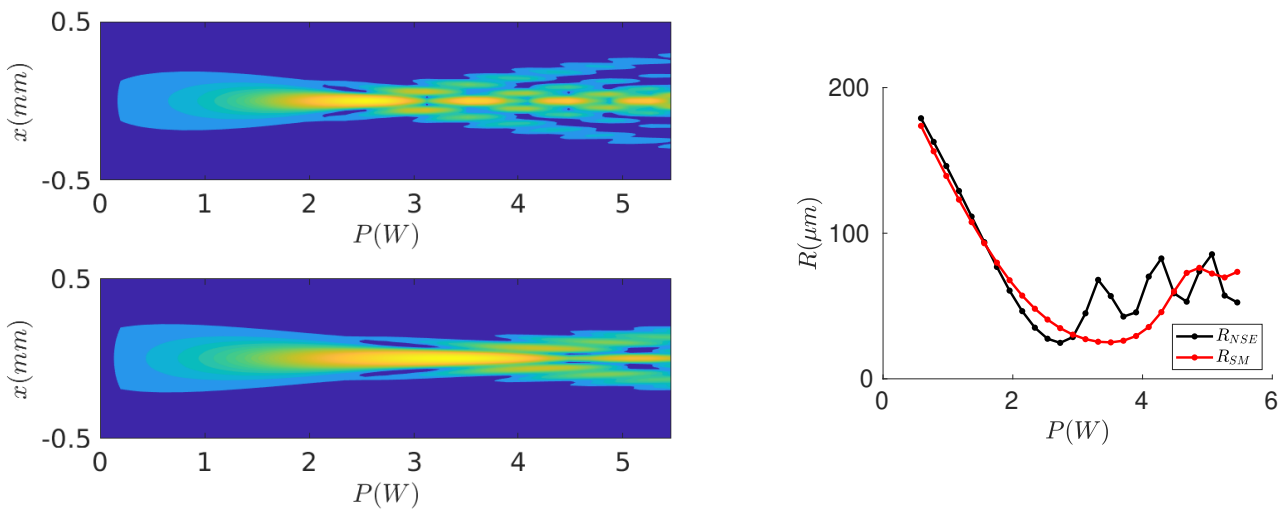

FIG. 3. Left plots: $y = 0$ slice of the beam intensity profile as a function of one transverse coordinate x and power, obtained from the NSE (top left) and SM model (bottom left); both plots are in logarithmic color-scale. Right plot: comparison between the outputs of the NSE simulation (black curve) and SM model (red curve) for the one dimensional average size of the beam profile as a function of power.

The figure 3 shows a quantitative comparison between the NSE and the SM models: the dynamics are qualitatively similar, showing in both cases a collapse followed by nonlinear oscillations. At low power, the difference between the structure of the output intensity profiles is quite small, while after the minimum of the $R(P)$ curve, the dynamics of the two systems start to differ significantly. In particular, one can see for the NSE an oscillating peak surrounded by concentric rings, while for the SM result the rings are less extended and the peak less pronounced (Fig. 4). Indeed, the NSE output intensity profile is in agreement with the one observed in the experiment, as at high power it is characterized by a central oscillating soliton surrounded by the classical solution, whereas the Snyder-Mitchell result is quite different, being more similar to a Fresnel diffraction pattern from a circular aperture.

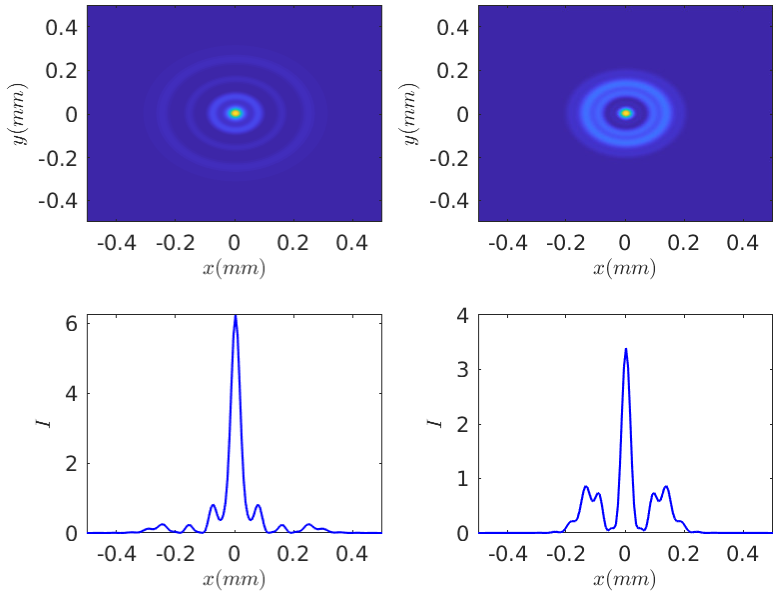

FIG. 4. Left plots: intensity profile predicted by the NSE model as a function of the two transverse spatial coordinates (top left) and $y = 0$ slice (bottom left). Right plots: intensity profile predicted by the SM model as a function of the two transverse spatial coordinates (top right) and $y = 0$ slice (bottom right). All plots are at P=5.5W, as in both cases the central peak is at an absolute maximum at that power.

We arrive at the same conclusions looking at the phase-space dynamics, shown in Fig. 5: at the beginning the two models are very similar, while at high powers, and in particular after the collapse ($P \approx 1.8\,\mathrm{W}$), the NSE model exhibits a more complicated dynamics (akin to the experimental Wigner distribution) compared with SM.

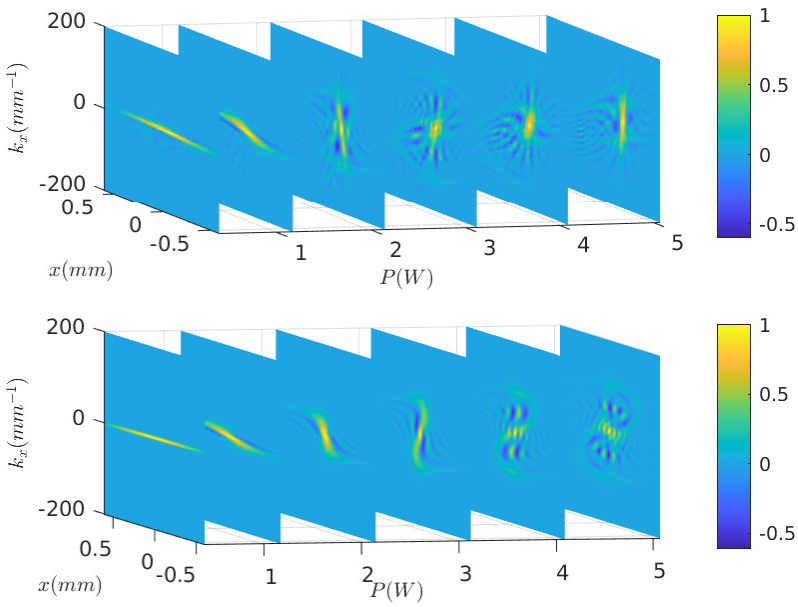

FIG. 5. Results of the NSE simulation (first row) and SM model (second row) for the $y = 0, k_y = 0$ profiles of the Wigner distribution.

These comparisons allow to discriminate the static an-harmonic potential and represent a further confirmation of presence of violent relaxation in the experimental system.

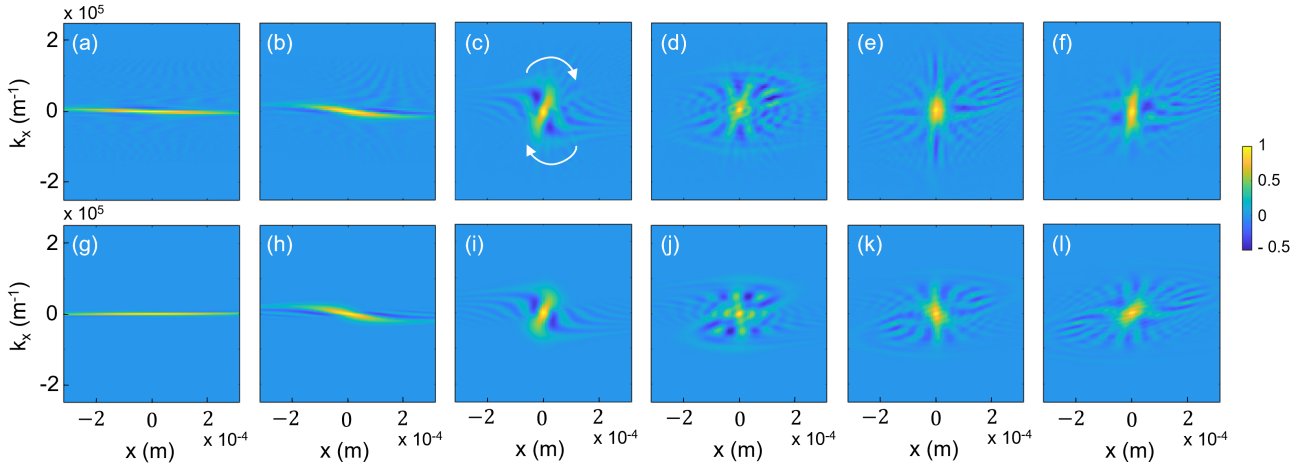

FIG. 6. Results of experiment - top row (a)-(f) - and simulation - bottom row (g)-(l) - for the $y = 0, k_y = 0$ profiles of the Wigner distribution at different powers: (a),(g) $P = 0.2$W, (b),(h) $P = 1$W,(c),(i) $P = 2$W,(d),(j) $P = 3$W,(e),(k) $P = 4$W,(f),(l) $P = 5$W.

Fig. 6 reports a comparison between the experimental and numerical results and see, here again, that they are in a good agreement. At the initial stage, the system has a Gaussian spatial distribution with a very narrow dispersion along the k_x-axis. As P increases, the phase mixing starts by first rolling up the phase-space (indicated by the white arrows) and then forming characteristic filaments [2].

TOTAL ENERGY CONSERVATION IN P

Let us consider the case with no losses, then for propagation described by Eq. (2) the total energy E is conserved as a function of z, where we can define the energy as $E = \int d\mathbf{r}_\perp \mathcal{E}^*(\mathbf{r}_\perp, z) \left[-\frac{\nabla_\perp^2}{2k} - \frac{k_0}{2}\Delta n(\mathbf{r}_\perp, z) \right] \mathcal{E}(\mathbf{r}_\perp, z)$ (see the main manuscript). It is possible to show analytically that the energy E is conserved as function of power P in the semi-classical regime by computing the energy at $z = 0$. Due to the conservation of E in z the same behaviour will be found at $z = L$. Let us consider the field initial condition Eq. (3), where f is the initial beam phase, s the initial waist and $A = \sqrt{P/(\pi s^2)}$ the amplitude, where we have used the fact that the integral over all space of the intensity corresponds to the power P, i.e. $P = \int |\mathcal{E}(r_\perp, z)|^2 dr_\perp = A^2 \pi s^2$. The initial kinetic energy $K(z = 0, P)$ results

$$K(z = 0, P) = \int \frac{|\nabla_\perp \mathcal{E}(r_\perp, z = 0)|^2}{2k} dr_\perp = \frac{\pi A^2}{2k} + \frac{\pi A^2 k_0^2 s^4}{2 f^2 k} = \frac{f^2 + k_0^2 s^4}{2 f^2 k s^2} P. \tag{7}$$

The first term in K corresponds to the quantum pressure, while the second term corresponds to the initial velocities of the modes (or of the particles, analogously). The potential as a function of the radial coordinate is calculated solving Poisson equation in polar coordinates. For simplicity we define $\Delta n(r_\perp, z = 0) \equiv v(r)$. In polar coordinates we have to solve the equation

$$v''(r) + \frac{1}{r} v'(r) = -\frac{\alpha\beta}{\kappa} A^2 e^{-r^2/s^2} \tag{8}$$

whose solution is

$$v(r) = \frac{P\alpha\beta Ei(-r^2/s^2)}{4\pi\kappa} + C_1 \ln(r) + C_2, \tag{9}$$

where $Ei(x) = \int_{-\infty}^{x} dt e^t/t$ is the exponential integral function and we used the fact that $A = \sqrt{P/(\pi s^2)}$. The constant C_1 is set asking that the solution $v(r)$ is regular in $r = 0$. Performing a Taylor series of Eq. (9) about $r = 0$, we get

$$v(r) = \frac{2\ln(r)(P\alpha\beta + 2C_1\pi\kappa) + P\alpha\beta(\gamma_E - 2\ln(s))}{4\pi\kappa} + C_2 + \mathcal{O}(r^2), \tag{10}$$

where γ_E is the gamma Euler constant. In order to cancel the log term in Eq. (11) we must have that $P\alpha\beta+2C_1\pi\kappa = 0$, which fixes C_1. The constant C_2 reflects the Gauge symmetry of the original equation. We choose C_2 in order to include the physical size of the nonlinear medium, such that $v(r = R) = 0$ with $R = D/2$, being the smallest distance between the beam of light and the crystal boundary in the (x, y) plane. In this way $v(r)$ is such that it is zero outside the material as in the Distributed Loss Model used in the numerical simulations (see above). We finally find

$$v(r) = \frac{P\alpha\beta}{4\pi\kappa}\left[Ei(-r^2/s^2) - Ei(-R^2/s^2) + 2\ln(R/r)\right]. \tag{11}$$

The initial potential energy is

$$V(z=0,P) = -\frac{k_0}{2}\int v(r_\perp)|\mathcal{E}(r_\perp, z=0)|^2 dr_\perp = \frac{\alpha\beta k_0(2\ln(s/R) + \ln(2) - \gamma_E + Ei(-R^2/s^2))}{8\pi\kappa}P^2. \tag{12}$$

If the initial phase curvature is negligible ($f \to \infty$) and $\chi \ll 1$, it is easy to show that the energy for the initial condition $E(z = 0, P)$ is mainly proportional to V, being that the initial kinetic energy $K(z = 0, P) \simeq 0$. It results then that for our experimental parameters (in particular $P > 0.5W$) the ratio between K and V is $K/V \simeq 1\%/P$ at $z = 0$. Since E is conserved in z, the same behaviour is expected at $z = L$. We show this numerically in the following. A remark is due at this point. The normalization is crucial for the energy conservation in P. Being that in the semi-classical regime $E(z = 0, P) \propto V(z = 0, P) = \text{constant} * P^2$, the quantity we need to look at is not E but rather E/P^2, which is the energy for the normalized field. Injecting more power in the crystal, the total energy will increase, however, the energy of the normalized field, or analogously, the energy for the unit of mass (the power P is linked to the mass M of the gravitational system), hence, the energy per particle, or per mode, is conserved. To show this, one can look at the numerically computed evolution of the 3 key quantities involved, the kinetic K and potential V energies and total normalized energy E for the case without losses. Figure 7 below shows that the normalized E is indeed conserved in P, being the variation of 1% maximum in the considered range of powers for the initial condition at $z = 0$ (see red dashed line). As expected, the variation of the normalized energy for $z = L$ replicates the trend observed for at $z = 0$ (blue continuous line). There is a remarkable agreement also with the analytical calculation, (see yellow line in Fig. 7(a-b)). The slight offset in panel (a) is due to the non-perfect overlap between the DLM model and the analytical calculation. This is due to the fact that in the DLM model the boundary is included as a distributed loss term in the temperature equation. In the analytical calculation instead, the heat equation is solved exactly and the boundary is set as a condition on C_2, setting a reference of the energy. This difference in the way of including the boundary condition appears as an offset in comparison to the DLM model, despite not affecting the energy trend. This shows that the DLM model - despite not being analytically solvable - is a valuable tool for simulating fields propagation in nonlinear media.[4].

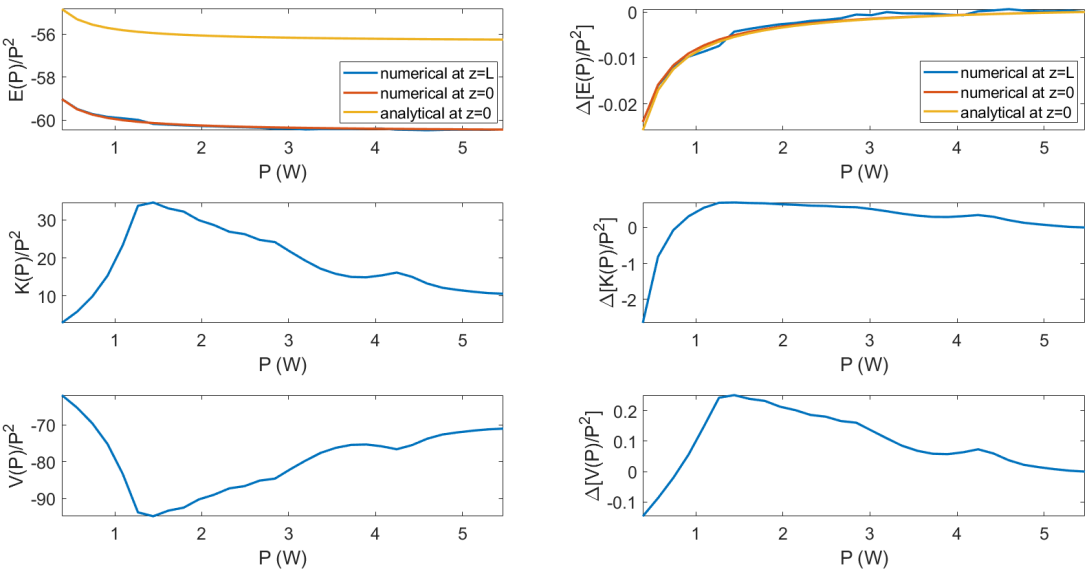

FIG. 7. Simulation of the normalized total energy (a), normalized total kinetic (c) and potential energy (e) as function of power. E, K, P are numerically calculated at $z = L$ (blue continuous line) and at $z = 0$ (red dashed line) and (a). Yellow line shows the analytical calculation (see Eqs. (7-12)). Variation of the normalized total energy (b), kinetic (d) and potential (f) energies as function of power at $z = L$ (blue continuous line) and at $z = 0$ (red dashed line) (b) and analytically calculated at z=0 (yellow line). The variation is calculated as $\Delta\left[E/P^2\right] = \frac{E(P_{max})/P_{max}^2 - E(P)/P^2}{E(P)/P^2}$.

FINITE χ EFFECTS IN THE EVOLUTION OF THE ENERGY DISTRIBUTION

We determine the importance of finite χ effects in the evolution of the energy distribution, performing simulations with different values of χ, without dissipation and reflections. We plot the evolution of the energy distribution in Fig. 8, for different values of z, expressed in units of $z_{\rm dyn}$. In the experiment $z_{\rm dyn} = 6.2\,cm$ for $P \approx 1.77\,W$ (see Tab. I). For values $z \lesssim 3\,z_{\rm dyn}$ we observe a weak finite χ effect, for all values simulated. For $z \gtrsim 3\,z_{\rm dyn}$ we observe a convergence for the smallest values of χ, which coincides with the corresponding values of χ used in the experiment. We can conclude that the experiment χ is sufficiently small in order to have little incidence on the change of the energy distribution compared with violent relaxation.

$z/z_{\rm dyn}$	P	χ
1.20	0.11	0.0680
1.84	0.26	0.0442
2.40	0.44	0.0340
3.02	0.70	0.0269
3.61	1.00	0.0225
4.81	1.77	0.0169
7.21	3.98	0.0113
8.32	5.30	0.0098

TABLE I. Values of z corresponding at the power P in the experiment with its associated value of χ.

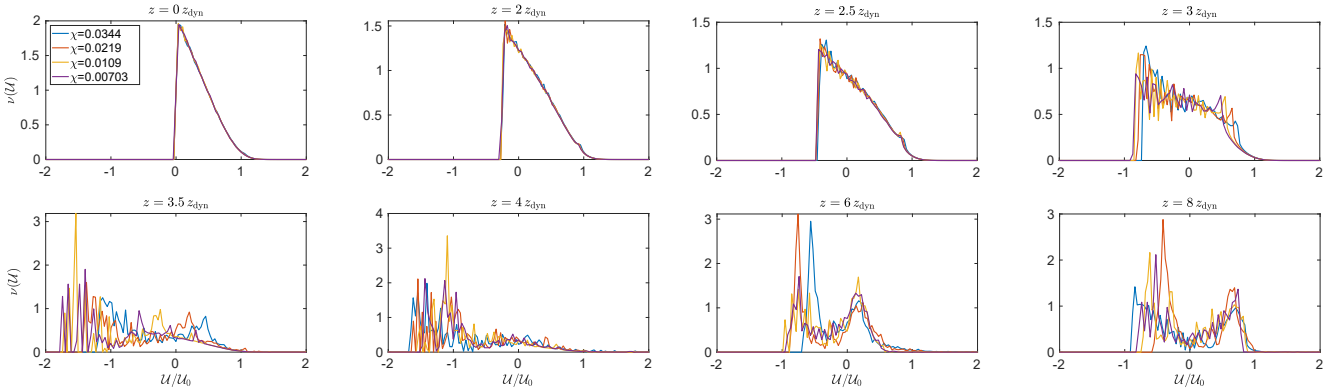

FIG. 8. Simulation of the evolution of the energy distribution for different values of the power χ. The energy axis is in units of $\mathcal{U}_0 = (\alpha\beta k_0 P)\,/\,(2\pi\kappa)$.

EFFECT OF LOSSES

In the absence of losses and in the limit $\chi \to 0$ the mapping between P and z used in the paper is perfect and the only mechanism responsible to the evolution of the energy distribution is violent relaxation. We have shown above that finite χ effects are small. We study here the relevance of losses.

First we investigate the effect of losses in the mapping between P and z. In Fig. (a)-(c) we show the difference in the evolution of the intensity $I = |\mathcal{E}|^2$ between studying the dynamics in z (which corresponds to the original system) or in terms of the power (which is the way according to which the experiment has been performed, as it is impossible to measure the amplitude of the beam inside the material). Specifically, in Fig. (a) we show the evolution of the beam intensity profile $I(x, y = 0, z; P = 5.5\,W)$ as a function of the propagation coordinate $z/z_{\rm dyn}$, at fixed power, obtained from a simulation without losses. In Fig. (c) on the other hand, we show the evolution of intensity profile $I(x, y = 0, z = L = 30\,cm; P)$, obtained from a simulation with losses, varying the power, and expressing the propagation coordinated as $L/z_{\rm dyn}$. The latter reproduces the experimental configuration. In both simulations we observe the same qualitative behaviour. In Fig. (b) we show the evolution of the transverse size of the system $R(z)$ for the same simulations presented in (a) and (c): without losses (blue curve) and with losses (black curve). The main difference is that the black curve collapses later compared with the blue one. This is due to the presence of losses, which slow-down the dynamics. For the same reason, the average beam size obtained varying the power at constant z, is shown to be slightly larger, compared to the blue curve. Despite these differences, the undergoing physics remains the same.

We investigate now the effect of losses in the evolution of the energy distribution after the collapse. In Fig. (d) we show the evolution of the energy distribution, obtained from numerical simulations, from the lowest power to the largest one. The orange curve corresponds to the experimental configuration, with losses. The yellow curve correspond to a simulation without losses. In order to have both curves corresponding to the same output intensity, the yellow one is multiplied by a factor $T^5 e^{-\alpha L}$, which take into account the losses. We observe that the difference form the initial energy distribution is much larger than the differences between these curves, which allows to conclude that the effect of violent relaxation dominates over losses in the evolution of the energy distribution.

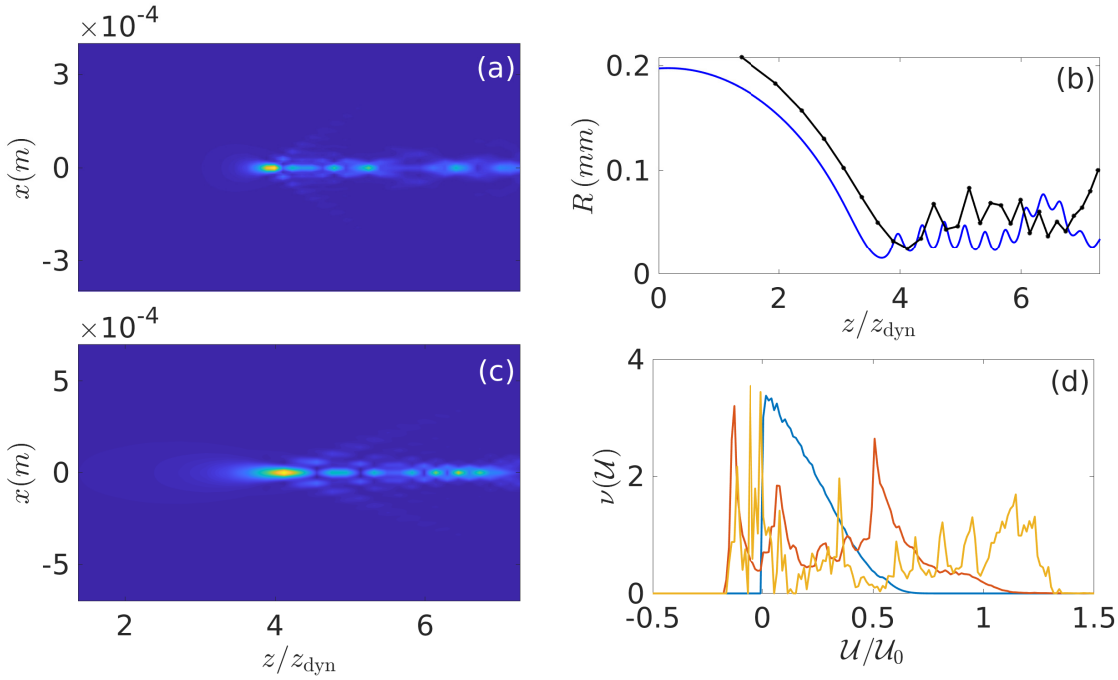

FIG. 9. (a): evolution of the intensity profile $I(x, y = 0, z; P = 5.5\,W)$ for a simulation without losses. (b): Evolution of the transverse size of the beam $R(z)$ without losses (blue curve) and with losses (black curve). (c): evolution of the intensity profile $I(x, y = 0, z = 30\,cm; P)$ for a simulation with losses, with P expressed in terms of $z/z_{\rm dyn}$ (see text). (d): evolution of the energy distribution from the initial condition (blue curve) to the largest power, with losses (orange curve) and without losses (yellow curve).

[1] Jacopo Bertolotti. Off-Axis Digital Holography Tutorial. `https://jacopobertolotti.com/tutorials.html`.
[2] James Binney and Scott Tremaine. Galactic Dynamics: Second Edition. Princeton University Press, 2008.
[3] Roger W Hockney and James W Eastwood. Computer simulation using particles. CRC Press, 2021.
[4] Thomas Roger, Calum Maitland, Kali Wilson, Niclas Westerberg, David Vocke, Ewan M Wright, and Daniele Faccio. Optical analogues of the newton–schrödinger equation and boson star evolution. Nature communications, 7(1):1–8, 2016.
[5] Allan W Snyder and D John Mitchell. Accessible solitons. Science, 276(5318):1538–1541, 1997.
[6] Eugene P Wigner. On the quantum correction for thermodynamic equilibrium. In Physical Chemistry, Solid State Physics, pages 110–120. Springer, 1997.

Integrating factor techniques applied to the Schrödinger-like equations. Comparison with Split-Step methods.

Martino Lovisetto, Didier Clamond and Bruno Marcos

Université Côte d'Azur, CNRS UMR 7351, LJAD, Parc Valrose, 06108 Nice cedex 2, France.

Abstract

The nonlinear Schrödinger and the Schrödinger–Newton equations model many phenomena in various fields. Here, we perform an extensive numerical comparison between splitting methods (often employed to numerically solve these equations) and the integrating factor technique, also called Lawson method. Indeed, the latter is known to perform very well for the nonlinear Schrödinger equation, but has not been thoroughly investigated for the Schrödinger–Newton equation. Comparisons are made in one and two spatial dimensions, exploring different boundary conditions and parameters values. We show that for the short range potential of the nonlinear Schrödinger equation, the integrating factor technique performs better than splitting algorithms, while, for the long range potential of the Schrödinger–Newton equation, it depends on the particular system considered.

1. Introduction

The nonlinear Schrödinger and the Schrödinger–Newton (also called Schrödinger–Poisson) equations describe a large number of phenomena in different physical domains. These equations are nonlinear variants of the Schrödinger one, which, in non-dimensional units, reads

$$\mathrm{i}\,\partial_t\,\psi \;+\; \tfrac{1}{2}\,\nabla^2\psi \;-\; V\,\psi \;=\; 0, \tag{1}$$

where ψ is a function of space and time, ∇^2 is the Laplace operator and V is a function of ψ, space and time.

For the nonlinear Schrödinger equation (hereafter NLS), the *local nonlinear* potential is

$$V \;=\; g\,|\psi|^2, \tag{2}$$

where g is a coupling constant. For $g > 0$ the interaction is repulsive, while it is attractive for $g < 0$. The NLS equation describes various physical phenomena, such as Bose–Einstein condensates [1], laser beams in some nonlinear optical media [2], water wave packets [3], etc.

In the case of the Schrödinger–Newton (SN) equation, the potential is given by the Poisson equation

$$\nabla^2\,V \;=\; g\,|\psi|^2, \tag{3}$$

where g is a coupling constant, the interaction being attractive if $g > 0$ and repulsive if $g < 0$. It is therefore *nonlinear* and *nonlocal*, giving rise to collective phenomena [4], appearing for instance in optics [5, 6, 7], Bose–Einstein condensates [8], astrophysics and cosmology [9, 10, 11] and theories describing the quantum collapse of the wave function [12, 13]. It is

also used as a numerical model to perform cosmological simulations in the semi-classical limit [14].

The SN equation takes a slightly different form when applied in cosmology [15]. Here, due to the expansion of the universe, the Poisson equation is modified [16] as

$$\nabla^2 V \;=\; a^{-1}\, g\left(|\psi|^2 - 1\right), \tag{4}$$

where $a(t)$ is a scaling factor. The modification of the Poisson equation (4) ensures that the potential is finite in an infinite universe.

These NLS and SN equations are special cases of the Gross–Pitaevskii–Poisson (GPP) equation

$$\mathrm{i}\,\partial_t\,\psi \;+\; \tfrac{1}{2}\,\nabla^2\,\psi \;-\; V_1\,\psi \;-\; V_2\,\psi \;=\; 0, \qquad \nabla^2 V_1 \;=\; g_1\,|\,\psi\,|^2, \qquad V_2 \;=\; g_2\,|\,\psi\,|^2. \tag{5}$$

This equation appears in many fields, such as optics [17, 18], Bose-Einstein condensates [19] and cosmology (to simulate scalar field dark matter) [20, 21, 22].

In order to solve the above equations, except for very special cases, numerical methods must be used. Two families of temporal numerical schemes are commonly used to solve the Schrödinger equation with a nonlinear potential: the integrating factor technique (generally attached with a Runge–Kutta scheme) and the Split-Step method. In this paper, we present an extensive comparison between integrating factor methods and splitting algorithms, considering both accuracy and computational speed. Comparisons are made exploring different types of boundary conditions, in one and two spatial dimensions, with parameters ranging in values close to many regimes of physical interest. The main reason for choosing these methods is that, in the literature, Split-Step solvers are commonly used to integrate both the SN and the NLS equations, while the integrating factor has been applied to integrate the NLS with very performing results [23, 24]. A natural question, which is also the main motivation of this work, is how the integrating factor technique performs when considering the long range interactions of the SN system instead of short range ones of the NLS. We show that the integrating factor performs better than splitting algorithms for local interactions (such as the NLS). When a long range interaction (such as the one appearing in the SN equation) is considered, the relative performance between the integrating factor and splitting algorithms depends on the system.

The paper is organized as follows. In section 2, the methods of numerical time integration are described. Section 3 concerns detailed comparisons between Split-Step integrators (order 2, 4 and 6 with fixed time-step and order 4 with adaptive time-step) and standard algorithms with adaptive time-step belonging to the Runge–Kutta family [25, 26, 27] together with the integrating factor technique. Conclusions are drawn in section 4.

2. Numerical algorithms

In this section, we describe the different numerical methods used for the temporal resolution of the equations considered in the paper. First, we outline the integrating factor technique attached with an adaptive embedded scheme of arbitrary order. Then, we describe the Split-Step algorithm, with both fixed and adaptive time-step.

Spatial resolution are performed with pseudo-spectral methods. In particular, we rely on methods based on fast Fourier transform (FFT) due to their efficiency and accuracy [28].

2.1. Integrating Factor

The integrating factor method can be applied to any differential equation of the form

$$\mathrm{i}\,\partial_t\,\psi \;=\; F(\boldsymbol{r},t,\psi)\,, \qquad \psi \;=\; \psi(\boldsymbol{r},t)\,, \tag{6}$$

where the right-hand side can be split into linear and nonlinear parts. This results in

$$\mathrm{i}\,\partial_t\,\psi \;+\; \mathcal{L}\,\psi \;=\; \mathcal{N}(\boldsymbol{r},t,\psi)\,, \tag{7}$$

where $\mathcal{L}$ is an easily computable (generally autonomous) linear operator and $\mathcal{N} \stackrel{\text{def}}{=} F + \mathcal{L}\psi$ is the remaining (usually) nonlinear part. At the n-th time-step, with $t \in [t_n, t_{n+1}]$, the change of dependent variable

$$\phi \;\stackrel{\text{def}}{=}\; \exp[\,(t-t_n)\,\mathcal{L}\,]\,\psi \qquad \Longrightarrow \qquad \mathrm{i}\,\partial_t\,\psi \;=\; \exp[\,(t_n-t)\,\mathcal{L}\,]\,(\,\mathrm{i}\,\partial_t\,\phi \,-\, \mathcal{L}\,\phi\,)\,, \tag{8}$$

yields the equation

$$\mathrm{i}\,\partial_t\,\phi \;=\; \exp[\,(t-t_n)\,\mathcal{L}\,]\,\mathcal{N}. \tag{9}$$

Note that this change of variable is such that $\phi = \psi$ at $t = t_n$. If the operator $\mathcal{L}$ is well chosen, the stiffness of (7) is considerably reduced and, for $t \in [t_n; t_{n+1}]$, the equation (9) can usually be well approximated by algebraic polynomials. Thus, standard time-stepping methods can efficiently solve (9). Here, we focus on adaptive Runge–Kutta methods [27, 29].

As explained in [30], it is possible to further improve and optimize the integrating factor method. The details of this improved version of the integrating factor technique are illustrated in Appendix A. We perform our numerical tests using this optimized version of the integrating factor technique, which hereafter is denoted as IFC.

2.1.1. Application to the Schrödinger equation

It is straightforward to apply these methods to the Schrödinger equation (1). Specifically, for the SN and NLS equations, the Laplacian term is a linear operator while the potential V is a nonlinear operator. Switching to Fourier space in position, the equation becomes

$$\mathrm{i}\,\partial_t\,\widehat{\psi} \;-\; \tfrac{1}{2}\,k^2\,\widehat{\psi} \;-\; \widehat{V\psi} \;=\; 0, \tag{10}$$

where "hats" denote Fourier transforms of the underneath quantity and $k \stackrel{\text{def}}{=} |\boldsymbol{k}|$ is the wavenumber. Therefore, the system is now in a form where the application of the integrating factor technique is straightforward. With the change of variable $\phi(\boldsymbol{k},t) = \widehat{\psi}(\boldsymbol{k},t)\,\mathrm{e}^{\mathrm{i}k^2(t-t_0)/2}$, one obtains

$$\partial_t\,\phi \;=\; -\mathrm{i}\,\mathrm{e}^{\mathrm{i}k^2(t-t_0)/2}\,\widehat{V\psi}\,. \tag{11}$$

In order to perform our numerical tests, we use the Dormand and Prince 5(4) [25] and Tsitouras 5(4) [26] integrators. Both schemes are Runge–Kutta pairs of order 5(4). However, we observe a speed difference between these solvers of maximum 10%, depending on the simulated system. For this reason, we choose for each case the fastest of the two: specifically for NLS and the periodical SN equations we use the Dormand and Prince scheme, while in all the other cases we rely on Tsitouras' one. The higher-order Fehlberg 7(8) integrator [27] is also used as *reference solutions* for accuracy comparisons (see section 3.1).

2.2. Split-Step methods

The Split-Step method [31] performs the temporal resolution of the Schrödinger equation separating the linear terms from the nonlinear ones, in a different manner compared with the integrating factor. Writing the equation as

$$\mathrm{i}\,\partial_t\,\psi \;=\; H\,\psi, \tag{12}$$

$H = \frac{1}{2}\nabla^2 + V$ being the Hamiltonian operator, the formal solution is

$$\psi(\boldsymbol{r},t) \;=\; \exp\!\left(-\mathrm{i}\int_{t_n}^{t} H\,\mathrm{d}t\right)\psi(\boldsymbol{r},t_n), \qquad t\in[t_n;t_{n+1}]. \tag{13}$$

Except for very few cases, the result of the operator $\exp(-\mathrm{i}H(t-t_n))$ applied to $\psi(\boldsymbol{r},t_n)$ is unknown. Nevertheless, for $t\in[t_n;t_{n+1}]$, it is possible to approximate $\exp(-\mathrm{i}H(t-t_n))$ as a product of exponentials, each one involving either the potential or the Laplacian term, with appropriate coefficients. For example, the approximation corresponding to the Split-Step method of order 2 is

$$\mathrm{e}^{-\int_{t_n}^{t}\mathrm{i}H\,\mathrm{d}t} \;=\; \mathrm{e}^{-\mathrm{i}K(t-t_n)/2}\,\mathrm{e}^{-\int_{t_n}^{t}\mathrm{i}V\,\mathrm{d}t}\,\mathrm{e}^{-\mathrm{i}K(t-t_n)/2} \;+\; O\left((t-t_n)^2\right), \tag{14}$$

where $K = \frac{1}{2}\nabla^2$.

At higher orders, the approximation of the operator $\exp(-\mathrm{i}H(t-t_n))$ is known as Suzuki-Trotter expansion [32]. It is generally more complicated than (14) and not unique, which can be determined with the Baker–Campbell–Hausdorff formula [33]. For our numerical tests, we consider the Split-Step of orders 2, 4 and 6, whose pseudo-codes are listed in Appendix B.

It is possible to design an adaptive time-step scheme with Split-Step methods. Here, we consider an adaptive embedded splitting pair [34] of order 4(3). This algorithm is characterized by a fourth-order splitting solver derived by Blanes and Moan [35] embedded with third order scheme constructed by Thalhammer and Abhau [34, 36]. The pseudo-code for this algorithm, hereafter denoted "SSa", is described in Appendix B.

3. Numerical comparison of the different time-integrators

In this section, we compare the efficiencies of the methods previously described. The comparisons focus on speed and accuracy of each algorithm, simulating systems with different potentials, boundary conditions and physical regimes. First, we outline the different estimators employed to determine the accuracy of each numerical integrator. Then, we list and summarize the results for every equations considered, in one and two spatial dimensions. We start with the NLS equation which is used as benchmark, since an analytical solution is known in the one dimensional case. Then we switch to the SN equation with both open and periodic boundary conditions. Finally, we present the results for the two dimensional Gross–Pitaevskii–Poisson equation, which can be considered as a hybrid version of the SN and NLS systems.

3.1. Estimators of the accuracy of the time-integration algorithms

The accuracy of each time-integration algorithm is estimated looking at three different indicators:

1. The energy conservation. The energy E is a constant of motion for the Schrödinger equation. For the NLS and SN equations, it is defined as

$$E = \frac{1}{2} \int \mathrm{d}\boldsymbol{r}\, \psi^* \left(-\nabla^2 + V\right) \psi. \tag{15}$$

Using the initial energy as reference, the error on the energy conservation is

$$\Delta E_i = \left| \frac{E(t_i)}{E(t_0)} - 1 \right|, \tag{16}$$

where t_0 is the initial time and t_i denotes the i-th time-step of the numerical integration. This error being (in general) time-dependent, we consider the error

$$\overline{\Delta E} = \max_i \left[\Delta E_i\right], \tag{17}$$

the latter being the maximal difference with respect to the initial value, during the whole simulation.

2. Another constant of motion for the considered equation, is the mass,

$$M = \int \mathrm{d}\boldsymbol{r}\, |\psi|^2. \tag{18}$$

This quantity is automatically conserved with machine precision when using splitting algorithms, while it is not in general the case with the integrating factor. For this reason, when the latter technique is employed, we impose mass conservation at each time-step, multiplying the solution ψ by $M_0 / \int \mathrm{d}\boldsymbol{r}\, |\psi|^2$, where M_0 is the initial mass.

3. The error on the solution performing time reversion tests. This quantity is obtained running a simulation up to a given time t_{fin}, then reversing the time and evolving back to the initial instant. The error is monitored using the L_∞-norm of the difference between the solution at the initial time, at beginning of the simulation and at the end of it. Denoting the "backward" solution by $\Delta\psi_{\mathrm{rev}}$, one has

$$\Delta\psi_{\mathrm{rev}} = \max_i \left(\left| \psi(x_i, t_0) - \psi_{\mathrm{backward}}(x_i, t_0) \right| \right). \tag{19}$$

4. The two estimators above favorize *a priori* time-splitting algorithms because they are symplectic and reversible, whereas the integrating factor is not. For this reason, we also compare the result of the simulations with a "reference one", very accurate, using an adaptive Fehlberg integrator of order 7 embedded within an order 8 scheme, with a very small tolerance, tol = 10^{-14}. Defining this estimator as $\Delta\psi_{\mathrm{ref}}$, one has

$$\Delta\psi_{\mathrm{ref}} = \max_i \left(\left| \psi(x_i, t_f) - \psi_{\mathrm{F7(8)}}(x_i, t_{\mathrm{fin}}) \right| \right), \tag{20}$$

where ψ is the numerical solution provided by the particular method considered and $\psi_{\mathrm{F7(8)}}$ is the one outputted by the Fehlberg 7(8) integrator.

3.2. 1D nonlinear Schrödinger equation

We first consider the case of the one dimensional NLS

$$\mathrm{i}\frac{\partial \psi}{\partial t} + \frac{1}{2}\frac{\partial^2 \psi}{\partial x^2} + |\psi|^2 \psi = 0, \tag{21}$$

Method	Δt	$\overline{\Delta E}$	$\Delta\psi_{\rm rev}$	$\Delta\psi_{\rm ref}$	$T(s)$
SS2	10^{-3}	$7.5\cdot10^{-13}$	$6.3\cdot10^{-10}$	$1.1\cdot10^{-4}$	86.7
SS4	$5\cdot10^{-3}$	10^{-15}	$8.2\cdot10^{-10}$	$5.8\cdot10^{-7}$	38.1
SS6	$2\cdot10^{-2}$	10^{-15}	$2.0\cdot10^{-10}$	$3.7\cdot10^{-9}$	29.3
SSa, tol = 10^{-6}	$2.1\cdot10^{-2}$	$1.6\cdot10^{-12}$	$3.5\cdot10^{-10}$	$6.5\cdot10^{-10}$	34.0
IFC, tol = 10^{-9}	$2.1\cdot10^{-2}$	10^{-15}	$1.2\cdot10^{-9}$	$7.8\cdot10^{-10}$	14.5

Table 1: Comparison for the 1D NLS equation between the IFC method and the Split-Step solvers. T is the total time required to run each simulation, measured in seconds. The Δt for adaptive algorithms is the averaged one.

which admits a simple analytical solution

$$\psi(x,t) \;=\; \sqrt{2}\,\mathrm{sech}\left(\sqrt{2}\,x\right)\exp(\mathrm{i}\,t). \tag{22}$$

We present a set of simulations in order to compare the Split-Step integrators with the IFC, looking at the energy conservation error, the error on the solution and the total time needed to run each simulation. In these simulations, the space is discretized with $N = 2048$ points, in a domain of length $L = 80$ and the analytical solution at $t = 0$ is used as initial condition. The results are summarized in table (1). We observe that the IFC solver is the fastest one by at least a factor 2, presenting at the same time the best results to all the indicators: it uses a larger time-step, presents equal or better energy conservation, returns only a slightly worse $\Delta\psi_{\rm rev}$ and it is one of the best comparing to the reference simulation.

3.3. 1D Schrödinger–Newton equation

We now focus on the SN system, starting from the case of a single spatial dimension,

$$\mathrm{i}\,\frac{\partial\,\psi}{\partial t} \;+\; \frac{1}{2}\,\frac{\partial^2\,\psi}{\partial x^2} \;-\; V\,\psi \;=\; 0, \qquad \frac{\partial^2\,V}{\partial x^2} \;=\; g\,|\psi|^2\,. \tag{23}$$

The solutions of (23) depend on the initial condition and on the single parameter g. The chosen initial condition is $\psi(x,t=0) = \exp(-x^2/2)/\sqrt[4]{\pi}$. The potential V is calculated using Hockney's method [37]. We perform a set of tests with different values of the parameter g, corresponding to different physical regimes. The case $g = 10$ corresponds to a system in the quantum regime, i.e., with an associated De Broglie wavelength of the order of the size of the system, while $g = 500$ corresponds to a system closer to the semi-classical regime, with an associated De Broglie wavelength about 20 times smaller than the size of the system. The typical evolution of this system is characterized by the initial condition which oscillates, exhibiting a complex dynamics. This is particularly visible in the semi-classical regime, in which high frequency oscillations appear in the wavefunction, as shown in Fig. 1. The simulation is run in a domain of length $L = 80$, discretized into $N = 2048$ points in the $g = 10$ case, while for $g = 500$ we set $L = 20$ and $N = 2048$. The characteristic time of dynamics is defined as $t_{\rm dyn} = |g|^{-1/2}$. In table (2), we compare the Split-Step integrators with the IFC, looking at the energy conservation error, the error on the solution and the total time needed to run each simulation. Here, splitting methods proved to be faster than the integrating factor. In addition, the SS4 and SS6 performed better than the adaptive integrators. This is due the fact

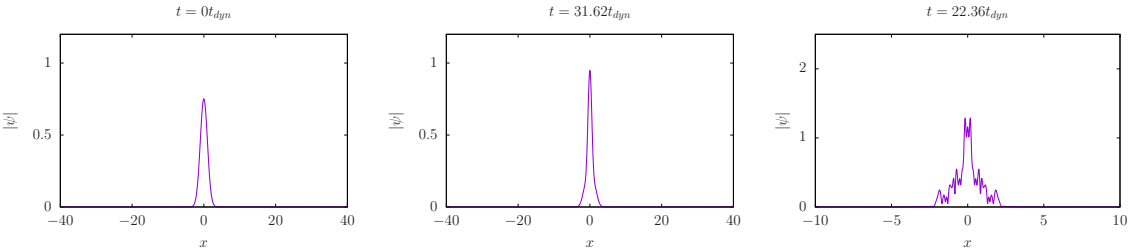

Figure 1: Snapshots of the modulus of the solution of the 1D SN equation $|\psi|$. The left plot is the initial condition, center plot and right plot correspond to the solution at the end of the simulation for $g = 10$ and $g = 500$ respectively.

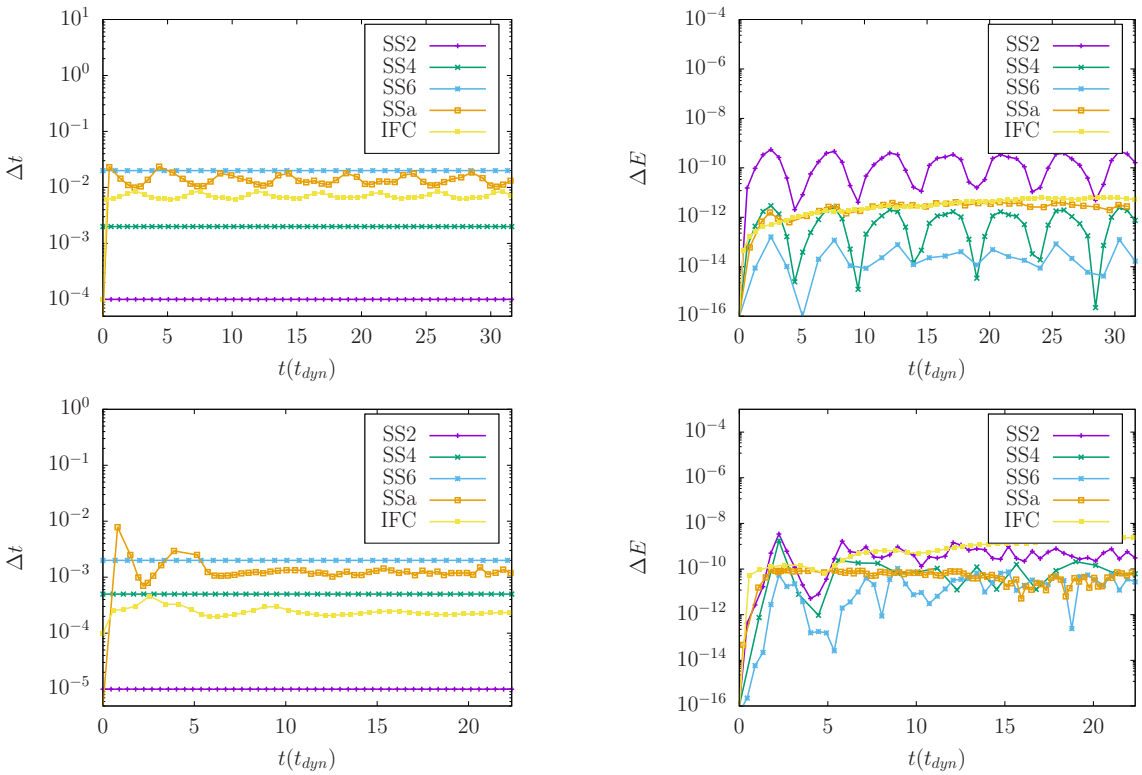

Figure 2: Comparison for the 1D SN equation between the time-step and the error on the energy conservation for the IFC method and the Split-Step solvers for both the cases $g = 10$ (upper plots) and $g = 500$ (lower plots).

g	Method	$\Delta t/t_{\rm dyn}$	$\overline{\Delta E}$	$\Delta\psi_{\rm rev}$	$\Delta\psi_{\rm ref}$	$T(s)$
10	SS2	$3.1\cdot10^{-4}$	$5.5\cdot10^{-10}$	$4.5\cdot10^{-11}$	$4.5\cdot10^{-9}$	123.3
	SS4	$6.3\cdot10^{-3}$	$2.9\cdot10^{-12}$	$2.5\cdot10^{-12}$	$5.5\cdot10^{-11}$	11.1
	SS6	$6.3\cdot10^{-2}$	$1.5\cdot10^{-13}$	$4.0\cdot10^{-12}$	$1.1\cdot10^{-11}$	3.5
	SSa	$4.3\cdot10^{-2}$	$4.2\cdot10^{-12}$	$8.5\cdot10^{-11}$	$5.9\cdot10^{-11}$	6.4
	IFC	$2.2\cdot10^{-2}$	$1.8\cdot10^{-12}$	$1.3\cdot10^{-10}$	$3.3\cdot10^{-11}$	5.0
500	SS2	10^{-5}	$6.0\cdot10^{-9}$	$1.1\cdot10^{-10}$	$5.2\cdot10^{-8}$	120.0
	SS4	$5\cdot10^{-4}$	$2.5\cdot10^{-9}$	$4.9\cdot10^{-12}$	$1.3\cdot10^{-7}$	5.4
	SS6	$2\cdot10^{-3}$	$1.8\cdot10^{-10}$	$2.8\cdot10^{-11}$	$7.6\cdot10^{-8}$	3.5
	SSa	$3.2\cdot10^{-2}$	$1.0\cdot10^{-10}$	$6.4\cdot10^{-8}$	$2.9\cdot10^{-8}$	6.7
	IFC	$5.4\cdot10^{-3}$	$1.8\cdot10^{-9}$	$2.3\cdot10^{-8}$	$1.5\cdot10^{-8}$	11.9

Table 2: Comparison for the 1D SN equation between the IFC method and the Split-Step solvers. The SSa simulations and IFC have been performed with a tolerance tol = 10^{-7} and tol = 10^{-10} respectively for $g = 10$ and tol = 10^{-6} and tol = 10^{-10} respectively for $g = 500$. The Δt for adaptive algorithms is the averaged one. T is the total time required to run each simulation, measured in seconds.

that, for this particular system, the extra computational cost due to the implementation of the adaptive-step is not fully compensated by the time-gain in terms of computational speed. Indeed, splitting algorithms with fixed time-step require a smaller number of computational operations to be implemented. For this reason, here, choosing a "proper" fixed time-step still results in a slightly faster numerical integration compared to an adaptive scheme.

3.3.1. Periodical case

We now switch to another version of the SN system, which has important applications in cosmology in order to simulate the formation of large-scale structures in the universe (4). We take $a = 1$, which in cosmology corresponds to the case of a static universe [38]; we do not expect modifications of our conclusions for different cosmological models. In one dimension the equations read

$$\mathrm{i}\,\frac{\partial\psi}{\partial t} + \frac{1}{2}\frac{\partial^2\psi}{\partial x^2} - V\psi = 0, \tag{24a}$$

$$\frac{\partial^2 V}{\partial x^2} = g\,(|\psi|^2 - 1), \tag{24b}$$

where the wavefunction $|\psi|^2$ is normalized to unity. The potential V is obtained calculating the inverse of the Laplacian in Fourier space and transforming back the result to real space. We take "cold" initial conditions (see [39, 40]), namely,

$$\psi(x, t = 0) = \sqrt{\rho_0 + \delta\rho(x)}\,\exp(\mathrm{i}\theta(x)), \tag{25}$$

where θ is a function whose gradient is proportional to the initial velocity field (set to zero for simplicity), ρ_0 is the background constant density and $\delta\rho(x)$ is the density fluctuations,

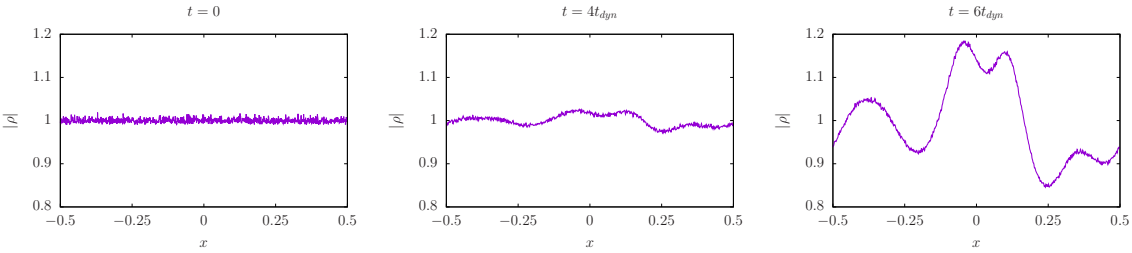

Figure 3: Snapshots of the modulus squared of the solution of the 1D SN equation (periodical case) $|\psi|^2$.

generated as

$$\delta\rho(x) \;=\; \mathcal{F}^{-1}\Big[\, R(k)\sqrt{P(k)}\,\Big], \tag{26}$$

where $R(k)$ is a Gaussian random field, with zero average and unity variance. The function $P(k)$ is called *Power Spectrum*, and it is defined as

$$P(k) \;=\; \frac{1}{L^d}\,\big|\,\widehat{\delta\rho}(k)\,\big|^2, \tag{27}$$

corresponding to the initial density fluctuations one wants to generate. The initial conditions are numerically initialized applying an additional filter $F(k)$ in Fourier space with the aim of setting to zero all the modes corresponding to a space scale comparable (or smaller) than the grid-step

$$F(k) \;=\; \mathrm{sech}\big((k/k_F)^{10}\big), \tag{28}$$

with $k_F = k_N/8$, where k_N is the Nyquist wavelength, defined as $k_N = \frac{N}{2L}$. Thus, the initial condition is

$$\psi(x, t=0) \;=\; \mathcal{F}^{-1}\Big[\, F(k)\,\mathcal{F}\Big[\sqrt{\rho_0 + \delta\rho(x)}\Big]\Big]. \tag{29}$$

In the simulations, space is discretized with $N = 1024$ points, in a domain of length $L = 1$ and a constant power spectrum is used as initial condition. We show the simulation results in the semi-classical regime. The latter corresponds to large values of the parameter g, as one has $g \propto \hbar^{-2}$. Specifically, we take $g = 10^6$ (we do not observe differences in the performance in the quantum regime, i.e., for smaller values of g) and $\rho_0 = 1$.

In Fig. (3), the typical evolution of the system in the cosmological context is shown: the initial condition is spatially homogeneous with small fluctuations. The fluctuations grow due to gravitational interactions, up to be dominated by the finite size of the simulation box. The characteristic time of dynamics is defined as $t_{\rm dyn} = |g|^{-1/2}$. In Fig. 4, the Split-Step integrators are compared with the IFC. We observe for $t \gtrsim 5t_{\rm dyn}$ that the time-step decreases; this is due to the fact that the dynamics switches from a regime where the largest scales are still linear, to a regime where all the scales are nonlinear [15]. It indicates that the integrating factor is particularly efficient in the weakly nonlinear regime, which is the regime of interest in cosmological simulations. The Split-Step integrators (except SS2) are observed to perform in the same manner in the weakly non-linear and strongly non-linear regime. We observe that IFC outperforms the tested Split-Step integrators in the first regime, whereas, in the second one it becomes equally efficient compared to the split-step methods. This is consistent with the observation of Sect. 3.3: since the dynamics corresponds to a highly nonlinear regime, the Split-Step method performs better than the IFC one in this case. Looking to Table (3), it is clear that (for the whole simulation of this system) the IFC is the most efficient integration method.

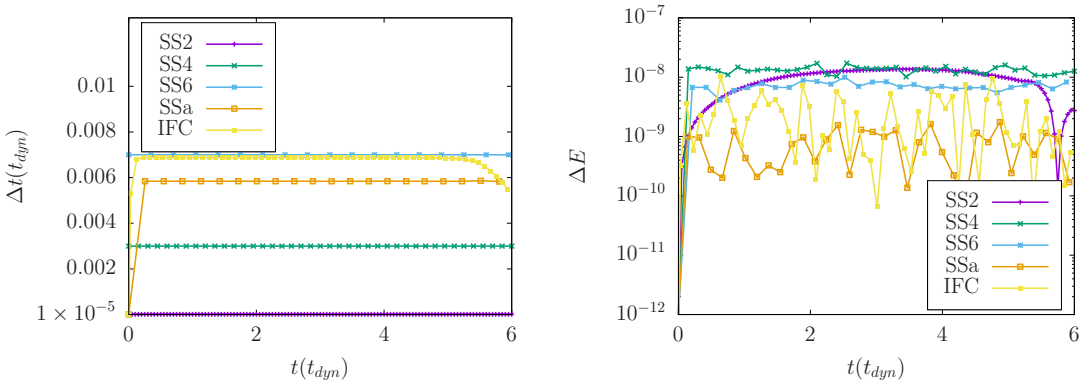

Figure 4: Comparison for the 1D SN equation (periodical case) between the time-step (left plot) and the error on the energy conservation (right plot) for the IFC method and the Split-Step solvers.

Method	$\Delta t/t_{\text{dyn}}$	$\overline{\Delta E}$	$\Delta\psi_{\text{rev}}$	$\Delta\psi_{\text{ref}}$	$T(s)$
SS2	10^{-5}	$1.6 \cdot 10^{-8}$	$8.3 \cdot 10^{-9}$	$8.5 \cdot 10^{-10}$	276.5
SS4	$3 \cdot 10^{-3}$	$1.9 \cdot 10^{-8}$	$1.3 \cdot 10^{-9}$	$1.5 \cdot 10^{-11}$	1.8
SS6	$7 \cdot 10^{-3}$	$1.1 \cdot 10^{-8}$	$1.1 \cdot 10^{-8}$	$3.1 \cdot 10^{-11}$	2.3
SSa, tol = 10^{-9}	$5.8 \cdot 10^{-3}$	$2.3 \cdot 10^{-9}$	$3.3 \cdot 10^{-9}$	$1.2 \cdot 10^{-11}$	4.3
IFC, tol = 10^{-12}	$6.7 \cdot 10^{-3}$	$1.1 \cdot 10^{-8}$	$1.8 \cdot 10^{-10}$	$6.7 \cdot 10^{-11}$	1.3

Table 3: Comparison for the 1D SN equation (periodical case) between the IFC method and the Split-Step solvers. T is the total time required to run each simulation, measured in seconds. The Δt for adaptive algorithms is the averaged one.

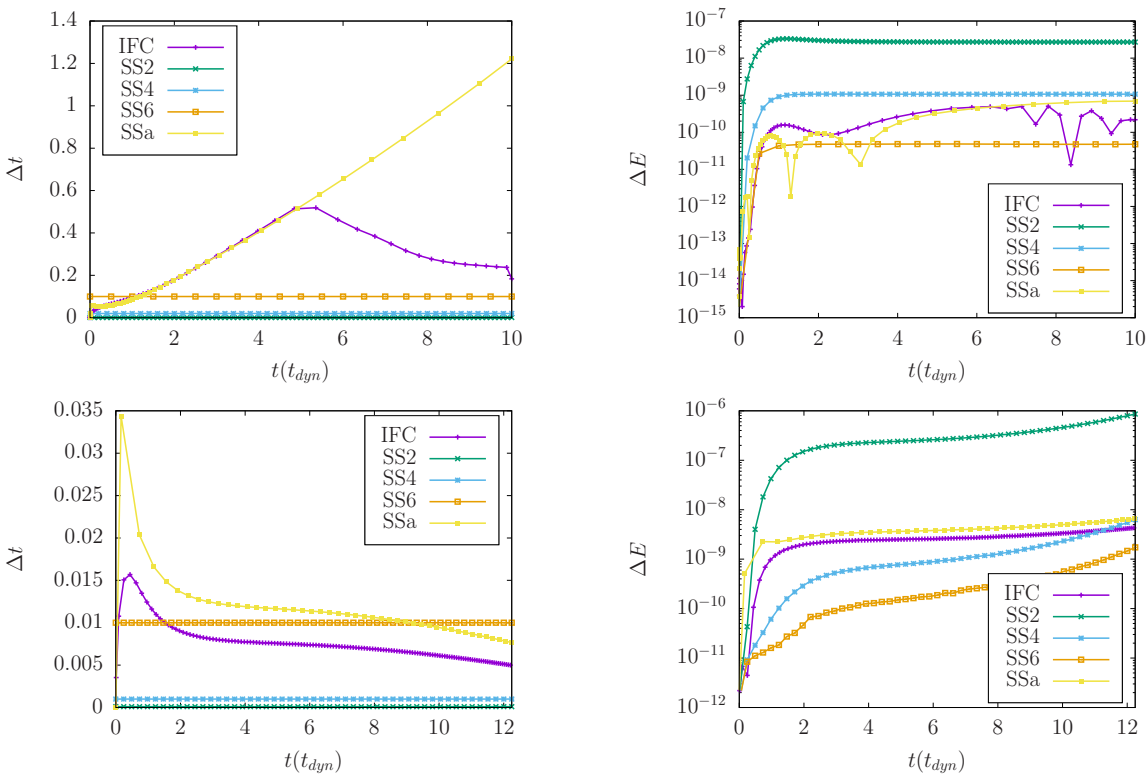

Figure 5: Comparison for the 2D NLS equation between the time-step (left panel) and the error on the energy conservation (right panel) for the IFC method and the Split-Step solvers. The top row corresponds to the $g = -1$ case while the bottom row to $g = -6$. The last time-step is chosen in such a way that the final time is the same in all simulations, in order to ensure that $\Delta\psi_{\rm rev}$ and $\Delta\psi_{\rm ref}$ are evaluated properly, which explain the step which appears for the last time point in Δt.

3.4. 2D nonlinear Schrödinger equation

In the 2D NLS case, one has

$$\mathrm{i}\,\partial_t\,\psi \;+\; \tfrac{1}{2}\,\nabla^2\,\psi \;-\; g\,|\psi|^2\,\psi \;=\; 0. \tag{30}$$

The dynamics of (30) presents a finite time singularity: it can be proven [41] that there exists a finite time when the norm of the solution or of one of its derivatives becomes infinity. This happens whenever the initial condition ψ_0 satisfies $E_g = \frac{1}{2}\int \mathrm{d}\boldsymbol{r}\,\psi_0\left(g\,|\psi_0|^2 - \nabla^2\right)\psi_0^* < 0$. The initial condition is taken as $\psi(\boldsymbol{r}, t = 0) = \mathrm{e}^{-r^2/2}/\sqrt{\pi}$ and we study the cases $g = -1$ and $g = -6$ with respective initial energies $E_{g=-1} \approx 0.42$ and $E_{g=-6} \approx 0.02$. Thus, the latter is associated with an initial energy closer to the singular regime than the former. The simulation is run in a box of side $L = 80$, discretized into $N = 1024 \times 1024$ points in the $g = -1$ case, while for $g = -6$ we set $L = 120$ and $N = 4096 \times 4096$. The characteristic time of dynamics is defined as $t_{\rm dyn} = |g|^{-1/2}$.

Split-Step integrators are compared with the IFC, looking at the energy conservation error, the error on the solution and the total time needed to run each simulation. The results are illustrated in Fig. (5) and table (4). The gain factor between splitting algorithms and the IFC method depends on the value of g. However, in both cases, the optimized integrating factor proved to be more efficient.

g	Method	$\Delta t/t_{\rm dyn}$	$\overline{\Delta E}$	$\Delta\psi_{\rm rev}$	$\Delta\psi_{\rm ref}$	$T(s)$
-1	SS2	10^{-3}	$3.3\cdot10^{-8}$	$4.5\cdot10^{-8}$	$5.0\cdot10^{-10}$	6939
	SS4	$2\cdot10^{-2}$	$1.1\cdot10^{-9}$	$3.5\cdot10^{-13}$	$7.0\cdot10^{-11}$	830
	SS6	10^{-1}	$4.5\cdot10^{-11}$	$2.5\cdot10^{-14}$	$6.2\cdot10^{-11}$	445
	SSa	$2.3\cdot10^{-1}$	$7.0\cdot10^{-10}$	$3.0\cdot10^{-10}$	$2.5\cdot10^{-11}$	267
	IFC	$1.7\cdot10^{-1}$	$4.5\cdot10^{-10}$	$3.0\cdot10^{-10}$	$1.6\cdot10^{-11}$	169
-6	SS2	$2.5\cdot10^{-4}$	$8.8\cdot10^{-7}$	$1.4\cdot10^{-11}$	$7.9\cdot10^{-7}$	405012
	SS4	$2.5\cdot10^{-3}$	$6.3\cdot10^{-9}$	$2.5\cdot10^{-12}$	$3.7\cdot10^{-9}$	82891
	SS6	$2.5\cdot10^{-2}$	$1.7\cdot10^{-9}$	$1.6\cdot10^{-12}$	$1.8\cdot10^{-9}$	24453
	SSa	$2.8\cdot10^{-2}$	$6.5\cdot10^{-9}$	$1.4\cdot10^{-10}$	$5.4\cdot10^{-9}$	29117
	IFC	$1.8\cdot10^{-2}$	$2.3\cdot10^{-9}$	$3.5\cdot10^{-9}$	$9.4\cdot10^{-9}$	22843

Table 4: Comparisons for the 2D NLS equation between different methods for the Dormand and Prince integrator. The Δt for adaptive algorithms is the averaged one. T is the total time required to run each simulation, measured in seconds. The tolerances of the integrator SS4(3) is tol = 10^{-6} and tol = 10^{-10} for the IFC.

3.5. 2D Schrödinger-Newton equation

In the 2D SN case, one has

$$\mathrm{i}\,\partial_t\,\psi \;+\; \tfrac{1}{2}\,\nabla^2\psi \;-\; V\,\psi \;=\; 0, \qquad \nabla^2 V \;=\; g\,|\psi|^2\,. \tag{31}$$

Similarly to the one dimensional case, we use a Gaussian initial conditions $\psi(\boldsymbol{r}, t = 0) = \mathrm{e}^{-r^2/2}/\sqrt{\pi}$ and two values of the coupling constant, $g = 10$ and $g = 500$. The former corresponds to a system in the quantum regime and the latter is closer to the semi-classical one. The potential V, as in the 1D case, is calculated using the Hockney method [37]. The simulation is run in a box of side $L = 40$, discretized into $N = 1024^2$ points in the $g = 10$ case, while for $g = 500$ we set $L = 20$ and $N = 1024 \times 1024$, the characteristic time of dynamics is defined as $t_{\rm dyn} = |g|^{-1/2}$.

In table (5) and Fig. (6), we compare the Split-Step and the IFC integrators, looking at the energy conservation error, the error on the solution and the total time needed to run each simulation.

For the 2D Schrödinger–Newton equation, adaptive splitting algorithms proved to be as efficient as the IFC. Similarly to the one-dimensional case, also here the SS6 split-step algorithm with constant time-step resulted to be the fastest among the ones we tested. This is due to the same reasons mentioned in section 3.3. Note that, here, the performance gap between the integrating factor and splitting algorithms is smaller than in the one-dimensional case. Indeed, as the dynamics gets more complicated and the number of spatial dimensions increase, algorithms with adaptive time-step shall always be preferred.

3.5.1. Periodical case

For the 2D periodical case, we run simulations in a box of side $L = 1$ with $N = 1024 \times 1024$, using again a constant power spectrum as initial condition with $g = 10^6$, $\rho_0 = 1$ and a zero

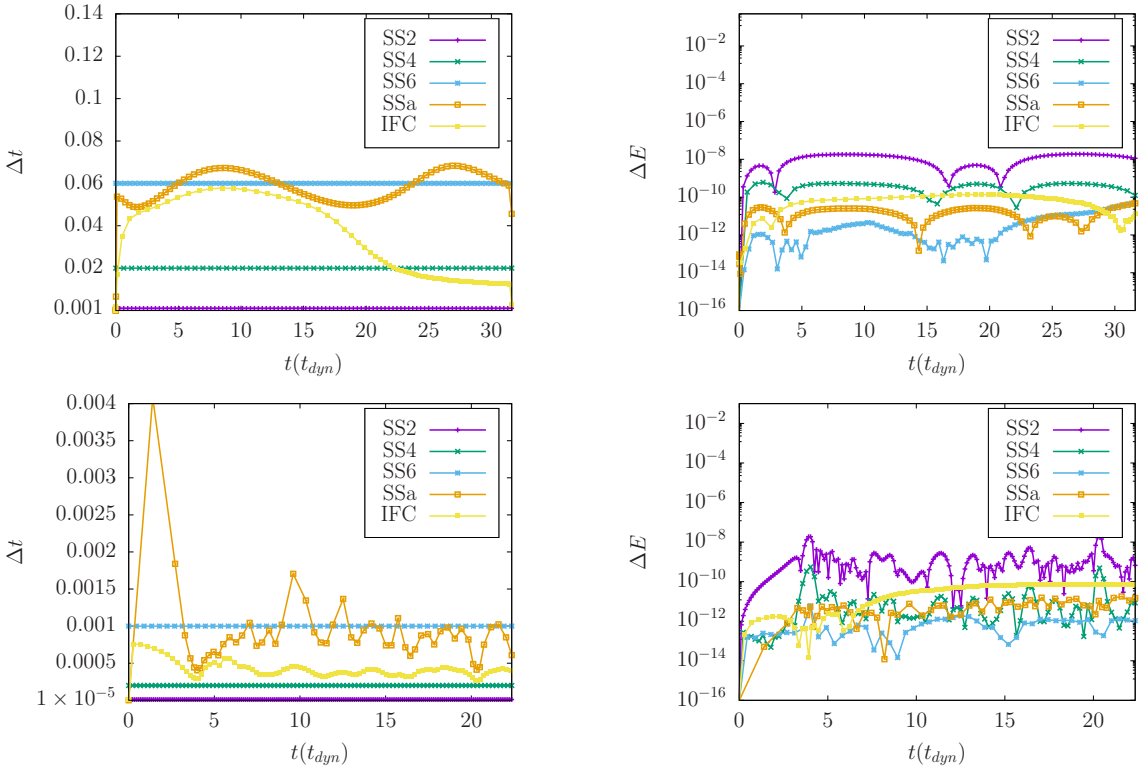

Figure 6: Comparison for the 2D SN equation between the time-step and the error on the energy conservation with the IFC method and the Split-Step solvers for both the cases $g = 10$ (upper plots) and $g = 500$ (lower plots).

g	Method	$\Delta t/t_{\text{dyn}}$	$\overline{\Delta E}$	$\Delta\psi_{\text{rev}}$	$\Delta\psi_{\text{ref}}$	$T(s)$
10	SS2	$3.2 \cdot 10^{-3}$	$1.8 \cdot 10^{-8}$	$3.5 \cdot 10^{-12}$	$1.0 \cdot 10^{-7}$	9070
	SS4	$6.3 \cdot 10^{-2}$	$6.0 \cdot 10^{-10}$	$1.4 \cdot 10^{-11}$	$3.8 \cdot 10^{-8}$	959
	SS6	$1.9 \cdot 10^{-1}$	$4.6 \cdot 10^{-11}$	$1.6 \cdot 10^{-7}$	$4.1 \cdot 10^{-8}$	932
	SSa	$1.7 \cdot 10^{-1}$	$4.7 \cdot 10^{-11}$	$1.4 \cdot 10^{-7}$	$3.9 \cdot 10^{-8}$	1174
	IFC	$8.4 \cdot 10^{-2}$	$1.3 \cdot 10^{-10}$	$5.8 \cdot 10^{-8}$	$2.9 \cdot 10^{-8}$	1172
500	SS2	$2.2 \cdot 10^{-4}$	$2.0 \cdot 10^{-8}$	$3.1 \cdot 10^{-10}$	$9.1 \cdot 10^{-8}$	84030
	SS4	$4.5 \cdot 10^{-3}$	$5.6 \cdot 10^{-10}$	$2.8 \cdot 10^{-11}$	$7.0 \cdot 10^{-9}$	8401
	SS6	$2.2 \cdot 10^{-2}$	$6.1 \cdot 10^{-12}$	$9.1 \cdot 10^{-11}$	$4.1 \cdot 10^{-9}$	5143
	SSa	$2.1 \cdot 10^{-2}$	$1.9 \cdot 10^{-11}$	$2.0 \cdot 10^{-11}$	$3.9 \cdot 10^{-9}$	6676
	IFC	$9.1 \cdot 10^{-3}$	$7.5 \cdot 10^{-11}$	$3.0 \cdot 10^{-10}$	$1.6 \cdot 10^{-9}$	6637

Table 5: Comparison for the 2D SN equation between the IFC method and the Split-Step solvers. The Δt for adaptive algorithms is the averaged one. The tolerance for the SSa algorithm is tol = 10^{-6} and tol = 10^{-7} for $g = 10$ and $g = 500$ respectively, and for the IFC algorithm tol = 10^{-10} and tol = 10^{-12} for $g = 10$ and $g = 500$ respectively.

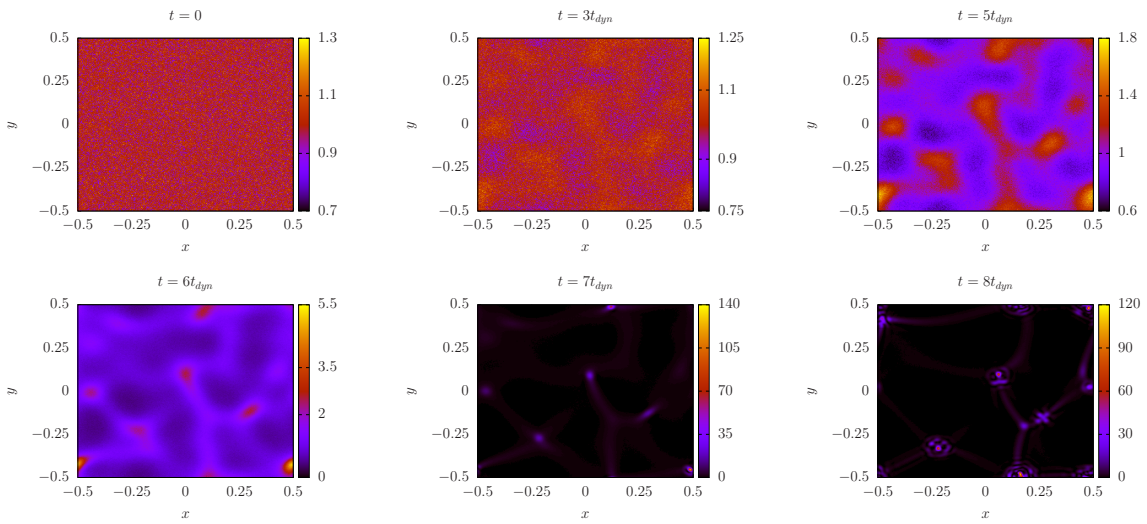

Figure 7: Snapshots of the modulus squared of the solution of the 2D SN equation (periodical case) $|\psi|^2$.

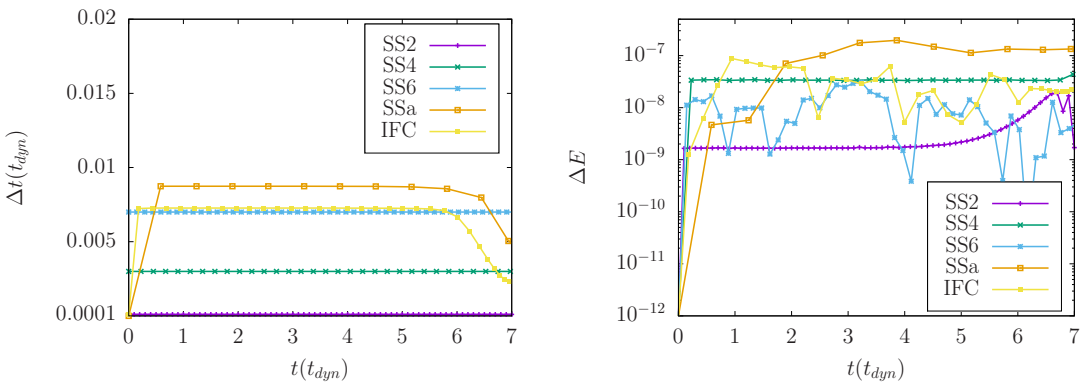

Figure 8: Comparison for the 2D SN equation (periodical case) between the time-step (left plot) and the error on the energy conservation (right plot) for the IFC method and the Split-Step solvers.

initial velocity field. In Fig. (7) some snapshots of the modulus squared of the solution are shown, expressing time in units of $t_{\rm dyn} = 1/\sqrt{g}$.

In table (6) and Fig. (8), we compare the Split-Step and IFC integrators, looking at the energy conservation error, the error on the solution and the total time needed to run each simulation. We obtain the same result than in one dimension, with the IFC being the most efficient method.

3.6. Gross–Pitaevskii–Poisson equation

We conclude by presenting the results for the 2D Gross–Pitaevskii–Poisson equation, which is a combination of the NLS and SN equations

$$\mathrm{i}\,\partial_t\,\psi \;+\; \tfrac{1}{2}\,\nabla^2\,\psi \;-V\,\psi \;=\; 0, \qquad V = V_1 + V_2, \qquad \nabla^2 V_1 \;=\; g_1\,|\,\psi\,|^2\,, \qquad V_2 \;=\; g_2\,|\,\psi\,|^2\,.$$

Based on the results presented so far, in the case of open boundary conditions, one expects the split-step or the integrating factors to outperform one the other, depending on the values of g_1 and g_2. We set them to $g_1 = -3$ and $g_2 = 100$ which are very close to the one typically

Method	$\Delta t/t_{\rm dyn}$	$\overline{\Delta E}$	$\Delta\psi_{rev}$	$\Delta\psi_{ref}$	$T(s)$
SS2	10^{-4}	$1.8\cdot10^{-8}$	$4.5\cdot10^{-9}$	$1.0\cdot10^{-5}$	31711
SS4	$3\cdot10^{-3}$	$4.2\cdot10^{-8}$	$3.1\cdot10^{-6}$	$5.3\cdot10^{-6}$	2485
SS6	$7\cdot10^{-3}$	$3.5\cdot10^{-8}$	$4.5\cdot10^{-10}$	$5.1\cdot10^{-6}$	3046
SSa, tol = 10^{-7}	$7.5\cdot10^{-3}$	$2.3\cdot10^{-7}$	$8.5\cdot10^{-7}$	$1.2\cdot10^{-6}$	3362
IFC, tol = 10^{-12}	$5\cdot10^{-3}$	$9.5\cdot10^{-8}$	$4.6\cdot10^{-6}$	$8.9\cdot10^{-7}$	2232

Table 6: Comparison for the 2D SN equation (periodical case) between the IFC method and the Split-Step solvers. T is the total time required to run each simulation, measured in seconds. The Δt for adaptive algorithms is the averaged one.

Method	Δt	$\overline{\Delta E}$	$\Delta\psi_{\rm rev}$	$\Delta\psi_{\rm ref}$	$T(s)$
SS6	$2.5\cdot10^{-3}$	$1.2\cdot10^{-9}$	$4.5\cdot10^{-11}$	$4.5\cdot10^{-8}$	32753
SSa, tol = 10^{-7}	$4\cdot10^{-3}$	$2.4\cdot10^{-11}$	$2.2\cdot10^{-8}$	$1.4\cdot10^{-8}$	63315
IFC, tol = 10^{-11}	$2\cdot10^{-3}$	$7.7\cdot10^{-10}$	$6.2\cdot10^{-8}$	$2.3\cdot10^{-8}$	28273

Table 7: Comparison for the 2D Gross–Pitaevskii–Poisson equation between the IFC and the Split-Step methods. T is the total time required to run each simulation, measured in seconds.

employed when simulating the collapse of a self-gravitating Bose-Einstein condensate with attractive self-interaction [21]. The numerical parameters are $N = 2048\times2048$, $L = 40$ and $t_f = 5$ while the initial condition is a Gaussian, $\psi(\boldsymbol{r}, t = 0) = \mathrm{e}^{-r^2/2}/\sqrt{\pi}$. In table 7 comparisons between the most efficient methods tested for the NLS (IFC method) and the SN in the non-periodical case (SS6 or SSa, depending on the parameters) are shown. For the values of g_1 and g_2 we use, the IFC method outperforms the split-step solvers. Moreover, we observe that for our particular initial condition, the smaller the g_1/g_2 ratio is, the better the IFC performs with respect to splitting methods, with a robust difference already appearing for $g_1/g_2 \lessapprox 0.1$. This confirms that the presence of a short-range interaction term puts the integrating factor method in a clear more performing position, compared to splitting methods.

4. Conclusion

We studied the numerical resolution of the nonlinear Schrödinger (NLS) and the Newton–Schrödinger (SN) equations using the optimized integrating factor (IFC) technique. This method was compared with splitting algorithms. Specifically, for the integrating factor, we tested fifth-order time-adaptive algorithms, while, for the Split-Step family, we focused on second-, fourth- and sixth-order schemes with fixed time-step, and a fourth-order algorithm with adaptive time-step. We performed extensive tests with systems in one and two spatial dimensions, with open or periodic boundary conditions.

The comparisons between the results obtained in the tested cases, show that the IFC method can be more efficient than splitting algorithms, especially in the NLS equation and periodical SN equation cases. For the SN equation in the non-periodical case on the other

hand, splitting algorithms proved to be more efficient, even though the optimized integrating factor provided competitive results in terms of both speed and accuracy. Moreover, the results obtained for the Gross–Pitaevskii–Poisson equation pointed out how the presence of a short-range interaction term puts the integrating factor method in a clear more performing position.

Finally, the achieved results indicate how, among the splitting algorithms at fixed step, working with higher order solvers is always more efficient. In particular the Split-Step order 6 proved to be around 10 times faster compared with the lower order ones, while conserving the energy with the same error.

References

[1] F. Dalfovo, S. Giorgini, L. P. Pitaevskii, S. Stringari, Theory of Bose–Einstein condensation in trapped gases, Reviews of Modern Physics 71 (3) (1999) 463.

[2] A. Hasegawa, Optical solitons in fibers, in: Optical Solitons in Fibers, Springer, 1989, pp. 1–74.

[3] C. Kharif, E. Pelinovsky, A. Slunyaev, Rogue waves in the ocean, Springer Science & Business Media, 2008.

[4] J. Binney, S. Tremaine, Galactic Dynamics: Second Edition, 2008.

[5] F. Dabby, J. Whinnery, Thermal self-focusing of laser beams in lead glasses, Applied Physics Letters 13 (8) (1968) 284–286.

[6] C. Rotschild, O. Cohen, O. Manela, M. Segev, T. Carmon, Solitons in nonlinear media with an infinite range of nonlocality: first observation of coherent elliptic solitons and of vortex-ring solitons, Physical review letters 95 (21) (2005) 213904.

[7] C. Rotschild, B. Alfassi, O. Cohen, M. Segev, Long-range interactions between optical solitons, Nature Physics 2 (11) (2006) 769–774.

[8] F. S. Guzman, L. A. Urena-Lopez, Gravitational cooling of self-gravitating Bose condensates, The Astrophysical Journal 645 (2) (2006) 814.

[9] W. Hu, R. Barkana, A. Gruzinov, Fuzzy cold dark matter: the wave properties of ultralight particles, Physical Review Letters 85 (6) (2000) 1158.

[10] A. Paredes, H. Michinel, Interference of dark matter solitons and galactic offsets, Physics of the Dark Universe 12 (2016) 50–55.

[11] D. J. Marsh, J. C. Niemeyer, Strong constraints on fuzzy dark matter from ultrafaint dwarf galaxy Eridanus ii, Physical review letters 123 (5) (2019) 051103.

[12] L. Diosi, Gravitation and quantumm-echanical localization of macroobjects, arXiv preprint arXiv:1412.0201 (2014).

[13] R. Penrose, On gravity's role in quantum state reduction, General relativity and gravitation 28 (5) (1996) 581–600.

[14] L. M. Widrow, N. Kaiser, Using the Schrödinger equation to simulate collisionless matter, The Astrophysical Journal 416 (1993) L71.

[15] P. J. E. Peebles, The large-scale structure of the universe, 1980.

[16] N. Banik, A. J. Christopherson, P. Sikivie, E. M. Todarello, Linear Newtonian perturbation theory from the Schrödinger–Poisson equations, Phys.Rev. D 91 (12) (2015) 123540. doi:10.1103/PhysRevD.91.123540.

[17] C. Conti, M. Peccianti, G. Assanto, Route to nonlocality and observation of accessible solitons, Physical review letters 91 (7) (2003) 073901.

[18] Y. Izdebskaya, W. Krolikowski, N. F. Smyth, G. Assanto, Vortex stabilization by means of spatial solitons in nonlocal media, Journal of Optics 18 (5) (2016) 054006.

[19] D. O'dell, S. Giovanazzi, G. Kurizki, V. Akulin, Bose–Einstein condensates with $1/r$ interatomic attraction: Electromagnetically induced "gravity", Physical Review Letters 84 (25) (2000) 5687.

[20] A. Suárez, P.-H. Chavanis, Cosmological evolution of a complex scalar field with repulsive or attractive self-interaction, Physical Review D 95 (6) (2017) 063515.

[21] P.-H. Chavanis, Collapse of a self-gravitating Bose–Einstein condensate with attractive self-interaction, Physical Review D 94 (8) (2016) 083007.

[22] A. Bernal, F. S. Guzman, Scalar field dark matter: Head-on interaction between two structures, Physical Review D 74 (10) (2006) 103002.

[23] P. Bader, S. Blanes, F. Casas, M. Thalhammer, Efficient time integration methods for Gross–Pitaevskii equations with rotation term, arXiv preprint arXiv:1910.12097 (2019).

[24] C. Besse, G. Dujardin, I. Lacroix-Violet, High order exponential integrators for nonlinear Schrödinger equations with application to rotating Bose–Einstein condensates, SIAM J. Numer. Anal. 55 (3) (2017) 1387–1411.

[25] J. R. Dormand, P. J. Prince, A family of embedded Runge–Kutta formulae, J. Comp. Appl. Math. 6 (1) (1980) 19–26.

[26] C. Tsitouras, Runge–Kutta pairs of order 5(4) satisfying only the first column simplifying assumption, Computers & Mathematics with Applications 62 (2) (2011) 770–775.

[27] R. Alexander, Solving ordinary differential equations i: Nonstiff problems (e. hairer, sp norsett, and g. wanner), Siam Review 32 (3) (1990) 485.

[28] C. Canuto, M. Y. Hussaini, A. Quarteroni, T. A. Zang, Spectral Methods. Fundamentals in Single Domains, 2nd Edition, Scientific Computation, Springer, 2008.

[29] J. C. Butcher, Numerical methods for ordinary differential equations, John Wiley & Sons, 2016.

[30] M. Lovisetto, D. Clamond, B. Marcos, Optimized integrating factor technique for schrödinger-like equations, Applied Numerical Mathematics 178 (2022) 329–336.

[31] S. Blanes, F. Casas, A. Murua, Splitting and composition methods in the numerical integration of differential equations, arXiv preprint arXiv:0812.0377 (2008).

[32] M. Suzuki, General theory of fractal path integrals with applications to many-body theories and statistical physics, Journal of Mathematical Physics 32 (2) (1991) 400–407.

[33] H. Holden, K. H. Karlsen, K.-A. Lie, Splitting methods for partial differential equations with rough solutions: Analysis and MATLAB programs, Vol. 11, European Mathematical Society, 2010.

[34] M. Thalhammer, J. Abhau, A numerical study of adaptive space and time discretisations for Gross–Pitaevskii equations, Journal of computational physics 231 (20) (2012) 6665–6681.

[35] S. Blanes, P. C. Moan, Practical symplectic partitioned Runge–Kutta and Runge–Kutta–Nyström methods, Journal of Computational and Applied Mathematics 142 (2) (2002) 313–330.

[36] M. Thalhammer, High-order exponential operator splitting methods for time-dependent Schrödinger equations, SIAM Journal on Numerical Analysis 46 (4) (2008) 2022–2038.

[37] R. W. Hockney, J. W. Eastwood, Computer simulation using particles, crc Press, 2021.

[38] S. Weinberg, Cosmology, OUP Oxford, 2008.

[39] G. Davies, L. M. Widrow, Test-bed simulations of collisionless, self-gravitating systems using the Schröd
The Astrophysical Journal 485 (2) (1997) 484–495. doi:10.1086/304440.
URL https://doi.org/10.1086/304440

[40] P. Mocz, L. Lancaster, A. Fialkov, F. Becerra, P.-H. Chavanis, Schrödinger–Poisson Vlasov–Poisson correspondence, Phys. Rev. D 97 (2018) 083519. doi:10.1103/PhysRevD.97.083519.
URL https://link.aps.org/doi/10.1103/PhysRevD.97.083519

[41] C. Sulem, P.-L. Sulem, The nonlinear Schrödinger equation: self-focusing and wave collapse, Vol. 139, Springer Science & Business Media, 2007.

Appendices

Appendix A. Optimized Integrating Factor

The optimized version of the integrating factor is based on the property that, for the Schrödinger equation, if the value of the potential V is modified by an additive constant $\mathcal{C}$, only the phase of the solution ψ is changed. Indeed, if ψ is a solution of (1) at a given time t, then $\Psi \stackrel{\text{def}}{=} \psi\, \mathrm{e}^{-\mathrm{i}\,\mathcal{C}\,t}$ is a solution of

$$\mathrm{i}\,\partial_t\,\Psi \;+\; \tfrac{1}{2}\,\nabla^2\Psi \;-\; (V+\mathcal{C})\;\Psi \;=\; 0, \tag{A.1}$$

as it can be easily verified. Thus, adding a constant $\mathcal{C}_n$ to V, the solution is modified as

$$\psi(t_n) \;\rightarrow\; \psi(t_n)\,\mathrm{e}^{-\mathrm{i}\varphi}, \qquad \varphi \stackrel{\text{def}}{=} \sum_{n=0}^{N_h} \mathcal{C}_n\, h_n, \tag{A.2}$$

where $h_n \stackrel{\text{def}}{=} t_{n+1} - t_n$ is the n-th time-step and N_h is the total number of time-steps.

The freedom provided by the gauge condition of the potential is exploited to compute an optimal value of $\mathcal{C}_n$, which allows to choose a larger time-step compared to the $\mathcal{C}_n = 0$ case and therefore speeding up the numerical integration. The resulting optimal value, $\tilde{\mathcal{C}}_n$, which is obtained at each time step n as the value of $\mathcal{C}_n$ minimising the L_2-norm of $\mathcal{N}$ [30], is

$$\tilde{\mathcal{C}}_n \stackrel{\text{def}}{=} -\left(\sum_{\ell=-[M/2]}^{[M/2]-1} V_\ell\, |\psi_\ell|^2\right) \Bigg/ \left(\sum_{\ell=-[M/2]}^{[M/2]-1} |\psi_\ell|^2\right) \tag{A.3}$$

where $\psi_\ell \stackrel{\text{def}}{=} \psi(\boldsymbol{r}_\ell)$ and $V_\ell \stackrel{\text{def}}{=} V(\boldsymbol{r}_\ell)$ at time t_n.

Appendix B. Split-Step pseudo-codes

We list below, in ALG. (1), the pseudo-codes for the Split-Step algorithms with fixed time-step. We consider the general case of order N, with $N \in \{2, 4, 6\}$.

Algorithm 1 : SSN, $N \in \{2, 4, 6\}$

$t \leftarrow t_0$
$\psi \leftarrow \psi(\boldsymbol{r}, t_0)$
while $t < t_f$ **do**
  $\psi \leftarrow \mathrm{FFT}^{-1}[\exp\left(-\mathrm{i}\hat{K} a_1 h\right) \mathrm{FFT}[\psi]]$
  $\psi \leftarrow \exp\left(-\mathrm{i} V b_1 h\right) \psi$
  $\vdots$
  $\psi \leftarrow \mathrm{FFT}^{-1}[\exp\left(-\mathrm{i}\hat{K} a_{\frac{N}{2}} h\right) \mathrm{FFT}[\psi]]$
  $\psi \leftarrow \exp\left(-\mathrm{i} V b_{\frac{N}{2}} h\right) \psi$
  $\psi \leftarrow \mathrm{FFT}^{-1}[\exp\left(-\mathrm{i}\hat{K} a_{\frac{N}{2}-1} h\right) \mathrm{FFT}[\psi]]$
  $\psi \leftarrow \exp\left(-\mathrm{i} V b_{\frac{N}{2}-1} h\right) \psi$
  $\vdots$
  $\psi \leftarrow \mathrm{FFT}^{-1}[\exp\left(-\mathrm{i}\hat{K} a_1 h\right) \mathrm{FFT}[\psi]]$
  $\psi \leftarrow \exp\left(-\mathrm{i} V b_1 h\right) \psi$
  $t \leftarrow t + h$

In the latter, h is the time step, FFT and FFT^{-1} denote the Fast Fourier Transform and its inverse respectively, $\hat{K}$ is the kinetic energy operator in Fourier space, V is the potential, and the values of a_i and b_i, $i \in \{1, 2, 3, 4, 5, 6\}$, are listed in table B.8.

SS2	SS4	SS6
$a_1 = \frac{1}{2}$	$a_1 = \frac{\omega}{2}$	$a_1 = 0.0502627644003922$
$b_1 = 1$	$b_1 = 1$	$b_1 = 0.148816447901042$
	$a_2 = \frac{1-\omega}{2}$	$a_2 = 0.413514300428344$
	$b_2 = 1 - 2\omega$	$b_2 = -0.132385865767784$
		$a_3 = 0.0450798897943977$
		$b_3 = 0.067307604692185$
		$a_4 = -0.188054853819569$
		$b_4 = 0.432666402578175$
		$a_5 = 0.541960678450780$
		$b_5 = 0.5 - (b_1 + b_2 + b_3 + b_4)$
		$a_6 = 1 - 2(a_1 + a_2 + a_3 + a_4 + a_5)$
		$b_6 = 1 - 2(a_1 + a_2 + a_3 + a_4 + a_5)$

Table B.8: Values of the parameters for the Split-Step algorithms. The quantity ω is given by $\omega = \frac{2+2^{\frac{1}{3}}+2^{-\frac{1}{3}}}{3}$.

In the case of SSa, the adaptive splitting algorithm, i.e. the SS4(3), both the solutions at the 4th and at the 3rd order must be evaluated. The pseudo-code is described in ALG. (2), while the coefficients are listed in B.9. In our numerical tests we set $\alpha = 0.9$, $\beta = 3$.

Algorithm 2 : SSa

$t \leftarrow t_0$
$\psi \leftarrow \psi(\boldsymbol{r}, t_0)$
while $t < t_f$ **do**
  $\psi \leftarrow \widetilde{\psi}$
  $\psi \leftarrow \mathrm{FFT}^{-1}[\mathrm{e}^{-\mathrm{i}\hat{K}a_1 h}\mathrm{FFT}[\psi]]$
  $\psi \leftarrow \mathrm{e}^{-\mathrm{i}Vb_1 h}\psi$
  $\vdots$
  $\psi \leftarrow \mathrm{FFT}^{-1}[\mathrm{e}^{-\mathrm{i}\hat{K}a_7 h}\mathrm{FFT}[\psi]]$
  $\psi \leftarrow \mathrm{e}^{-\mathrm{i}Vb_7 h}\psi$
  $\widetilde{\psi} \leftarrow \mathrm{FFT}^{-1}[\mathrm{e}^{-\mathrm{i}\hat{K}\overline{a}_1 h}\mathrm{FFT}[\widetilde{\psi}]]$
  $\widetilde{\psi} \leftarrow \mathrm{e}^{-\mathrm{i}V\overline{b}_1 h}\widetilde{\psi}$
  $\vdots$
  $\widetilde{\psi} \leftarrow \mathrm{FFT}^{-1}[\mathrm{e}^{-\mathrm{i}\hat{K}\overline{a}_7 h}\mathrm{FFT}[\widetilde{\psi}]]$
  $\widetilde{\psi} \leftarrow \mathrm{e}^{-\mathrm{i}V\overline{b}_7 h}\widetilde{\psi}$
  $err \leftarrow \sqrt{\frac{\sum_{i=1}^{N}\left|\psi(\boldsymbol{x}_i,t_n)-\widetilde{\psi}(\boldsymbol{x}_i,t_n)\right|^2}{\sum_{j=1}^{N}\left|\psi(\boldsymbol{x}_j,t_n)\right|^2}}$
  if $err \leq \mathrm{tol}$ **then**
    $t \leftarrow t + h$
  else

19: $\psi \leftarrow \widetilde{\psi}$

20: $h \leftarrow h \min\left\{\alpha\left(\frac{\text{tol}}{\Delta_n}\right)^{\frac{1}{4}}, \beta\right\}$

SSa			
Order 4		Order 3	
a_1	0	$\tilde{a}_1$	0
b_1	0.0829844064174052	$\tilde{b}_1$	0.0829844064174052
a_2	0.245298957184271	$\tilde{a}_2$	0.245298957184271
b_2	0.3963098014983680	$\tilde{b}_2$	0.3963098014983680
a_3	0.604872665711080	$\tilde{a}_3$	0.604872665711080
b_3	-0.0390563049223486	$\tilde{b}_3$	-0.0390563049223486
a_4	0.5 - $(a_2 + a_3)$	$\tilde{a}_4$	0.5 - $(a_2 + a_3)$
b_4	1. - $2(b_1 + b_2 + b_3)$	$\tilde{b}_4$	1. - $2(b_1 + b_2 + b_3)$
a_5	0.5 - $(a_2 + a_3)$	$\tilde{a}_5$	0.3752162693236828
b_5	-0.0390563049223486	$\tilde{b}_5$	0.4463374354420499
a_6	0.604872665711080	$\tilde{a}_6$	1.4878666594737946
b_6	0.3963098014983680	$\tilde{b}_6$	-0.0060995324486253
a_7	0.245298957184271	$\tilde{a}_7$	-1.3630829287974774
b_7	0.0829844064174052	$\tilde{b}_7$	0

Table B.9: Values of the parameters for the SSa.

Applied Numerical Mathematics 178 (2022) 329–336

Contents lists available at ScienceDirect

Applied Numerical Mathematics

www.elsevier.com/locate/apnum

Optimized integrating factor technique for Schrödinger-like equations

M. Lovisetto *, D. Clamond, B. Marcos

Université Côte d'Azur, CNRS UMR 7351, Laboratoire J. A. Dieudonné, Parc Valrose, 06108 Nice cedex 2, France

ARTICLE INFO

Article history:
Received 18 January 2022
Received in revised form 31 March 2022
Accepted 12 April 2022
Available online 15 April 2022

Keywords:
Gauge optimization
Time-stepping
Integrating factor
Schrödinger-like equations
Lawson methods

ABSTRACT

The integrating factor technique is widely used to solve numerically (in particular) the Schrödinger equation in the context of spectral methods. Here, we present an improvement of this method exploiting the freedom provided by the gauge condition of the potential. Optimal gauge conditions are derived considering the equation and the temporal numerical resolution with an adaptive embedded scheme of arbitrary order. We illustrate this approach with the nonlinear Schrödinger (NLS) and with the Schrödinger–Newton (SN) equations. We show that this optimization increases significantly the overall computational speed, sometimes by a factor five or more. This gain is crucial for long time simulations, as, with larger time steps, less computations are performed and the overall accumulation of round-off errors is reduced.

1. Introduction

The Schrödinger equation is used in many fields of Physics. In dimensionless units, it takes the form

$$\mathrm{i}\,\partial_t\,\psi \;+\; \tfrac{1}{2}\,\nabla^2\psi \;-\; V\,\psi \;=\; 0, \tag{1}$$

where ψ is a function of the spatial coordinates $\boldsymbol{r}$ and of the time t, ∇^2 is the Laplace operator, and the potential V is generally a function of space and time and, possibly, a functional of ψ. In this paper, we focus more specifically on the nonlinear Schrödinger equation (V proportional to $|\psi|^2$) and on the Schrödinger–Newton (or Schrödinger–Poisson) equation in which the Laplacian of the potential is proportional to $|\psi|^2$. These special cases were chosen for clarity and because they are of practical interest, but the method presented here can be extended to more general potentials (and equations).

With the nonlinear Schrödinger equation (NLS) considered here, the (local nonlinear) potential is

$$V \;=\; g\,|\psi|^2, \tag{2}$$

where g is a coupling constant. For $g > 0$ the interaction is repulsive, while, for $g < 0$ it is attractive. The NLS describes various physical phenomena, such as Bose–Einstein condensates [10], laser beams in some nonlinear media [15], water wave packets [18], etc.

With the Schrödinger–Poisson equation, the potential is given by the Poisson equation

$$\nabla^2\,V \;=\; g\,|\psi|^2, \tag{3}$$

* Corresponding author.
E-mail address: Martino.LOVISETTO@univ-cotedazur.fr (M. Lovisetto).

https://doi.org/10.1016/j.apnum.2022.04.011
0168-9274/

where g is another coupling constant, the interaction being attractive if $g > 0$ and repulsive if $g < 0$. It is therefore *nonlinear* and *non-local*, giving rise to collective phenomena [5], appearing for instance in optics [9,24,25], Bose–Einstein condensates [14], cosmology [17,21,22] and theories describing the quantum collapse of the wave function [11,23]. It is also used as a model to perform cosmological simulations in the semi-classical limit [29].

The above equations cannot be solved analytically (except for very special cases) and numerical methods must be employed. In this paper, we focus on spectral methods for the spatial resolution, i.e., methods that are based on fast Fourier transform (FFT) techniques, that are specially efficient and accurate [8]. For the temporal resolution, two families of methods are commonly employed to solve Schrödinger-like equations: integrating factors [20] and split-step integrators [6]. The latter methods have been used to integrate both the SN and NLS equations, but the former is used essentially to solve the NLS, with very performing results [2–4]. In this note, we focus on the former technique, which consists in integrating analytically the linear part of the equation and integrating numerically the remaining nonlinear part with a classical method [20]. The principle of the method is described as follows.

Writing the Schrödinger equation in the generic form

$$\mathrm{i}\,\partial_t\,\psi \;=\; F(\boldsymbol{r},t,\psi)\,, \qquad \psi \;=\; \psi(\boldsymbol{r},t)\,, \tag{4}$$

the right-hand side is split into linear and nonlinear parts

$$\mathrm{i}\,\partial_t\,\psi \;+\; \mathcal{L}\,\psi \;=\; \mathcal{N}(\boldsymbol{r},t,\psi)\,, \tag{5}$$

where $\mathcal{L}$ is an easily computable autonomous linear operator and $\mathcal{N} \stackrel{\text{def}}{=} F + \mathcal{L}\psi$ is the remaining (usually) nonlinear part. At the n-th time-step, with $t \in [t_n, t_{n+1}]$, considering the change of dependent variable

$$\phi \;\stackrel{\text{def}}{=}\; \exp[\,(t-t_n)\,\mathcal{L}\,]\,\psi \qquad \Longrightarrow \qquad \mathrm{i}\,\partial_t\,\psi \;=\; \exp[\,(t_n-t)\,\mathcal{L}\,]\,(\,\mathrm{i}\,\partial_t\,\phi \;-\; \mathcal{L}\phi\,)\,, \tag{6}$$

so $\phi = \psi$ at $t = t_n$, the equation (5) is rewritten

$$\mathrm{i}\,\partial_t\,\phi \;=\; \exp[\,(t-t_n)\,\mathcal{L}\,]\,\mathcal{N}. \tag{7}$$

The operator $\mathcal{L}$ being well chosen, the stiffness of (5) is considerably reduced and the equation (7) is (hopefully) well approximated by algebraic polynomials for $t \in [t_n; t_{n+1}]$. Thus, standard time-stepping methods, such as an adaptive Runge–Kutta method [1,7], can be used to efficiently solve (7). To do so, the solution is evaluated at two different orders and a local error is estimated as the difference between those quantities. Popular integrators can be found in [1,12].

Notice that, for finite domains, the integrating factor must be implemented such that boundary conditions and the domain geometry are properly taken into account. However, here, we focus on periodic domains, therefore there are no conditioning issues with the method, as explained in [16].

It is straightforward to apply this strategy to the Schrödinger equation (1) since $\frac{1}{2}\nabla^2\psi$ and the potential V are, respectively, linear and nonlinear operators of ψ. By switching to Fourier space in position, the equation becomes

$$\mathrm{i}\,\partial_t\,\widehat{\psi} \;-\; \tfrac{1}{2}\,k^2\,\widehat{\psi} \;-\; \widehat{V\,\psi} \;=\; 0, \tag{8}$$

where "hats" denote the Fourier transform of the underneath quantity and $k \stackrel{\text{def}}{=} |\boldsymbol{k}|$ ($\boldsymbol{k}$ the wave vector). The equation is now in a form where the application of the integrating factor (IF) method is straightforward, i.e., (8) becomes

$$\mathrm{i}\,\partial_t\,\phi \;=\; -\mathrm{i}\,\exp[\tfrac{\mathrm{i}}{2}k^2(t-t_n)]\,\widehat{V\,\psi}, \tag{9}$$

where $\phi(\boldsymbol{k},t) \stackrel{\text{def}}{=} \widehat{\psi}(\boldsymbol{k},t)\exp[\frac{\mathrm{i}}{2}k^2(t-t_n)]$. If the nonlinear part of the equation is zero, then $\mathrm{i}\,\partial_t\,\phi = 0$ and any (reasonable) temporal scheme will produce the exact solution $\phi(t) = \phi(t_n)$. In other words, the integrating factor technique is exact for linear equations. This indicates that the numerical errors depend on the magnitude of the nonlinear part. Therefore, in order to minimise these errors, a strategy consists in minimizing the magnitude of $\mathcal{N}$ at each time-step. To do so, we exploit the gauge invariance of the Schrödinger equation: if ψ is a solution of (1) at a given time t, then $\Psi = \psi(\mathbf{r},t)\mathrm{e}^{-\mathrm{i}\int_{t_0}^{t}\mathrm{d}s\,\mathcal{C}(s)}$, with $\mathcal{C}(t_0) = 0$, is a solution of

$$\mathrm{i}\,\partial_t\,\Psi \;+\; \tfrac{1}{2}\,\nabla^2\Psi \;-\; (V + \mathcal{C}(t))\;\Psi \;=\; 0, \tag{10}$$

as one can easily verify. Thus, at each time-step, adding a constant $\mathcal{C}_n$ to V in (1), modifies the solution as

$$\psi(t_n) \;\to\; \psi(t_n)\,\mathrm{e}^{-\mathrm{i}\varphi}, \qquad \varphi \;\stackrel{\text{def}}{=}\; \sum_{j=0}^{n}\mathcal{C}_j\,h_j, \tag{11}$$

where $h_j \stackrel{\text{def}}{=} t_{j+1} - t_j$ is the j-th time-step. Of course, at the end of the computations, the operation (11) can be easily reverted if the original phase is relevant. Using this procedure, we observed up to a five-fold speed increase (the overall

computational time is divided by about five) compared to taking $\mathcal{C}_n = 0$. Of course, the speed-up varies depending on the initial condition, of the (spatial and temporal) numerical schemes and on the choice of gauge corresponding to $\mathcal{C}_n = 0$.

In this paper, we derive some analytic formulas giving an optimal $\mathcal{C}_n$ in order to maximise the time-step, i.e., to minimize the overall computational time of the numerical resolution. We emphasize that the thus obtained optimal values of $\mathcal{C}_n$ do not affect the accuracy of the numerical solution, leaving it unchanged with respect to the $\mathcal{C}_n = 0$ case. Two strategies are presented. In section 2, a first 'natural' approach to derive a suitable $\mathcal{C}_n$ is based on the analytical structure of the equation and it is independent of the numerical algorithm employed for its resolution. More precisely, $\mathcal{C}_n$ is obtained minimizing a norm of the right-hand side of the equation (5). This provides an easy manner to obtain a formula that is moreover computationally 'cheap'. This expression is however only near optimal, so a 'better' expression is subsequently derived. Considering both the equations and the numerical algorithms, a second optimal expression for $\mathcal{C}_n$ is derived in section 3. This approach consists in minimizing exactly the numerical error and thus explicitly dependents on the numerical scheme. This provides a more accurate, but computationally expensive, solution. The advances of these special choices are illustrated numerically in section 4. Finally, a summary and perspectives are drawn in section 5.

2. Near optimal $\mathcal{C}_n$

As mentioned above, if properly chosen, the integrating factor is able to reduce the stiffness of the equation, making the numerical integration more efficient. In addition, the magnitude of the nonlinear part of (7) also contributes to the efficiency of the numerical integration. Specifically, if $\mathcal{N}$ is zero, $\partial_t \phi = 0$ and the integrating factor technique is exact. Thus, the efficiency of the algorithm is expected to increase as the magnitude of $\mathcal{N}$ gets smaller, and subsequently the overall computational time should be reduced. Here, we show how to choose the arbitrary constant $\mathcal{C}_n$ in order to reduce the magnitude of the nonlinear part $\mathcal{N}$. In the case of the Schrödinger equation, we have

$$\mathcal{N}(\boldsymbol{k}, t; \phi; \mathcal{C}_n) \;=\; -\mathrm{i}\, \exp[\tfrac{\mathrm{i}}{2} k^2 (t - t_n)]\, \mathcal{F}\{(V + \mathcal{C}_n)\ \psi\}, \tag{12}$$

where $\mathcal{F}$ denotes the Fourier transform, and $\psi(\boldsymbol{x}, t) = \mathcal{F}^{-1}\{\exp[-\frac{\mathrm{i}}{2} k^2 (t - t_n)]\, \phi(\boldsymbol{k}, t)\}$.

A natural strategy is to minimise the L_2-norm, namely

$$\mathcal{G}_n(\mathcal{C}_n) \stackrel{\text{def}}{=} \frac{1}{M} \sum_{m=-[M/2]}^{[M/2]-1} |\mathcal{N}(\boldsymbol{k}_m, t_n; \phi; \mathcal{C}_n)|^2, \tag{13}$$

where M is the number of spatial modes, square brackets denote the integer part and $\boldsymbol{k}_m$ is the m-th Fourier mode. Indeed, in the latter expression, we considered discrete Fourier transforms, given that we are in the context of numerical simulations. The explicit expression of $\mathcal{G}_n$ can be found exploiting the definition of the discrete Fourier transform. For simplicity, we do the calculations in one dimension (1D) without loss of generality, since the final result is independent of the spatial dimension d. From Parseval theorem, one obtains

$$\mathcal{G}_n(\mathcal{C}_n) \;=\; \sum_{\ell=-[M/2]}^{[M/2]-1} (V_\ell + \mathcal{C}_n)^2\, |\psi_\ell|^2, \tag{14}$$

where $\psi_\ell \stackrel{\text{def}}{=} \psi(\boldsymbol{x}_\ell)$ and $V_\ell \stackrel{\text{def}}{=} V(\boldsymbol{x}_\ell)$ at time t_n. Since the function $\mathcal{G}_n(\mathcal{C}_n)$ is a second-order polynomial in $\mathcal{C}_n$, it admits an unique minimum, which is obtained from the equation $\mathrm{d}G_n(\mathcal{C}_n)/\mathrm{d}\mathcal{C}_n = 0$, yielding

$$\mathcal{C}_n \;=\; -\left(\sum_{\ell=-[M/2]}^{[M/2]-1} V_\ell\ |\psi_\ell|^2 \right) \Bigg/ \left(\sum_{\ell=-[M/2]}^{[M/2]-1} |\psi_\ell|^2 \right) \stackrel{\text{def}}{=} \tilde{\mathcal{C}}_n. \tag{15}$$

Therefore, at each time step n, $\tilde{\mathcal{C}}_n$, which is the value of $\mathcal{C}_n$ minimizing the L_2-norm of $\mathcal{N}$, is obtained from (15). We show below that even though this approach is not unique (i.e., different norms could be considered), the provided solution is quite advantageous compared to others, being computationally cheap and independent on the order of the numerical scheme.

3. Optimal $\mathcal{C}_n$

We show here another way to choose the arbitrary constant $\mathcal{C}_n$ in order to improve the algorithm efficiency and reduce the overall computational time. This approach is based on the principles of the adaptive time-step procedure, where at each time step n, an error Δ_n between two approximated solutions of different orders is estimated. Since the smaller this quantity the larger the time-step, minimizing Δ_n allows to choose a larger time-step, speeding-up the numerical integration and keeping roughly the same numerical error. More specifically, the error Δ_n depends on the arbitrary constant $\mathcal{C}_n$, hence the minimization can be performed (see below) choosing an appropriate $\mathcal{C}_n$. In this section, we first recall the method for determining the size of the time step used in the Runge–Kutta procedures; interested readers should refer to [1] for

further details. Although the determination of $\mathcal{C}_n$ can be formally presented for any embedded Runge–Kutta schemes, this results in very cumbersome calculations with little insights. Thus, for brevity and clarity, we illustrate the method with the Heun method (that is a second-order Runge–Kutta method with an embedded first-order explicit Euler scheme for the time stepping [27]). We then sketch-out how this procedure can be implemented for generic embedded Runge–Kutta methods.

3.1. Principle of the adaptive time-step procedure

For the time stepping, embedded Runge–Kutta methods estimate the quadrature error comparing the results of two orders of the time integrator [1]. For a solver of order N with an embedded $(N-1)$-order scheme (hereafter schemes of orders $\{N, N-1\}$), at the n-th time step, the error Δ_n is [28]

$$\Delta_n \stackrel{\text{def}}{=} \sqrt{\frac{1}{M}\sum_{m=-[M/2]}^{[M/2]-1}\left(\frac{\left|\phi(\boldsymbol{k}_m,t_n)-\widetilde{\phi}(\boldsymbol{k}_m,t_n)\right|}{\text{Tol}+\max\Big(|\phi(\boldsymbol{k}_m,t_n)|\,,\left|\tilde{\phi}(\boldsymbol{k}_m,t_n)\right|\Big)\times\text{Tol}}\right)^2}\,, \tag{16}$$

where M is the number of spatial modes, square brackets denote the integer part, $\phi(\boldsymbol{k}_m,t_n)$ is the N-th order solution at the m-th Fourier mode, the "tilde" notation indicating the solution at order $N-1$, and Tol is the tolerance (parameter defining the desired precision of the time-integration). The time step h_n is accepted if the error Δ_n is smaller than the tolerance Tol, otherwise h_n is reduced and this step is recomputed. h_n being accepted, the next time step h_{n+1} is obtained assuming the largest error equal to the tolerance. In order to avoid an excess of rejected time steps, we use the Proportional Integral (PI) Step Control [28], which chooses the optimal time step h_{n+1} as

$$h_{n+1} \;=\; h_n\,\Delta_n^{-b}\,\Delta_{n-1}^{c}, \tag{17}$$

where $b=0.7/p$, $c=0.4/p$, p being the order of the chosen integrator [13]. Interested readers should refer to [1] for details on this classical procedure.

3.2. Optimum time step

Since the constant $\mathcal{C}_n$ can be chosen freely, we seek for the value of $\mathcal{C}_n$ providing the largest h_{n+1}, namely, to maximise the right-hand side of (17). Since h_n and Δ_{n-1} are determined at the previous time-step, only Δ_n in (17) depends on $\mathcal{C}_n$. Thus, in order to maximize h_{n+1}, Δ_n must be minimized, i.e., one must solve $\mathrm{d}\Delta_n/\mathrm{d}\mathcal{C}_n=0$. This derivation being characterized by cumbersome algebra for general embedded Runge–Kutta schemes, we illustrate the case of the Heun algorithm (that is a second-order Runge–Kutta method with an embedded first-order explicit Euler scheme for the time stepping [27]), the principle being the same for higher order integrators. Also for simplicity, we give the calculations in one dimension (1D) without loss of generality, since the final result is independent of the spatial dimension.

3.2.1. Optimum $\mathcal{C}_n$ for Heun's method

Heun's method consists, here, in solving the initial value problem (for $t \geqslant t_n$)

$$\mathrm{i}\,\partial_t\,\phi \;=\; f(\boldsymbol{k},t;\phi;\mathcal{C}_n) \stackrel{\text{def}}{=} -\mathrm{i}\,\exp\Big[\,\tfrac{\mathrm{i}}{2}\,k^2\,(t-t_n)\,\Big]\,\mathcal{F}\{\,(V+\mathcal{C}_n)\,\psi\,\}, \tag{18}$$

and

$$\phi(\boldsymbol{k},t) \stackrel{\text{def}}{=} \exp\Big[\,\tfrac{\mathrm{i}}{2}\,k^2\,(t-t_n)\,\Big]\,\mathcal{F}\{\psi(\boldsymbol{x},t)\}. \tag{19}$$

Hereafter, for brevity, we denote

$$\phi_n \;=\; \phi_n(\boldsymbol{k}) \stackrel{\text{def}}{=} \phi(\boldsymbol{k},t_n), \qquad \psi_n \;=\; \psi_n(\boldsymbol{x}) \stackrel{\text{def}}{=} \psi(\boldsymbol{x},t_n), \qquad V_n \;=\; V_n(\boldsymbol{x}) \stackrel{\text{def}}{=} V(\boldsymbol{x},t_n). \tag{20}$$

At time $t=t_{n+1}$, the first- and second-order (in h_n) approximations of ϕ, respectively $\widetilde{\phi}_{n+1}$ and ϕ_{n+1}, are

$$\widetilde{\phi}_{n+1} \;=\; \phi_n \;+\; h_n\,f(\boldsymbol{k},t_n;\phi_n;\mathcal{C}_n), \tag{21}$$

$$\phi_{n+1} \;=\; \phi_n \;+\; \tfrac{1}{2}\,h_n\,[\,f(\boldsymbol{k},t_n;\phi_n;\mathcal{C}_n) \;+\; f(\boldsymbol{k},t_n+h_n;\phi_n+h_n f(\boldsymbol{k},t_n;\phi_n;\mathcal{C}_n);\mathcal{C}_n)\,]\,. \tag{22}$$

The next time-step h_{n+1} is chosen using equation (17). For our equation, the difference between the first- and second-order approximations $\Delta\phi_{n+1} \stackrel{\text{def}}{=} \left|\phi_{n+1}-\widetilde{\phi}_{n+1}\right|$ is such that

$$\begin{aligned}(\Delta\phi_{n+1})^2 \;&=\; \tfrac{1}{4}\,h_n^2\,|\,f(\boldsymbol{k},t_n;\phi_n;\mathcal{C}_n) \;-\; f(\boldsymbol{k},t_n+h_n;\phi_n+h_n f(\boldsymbol{k},t_n;\phi_n;\mathcal{C}_n);\mathcal{C}_n)\,|^2\\ &=\; \tfrac{1}{4}\,h_n^2\,\Big|\,f(\boldsymbol{k},t_n;\phi_n;\mathcal{C}_n) \;+\; \mathrm{i}\,\mathrm{e}^{\mathrm{i}k^2h_n/2}\times\\ &\qquad\qquad \mathcal{F}\Big\{(V_{n+1}+\mathcal{C}_n)\mathcal{F}^{-1}\Big\{\mathrm{e}^{-\mathrm{i}k^2h_n/2}\,(\phi_n+h_n f(\boldsymbol{k},t_n;\phi_n;\mathcal{C}_n))\Big\}\Big\}\Big|^2\,,\end{aligned} \tag{23}$$

where $V_{n+1} = V(\boldsymbol{x}, t_n + h_n)$. We note that the absolute value in (23) is of first-order in h_n, as one can easily check with a Taylor expansion around $h_n = 0$, so $(\Delta\phi_{n+1})^2 = O\left(h_n^4\right)$. More precisely, after some elementary algebra, one finds

$$(\Delta\phi_{n+1})^2 = \tfrac{1}{4} h_n^4 \left| \mathcal{F}\left\{(V_n + \mathcal{C}_n)^2 \psi_n\right\} + \mathrm{i}\,\mathcal{F}\{\partial_t V_n \psi_n\} + \mathcal{F}\{\partial_x V_n \partial_x \psi_n\} + \tfrac{1}{2}\mathcal{F}\{\partial_{xx} V_n \psi_n\} \right|^2 + O\left(h_n^5\right), \tag{24}$$

which, defining

$$\alpha(\boldsymbol{x}, t; \mathcal{C}_n) \stackrel{\text{def}}{=} (V_n + \mathcal{C}_n)^2 \psi_n, \qquad \beta(\boldsymbol{x}, t) \stackrel{\text{def}}{=} \mathrm{i}\,\partial_t V_n \psi_n + \partial_x V_n \partial_x \psi_n + \tfrac{1}{2}\partial_{xx} V_n \psi_n, \tag{25}$$

can be rewritten as

$$(\Delta\phi_{n+1})^2 = \tfrac{1}{4} h_n^4 \left|\mathcal{F}\{\alpha(\mathcal{C}_n) + \beta\}\right|^2 + O\left(h_n^5\right). \tag{26}$$

Introducing the mean quadratic error

$$E_n(\mathcal{C}_n) \stackrel{\text{def}}{=} \frac{1}{M} \sum_{m=-[M/2]}^{[M/2]-1} \Delta\phi_{n+1}^2(\boldsymbol{k}_m, t_n; \mathcal{C}_n), \tag{27}$$

substituting (26) into (27) and exploiting the definition of the discrete Fourier transform, one obtains (using Parseval theorem)

$$\begin{aligned} E_n(\mathcal{C}_n) &= \frac{1}{M} \sum_{m=-[M/2]}^{[M/2]-1} \left| \sum_{\ell=-[M/2]}^{[M/2]-1} \mathrm{e}^{-2\mathrm{i}\pi m\ell/M} (\alpha_\ell(\mathcal{C}_n) + \beta_\ell) \right|^2 \tfrac{1}{4} h_n^4 + O\left(h_n^5\right) \\ &= \sum_{\ell=-[M/2]}^{[M/2]-1} |\alpha_\ell(\mathcal{C}_n) + \beta_\ell|^2 \tfrac{1}{4} h_n^4 + O\left(h_n^5\right). \end{aligned} \tag{28}$$

The minimum of $E_n(\mathcal{C}_n)$, obtained from the equation $\mathrm{d}E_n(\mathcal{C}_n)/\mathrm{d}\mathcal{C}_n = 0$, is such that

$$\sum_{\ell=-[M/2]}^{[M/2]-1} \frac{\mathrm{d}\,|\alpha_\ell(\mathcal{C}_n)|^2}{\mathrm{d}\mathcal{C}_n} + 2\,\mathrm{Re}\left(\frac{\mathrm{d}\alpha_\ell(\mathcal{C}_n)}{\mathrm{d}\mathcal{C}_n}\beta_\ell^*\right) = 0. \tag{29}$$

Therefore, the optimum $\hat{\mathcal{C}}_n$ providing the largest h_{n+1}, in the case of Heun's method, is a solution of (29).

3.2.2. Optimum $\mathcal{C}_n$ for generic embedded Runge–Kutta schemes

The optimum $\mathcal{C}_n$ for general embedded Runge–Kutta schemes can be obtained following the same principles illustrated above with the Heun algorithm. However, the algebraic calculations get rapidly very cumbersome, leading to expensive computations that, in most cases, exceeds the time gained with a larger step. Here, we sketch-out the procedure for generic embedded Runge–Kutta methods, considering solvers of order N with an embedded $(N-1)$-order scheme (for other embedded or extrapolation methods, the procedure is completely analogue). For a s-stage method, the error $\Delta\phi_{n+1}$ can be written as [28]

$$(\Delta\phi_{n+1})^2 = \left|\sum_{\ell=1}^{s} d_\ell\, w_\ell\right|^2, \quad d_\ell \stackrel{\text{def}}{=} a_{s,\ell} - b_\ell, \quad w_\ell \stackrel{\text{def}}{=} h_n\, f\left(\boldsymbol{k}, t_n + c_\ell h_n; \phi_n + \sum_{r=1}^{\ell-1} a_{\ell,r}\, w_r; \mathcal{C}_n\right), \tag{30}$$

where $a_{\ell,r}$, b_ℓ and c_ℓ are the coefficients of the Butcher tableau which characterizes the integrator [28]. Using Taylor expansions and un-nesting the scheme, it is possible to prove that a result with a similar structure compared with (26) is obtained. In this case, the number of stages s appears as exponent in the function α, which takes the form $\alpha(\boldsymbol{x}, t; \mathcal{C}_n) = (V_n + \mathcal{C}_n)^{2s}\psi_n$. The function β, on the other hand, becomes explicitly dependent on $\mathcal{C}_n$, involving a number of terms growing exponentially with s. For this reason, even though the exact result can always be achieved, the computational time needed to minimize the error (16) is often larger than the time gained with a larger step, especially for higher order schemes ($s > 3$). In the next section, we show how, for practical applications, an exact solution is not necessary to improve the algorithm, and (15) represents a fast and accurate method.

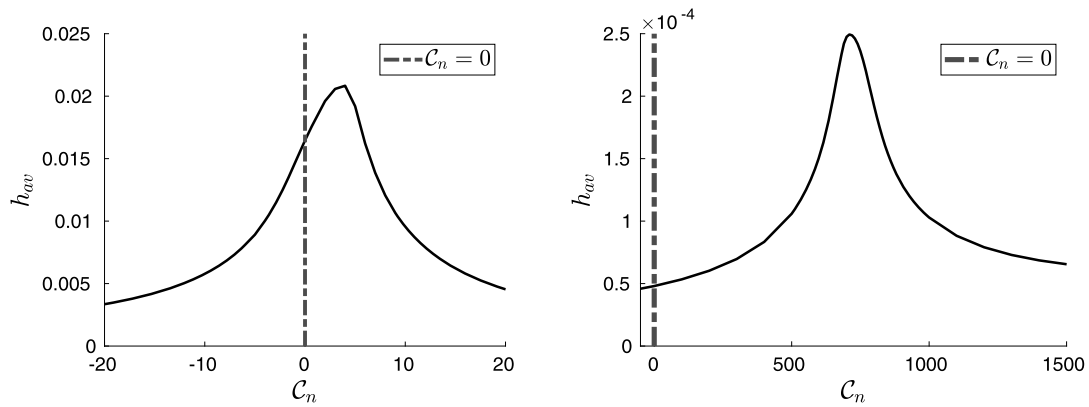

Fig. 1. Average time-step $h_{av} = \frac{1}{N_h}\sum_{n=1}^{N_h} h_n$ with a constant $\mathcal{C}_n$ for the IF method applied to the one dimensional NLS (left) and SN (right) equations.

Table 1
Comparisons for the SN and the NLS equations, in one and two spatial dimensions, between different values of $\mathcal{C}_n$.

Eq.	SN_{1D}	SN_{1D}	SN_{2D}	SN_{2D}	NLS_{1D}	NLS_{1D}	NLS_{2D}	NLS_{2D}
$\mathcal{C}$	0	$\tilde{\mathcal{C}}_n$	0	$\tilde{\mathcal{C}}_n$	0	$\tilde{\mathcal{C}}_n$	0	$\tilde{\mathcal{C}}_n$
$N_{\Delta t}$	20819	3871	8382	2682	6047	4781	754	690
$T\,(s)$	66.7	12.1	12856	4736	18.9	14.5	23769	22843

4. Numerical examples

Here, we consider numerical examples where we apply this method, focusing on both the SN and NLS equations solved with the Dormand and Prince 5(4) integrator [12] in one and two spatial dimensions. In all cases, we set open boundary conditions for the potential, while the initial conditions and the value of the physical parameters are chosen to be very close to regimes of physical interest, as described in [10,15,18]. Notice that, in the most general case, one should take into account the geometry of the domain and the nature of boundary conditions to calculate the potential V in the SN case. This operation is however straightforward in the considered examples, as we focused on rectangular domains using pseudo-spectral methods. Details on the numerical simulations can be found in Appendix A. The gain factor provided by the method depends on the optimal value of $\mathcal{C}_n$ compared to the $\mathcal{C}_n = 0$ case, which changes from case to case as a function of the boundary conditions for the potential and of the profile of the solution. Specifically, since the gain factor is evaluated with respect to the $\mathcal{C}_n = 0$ case, the more the optimal value of $\mathcal{C}_n$ is far from zero, the larger the gain factor gets.

For the one-dimensional NLS, some analytical stationary solutions are known. We then use one of these solutions (see Appendix A) as initial condition. For all other cases (SN and NLS 2D), no such stationary solutions are known, so we use gaussian initial conditions.

In Fig. 1, we show the average time-step $h_{av} = \sum_{n=1}^{N_h} h_n / N_h$, for an entire simulation with N_h time steps, as a function of $\mathcal{C}_n$ for the one-dimensional SN and NLS equations. These plots are generated taking $\mathcal{C}_n$ constant for the entire simulations, in order to better appreciate the strong dependence of the time-step on the choice of the gauge for the potential. In Fig. 2, we report the result of simulations performed choosing the near optimal $\mathcal{C}_n = \tilde{\mathcal{C}}_n$ at each time-step. Note that, for the one-dimensional NLS, the solution being stationary, h_n and the optimum $\mathcal{C}_n$ do not change in time, that is not the case in 2D. We show the time-step h_n as a function of time for the one-dimensional SN and NLS equations, comparing the $\mathcal{C}_n = 0$ case with $\mathcal{C}_n = \tilde{\mathcal{C}}_n$. In both cases, the time-step chosen by the algorithm with the optimisation of the gauge constant proves to be larger, compared to the $\mathcal{C}_n = 0$ case. In Table 1, we show the number of time-loops $N_{\Delta t}$ required to run each simulation and the time T needed to run the simulation (in seconds) for the cases $\mathcal{C}_n = 0$ and $\mathcal{C} = \tilde{\mathcal{C}}_n$. For NLS, in the one dimensional case we achieve roughly a 30% improvement in terms of speed gain between the $\mathcal{C} = 0$ and $\mathcal{C} = \tilde{\mathcal{C}}_n$ cases, while in two dimensions the speed gain is only approximately 10% since, here, the value of $\tilde{\mathcal{C}}_n$ is very close to zero. As long as the SN equation is concerned, (15) proved to reduce remarkably both the number of time loops and the effective time for the total simulation, providing up to a factor 5 of improvement with respect to the $\mathcal{C}_n = 0$ case in 1D and up to a factor 3 in 2D.

5. Conclusion

Exploiting a gauge condition on the potential, we optimized the integrating factor technique applied to the nonlinear Schrödinger and Schrödinger–Newton equations. Although the exact values of the piecewise constant $\mathcal{C}_n$ minimizing the error (16) (therefore maximizing the time-step) is in principle always possible to compute (e.g., with a computer algebra system), its expression depends on the particular numerical scheme chosen and it becomes complicated as the order of the method increases, resulting in a high computational cost. However, the near-optimal value obtained from the first approach

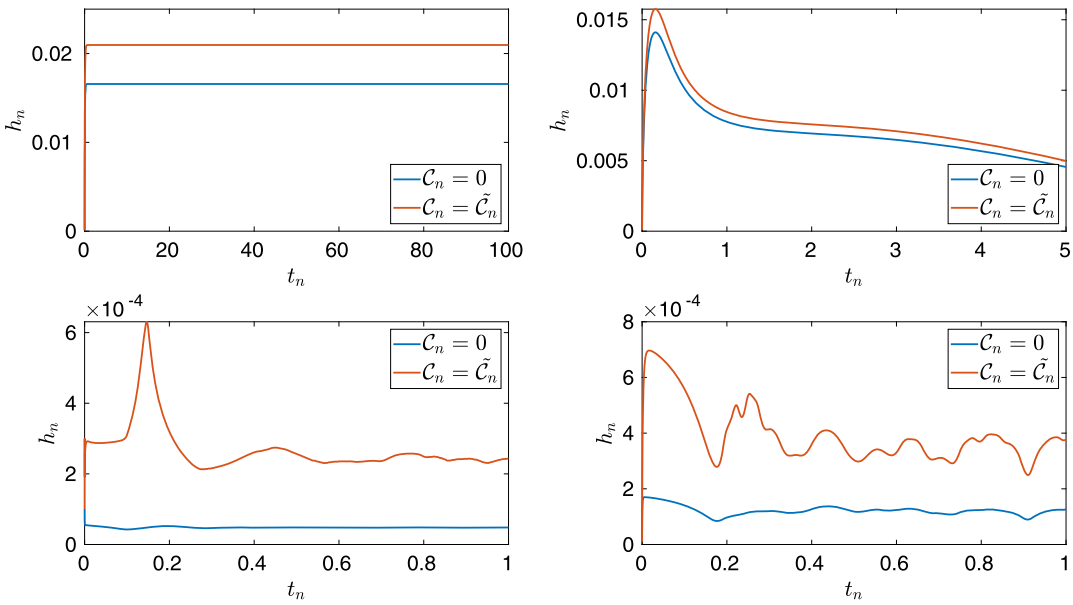

Fig. 2. Comparison between $\mathcal{C}_n = \tilde{\mathcal{C}}_n$ and $\mathcal{C}_n = 0$ for time-step h_n as a function of time, for the IF method applied to the NLS_{1D} (top left), NLS_{2D} (top right), SN_{1D} (bottom left) and SN_{2D} (bottom down).

we described, based on the minimization of the L_2-norm of the nonlinear part of the equation, proved to be an accurate and efficient solution in the tested cases. Thus, being computationally extremely cheap and independent of the particular numerical scheme employed, this is the approach one should choose for most simulations, at least when the computation of $\mathcal{N}$ is not very expensive. For Schrödinger-like equations with hard to compute potentials, most of the computational time is spent in the calculation of $\mathcal{N}$. For these very demanding equations, the extra cost needed to compute the optimum $\hat{\mathcal{C}}_n$ (instead of the near optimum $\tilde{\mathcal{C}}_n$) is negligible in comparison, so $\hat{\mathcal{C}}_n$ could be preferable.

For the cases tested here, we found a speed-up in the computation time up to a factor 5, the speed-up depending on the equation and on the physical regime. These examples show that this approach provides significant speed improvements, that with minor modifications of the original algorithm. Though we focused on the nonlinear Schrödinger and Schrödinger–Newton equations, the method principle is independent on the particular potential considered, so this approach can be extended to other Schrödinger-like equations. More generally, the idea behind the method presented in this note can be, at least in principle, generalized and extended to other equations with similar gauge conditions.

Appendix A. Numerical simulations

For the one-dimensional NLS, we considered the case $g = -1$ (see eqs. (1) and (3)) and we used $\psi(x, t = 0) = \sqrt{2}\,\mathrm{sech}\left(\sqrt{2}\,x\right)$ as initial condition. We discretized the space with $N = 2048$ points, in a computational box of length $L = 80$. The two-dimensional NLS, which is often employed in optics to model self-focusing beams in a medium with a cubic non-linearity [19,30], presents a finite time (blow-up) singularity [26]. More specifically, whenever the initial condition ψ_0 satisfies $E_g = \int \mathrm{d}\boldsymbol{r}\, \psi_0, \left(-\frac{1}{2}\nabla^2 + \frac{g}{2}\,|\psi_0|^2\right) \psi_0^* < 0$, the norm of the solution, or of one of its derivatives, becomes unbounded in finite time. For this reason, we stop the simulation at $t_{\mathrm{fin}} = 5$, i.e., before the singularity occurs. We set $\psi(\boldsymbol{r}, t = 0) = \mathrm{e}^{-r^2/2}/\sqrt{\pi}$ as initial condition and we consider the $g = -6$ case, for which the corresponding initial energy is $E(g = -6) \approx 0.02$, hence quite close to the singular regime; for the spatial discretization we used $L = 120$ and $N = 4096^2$ (squared box with side $L = 120$ discretized with 4096×4096 nodes). For both the one and two dimensional SN equations, we set $g = 500$ and considered a Gaussian initial condition, $\psi(\boldsymbol{x}, t = 0) = \mathcal{N}\mathrm{e}^{-|\boldsymbol{x}|^2/2}$ where $\mathcal{N}$ is the normalisation factor, fixed such that $\int \mathrm{d}\boldsymbol{x}\,|\psi(\boldsymbol{x}, t = 0)|^2 = 1$. The parameters of the spatial discretization are $L = 20$ and $N = 2048$ in 1D, while for the 2D case we set $L = 20$ and $N = 1024^2$. To solve the SN and the NLS equation we used the Dormand and Prince 5(4) integrator [12].

References

[1] R. Alexander, Solving ordinary differential equations i: nonstiff problems (e. hairer, sp norsett, and g. wanner), SIAM Rev. 32 (3) (1990) 485.
[2] W. Auzinger, I. Březinová, A. Grosz, H. Hofstätter, O. Koch, T. Sato, Efficient adaptive exponential time integrators for nonlinear Schrödinger equations with nonlocal potential, J. Comput. Math. Data Sci. 1 (2021) 100014.
[3] P. Bader, S. Blanes, F. Casas, M. Thalhammer, Efficient time integration methods for Gross–Pitaevskii equations with rotation term, arXiv preprint arXiv:1910.12097.
[4] C. Besse, G. Dujardin, I. Lacroix-Violet, High order exponential integrators for nonlinear Schrödinger equations with application to rotating Bose–Einstein condensates, SIAM J. Numer. Anal. 55 (3) (2017) 1387–1411.

[5] J. Binney, S. Tremaine, Galactic Dynamics, second edition, 2008.
[6] S. Blanes, F. Casas, A. Murua, Splitting and composition methods in the numerical integration of differential equations, arXiv preprint arXiv:0812.0377.
[7] J.C. Butcher, Numerical Methods for Ordinary Differential Equations, John Wiley & Sons, 2016.
[8] C. Canuto, M.Y. Hussaini, A. Quarteroni, T.A. Zang, Spectral Methods. Fundamentals in Single Domains, 2nd edition, Scientific Computation, Springer, 2008.
[9] F. Dabby, J. Whinnery, Thermal self-focusing of laser beams in lead glasses, Appl. Phys. Lett. 13 (8) (1968) 284–286.
[10] F. Dalfovo, S. Giorgini, L.P. Pitaevskii, S. Stringari, Theory of Bose–Einstein condensation in trapped gases, Rev. Mod. Phys. 71 (3) (1999) 463.
[11] L. Diosi, Gravitation and quantumm-echanical localization of macroobjects, arXiv preprint arXiv:1412.0201.
[12] J.R. Dormand, P.J. Prince, A family of embedded Runge–Kutta formulae, J. Comput. Appl. Math. 6 (1) (1980) 19–26.
[13] K. Gustafsson, Control theoretic techniques for stepsize selection in explicit Runge–Kutta methods, ACM Trans. Math. Softw. 17 (4) (1991) 533–554.
[14] F.S. Guzman, L.A. Urena-Lopez, Gravitational cooling of self-gravitating Bose condensates, Astrophys. J. 645 (2) (2006) 814.
[15] A. Hasegawa, Optical solitons in fibers, in: Optical Solitons in Fibers, Springer, 1989, pp. 1–74.
[16] M. Hochbruck, J. Leibold, A. Ostermann, On the convergence of Lawson methods for semilinear stiff problems, Numer. Math. 145 (3) (2020) 553–580.
[17] W. Hu, R. Barkana, A. Gruzinov, Fuzzy cold dark matter: the wave properties of ultralight particles, Phys. Rev. Lett. 85 (6) (2000) 1158.
[18] C. Kharif, E. Pelinovsky, A. Slunyaev, Rogue Waves in the Ocean, Springer Science & Business Media, 2008.
[19] K. Konno, H. Suzuki, Self-focussing of laser beam in nonlinear media, Phys. Scr. 20 (3–4) (1979) 382.
[20] J.D. Lawson, Generalized Runge–Kutta processes for stable systems with large Lipschitz constants, SIAM J. Numer. Anal. 4 (3) (1967) 372–380.
[21] D.J. Marsh, J.C. Niemeyer, Strong constraints on fuzzy dark matter from ultrafaint dwarf galaxy Eridanus ii, Phys. Rev. Lett. 123 (5) (2019) 051103.
[22] A. Paredes, H. Michinel, Interference of dark matter solitons and galactic offsets, Phys. Dark Universe 12 (2016) 50–55.
[23] R. Penrose, On gravity's role in quantum state reduction, Gen. Relativ. Gravit. 28 (5) (1996) 581–600.
[24] C. Rotschild, O. Cohen, O. Manela, M. Segev, T. Carmon, Solitons in nonlinear media with an infinite range of nonlocality: first observation of coherent elliptic solitons and of vortex-ring solitons, Phys. Rev. Lett. 95 (21) (2005) 213904.
[25] C. Rotschild, B. Alfassi, O. Cohen, M. Segev, Long-range interactions between optical solitons, Nat. Phys. 2 (11) (2006) 769–774.
[26] C. Sulem, P.-L. Sulem, The Nonlinear Schrödinger Equation: Self-Focusing and Wave Collapse, Vol. 139, Springer Science & Business Media, 2007.
[27] E. Süli, D.F. Mayers, An Introduction to Numerical Analysis, Cambridge University Press, 2003.
[28] G. Wanner, E. Hairer, Solving Ordinary Differential Equations II, Springer, Berlin Heidelberg, 1996.
[29] L.M. Widrow, N. Kaiser, Using the Schrödinger equation to simulate collisionless matter, Astrophys. J. 416 (1993) L71.
[30] V. Zakharov, V. Synakh, The nature of the self-focusing singularity, Zh. Èksp. Teor. Fiz. 68 (1975) 940–947.